# PROCEEDINGS

## NINETEENTH WORKSHOP
## GEOTHERMAL RESERVOIR ENGINEERING

**January 18-20, 1994**

Henry J. Ramey, Jr., Roland N. Horne,
Paul Kruger, Frank G. Miller,
William E. Brigham, Jean W. Cook
Stanford Geothermal Program
Workshop Report SGP-TR-147

Library of Congress Catalog Card No. 86-643338
ISSN 1058-2525

# TABLE OF CONTENTS

## SCIENCES I



## INJECTION II



## MODELING II



## ADSORPTION

## MODELING III/SCIENCES II



## SCIENCES II



## PRODUCTION II



## SCIENCES III

# PREFACE

The Nineteenth Workshop on Geothermal Reservoir Engineering was held at Stanford University on January 18-20, 1994. This workshop opened on a sad note because of the death of Prof. Henry J. Ramey, Jr. on November 19, 1993. Hank had been fighting leukemia for a long time and finally lost the battle. Many of the workshop participants were present for the celebration of his life on January 21 at Stanford's Memorial Church. Hank was one of the founders of the Stanford Geothermal Program and the Geothermal Reservoir Engineering Workshop. His energy, kindness, quick wit, and knowledge will long be missed at future workshops. Following the Preface we have included a copy of the Memorial Resolution passed by the Stanford University Senate.

There were one hundred and four registered participants. Participants were from ten foreign countries: Costa Rica, England, Iceland, Italy, Japan, Kenya, Mexico, New Zealand, Philippines and Turkey. Workshop papers described the performance of fourteen geothermal fields outside the United States.

Roland N. Horne opened the meeting and welcomed the visitors to the campus. The key note speaker was J.E. "Ted" Mock who gave a presentation about the future of geothermal development. The banquet speaker was Jesus Rivera and he spoke about Energy Sources of Central American Countries.

Forty two papers were presented at the Workshop. Technical papers were organized in twelve sessions concerning: sciences, injection, production, modeling, and adsorption. Session chairmen are an important part of the workshop and our thanks go to: John Counsil, Mark Walters, Dave Duchane, David Faulder, Gudmundur Bodvarsson, Jim Lovekin, Joel Renner, and Iraj Ershaghi.

The Workshop was organized by the Stanford Geothermal Program faculty, staff, and graduate students. We wish to thank Pat Ota, Ted Sumida, and Terri A. Ramey who also produces the Proceedings Volumes for publication. We owe a great deal of thanks to our students who operate audiovisual equipment and to Xianfa Deng who coordinated the meeting arrangements for the Workshop.

Roland N. Horne
Frank G. Miller
Paul Kruger
William E. Brigham
Jean W. Cook

*Memorial Resolution*

# Henry J. Ramey, Jr.

1925-1993

Henry Jackson Ramey, Jr., Keleen and Carlton Beal Professor of Petroleum Engineering, died November 19, 1993 of leukemia. He is survived by his wife, Alyce and three children Jonna, Terri and Taigh. It would be hard to overstate Hank's contributions to the petroleum engineering profession, to the Departments of Petroleum Engineering at Stanford and Texas A&M University, and to the lives of the many students, faculty, staff, and practicing engineers with whom he worked during his long career.

Hank was a pioneer. He personally led the development of three distinct areas of petroleum engineering technology: *in situ* combustion for recovery of heavy oil, the engineering of recovery of steam from geothermal reservoirs, and the design and interpretation of pressure transient tests of oil and gas wells to determine properties of reservoir rocks. Hank made fundamental contributions to each of those areas at their inception and he wove the three strands into a research effort that continued until his death.

Hank was born in Pittsburgh in 1925. Hank's education was interrupted by World War II. He served as a navigator and B-29 crew member in the South Pacific. After the war he completed his BS (1949) and Ph.D. (1952) degrees in Chemical Engineering at Purdue University. Hank married Alyce in September 1948. He began his research career in 1952 with Magnolia Petroleum Company, a predecessor of Mobil Oil. Over the next eleven years, he held positions in research, production engineering and reservoir engineering with Magnolia, General Petroleum Corporation (another Mobil predecessor), Mobil, and the Chinese Petroleum Corporation in Taiwan (on loan from Mobil). He began his teaching career as a part-time Graduate School Lecturer at the University of Southern California in 1960/61. He moved fully into the academic arena in 1963 as Professor of Petroleum Engineering at Texas A&M University. He came to Stanford in 1966. He chaired the Petroleum Engineering Department for ten years (1976-86), leading its growth and building its stature. He was named to the Keleen and Carlton Beal Chair in 1981.

Hank is known worldwide for his contributions to pressure transient well testing, a technique by which the transient change of pressure in a well after production or injection has ceased can be interpreted to yield information about the properties and size of the reservoir. Hank and his students were responsible for much of the mathematical and practical development of modern well testing. The theory they developed includes the effects of complex fluid flows in and near the wellbore, and with that theory, useful

information can be extracted from experimental observations that would otherwise be uninterpretable.

Hank was a key innovator in the development of thermal oil recovery methods, which are applied to displace the heavy viscous crude oils that are abundant in California and elsewhere (Canada, Venezuela, and Indonesia to name a few). In the late 1950's he led the South Belridge Thermal Recovery Experiment, a field test of the new *in situ* combustion technique supported by eleven oil companies. Throughout his career he worked with many students to analyze and develop engineering science descriptions of *in situ* combustion and steam injection methods for heavy oil recovery.

Hank pioneered the field of geothermal reservoir engineering. In the 1960's he began to apply the principles of petroleum reservoir engineering to the recovery of energy in the form of steam from geothermal reservoirs. In 1972 the Stanford Geothermal Program was established, and it remains the premier geothermal reservoir engineering research curriculum in the world today. For his work in this area, he recently received the Department of Energy Award for Exceptional Public Service, the highest civilian award given by the U.S. Government.

Many other awards were bestowed on Hank. He won every major award given by the Society of Petroleum Engineers, and he served twice as a Distinguished Lecturer. He was elected to the National Academy of Engineering in 1981. Hank's professional colleagues know and appreciate his many technical contributions.

While Hank's research is known to all, he will be remembered most for his personal warmth, his sense of humor, and for his steadfast concern for students. His example created an environment in which good students could develop their intellectual skills in an atmosphere of respect. On the news of his death, messages of regret flooded in from former students from all corners of the globe.

Hank was multidimensional. He read voraciously, researched the history of petroleum engineering, especially at Stanford and had an ardent interest in aircraft.. He and his son Taigh helped fly a relic B-29 from the U.S. to Britain. The aircraft was restored for museum exhibition after that flight. At the time it was barely air worthy. Hank's celestial navigation made the flight a success.

Navigation was both a personal and a professional specialty for Hank. His leadership of Petroleum Engineering at Stanford used those skills as well. He always knew where he was, where he had been, and where he was going and he was a leader in charting a course for the Petroleum Engineering Department at Stanford. He will be terribly missed by those whose love and respect he will always hold.

PROCEEDINGS, Nineteenth Workshop on Geothermal Reservoir Engineering
Stanford University, Stanford, California, January 18-20, 1994
SGP-TR-147

# EXPANDED RESOURCE BASE -- THE KEY TO FUTURE GEOTHERMAL DEVELOPMENT

John E. Mock, Director
Geothermal Division
U.S. Department of Energy

Gene V. Beeland
DynCorp•Meridian
Alexandria, Virginia

## ABSTRACT

According to analyses by the Department of Energy's Energy Information Administration (EIA), geothermal electric power capacity could nearly quadruple over the next 20 years, and there is a tremendous potential for growth in the direct uses of geothermal energy. However, for a high rate of development to occur in either of these applications, the identified resource base must be expanded. To this end, the Department is supporting R&D efforts to 1) share with industry the costs and risks of evaluating promising new resource prospects with power potential; 2) reduce the costs of exploration to enhance industry's cost-competitive posture; and 3) assess the location and characteristics of low-temperature resources.

This paper describes DOE's new cost-shared industry-coupled exploratory drilling program to be initiated with a solicitation by the Idaho National Engineering Laboratory, field manager of DOE's reservoir technology activities. Proposals will be requested for drilling either core holes or full-size wells on prospects from which some information had already been gathered, such as surface geophysics or shallow heat flow.

The paper also discusses the status of the project designed to demonstrate whether a geothermal reservoir can be identified and adequately evaluated to meet investment requirements with slimholes rather than the much more costly production-size wells. Results to date of testing at the Far West 24 MWe plant site at Steam Boat Hills, Nevada, are reported, and plans for related technology development to make slimhole exploration accessible even to small developers are described.

In addition, the paper describes the components of a Low-Temperature Assessment Program and its objectives and identifies the state resource assessment teams.

It is concluded that the successful execution of each of these projects will help to ensure a secure future for geothermal energy in this country, thus enhancing the environment wherever geothermal energy substitutes for the combustion of fossil fuels.

## INTRODUCTION

According to analyses by the Department of Energy's Energy Information Administration, geothermal electric power capacity could nearly quadruple over the next 20 years. It is also estimated that, if the new DOE/industry cooperative program, tentatively called GEO - PACT (Geothermal Program to Accelerate Commercialization of Technology) is funded at requested levels, earlier increases in both power capacity and direct use applications could result by the year 2000:

- 1,200 MWe capacity in the U.S.
- 2,000 MWe capacity in the rest of the world
- 40 trillion BTUs per year in direct heat
- 700,000 geothermal heat pump units.

Accomplishment of this degree of growth in geothermal use alone will offer dramatic support to President Clinton's Climate Change Action Plan, which calls for a reduction of greenhouse gas emissions in the U.S. to 1990 levels by 2000, and to similar worldwide efforts for a healthier future environment. It is estimated that a geothermal response of this magnitude would reduce carbon dioxide emissions by nearly 100 million tons per year, of sulfur dioxide by one million pounds per year, and of nitrogen oxides by 330,000 pounds per year. (These quantities were determined by comparison of emissions from clean geothermal power plants with those from the average coal-fired plant in the U.S. using 1990 data from EIA). Since coal is one of the most polluting fuels, it is expected that accelerated geothermal development would have greatest impact on coal among all competing fuels, and would lead directly to reduced coal use.

Before growth of the magnitude suggested above can occur, however, a greatly expanded resource

data base is necessary. Acquiring the knowledge needed to assure continuing growth in power capacity will involve 1) exploration to confirm that currently unknown reservoirs are present at commercially viable temperatures and quantities at economically accessible depths, and 2) more detailed characterization of promising reservoirs in order to design strategies for their production. These development steps are the particular province of the participants in the Stanford Reservoir Engineering Workshop whose contributions to the current resource data base and to exploration and resource assessment techniques are recognized worldwide. Thus, it is not necessary to elaborate here on the details of the great costs involved in discovering and evaluating reservoirs. It is only emphasized once again that with current technology these functions are beyond industry's economic means, and government assistance appears essential if geothermal energy is to make a substantial contribution to the President's climate change plan.

Concomitantly, accelerated development of low-temperature geothermal resources in direct uses of the magnitude suggested above hinges to a large extent on compilation and characterization of reservoirs suitable for these applications, particularly those within five miles of population centers.

## EXPANSION OF GEOTHERMAL RESOURCE DATA BASE

As one of the coordinated initiatives envisioned by the GEO-PACT program, planning is underway in the Geothermal Division to establish a government/industry cooperative exploratory drilling project. The objective of this project is to increase the inventory of known U.S. geothermal resources and to assist industry in determining the feasibility of economic development of particular resource areas in order to accelerate development and investment decisions.

As planned, the mechanics of this project will be very similar to the Industry-Coupled Cost-Shared Program initiated in the 1970s when a working data base for geothermal resources did not exist. The only source of this information at the time was the energy companies themselves who regarded it as proprietary.

The program was initiated to: 1) stimulate industry exploration through cost and risk sharing; 2) make data generated from the program available for unrestricted use; 3) develop case histories of geothermal exploration in various geologic environments for determining optimum exploration techniques; and 4) confirm resource potential at selected geothermal sites. The program included 21 deep exploratory wells with an average depth of about 7,000 feet, numerous shallow thermal gradient test holes, and geoscience investigative surveys. These efforts are summarized in Exhibit 1.

Nine major data packages were developed and are still available through the Earth Science Laboratory of the University of Utah Research Institute, and excellent results were achieved, with eight of the 14 sites investigated in commercial production today.

While development has not yet reached the full estimated megawatt capacity of any of the eight reservoirs, their remaining potential is not enough to support major industry growth. The sites are as follows:

| Nevada | Utah |
|---|---|
| Beowawe | Roosevelt Hot Spings |
| Desert Peak | Cove Fort |
| Dixie Valley | |
| San Emedio | |
| Soda Lake | |
| Stillwater | |

If the new project is funded as proposed, it will be open to all interested companies for geothermal exploration anywhere in the U.S. Core holes or exploratory wells may be proposed, and bidders will be requested to provide any knowledge of a proposed prospect area already gained through activities such as surface geophysics or shallow heat flow measurements. An indication of the ultimate user -- utility or independent producer -- of sites deemed suitable for development will also be requested. The proposer must agree to pay 50 percent of the drilling cost and provide estimates of the depth to the resource and of the total drilling costs.

## REDUCED FIELD DEVELOPMENT COSTS

Industry has expressed strong interest in technology advancements to reduce exploration costs so that industry can conduct more aggressive exploration programs on its own. As a result, a project was designed to investigate whether slimholes, rather then full-sized exploratory wells, can provide adequate information on a reservoir to satisfy investor requirements.

Slimholes are cheaper than wells because lost circulation zones can be drilled through without loss of drilling fluid, smaller rigs and crews as well as smaller drill sites are needed, road and permit requirements and environmental impact are reduced, and problems can be predicted and fixed

## EXHIBIT 1

**SUMMARY OF INDUSTRY-COUPLED PROGRAM EFFORTS**

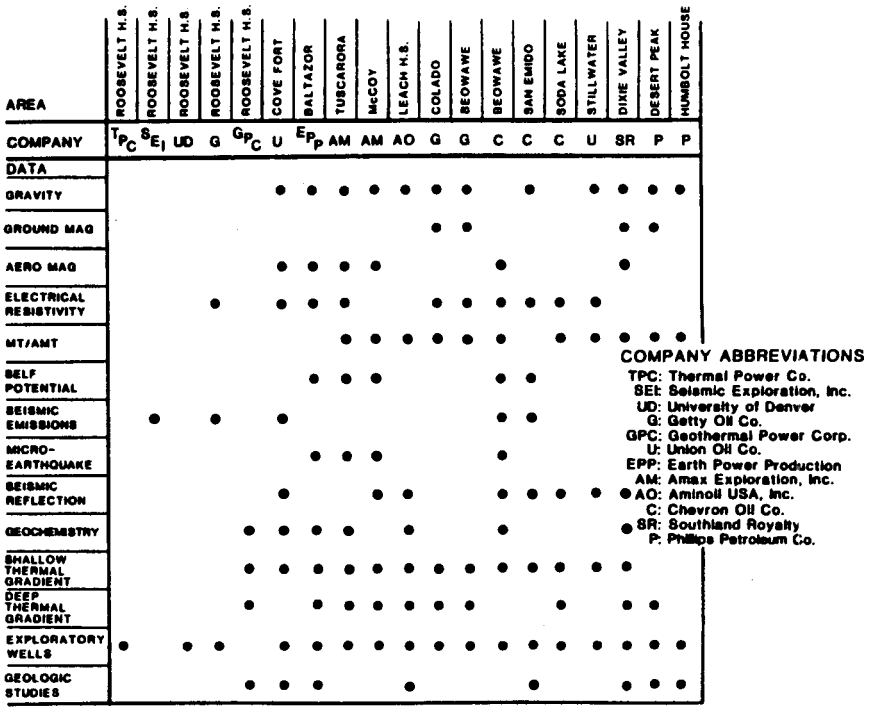


more easily. The cost analysis of a test of an existing core hole at the Far West Capital site at Steamboat Hills, Nevada, indicated the cost at $151/foot for the slimhole compared to $377/foot for an adjacent production well.

The project is under the direction of the Sandia National Laboratories which is working with a group that includes personnel from Sandia, Lawrence Berkeley Lab, University of Utah Research Institute, U.S. Geological Survey, independent consultants, and geothermal operators. This group is involved to a greater or lesser extent in all decisions affecting the direction of the research. Specific tasks, as outlined by John Finger of Sandia at last year's geothermal program review, include:

- Correlation of fluid flow and injection tests between slimholes and production size wells.
- Transfer of slimhole exploration drilling and reservoir assessment to industry so that slimhole drilling becomes an accepted method for geothermal exploration.
- Development and validation of a coupled wellbore-reservoir flow simulator which can be used for reservoir evaluation from slimhole flow data.
- Collection of applicable data from commercial wells in existing geothermal fields.
- Drilling of at least one new slimhole and using it to evaluate a geothermal reservoir.

The initial tests, on coreholes at Far West, a well-characterized field, yielded flow data which were in excellent agreement with results obtained by using measured downhole conditions as input for wellbore simulator codes. Further intensive testing is planned. Investigation of existing wellbore and reservoir codes indicates that they can be combined and/or slightly modified to produce a useful tool for analysis of reservoir parameters from wellbore flow data.

Plans to drill slimholes at two other well documented sites -- Coso Hot Springs and Wendell-Amedee, both in California -- this year are pending continued funding for this project. Its ultimate goal is to develop tools that will make slimhole exploration accessible even to the small, independent geothermal developer. These include, among others:

- guidelines for drilling and completing exploration slimholes
- recommended test procedures and strategies, including data requirements
- improved downhole instrumentation
- data interpretation techniques, possibly in the form of a PC-compatible flow simulator which could be distributed at a nominal expense to independent developers.

## ASSESSMENT OF LOW- AND MODERATE-TEMPERATURE GEOTHERMAL RESOURCES

The objectives of the ongoing low- and moderate-temperature resources assessment is to promote accelerated use of these non-polluting resources in lieu of fossil-fuels for heating, and, in some climates, cooling. According to the Geo-Heat Center at the Oregon Institute of Technology, space heating in the 50-82°C (120°-180°F) range is by far the largest single U.S. energy use, representing 45 percent of all energy uses below 260°C (500°F). Customers of geothermal district heating systems commonly realize a 50 percent saving over the use of natural gas, with the payback period for initial installation determined by variations required by site-specific conditions.

Geothermal heat pumps represent similar operations cost savings over most alternatives, and the Environmental Protection Agency has found that they are the least polluting of all alternatives in most areas of the country. The Department of Defense has concluded, as enunciated in a military handbook on energy use, that the GHP is "the most efficient method of using electric power for heating." Thus, DOD has embarked on a program to accelerate the installation of GHPs at its facilities "to contribute to modernization and energy efficiency by reducing power consumption and maintenance costs." The circle of GHP proponents also includes utilities which are seeking the benefits of GHPs through reduced peak demand and higher annual load factors by offering various incentives to their customers to offset the upfront installation costs.

Thus, increased use of geothermal direct heat technologies will not only make a major contribution to reductions in greenhouse gas emissions, but will increase energy efficiency and cost savings, all of which are major objectives of DOE. It is believed that the products to result from the low- and moderate-temperature resource assessment will hasten the achievement of these objectives.

One product, which is nearly finished, is a nationwide set of maps indicating the potential locations for GHP installation. These are being prepared by the various state water resources research institutes.

Another product, also nearing completion, is an updated and refined inventory of the low- and moderate-temperature resources of the western states. Maps prepared for 18 of these states under the DOE State-Coupled Resource Assessment program of the late 1970s provided an excellent starting point for the current work. They identified wells and springs with anomalous temperatures and, along with supporting reports, have been very useful.

The current effort is focused on "cleaning up" the data base to provide good and usable data without errors. Drilling records and other information are being reviewed to identify new resources and verify temperatures and flow rates which may have changed substantially since the earlier State-Coupled program.

The Geo-Heat Center has selected the preliminary data base from the Utah Geological Survey as a model for the digital data base in table format. Information to be contained in the tables is as follows:

Table 1. Location: ID number, source name, county code, latitude and longitude.

Table 2. Description: ID number, source name, type of source, temperature (°C), flow rate (L/min), depth of wells (m), current resource use, and references to relevant studies (geology, geophysics, geochemistry, hydrology) completed for the site.

Table 3. Geochemistry: ID number, source name, pH, TDS, major cations, major anions, cation-anion balance, chemical species that may cause scale and corrosion products, and light stable isotopes.

Resource maps at a scale of 1:1,000,000 are also in preparation.

Program participants include, in addition to the Geo-Heat Center, the University of Utah Research Institute, the Idaho Water Resources Research Institute and agencies of state governments or universities in most of the western states.

## CONCLUSION

The highest levels of experience and expertise in the U.S. geothermal community are being brought to bear on each of these projects. It can thus be expected that they will be executed with a maximum degree of success. To that end, they will enhance geothermal development, for both power generation and direct use applications, in this country and abroad, and, in turn, enhance the environment worldwide.

PROCEEDINGS, Nineteenth Workshop on Geothermal Reservoir Engineering
Stanford University, Stanford, California, January 18-20, 1994
SGP-TR-147

# FEASIBILITY STUDY FOR THE THELAMÖRK LOW-TEMPERATURE SYSTEM IN N-ICELAND

Grímur Björnsson, Gudni Axelsson and Ólafur G. Flóvenz

National Energy Authority, Grensásvegur 9, 108 Reykjavík, ICELAND

## ABSTRACT

*The Thelamörk low-temperature geothermal system in N-Iceland has for the last decade been considered as a possible source of hot water for the Akureyri District Heating Service. A productive well was drilled in the summer of 1992 after 10 years of geothermal research in the area. Following that a feasibility study was performed in order to determine whether harnessing the geothermal system for space heating would be economical. This study consisted of a nine month full scale production test along with partial reinjection and tracer tests. It also involved careful monitoring of production rates, water level changes and chemistry. Finally, the data collected were analyzed on the basis of simple reservoir models. The results of the analysis indicate that the system will sustain a production of 19-20 l/s, initially at 91 °C, for the next 10 years, given that 3 l/s will be reinjected. However, a cooling of 9-12 °C is predicted due to infiltration of colder groundwater and the reinjection. The results also suggest that harnessing the geothermal system will be economical, despite the high cost of exploration and an 11 km insulated pipeline to Akureyri.*

## INTRODUCTION

*Hitaveita Akureyrar* (the Akureyri District Heating Service) provides hot water for space heating in the town of Akureyri in Central North Iceland (pop. 16,000). For this purpose water is produced from four low-temperature hydrothermal systems in the vicinity of the town, shown in Figure 1, namely: Glerárdalur, Ytri-Tjarnir, Laugaland and Botn (Axelsson and Björnsson, 1993). In 1992 the annual production from each of these four systems ranged between 13 and 42 l/s of 60-95 °C water (Flóvenz et al., 1993). This amounts to 228 $GWh_t$ of thermal energy, assuming a return water temperature of 30 °C. The production rate has increased by 2 % annually during the last decade and the demand of the space heating market is expected to continue to rise. The total production capacity of the four systems, however, is estimated at only 248 $GWh_t$/year, assuming the present system of production wells and downhole pumps (Axelsson et al., 1988). This forces Hitaveita Akureyrar to acquire additional sources of energy within a few years.

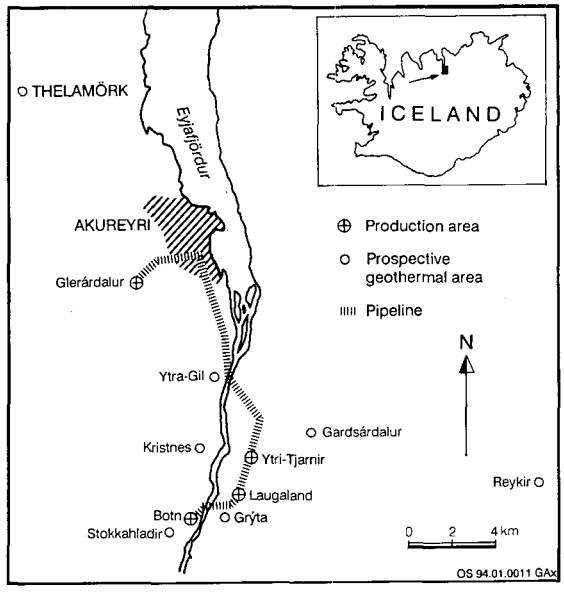


**Figure 1:** *Location of the Thelamörk field and the geothermal areas presently utilized by Hitaveita Akureyrar.*

The search for more energy has focused on a few unharnessed geothermal fields in the vicinity of Akureyri. One of the areas considered is the Thelamörk geothermal field, located about 11 km north of Akureyri (Figure 1). At Thelamörk the only manifestations of geothermal activity were a small hot spring flowing 0.3 l/s of 45 °C water together with ancient silica precipitation. Yet geothermometers suggested an underlying geothermal reservoir of 90-100 °C. The initial exploration phase, which ended in 1970 (Table 1), was not fully successful. Thus plans for utilization of the Thelamörk field were abandoned.

Rapid development of exploration techniques along with the marginal power capacity of Hitaveita Akureyrar restored the interest in the Thelamörk field in 1983. After conducting resistivity and magnetic surveys, geological mapping and exploration drilling, a successful well was drilled in the summer of 1992. Following that the feasibility of harnessing the geothermal system was studied (Flóvenz et al., 1994). This was done by producing from the new well for nine months and by observing and analyzing the systems response.

**Table 1.** *Wells drilled in the Thelamörk geothermal field.*

| Well | Drilled | Depth (m) | Type |
|---|---|---|---|
| 1 | 1944 | 375 | Expl. well |
| *2* | *1965* | *1088* | *Prod. well* |
| 3 | 1970 | 667 | Expl. well |
| 4 | 1970 | 711 | Expl. well |
| 5 | 1989 | 239 | Expl. well |
| 6 | 1989 | 361 | Expl. well |
| 7 | 1989 | 208 | Expl. well |
| 8 | 1989 | 251 | Expl. well |
| 9 | 1990 | 367 | Expl. well |
| 10 | 1992 | 914 | Expl. well |
| *11* | *1992* | *452* | *Prod. well* |

In this paper a brief description of the production test and the data collected is given. The simple reservoir models used to analyze the data are presented along with their predictions on the following:

1. Future water level changes in the reservoir.
2. Reservoir cooling due to infiltration of colder groundwater.
3. Heat mining and water level maintenance by reinjection.

Finally, a cost estimate for the Thelamörk project is shown and compared to the cost of space heating by sources of energy, other than geothermal.

In the initial work more complicated, distributed parameter models were considered. They were, however, rejected at this stage due to a very tight time schedule for the feasibility study and the limited data available (i.e. a primitive conceptual model).

## GEOTHERMAL EXPLORATION

Like most low-temperature geothermal systems in Iceland, the Thelamörk system was believed to be characterized by near vertical structures, such as fracture-zones or dykes. The upflow of hot water is along permeable parts of these structures. Therefore the geothermal exploration phase aimed at locating vertical formations, in particular the permeable ones. Figure 2 shows the results of the exploration (Flóvenz et al., 1984). On the basis of a ground magnetic survey, together with geological mapping and analysis of drill cuttings, several dykes were located, most of them directed between N and NW. Also located were two NNE-trending faults, dipping to the east. Head-on resistivity profiling located two low-resistivity structures directed NNW and a third one along the Hörgá river, apparently connecting the other two (Flóvenz, 1984).

Due to the complexity of the subsurface structure, five additional exploration wells were drilled in 1989 and 1990 (Table 1) to obtain more detailed information on the system, in particular on the temperature distribution (Flóvenz et al., 1990, Milicevic, 1990). Integrated modeling of the formation temperature, well log data, drill cutting analysis and results of resistivity- and ground magnetic surveys strongly indicated that the upflow zone was restricted to a narrow part of either the low-resistivity fracture along the river or the dyke marked A in Figure 2. The upflow zone might even be restricted to the intersection of the fracture and the dyke. The dip of the fracture along the river was assumed to be about 6 ° to the south. Well 10 was drilled in the summer of 1992 and targeted to intersect the fracture at 600-900 m depth. This well turned out to be unsuccessful and temperature data from the well indicated that the fracture was, in fact, dipping to the north (Flóvenz et al., 1994).

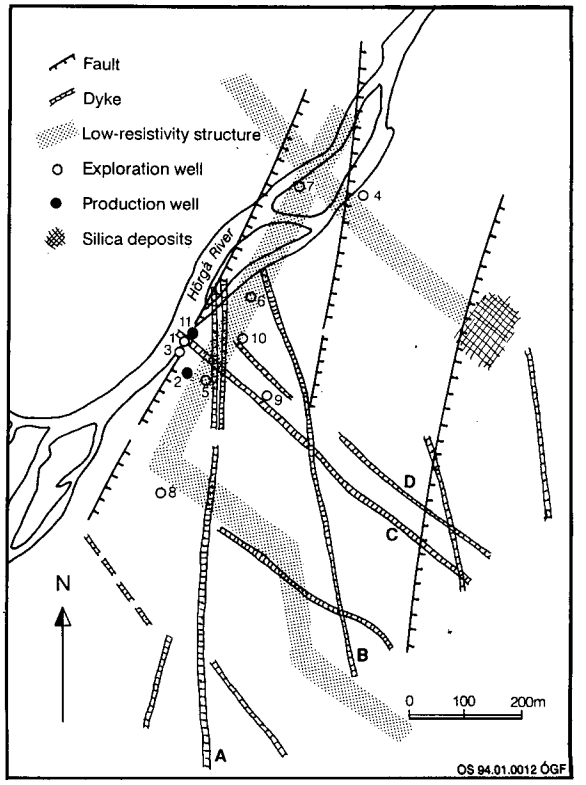


**Figure 2:** *A geological map of the Thelamörk area showing dykes, faults, low resistivity structures and wells.*

Well 11, which was drilled later that summer, was successful. It intersected highly productive feedzones at 430-450 m depth, and thus confirmed the conclusion on the dip of the permeable fracture. Brief testing by air-lifting at the conclusion of drilling yielded 40-60 l/s of 85-90 °C water. However, a rapidly increasing draw-down was observed in well 11 and most of the exploration wells during these short periods of testing.

## THE PRODUCTION TEST

The rapidly increasing draw-down during air-lifting of well 11 indicated that the long-term productivity of the well might be limited, in spite of its great initial pro-

ductivity. It was, therefore, decided that the Thelamörk field would be tested carefully before any plans of connecting it to Hitaveita Akureyrar would be made. This testing was done by producing from well 11 for a period of nine months. A rotary-shaft pump was installed in the well along with an air tube for water level measurements and a flowmeter. Other wells in the area were also prepared for water level monitoring. Pumping started on November 11, 1992 and continued until August 11, 1993.

During the test 15 - 20 l/s of 91.5 °C water were produced from well 11. In addition about 6 l/s were reinjected into wells 6 and 8 during the last 2 1/2 months of the test. Figure 3 shows the production rate along with the injection into wells 6 and 8. The flow rates, water temperature, chemical concentration of water samples and water level in most of the wells in the area were monitored carefully throughout the test. As an example more than 2500 water level readings were taken.

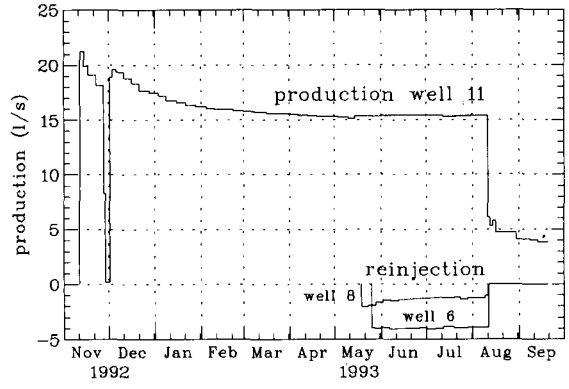


**Figure 3:** *Rates of production from well 11 and reinjection into wells 6 and 8.*

Figure 4 shows the water level data collected in well 11. It should be noted that the brief water level recovery in December 1992 was due to a failure of the pump in well 11.

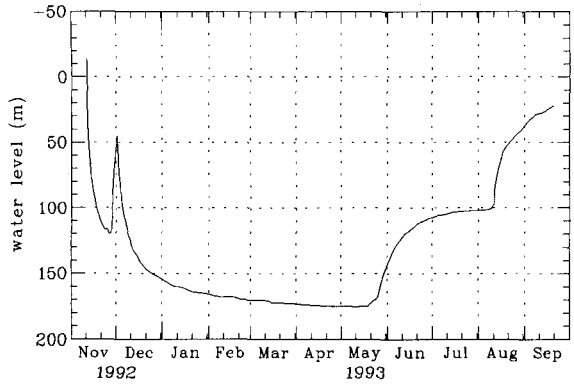


**Figure 4:** *Water level in well 11 during the pumping test.*

Tracer tests were carried out concurrently with the reinjection in order to evaluate the connections between possible injection wells and the production well. These will be discussed later in the paper.

## FUTURE WATER LEVEL

Most of the wells at Thelamörk showed similar water level changes during the production test. The draw-down in well 2 was about 190 m, equaling the draw-down in well 11. In wells 3, 5, 6, 8 and 9 water levels fell by about 160 m. The maximum draw-down in wells 4, 7 and 10, however, was between 10 and 70 m. The similar draw-down in the former group is most likely due to their direct connection to the permeable fracture zone discussed earlier. The water level in the latter group, on the other hand, is dominated by the pressure in the rock matrix outside the fracture zone.

The interference data from the exploration wells were simulated by the response of a conventional Theis-model of an infinite, confined and isotropic layer of porous material. An example of the results is presented in Figure 5, which shows the observed and calculated draw-down in well 6 during the first 16 days of the production test. A transmissivity $khg/\nu$ = $3.9 \times 10^{-5}$ $m^2/s$ and a storativity $c_t h\rho g$ = $2.3 \times 10^{-4}$ were estimated for this well pair. The transmissivity corresponds to a permeability thickness (kh) of only 1.3 Dm. This represents the average reservoir permeability in the production part of the geothermal system. This is comparable to the lowest such values estimated for geothermal systems utilized in Iceland (Björnsson and Bodvarsson, 1990).

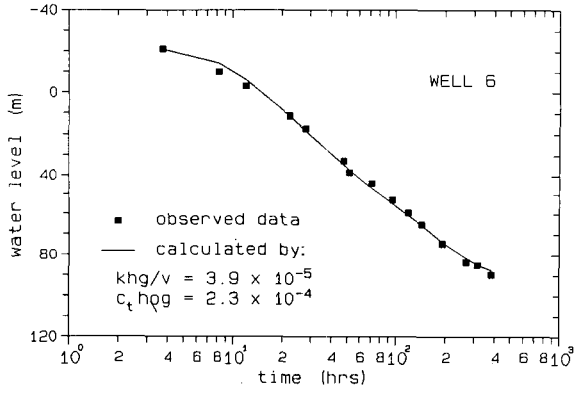


**Figure 5:** *Simulated interference data from well 6.*

Lumped reservoir modeling was used to simulate the water level data from the production test and to predict the draw-down in the reservoir due to long-term production from well 11 as well as to estimate the reservoir volume. Lumped models have been used successfully to simulate and predict pressure response data from several low-temperature reservoirs in Iceland (Axelsson, 1989 and 1991). An automatic method which tackles the simulation as an inverse problem was applied (Axelsson and Arason, 1992).

Figure 6 shows the three tank lumped model used to simulate the water level data from well 11. The innermost tank, which has a mass storage coefficient $\kappa_1$, simulates the production part of the geothermal system. This tank is connected by a conductor $\sigma_1$ to the second tank ($\kappa_2$), which simulates the outer and deeper parts of the reservoir. The conductor simulates the fluid conductivity between those two parts. The second tank is finally connected to the third tank ($\kappa_3$), which simulates recharge to the geothermal system. This tank simulates probably both the deeper parts of the geothermal system and the overlaying groundwater system. Figure 7 shows the match between the observed and simulated water levels.

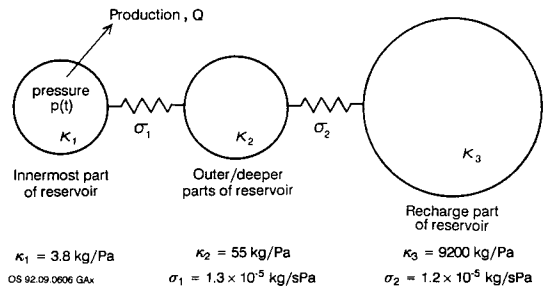


**Figure 6:** *A lumped reservoir model of the Thelamörk geothermal system.*

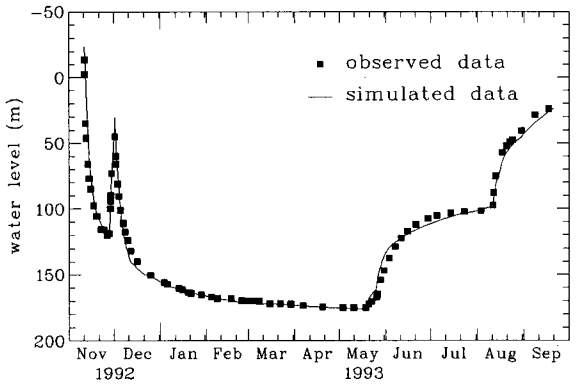


**Figure 7:** *Observed and simulated water level changes in well 11.*

In this study a closed reservoir model was used rather than an open one. This results in pessimistic water level predictions in contrast to optimistic predictions made by open models. The storage coefficient of the outermost tank was, in fact, adjusted such that the simulated water level declined by 5 m/year at 15 l/s net production. This equals the decline rate observed during the middle of the production test, before the reinjection. It is, however, unlikely that a decline rate so high will persist during long-term production.

The mass storage coefficient of the innermost tank corresponds to a volume of 0.095 km$^3$, assuming an average porosity of 5 %. The outer and deeper parts of the model (tank 2) simulate a volume of 1.4 km$^3$, assuming the same porosity. The recharge part of the system appears to be unconfined, which is reflected in a very large mass storage coefficient (Figure 6). The storage coefficient of an unconfined reservoir depends on its area rather than its volume (Axelsson, 1989). The storage coefficient of the third tank corresponds to an area of 0.9 km$^2$, assuming a porosity of 10 %.

The above results indicate that the reservoir volume, affected by the new well, is small with a low average permeability. The Thelamörk geothermal system appears, however, to be connected to much larger recharge systems, perhaps a geothermal reservoir at greater depth, as well as the surrounding groundwater systems.

Finally, the lumped model was used to predict the water level draw-down in well 11 for three cases of constant future production, for a ten year period. The results are presented in Figure 8 but will be discussed in a later section.

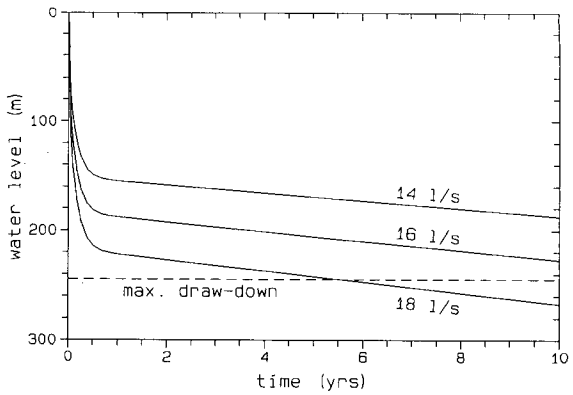


**Figure 8:** *Predicted water level changes in well 11 at Thelamörk.*

## COOLING BY INFLOW OF COLDER WATER

The chemical concentration of the water from well 11 was monitored during the production test. The most noteworthy change was a decline in silica concentration, from 129 ppm initially to 124 ppm in late May, when the reinjection began. This decline is believed to be the result of colder fluids seeping into the production part of the reservoir, partially as internal flow in the exploration wells and partially through fractures extending to the surface. A simple lumped model was used to simulate these data and to predict cooling of the water produced from well 11 in the future. This model is described in more detail in Appendix A.

The match between the observed and calculated silica concentration is shown in Figure 9. In the model mixing of geothermal water and cold groundwater takes place in a small subvolume (V) of the geothermal

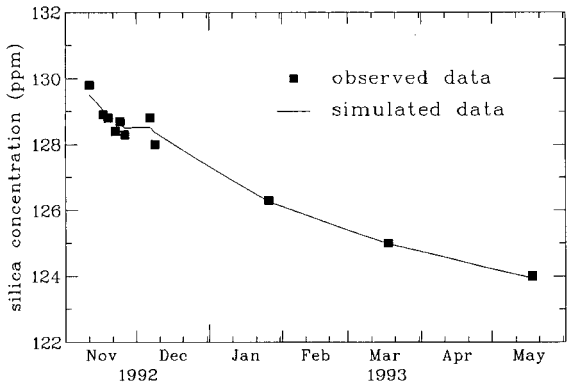


**Figure 9:** *Measured and simulated silica concentration in water produced from well 11.*

reservoir. The product of this volume and porosity ($\phi$) equals 0.0007 $km^3$. This corresponds to a volume of 0.015 $km^3$, assuming an effective porosity of 5 %. In the model the base inflow (R) is about 78 % of the production, whereas the colder down-flow (q) is about 22 %, with a silica concentration (C′) of 50 ppm. This model does not constitute a unique solution. A greater volume and more down-flow with, however, a greater silica concentration and higher temperature would result in a similar fit. This non-uniqueness does not influence the cooling predictions seriously and the model used predicts, in fact, the greatest long-term cooling. The model is, in other words, pessimistic.

The simple model of Appendix A was finally used to predict the possible temperature decline due to down-flow of colder water. This was done for 5 % and 10 % reservoir porosities and assuming that the temperature of the down-flow was 25 °C. The results are presented in Figure 10. An effective porosity of 5 % is considered to be most realistic due to the fractured nature of the Thelamörk geothermal system. This is supported by a negligible temperature decline during the nine month production test.

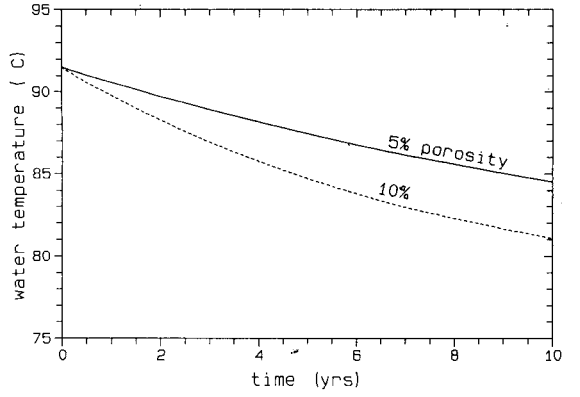


**Figure 10:** *Predicted temperature decline due to down-flow of colder water for 16 l/s production.*

## HEAT MINING BY REINJECTION

The objective of the tracer studies at Thelamörk was to evaluate the nature of the fracture system connecting injection and production wells. The water produced from well 11 was recirculated at rates of 4 and 2 l/s into wells 6 and 8, respectively, from late May until the middle of August, 1993 (Figure 4). The water level of all wells was monitored meanwhile. When a semi steady-state had been reached, a known mass of bromide and fluorescein was injected instantaneously into wells 6 and 8, respectively. Water samples where taken frequently from well 11 and the two tracer concentrations measured. Figure 11 shows the observed data for the bromide injected into well 6. Also shown is the data corrected for the extra bromide that was recirculated from well 11 into wells 6 and 8 (Arason et al., 1993). The corrected data shows that 9.3 kg of the 15.5 kg of bromide injected were recovered, or 60 %. The tracer recovery for well 8 was similar, yet somewhat slower because of the greater distance between wells 8 and 11. About 0.24 kg of fluorescein were recovered compared to the 1 kg injected.

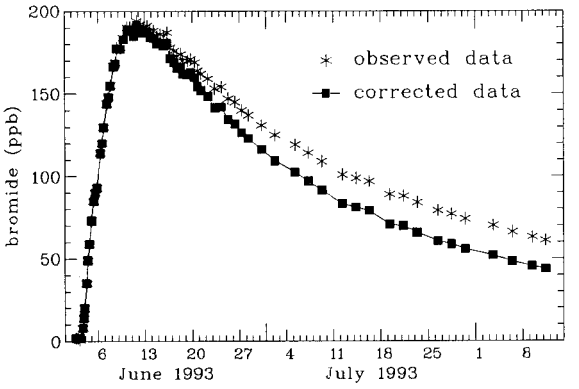


**Figure 11:** *Observed and corrected tracer recovery curves for the well dipole 6-11.*

The tracer return curves were analyzed by a simple one-dimensional fracture-zone model. A brief description of the method used is given in Appendix B. Figure 12 shows the measured and simulated tracer return curves for the bromide injected into well 6. Two flow channels between the injector and the producer were assumed. The first channel accounts for 15 % of the recovered tracer and is taken to be the shortest distance between the two wells (120 m). The second channel, on the other hand, transported 85 % of the tracer mass. This flow channel is assumed to be a fracture zone connecting the major feedzones of the two wells. Table 2 presents the model parameters used in the simulation.

The variable $M_i$ in Table 2 above denotes the calculated mass recovery of tracer through the corresponding channel until infinite time. According to this study, a maximum recovery of 77 % is predicted for the channels connecting wells 6 and 11. Similar results were

**Table 2:** *Model parameters used to simulate the tracer recovery of bromide. See Appendix B for nomenclature.*

| Channel length (m) | u (m/s) | $A\phi$ ($m^2$) | $\alpha_L$ (m) | $M_i/M$ |
|---|---|---|---|---|
| 120 | $1.92 \times 10^{-4}$ | 18.8 | 51 | 0.11 |
| 320 | $1.45 \times 10^{-4}$ | 24.0 | 193 | 0.66 |

obtained for the fluorescein injected into well 8, although the predicted maximum tracer recovery is only 40 %.

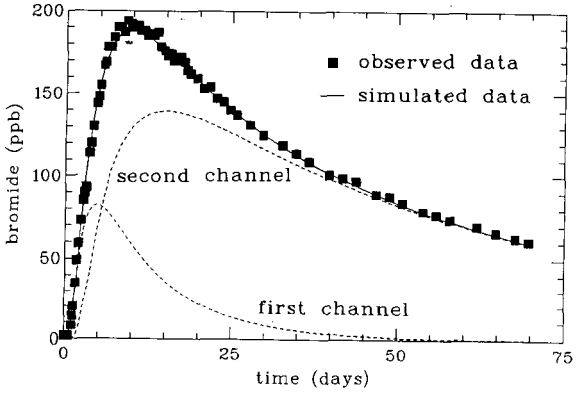


**Figure 12:** *Observed and simulated tracer recovery curves for the well dipole 6-11.*

The fracture properties obtained through the tracer studies were finally used to estimate the heat absorbed by the injected fluid in the fracture system. The one-dimensional fracture model applied is presented in Appendix B. The assumption is made that the fluid passes a fracture zone of width 1 m and porosity 30 %. This gives, according to table 2, a flow channel height (h) of 80 m for the well dipole 6-11.

Figure 13 shows the predicted temperature of injected water as it enters well 11. Several injection rates into wells 6 and 8 were considered. The study indicates an effective heat mining for all the cases. Mixing calculations for well 11 show, however, that injection rates should be limited to 1-2 l/s per well for less than 2 °C cooling of the produced fluid. Note that the 30 °C temperature of the injected fluid corresponds to the return temperature of geothermal water used locally for space heating.

## PREDICTING THE OVERALL RESERVOIR PERFORMANCE

The reservoir models described above simulate and predict independently three different aspects of the response of the Thelamörk geothermal system to production and injection. Their results, presented in figures 8, 10 and 13, may be combined to predict the overall performance of the system. The fact that the

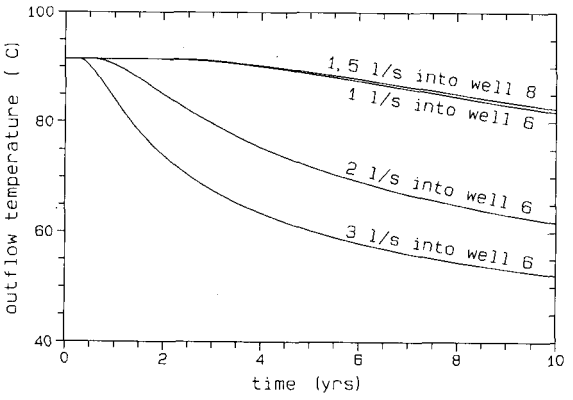


**Figure 13:** *Heat mining for a few cases of injection into wells 6 and 8. The injection fluid temperature is 30 °C.*

data were not integrated into a single reservoir model probably results in more pessimistic predictions. It is, for example, unlikely that the reservoir will behave as a closed system during long-term production if a considerable inflow of colder groundwater takes place.

The key result of this study, as requested by Hitaveita Akureyrar, is an estimate of the production capacity and, furthermore, a production strategy for the Thelamörk reservoir. The production capacity is limited by a maximum 245 m draw-down in the production well, assuming a conventional rotary shaft pump. Another limit is the production temperature of well 11. The down-flow study indicates that a cooling by some degrees during a period of ten years is very likely, due to infiltration from above. In addition, reinjection will lead to some cooling. The reinjection, on the other hand, reduces the pressure draw-down and thereby allows an increase in production.

Figures 8 and 10 show that the Thelamörk system sustains a maximum, net production of 16-17 l/s for the next decade, and 7 - 10 °C temperature decline is predicted at the end of this time period. Mixing calculations, based on Figure 13, also show that 1.5 l/s injection into each of wells 6 and 8 will result in an additional 2 °C cooling of well 11 for this production. Because of the reduced draw-down, an injection of 3 l/s will increase the total production to 19-20 l/s, although the net production remains 16-17 l/s. This provides a 20 % increase in flowrates from well 11 and a 15 % increase in the thermal energy recovered.

## ECONOMICS OF THE THELAMÖRK PROJECT

Table 3 presents a simplified evaluation of the economy of exploiting the Thelamörk field. Two production scenarios are considered, one without injection and the other with reinjection of local return water. The evaluation is based on a project lifetime of 20 years, such that the above predictions on water temperature have been extrapolated for another 10 years resulting in the average water temperature shown in the table. The 20 year project lifetime is very conserva-

tive, as the geothermal system is expected to supply hot water for much longer. However, drilling of a new production well may become necessary during these 20 years, due to the foreseen cooling of well 11. The numbers in table 3 are based on an exchange rate of 72.5 Icelandic kronur per U.S. dollar.

**Table 3.** *Economy of exploiting the Thelamörk field.*

| Assumptions | Case A | Case B |
|---|---|---|
| Production rate | 16 l/s | 19 l/s |
| Local use | 3 l/s | 3 l/s |
| Pumping to Akureyri | 13 l/s | 16 l/s |
| Reinjection | 0 l/s | 3 l/s |
| Average water temp. | 86 °C | 84 °C |
| Cooling in pipeline | 7 °C | 6 °C |
| Thermal energy[1)] | 23.4 $GWh_t$/yr | 28.2 $GWh_t$/yr |
| Exploration & drilling | $ 620,000 | $ 620,000 |
| Pipeline, pumps etc. | $ 1,100,000 | $ 1,100,000 |
| Interest rate | 6 % | 6 % |
| Project lifetime | 20 yrs | 20 yrs |
| Pumping costs | $ 46,000/yr | $ 55,000/yr |
| Operating costs | $ 21,000/yr | $ 21,000/yr |
| Energy price | 9.3 mills/$kWh_t$ | 8.0 mills/$kWh_t$ |

[1)] assuming a 30 °C return water temperature.

The energy price in the table may be compared to the following 1993 consumer prices in Iceland:

| | |
|---|---|
| Geothermal heating in Akureyri | 29 mills/$kWh_t$ |
| Average hot water price | 11 mills/$kWh_t$ |
| Heating by oil | 42 mills/$kWh_t$ |
| Electricity for space heating (government subsidized) | 34 mills/$kWh_e$ |

This comparison shows that the Thelamörk project will be highly economical in spite of the relatively high cost of exploration and drilling, a long pipeline and a limited productivity of the geothermal system. Case B will be more economical notwithstanding a greater temperature decline and will provide an additional income for Hitaveita Akureyrar of about $ 35,000 per year. This happens to be approximately the cost of drilling a 500 m deep reinjection well.

## CONCLUDING REMARKS

The main conclusions of the feasibility study for the Thelamörk low-temperature system are:

1. The geothermal system is characterized by a fracture zone, and a few dykes. It is very small in volume ($\approx 1\ km^3$) and has a low permeability thickness ($\approx 1$ Dm). This leads to a great pressure draw-down during production.
2. The results of lumped modeling indicate that the maximum, long-term production from well 11 is on the order of 16-17 l/s, (maximum draw-down 245 m). Injection of local return water (3 l/s) can increase the total production to 19-20 l/s.
3. The production reservoir appears to be connected to the overlying groundwater system. Some cooling due to down-flow of colder water may, therefore, accompany long term production.
4. Injection and tracer studies show that well 11 and possible injection wells are directly connected, most likely through the reservoir fracture system. Therefore, injection rates must be restricted to 1-2 l/s per well, for an efficient heat recovery.
5. The initial temperature of the water produced from well 11 is 91.5 °C. Colder down-flow and reinjection may result in a 9-12 °C temperature decline during 10 years of production.
6. The production cost for hot water from the Thelamörk field is estimated at 9.3 mills/$kWh_t$ without reinjection and 8.0 mills/$kWh_t$ if 3 l/s are reinjected. This shows that a reinjection program (wells and surface equipment) will pay off in 2-3 years.
7. An energy price of 8-9 mills/$kWh_t$ compares favorably with the average hot water consumer price in Iceland of about 11 mills/$kWh_t$. Therefore, small scale geothermal projects, such as Thelamörk, appear to be economical.

On the basis of this study, Hitaveita Akureyrar has already decided to exploit the Thelamörk area. Hot water from the field is expected to start flowing to Akureyri in the fall of 1994.

The cooling predicted may cause well 11 to cease to be economical sometime in the future. However, the known strike and dip of the upflow zone allows for a precise location of a new production well that will intersect the upflow at a greater depth than well 11, where little or no cooling is expected.

Finally, it should be mentioned that Thelamörk is the first low-temperature geothermal system in Iceland where such extensive testing is carried out before plans for utilization are made. The production test and its analysis may serve as a model for other similar projects in the future.

## ACKNOWLEDGEMENTS

The authors would like to thank Hitaveita Akureyrar for allowing publication of the data from the Thelamörk geothermal field. We also thank the staff of Hitaveita Akureyrar for their cooperation during the production test, in particular Mr. Ari Rögnvaldsson, and Drs. Valgardur Stefánsson and Þórdur Arason at Orkustofnun for critically reviewing the paper.

## REFERENCES


Arason, Þ., G. Axelsson and G. Björnsson, 1993: The TR-family of programs for analyzing tracer test data (User's Guide). National Energy Authority, Reykjavík, unpublished report.

Axelsson, G., 1991: Reservoir engineering studies of small low-temperature hydrothermal systems in Iceland. *Sixteenth Workshop on Geothermal Reservoir Engineering, Jan. 1991*, Stanford University, 143-149.

Axelsson, G., 1989: Simulation of pressure response data from geothermal reservoirs by lumped parameter models. *Fourteenth Workshop on Geothermal Reservoir Engineering, Jan. 1989*, Stanford University, 257-263.

Axelsson, G. and G. Björnsson, 1993: Detailed three-dimensional modeling of the Botn hydrothermal system in N-Iceland. *Eighteenth Workshop on Geothermal Reservoir Engineering, Jan. 1993*, Stanford University, 8 pp.

Axelsson, G., and Þ. Arason, 1992: LUMPFIT. Automated simulation of pressure changes in hydrological reservoirs. User's Guide, version 3.1, September 1992, 32 pp.

Axelsson, G., H. Tulinius, Ó.G. Flóvenz and Þ. Thorsteinsson, 1988: Geothermal resources of Hitaveita Akureyrar. The future outlook in 1988 (in Icelandic). Report OS-88052/JHD-10, National Energy Authority, Reykjavík, 35 pp.

Björnsson, G. and G.S. Bodvarsson, 1990: A survey of geothermal reservoir properties. *Geothermics, 19*, 17-27.

Bödvarsson, G., 1972: Thermal problems in the siting of reinjection wells. *Geothermics, 1*, 63-66.

Carslaw, H.W. and J.C. Jaeger, 1959: *Conduction of Heat in Solids.* Second Edition, Claredon Press, Oxford, 403 pp.

Flóvenz, Ó.G., 1984: Application of the head-on resistivity profiling method in geothermal exploration. *Geoth. Resources Council Trans., 8*, 493-498.

Flóvenz, Ó.G., G. Björnsson, G. Axelsson, G. Sverrisdóttir, H. Sigvaldason, J. Tómasson and S. Benediktsson, 1994: Laugaland at Thelamörk. Drilling and production testing during 1992 and 1993 (in Icelandic). National Energy Authority, Reykjavík, report in press.

Flóvenz, Ó.G., G. Axelsson, G. Sverrisdóttir and G. Björnsson, 1993: Geothermal resources of Hitaveita Akureyrar. The future outlook in 1993 (in Icelandic). Report OS-93025/JHD-06, National Energy Authority, Reykjavík, 48 pp.

Flóvenz, Ó.G., J. Tómasson and G. Björnsson, 1990: Exploration drilling at Thelamörk during 1989 (in Icelandic). Report OS-90014/JHD-02, National Energy Authority, Reykjavík, 38 pp.

Flóvenz, Ó.G., M. Kjartansdóttir, S. Einarsson, H. Eysteinsson and S.S. Gudlaugsson, 1984: Laugaland at Thelamörk. Geothermal research 1983-1984 (in Icelandic). Report OS-84095/JHD-17, National Energy Authority, Reykjavík, 78 pp.

Javandel I., C. Doughty and C.F. Tsang, 1984: *Groundwater Transport. Handbook of Mathematical Models.* Water Resources Monograph Series, 10, Am. Geophys. Union, 228 pp.

Milicevic, B., 1990: Interpretation and modeling of the temperature distribution at Thelamörk, N-Iceland, Report 90-10, UNU Geothermal Training Programme, Reykjavík, 36 pp.

Wang, G., 1991: Modeling of the Urridavatn low-temperature system in E-Iceland. Report 91-12, UNU Geothermal Training Programme, Reykjavík, 40 pp.


## APPENDIX A: DOWN-FLOW OF COLDER GROUNDWATER

A simple model is used to simulate the effects of down-flow of colder groundwater into a geothermal system during production (see also Wang, 1991 and Flóvenz et al., 1994). The model is presented in Figure A.1. It consists of an infinite groundwater system with a water temperature T´ and solute concentration C´. The production part of the geothermal system has a volume V, variable temperature T(t) and solute concentration C(t). The initial temperature and concentration are denoted by $T_0$ and $C_0$. In addition there is a constant inflow of R kg/s from the outer and deeper parts of the geothermal system with temperature $T_R$ and concentration $C_R$. A variable production of Q kg/s starts at time t = 0. The down-flow of groundwater is q kg/s, which is also variable. The conservation of the solute involved is given by:

$$V \frac{d(\rho_v \phi C)}{dt} + Q\,C = q\,C' + R\,C_R \qquad \text{(A-1)}$$

where $\rho_v$ is the density of water and $\phi$ the porosity of rocks in the production part of the system. This equation may be rewritten:

$$\frac{dC}{dt} + \alpha\,(q + R)\,C(t) = \alpha\,q\,C' + \alpha\,R\,C_R \qquad \text{(A-2)}$$

$$\text{with} \quad \alpha = 1 / (V \rho_v \phi)$$

The production may be approximated by

$$Q(t) \approx Q_i \quad \text{for} \quad t_{i-1} \le t < t_i\,, \quad i=1,2,\ldots \qquad \text{(A-3)}$$

with $t_0 = 0$. One may also define:

$$C_i = C(t_i) \quad \text{for} \quad i=0,1,2,\ldots \qquad \text{(A-4)}$$

with $C_0 = R$. In most instances one can assume that pressure changes occur much more rapidly than changes in chemistry and temperature. Therefore q(t) may be considered to be constant during each of the time intervals defined in equation (A-3), i.e. $q_i \approx Q_i - R$. The solution to equation (A-2) is then given by:

$$C_i \approx C_{i-1}\, e^{-\alpha Q_i \Delta t_i} + \frac{(Q_i - R)C' + RC_0}{Q_i} (1 - e^{-\alpha Q_i \Delta t_i}) \qquad \text{(A-5)}$$

$$\text{for} \quad i=1,2,\ldots$$

The conservation of energy in the model is given by:

$$V\frac{d((\rho c)T)}{dt} + c_v Q T = c_v q T' + c_v R T_R \qquad \text{(A-6)}$$

where $(\rho c)$ is the volumetric heat capacity of the reservoir and $c_v$ the heat capacity of water. This equation is of exactly the same form as equation (A-1) above. The solution for the temperature of the water produced is therefore given by:

$$T_i \approx T_{i-1}\, e^{-\beta Q_i \Delta t_i} + \frac{(Q_i - R)T' + RT_0}{Q_i}\left(1 - e^{-\beta Q_i \Delta t_i}\right) \qquad \text{(A-7)}$$

$$\text{for } i = 1,2,\ldots \qquad \text{with } \beta = \frac{c_v}{V(\rho c)}$$

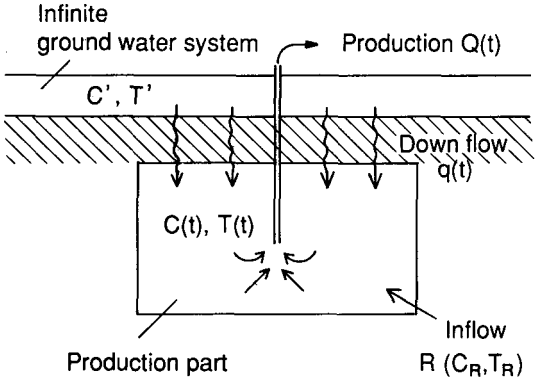


**Figure A.1:** *The simple model used for simulating down-flow of colder groundwater.*

## APPENDIX B: HEAT MINING BY INJECTION

The model used to simulate tracer return curves and predict heat mining by injection is shown schematically in Figure B.1. A constant mass flowrate, q, is pumped into an injection well and a constant mass rate, Q, pumped from a production well. A basic assumption in the formulation is that the flow channel, connecting the two wells, is along a narrow fracture zone. Furthermore, a near one-dimensional flow is assumed in the channel. The cross sectional area of the flow channel is $A = h \times b$, where h is its height and b is the width. The porosity of the flow channel is $\phi$ and its longitudinal dispersivity is denoted by $\alpha_L$. Molecular diffusion is neglected. The differential equation describing the tracer concentration in the channel, C, is as follows (Javandel et al., 1984):

$$D\frac{\partial^2 C}{\partial x^2} = u\frac{\partial C}{\partial x} + \frac{\partial C}{\partial t} \qquad \text{(B-1)}$$

where x is the distance from the injection well, t the time, u the mean velocity of the flow ($u = q/\rho A\phi$) and D the dispersion coefficient of the flow channel ($D = \alpha_L u$).

At time t = 0, a mass M of some tracer is injected and consequently transported along the flow channel to the production well. The tracer concentration in the produced fluid, c, is correlated to the fracture zone concentration by using the conservation of mass, i.e. $c\,Q = C\,q$. Therefore, solving the governing equations results in:

$$c(t) = \frac{uM}{Q}\frac{1}{2\sqrt{\pi Dt}}\, e^{-(x-ut)^2/4Dt} \qquad \text{(B-2)}$$

An automatic, least square computer code, TRINV, was developed to simulate tracer return curves in terms of M/Q, D and u in the above equation (Arason et al., 1993). The TRINV code allows for multiple flow channels connecting the two wells.

The analysis of tracer return curves provides an estimate of the cross sectional area A of the flow channel and, hence, the total contact area between the reservoir rock and the flow channel. Given the flow channel inlet temperature $T_n$, the channel height, length and width as well as the undisturbed rock temperature $T_0$, one can estimate the temperature of the injected fluid at any distance x along the flow channel. This is based on a formulation which considers a coupling between the heat convected along the flow channel and the heat conducted from the reservoir rock to the channel fluid. The solution to similar problems is, for example, presented by Carslaw and Jaeger (1959) and Bödvarsson (1972). The analytical solution for the fluid temperature $T_q(x,t)$, is:

$$T_q(x,t) = T_n + (T_0 - T_n)\,\mathrm{erf}\left[\frac{kxh}{c_w q\sqrt{\kappa(t - x/\beta)}}\right] \qquad \text{(B-3)}$$

valid at times $t > x/\beta$, with $\beta$ defined as $q/\rho_w hb$. Here k is the thermal conductivity of the reservoir rock and $\kappa$ its thermal diffusivity. In addition, $\rho_w$ is the density and $c_w$ the heat capacity of water. The temperature of the produced fluid, assuming a constant temperature, $T_0$, for all feedzones in the production well, except the one connected to the flow channel, is finally given by:

$$T(t) = T_0 - \frac{q}{Q}\left(T_0 - T_q\right) \qquad \text{(B-4)}$$

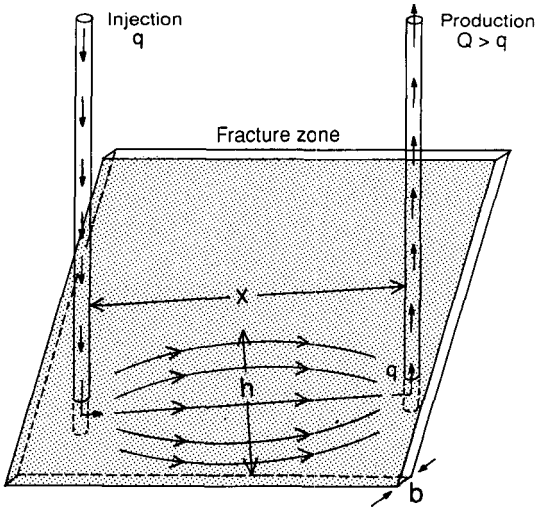


**Figure B.1:** *A simple model of a fracture-zone connecting a reinjection-production well dipole.*

PROCEEDINGS, Nineteenth Workshop on Geothermal Reservoir Engineering
Stanford University, Stanford, California, January 18-20, 1994
SGP-TR-147

# CHARACTERIZATION OF SUBSURFACE FRACTURE PATTERNS IN THE COSO GEOTHERMAL RESERVOIR BY ANALYZING SHEAR-WAVE SPLITTING OF MICROEARTHQUAKE SEISMOGRAMS

*Min Lou and Jose A. Rial*

*Wave Propagation Laboratory, Department of Geology*
*University of North Carolina at Chapel Hill, NC27599*

## ABSTRACT

A large number of microearthquake seismograms have been recorded by a downhole, three-component seismic network deployed around the Coso, California geothermal reservoir. Shear-wave splitting induced by the alignment of cracks in the reservoir has been widely observed in the recordings. Over 100 events with body wave magnitude greater than 1.0 from microearthquakes recorded since March of 1992. have been processed. The results show that most events with paths within the critical angle that defines the shear-wave window, display clear shear-wave splitting, and the fast shear waves have predominant polarization directions for most stations. The rose diagrams of fast shear-wave particle motion suggest that there are three predominant fracture strikes (or directions of maximum horizontal stresses) in the Coso geothermal field: *N 40°-60°E*, *N 0°-25°E*, and *N 25°-35° W*, which are consistent with photographically or magnetically mapped alignments on the surface. From the delay time of split shear waves, we estimate that the crack density in the most active geothermal reservoir area (above *3.00km* depth) ranges between *0.030* and *0.055*, values commonly found in other hydrocarbon or geothermal reservoirs.

## 1. INTRODUCTION

Shear-wave splitting due to the alignment of vertical cracks in the crust has been widely observed in a variety of tectonic settings and data gathering experiments; from earthquake recordings to controlled-source seismic data. It has also been recognized that the polarization of the fast split shear wave is usually parallel to the local strike of cracks (or direction of the maximum horizontal stress), and the time delay between fast and slow shear waves is directly related to the intensity of crack-induced anisotropy in the medium (Figure 1; see also Crampin 1987, Crampin and Lovell 1991).

Therefore, the interpretation of shear-wave splitting is an important diagnostic tool to determine the direction and evaluate the bulk density of subsurface fractures in hydrocarbon or geothermal reservoirs (Cliet et al 1991, Muller 1991, Sachpazi and Hirn 1991, Sato et al 1991). We here report on the determination of fracture patterns and crack density in the Coso geothermal field by the above mentioned methods using a large number of microearthquake seismograms recorded by a downhole, three-component seismic network (Malin 1993).

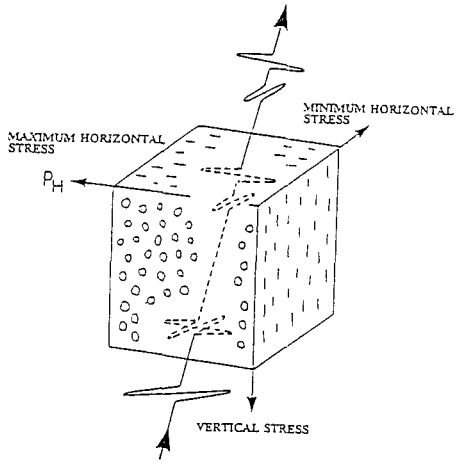


Fig. 1. Schematic illustration of stress-aligned cracks and shear-wave splitting. The cracks are aligned by the typical stress relationships in the subsurface crust. the leading split shear wave is polarized parallel to the strike of cracks (after Crampin 1987).

*Methodology*

Shear-wave splitting is best identified by the examination of polarization diagrams of the two horizontal orthogonal components of shear-wave arrivals. Almost all shear-wave first arrivals are observed to have linear polarization. After a delay of usually hundredths of a second, the first motions are followed by abrupt changes in direction that evolve into elliptical motion, or further linear motion along different polarization directions as the time delay becomes long enough to separate the late signal from the initial arrival (e.g. see Figure 2).

To quantitatively determine the polarization and time delay of split shear waves, the following processing method is used: First, the two horizontal components of the shear wave seismograms are numerically rotated to search for the orientation along which the ratio of the projections of the particle displacement reaches a maximum. In a time window that contains only the fast shear-wave arrival, the azimuth at which this maximum ratio occurs is taken as the polarization direction of fast shear wave (Shih, Meyer and Schneider 1989). Second,

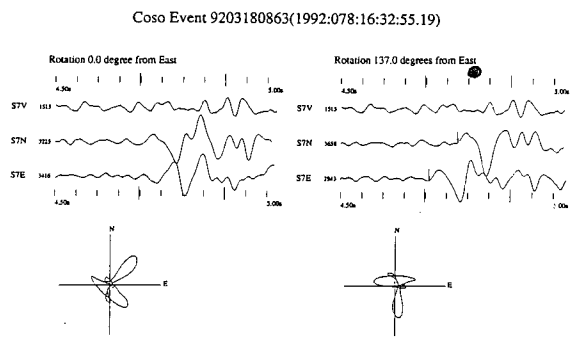


Fig. 2. Shear-wave splitting recorded on station S7, from event 9203180863. The splitting is best detected from the polarization diagram of the horizontal components(S7N, S7E) over a windowed shear-wave train. The polarization direction of the leading shear-wave is about $137^{o}$ measured counter-clockwise from an assumed East* direction. The two split shear waves (fast and slow) are clearly identified after the seismograms are rotated into the polarization directions corresponding to the fast and slow shear waves.

after the appropriate rotation of the seismogram components to the azimuth angle previously determined has been performed, the time delay between the split shear waves is measured by a standard cross-correlation function.

Although straightforward, the detection and analysis of shear-wave splitting must be based on a large set of shear-wave seismogram data. The behavior of shear-wave splitting above small earthquakes is usually very complicated, because of the complexity of the source signal, subsurface geology structure, and surface topography. One major restriction to the analysis of shear-wave splitting is that, to obtain correct interpretation of split shear-waves, the recording site needs to be within the shear-wave window. The shear-wave window beneath a recording site is defined by the critical angle *arcsin (Vs/ Vp)*. For angles of incidence greater than the critical angle (outside the shear-wave window), shear waves have such interaction with the free surface that almost all similarities with the incoming waveform are irretrievably lost (Booth and Crampin 1985). The critical angle defining the shear-wave window is about $35^{o}$ in a half space with a Poisson' ratio of *0.25*. However, ray curvature due to low-velocity surface layers usually allows the effective window to be enlarged to angles of incidence of $45^{o}$ or $50^{o}$.

## 2. SHEAR-WAVE SPLITTING FROM THE COSO MICROEARTHQUAKE SEISMOGRAMS

The Coso geothermal area is a very active seismic zone with an average of 20 microearthquakes per day; about half of them associated with the geothermal field activity (Malin 1993). Most of these events have been located and cataloged by Peter Malin's seismology group at Duke University. These seismic data offer a unique opportunity to study shear-wave splitting and anisotropy in the reservoir area.

From the numerous Coso microearthquakes recorded since March of 1992, we restricted the shear-wave analysis to those events with body wave magnitudes greater than *1.0*. The analysis was restricted to high signal/noise ratio, clear seismograms, not suspect of complications and presenting an impulsive and short shear-wave signal with shear-wave motion polarized primarily in the horizontal plane, i.e., events with paths within the shear-wave window.

To illustrate, Figure 2 shows a typical example of shear-wave splitting recorded on station S7, from event 9203180863. The splitting is clearly detected on the polarization diagram of the horizontal components. Figure 3 shows the azimuth function, i.e., the ratio of the horizontal components of particle displacement in a time window that contains only the fast shear-wave arrival. From the azimuth function we determine by inspection that the polarization direction of the leading shear-wave is along the azimuth $137^{o}$ measured counter-clockwise from the East (E*) direction[1]. In Figure 2 the two split shear waves (fast and slow) are clearly identified after the seismograms are rotated so as to coincide with the

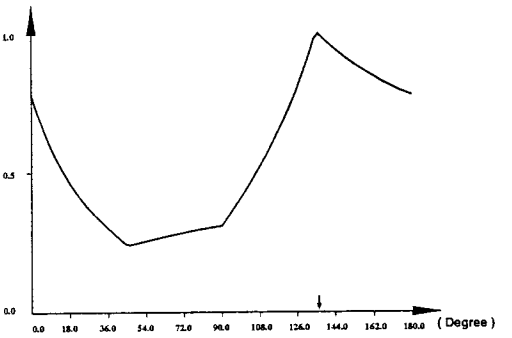


Fig. 3. The polarization direction of the leading shear-wave is found at azimuth $137^{o}$ measured counter-clockwise from the East* direction, for event 920380863.

polarization directions of the fast and slow shear waves. From the cross-correlation function of these two rotated components we measure the time delay (about 66 ms in this example) at which the maximum in the cross-correlation function occurs (Figure 4). To illustrate the consistency of the results, Figures 5a - b show the shear-wave splitting recorded on the same station S7 as in

[1]This is the East direction in the down-hole instrument frame. The actual, geographical direction of polarization is obtained after correcting for instrument mis-orientation. The correct geographical directions of each station's components are obtained from the polarization of the first arrivals of P-waves from a number of well-located regional microearthquakes. In the following the notation E* is used to indicate (uncorrected) instrumental East direction.

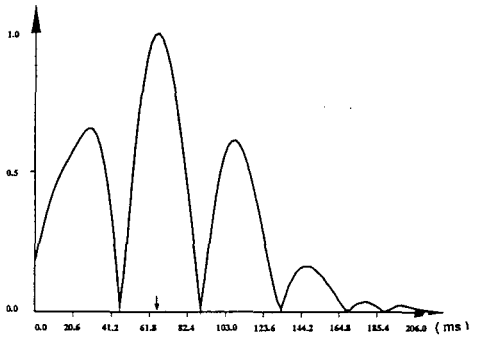


Fig. 4. The cross-correlation function of the two rotated horizontal components (fast and slow) of the seismograms recorded on station S7, from the event 9203180863. The time delay of split shear waves is taken as *66 ms*, at which the maximum of the cross-correlation function occurs.

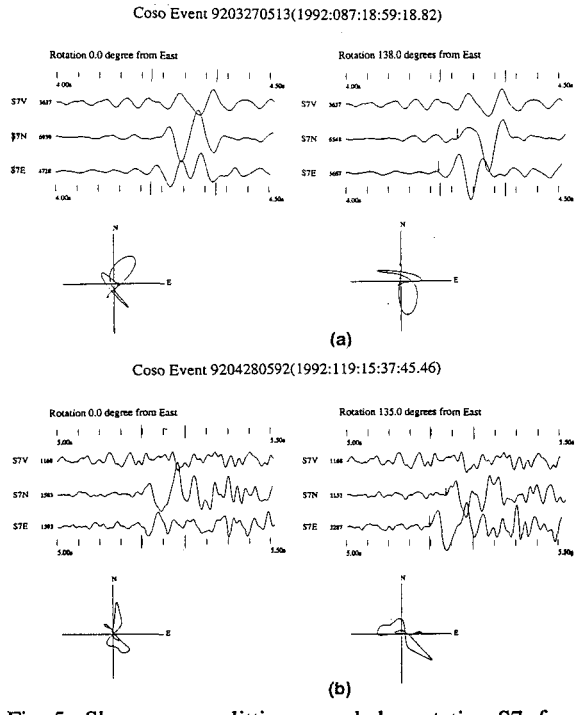


Fig. 5. Shear-wave splitting recorded on station S7, from (a) event 9203270513, and (b) event 9204280592. The polarization directions of the leading shear wave of the two events are about $138^o$ and $135^o$, respectively, measured counter-clockwise from the East* direction. They are almost the same azimuth as the event in Figure 2. The time delays of split shear waves of both events are about *40ms*, which can be easily measured after the two horizontal components of shear waves are rotated into fast and slow shear wave polarization directions.

Figure 2, but from two different events, 9203270513 and 9204280592, which approach the station from different directions. The polarization directions of the leading shear waves for two events are $138^o$ and $135^o$ from the E* direction. Time delays for both events are about *40 ms*. Thus, the polarization directions of the leading shear waves recorded at station S7 are almost the same (within 2 degrees) for all three events. This implies that the observed shear-wave polarizations are not due to the source radiation but the result of crack-induced anisotropic structure between the sources and the station.

Similarly, in Figures 6a -c, we show the shear-wave splitting recorded on a different station, N4, from three different events 9306030128, 93060040151 and 93060040155. We find almost the same polarization direction ($70^o$ measured counter-clockwise from the E* direction in this case) for three events. The time delays of split shear-waves for these three events are *56ms*, *53ms* and *41ms*, respectively.

## 3. RESULTS

We processed and analyzed shear-wave splitting from over 100 microearthquake events around the Coso geothermal area. A catalog containing shear-wave splitting (polarization direction and time delay) and source locations has been assembled. From the catalog of shear-wave splitting, we infer the following information on the strike of fracture (or direction of the maximum horizontal stress) and crack density in the Coso geothermal field:

### (1) STRIKE OF FRACTURES (OR DIRECTION OF THE MAXIMUM HORIZONTAL STRESS)

To infer the local strike of fracture in the Coso area, we have plotted the rose diagrams of the fast shear-wave polarization direction vs frequency for most Coso network stations. Figure 7 shows the rose diagrams of the corrected polarization directions of leading shear wave for eight stations. Almost every rose diagram has a dominant polarization direction, which is here interpreted as the local strike of fracturing or direction of the maximum horizontal stress. Basically, there are three predominant strike groups observed in these rose diagrams: $N\ 40^o\text{-}60^o\ E$(for stations S2, S7, N5), $N\ 0^o\text{-}25^o\ E$(for stations S1, S4, S8, N1), and $N\ 25^o\text{-}35^o\ W$(for station N4). These three predominant fracture trends seem to be generally consistent with the photographically mapped lineaments ($N60^oE$, *N-S*, and $N35^oW$) (Bryan et al. 1990), and magnetically mapped lineaments ( $N40^oE$, *N-S*, and $N55^oW$) (Moore and Erskine, 1990). The Coso surface geology map (Stinson 1977) suggests that the three predominant strikes are related to north and northeast trending faults, as well as northwest trending intrusive dike features.

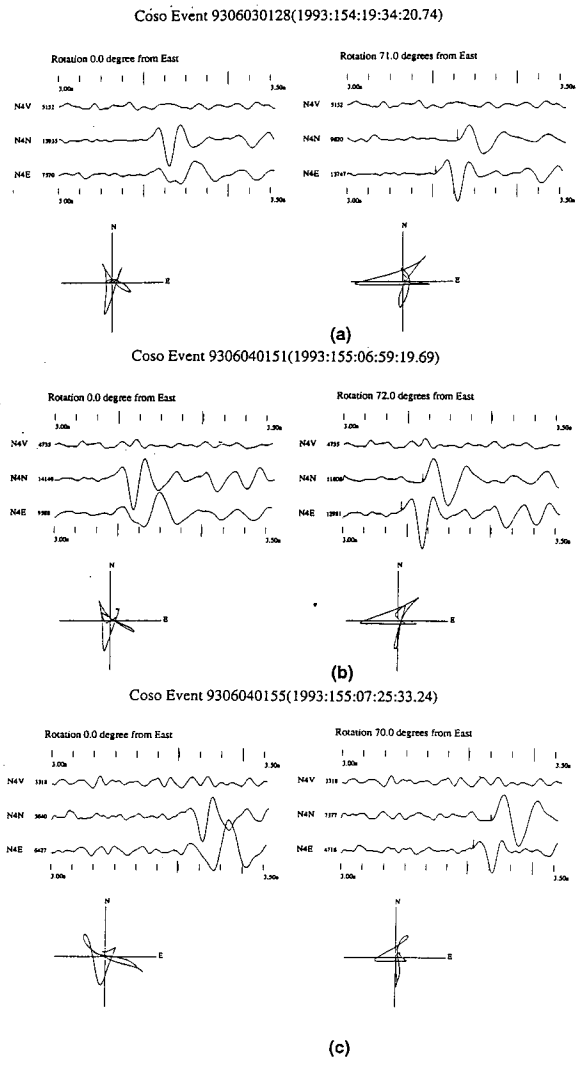


Fig. 6. Shear-wave splitting recorded on station N4, from (a) the event 9306030128, (b) event 93060040151, and (c) event 93060040151. The three events have the almost same polarization direction of the leading shear waves (about $70^o$ measured counter-clockwise from the East* direction). The time delays of split shear waves of these three events are *56ms*, *53ms* and *41ms*, respectively.

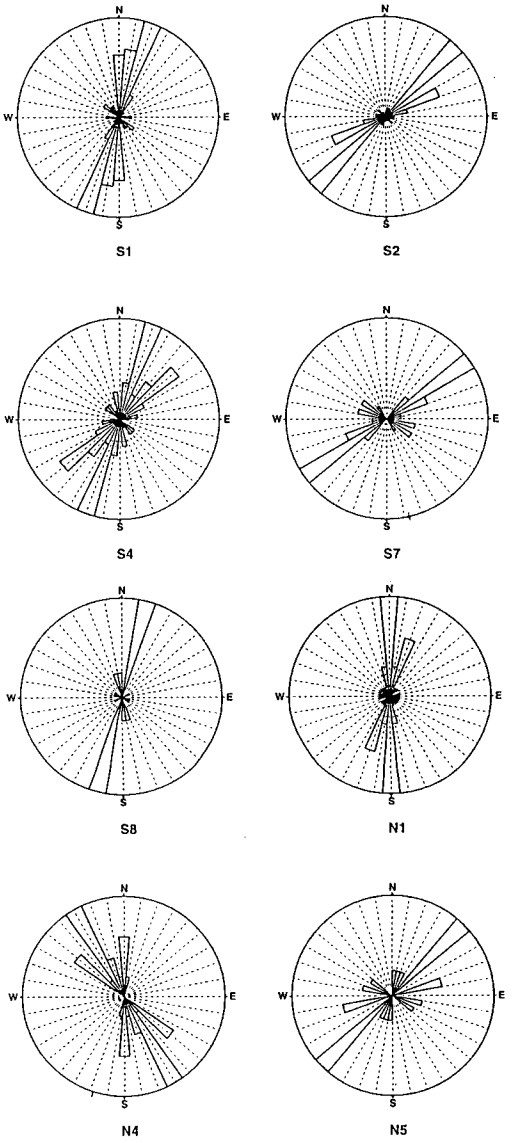


Fig. 7. Rose diagrams of the polarization directions of leading shear waves for the stations S1, S2, S4, S7, S8, N1, N4, and N5 of the Coso seismic network, which show the predominant strike of fractures (directions of the maximum horizontal stress).

## (2) TIME DELAYS OF SPLIT SHEAR WAVES AND CRACK DENSITIES

We have measured the time delays of split shear waves for each processed event. We use the crack density (*CD*) ($CD=Na^3/V$, where $N$ is the number of cracks of average radius $a$ in volume $V$) instead of the time delay to measure the intensity of crack-induced anisotropy in the medium. If we assume that anisotropy is caused by aligned water-filled cracks contained in an otherwise isotropic homogeneous medium, and that each crack is like a thin disk opening radius much smaller than wavelength of shear-waves, then the velocities of two split shear waves can be written (Hudson 1981):

$$V_{SP}^2=\beta^2\,[1 - 8/3\,\varepsilon\,\alpha^2/(3\alpha^2-2\beta^2)\,(cos4\theta +1)] \quad (1)$$

$$V_{SR}^2 = \beta^2 [1 - 8/3\, \varepsilon\, a^2/(3\alpha^2 - 2\beta^2)(\cos 2\theta + 1)] \quad (2)$$

Here $V_{SP}$ and $V_{SR}$ are velocities of quasi- shear waves that are polarized parallel and at right-angle to the plane of incidence, respectively; $\varepsilon$ is crack density (*CD*); $\theta$ is the angle of propagation from the strike of cracks; $\alpha$ and $\beta$ are compressional and shear wave velocities in the isotropic rock matrix, respectively.

The time delay $\tau$ is given by the expression

$$\tau = ( 1/V_{SP} - 1/V_{SR} ) L \quad (3)$$

where $L$ is a propagation distance between source and receiver.

If we assume that the Poission's ratio of the isotropic rock matrix is 0.25, and $\varepsilon << 1$, we have the following approximation relation between $\tau$ and $\varepsilon$ ( Sato et. al., 1991):

$$\tau = 4\varepsilon ( \cos 4\theta - \cos 2\theta ) L / 7\beta. \quad (4)$$

Using the above formulation and the isotropic velocity model in the Coso area (Malin and Erskine 1990, Alvarez 1992), we estimate that the crack density ranges between *0.010* and *0.055* throughout the Coso area, changing with different depths and locations. Statistically, the Coso area seems to be divided into three depth layer groups with different crack densities: For a layer above the depth of *2.50km*, the crack density is between *0.040-0.055*. This crack density is higher than those (<=0.04) commonly found in normally cracked sedimentary, metamorphic, and igneous rocks (Crampin et al. 1986, Crampin and Booth 1985, Robert and Crampin 1986), but since above this depth there is an active geothermal reservoir area, the higher crack density is expected. The crack density in this depth area is also near to that (>=0.05) found in a Japanese geothermal reservoir (Sato, Matsumoto and Nitsuma 1991). For layer depth between *2.50km* and *3.00km*, the crack density ranges between *0.030* and *0.040*. This is a crack density commonly found in a number of hydrocarbon sedimentary reservoir rocks (Crampin et al 1986). For layer depth below *3.00km*, the crack density varies from *0.010* to *0.030*, which is consistent with the known crack density in the crust.

## 4. CONCLUSIONS AND DISCUSSION

Shear-wave splitting induced by the alignment of cracks in the Coso geothermal field has been clearly identified from most events with paths within the critical angle that defines the shear-wave window. The polarization directions of leading shear-waves suggests that there are three predominant fracture strikes around the area: *N 40°-60° E*, *N 0°-25° E*, and *N25°-35°W*, which are generally consistent with photographically or magnetically mapped alignments on the surface. From the delay time of split shear waves, we estimate that the crack density in the most active geothermal reservoir area (above *3.00km* deep) ranges between *0.030* and *0.055*, which is commonly found in other geothermal or hydrocarbon reservoirs. The variation in time delays of split shear waves and crack density observed among different depths and stations in the Coso area suggests that near-station effects may contribute heavily to anisotropy effects. A local stronger near-surface anisotropy may overlie a small deeper crustal anisotropy (Sachpazi and Hirn 1991). It appears necessary to use a tomographic inspection method to delineate those portions of the reservoir having different crack densities by inverting the shear-wave delays of different paths. Shear wave trains contain more information than P-wave trains, and shear-wave splitting is very sensitive to the change of the orientation, distribution, and saturation of fractures in the rockmass. Therefore, any time change in the shear-wave splitting character of the recorded seismograms excited by pumping and injection activities may be used to monitor the production and operation process in the geothermal reservoirs.

## ACKNOWLEDGEMENTS

This research is co-sponsored by the US Navy (Geothermal Program Office, Naval Air Weapons Station, China Lake), Idaho National Engineering Laboratory (EG&G), the California Energy Company, Inc., and the Department of Energy (Geothermal Division), under subcontract No. C93-160437.
We thank Peter Malin for many helpful discussions and suggestions.

## REFERENCES

Alvarez, M.G. (1992) *The seismotectonics of the southern Coso range observed with a new borehole seismographic network*, Master degree thesis, Duke University.

Booth, D.C. and S. Crampin (1985) Shear-wave polarizations on a curved wavefront at an isotropic free-surface, *Geophys. J. R. astr. Soc.*, **83**, 31-45.

Bryan, J.G., E. Baumgrartner, and W. Austin (1990) Remotely sensed controls on heat flow within the Coso geothermal area: implications for further exploration, Coso Field Trip, edited by Moore J. and Erskine M., AAPG EMD **1**, 41-60.

Cliet, Ch., L. Brodov, A. Tikhonov, D. Marin and D. Michon (1991) Anisotropy survey for reservoir definition, *Geophys. J. Int.*, **107**, 417-427.

Crampin, S. (1987) Geological and industrial implications of extensive-dilatancy anisotropy, *Nature*, **328**, 491-496.

Crampin, S. and D.C., Booth (1985) Shear-wave polarization near the North Anatolian Faults. II. Interpretation in terms of crack induced anisotropy. *Geophys. J. Roy. Astr. Soc*, **83**, 75-92.

Crampin, S., I. Bush, C. Naville, and D.B., Taylor (1986) Estimating the internal structure of reservoirs with shear-wave VSPs. The Leading Edge, **5**, 11, 35-39.

Crampin, S and J. Lovell (1991) A decade of shear-wave splitting in the Earth's crust: what does it mean? what use can we make of it? and what should we donext?, *Geophys. J. Int.* **107**, 387-407.

Crampin, S., R. Evens and S.B. Ucer (1985) Analysis of records of local earthquakes: the Turkish Dilatancy Projects (TDP1 and TDP2), *Geophys. J. R. astr. Soc.*, **83**, 31-45.

Hudson, J.A. (1981) Wave speeds and attenuation of elastic waves in material containing cracks, *Geophys. J. R. astr. Soc.*, **64**, 133-150.

Malin, P. (1993), Report on workshop on extensional Process in Coso and Indian Wells Valley Area, July 23, 1993, Duke University.

Malin, P.E. and M.C. Erskine (1990) Coincident P and SH reflection from Basement rocks at the Coso geothermal field, *AAPG Bulletin plus abstracts 1990 San Francisco meeting, June 6 to 8, 1990.*

Moore J. and M. Erskine M (editors) (1990) Coso Field Trip, AAPG EMD 1, 41-61.

Mueller, M.C (1991) Prediction of lateral variability in fracture intensityusing multicomponent shear-wave surface seismic as a precursor to horizontal drilling in the Austin Chalk, *Geophys. J. Int.*, **107**, 409-415.

Robert, G. and S. Crampin (1986) Shear-wave polarization in a Hot Rock geothermal reservoir: Anisotropic effects of fractures, *Int. J. Rock Mech Min. Sci. Geomech. Abstr.* **23**, 291-302.

Sachpazi, M and A. Hirn (1991) Shear-wave anisotropy across the geothermal field of Milos, Aegean volcanic arc. *Geophys. J. Int.*, **107**, 673-685.

Sato, M., N. matsumoto and H. Niitsuma (1991) Evaluation of geothermal reservoir cracks by shear-wave splitting of acoustic emission, *Geothermics,* **20**, 197-206.

Shih, X.R., P. Meyer, P. and J.F. Schneider (1989) An automated, analytical method to determine shear-wave splitting. *Tectonophysics*, **165**, 271-278.

Stinson, M (1970). Geology of the Haiwee Reservoir 15' Quadrangle, Inyo County, California: California Division of mines and Geology, Map Sheet 37.

PROCEEDINGS, Nineteenth Workshop on Geothermal Reservoir Engineering
Stanford University, Stanford, California, January 18-20, 1994
SGP-TR-147

# MEASUREMENT OF INJECTIVITY INDEXES IN GEOTHERMAL WELLS WITH TWO PERMEABLE ZONES

Jorge A. Acuna

Department of Geothermal Resources, ICE
Instituto Costarricence de Electricidad
P.O.Box 10032-1000, San Jose, Costa Rica

## ABSTRACT

Injectivity tests in wells with two permeable zones and internal flow is analyzed in order to include the usually severe thermal transient effects. A theoretical analysis is performed and a method devised to obtain information from the thermal transient, provided that temperature is measured simultaneously with pressure. The technique is illustrated with two real tests performed at Miravalles, Costa Rica. It allows to estimate total injectivity index as well as the injectivity index of each one of the two zones separately. Correct position of measuring tools and nature of spontaneous internal flow is also discussed.

## INTRODUCTION

Miravalles geothermal field in Costa Rica is a water dominated reservoir whose permeability is attributed to fracture systems embedded in an otherwise low permeability geologic formation. Permeable zones are usually localized and many wells present two or more zones between which spontaneous flow occurs. To characterize these wells with respect to their productivity potential previously to production tests, two parameters are looked for, the injectivity index and hydraulic transmissivity from pressure transient injection tests.

The injectivity index of a well is a measurement related to permeability, but considered poorer in quality when compared to transmissivity obtained from pressure transient tests. Wells in fractured systems, however, that intercept only a few fractures often deviate from conventional models for fractured systems [3]. During pressure transient tests, systems of fractures with only a few feeding points to a well may behave as networks with fractal geometry [1]. This type of systems may approach asymptotically a constant pressure when subject to injection at constant flow rate, even when they are still behaving as systems of infinite size [1]. This fact corroborated numerically [1] and observed in real tests [2] [3], gives new reliability to the old injectivity index measurement.

Injectivity indexes have been proven reliable in Miravalles to assess productivity of wells and also to predict performance of injector wells. Our experience, as well as the experience in other geothermal fields [5], shows that this simple measurement relates closely to the productivity index of wells. Injectivity is also easy to obtain during drilling and just after completion of new wells.

Pressure transient analysis of injection tests in geothermal wells, such as fall-offs and step rate tests, may yield hydraulic transmissivity and a product of storativity-skin factor in wells of low permeability [4]. In wells of high permeability, such as many wells at Miravalles, thermal transients caused by different temperature of the injected fluid, spontaneous internal flow and thermal recovery of wells usually dominate over the comparatively small pressure transient response and the interpretation becomes too complicated [5].

To minimize thermal effects it is recommended to locate the pressure tool in the main permeable zone [5]. However, there is no recipe for wells with more than one permeable zone and none of them appearing as clearly dominant. In some wells with two zones at Miravalles, it was attempted to locate the tool in the upper zone and later in the lower zone, obtaining severe thermal effects in both cases. This causes the determination of the hydraulic transmissivity $kh$ from injection tests to be quite ambiguous. Thus, we have to rely only on injectivity tests.

In these tests, the normal practice is to eliminate thermal effects by making a massive injection to cool down the well before the test [4], and then proceed with the test itself. In practice, however, it is often difficult to supply the usually large amounts of water required. Drilling rig time expense is also a concern.

This paper describes the theory and practical application of a simple approach to obtain good values of injectivity indexes in wells with two permeable zones previously identified. It is argued that information from thermal transients can be used to characterize each one of two permeable zones separately or, at least, improve interpretation of tests affected by severe thermal effects.

## THEORETICAL MODEL AND ASSUMPTIONS

It is assumed that we have a well with two permeable zones with injectivity index $ii_{up}$ for the upper zone and $ii_{lo}$ for the lower zone. It is also assumed that the indexes remain constant to changes in flow rate and temperature of the circulating fluid.

For short tests, such as the ones we perform at Miravalles, the extension of the cold spot caused by injection is small, therefore, properties of reservoir fluid, not injected fluid, are the ones that dominate the behavior [4][6]. The assumption of no change of the injectivity with changes in temperature of the injected fluid is, thus, justified.

The two zones are separated by a distance $H$ and the upper zone has an overpressure $SP$ with respect to the lower zone (this overpressure could also be an underpressure). Reservoir pressure in the upper zone is $p^*_{up}$ and the reservoir is initially at the same temperature $T^*$.

### SPONTANEOUS FLOW WITHOUT INJECTION

Based on the initial conditions it is possible to establish the reservoir pressure in the lower zone $p^*_{lo}$ as

$$p^*_{lo}=p^*_{up}-SP+\rho_{T^*}gH \qquad (1)$$

where $\rho_{T^*}$ is the density of the reservoir fluid at its initial temperature $T^*$.

Once the well has been drilled and the two permeable zones are communicated, spontaneous flow is established. Assuming isothermal temperature profile, the flow rate produced by one zone is the same one accepted by the other and we have

$$ii_{up}(p^*_{up}-p_{up})=-ii_{lo}(p^*_{lo}-p_{lo}) \qquad (2)$$

Considering also negligible friction pressure losses in the well, pressure at the lower zone can be calculated from the pressure in the well at the upper zone as $p_{up}+\rho gH$, where $\rho$ is the density of the fluid in the well that changes as the well recovers thermally. An expression for pressure at the upper zone of the well at a given time can be written as

$$p_{up}=p^*_{up}-\frac{ii_{lo}}{ii_{up}+ii_{lo}}(SP+\Delta\rho gH) \qquad (3)$$

where $\Delta\rho=\rho-\rho_{T^*}$.

According to equation (3), in wells with spontaneous flow, the "static" pressure does not reflect the reservoir pressure even if measured in front of one of the permeable zones.

The circulating flow rate can then be calculated as

$$Q_{up}=-Q_{lo}=\frac{ii_{up}ii_{lo}}{ii_{up}+ii_{lo}}(SP+\Delta\rho gH) \qquad (4)$$

Even when $SP=0$ there will be flow between the two zones. Thus, spontaneous internal flow may be caused only by the pressure gradient created by changes in density due to cooling of the well. If this is the case, flow should stop once the well reaches thermal equilibrium with the formation. A fundamental characteristic of this type of flow is that its direction must be downwards (down-flow) because it is driven by gravity forces.

### FLUID INJECTION

To consider injection of fluid, the mass balance equation is stated again but including the injected flow rate $Q$, in this case well pressure in the upper zone is given by

$$p_{up}=p^*_{up}-\frac{ii_{lo}}{ii_{up}+ii_{lo}}(SP+\Delta\rho gH)+\frac{Q}{ii_{up}+ii_{lo}} \qquad (5)$$

The corresponding expression for produced (positive) or accepted

(negative) flow rate in the upper zone is

$$Q_{up}=\frac{ii_{up}}{ii_{up}+ii_{lo}}(ii_{lo}(SP+\Delta\rho gH)-Q) \quad (6)$$

Flow rate from the formation to the well in the upper zone $Q_{up}$ can be zero when the injected flow rate $Q$ is equal to $k_{lo}(SP+\Delta\rho gH)$. If, however, injected flow rate is less than that, there will be production of fluid from the upper zone, otherwise, the upper zone will accept injected fluid.

The lower zone, on the other hand, will always accept fluid at a flow rate given by

$$Q_{lo}=-\frac{ii_{lo}}{ii_{up}+ii_{lo}}(ii_{up}(SP+\Delta\rho gH)+Q) \quad (7)$$

All previous equations are valid at a given time because it is assumed that temperature is changing continuously. To incorporate the variable time in the analysis we discretize the process in injection stages as follows.

Let us assume that there are two stages of injection at flow rates $Q_a$ and $Q_b$ that could be equal. It is also assumed that temperature of the well between the two zones is such that the respective densities are $\rho_a$ and $\rho_b$. It can be shown that the pressure change $\Delta p$ measured in the upper zone is related to the change in flow rate $\Delta Q=Q_b-Q_a$ and to the change in density $\Delta\rho=\rho_b-\rho_a$ as follows

$$\Delta p_{up}=\frac{\Delta Q}{ii_{up}+ii_{lo}}-\frac{ii_{lo}}{ii_{up}+ii_{lo}}gH\Delta\rho \quad (8)$$

If the second flow rate $Q_b$ is larger than the first one $Q_a$, the change in flow rate will be positive as well as the density change, therefore, if there is an important difference between temperature between both stages, the pressure change would be **underestimated** if the tool is located at the upper zone. If the injectivity index is calculated in the conventional way as $ii=\frac{\Delta Q}{\Delta p}$, it will be overestimated. Notice the possibility of having negative pressure changes when the lower zone has good injectivity with respect to the upper zone and when the temperature changes are large.

The pressure change in the lower zone is given by

$$\Delta p_{lo}=\frac{\Delta Q}{ii_{up}+ii_{lo}}+\frac{ii_{up}}{ii_{up}+ii_{lo}}gH\Delta\rho \quad (9)$$

According to equations (8) and (9), thermal effects on the total pressure change depend on the relative magnitude of the injectivity of the two zones. This relationship constitutes the basis for extracting information of the two zones separately.

In general, when the pressure change at a depth $X$ $(0 < X < H)$ below the upper zone is considered, we have

$$\Delta p=\frac{\Delta Q}{ii_{up}+ii_{lo}}+\frac{X(ii_{up}+ii_{lo})-Hii_{lo}}{ii_{up}+ii_{lo}}g\Delta\rho \quad (10)$$

An important result of this expression is that there is a given depth $X_o$ where measurements are not affected by thermal effects and this depth is given by

$$X_0=H\frac{ii_{lo}}{ii_{up}+ii_{lo}} \quad (11)$$

As expected, this distance approaches zero (upper zone) only when the index of the upper zone is very large with respect to the one of the lower zone and $H$ when the injectivity of the lower zone is very large with respect to the one of the upper zone. In practice, however, this equation is important once the individual injectivity indexes are known because it allows to measure pressure changes without thermal interference, a feature highly desirable in pressure transient tests.

## PRACTICAL APPLICATION OF THE MODEL

As mentioned above, before applying the described model for injection test interpretation, it is necessary to know the location of the two permeable zones. We usually do this by means of two temperature profiles of the well. The first one is done without injecting and after several hours of thermal recovery. Immediately after this first profile, injection is started at a flow rate of 15 to 20 liters per second. The second profile is the injecting profile that is made one or two hours after starting injection.

Figure 1 shows this two profiles for well A in Miravalles geothermal field. The "static" profile shows a thermal peak that corresponds to the upper permeable zone. Immediately below, there is a zone with constant temperature in which the spontaneous

flow is taking place. The injecting profile shows the location of the upper zone as a small change of gradient but it shows clearly the lower zone. With this information it is possible to conclude that the two zones are separated by a distance close to 550 m and both are accepting injected water.

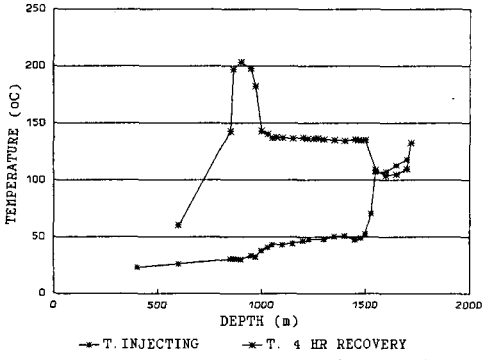


**Figure 1.** Temperature profiles with and without injection for well A in Miravalles, Costa Rica, showing the location of two permeable zones separated 550 m approximately.

To apply the model to injectivity test interpretation, we use equations (8) and (9) for the increments of pressure that occur between successive times of the test.

Although $\Delta Q$ should include wellbore storage effects, these are disregarded because they disappear after short time. On the other hand, $\Delta\rho$ should take into consideration the temperature change in the entire column of fluid between the two zones. It was assumed before, however, that the entire column of fluid has the same temperature equal to the one measured by the tool located inside the internal flow region.

To perform an injectivity test we introduce in the well a tandem of tools to measure pressure and temperature. The tandem must be located the closest possible to the selected permeable zone but always inside the region where the internal flow occurs.

The analysis technique consists of calculating density for each time based on the corresponding pressure and temperature. It has to be remembered that the dependence between density of liquid water and pressure is very small. Using consecutive data, changes $\Delta Q$ and $\Delta\rho$ are calculated. Even when measured temperature may not correspond to the actual average temperature of the region between permeable zones, the change in temperature and, thus, the change in density is very likely to correspond better to the true change in average density. Using guessed values for $ii_{up}$ and $ii_{lo}$, the pressure change $\Delta p$ can be calculated using equation (8) or (9) depending on the location of the tandem of tools.

The theoretical pressure for a given time would be equal to an initial pressure plus the summation of the pressure changes that occur up to that given time. The final step is to adjust the values of the indexes $ii_{up}$ and $ii_{lo}$ to obtain a reasonable match between the measured and calculated pressures. The initial pressure is usually set equal to the one measured by the tool, but it can also be adjusted, keeping the difference below the error associated with the tool for measurement of absolute pressure.

## APPLICATION TO ACTUAL CASES

The first case to be analyzed corresponds to an injectivity test in well A at Miravalles. As shown in Figure 1, the permeable zones are separated 550 m. Figure 2 shows the injectivity test performed with the tandem of instruments in the upper zone at 970 m. The temperature curve shows a maximum temperature above 200°C. This indicates that the tool was located a little above the spontaneous flow

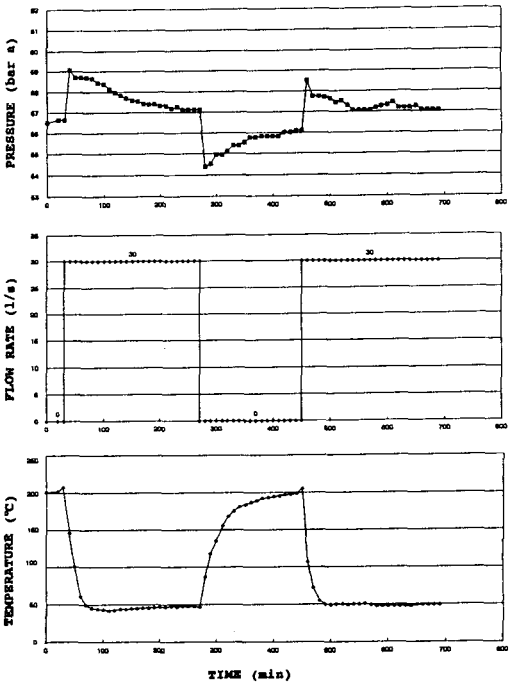


**Figure 2.** Variation of pressure, flow rate and temperature during injectivity test of well A. Tools located in the upper permeable zone.

region. The "static" profile of Figure 1 shows that the maximum temperature that occurs in this region after four hours of recovery is approximately 140°C. The stage without pumping lasts 3 hours, therefore, the thermal variation that occurs during the injectivity test is linearly corrected to give a maximum temperature of 140°C, keeping the same minimum temperature.

Figure 3 shows the best fit for the pressure curve obtained after manual matching. The index in the upper zone $ii_{up}$ is 2.5 (l/s)/bar, the one of the lower zone $ii_{lo}$ is 5 (l/s)/bar. The total injectivity index of this well is, therefore 7.5 (l/s)/bar.

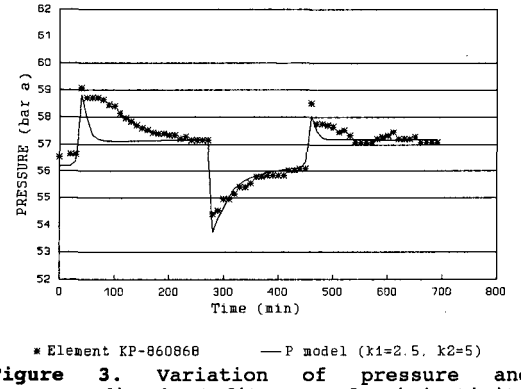


**Figure 3.** Variation of pressure and corresponding best fit curve for injectivity test of well A.

The match is good except for the first stage of pumping where cooling of the fluid column inside the well occurs slower than that measured by the temperature tool located in the upper zone. The assumption of making the average temperature of the well equal to the one measured by the tool, however, appears to give reasonable results for the following parts of the test.

The second case to be presented corresponds to an injectivity test for well B in Miravalles. This well also has two permeable zones. The first one located in the interval 1000-1100 m and the second one in the interval 1450-1550 m. For this test the tandem of tools was located in the lower zone at 1550 m deep. Figure 4 shows the profiles with and without injection. The profile without injection shows the characteristic length of at least 450 m with constant temperature caused by the spontaneous flow. The injecting profile shows how the assumption of constant temperature during injection for the entire segment between permeable zones is a reasonable one.

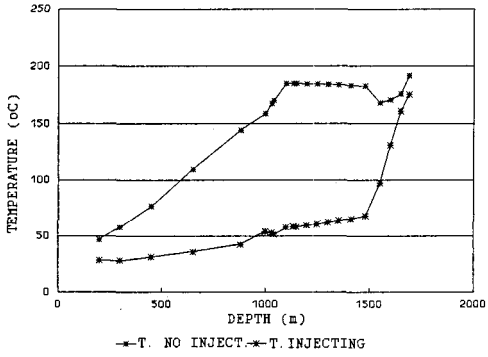


**Figure 4.** Temperature profiles with and without injection for well B in Miravalles, Costa Rica, showing two permeable zones separated 450 m approximately.

Figure 5 shows the variation of pressure, flow rate and temperature for this test that concluded with a fall-off. Based on the thermal variation shown in Figure 5 and its comparison with the injecting profile of Figure 4, it seems that the tool was located a little below the internal flow region. Therefore, the temperature curve is corrected linearly so that the initial temperature of the graph is equal to the respective temperature in the injecting profile. The minimum temperature remains the same as well as the fall-off part of measurement.

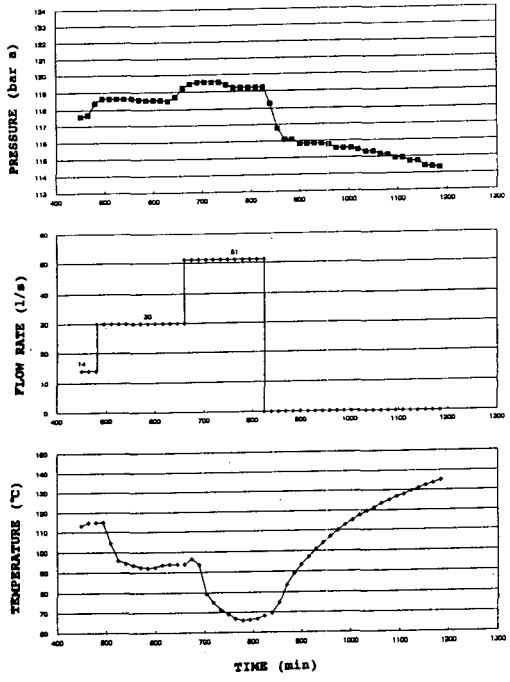


**Figure 5.** Variation of pressure, flow rate and temperature for injectivity test and fall-off for well B. Measuring tools located in the lower zone.

The slope of the fall-off curve is very large. If this curve is conventionally interpreted with the multiple flow rate pressure transient technique, it would give conductivities of the order of 1 Darcy-m, a value extremely low for this well. Actually, the fall-off part of the test is severely affected by thermal effects and should not be used to determine hydraulic transmissivity ***kh***, nevertheless, it is important to obtain the best fit curve for injectivity indexes as shown below.

Figure 6 shows the measured pressure curve and the theoretical best-fit curve. The match is good even for the fall-off part of the test. The best-fit values for $ii_{up}$ and $ii_{lo}$ are 18 and 1 (l/s)/bar respectively. The shape of the fall-off curve allows to determine that the value of injectivity of the upper zone is much larger than that of the lower zone.

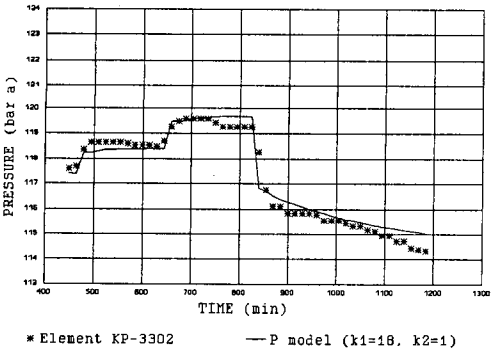


**Figure 6.** Variation of measured pressure and respective best fit curve for injectivity and fall-off test of well B.

## CONCLUSIONS

Spontaneous flow between two permeable zones in a well can be established without the existence of an overpressurized zone. It is only necessary to induce cooling of the well such as the one that occurs during drilling. If the flow is caused by simple cooling, the flow should stop once the well has stabilized thermally, if, however, there is overpressure, the flow will not stop even with the well thermally stabilized.

During an injectivity test in a well with two permeable zones, the upper zone may produce or accept fluid depending on the flow rate injected according to equation (6).

Thermal effects on injectivity tests and fall-offs in wells with two permeable zones can be utilized to extract information about the two zones separately. The procedure is quite simple and uses measurements of temperature and flow rate to obtain a theoretical response that is matched against measured pressure data by adjusting the value of injectivity indexes of the two permeable zones.

The technique proposed has the uncertainty associated with the assumptions made, especially the one regarding temperature of the liquid column between the permeable zones. Practical application of this method would benefit substantially if measurements of pressure and temperature were made in the two permeable zones simultaneously.

## ACKNOWLEDGEMENTS

The support of the Costarican Institute of Electricity (ICE) in the preparation and publication of this work is gratefully acknowledged.

## REFERENCES

1. J.A. Acuna, Numerical Construction and Fluid Flow Simulation in Networks of Fractures Using Fractal Geometry. Ph.D. Dissertation, University of Southern California, 1993.

2. J.A. Acuna, I. Ershaghi and Y.C. Yortsos. Fractal Analysis of Pressure Transients in The Geysers Geothermal Field. Paper presented at the 17th Annual Workshop on Geothermal Reservoir Engineering, Stanford, CA, January 29-31, 1992.

3. J.A. Acuna, I. Ershaghi and Y.C. Yortsos, Practical Application of Fractal Pressure Transient Analysis in Naturally Fractured Reservoirs. SPE paper 24705. Presented at the 67th SPE Technical Conference and Exhibition. October 4-7, Washington D.C., 1992.

4. G. S. Bodvarsson, S. M. Benson, O. Sigurdsson, V. Stefansson and E.T. Eliasson. The Krafla Geothermal Field, Iceland. 1. Analysis of Well Test Data. Water Resources Research, **20** (11): 1515, 1984.

5. M.A. Grant, I.G. Donaldson and P.F. Bixley. Geothermal Reservoir Engineering. Academic Press, 1982.

6. S.M. Benson, J. Dagget, J. Ortiz and E. Iglesias. Permeability Enhancement Due to Cold Water Injection: A Case Study at Los Azufres Geothermal Field. Document LBL-27350. Lawrence Berkeley Laboratory. Earth Sciences Division, 1989.

PROCEEDINGS, Nineteenth Workshop on Geothermal Reservoir Engineering
Stanford University, Stanford, California, January 18-20, 1994
SGP-TR-147

# INJECTION PERFORMANCE EVALUATION IN UNIT 13, UNIT 16, SMUDGEO #1, AND BEAR CANYON AREAS OF THE SOUTHEAST GEYSERS

K. P. Goyal

Calpine Corporation
1160 N. Dutton Ave., Suite 200
Santa Rosa, CA 95401

## ABSTRACT

Steam production data from wells surrounding Unit 13 injection well CA 956A-1 and Unit 16 injection well Barrows-1 were analyzed to estimate annual and cumulative recovery factors due to water injection into these wells. Production and injection data from SMUDGEO#1 and Bear Canyon wellfields were also analyzed to obtain recovery of the injected water in those wellfields. The results of this study may be useful in designing future injection projects in vapor dominated systems.

## INTRODUCTION

Several steam field operators have found that water injection into the vapor dominated reservoir can be very useful if performed properly (Goyal and Box, 1992; Enedy et al, 1991; Hanano et al.,1991; Gambill, 1990; Bertrami et al., 1985 and Cappetti et al, 1982). The positive contributions of water injection include providing reservoir pressure support, maintaining steam production rate, reducing makeup well requirements, increasing reserves and life of the field by recovering a portion of the approximate 90% heat which is stored in the rocks of the vapor dominated systems. On the other hand, injection can reduce well productivity or even drown a production well by breakthrough of the injected cold water into a production well through some high permeability fracture conduits. It can also create obstructions in the wellbore and reduce steam flow rate by silica precipitation. Workovers, sometimes costly, may be needed to clean such wells.

In this paper I present the results of injection in four wellfields: Unit 13, Unit 16, SMUDGEO#1 and Bear Canyon, and try to quantify steam recovery due to injection in each wellfield by calculating recovery factors from the production data. The results for Units 13 and 16, already presented in Goyal and Box (1992), have been updated through May 1993. Discussions about SMUD and Bear Canyon wellfields are new.

The "recovery factor" is defined as the ratio of additional steam provided by injection to the amount of water injected over the same period of time. Additional steam is the steam produced at the new decline rate or improvement rate established due to injection minus the steam production calculated at a decline rate without injection. The improvement rate is defined as the annual exponential (or harmonic) increase in the steam flow rate. This definition is similar to the annual exponential (or harmonic) decline rate but represents an increase in flow rate rather than a decrease.

Gambill (1990), Beall et al., (1989) and Beall (1993) have used geochemical data such as deuterium isotope and/or ammonia to estimate the recovery of injected water in various parts of The Geysers geothermal field. The recovery factor defined on the basis of production data may be different than that defined on the basis of geochemical data if considered on a well by well basis. However, the combined recovery from all production wells affected by one or more injection wells should ultimately agree by both methods given sufficient time, since (i) the total amount of boiled water should appear as steam in the production wells and be reflected in the production data and (ii) the steam originally to be produced by a given well but replaced by injection derived steam (IDS) should eventually be produced in other well(s). Water injection may create unfavorable situations where the determination of the recovery factor from decline analysis may not produce reliable results. Such situations include (i) a decrease in steam flow rate due to water breakthrough, (ii) scale deposits in the wellbore, (iii) the fluctuating flow rate, and (iv) the completion of additional production wells in injection affected areas which impact the decline rates of nearby production wells as seen in the Unit 16 analysis.

## UNIT 13 INJECTION WELL CA 956A-1:

Originally a steam production well since the plant start-up in May 1980, well CA 956A-1 was converted to an injection well on October 30, 1989 as discussed in Goyal and Box (1992). From October 1989 to April 1993, most of Unit 13 injectate was divided between wells CA 956A-1 and an NCPA/Calpine joint injection well C-11 (Enedy et al, 1991) with a small amount going into Thorne-7. Due to lower than expected direct benefits to Calpine, the water from Unit 13 to the joint well C-11 has been stopped effective April 1993. All of Unit 13 steam condensate is now injected into CA 956A-1 and CA 956-2. Originally a production well, well CA 956-2 was converted into an injection well in October 1993.

Production Wells Surrounding The Injection Well CA 956A-1:

Twelve wells surrounding the injection well CA 956A-1 and shown by solid circles in Figure 2 were monitored for their flow rate and decline rate behavior. Most wells displayed a reduction in decline rate but the wells located within the dashed outline exhibited an increase in their flow rate (Goyal and Box, 1992).

The flow rate increase observed in these wells suggest that most of the injected water into CA 956A-1 took a southwestern route and appeared as steam in wells located within the dashed outline (Figure 2). The pressure support to these wells from C-11, located south of the Unit 13 lease boundary, was minimal as suggested by the tracer test conducted in C-11 in February 1991 (Adams et al., 1991). The tracer recovery in Unit 13 wells was of one order of magnitude lower compared to NCPA wells. Additionally, injection into C-11 was stopped from June 1990 to November 1990 but the improved performance of these wells continued (Figure 3). These observations suggest that recovery in these wells is predominantly due to injection into CA 956A-1.

Recovery Factors (RF) due to Injection into CA 956A-1:

The combined normalized flow rate of 12 wells plus CA 956A-1 at 110 psig wellhead pressure (WHP) is presented in Figure 3 from January 1988 to May 1993. Due to conversion of production well CA 956A-1 into an injection well, the flow rate of only 12 wells is plotted after October 1989. Decline rates, shown in Figure 3, are estimated by excluding the data points affected by plant outages and testing. The 13 production wells, including CA 956A-1, exhibit an annual exponential decline of 26% in 1988 and 20% in 1989 before the start of injection into CA 956A-1. During the next four months, the flow rate increased by 110 klbm/hr. This increase was experienced by the 12 wells (13 wells minus CA 956A-1) and was over and above the flow rate of the original 13 wells. Subsequently, the flow rate of these wells declined but at a moderate rate of 10.5% as shown in Figure 3. Injection into CA 956A-1 has helped in two ways: one in reducing decline rates by 9.5% and the other in providing an increase in the flow rate. The injection rate (gpm) averaged over a month since the start up in October 1989 is also shown in this figure which ranges from 300 gpm to 800 gpm.

The hatched area in Figure 3 is used to calculate the recovery of the injected water. In these calculations, it is assumed that the original 13 wells would have declined at 20% harmonic rate starting October 1989. This assumption is consistent with the behavior of these wells in 1988 and 1989 (Figure 3) and is supported by the modeling effort of the Technical Advisory Committee appointed by the California Energy Commission (GeothermEx, 1992).

Cumulative steam recovery and recovery factors (RF) for 3 years are shown in Figure 4. Steam recovery exhibits an increasing trend with time. A cumulative three year recovery factor of 61% is shown in Figure 4b. A slight decrease in the third year RF may be caused by a 30% increase in the injected water in that year as presented in Table 1.

Annual recovery factors (RF) of 56%, 73% and 57% were estimated for the first, second and third year respectively (Table 1). Reduced RF in the third year implies that increased injection did not enhance steam recovery correspondingly. It may be noted that steam recovery in the second and third year was almost equal even though the annual injection in the third year was 30% higher than the second year (Table 1). This suggests that the injection rate should be kept close to the second year level of about 2500 million lbm or 600 gpm for an optimum boiling of the injected water.

First year recovery factor of 56% is lower than 63% reported in Goyal and Box (1992). This difference is mainly caused by the amount of the injection water used in the first year. Previously we considered the annual injection water to be 2.12 billion lbm from October 30, 1989 to September 30, 1990. In this study, we considered the first year injection of 2.36 billion lbm from October 30, 1989 to October 31, 1990 because injection into CA 956A-1 during October 1989 was only for two days.

The annual steam recovery presented in Table 1 can be converted in to MWh by using the Unit 13 steam usage factor of 20.5 klbm/MWh. This suggests that injection into CA 956A-1 provided 64,449 MWh (7.4 MW), 86,976 MWh (9.9 MW) and 88,498 MWh (10.1 MW) in the first, second and third year respectively.

In summary, water injection into the southwest area of Unit 13 provided a total cumulative three year recovery of about 61% and generation of 239,923 MWh. This recovery may be slightly on the high side due to some pressure support provided by water injection into the joint NCPA/Calpine well C-11. To date, no adverse injection effects such as cooling or water breakthrough have been noted in the production wells in this area due to water injection into CA 956A-1.

UNIT 16 INJECTION WELL BARROWS-1:

Originally a steam producer since the plant start-up in October 1985, Barrows-1 was converted into an injection well on October 1, 1990. The water breakthrough to a nearby producer in early 1992 prompted Barrows-1 examination. Its casing was found to be parted at 2500'. This problem was fixed by installing a 6-5/8" liner inside the original casing. The well was put back in service in April 1992. After this repair, it received a major portion of Unit 16 water until November 1993 when the injection rate was reduced to about 100 gpm due to water breakthrough to nearby producers.

| Wellfield | Injection Well | Annual Data | First year | Second year | Third year |
|---|---|---|---|---|---|
| Unit 13 | CA 956A–1 | Injection (Mlbm) | 2,363.5 | 2,451.1 | 3,190.5 |
| | | Recovery (Mlbm) | 1,321.2 | 1,783.0 | 1,814.2 |
| | | Recovery Factor | 56% | 73% | 57% |
| | | Recovery (MWh) | 64,449 | 86,976 | 88,498 |
| | | Recovery (av. MW) | 7.4 | 9.9 | 10.1 |
| Unit 16 | Barrows–1 | Injection (Mlbm) | 2,658.3 | 2,195.5 | |
| | | Recovery (Mlbm) | 540.3 | 1,114.8 | |
| | | Recovery Factor | 20% | 51% | |
| | | Recovery (MWh) | 30,017 | 61,933 | |
| | | Recovery (av. MW) | 3.4 | 7.1 | |
| SMUD | CA 1862–18 | Injection (Mlbm) | 2,027.9 | 3,375.0 | |
| | | Recovery (Mlbm) | 11.2 | 25.9 | |
| | | Recovery Factor | 0.6% | 0.8% | |
| | | Recovery (MWh) | 772 | 1,786 | |
| | | Recovery (av. MW) | 0.1 | 0.2 | |
| Bear Canyon | DE–7 | Injection (Mlbm) | 987.6 | | |
| | | Recovery (Mlbm) | 28.4 | | |
| | | Recovery Factor | 2.9% | | |
| | | Recovery (MWh) | 1,732 | | |
| | | Recovery (av. MW) | 0.2 | | |

**TABLE 1: Annual Injection Data and Recovery Factors**

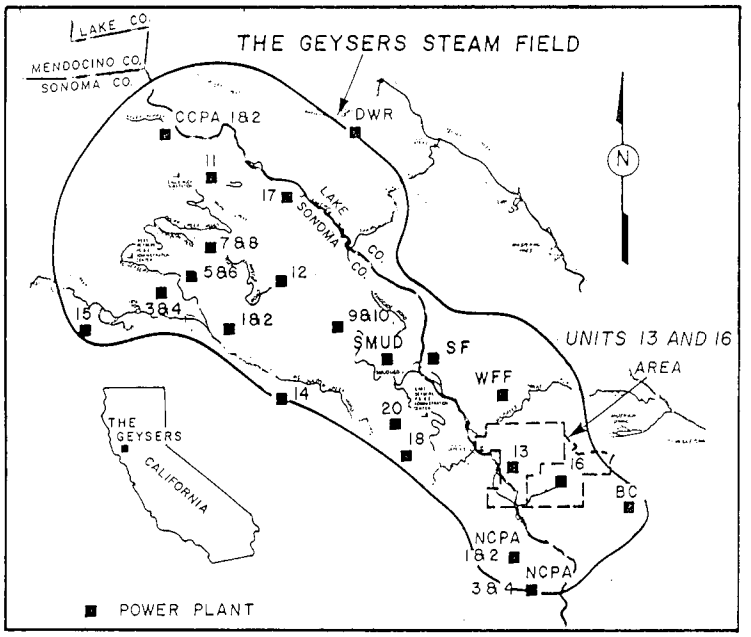


**FIGURE 1: The Location Map**

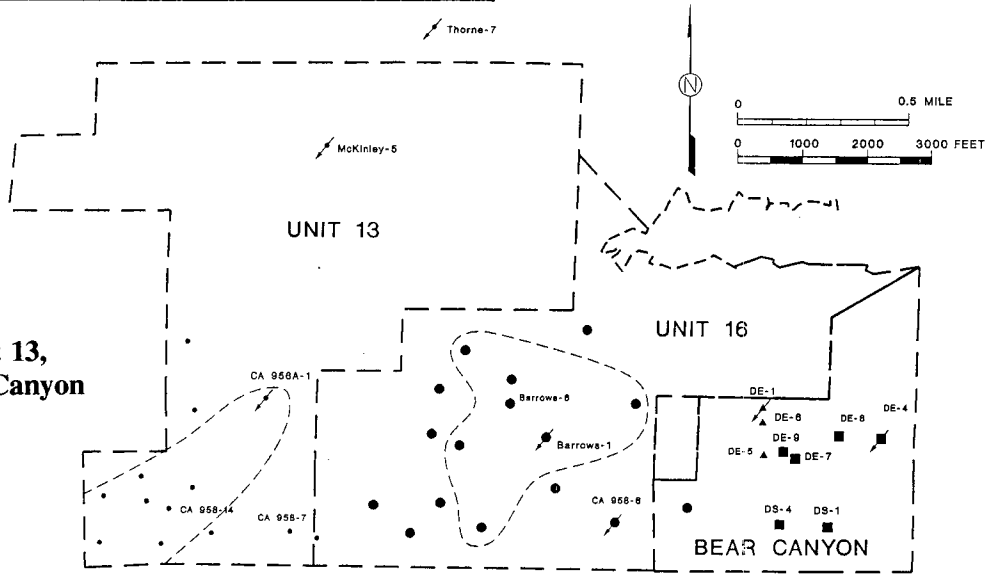


**FIGURE 2:**

**Study Area in Unit 13, Unit 16 and Bear Canyon**

Recovery Factors due to Water Injection into Barrows-1:

In the Unit 16 area, a total of 15 production wells are used in this analysis: 7 wells located within the dashed outline showing maximum injection benefit and 8 nearby wells located outside the dashed outline showing some injection benefit (Figure 2). The eastern most well of this group belongs to the Bear Canyon lease. The combined flow rate of all 15 wells normalized at 110 psig wellhead pressure is presented in Figure 5 from March 1989 to April 1993. Due to the conversion of Barrows-1 into an injection well, the flow rate of only 14 wells is plotted after September 1990. All 15 wells display a combined annual exponential decline rate of 12% before the start of injection into Barrows-1. The shift of most of Unit 16 injection to Barrows-1 since October 1, 1990 has reduced the decline rate to 4% as shown in Figure 5. An increase in flow rate, similar to that seen in the Unit 13 area (Figure 3), is not seen in the Unit 16 area. Additionally, the effect of makeup well drilling in 1992 is reflected by an increase in the decline rate from 4% to 20%.

The injection rate (gpm) into Barrows-1 and into the Unit 16 area (Barrows-1 plus CA 958-6) averaged over a month from March 1989 to April 1993 is also shown in figure 5. The injection rate into Barrows-1 and the Unit-16 area ranges from about 300 gpm to 700 gpm and 600 to 1100 gpm respectively (Figure 5).

The hatched area in Figure 5 is used to calculate the steam recovery due to injection into Barrows-1. The following assumptions were made in these calculations.

1. The decline rate of the 15 wells without injection into Barrows-1 is projected as harmonic at 12% rate from September 1990 until March 1992. This assumption is similar to that assumed in Unit-13 calculations.

2. The steam recovery during the next six months (high decline period) after March 1992 is equal to the steam recovery during the first six months. This assumption implies that steam recovery by injection during the 20% decline rate period has not diminished. This is reasonable since the increase in the decline rate is caused by 17% more steam withdrawal from the area by new makeup wells. This increased withdrawal is expected to enhance the boiling rate due to reduced boiling temperature associated with lower reservoir pressures. This assumption was supported by a tracer test conducted in Barrows-1 in February 1993 where 66% of the tracer came back from the surrounding 10 wells in 30 days. More than 80% of the total recovered tracer came from the nearest new makeup well CA 958-16 (J. J. Beall-Personal communication, 1993).

3. The decline history of 15 wells, shown in Figure 5, during 1989-90 and the 12% harmonic projection

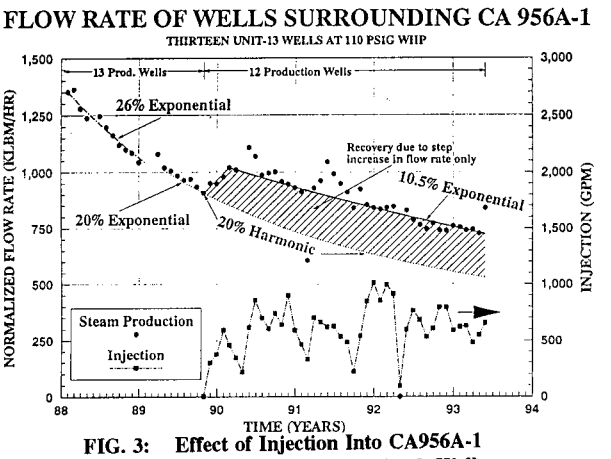


**FIG. 3: Effect of Injection Into CA956A-1 on Some Surrounding Prod. Wells.**

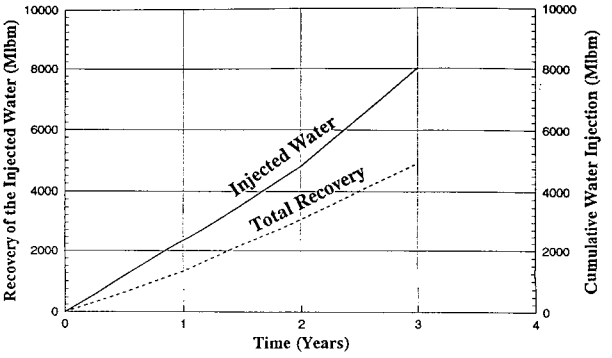


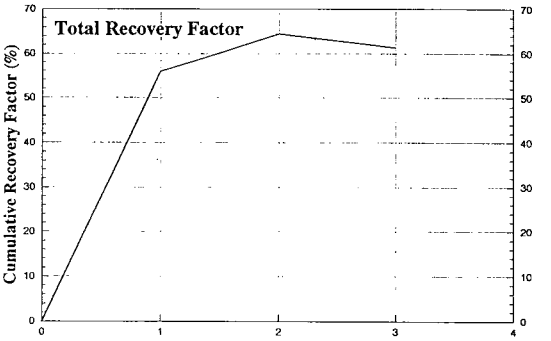


**FIG. 4: Total Cumulative Recovery Factors Due to Injection into CA956A-1**

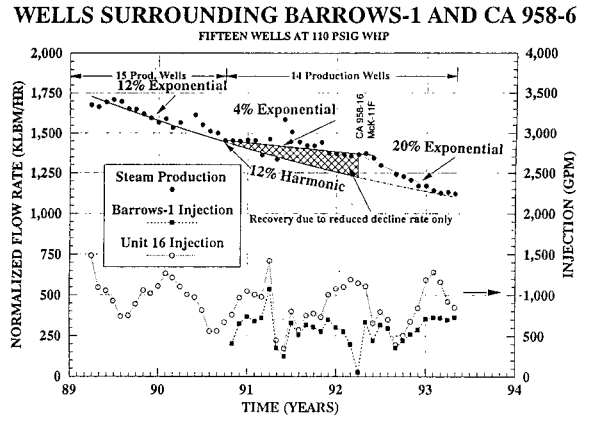


**FIG. 5: Effect of Injection in Barrows-1 on Surrounding Wells**

from September 1990 already takes into account the injection support provided by the water injection into CA 958-6. A decrease in water injection into this well can only result in an increase in the decline rate of the 15 wells to more than 12%. Therefore, the hatched area shown in Figure 5 and the calculated recovery factors are considered conservative.

Cumulative steam recovery and water injection in Barrows-1 and in the Unit-16 area are presented in Figure 6. A two year cumulative recovery factors of 34% is also shown in this figure. Annual recovery factors of 20% for the first year and 51% for the second year are presented in Table 1. The annual steam recovery in Table 1 is equivalent to 30,017 MWh (3.4 MW) and 61,933 MWh (7.1 MW) in the first and second year respectively for a Unit 16 steam usage factor of 18 klbm/MWh.

In summary, water injection in Barrows-1 provided a two year cumulative recovery of 34%. Recently, a decrease in flow rate of two nearby production wells has been observed. This phenomenon is believed to be caused by water breakthrough from the injection well Barrows-1. Therefore, the injection rate into this well is presently reduced to about 100 gpm.

SMUDGEO#1 INJECTION HISTORY:

The SMUDGEO#1 wellfield is located northwest of Unit 13 as shown in Figure 1. This 78 MWG unit came on line in October 1983 with 11 production wells and one injection well. Presently, there are 19 production wells and one injection well. In fact, total producing legs in the SMUD area are 23 which include one production well with 2 forks and two wells with a single fork each. The outline of the SMUD wellfield and the location of injection and the nearby production wells is shown in Figure 7.

CA 1862-6 was used as an injection well from the plant start up in October 1983 through July 1985. Water breakthrough to nearby producers, resulting from the poor completion of this well, prompted the drilling of a new injection well CA 1862-17. The original injection well CA 1862-6 was redrilled and completed as a producer in September 1985. CA 1862-17 accepted water from July 1985 to August 1991. In an effort to obtain better returns of the injectate, the redrilled well CA 1862-6 was converted to an injection well in August 1991. The former injection well CA 1862-17 was kept as a standby injector for 15 months until it was plugged and abandoned in November 1992 due to the damaged casing.

Injection Well CA 1862-6:

This well has been accepting all the condensate from the SMUD plant since August 27, 1991. No perforated liner was installed in this well, allowing the injectate to leave the wellbore below the casing shoe at 4038'. Recently, due to obstruction in the wellbore injectate started exiting at shallow depth, affecting the nearby producers. Therefore, a workover was performed in December 1993 and a 6-5/8" liner was installed from the surface to 4695'.

A tracer test was conducted in this well in December 1991 by injecting 232 pounds of R-13 Freon tracer (chlorotrifluoromethane). A total of 74% of the tracer was recovered in 60 days, mostly from the wells in the SMUD area. In fact, 68% of the total tracer was recovered from three wells: 55% from CA 1862-18, 12% from CA 1862-19 and 1% from CA 1862-13 (personal comm., J.J. Beall, 1992). The proximity of these wells to the injection well suggests that most of the injected water benefits remained within the SMUD lease (Figure 7).

Recovery Factors due to injection into CA 1862-6:

Consistent with the tracer data, well CA 1862-18 derived the maximum benefit from this injection. Its decline rate decreased from 20% exponential to 15% harmonic (Figure 8). The effect on other nearby wells was too small to analyze. The overall impact of the injection on the flow rate and the decline rate of the nearby 3 wells was minimal as shown in Figure 9.

A flow rate increase seen in 1991 in Figures 8 and 9 was caused by a high header pressure operation of the surrounding PG&E units resulting in reduced steam withdrawal from the reservoir offsetting the SMUD lease (TAC Consortium, 1992). Therefore, the flow rate just before injection is used as the initial condition to evaluate injection benefits in the SMUD area.

The combined normalized flow rate of wells CA 1862-18, CA 1862-19 and CA 1862-13 displays an annual exponential decline rate of 20% during 1989-90. The decline rate reduced to 6% exponential for about 8 months after the start up of injection into CA 1862-6. Thereafter the decline rate increased substantially as shown in Figure 9. The flow rate data from August 1991 to August 1993 suggest an overall decline rate of 20% harmonic. Using the methodology discussed earlier, the net gain in these 3 wells due to injection is zero. Additionally, an injection rate above 500 gpm has a positive impact on the flow rate of these wells as shown in Figure 9.

Using the hatched area in Figure 8 for CA 1862-18, annual recovery factors of 0.6% for the first year and 0.8% for the second year were calculated (Table 1). A two year cumulative recovery factor of 0.7% was also computed. These translate into a two year generation of 2,558 MWh for a steam usage factor of 14,500 pound per MWh (Table 1).

BEAR CANYON INJECTION HISTORY:

The Bear Canyon project is located east of Unit 16 as shown in Figure 2. It is a 24 MWG unit which came on line in September 1988 with only 5 production wells and 1 injection well. Presently it has 8 production wells and one redrilled injection well. The actual producing legs in this wellfield are 11 which include two wells: one with 3 legs and the other with 2 producing legs.

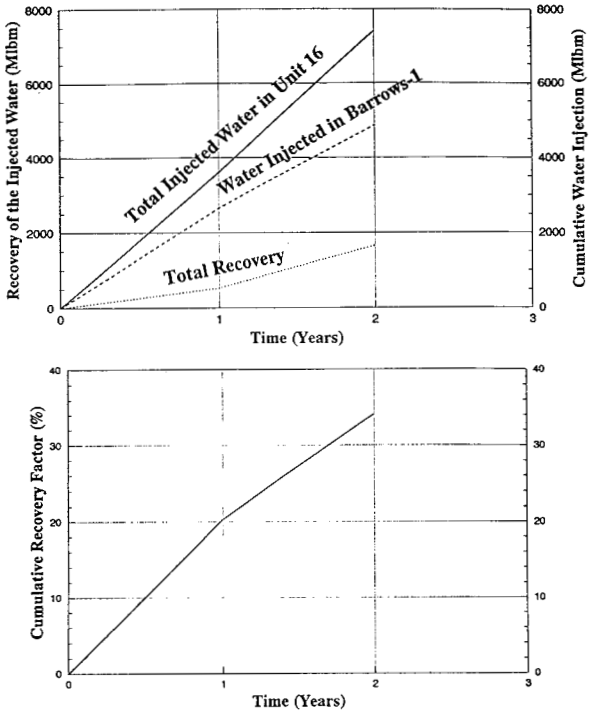


**FIG. 6: Cumulative Recovery Factors Based on Injection into Barrows-1.**

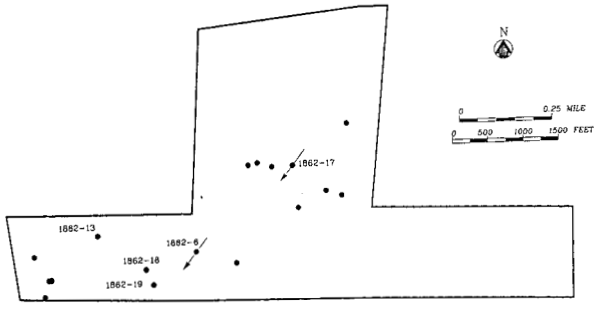


**FIGURE 7: Injection Well CA1862-6 & the Surrounding Production Wells in the SMUD Area.**

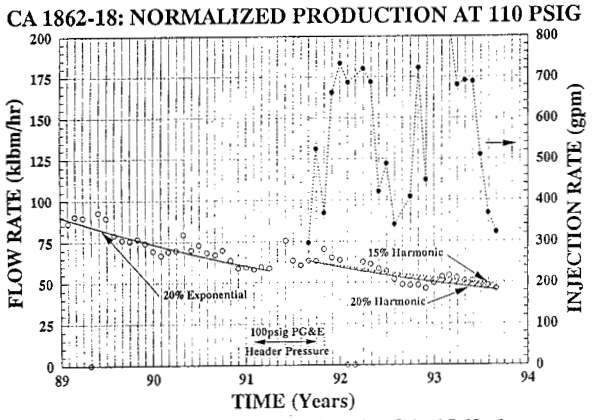


**FIG 8: Effect on Injection in CA 1862-6 on the Production Well CA 1862-18.**

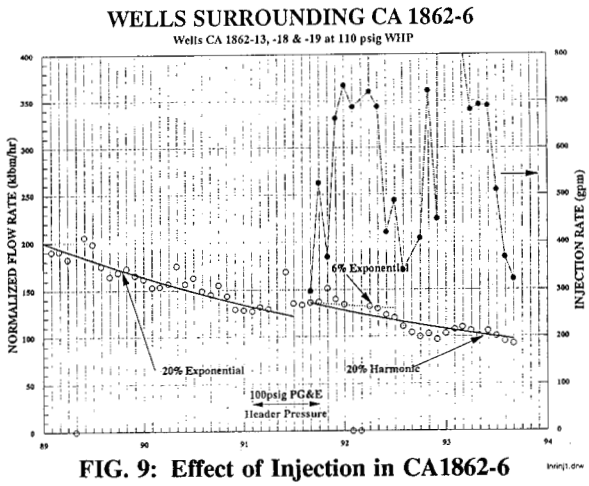


**FIG. 9: Effect of Injection in CA1862-6 on the Surrounding Wells.**

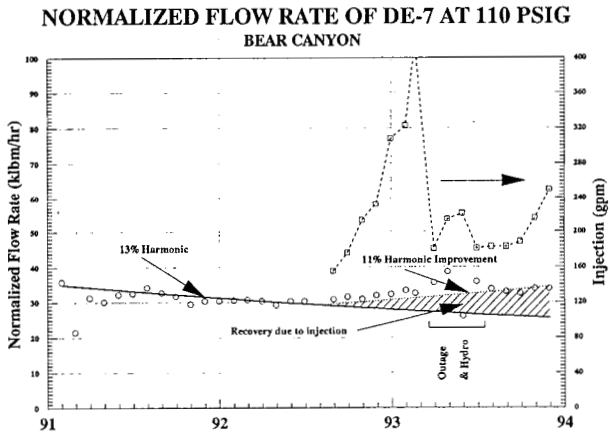


**FIG. 10: Effect of Injection in DE-4 on the Flow Rate of DE-7.**

Injection Well Davies Estate-4 (DE-4):

DE-4 has been accepting all the water from the plant since its start up in 1988. However, the original location of DE-4 was such that it resulted the water being injected to the east of the lease without obvious benefits to the production wells. Therefore, the original leg of DE-4 was plugged and a new leg was drilled towards the production area in June-July 1992. The new leg has been accepting all the water from the plant since August 1992. No adverse injection impact has been observed so far.

A tracer test was conducted in April 1993 by injecting 160 lbm of R-13 Freon tracer to evaluate the potential benefits derived from this well. The tracer was not seen in any of the wells for the first 13 days. Subsequently, a small amount of tracer was recovered from DE-9 followed by Davies State 5206-4 (DS-4), DE-7, DE-8 and DS-1 (J. J. Beall, Personal Communication 1993). The cumulative tracer recovery in the Bear Canyon area was less than 1% even 110 days after the test suggesting a slow boiling process of the injected water in this area. High reservoir pressure and the geology (not so high fracturing) appear to be responsible for slow boiling.

Recovery Factors due to injection into DE-4:

The tracer test indicated a maximum recovery in wells DE-8 and DE-9. However, the effect of injection on the flow rate of these wells was too small to analyze. The data of only one well, DE-7, was analyzable. The normalized flow rate of DE-7 from January 1991 to November 1993 is shown in Figure 10. The injection into DE-4 from July 1992 to November 1993 is also indicated in this figure.

DE-7 displays a 13% harmonic decline rate in 1991-92 until the start up of injection into DE-4 in August 1992. Since then, its flow rate shows an improvement at a harmonic rate of 11% as presented in Figure 10. The recovery of the injected water is shown by the hatched area in this figure. On the basis of this area, a first year recovery of 28.4 million pounds is calculated. This amounts to a first year recovery factor of 2.9% for an annual water injection of 987.6 million pounds. This steam recovery is worth 1732 MWh (0.2 MW) for a steam usage factor of 16.4 klbm per MWh.

## CONCLUSIONS:

The highest annual recovery factors of 56%, 73% and 57% were estimated for the southwest area of Unit 13 for the first, second and third year respectively. A three year cumulative recovery factor of 61% was obtained. Low reservoir pressure (low boiling temperature) and large heat transfer area (high fracturing) were thought to be responsible for the efficient boiling of the injectate in this area. Unit 13 recovery factors may be slightly on the high side due to pressure support provided by water injection into the joint NCPA/Calpine well C-11. To date no adverse impact such as cooling or water breakthrough has been observed by the injection into CA 956A-1.

Injection into Barrows-1 provided an annual recovery factor of 20% for the first year and 51% for the second year. The two year cumulative recovery factor was 34%. Higher reservoir pressure and higher fracture connectivity between production and injection wells in the Unit 16 area compared to the southwest area of Unit 13 are believed to result in lower recovery factors. The injection in the Unit 16 area has not been trouble free. Water breakthrough problems do appear from time to time requiring workover of the injection wells.

Injection into the SMUD well CA 1862-6 has provided minimal benefits. One well CA 1862-18 did exhibit a reduction in the decline rate from 20% exponential to 15% harmonic. However, the annual and cumulative recovery factors were less than 1%. The injection recovery in the SMUD area is very poor though the reservoir pressure is almost the lowest out of the four wellfields presented in this paper. The poor heat transfer characteristics in this area (geology) prevent efficient boiling of the injectate. Problems related to water breakthrough and injection well workover were also encountered in the SMUD wellfield.

In spite of slow boiling, injection has been helpful in the Bear Canyon area. Well DE-7 displays a continuous increase in its flow rate since the start up of injection in the redrilled well DE-4. The production data of DE-7 suggests a first year recovery factor of 2.9% and an electric generation of 1732 MWh. No adverse impact is observed by injection into DE-4 so far.

## ACKNOWLEDGEMENTS:

I would like to thank Tom Box for his helpful comments and Calpine Corporation and Santa Fe Geothermal for permission to publish this paper.

## REFERENCES:

Adams, M.C., Beall, J.J., Enedy, S.L., and Hirtz, P. (1991), "The Application of Halogenated Alkanes as Vapor-Phase Tracers: A Field Test in the Southeast Geysers," Geothermal Res. Counc. Trans., Vol. 15, October 1991, pp. 457-463.

Beall, J.J., Enedy, S.L., and Box, W.T. Jr. (1989), "Recovery of injected condensate as steam in the south Geysers field," Geothermal Resource Council, Transactions, v. 13, pp. 351-358.

Beall, J.J. (1993), "The history of injection recovery in the units 13 and 16 area of the Geysers Steamfield", Geothermal Resources Council, Transactions, v. 17, pp. 211-214.

Bertrami, R., Calore, C., Cappetti, G., Celati, R. and D'Amore, F. (1985), "A three year recharge test by reinjection in the central area of Larderello field: analysis of production data", *Geothermal Resources Council Transactions* **9(II)**, 293-298.

Cappetti, G., Giovannoni, A., Ruffilli, C., Calore, C. and Celati, R. (1982), "Reinjection in the Larderello geothermal field", International Conference on geothermal energy, Florence Italy, May 11-14, 1982, Paper F1.

Enedy S., Enedy K. and Maney J. (1991), "Reservoir Response to Injection in the Southeast Geysers", *Proc. 16th workshop on Geothermal Reservoir Engineering, Stanford University,* pp.75-82.

Gambill, D.T. (1990), "The Recovery of Injected Water as Steam at The Geysers", Geothermal Resources Council Transactions, Vol 14, Part II, August 1990, pp. 1655-1660.

GeothermEx, Inc.(1992), "Fieldwide reservoir modeling of the Geysers Geothermal field, California", prepared for Lake and Sonoma Counties under a grant from the California Energy commission, 6-3p.

Goyal, K.P. and Box, W.T. Jr. (1992), "Injection recovery based on production data in unit 13 and unit 16 areas of the Geysers field", *Proc. 17th Annual Workshop on Geothermal Reservoir Engineering, Stanford University,* pp. 103-109.

Hanano, M., Ohmiya, T. and Sato, K. (1991), "Reinjection experiment at the Matsukawa vapor-dominated geothermal field: Increase in steam production and secondary heat recovery from the reservoir", *Geothermics,* **20(5/6)**, 279-289.

TAC Consortium (1992), "Progress Report on Implementation of the Coordinated Resource Management Plan for The Geysers", Prepared by Calpine Corporation, Unocal Corp., NCPA, PG&E, SMUD and Russian River Energy Company, 41 p.

PROCEEDINGS, Nineteenth Workshop on Geothermal Reservoir Engineering
Stanford University, Stanford, California, January 18-20, 1994
SGP-TR-147

# AN INVERSE PROBLEM SOLUTION TO THE FLOW OF TRACERS IN NATURALLY FRACTURED RESERVOIRS

JETZABETH RAMÍREZ S., FERNANDO SAMANIEGO V., FERNANDO RODRÍGUEZ, AND JESÚS RIVERA R.

UNIVERSIDAD NACIONAL AUTÓNOMA DE MÉXICO
FACULTAD DE INGENIERÍA, 04510 MÉXICO, D.F.

## ABSTRACT

This paper presents a solution for the inverse problem to the flow of tracers in naturally fractured reservoirs. The models considered include linear flow in vertical fractures, radial flow in horizontal fractures, and cubic block matrix-fracture geometry. The Rosenbrock method for nonlinear regression used in this study, allowed the estimation of up to six parameters for the cubic block matrix fracture geometry. The nonlinear regression for the three cases was carefully tested against syntetical tracer concentration responses affected by random noise, with the objective of simulating as close as possible step injection field data. Results were obtained within 95 percent confidence limits. The sensitivity of the inverse problem solution on the main parameters that describe this flow problem was investigated. The main features of the nonlinear regression program used in this study are also discussed. The procedure of this study can be applied to interpret tracer tests in naturally fractured reservoirs, allowing the estimation of fracture and matrix parameters of practical interest (longitudinal fracture dispersivity $\alpha$, matrix porosity $\phi_2$, fracture half-width w, matrix block size d, matrix diffusion coefficient $D_2$ and the adsorption constant $k_d$). The methodology of this work offers a practical alternative for tracer flow tests interpretation to other techniques.

## INTRODUCTION

Most of the geothermal reservoirs currently under exploitation are found in naturally fractured formations. The behavior of these reservoirs is quite different from that of "homogeneous"-conventional-reservoirs. The complex matrix-fracture interaction of these systems makes their characterization a challenging task. Among the different tools currently available to accomplish this endeavor, tracer test interpretation is taking an ever increasing role. These interwell tracer tests have significantly contributed to the better understanding of the fluid flow in these systems. Radioactive and chemical tracers have been used for many years in groundwater hydrology to analyze the movement of water through porous formations, but their use in geothermal reservoir engineering is more recent (Jensen, 1983).

It has been recognized, as already stated, that tracer test interpretation, in addition to well-to-well pressure transient tests (Brigham and Abbaszadeh-Dehgani, 1987), is a very important contribution towards accomplishing the characterization of naturally fractured reservoirs. As concluded by these authors, these two testing techniques are complementary, not competing.

There are several papers that discuss the flow of tracers in naturally fractured reservoirs. For a review of the recent work the papers of Ramírez et al. (1990, 1991, 1992) may be consulted. Most of these studies deal with the direct problem (i.e., predicting the tracer response behavior from the knowledge of pertinent reservoir and tracer parameters). Methods for solving the inverse problem (i.e., estimating reservoir and tracer parameters from the interpretation of the tracer response), are much less numerous than solutions to the direct problem. This situation gets worst when dealing with naturally fractured reservoirs.

Fossum and Horne (1982) used the model of Horne and Rodríguez (1983), that accounts for dispersion during fluid flow through the fractures, to analyze tracer return profiles for the Wairakei geothermal field.

Jensen (1983) presented the application of a double porosity model, in a nonlinear least-squares procedure of curve fitting of tracer concentration responses. Fossum (1984) presented an application of a reformulated two dimensional double porosity model, using the same nonlinear least-squares procedure used by Jensen (1983). This model represented the fractured medium by a mobile region, in which convection, diffusion, and adsorption are allowed, and an immobile region in which only diffusion and adsorption are allowed. Other authors (Shinta and Kazemi, 1993), have recently considered the application of a two dimensional and two phase model to interpret an actual field test.

The purpose of this study is to present a solution for the inverse problem to the flow of tracers in naturally fractured reservoirs. The models considered include linear flow in vertical fractures, radial flow in horizontal fractures, and cubic block matrix-fracture geometry. The Rosenbrock method (1960) for nonlinear regression used in this study allowed the estimation of up to six parameters for the cubic block matrix-fracture geometry.

## MATHEMATICAL MODELS

Models considered in this study are shown in Figs. 1 to 4. The naturally fractured medium, Fig. 1, is represented by means of Figs. 2 to 4, which correspond to the flow ge-

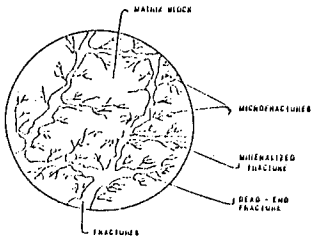


Fig. 1 Naturally fractured reservoir

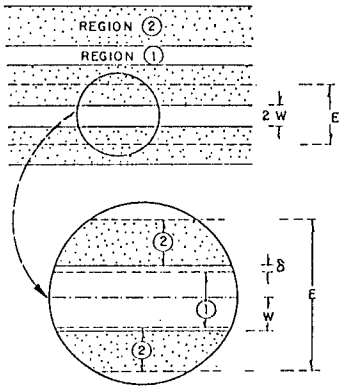


Fig. 2 Vertical fractures - linear flow - model

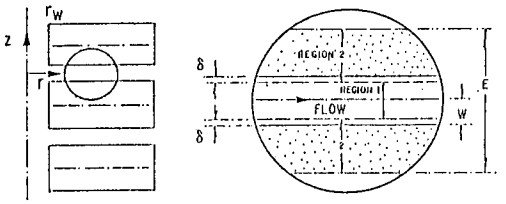


Fig. 3 Radial flow - horizontal fractures - model

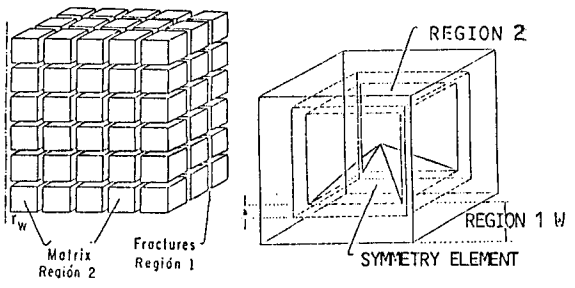


Fig. 4 Cubic matrix proposed model for representation of the flow of a tracer in a naturally fractured medium

ometries commonly present in these formations. Idealized models of naturally fractured reservoirs used to describe linear flow (vertical fractures), and radial flow (horizontal fractures) shown in Figs. 2 and 3, represent the fractured medium by means of a system of equally spaced parallel fractures, alternated with matrix blocks. Fig. 4 shows the ideal representation for the case of radial flow considering cubic matrix-fracture geometry, where the fractured medium is represented by means of a system of identical cubic blocks separated by an orthogonal network of fractures.

The system shown in these figures consists of two regions: 1) a mobile region constituted by the fracture network and 2) a stagnant or immobile region, constituted by the matrix blocks. This type of visualization of the problem has been used in previous works (Jensen, 1983; Ramírez et al., 1990, 1991, 1992). It is considered that these regions are interconnected by means of a thin layer of fluid, contained within the immobile region, which controls the mass transfer by diffusion between both regions.

The main assumptions considered in the three models are the following:
1. Constant density for species "A".
2. No velocity component in direction perpendicular to flow.
3. In the mobile region, the concentration gradient in the transverse flow direction is considered negligible.
4. The volume of the mobile region remains constant.
5. Adsorption takes place by means of a first order chemical reaction.
6. The mass transfer between the fracture and matrix systems is controlled by a fluid layer of infinitesimal thickness, $\delta$, located at the interface between matrix blocks and surrounding fractures.
7. Tracer transport takes place by means of the following mechanims:
*Mobile region (fractures)*: Difussion + Convection.
*Stagnant region (Matrix blocks and dead-end fractures)*: Difussion + Adsorption.

The main difference between the linear and radial models is, that in the first case the velocity is constant, while for the radial cases, the velocity depends on the radial distance and therefore, the dispersion coefficient, $D_r$, is also a function of this radial distance. For the cases of radial flow under constant rate injection, the velocity is defined as:

$$v_r = \frac{a}{r} \tag{1}$$

where:

$$a = \frac{q}{2\pi h \phi_1} \tag{2}$$

where $h$ is the reservoir thickness and $\phi_1$ is the fracture porosity.

The solutions for the flow problems of vertical fractures (Ramírez et al., 1990), for the horizontal fractures (Ramírez et al., 1991), and for the cubic block matrix-fracture geometry (Ramírez and Samaniego, 1992), derived using the

Laplace tranform method, result for the case of linear flow in an analytic solution of the integral type and for the cases of radial flow, in a solution in Laplace space in terms of Airy functions. The solutions for the case of continuous tracer injection for the three models are as follows:

**Linear Flow**

$$C_{D1}(x_D,t_D) = \frac{1}{\sqrt{\pi}} exp\left(\frac{x_D P_{e1}}{2}\right) \int_0^{\infty} \frac{1}{(\tau'')^2} \cdot$$

$$exp\left[-\left(\frac{1}{\tau''}-1\right)^2 - \frac{P_{e1}x_D^2}{4\left(\frac{1}{\tau''}-1\right)^2}\left(\frac{P_{e1}}{4}+\gamma\right)\right] \cdot$$

$$\{F_1 + F_2\} U\left(t_D - \frac{P_{e1}x_D^2}{4\left(\frac{1}{\tau''}-1\right)^2}\right) d\tau'' \qquad (3)$$

where:

$$F_1 = \{exp(-A_1)\, erfc\{B_1 - C_1\}\} \qquad (4)$$

and

$$F_2 = \{exp(A_1)\, erfc\{B_1 + C_1\}\} \qquad (5)$$

where:

$$A_1 = \frac{x_D^2 P_{e1}\alpha}{4\left(\frac{1}{\tau''}-1\right)^2}\sqrt{\gamma} \qquad (6)$$

$$B_1 = \frac{x_D^2 P_{e1}\alpha}{8\left(\frac{1}{\tau''}-1\right)^2\sqrt{t_D - \frac{P_{e1}x_D}{4\left(\frac{1}{\tau''}-1\right)^2}}} \qquad (7)$$

and

$$C_1 = \sqrt{\gamma\left(t_D - \frac{P_{e1}x_D^2}{4\left(\frac{1}{\tau''}-1\right)^2}\right)} \qquad (8)$$

**Radial Flow**

Laplace space solutions to both horizontal fractures and cubic block-matrix fracture geometry cases, may be written in the following general form:

$$\overline{C}_{D1}(r_D,s) = \frac{1}{s} exp\left(\frac{Y-Y_0}{2}\right) \frac{A_i\left(\xi_r^{1/3}Y\right)}{A_i\left(\xi_r^{1/3}Y_0\right)} \qquad (9)$$

where:

$$Y = r_D + \frac{1}{4\xi_r} \qquad (10)$$

$$Y_0 = r_{D0} + \frac{1}{4\xi_r} \qquad (11)$$

The variable $\xi_r$ depends on the geometry of the matrix-fracture system. For the layered matrix-fracture geometry, it is given as follows:

$$\xi_r = s + \gamma + \frac{D_{D2}}{z_{D0}}\beta_r . tanh\left\{4\beta_r\left(\frac{E_D}{2} - z_{D0}\right)\right\} \qquad (12)$$

and for tho cubic block matrix-fracture geometry:

$$\xi_r = s + \gamma + \varepsilon\left\{\beta_r\, coth\left(z_{D0}\,\beta_r\right) - \frac{1}{z_{D0}}\right\} \qquad (13)$$

where:

$$\varepsilon = \frac{6}{d_D}\frac{\phi_2}{\phi_1} D_{D2} \qquad (14)$$

$$\beta_r = \sqrt{\frac{s+\gamma}{RD_{D2}}} \qquad (15)$$

The integral of Eq. 3 was numerically integrated using the algorithm of O'Hara and Smith (1969). The solution for the radial flow models in real space was obtained using the algorithm of Crump (1976) as numerical invertor, and the Airy functions were computed according to Abramowitz and Stegun (1970).

A solution for the finite step injection case may be obtained through the use of Eqs. 3 and 9 and the principle of superposition.

In some tests, the tracer is injected for a short period and are referred to as"spike" injection tests (Walkup, 1984). It has been stated (Walkup and Horne, 1985; Walkup, 1984), that the solution for the spike injection test can be derived through the time derivative of the continuous solution.

## OPTIMIZATION ALGORITHM

Optimization of the model parameters is accomplished using a nonlinear least-squares method of curve fitting. The objective function to be minimized is given by Eq. 16:

$$F(\alpha_1,\alpha_2,...,\alpha_j) = \sum_{i=1}^{N}[C(t_i) - C^*(t_i,\alpha_1,\alpha_2,...,\alpha_j)]^2 \qquad (16)$$

where:

| | |
|---|---|
| $C(t_i)$ | = measured tracer concentrations |
| $C(t_i,\alpha_j)$ | = calculated tracer concentrations |
| $\alpha_j$ | = matching parameters |
| $t$ | = time |
| $N$ | = number of data points |

It must be kept in mind that the reservoir-tracer parameters that could be estimated through the interpretation of a

tracer test, depend on the model used for this purpose. In this study the number of matching parameters used were 2, 5, and 2, 4 and 6, for the vertical (linear flow) fractures, horizontal (radial flow) fractures and cubic-block matrix fracture geometry, respectively.

The algorithm used to minimize the objective function given by Eq. 16 was that of Rosenbrock (1960). This is a direct search strategy method, where the direction of search and step lengths are fixed heuristically, or through a specific scheme, rather than through and optimal mathematical way (Fuentes, 1993). The main attraction of direct search methods rests on their proved simplicity and practicality.

The computer program used in this study to minimize the objective function given by Eq. 16 consists of a main program and four functions: a) The objective function; b) Function CX for the estimation of the matching parameters $\alpha_j$; c) Function CG for the lower restrictions set on the $\alpha_j$ parameters; and d) Function CH for the upper restrictions of the $\alpha_j$ paramters. This optimization procedure does not limit the number of parameters to be matched, neither the type of restrictions. The required partial derivatives with respect to the matching parameters are calculated numerically; for example for the parameters $\alpha_1$:

$$\frac{\partial F}{\partial \alpha_1} = \frac{F[\alpha_1 + \Delta\alpha_1, \alpha_2, ..., \alpha_j] - F[\alpha_1, \alpha_2, ..., \alpha_j]}{\Delta\alpha_1} \tag{17}$$

where $\Delta\alpha_1$ is a small differential increment.

This procedure requires an initial estimation for the matching parameters, and for the length of the optimization step, e, used in the solution of this problem.

For the initialization of this process, the objective function given by Eq. 16 is first evaluated with the initial data. Next, the objective function is evaluated with the result of incrementing the initial estimate by the optimization step e. If the function F decreases, we are moving in the right direction and the step e is multiplied by $\alpha_R(\alpha_R > 1)$. On the other hand, if F increases the step e is multiplied by - $\beta_R(0 \leq \beta_R \leq 1)$, and the direction of search is reversed. This procedure is followed for all the matching parameters. After each function evaluation, a check is made to determine whether the constraints are verified and boundary zones are not violated. The restrictions for the matching parameters were fixed based on the range of variation of the physical parameters reported in the literature (Grisak and Pickens, 1981; Weber and Baker, 1981; Hensel, 1981), as shown in Table 1.

## DISCUSSION OF RESULTS

The results of this section are synthetic, generated for the injection of the radioactive tritium tracer in naturally fractured reservoirs. The tracer responses were computed by means of solutions given by Eqs. 3 and 9, in addition to Eqs. 12 and 13. As mentioned, the range of the data used for the generation of these results is presented in Table 1.

**TABLE 1** RANGE OF THE PARAMETERS USED IN THIS STUDY (Partially taken from Pickens and Grisak, 1981; Weber and Baker, 1981; Hensel, 1989)

| | | | |
|---|---|---|---|
| Injection rate, | $10 \leq$ | $w, ton/hr$ | $\leq 300$ |
| Radial distance, | $200 \leq$ | $r, m$ | $\leq 1000$ |
| Formation thick., | $4.11 \leq$ | $h, m$ | $\leq 100$ |
| Fracture width, | $.0001 \leq$ | $, m$ | $\leq 0.01$ |
| Block size, | $2.05 \leq$ | $d, m$ | $\leq 25$ |
| Fracture disper., | $0.5 \leq$ | $\alpha, m$ | $\leq 400$ |
| Matrix porosity, | $0.01 \leq$ | $\phi_2$,frac. | $\leq 0.35$ |
| Matrix diff coef, | 1E-12$\leq$ | $D_2, m^2/D$ | $\leq$ 1.38E-5 |
| Adsorption const, | $.5 \leq$ | $R$,dimens. | $\leq 1$ |

With the purpose of simulating as close as possible real field conditions, random noise was introduced to the calculated tracer responses. The white noise consisted of a sorted non correlated sequence of numbers $a_i$, with a normal distribution with mean equal to zero and variance $\sigma_a^2$(Davis, 1973). The method used is based on the residual analysis (Montgomery, 1984), that considers that the independent random errors have a normal distribution, with mean equal to zero and variance equal to 1. The expresion used is given by Eq. 18:

$$C_{Di} = C_{Di} + a_i \tag{18}$$

where $C_{Di}$ is either the tracer concentration at time $t_i$ or that computed with Eqs. 3 and 9, $a_i$ is the random error and $C_{Di}$ is the concentration that simulates field data conditions.

This section presents results for conditions of finite step injection, for the three cases already mentioned. It is important to notice that for the case of vertical fractures only one fracture is considered; thus, due to the difference in pore volume between this case and the radial systems, smaller injection times were used in the linear example. Results presented are divided in two main groups. First the inverse problem is solved for "good data", which means synthetic data without noise. This is considered useful as a preliminary test of the capability of the optimization algorithm. Second, the algorithm is applied, as already mentioned, in a final test to noisy data. For the minimization of the objective function given by Eq. 16, a set of 34 data points was used.

Results of this study were generated for fixed values of the physical parameters that fall in the ranges presented in Table 1, included in Table 2. The values of column 2 of this table were taken from Jensen (1984). The exception is the value of fracture dispersivity $\alpha$, which was considered in accordance to the finding of Pickens and Grisak (1981), stating that dispersivity is a function of the mean travel distance. The injection rate is considered in this linear case through the definition of the Peclet number for the

fractured region $P_{e1}$. In other words, we choose a fixed value of this parameter for each simulation, for these cases equal to 5. For this linear case the thickness corresponds to the horizontal thickness E of the repetitive element shown in Fig.2 (Ramírez et al., 1990), which has been shown by these authors that for practical purposes does not importantly affect the results. This assumption is considered in Eq. 3.

**TABLE 2** DATA USED FOR THE TRACER RESPONSE EXAMPLES OF THIS STUDY

| | Linear | Radial |
|---|---|---|
| Injection rate, $q\ m^3/D$ | – | 2400 |
| Distance, $L$ or $r\ m$ | 210 | 250 |
| Formation thick., $h\ m$ | – | 4.11 |
| Fracture width, $w\ m$ | $1.8E-4$ | $1.0E-4$ |
| Block size, $d\ m$ | – | 2.05 |
| Fracture disper., $\alpha\ m$ | 21 | 25 |
| Matrix porosity, $\phi_2$ | 0.01 | 0.01 |
| Matrix diff coef, $D_2\ m^2/D$ | $1.E-8$ | $1.38E-5$ |
| Adsorption const, $k_d$ | 1 | 1 |
| Velocity, $v_L\ m/D$ | 909.6 | – |
| Radioactive decay const.,$\lambda\ 1/D$ | – | $1.534E-4$ |

As a starting point, Fig. 5 presents results for the linear flow of a chemical tracer in a vertical fractures case, for a finite step injection time $t_D$=0.85. The matching dimensionless parameters used are the Peclet number for the mobile or fractured region $P_{eL}$ and the $\alpha$ parameter, which combines the parameters of the immobile region. The precision used to obtain these results was $1 \times 10^5$, yielding an optimized objective function of $1.02 \times 10^5$, with matching parameters reported in Table 3.

**TABLE 3** LINEAR FLOW

| | Fig. 5 "Good Data" | | Fig. 6 "Noisy Data" | |
|---|---|---|---|---|
| Real parameters | Initial | Matched | Initial | Matched |
| $\alpha_1 = P_{e1} = 10$ | 5 | 10.07 | 8 | 10.26 |
| $\alpha_2 = \alpha = .0027$ | .004 | .0045 | .0015 | .0098 |

Fig. 6 shows the results of Fig. 5 after being altered to include random noise. In this graph and those to follow, the continuous curve represents the match, and the individual symbols the data to be matched. The discontinuous curves, as indicated, correspond to the 95% confidence intervals. The precision used to obtain these results was $1 \times 10^5$, yielding an optimized objective function of $1.23 \times 10^2$, with matching parameters reported in Table 3. We can observe that despite the dispersion of the noisy data, most of it fall within the confidence interval bandwith. Table 3 shows a comparion of matched results of Figs. 5 and 6. Two points are noteworthy. First, the initial data was selected closer to the real parameters for the noisy data match of Fig. 6, and second, the match is more sensitive to the Peclet number for the fracture region than to the $\alpha$ parameter. This is clearly noticed by the big percentage error of the $\alpha$ matched parameter value with respect to the real value, greater than 100%.

Next, results of a radial flow five parameters noisy data match for a layered (horizontal fractures) reservoir, are presented in Fig. 7 and Table 4. The matching parameters used were the fracture dispersivity $\alpha$, matrix porosity $\phi_2$, fracture half-width $w$, matrix diffusion coefficient $D_2$, and the dimensionless retardation parameter $R$. It is important to notice that these matching parameters directly correspond to the real variables of the tracer flow problem, with the exception of the retardation factor $R$ that requires the formation density to estimate the adsorption constant $k_d$. The finite step injection time considered was $t_D$=52.5. Results were computed through Eqs. 9 and 12,

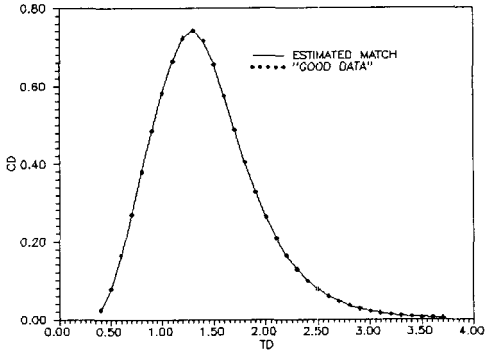


Fig. 5 Tracer response match of "good data" through two parameters, linear flow (vertical fracture).

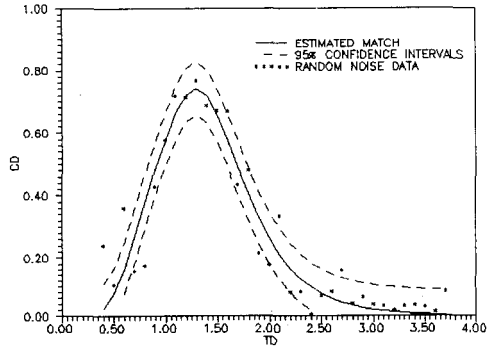


Fig. 6 Random noise tracer response match through two parameters, linear flow (vertical fractures).

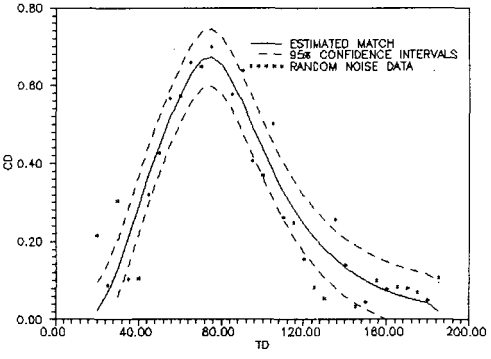


Fig. 7 Random noise tracer response match through five parameters, radial flow for a layered (horizontal fractures) reservoir.

considering only a horizontal fracture, as indicated in Fig. 3, which means that the reservoir thickness $h$ is equal the thickness of the symmetry element $E$ of this figure. The precision used was the same stated previously for the linear flow case, yielding an optimized objective function of $2.362\times10^2$, with matching parameters reported in Table 4. It can be observed from this figure that despite the dispersion of the noisy data, the match is considered reasonable due to the fact that most of the data fall within the 95% confidence interval bandwidth. For this match results, as also previously pointed out for the linear flow case, and the rest to follow, the fracture dispersivity $\alpha$ was found to be the most sensitive parameter on the inverse solution.

**TABLE 4** LAYERED MATRIX-FRACTURE GEOMETRY, FIVE MATCHING PARAMETERS

| | Fig. 7 | |
|---|---|---|
| Real parameters | Initial | Matched |
| $\alpha_1 = \alpha = 25\,m$ | 23 | 25.1672 |
| $\alpha_2 = \phi_2 = 0.01$ | .009 | 0.0128 |
| $\alpha_3 = w = .0001\,m$ | 0.00008 | .000085 |
| $\alpha_4 = D_e = 1.38\text{E-}5m^2/d$ | $1E-5$ | $1.278E-5$ |
| $\alpha_5 = R$=1.0 | .8 | .7528 |

Last, we present results for the cubic block matrix-fracture geometry systems. This geometry is considered a more realistic visualization of a naturally fractured reservoir (Ramírez and Samaniego, 1992). All results are for noisy data matches, presented in Figs. 8-10 and Tables 5-7. The six matching parameters for the general case 3 were those five already mentioned for the layered case, in addition to the matrix block size parameter $d$, with the same correspondence to real variables and exception previously discussed for the layered case. Cases 1 and 2 are particularizations of case 3, with matching parameters for the former being matrix porosity $\phi_2$ and matrix block size $d$, and for the latter, in addition to these of case 1, the fracture dispersivity $\alpha$ and the fracture half-width $w$. The finite step injection time considered was $t_D$=52.5. The original tracer response before being noisly altered, was computed by means of Eqs. 9 and 13. The precision used was the same stated previously for the linear flow case, yielding values of the optimized objective function of approximately 0.02 for cases 1 to 3, with matching parameters reported in Tables 5-7.

**TABLE 5** CUBIC BLOCK MATRIX-FRACTURE GEOMETRY, CASE 1, TWO MATCHING PARAMETERS

| | Fig. 8 | |
|---|---|---|
| Real parameters | Initial | Matched |
| $\alpha_1 = \phi_2 = .01$ | 0.03 | 0.0134 |
| $\alpha_2 = d = 2.05m$ | 1.0 | 2.29 |

It can be observed from Figs. 8-10 that despite the dispersion of the noisy data, the match is considered reasonable due to the fact that most of the data fall within the 95% confidence interval bandwidth. Further analysis of these matches based on the results presented in Tables 5-7, indicates important percentage differences of the matched results with respect to the real parameters, with the exception previously mentioned of the fracture dispersivity $\alpha$, in addition to the retardation factor $R$.

**TABLE 6** CUBIC BLOCK MATRIX-FRACTURE GEOMETRY, CASE 2, FOUR MATCHING PARAMETERS

| | Fig. 9 | |
|---|---|---|
| Real parameters | Initial | Matched |
| $\alpha_1 = \alpha = 25m$ | 20 | 25.35 |
| $\alpha_2 = \phi_2 = .01$ | .02 | 0.045 |
| $\alpha_3 = w = .0001m$ | .0015 | .00147 |
| $\alpha_4 = d = 2.05m$ | .9 | 1.618 |

**TABLE 7** CUBIC BLOCK MATRIX-FRACTURE GEOMETRY, CASE 3, SIX MATCHING PARAMETERS

| | Fig. 10 | |
|---|---|---|
| Real parameters | Initial | Matched |
| $\alpha_1 = \alpha = 25\,m$ | 23 | 24.867 |
| $\alpha_2 = \phi_2 = 0.01$ | .015 | 0.0153 |
| $\alpha_3 = w = .0001\,m$ | 0.0001 | .000085 |
| $\alpha_4 = d = 2.05\,m$ | 1.5 | 2.804 |
| $\alpha_5 = D_e = 1.38\text{E-}5m^2/d$ | $9.9E-6$ | $9.88E-6$ |
| $\alpha_6 = R$=1.0 | .98 | .99 |

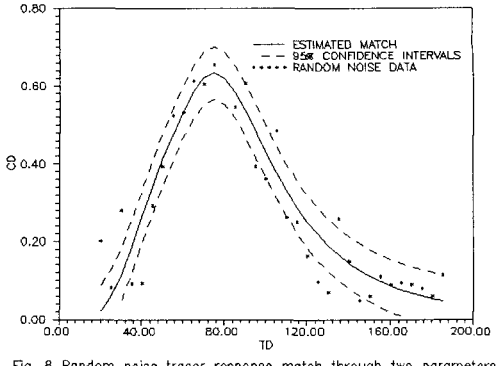

Fig. 8 Random noise tracer response match through two parameters, cubic matrix-fracture geometry.

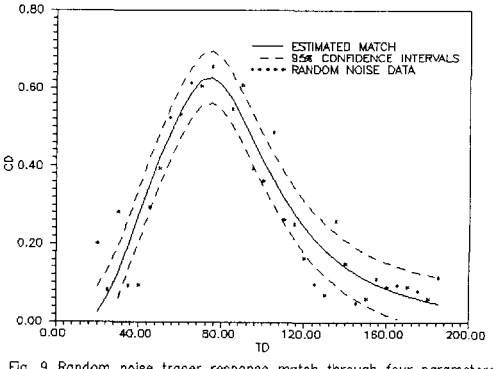

Fig. 9 Random noise tracer response match through four parameters, cubic matrix-fracture geometry.

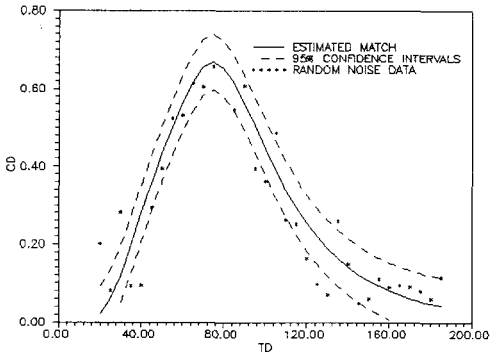


Fig. 10 Random noise tracer response match through six parameters, cubic matrix–fracture geometry

Further match analysis of "good data" results of Fig. 5 and Table 3, and of noisly altered tracer responses of Figs. 6-10 and Tables 4-7, concludes that the percentage errors between the matched and the real parameters values, depend first on the quality of the tracer concentration response, because it has been shown that these errors increase for the latter responses. Based on this finding, it can be stated that for reservoir characterization purposes it is necessary to have data as accurate and representative as possible. Smoothing and filtering data techniques can be used to accomplish this task. Second, results not completely shown in this paper (Ramírez, 1992), indicate that the errors also depend in the closeness of the initial or starting data. Thus, we should follow a synergy oriented interpretation, using information coming from all possible sources, i.e., geological, geophysical, petrophysis, well test analysis, etc.

## CONCLUSIONS

The main purpose of this study has been to present a solution for the inverse problem to the flow of tracers in naturally fractured reservoirs. The cases discussed consider mainly radioactive tracers but the solutions used are general, and a particular case would be the flow of chemical tracers.

Based on the material presented in this paper, the following conclusions are pertinent.

1. The Rosenbrock method for nonlinear regression used in this study has proved to be a powerful tool for providing an inverse solution to the flow of tracers.

2. The inverse problem analysis has included the linear flow vertical fractures, and the radial flow cases of horizontal fractures, and cubic block matrix-fracture geometry.

3. The maximum number of possible matching parameters was six, corresponding to the cubic block case.

4. The parameters that showed the most sensitivity on the inverse solutions were the Peclet number for the fracture region $P_{e1}$ for linear flow, and the fracture dispersivity $\alpha$ for the radial cases.

5. The errors between the matched and the real parameters values depend on the quality of the tracer concentration response, and on the closeness of the initial data to the real parameters.

6. A synergy oriented approach should be followed for the interpretation of a tracer test.

## NOMENCLATURE

$a$ = advection parameter, Eq. 2, $L^2/t$
$A_i(x)$ = Airy function
$B_1$ = function defined by Eq. 7
$C$ = tracer concentration
$C_1$ = function defined by Eq. 8
$C(t,\alpha_j)$ = calculated tracer concentration
$C_D$ = dimensionless tracer concentration
$\overline{C}_D$ = Laplace space dimensionless .. tracer concentration
$C_{Di}$ = calculated dimensionless tracer concentration .. at $t_i$
$C_{Di}$ = dimensionless noisy tracer concentration .. at $t_i$
$d$ = matrix block size, $L$
$d_D$ = dimensionless matrix block size, .. d / $\alpha$
$D_L$ = longitudinal dispersion coefficient .. for linear flow, $L^2/t$
$D_2$ = matrix diffusion coefficient, $L^2/t$
$D_{D2}$ = dimensionless matrix diffusion coefficient, .. $D_2/a$
$D_r$ = longitudinal dispersion coefficient .. for radial flow, $L^2/t$
$E$ = fracture spacing, $L$
$F$ = objective function, Eq. 16.
$F_1$ = function defined by Eq. 4
$F_2$ = function defined by Eq. 5
$h$ = reservoir thickness, $L$
$k_d$ = adsorption constant, $L^3/M$
$L$ = distance from injector to producer, $L$
$ND$ = number of cubic blocks in reservoir .. thickness $h$
$P_{e1}$ = Peclet number, dimensionless $v_L L/D_1$
$q$ = constant injection rate, $L^3/t$
$r$ = radial distance, $L$
$r_D$ = dimensionless radial distance
$r_w$ = wellbore radius,$L$
$r_{D0}$ = dimensionless wellbore radius
$R$ = dimensionless parameter, .. $\phi_2/[\phi_2 + \rho k_d(1-\phi_2)]$
$s$ = Laplace space parameter
$t$ = time, $t$
$t_D$ = dimensionless time, $qt/2\pi h\phi_1\alpha^2$ = .. $at/\alpha^2$
$U$ = step function, Eq. 3
$v$ = fluid velocity, Eq. 1, $L/t$
$w$ = fracture half-width, $L$
$x$ = distance in the $x$ direction, linear flow
$x_D$ = dimensionless distance in the $x$ direction, .. x/L

$y$ = distance in the $y$ direction, linear flow
$y_D$ = dimensionless distance in the $y$ direction, .. y/L
$Y$ = dimensionless parameter defined .. by Eq. 10
$Y_0$ = dimensionless parameter defined .. by Eq. 11
$z$ = vertical coordinate, radial flow, $L$
$z_{D0}$ = dimensionless vertical distance of the .. fluid film, $(d/2+\delta)\alpha$

### Greek symbols

$\alpha$ = dimensionless parameter, $\phi_2\sqrt{P_{e2}}/(w-\delta)$
$\alpha_L$ = longitudinal fracture dispersivity, $L$
$\alpha_i$ = dimensionless matching parameters, Eq. 16
$\beta_r$ = dimensionless parameter, Eq. 15
$\beta_R$ = constant used to multiply the optimization .. step e when the objective function increases.
$\gamma$ = dimensionless parameter, $\lambda\alpha^2/a$
$\delta$ = stagnant fluid film thickness, $L$
$\varepsilon$ = dimensionless parameter, Eq. 14
$\lambda$ = radioactive decay constant, $1/t$
$\xi$ = dimensionless parameters, Eqs. 12 and 13
$\rho$ = porous media density, $M/L^3$
$\tau$ = dummy variable of integration, Eq. 3
$\phi$ = porosity, fraction

### Subscripts

$c$ = cubic
$D$ = dimensionless
$L$ = linear
$i$ = initial, index (Eq. 16)
$r$ = radial
0 = origin or related to tracer injection .. concentration
1 = mobile or fractured region
2 = immobile (fluid layer and porous matrix) .. region

## REFERENCES


Abramowitz, M. and Stegun, I.A., 1970. Handbook of Mathematical Functions with Formulas, Graphs and Mathematical Tables. National Bureau of Standards, Washington, D.C.

Brigham, W.E. and Abbaszadeh-Dehghani, M., 1987. Tracer Testing for Reservoir Description J. Pet. Tech., Vol. 35, No. 5 (May) 519-527.

Crump, K.S., 1976. Numerical Inversion of Laplace Transforms Using a Fourier Series Approximation. J. ACM, Vol. 23, No. 1 (Jan.) 89-96.

Davis, C.J., 1973. Statistics and Data Analysis in Geology. John Wiley and Sons, New York.

Fossum, M. P. and Horne, R. N., 1982. Interpretation of Tracer Return Profiles at Wairakei Geothermal Field Using Fracture Analysis. Geothermal Resources Counsil, Transactions, Vol. 6.

Fossum, M. P., 1984. Tracer Analysis in a Fractured Geothermal Reservoir: Field Results from Wairakei, New Zealand. Stanford Geothermal Program, SGP-TR-56, Stanford, Ca.

Fuentes-Nucamendi, F.A., 1993. Optimization of Dry Gas Production Systems. M. Sc. report, Department of Petroleum Engineering, Stanford University, Stanford, Ca.

Hensel, W.M., Jr., 1989. A Perspective-Look at Fracture Porosity. SPE Formation Evaluation J., Vol. 4, No. 4 (Dec.) 531-534.

Horne, R.N., and Rodríguez, F., 1983. Dispersion in Tracer Flow in Fractured Geothermal Systems. Geophysical Research Letters, Vol. 10, No. 4, 288-292.

Jensen, C.L., 1983. Matrix Diffusion and Its Effect on the Modeling of Tracer Returns From the Fractured Geothermal Reservoir at Wairakei New Zealand. Stanford Geothermal Program, SGP-TR-71, Stanford, Ca.

Montgomery, D., 1984. Design and Analysis of Experiments. John Wiley and Sons, New York.

O'Hara, H. and Smith, F.J., 1969. The Evaluation of Definite Integrals by Interval Subdivision. Computer Journal, Vol. 12, 179-182.

Pickens, J.F. and Grisak, G.E., 1981. Modeling of Scale-Dependent Dispersion in Hydrogeologic Systems. Water Resour. Res., Vol. 17, No. 6 (Dec.) 1701-1711.

Ramírez, S.J., Rivera, R.J., Samaniego, V.F., and Rodríguez F., 1990. A Semianalytical Solution for Tracer Flow in Naturally Fractured Reservoirs. Proceedings, Fifteenth Workshop on Geothermal Reservoir Engineering, SGP-TR-130, Stanford U., Stanford, Ca., January 23-25.

Ramírez, S.J., Samaniego, V.F., Rivera, R.J., and Rodríguez F., 1991. An Investigation of Radial Tracer Flow in Naturally Fractured Reservoirs Proceedings, Sixteenth Workshop on Geothermal Reservoir Engineering, SGP-TR-134, Stanford U., Stanford, Ca., January 23-25.

Ramírez, S.J., and Samaniego V.F., 1992. A Cubic Matrix-Fracture Geometry Model for Radial Tracer Flow in Naturally Fractured Reservoirs Proceedings, Seventeenth Workshop on Geothermal Reservoir Engineering, SGP-TR-141, Stanford U., Stanford, Ca., January 29-31, 1992.

Ramírez, S.J., 1992 "Flujo de Trazadores en Yacimientos Naturalmente Fracturados", Ph.D dissertation, School of Engineering, National University of Mexico, Nov.

Rosenbrock, H.H., 1960. An Automatic Method for Finding the Greatest or Least Value of a Function. Computer Journal, 3, 175-184.

Shinta, A.A. and Kazemi, H., 1993. Tracer Transport in Characterization of Dual-Porosity Reservoirs. Paper SPE 26636, presented at SPE Annual Technical Conference and Exhibition, Houston, Tx., 3-6 October.

Walkup, G.W., 1984. Characterization of Retention Processes and Their Effect on Analysis of Tracer Tests in Fractured Reservoirs. Stanford Geothermal Program, SGP-TR-77, Stanford, Ca., June.

Walkup, G.W., and Horne, R. N., 1985. Characterization of Tracer Retention Processes and Their Effect on Tracer Transport in Fractured Geothermal Reservoirs. Paper SPE 13610, presented at California Regional Meeting, Bakersfield, Ca., March 27-29.

Weber, K.J. and Baker, M., 1981. Fracture and Vuggy Porosity. Paper SPE 10332, presented at SPE Annual Fall Technical Conference and Exhibition, San Antonio, Tx., 5-7 Oct.

PROCEEDINGS, Nineteenth Workshop on Geothermal Reservoir Engineering
Stanford University, Stanford, California, January 18-20, 1994
SGP-TR-147

# LIQUID-PHASE DISPERSION DURING INJECTION INTO VAPOR-DOMINATED RESERVOIRS

Karsten Pruess

Earth Sciences Division, Lawrence Berkeley Laboratory
University of California, Berkeley, CA 94720

## ABSTRACT

The behavior of water injection plumes in vapor-dominated reservoirs is examined. Stressing the similarity to water infiltration in heterogeneous soils, we suggest that ever-present heterogeneities in individual fractures and fracture networks will cause a lateral broadening of descending injection plumes. The process of lateral spreading of liquid phase is viewed in analogy to transverse dispersion in miscible displacement. To account for the postulated "phase dispersion" the conventional two-phase immiscible flow theory is extended by adding a Fickian-type dispersive term.

The validity of the proposed phase dispersion model is explored by means of simulations with detailed resolution of small-scale heterogeneity. We also present an illustrative application to injection into a depleted vapor zone. It is concluded that phase dispersion effects will broaden descending injection plumes, with important consequences for pressure support and potential water breakthrough at neighboring production wells.

## INTRODUCTION

Water injection into depleted vapor zones has similarities as well as differences to water injection into unsaturated zones above the water table. In both cases the medium contains a gas (or vapor) phase with very small vertical pressure gradient. Water migrates in response to the combined action of pressure, capillary, and gravity forces. Special effects arise in the geothermal injection problem from the strong coupling between fluid flow and heat transfer, giving rise to boiling and condensation processes and associated two-phase flow effects. Injection of liquid water into vapor-dominated reservoirs generates heat pipe effects (water-vapor counterflow), with very efficient heat transfer (Calore et al., 1986).

In response to liquid injection the water saturation near the injection point will increase. Water saturation may rise all the way to 100 %, establishing single-phase liquid conditions with pressure buildup and consequent lateral flow. If the permeability of the medium is sufficiently high, or water fluxes sufficiently low, the medium will remain in two-phase conditions. Then under isothermal conditions no pressure buildup will occur, and water flow will be affected only by gravity and capillary forces. In media with large pores, such as coarse-grained soils, or "large" fractures in hard rocks, capillary effects tend to be weak, and water flow will be dominated by gravity effects. In this case water will move primarily downward, but "straight" downward flow is only possible when appropriate permeability is available in the vertical direction. Water flowing downward in coarse soils, or in large (sub-)vertical fractures, may encounter low-permeability obstacles, such as silt or clay lenses in soils, or asperity contacts between fracture walls. Water will pond atop the obstacles and be diverted sideways, until other predominantly vertical pathways are reached (Fig. 1).

When the permeable medium into which water is injected is modeled as homogeneous, with weak capillary effects, injection plumes are predicted to remain narrow and slump essentially vertically downward (Calore et al., 1986; Lai and Bodvarsson, 1991; Shook and Faulder, 1991; Pruess, 1991a). However, horizontal diversion of water from smaller-scale heterogeneities may be an important process. It would tend to broaden injection plumes, with important consequences for heat transfer and vaporization.

The conventional treatment of two-phase flow can model horizontal flow due to pressure and capillary effects. However, horizontal flow diversion from media heterogeneities can be represented only if such heterogeneity is modeled in full explicit detail. In practical applications of reservoir modeling, explicit modeling of small-scale reservoir heterogeneities would require prohibitively large numbers of grid blocks, because heterogeneities occur on many different scales (impermeable lenses, individual fractures, fracture networks, lithologic units, etc.).

It is the purpose of this paper to propose an extension of conventional two-phase flow theory that attempts to capture the essential effects of smaller-scale heterogeneity in an approximate fashion, by adding a dispersive flow term to the governing equations. The validity of the proposed model is examined by means of simulations that represent small-scale heterogeneity in full explicit detail. The paper concludes with illustrative applications to water injection into depleted vapor zones. The simulations were performed with LBL's general-purpose reservoir simulator TOUGH2 (Pruess, 1991b), enhanced with a set of preconditioned conjugate gradient routines to be able to solve problems with of the order of 10,000 grid blocks (G. Moridis, private communication, 1993).

## MATHEMATICAL MODEL

The mass balance equation for two-phase single-component flow of water and vapor is customarily written as

$$\frac{\partial}{\partial t} \sum_{\substack{\beta=\text{liquid,}\\ \text{vapor}}} \phi\, S_\beta\, \rho_\beta \;=\; -\,\text{div} \sum_{\substack{\beta=\text{liquid,}\\ \text{vapor}}} \mathbf{F}_\beta \qquad (1),$$

where $\phi$ is porosity, S is saturation, $\rho$ is fluid density, and fluid fluxes $\mathbf{F}_\beta$ in liquid and vapor phases are given by a multiphase version of Darcy's law, as follows.

$$\mathbf{F}_\beta = -k\frac{k_{r\beta}}{\mu_\beta}\rho_\beta\left(\nabla P_\beta - \rho_\beta \mathbf{g}\right) \qquad (2).$$

The index $\beta$ denotes liquid or vapor phase, k is the absolute permeability, $k_{r\beta}$ is relative permeability for phase $\beta$, $\mu$ is viscosity, $P_\beta$ is pressure in phase $\beta$, and **g** is acceleration of gravity. Our proposed Fickian-type diffusion model for phase dispersion involves adding a dispersive flux term for liquid phase to Eq. (2) which, in analogy to solute dispersion in miscible flow (de Marsily, 1986), is written as

$$\mathbf{F}_{l,dis} = -\rho_l \phi \mathbf{D}_{dis} \nabla S_l \qquad (3).$$

We now specialize to conditions where advective flow is dominated by gravity. Introducing the propagation velocity v of saturation disturbances in the absence of capillary effects (Pruess, 1991a),

$$v = \frac{k}{\phi}\frac{\rho_l g}{\mu_l}\frac{dk_{rl}}{dS_l}\frac{\mathbf{g}}{g} \qquad (4),$$

the dispersion tensor $\mathbf{D}_{dis}$ is written as (Pruess, 1993)

$$\mathbf{D}_{dis} = v\left(\alpha_T\left[\mathbf{e}_x\mathbf{e}_x + \mathbf{e}_y\mathbf{e}_y\right] + \alpha_L\mathbf{e}_z\mathbf{e}_z\right) \qquad (5).$$

Here we have introduced transverse and longitudinal dispersivities $\alpha_T$, $\alpha_L$, and unit vectors **e** in the x, y, and z-directions. (Positive z-direction is upward.) g and v are the magnitudes, respectively, of the gravitational acceleration and velocity vectors. Inserting Eqs. (4, 5) into (3), the dispersive liquid flux becomes

$$\mathbf{F}_{l,dis} = -k\frac{\rho_l g}{\mu_l}\rho_l\left(\alpha_T\left[\mathbf{e}_x\mathbf{e}_x + \mathbf{e}_y\mathbf{e}_y\right] + \alpha_L\mathbf{e}_z\mathbf{e}_z\right)\nabla k_{rl} \qquad (6).$$

The flux given by Eq. (6) has been added to Eq. (2), and has been incorporated into our general-purpose reservoir simulator TOUGH2 (Pruess, 1991b). Standard first-order finite difference approximations have been used for discretizing the components of the relative permeability gradient vector.

We note in passing that capillary-driven liquid flux can be written, from Eq. (2), as

$$\begin{aligned}\mathbf{F}_{l,cap} &= -k\frac{k_{rl}}{\mu_l}\rho_l \nabla P_{cap} \\ &= -k\frac{\rho_l g}{\mu_l}\rho_l\left(\frac{1}{\rho_l g}\frac{dP_{cap}}{d\ln k_{rl}}\right)\nabla k_{rl}\end{aligned} \qquad (7).$$

Comparing with Eq. (6), it is seen that the proposed phase-dispersive flux, apart from being anisotropic, has the same structure as capillary flux. The capillary dispersivity is given by

$$\alpha_{cap} = \frac{1}{\rho_l g}\frac{dP_{cap}}{d\ln k_{rl}} \qquad (8).$$

From the correspondence between phase-dispersive and capillary fluxes, we expect that phase dispersion effects may be important when capillary effects are weak, i.e., for liquid flow in "coarse" heterogeneous media such as large fractures and coarse-grained soils. Longitudinal (vertical) phase dispersion will modify the predominant downward advective flow. Transverse dispersion may lead to qualitatively new behavior, causing a lateral (horizontal) spreading of liquid plumes even when capillary pressures are weak. In the remainder of the paper we will focus on transverse dispersion effects.

## NUMERICAL EXPERIMENTS

To examine the validity of the proposed phase dispersion model we have performed numerical simulation experiments. In these simulations, small-scale medium heterogeneity was resolved in detail, and no explicit allowance for phase dispersion as in Eq. (6) was made. Liquid plume behavior was explored in media with different types of deterministic and random heterogeneities. As an example, Fig. 2 shows a 2-D vertical section of a medium that features a random distribution of impermeable obstacles. The problem was designed to capture a heterogeneity structure as may be encountered in shallow sedimentary soils (see specifications given in Table 1). Similar parameters may be applicable to individual fractures in vapor-dominated reservoirs. The impermeable obstacles can be interpreted as representing shale, silt, or clay bodies (Begg et al., 1985). In the present context they may be thought of as representing (nearly) impermeable asperity contacts between fracture walls.

TABLE 1. PARAMETERS FOR TEST PROBLEMS WITH DETAILED EXPLICIT HETEROGENEITY.

| | |
|---|---|
| Permeability<br>Porosity | $k = 10^{-11}$ m$^2$<br>$\phi = 0.35$ |
| Relative Permeability | |
| van Genuchten function (1980)<br>$k_{rl} = \sqrt{S^*}\left\{1-\left(1-\left[S^*\right]^{1/\lambda}\right)^{\lambda}\right\}^2$ | $S^* = (S_l - S_{lr})/(1 - S_{lr})$ |
| irreducible water saturation<br>exponent | $S_{lr} = 0.15$<br>$\lambda = 0.457$ |
| Geometry of Flow Domain | |
| 2-D vertical (X-Z) section<br>width (X)<br>depth (Z)<br>gridding | <br>20 m<br>15 m<br>80 x 120 = 9600 blocks<br>$\Delta X$ = .25 m<br>$\Delta Z$ = .125 m |
| heterogeneity:<br>random distribution of impermeable obstacles | |
| Initial Water Saturation | |
| for $6.5 \le X \le 13.5$ m and $-3.5 \le Z \le 0$ m<br>remainder of domain | $S_l = 0.99$<br>$S_l = 0.15$ |

The numerical experiments involve placing a localized plume of enhanced liquid saturation into a medium such as shown in Fig. 2. The plume is then permitted to flow in

response to gravitational force in isothermal mode, not considering any phase change processes. Plume behavior is analyzed by evaluating spatial moments (Essaid et al., 1993), defined by

$$M_{ijk} = \int x^i y^j z^k \phi\left(S_l - S_{l0}\right) dV \qquad (9).$$

Plume spreading in the transverse direction is expressed by the mean square plume size, or variance,

$$\sigma_T^2 = \frac{M_{200}}{M_{000}} - \langle x \rangle^2 \qquad (10).$$

The center of mass coordinates of the plume are given by

$$\langle x \rangle = M_{100}/M_{000} \qquad (11a)$$

$$\langle z \rangle = M_{001}/M_{000} \qquad (11b).$$

It is well known that an effective diffusivity for a localized spreading plume can be calculated as (Sahimi et al., 1986; Freyberg, 1986)

$$D_T = \frac{1}{2}\frac{d}{dt}\left(\sigma_T^2\right) \qquad (12).$$

Dividing by the downward velocity $d\langle z \rangle/dt$ of plume movement yields the transverse dispersivity

$$\alpha_T = \frac{D_T}{(d\langle z \rangle/dt)} \qquad (13).$$

Fig. 3 shows transverse dispersivites calculated for two heterogeneous media with different distribution of random obstacles. Initially, dispersivities undergo some transient changes. These are caused by the extreme discontinuity of the initial saturation distribution. For the large initial water saturation of $S_l = .99$ in the plume water flow rates are large. The consequent rapid saturation changes are poorly resolved with the space and time discretization used in the simulation. As rates of water flow and saturation change slow down the dispersivities are seen to stabilize at very nearly constant values. These results as well as others not shown here confirm that transverse plume spreading from the intrinsic heterogeneities of the medium indeed gives rise to a Fickian diffusion process. We conclude that the heterogeneous medium behaves like an effective dispersive medium.

## APPLICATION

To explore and illustrate phase-dispersive effects during water injection into vapor-dominated reservoirs we consider a two-dimensional radially symmetric problem (Fig. 4). An injection well penetrates the top 500 m of a 1000 m thick reservoir. Problem parameters are intended to be representative of conditions in depleted zones at The Geysers (see Table 2; Pruess and Enedy, 1993). The reservoir is described as an effective single-porosity medium, using a large irreducible water saturation of $S_{lr}$ = 80 % to approximate dual-permeability (fracture-matrix) behavior (Pruess, 1983). Initial conditions are a temperature of 240 °C throughout, and gravity-equilibrated pressures relative to 10 bars at the reservoir top. These conditions are maintained at the outer radius of R = 220 m, corresponding to an area of approximately 40 acres for the injection well. Liquid water is injected at a rate of 25 kg/s, and results for water saturation distributions and reservoir pressures after 691.9 days of injection are shown in Figs. 5 and 6.

In the absence of phase dispersion, the injection plume shows a predominant downward movement (Calore et al., 1986; Lai and Bodvarsson, 1991; Shook and Faulder, 1991). Downward as opposed to lateral flow would be even more pronounced for larger permeability, lower injection rate, or coarser discretization with larger cross-sectional area for downward flow of injectate. Gridding in our simulation is fine enough that considerable lateral movement of the injected water takes place. The radius $R_g$ to which the injection plume would have to grow so that water could flow downward under gravity drive at a rate equal to the entire injection rate can be estimated from Eq. (2). For a vertical permeability of $50 \times 10^{-15}$ m$^2$ and a rate of 25 kg/s, excluding vaporization effects, we obtain $R_g$ = 52.1 m for T = 240 °C water, and $R_g$ = 120.6 m for T = 25 °C water.

Phase dispersion enhances the lateral and diminishes the downward movement of injectate, as expected (Figs. 5b, c). An obvious implication is that neglect of phase-dispersive processes may underestimate the potential for water breakthrough at laterally offset production wells.

TABLE 2. PARAMETERS FOR TWO-DIMENSIONAL R-Z INJECTION PROBLEM.

| | |
|---|---|
| permeability | $k = 50 \times 10^{-15}$ m$^2$ |
| porosity | $\phi = .04$ |
| Rock Properties | |
| density | $\rho_R = 2600$ kg/m$^3$ |
| specific heat | $c_R = 1000$ J/kg °C |
| heat conductivity | $K_R = 2.51$ W/m °C |
| Relative Permeability | |
| Corey-curves | |
| irreducible water saturation | $S_{lr} = .15$ |
| irreducible gas saturation | $S_{gr} = .05$ |
| Initial Conditions | |
| temperature | 240 °C |
| pressure | 10 bars (at reservoir top) |
| Injection Specifications | |
| rate | 25 kg/s |
| enthalpy | $8.4 \times 10^4$ J/kg |

It is interesting to note that inclusion of phase dispersion diminishes the volume of the single-phase liquid zone and gives rise to very broad two-phase regions. The pressure response from injection shows much detailed spatial structure, with pressures increasing in some regions, decreasing in others (Figs. 6a-c). When phase dispersion is included, more heat transfer and vaporization of injectate are predicted to occur at shallower depths. In the case without phase dispersion most pressure support is coming from the deepest regions. Increasing levels of phase dispersion will confine vaporization and pressure support to shallower depths, but extending to greater distance from the injection well. Pressures near the injection well are considerably lower than in the absence of phase dispersion, especially near the top of the injection interval. These low-pressure regions consume considerable

amounts of vapor by condensation (Pruess and Enedy, 1993). Nearby production wells may respond with flow rate increases or decreases, depending on the elevation difference between open intervals. Production interference will be time-dependent as zones of increased as well as decreased pressures migrate outward from the injector.

## DISCUSSION AND CONCLUSIONS

Injection response in vapor-dominated reservoirs is expected to be strongly influenced by heterogeneous reservoir permeability. Even though injected water is likely to flow primarily downward in response to gravitational body force, such flow will be strictly vertical only if appropriate permeability is available. Descending injection plumes will tend to pond atop regions of lower permeability, and will be diverted sideways until again predominantly downward pathways are encountered. Thus, reservoir heterogeneity is expected to cause a lateral broadening of injection plumes.

Stressing the analogy to solute (tracer) dispersion in heterogeneous media, we have proposed a mathematical model that approximates injection plume spreading as a Fickian diffusion process. Support for this concept was provided by simulations with detailed explicit resolution of small-scale permeability heterogeneity. Phase dispersion effects were illustrated by means of an example that is representative of water injection into depleted vapor zones at The Geysers. It was shown that phase dispersion can significantly affect water breakthrough at neighboring production wells. Pressure support through boiling of injectate was predicted to occur below the injection interval, while at shallower depths reservoir steam is consumed by condensation, with associated pressure decline.

It appears that phase dispersion may cause important effects during liquid injection into heterogeneous vapor-dominated reservoirs, and that it should be included in mathematical models. Work is needed to identify appropriate values for phase dispersivities for use in field simulations.

## ACKNOWLEDGEMENT

This work was supported by the Assistant Secretary for Energy Efficiency and Renewable Energy, Geothermal Division, of the U.S. Department of Energy under Contract No. DE-AC03-76SF00098. The author thanks his colleague George Moridis for providing a package of preconditioned conjugate gradient routines that made possible the simulation of problems with of the order of 10,000 grid blocks. For a critical review of the manuscript and the suggestion of improvements thanks are due to George Moridis and Marcelo Lippmann.

## REFERENCES

Begg, S.H., D.M. Chang, and H.H. Haldorsen. A Simple Statistical Method for Calculating the Effective Vertical Permeability of a Reservoir Containing Discontinuous Shales, paper SPE-14271, presented at the 60th Annual Technical Conference and Exhibition of the Society of Petroleum Engineers, Las Vegas, NV, September 1985.

Calore, C., K. Pruess, and R. Celati. Modeling Studies of Cold Water Injection into Fluid-Depleted, Vapor-Dominated Geothermal Reservoirs, Proc., 11th Workshop Geothermal Reservoir Engineering, pp. 161-168, Stanford University, Stanford, California, January 1986.

de Marsily, G. *Quantitative Hydrogeology*, Academic Press, Orlando, FL, 1986.

Essaid, H.I., W.N. Herkelrath and K.M. Hess. Simulation of Fluid Distributions Observed at a Crude Oil Spill Site Incorporating Hysteresis, Oil Entrapment, and Spatial Variability of Hydraulic Properties, *Water Resources Res.*, Vol. 29, No. 6, pp. 1753-1770, 1993.

Freyberg, D.L., A Natural Gradient Experiment on Solute Transport in a Sand Aquifer. 2. Spatial Moments and the Advection and Dispersion of Nonreactive Tracers, *Water Resources Res.*, Vol. 22, No. 13, pp. 2031-2046, 1986.

Lai, C. H. and G. S. Bodvarsson. Numerical Studies of Cold Water Injection into Vapor-Dominated Geothermal Systems, paper SPE-21788, presented at Society of Petroleum Engineers Western National Meeting, Long Beach, CA, March 1991.

Pruess, K. Heat Transfer in Fractured Geothermal Reservoirs with Boiling, *Water Resources Res.*, Vol. 19, No. 1, pp. 201-208, 1983.

Pruess, K. Grid Orientation and Capillary Pressure Effects in the Simulation of Water Injection into Depleted Vapor Zones, *Geothermics*, 20 (5/6), 257-277, 1991a.

Pruess, K. TOUGH2 - A General Purpose Numerical Simulator for Multiphase Fluid and Heat Flow, Report No. LBL-29400, Lawrence Berkeley Laboratory, Berkeley, CA, May 1991b.

Pruess, K. Dispersion of Immiscible Fluid Phases in Gravity-Driven Flow: A Fickian Diffusion Model, *Water Resources Res. (submitted)*, LBL-33914, June 1993.

Pruess, K. and S. Enedy. Numerical Modeling of Injection Experiments at The Geysers, Lawrence Berkeley Laboratory Report LBL-33423, presented at 18th Workshop on Geothermal Reservoir Engineering, Stanford University, Stanford, CA, January 26-28, 1993.

Sahimi, M., B. D. Hughes, L. E. Scriven and H. T. Davis. Dispersion in Flow Through Porous Media - I. One-Phase Flow, *Chem. Eng. Sci.*, 41 (8), 2103-2122, 1986.

Shook, M. and D. D. Faulder. Analysis of Reinjection Strategies for The Geysers, Proc., Sixteenth Workshop Geothermal Reservoir Engineering, pp. 97-106, Stanford University, Stanford, CA, January 1991.

van Genuchten, M. Th., A Closed-Form Equation for Predicting the Hydraulic Conductivity of Unsaturated Soils, *Soil Sci. Soc. Am. J.*, Vol. 44, pp. 892-898, 1980.

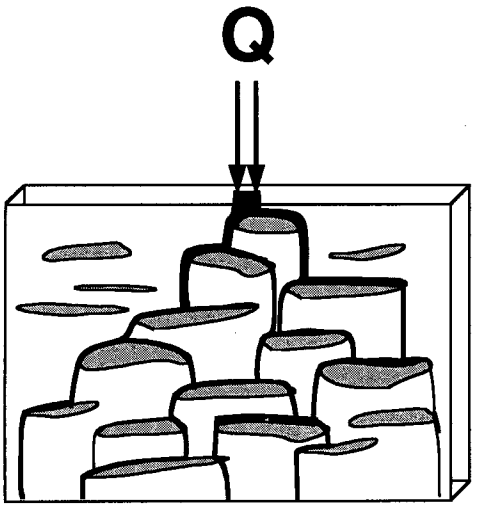


Figure 1. Schematic of water infiltration in a heterogeneous medium. Regions of low permeability (shaded areas) divert water flux sideways and cause a lateral spreading of the infiltration plume.

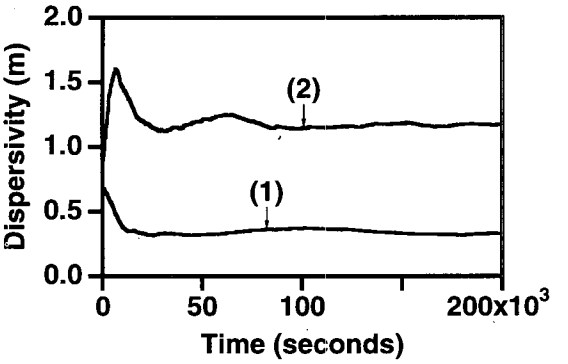


Figure 3. Simulated transverse dispersivities for heterogeneous media with random distributions of 150 impermeable obstacles. Curve (a) is for the medium of Fig. 2; curve (b) is for a medium with length of obstacles uniformly distributed in the range of 1-3 m.

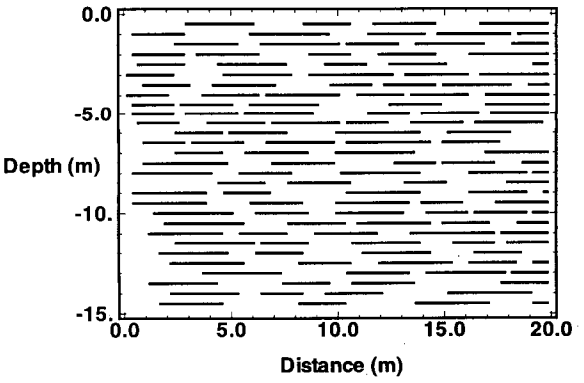


Figure 2. Heterogeneous medium with a random distribution of 150 impermeable obstacles (black segments). Length of obstacles is uniformly distributed in the range of 2-4 m

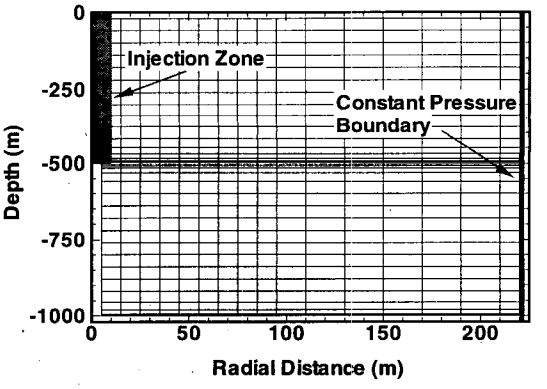


Figure 4. Gridding for two-dimensional R-Z injection problem.

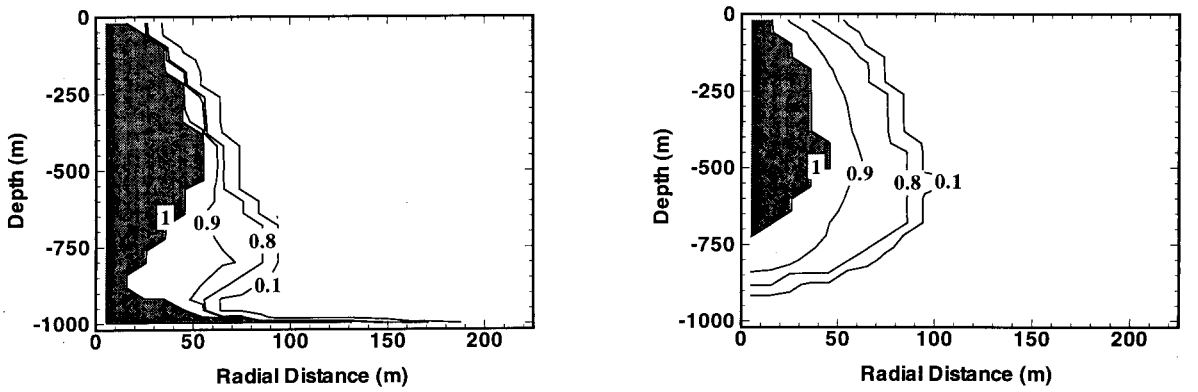


a) b)

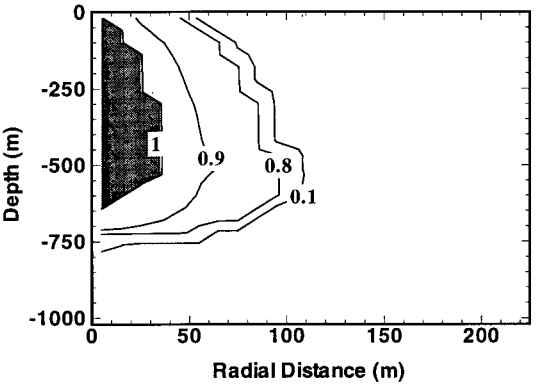


c)

Figure 5. Simulated injection plumes for different transverse dispersivities. Liquid saturation contours after 691.9 days of injection are shown for (a) $\alpha_T = 0$, (b) $\alpha_T = 5$ m, (c) $\alpha_T = 10$ m.

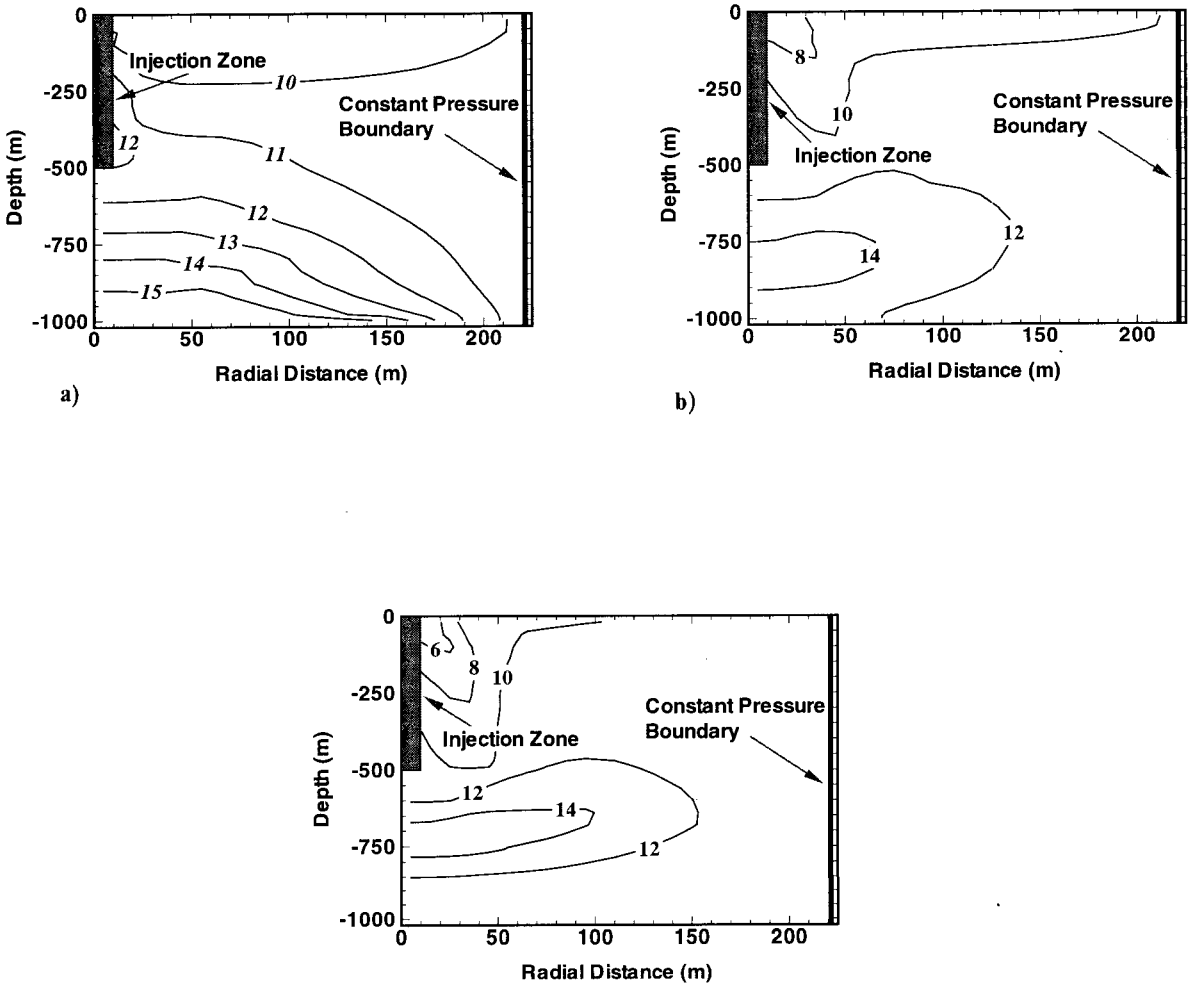


Figure 6. Simulated pressures (in bars) after 691.9 days of injection for phase dispersivities of (a) $\alpha_T = 0$, (b) $\alpha_T = 5$ m, (c) $\alpha_T = 10$ m.

PROCEEDINGS, Nineteenth Workshop on Geothermal Reservoir Engineering
Stanford University, Stanford, California, January 18-20, 1994
SGP-TR-147

# HEAT EXTRACTED FROM THE LONG TERM FLOW TEST IN THE FENTON HILL HDR RESERVOIR

Paul Kruger
Civil Engineering Department
Stanford University
Stanford CA 94305

and

Bruce Robinson
Earth Sciences Division
Los Alamos National Laboratory
Los Alamos NM 87545

## ABSTRACT

A long-term flow test was carried out in the Fenton Hill HDR Phase-2 reservoir for 14 months during 1992-1993 to examine the potential for supplying thermal energy at a sustained rate as a commercial demonstration of HDR technology. The test was accomplished in several segments with changes in mean flowrate due to pumping conditions. Pre-test estimates of the extractable heat content above a minimum useful temperature were based on physical evidence of the size of the Fenton Hill reservoir. A numerical model was used to estimate the extent of heat extracted during the individual flow segments from the database of measured production data during the test. For a reservoir volume of $6.5 \times 10^6$ m$^3$, the total heat content above a minimum temperature of 150° C was $1.5 \times 10^{15}$ J. For the total test period at the three sustained mean flowrates, the integrated heat extracted was $0.088 \times 10^{15}$ J, with no discernable temperature decline of the produced fluid. The fraction of energy extracted above the abandonment temperature was 5.9 %. On the basis of a constant thermal energy extraction rate, the lifetime of the reservoir (without reservoir growth) to the abandonment temperature would be 13.3 years, in good agreement with the pre-test estimate of 15.0 years for the given reservoir volume.

## INTRODUCTION

Successful development of geothermal energy as an important contribution to world energy supply, beyond the few easily utilized hydrothermal systems, depends on improved technology for efficient heat extraction from a natural variety of subsurface concentrations of thermal energy deposited in accessible volumes of rock formations over a wide range of useful temperature and containing a range of in-place heat-carrier fluid, from HDR (none) to hydrothermal (abundant) systems.

Engineering experience is needed to attain successful development of heat extraction technology. It is also important to acquire reliable means to evaluate the potential for thermal energy extraction at an early stage in the development of prospective resources for commercial utilization. The key uncertainties of HDR geothermal resources for heat extraction include:

(1) fractured rock volume available for heat transfer to the circulating fluid that determines the total accessible heat content;

(2) distribution of rock-block sizes and fracture flowpaths that determine the optimum heat extraction rate;

(3) production flowrate strategy for sustainable deliverability at sufficient power level and longevity to provide commercial incentive for development.

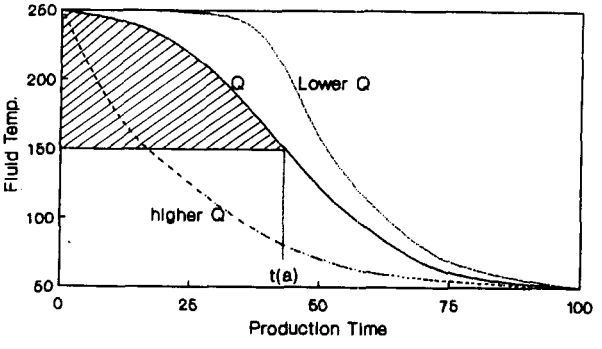


Fig.1 Relationship of fraction produced (shaded area) above a given abandonment temperature to the production flowrate (from Kruger, 1993).

Figure 1, from Kruger (1993), notes the relationship for a reservoir of given thermal properties between production flowrate, Q, and thermal energy extraction, the area under the cooldown curve. The difficult management decision on balancing maximum power output (higher Q for greater current income) and maximum thermal extraction efficiency (lower Q for greater total return) over a longer amortization period also requires knowledge of these key parameters. In both cases, the parameters need to be evaluated with sufficient confidence for investment and management decisions.

Experiments to establish technical means to provide reliable estimates of the key parameters are available in the form of long-term constant-flowrate reservoir testing. Long term signifies a period sufficient to estimate the available heat content above the application minimum temperature and the range of heat extraction rate - lifetime

relations for optimum reservoir management. Only a few such experiments have been performed throughout the world; they include the 3-year circulation test at Rosemanowes, Cornwall, England, the 90-day circulation test at Hijiori, Honshu, Japan, and, now, the 14-month long-term flow test (LTFT) at Fenton Hill, New Mexico, USA.

The three-year circulation test at Rosemanowes was carried out as part of the U.K. HDR program described by Symons (1991) to evaluate the potential for electric power generation in the United Kingdom from the vast thermal energy stored in the Cornwall granitic formations. A description of the test was given by Parker (1989). It ran for over 1220 days in which the temperature decline was measured from an initial reservoir temperature of 80° C to an abandonment temperature of 52° C. From production data supplied by the test operators (Nicol, private communication, 1989), Kruger (1990) was able to match the observed exponential cooldown over the three-year period by fitting of reservoir volume and mean fracture spacing (MFS) parameters for heat transfer. The match reservoir volume of $3.25 \times 10^6$ m$^3$ was in agreement with the volume of $5 \times 10^6$ m$^3$ estimated by Nicol and Robinson (1990) from tracer and seismic measurements. The MFS was indicative of the uniform flow conditions for heat transfer for the mean production flowrate.

The 90-day circulation test at Hijiori was the first (and thus far, only) multi-production (three) well test in the world. The test was described by Yamaguchi, et al. (1992). It was run with three major events for different objectives, (1) an initial sharp increase in flowrate to examine the potential for increasing reservoir size, (2) with two of the three wells shutin for two weeks in succession to test the individual production wells, and (3) at constant injection rate to evaluate reservoir performance.

The Hijiori test was run with accumulation of extensive diagnostic data and frequent downhole logs to describe the flow geometries and downhole temperature history. The measurements identified a number of entry zones into each well. An analysis of the observed cooldown data was reported by Kruger and Yamaguchi (1993) based on allocation of the constant injection flowrate among the multiple entry zones of the three production wells, adjusted for observed water loss. The cooldown simulations by zonal sectors provided an estimate of the sector volumes and the corresponding heat content. Analysis of the test was made difficult by the early flowrate excursion and the two-week shutins. The experience, however, will be useful in execution of the deepened Hijiori reservoir which will be used for a longer flow test.

The 14-month LTFT at Fenton Hill was carried out as part of the HDR technology development program at the Los Alamos National Laboratory since the early 1970's. The latest test was run in the Phase II part of the program, designed to demonstrate, at a sub-commercial scale, the feasibility of extracting heat from a HDR geothermal reservoir.

This paper reviews the heat extraction results obtained for the long-term flow test (LTFT) at Fenton Hill. A numerical method was used to integrate the continuous flowrate and temperature data collected during the several segments of the test to obtain the amount of heat extracted from the reservoir in relation to the calculated reservoir heat content. In addition, review is given of the corresponding estimates for the Rosemanowes and Hijiori circulation tests by analytical means.

## THE FENTON HILL LONG-TERM FLOW TEST

The Long-Term Flow Test (LTFT) at Fenton Hill in 1992-3 culminates over 20 years of experimental development of the technology for HDR geothermal energy resource utilization. The objectives for the LTFT were guided by both the need to continue development of the technology for optimum energy extraction and the need to operate the reservoir at constant production to demonstrate its long-term viability as a significant source of power. These conflicting objectives resulted in a test designed to operate at a reduced power extraction level to prevent seismic activity and growth of fracture volume in the reservoir.

A description of the Fenton Hill HDR Reservoir and plans for the LTFT was reported by Brown (1993). After a series of hydraulic fracturing experiments and redrilling of the wellbores, the surface plant was constructed and the test was initiated in April 1992. The surface equipment and data acquisition and control system were designed to provide a detailed record of the operating conditions with maximum automation. In addition, numerous tracer tests and geochemical analyses were carried out to monitor the behavior of the system during long-term operation. Although the plan for the test was to accomplish steady-state power production for a period of one year or longer, circulation through the reservoir was achieved for only eight months, due to mechanical pump failure and exhaustion of project funding. Nonetheless, significant performance information was obtained, including data on the thermal behavior of the system.

A summary of the experimental details of the LTFT was given by Brown (1993). The production period for the test is conveniently divided into a number of segments of quasi-steady state conditions, based on the history of the pump failures and replacements. A summary of the segment chronology is given in Table 1, and a summary of the production conditions is shown in Figure 2 , derived from Brown (1993).

The production history of the LTFT has been divided into four periods. The first segment (LTFT Phase I) was one of steady-state operation from test startup on 9 April 1992 until it ended abruptly on 31 July when the fluid injection

Table 1
Chronology of Fenton Hill Production Periods

| Period No. | Production Segment Name | Production Dates (1992-93) | Mean Flowrate (kg/s) |
|---|---|---|---|
| 1 | Pre-LTFT | Jan - Mar | 6.3 |
| 2 | LTFT Phase I | 9Apr - 31Jul | 6.0 |
| 3 | IFT Phase I | 20Aug - 2Oct | 4.1 |
| 4 | IFT Phase II | Nov - Dec | 5.4 |
| 5 | LTFT Phase II | 22Feb - 17Apr | 6.0 |
| 6 | Post-LTFT | Apr - May | 7.7 |

pumps failed. The test was then operated as an Interim Flow Test, first as IFT Phase I at lower flowrates with a back-up injection pump from 20 August through 2 October and then as IFT Phase II during the months of November and December with a leased pump more suitable for long-term operation. These two IFT phases allowed testing of reservoir flow behavior at two different production well pressures. The fourth segment of the Test (LTFT Phase II) commenced on 22 February 1993 with a new centrifugal pump capable of flowrates similar to the original LTFT conditions and continued until 17 April when the test was abandoned. One additional period of operation (post-LTFT) was carried out to examine the performance of the reservoir in response to short, planned shut-ins of the production wellbore.

The thermal performance of the reservoir was very stable after short-term transients observed at the startup of each segment. The temperature in the production well at the depth of the highest fracture entrance remained constant at 228 °C throughout the entire test period. Thermal cooldown of the produced fluid was not observed, although changes throughout the reservoir region were observed from a series of temperature logs.

The produced fluid temperature measured continuously at the surface varied with flowrate and time since startup for each segment. Calculation of 'continuous' down-hole temperature was accomplished with the wellbore heat transmission model of Ramey (1962). The data exhibited a sharp transient during the first few days of operation as the rock around the well was heated. The process approaches a quasi-steady state, flowrate dependent heat loss at longer times. Under the LTFT segment conditions, a temperature decline of 40 to 50 °C was observed over the wellbore depth to the surface. At higher flowrates, the temperature drop was smaller. A similar effect was observed in the injection well, where heatup of the injected fluid occurred rather than cooldown.

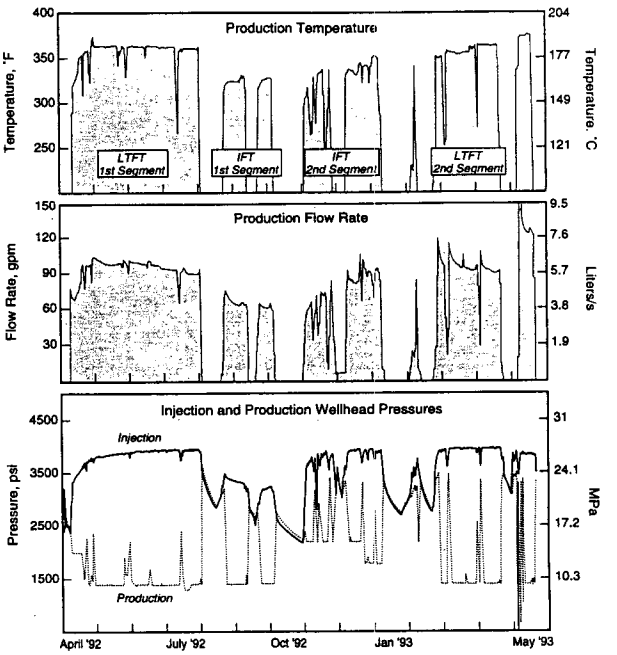


Fig.2 Production history of the Long-Term Flow Test at Fenton Hill, 1992-93 (from Brown, 1993).

## HEAT EXTRACTION FROM HDR RESERVOIRS

A HDR geothermal reservoir may be considered as the rock volume above some minimum utilization temperature that can be stimulated to provide adequate surface area for heat transfer to a circulating fluid (Kruger, 1993). The available heat content, HC, (J), of the useful reservoir volume with temperature above a minimum application temperature is given by

$$HC = (\rho V)\, C_p\, (T_o - T_a) \qquad (1)$$

where $V$ = reservoir volume ($m^3$)
$\rho$ = rock density ($kg/m^3$)
$C_p$ = rock specific heat (J/kg-C)
$T_o$ = mean initial formation temperature (C)
$T_a$ = application abandonment temperature (C)

The thermal energy extracted, HE, (J), through production time, t, is given by

$$HE = \int_{t_a}^{t_o} Q(t)\, \Delta h(T_i, T_f, t)\, dt \qquad (2)$$

where
$Q$ = production flowrate (kg/s)
$h$ = fluid enthalpy (kJ/kg)
$T_i$ = injection fluid temperature (C).
$T_f$ = produced fluid temperature (C)

$\Delta h(T_i,T_f)$ is the increase in enthalpy of the produced fluid above the enthalpy of the injected fluid. For an amortization period in which the temperature difference $(T_o-T_a)$ is small compared to the temperature difference $(T_o-T_i)$, the heat extracted can be approximated from the parameter mean values as

$$HE = \overline{Q}\ \overline{\Delta h}\ \Delta t \qquad (3)$$

The fraction of thermal energy produced, FP, is the ratio

$$FP = HE/HC \qquad (4)$$

Table 2
Heat Extraction Parameters for the LTFT

| Parameter | Value |
|---|---|
| Reservoir Volume | $6.45 \times 10^6$ m$^3$ |
| Init. Reserv. Temp | 228 °C |
| Abandonment Temp | 150 °C |
| Rock Density | 2700 kg/m$^3$ |
| Rock Specific Heat | 954 J/kgC |

## HEAT EXTRACTED FROM THE LTFT RESERVOIR

Calculation of the heat extracted from the six test segments listed in Table 1 were carried out with a computer program to numerically integrate Equ.2 with the database acquired for the LTFT. The input to the program were the measured inlet and outlet temperatures and production flowrate at discreet times during the test. After filtering out data points that represent spurious noise in the data, the program integrates the data using Euler's method. To compute the enthalpy of the fluid at the inlet and outlet temperature, steam table enthalpy data were fit using the quotient of rational polynomial expressions involving pressure and temperature to powers up to 3, after Zyvoloski and Dash (1991). The enthalpy computed in this way are accurate to within 0.062 %. The pressure, an independent variable of secondary importance compared to temperature, was assumed constant at 37.5 MPa, the approximate value at downhole conditions. The program was verified against a fictitious example problem of changing flowrate and declining temperature, and the program yielded results that agreed with a manual calculation using the steam tables to within 2 %. Reservoir properties for the heat extraction calculations are listed in Table 2.

Table 3 shows the results of the calculations of the heat extracted from the reservoir during each segment of the circulation tests. Also included are the cumulative heat extracted up until the end of each segment, as well as the percent of the total available heat content, based on an abandonment temperature of 150 °C and a reservoir volume of $6.45 \times 10^6$ m$^3$ (Robinson and Kruger, 1992).

The two circulation test segments with the largest heat extraction are phases I and II of the LTFT. The other 4 test periods contributed relatively little to the total heat extracted. For all six segments, the total heat extracted was only 5.9% of the available heat content. It is, therefore, not surprising that within the uncertainty of temperature measurement in the series of downhole temperature logs taken during the test period, there was no decline in the produced fluid temperature.

The small fraction of the available heat content removed during the LTFT confirms that Phase II reservoir at Fenton Hill is a large geothermal resource. Continued testing of the reservoir could apparently be operated in the future without serious thermal degradation, at least initially. On the basis of a constant thermal energy extraction rate, the lifetime of the reservoir to the abandonment temperature (even without reservoir growth) would be 13.3 years, in good agreement with the pre-test estimate of 15.0 years (in Robinson and Kruger, 1992) for the given reservoir volume.

The differences in the heat extracted from the reservoir and the heat recovered at the surface shown in Table 3 are quite small. The temperature loss as fluid travels up the production well is roughly 50 °C, which approximately balances the temperature gain of fluid travelling down the injection well. Thus, the computations for heat extracted from surface data (where temperature measurements are much easier to make) provide a fairly accurate estimate of the amount of heat extracted from the reservoir. However, the lower temperature of the production fluid at the surface compared to downhole results in a poorer electric conversion efficiency. Heat losses would decline at higher flow rates, and completion of the wellbore with insulating materials could further reduce wellbore heat loss.

## HEAT EXTRACTED FROM OTHER TESTS

The results of estimated heat extracted from the Fenton Hill reservoir can be compared to the results from the Rosemanowes and Hijiori circulation tests.

### Rosemanowes

Estimates of heat extraction were obtained both analytically and numerically. The analytical estimate was based on the observed exponential temperature decline (Kruger, 1990) over the 3-year circulation test. For the fitted equation

$$T_f = T_o\, e^{-k(T)t} \qquad (5)$$

Table 3
Heat Extraction from the Fenton Hill Reservoir

| Prodn Period No. | Heat Extraction Reservoir (TJ) | (%) | Heat Extraction at Surface (TJ) | (%) | Cumulative HE Reservoir (TJ) | (%) | Cumulative HE at Surface (TJ) | (%) |
|---|---|---|---|---|---|---|---|---|
| 1 | 6.12 | 0.41 | 5.17 | 0.35 | 6.12 | 0.41 | 5.17 | 0.35 |
| 2 | 38.0 | 2.54 | 38.5 | 2.57 | 44.1 | 2.95 | 43.7 | 2.92 |
| 3 | 8.59 | 0.57 | 6.92 | 0.46 | 52.7 | 3.52 | 50.6 | 3.38 |
| 4 | 9.43 | 0.63 | 7.99 | 0.53 | 62.1 | 4.15 | 58.6 | 3.91 |
| 5 | 20.0 | 1.34 | 18.0 | 1.20 | 82.1 | 5.49 | 76.6 | 5.11 |
| 6 | 6.17 | 0.41 | 5.97 | 0.40 | 88.3 | 5.90 | 82.6 | 5.51 |

it was assumed that the fluid enthalpy difference also declined exponentially with decline constant, k(h). For Rosemanowes test conditions of $T_o$=82° C (h=342.2kJ/kg), $T_a$=50° C (h=221.9kJ/kg), and $T_i$=20.3° C (h=85.2kJ/kg) at mean Q=14.5kg/s, the value of k(h) was obtained from

$$\Delta h = \Delta h(o)\, e^{-k(h)t} \qquad (6)$$

and the heat extracted was obtained by substitution of Δh into Equ.(2). The heat content of the reservoir from Equ.(1) was $2.40 \times 10^{14}$ J. The heat extracted was $2.88 \times 10^{14}$ J, with a fraction produced of 120 %. For a FP=1.00, the corresponding reservoir volume could be $V_r = 3.90 \times 10^6$ m$^3$ in lieu of the matched reservoir volume, $V_r = 3.25 \times 10^6$ m$^3$. Other sources of discrepancy could be a mean flowrate of 12.1 kg/s in lieu of 14.5 kg/s or heat transfer in both the injection and production wells.

The numerical estimate for heat extracted was made with the Fenton Hill model modified for the Rosemanowes data provided by CSMA (Nicol, private communication, 1989). For the same conditions as the analytical estimate, the integrated daily product of recorded production flowrate and injection and production temperatures yielded a heat extracted of $2.36 \times 10^{14}$ J, with a fraction produced of 98.0%.

### Hijiori

Thermal analysis of the Hijiori 90-day circulation test (Kruger and Yamaguchi, 1993) was made with a model in which the constant flow was divided into a number of zonal sector flows based on individual well production and logged depth of feed fractures. The largest flow zonal sector for each of the three production wells was evaluated to obtain the closest fit to the observed cooldown curve. The simulation results for the three zonal sectors showed a mean fracture spacing around 15-20 m for heat transfer, and the fractions produced for the geometric zonal sectors ranged from 129 to 266 %. An example was zonal sector 4 in well 1, where the fraction produced was 236 % for a sector of dimensions: R = 41 m and Z = 13 m. For the simulation run with FP = 67 % for the best match to the observed cooldown, the adjusted equal-aspect-ratio dimensions were: R = 62 m and Z = 20 m. If it is further assumed that this sector is representative of the whole reservoir, then the total heat extracted can be estimated from the ratio of sector flow to total injection flow, adjusted for the water lost from the production total. The data also allowed for an estimate of the reservoir volume and heat content.

## CONCLUSIONS

The results of the calculations of heat extracted from the LTFT at Fenton Hill, augmented by the results observed at the Rosemanowes and Hijiori sites, provide confidence that estimates of commercial quality of prospective HDR geothermal resources can be obtained from early results of circulation testing in the stimulated reservoir. The main parameters that require early evaluation are the extent of flow-connected volume created by the stimulations, the size distribution of the heat providing rock blocks, and a optimum production rate strategy that provides sufficient return over a sufficiently long amortization period.

Over the 14-month production period of the LTFT, both the small calculated fraction produced of the estimated reservoir heat content and the observed constant downhole production temperature imply that the conservatively calculated reservoir volume was sufficiently large to sustain constant production for about 15 years to the given abandonment temperature of 150 °C for application as steam for electric power generation. The prospect of further reservoir stimulation to increase the reservoir size during long-term production and to recover the non-produced injected fluid needs to be technically explored in the Fenton Hill reservoir.

The results of the other two circulation tests support the basis for estimating heat extraction. Although the Rosemanowes reservoir was sufficiently large for long-term operation, the small initial temperature at reservoir depth was too small for electric power generation, but

could serve as a hot-water supply. The agreement with calculated heat extraction by the numerical model and the approximating analytical model shows the ability to plan such an application. The results of the Hijiori test show a rapid extraction in a highly fractured small reservoir, but it provides engineering data for design of the deeper reservoir planned for further technical development.

REFERENCES


Brown, D.W., "Recent Flow Testing of the HDR Reservoir at Fenton Hill, New Mexico", Geoth.Res.Council Bull. 22, 208-214 (1993).

Kruger, P., "Heat Extraction from Microseismic Estimated Geothermal Reservoir Volume", Trans.Geoth.Res.Council 14, pt.II, 1225-1232 (1990).

Kruger, P., "The Concept of Geothermal Energy Mining", Proceedings, EPRI HDR Geothermal Workshop Report on 'Hot Dry Rock Geothermal Energy for U.S. Electric Utilities', Project RP1994-06, June, 1993.

Kruger, P. and T. Yamaguchi, "Thermal Drawdown Analysis of the Hijiori 90-Day Circulation Test", Proceedings, Eighteenth Stanford Geothermal Workshop, SGP-TR-145, January, 1993.

Nicol, D.A.C. and B.A. Robinson, "Modelling the Heat Extraction from the Rosemanowes HDR Reservoir", Geothermics 19, No.3, 247-257 (1990).

Parker, R.H., "Hot Dry Rock Geothermal Energy, Phase 2B Final Report of the Camborne School of Mines Project" (Pergamon Press, Oxford, 1989).

Ramey, H.J., "Wellbore Heat Transmission", J.Petro.Tech. 427-435 (April, 1962).

Robinson, B.A. and P. Kruger, "Pre-Test Estimates of Temperature Decline for the LANL Fenton Hill Long-Term Flow Test", Trans.Geoth.Res.Council 16, 473-479 (1992).

Symons, G.D., "The 1990 Geothermal HDR Programme Review", ETSU-R-53 (Harwell, UK, 1991).

Yamaguchi, T., N. Hiwaki, A. Tsuyoshi, and Y. Oikawa, "90-Day Circulation Test at Hijiori HDR Test Site", Geoth.Res.Coun.Trans. 16, 417-422, (1992).

Zyvoloski, G.A. and Z.V. Dash, "Verification Report for the Code FEHMN", Los Alamos National Laboratory Internal Report No. LA-UR-91-609 (1991).

PROCEEDINGS, Nineteenth Workshop on Geothermal Reservoir Engineering
Stanford University, Stanford, California, January 18-20, 1994
SGP-TR-147

# A METHOD FOR THE FLOW DIAGNOSIS AND INTERPRETATION OF A WELL TEST THROUGH THE USE OF THE PRESSURE DERIVATIVE FUNCTION

Fernando Ascencio Cendejas (†), Fernando Samaniego Verduzco (‡)
Jesús Rivera Rodríquez (‡)
(†) Gerencia de Proyectos Geotermoeléctricos, CFE and UNAM.
Apartado Postal 31-C. Morelia, Mich., MEXICO. CP 58290.
(‡) División de Estudios de Posgrado. UNAM. MEXICO, D.F.

## ABSTRACT

This paper presents an alternative technique for transient pressure analysis. The new method is based on the pressure derivative function and the impulse theory. This method uses a mathematical and graphical evaluation of an equation of the type $[t_{corr,f}]\ t^{n_f}\Delta p'_1 = m_f^1$, where $n_f$ is related to the specific flow pattern toward the well and the constant $m_f^1$ with the formation conductivity. This procedure simultaneously allows the diagnosis of the flow pattern through the presence of a horizontal line of a graph of $[t_{corr,f}]\ t^{n_f}\Delta p'_1$ versus $t$, and an estimation of the formation conductivity through the value of the constant $m_f^1$, given by the intersection of this line with the ordinate axis. In the ordinate graphing group, $t_{corr,f}$ is a correction factor for variable rate producing conditions, approximately equal to unity for long producing times. For constant rate drawdown tests this factor is equal to one. $f$ in this graphing group stands for the type of flow prevailing during a specific period of the test, i.e., spherical, linear, or radial. Variable well flow rates are also considered in the theory of analysis presented in this study. This new method is successfully applied to three field cases published in the literature.

## INTRODUCTION

Forecasting reservoir perfomance requires complete information on reservoir definition and formation and fluid properties, among other things. Pressure transient testing when using an integrated approach, has proved to be a reliable method for the estimation of formation properties and characterization of several reservoir heterogeneities. Over the last five decades, hundreds of technical papers have been written on well test analysis (*Matthews and Russell* [1967];*Ramey et al.* [1973]; *Earlougher* [1977]; *Energy Resources Conservation Board* [1975]; *Streltsova* [1987]; *Horne* [1990];*Sabet* [1990]; *Stanislav and Kabir* [1990]; *Samaniego and Cinco* [1994]); this material includes solutions for transient flow problems, methods of analysis and practical aspects of testing procedures.

Different authors have addressed the question of a general approach to the analysis of a well test (*Gringarten* [1985];*Gringarten* [1987a]; *Ehlig-Economides* [1988]; *Cinco Ley and Samaniego* [1989]; *Ehlig-Economides et al.* [1990]; *Stanislav and Kabir* [1990]; *Horne* [1990]; *Ramey* [1992]; *Samaniego and Cinco Ley* [1994]). This approach consists of four main steps: 1) Estimation of the influence function or unit flow rate response through the deconvolution process; 2) Diagnosis of flow regime, ussually through the use of the pressure derivative function; 3) Application of specific graphs of analysis; 4) Non-Linear regression of the pressure data. It has been accepted that if

this general methodology for the interpretation of a well test is used, following an integrated or synergy oriented approach, the goal of characterizing a reservoir system, and obtaining good estimates of its main parameters, can in most cases be achieved under favorable circumstances.

Recently *Jelmert* [1993a] and [1993b] has presented a methodology for flow diagnosis and type curve matching based on a polynomial derivative function. The main objective of this techique is to highlight both the slope and the intercept terms simultaneously. This is achieved by plotting the pressure data in the form of horizontal lines, which are easy to detect visually.

The purpose of this paper is to present an alternative technique for transient pressure analysis, which is based on the pressure derivative function and the impulse theory. This method uses a mathematical and graphical evaluation of an equation of the type $[t_{corr,f}]t^{n_f}\Delta p'_1 = m_f^1$, where $n_f^1$ is related to the specific flow pattern toward the well and the constant $m_f^1$ with the formation conductivity. Thus, this procedure simultaneously allows the diagnosis of the flow pattern through the presence of a horizontal line in a log-log graph, and an estimation of the formation conductivity.

# BASIC THEORY

The analysis of a transient pressure test is based in general, on a solution to a diffusivity type equation, that describes the flow of a specific fluid through a producing formation having constant porosity and permeability, which is given by Eq. 1:

$$k\nabla\cdot(\frac{\rho}{\mu}\nabla p) = \phi\rho c_t\frac{\partial p}{\partial t} \qquad (1)$$

Eq. 1 may be expressed in an alternate way if the general pseudopressure $\psi(p)$ defined by Eq. 2 is used:

$$\psi(p) = \int_{p_o}^{p}\frac{\rho}{\mu}dp \qquad (2)$$

Substituting Eq. 2 into Eq. 1:

$$k\nabla^2\psi(p) = \phi\mu c_t\frac{\partial\psi}{\partial t} \qquad (3)$$

Eq. 3 is general in the sense that due to the nature of the definition of the pseudopressure $\psi$ given by Eq. 2, the fluid considered can be either water or steam. In addition, it does not include the usual conventional diffusivity equation assumption of negligible square pressure gradients.

The diffusion type equation 3 can be written for the different flow regimes as follows:

$$(\frac{\partial^2\Delta\psi}{\partial r^2} + \frac{\mathbf{n}}{r}\frac{\partial\Delta\psi}{\partial r}) = \frac{1}{\eta}\frac{\partial\Delta\psi}{\partial t} \qquad (4)$$

where $\eta$ is the hydraulic diffusivity and $\mathbf{n}$ refers to the flow geometry, with values of 0,1, and 2 for linear (L), radial (R) and spherical (S) flow, respectively; $\Delta\psi$ is the pseudopressure drop $\psi_i - \psi(r,t)$.

Solutions to Eq. 4 can be obtained considering an instantaneous extraction of a mass of fluid $W$, through a point, line or plane source, corresponding to the three different flow geometries already mentioned (*Carslaw and Jaeger* [1959]; *Gringarten and Ramey* [1973]; *Hantush and Jacob* [1955]):

a). Linear flow period:

$$\Delta\psi_{ins,L}(r,t) = \frac{W}{\sqrt{k}\cdot A\ (4\pi\phi\mu c_t)^{1/2}}\frac{e^{-r^2/4\eta t}}{t^{1/2}} \qquad (5)$$

b). Radial flow period:

$$\Delta\psi_{ins,R}(r,t) = \frac{W}{4\pi\ k\cdot h}\frac{e^{-r^2/4\eta t}}{t} \qquad (6)$$

c). Spherical flow period:

$$\Delta\psi_{ins,E}(r,t) = \frac{(\phi\mu c_t)^{1/2}W}{8\pi^{3/2}\ k^{3/2}}\frac{e^{-r^2/4\eta t}}{t^{3/2}} \qquad (7)$$

Solutions given by Eqs. 5-7 have been used in the analysis of impulse tests ( *Ferris and Knowles* [1954]; *Cinco Ley et al.* [1986]; *Ayoub et al.* [1988]), where fluid extraction is carried out during a short time interval. It

is important to notice that Eq. 6 includes the formation conductivity $k \cdot h$, while in Eq. 7 the permeability $k$ appears raised to the 3/2 power, the units in both cases being the same $L^3$. Last, Eq. 5 for linear flow includes the product $\sqrt{k} \cdot A$ as a characteristic parameter, again with units $L^3$.

The influence function $\Delta\psi_1$ has been defined as a unit mass flow rate response (*Coats et al.* [1964]; *Cinco Ley et al.* [1986]), $\Delta\psi(r,t) = w\Delta\psi_1(r,t)$. Using this definition, the concept of an instantaneous source can be developed through the consideration of a continuous source during the time interval $\tau$, of strength $w$, located at a point $(x', y', z')$ (*Tijonov and Samarsky* [1983]). This source is equivalent to sources of strength $+w$ and $-w$, the first starting at $t = 0$ and the second at $t = \tau$. The pseudopressure distribution may be expressed:

$$\Delta\psi_\tau(r,t) = w[\Delta\psi_1(r,t) - \Delta\psi_1(r,t-\tau)] \quad (8)$$

During the time interval $\tau$ a total mass of fluid $W = w\tau$ is produced. Thus, Eq. 8 can be written:

$$\Delta\psi_\tau(r,t) = W[\frac{\Delta\psi_1(r,t) - \Delta\psi_1(r,t-\tau)}{\tau}] \quad (9)$$

Taking limits for $\tau \to 0$, considering a constant $w$, we obtain:

$$\lim_{\tau\to 0} \Delta\psi_\tau(r,t) = \Delta\psi_{ins}(r,t) = W\frac{\partial\Delta\psi_1(r,t)}{\partial t} \quad (10)$$

An alternate form to Eq. 10 is as follows:

$$\Delta\psi_{ins\ 1} = \frac{\Delta\psi_{ins}(r,t)}{W} = \frac{\partial\Delta\psi_1(r,t)}{\partial t} \quad (11)$$

In general, for a variable rate flow test, the pseudopressure drop $\Delta\psi(t)$ can be written:

$$\Delta\psi(t) = \sum_{i=1}^{N}(w_i - w_{i-1})\Delta\psi_1(t - t_{i-1}) \quad (12)$$

Taking the derivative of this expression and using Eq. 11:

$$\frac{\partial\Delta\psi(t)}{\partial t} = \sum_{i=1}^{N}(w_i - w_{i-1})\frac{\partial\Delta\psi_1(t-t_{i-1})}{\partial t}$$
$$= \sum_{i=1}^{N}(w_i - w_{i-1})\psi_{ins\ 1}(t - t_{i-1}) \quad (13)$$

For flow diagnosis and interpretation purposes, using Eq. 11, Eqs. 5-7 can be expressed in general form, for the producing well $r = 0$, as follows:

$$t^{n_f}\frac{\partial\Delta\psi_1}{\partial t} = m_f \quad (14)$$

where the expressions for the slope $m_f$ and the values of the exponent $n_f$, for the three flows regimes corresponding to Eqs. 5-7, are presented in Table 1.

**TABLE 1. EXPRESSION FOR THE SLOPE $m_f$ AND THE EXPONENT $n_f$ FOR LINEAR, RADIAL AND SPHERICAL FLOW.**

| *Type of Flow* | $n_f$ | $m_f$ |
|---|---|---|
| Linear (L) | $\frac{1}{2}$ | $1/\sqrt{k} \cdot A\ (4\pi\phi\mu c_t)^{1/2}$ |
| Radial (R) | 1 | $1/4\pi\ k \cdot h$ |
| Spherical (S) | $\frac{3}{2}$ | $(\phi\mu c_t)^{1/2}/8\pi^{3/2}k^{3/2}$ |

For variable flow rate conditions, using Eq. 11 and Eqs. 5-7, Eq. 13 can be written:

$$[t_{corr,f}]\ t^{n_f}\frac{\partial\Delta\psi_1(t)}{\partial t} = [t_{corr,f}]\ t^{n_f}\Delta\psi_1'(t) = m_f \quad (15)$$

where $t_{corr,f}$ is a correction time for variable rate producing conditions,

$$t_{corr,f} = [\frac{w_1}{w_N} + \frac{1}{w_N}\sum_{i=2}^{N}(w_i - w_{i-1})\frac{t^{n_f}}{(t-t_{i-1})^{n_f}}]^{-1} \quad (16)$$

and the influence function $\Delta\psi_1$ is equal to $\Delta\psi/w_N$.

For radial flow, two particular cases of the correction time $t_{corr,f}$ deserve discussion. First, a constante rate drawdown test, $w_1 = w_2 = \ldots = w_N$, results in $t_{corr,R} = 1$. Second, a buildup test after constant rate producing conditions gives $t_{corr,f}$ expressed by Eq. 17:

$$t_{corr,R} = \frac{(t_p + \Delta t)}{\Delta t} \tag{17}$$

with $t^{n_f}$ in Eq. 15 being $\Delta t^{n_f}$.

For linear and spherical flow conditions, constant rate buildup tests result in the following expressions for $t_{corr,f}$:

$$t_{corr,L} = \frac{(t_p + \Delta t)^{1/2}}{(t_p + \Delta t)^{1/2} - \Delta t^{1/2}} \tag{18}$$

$$t_{corr,S} = \frac{(t_p + \Delta t)^{3/2}}{(t_p + \Delta t)^{3/2} - \Delta t^{3/2}} \tag{19}$$

Eq. 15 suggest that if for a fixed value of the exponent $n_f$ a horizontal line in a log-log paper, of at least 3/4 of a cycle, is defined, we would be able to diagnostic the flow pattern prevailing during the test, allowing through the value of the constant ordinate of this line and the particular expression for $m_f$ (Table 1), the estimation of the permeability related parameter, $\sqrt{k} \cdot A$, $k \cdot h$ or $k^{3/2}$, for linear, radial or spherical flow, respectively.

To evaluate the influence function derivative $\Delta\psi_1'$ that appears in Eq. 15, the following expression based on the chain rule of differentiation and Eq. 2 can be used:

$$\frac{\partial \Delta\psi}{\partial t} = \frac{\rho}{\mu}\frac{\partial \Delta p}{\partial t} \tag{20}$$

where the pressure drop $\Delta p$ is defined by $p_i - p$.

If the phase flowing through the formation is liquid water, substituting Eq. 20 in Eq. 15 results:

$$[t_{corr,f}]t^{n_f}\Delta p_1' = m_f^1 \tag{21}$$

where the constant $\alpha_w$ is equal to $1E6$ for pressure expressed in $MPa$, the influence function $\Delta p_1$ is defined by $\Delta p / w_N$, and $m_f^1$ for water flow conditions is given by:

$$m_f^1 = \frac{\mu}{\alpha_w \rho} m_f \tag{22}$$

It has been assumed that average values for the viscosity and density within the pressure interval of interest can be assigned.

For steam flowing through the formation similarly, using the general gas law for real gases (*Katz et al.* [1959], Eq. 15 can be expressed:

$$[t_{corr,f}]t^{n_f}(\Delta p_1^2)' = m_f^1 \tag{23}$$

where $\Delta p_1^2 = (p_i^2 - p^2)/w_N$ and the constant $\alpha_s$ is iqual to $1E12$ for pressure expressed in $MPa$, and $m_f^1$ for steam flow conditions is given by:

$$m_f^1 = \frac{2\mu ZRT}{\alpha_s M} m_f \tag{24}$$

A similar average values assumption to that just made for the case of water has to be taken with regard to viscosity and the compressibility factor Z.

There are some physical conditions present in geothermal reservoirs where the previous assumption of average property values does not strictly apply, among them the case of a water with high dissolved solids content and of steam with a high non-condensible gases percentage. In these cases it is preferable to evaluate the pseudopressure defined by Eq. 2 following the procedure suggested by *Al-Hussainy, Ramey and Crawford* [1966].

# EXAMPLES OF APLICATION

In this section the proposed technique of analysis presented in this paper is applied to three field tests. Previous to the analysis, the pressure data were properly smoothed.

*Example A.* This example corresponds to a buildup test carried out in a water producing well H-16 of the Los Humeros geothermal field, Mexico. The data for this test is shown in Table 2. The diagnostic graph for this example, and examples B y C to follow, is constructed by means of Eqs. 21 and 23, with $t_{corr,f}$ given by Eqs. 17 and 18, and it is shown in Fig. 1. It can be observed that the pressure behavior follows a horizontal line for radial flow conditions, for approximately one log cycle. The values of the ordinate $m_R^1$ is $0.045 MPa\ kg/s$.

Thus, the estimate for the formation conductivity through the right hand side of Eq. 21, also given by Eq. 22, and Table 1 is as follows.

$$\begin{aligned} kh &= \frac{\mu}{\alpha_w \rho\ 4\pi m_R^1} \\ &= \frac{9.08E{-}5}{(1E6)(695)(4\pi)(0.045)} \\ &= 2.31E{-}13m^3 \end{aligned}$$

**TABLE 2. PRESSURE DATA FOR THE BUILDUP TEST IN WELL H-16**

| | |
|---|---|
| Production rate, $w$, $kg/s$ | 11 |
| Production time, $t_p$, $h$ | 2736 |
| Temperature, $T$, $°C$ | 315 |
| Water density, $\rho$, $kg/m^3$ | 695 |
| Water viscosity, $\mu$, $Pa\ s$ | $9.08E{-}5$ |

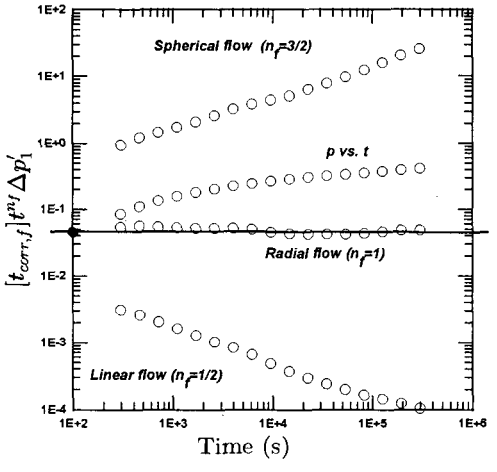


Figure 1: Diagnostic graph for Well H-16.

*Example B.* A pressure buildup test in a steam producing well Az-17 of Los Azufres geothermal reservoir, México (*S. Upton and Horne* [1989]), is analyzed. Data for this test are presented in Table 3, below. The diagnosis graph is shown in Fig 2. It can be noticed that the pressure bahavior follows a horizontal line for linear flow conditions, for approximately two log cycles. This finding is very much geologically supported by the fault Puentecillas, which is intersected by this well. The value of the ordinate $m_L^1$ is 0.0007 $s^{1/2}MPa^2$ $kg/s$. Thus, the estimate for the product $\sqrt{k}{\cdot}A$ through the right hand side of Eq. 23, also given by Eq. 24, and table 1 is as follows:

$$\begin{aligned} \sqrt{k}\cdot A &= \frac{2\mu ZRT}{\alpha_s M(4\pi\phi\mu c_t)^{1/2} m_L^1} \\ &= \frac{2(1.8E{-}5)(1)(8314.3)(537)}{1E12(18.016)(2.83E{-}12)^{1/2}(0.0007)} \\ &= 7.58E{-}3m^3 \end{aligned}$$

**TABLE 3. PRESSURE DATA FOR THE BUILDUP TEST IN WELL AZ-17**

| | |
|---|---|
| Production rate, $w$, $kg/s$ | 9.81 |
| Production time, $t_p$, $h$ | 144 |
| Temperature, $T$, $°K$ | 537 |
| Steam viscosity, $\mu$, $Pa\ s$ | $1.8E-5$ |
| Compressibility, $c_t$, $Pa^{-1}$ | $0.2495E-6$ |
| Porosity, $\phi$, | 0.05 |

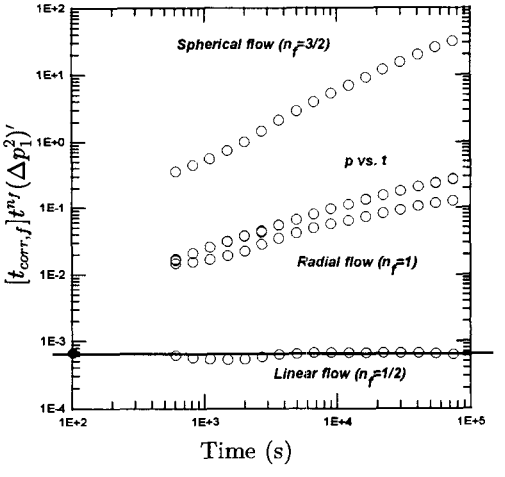


Figure 2: Diagnostic graph for Well AZ-17.

*Example C.* This is a drawdown test in a steam well reported by *Economides et al.* [1982]. The basic data are presented in Table 4. The diagnosis graph is shown in Fig. 3, observing that the pressure behavior follows a horizontal line for radial flow conditions, for approximately three quarters of a log cycle.
The ordinate $m_R^1$ is $0.0425s^{1/2}MPa$ $kg/s$. The formation conductivity $k \cdot h$ can be estimated through the right hand side of Eq. 23, also expressed by Eq. 24, and Table 1:

$$
\begin{aligned}
kh &= \frac{2\mu ZRT}{\alpha_s 4\pi M m_R^1} \\
&= \frac{2(1.7E{-}5)(0.84)(8314.3)(513)}{(1E12)(4\pi)(18.016)(0.0425)} \\
&= 1.26E{-}11 m^3 = 4.2E4md - ft.
\end{aligned}
$$

This estimation for the conductivity compares very well with the reported value by Economides et al. of $4.26E4md - ft$.

**TABLE 4. PRESSURE DATA FOR THE DRAWDOWN TEST IN EXAMPLE C**

| | |
|---|---|
| Production rate, $w$, $kg/s$ | 21 |
| Temperature, $T$, $°K$ | 513 |
| Steam viscosity, $\mu$, $Pas$ | $1.7E{-}5$ |
| Compressibility Factor, $Z$ | 0.84 |

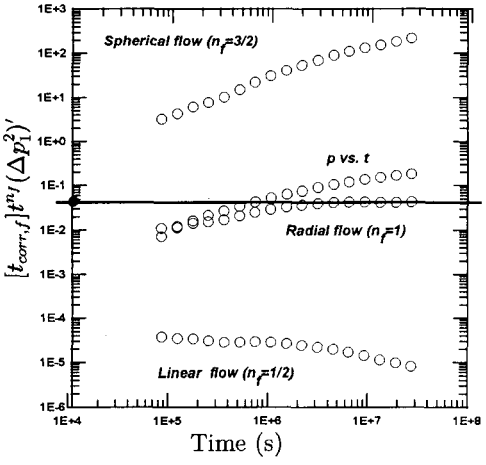


Figure 3: Diagnostic graph for example C.

# CONCLUSIONS

The principal purpose of this paper has been to present an alternative technique for transient pressure analysis, which is based on the pressure derivative function and the impulse theory.

The main conclusions of this work are as follows:

1. This method is based on a mathematical and graphical evaluation of an equation of the type $[t_{corr,f}]\, t^{n_f} \Delta p_1' = m_f^1$, where $n_f$ is related to the specific flow pattern towards the well and the constant $m_f^1$ with the formation conductivity.

2. This procedure simultaneously allows the diagnosis of the flow pattern through the presence of a horizontal line in a log-log graph, and an estimation of the formation conductivity.

3. The type of flow tests considered in this technique are drawdown and buildup tests, for both constant and variable rate conditions.

4. The different flow patterns analized are linear, spherical and radial.

5. This method was successfully applied to three field cases.

# NOMENCLATURE

$A$ = Area for linear flow, $m$.

$c_t$ = Total system compressibility, $Pa^{-1}$.

$h$ = Formation thickness, $m$.

$k$ = Formation permeability, $m^2$.

$k \cdot h$ = Formation conductivity, $m^3$.

$\sqrt{k} \cdot A$ = Product of the square root of permeability and the area perpendicular for linear flow, $m^3$.

$m_f^1$ = Slope of the pseudopressure behavior graph, Eq. 15.

$M$ = Molecular weight, $kg/kmol$.

$n_f$ = Parameter that refers to the flow geometry, Table 1 and Eq. 21.

$N$ = Number of different flow rates for a fixed time $t$.

$p$ = Pressure, $Pa$.

$p_i$ = Initial pressure, $Pa$.

$\Delta p_1$ = Influence function, Eq. 21.

$r$ = Distance from the producing point, $m$.

$R$ = Gas constant, 8314.3 $J/kmol\ °K$.

$r_w$ = Wellbore radius, $m$.

$t$ = Time, $s$.

$t_p$ = Producing time, $s$.

$\Delta t$ = Shut-in time, $s$.

$w$ = Mass flow rate, $kg/s$.

$W$ = Instantaneous fluid mass extraction, $kg$.

$\Delta$ = Difference.

$\alpha_s$ = Unit conversion constant for steam flow for pressure expressed in $MPa$, $1E12$, Eq. 23.

$\alpha_w$ = Unit conversion constant for water flow for pressure expressed in $MPa$, $1E6$, Eq. 21.

$\mu$ = Viscosity, $Pa\ s$.

$\eta$ = hydraulic diffusivity, $k/\phi\mu c_t$, $m^2/s$.

$\rho$ = Density, $kg/m^3$.

$\phi$ = Porosity, (fraction).

$\tau$ = Time interval, Eq. 8.

$\psi(r,t)$ = Pseudopressure, Eq. 2, $kg/m^3 s$.

$\Delta\psi(r,t)$ = Pseudopressure change, $\psi_i - \psi(r,t)$.

$\Delta\psi_1(r,t)$ = Influence Function, Eq. 8.

$\Delta\psi_{ins\ 1}(r,t)$ = Derivative with respect to time of the influence Function, Eq. 11.

$\nabla\cdot$ = Divergence operator.

$\nabla^2$ = Laplacian operator.

**Subscripts**

$o$ = reference, Eq. 2

1 = influence function

$f$ = phase

$i$ = initial or index

$ins$ = instantaneous

L= linear, Eq. 5

R= radial, Eq. 6

S= spherical, Eq. 7

**Superscripts**

$'$ first derivative.

# REFERENCES


Al-Hussainy,R., Ramey,H.J.,Jr, and Crawford, P.B. (1966): *The Flow of Real Gases Through Porous Media.* J. Pet. Tech., Vol.18, No.5 (May) 624-636.

Ayoub,J.A., Bourdet,D.P. and Chauvel, Y.L. (1988): *Impulse Testing.* SPE Formation Evaluation, Vol.3, No.3 (Sept.) 534-546.

Carslaw,H.S. and Jaeger,J.C. (1959): *Conduction of Heat in Solids.* Oxford at the Clarendon Press, Oxford, U.K.

Cinco-Ley,H. and Samaniego,F. (1981): *Transient Pressure Analysis for Fractured Wells.* J. Pet. Tech., Vol.33, No.9(Sept.) 1749-1766.

Cinco Ley,H. *et al.* (1986): *Analysis of Pressure Tests Through the Use of Instantaneous Source Response Concepts.* Paper SPE 15476, presented at 61st Annual Technical Conference and Exhibition, New Orleans,LA., Oct. 5-8.

Coats,K.H., Rapoport,L.A., McCord, J.R., and Drews, W.P. (1964): *Determination of Aquifer Influence Functions Data.* J. Pet. Tech., Vol. 16, No. 12 (Dec) 1417-1424.

Earlougher,R.C.,Jr. (1977): *Advances in Well Test Analysis.* Monograph Series, Society of Petroleum Engineers of AIME, Dallas, Tex., 5.

Economides, M.J., Ogbe,D.O., Miller,F.G., and Ramey,H.J.,Jr. (1982): *Geothermal Steam Well Testing:State of the Art.* J. Pet. Tech., Vol. 34, No. 5 (May) 976-988.

Ehlig-Economides,C.A. (1988): *Use of the Pressure Derivative forDiagnosing Pressure-Transient Behavior.* J. Pet. Tech., Vol.40, No.10(Oct.) 1280-1282.

Ehlig-Economides,C.A., Joseph,J.A., Ambrose, R.W.,Jr., and Norwood,C. (1990): *A Modern Approach to Reservoir Testing.* J. Pet. Tech., Vol.42, No.12 (Dec.) 1554-1563.

Energy Resources Conservation Board, (1975): *Theory and Practice of the Testing of gas Wells.* 3er ed. Pub ERCB-75-34, Calgary, Canada.

Ferris,J.G. and Knowles,D.B.(1954):*The Slug Test for Estimating Transmissibility.* Ground Water Note 26. U.S. Geological Survey.

Grant,M.A. (1979):*The Pseudo-pressure of Saturaded Steam.* Proc. Fourth Workshop on Geothermal Reservoir Engineering, Stanford University. Dec. 13-15.

Gringarten,A.C. and Ramey,H.J.,Jr. (1973): *The Use of Source and Green's Functions in Solving Unsteady-Flow Problems in Reservoirs.* Soc. Pet. Eng. J.,Vol.12, No.4 (Oct.)285-296.

Gringarten,A.C., (1985):*Interpretation of Transient Well Test data.* Developments in Petroleum Engineering-I, R.A. Dawe and D.C. Wilson, London: Elsevier Applied Science Publisher.

Gringarten,A.C., (1987a): *Type-Curve Analysis: What it Can and Can not Do.* J. Pet. Tech., Vol.39, No.1 (Jan.)11-13.

Hantush,M.S., and Jacob,C.E.,(1955):*Non-Steady Green's Functions for an Infinite Strip of Leaky Aquifer.* Trans. AIME. Vol.36.

Horne,R.N., (1990):*Modern Well Test Analysis.* Petroway Inc., Palo Alto, Ca.

Jelmert,T.A.,(1993):*A Note on Flow-Period Diagnostics in Well Testing.* Jour. of Pet. Science and Eng., Vol.8,No.4(Jan.) 329-332.

Jelmert,T.A.,(1993):*Theory and Application of Polinomial Type Curves.* Paper SPE 25876, presented at Rocky Mountain Regional/Low Permeability Reservoir Symposium, Denver, Co., April 26-28.

Katz,D.L., Cornell,D., Kobayashi,R., Poettmann,F.H., Vary,J.A., Elenbaas,J.R., and Weinaug,C.F.,(1959):*Handbook of Natural gas Engineering.* McGraw-Hill Book Co., New York.

Matthews,C.S. and Russell,D.G.,(1967): *Pressure Buildup and Flow Tests in Wells.* Monograph Series, Society of Petroleum Engineers of AIME, Dallas, Tex.,1.

Ramey,H.J.,Jr., Kumar,A., and Gulati,M.S., (1973):*Gas Well Test Analysis Under Water Drive Conditions.* American Gas Association, Alington, Va.

Ramey,H.J.,Jr.,(1992):*Advances in Practical Well-Test Analysis.* J. Pet. Tech., Vol.44,No.6 (June) 650-659.

Sabet,M.A., (1991):*Well Test Analysis.* Gulf Publishing Co., Houston, Tex.

Samaniego,V.F. and Cinco Ley,H., (1994):*Well Test Analysis for Carbonate Reservoirs.* Chapter 6. In:G.V. Chilingarian and S.J. Mazzullo (Editors), Carbonate Reservoir Characterization: A Geologic-Engineering Analysis, Part II. Elsevier, New York (To be publish).

Stanislav, J.F. and Kabir,C.S., (1990):*Pressure Transient Analysis.* Prentice-Hall, Englewood Cliffs, N.J.

Streltsova, T.D., (1988):*Well Testing in Heterogeneous Formations.* John Wiley & Sons., New York.

S. Upton,P., and Horne,R.N.,(1989):*Análisis de Pruebas en Pozos: Interpretación de una Prueba de Incremento Presión en el Pozo A-17 del Campo Geotérmico de Los Azufres, Mich., México.* Trabajo del convenio CFE-DOE.

Tijonov,A.N. and Samarsky,A.A. (1983):*Ecuaciones de la Física Matemática.* Spanish translation from the russian version, Mir, Moscow.

PROCEEDINGS, Nineteenth Workshop on Geothermal Reservoir Engineering
Stanford University, Stanford, California, January 18-20, 1994
SGP-TR-147

# ESTIMATING OF EQUILIBRIUM FORMATION TEMPERATURE BY CURVE FITTING METHOD AND IT'S PROBLEMS

Kenso Takai, Masami Hyodo, and Shinji Takasugi

Geothermal Energy Research and Development Co., Ltd., Tokyo 103, Japan

## ABSTRACT

Determination of true formation temperature from measured bottom hole temperature is important for geothermal reservoir evaluation after completion of well drilling. For estimation of equilibrium formation temperature, we studied non-linear least squares fitting method adapting the Middleton Model (Chiba et al., 1988). It was pointed out that this method was applicable as simple and relatively reliable method for estimation of the equilibrium formation temperature after drilling.

As a next step, we are studying the estimation of equilibrium formation temperature from bottom hole temperature data measured by MWD (measurement while drilling system). In this study, we have evaluated availability of non-linear least squares fitting method adapting curve fitting method and the numerical simulator (GEOTEMP2) for estimation of the equilibrium formation temperature while drilling.

## 1. INTRODUCTION

Determination of true formation temperature from measured bottom-hole temperature is important for geothermal reservoir evaluations after the completion of well drilling, and sometimes useful in selecting lost circulation materials for remedy work. However, the original temperature field around a borehole is disturbed by circulating mud during drilling, and it takes a considerably long time to reach temperature equilibrium between the formation and drilling mud after drilling and mud circulation has ended. The Horner-plot method (Parasnis, 1971; Dowdle and Cobb, 1975; Fertl and Winchmann, 1977) has popularly been in use for estimating the formation temperature. But this method requires long-period temperature logging data up to about 120 hours to get the reliable estimation, particularly in case the geothermal gradient is relative high as in geothermal wells. Several mathematical models for bottom-hole temperature stabilization have been proposed for estimation of formation temperature from short-period logging data after cessation of circulation of drilling mud.

In this paper we, at first, tested some mathematical well models to estimate the equilibrium formation temperature using short-period logging data. Then, we applied an appropriate model to the estimation of formation temperature after and while drilling. For the temperature estimation while drilling, we also introduced the method of numerical simulation in addition to the curve fitting method.

## 2. OUTLINE OF THE CURVE FITTING METHOD

### 2.1 Mathematical Temperature Stabilization Model

Several mathematical temperature stabilization models were proposed in the past, such as Carslaw and Jaeger (1959), Luikov (1968), and Middleton (1979). Although Middleton's square well model does not look adequate as shown in Fig. 1, estimated formation temperature is more accurate than the others (refer to Table 2).

Middleton (1979) considered that a vertical cylinder of small radius could be approximated by a square cylinder in rectangular coordinates. Therefore, the temperature distribution BHTc (x, y, t), around a vertical cylinder of infinite length after cessation of mud circulation could be expressed as the following equation:

$$BHTc(x,y,t)=Tm+\frac{1}{4}(Tf-Tm)\times\left\{erfc\left(\frac{R-x}{\tau}\right)+erfc\left(\frac{R+x}{\tau}\right)\right\}\times\left\{erfc\left(\frac{R-y}{\tau}\right)+erfc\left(\frac{R+y}{\tau}\right)\right\} \quad \cdots\cdots (1)$$

*where,*

$$\tau=\sqrt{4Kt}$$

$$erfc(x)=\frac{2}{\sqrt{\pi}}\int_x^{\infty} exp(-t^2)dt$$

Tm is the mud temperature in the borehole at the instant that circulation ceases, Tf is the formation equilibrium temperature, R is the effective radius of the region affected by drilling, K is the thermal diffusivity of the well contents, x, y are the Cartesian coordinates in the horizontal plane, and t is the shut-in time after the termination of mud circulation.

Assuming that the measurement is made at the center of the well (x = 0, y = 0), temperature becomes a function of time only:

$$BHTc(t)=Tm+(Tf-Tm)\times\left\{erfc\left(\frac{R}{\sqrt{4Kt}}\right)\right\}^2 \quad \cdots\cdots (2)$$

As apparent from the above equation, knowledge of circulation time of the drilling fluids, which is required in the Horner-plot method of correction for borehole temperature disturbance, is not necessary in this model. Because of this, the curve fitting method is more sensitive the Horner-plot method. The initial temperature distribution given by Equation (1) is shown in Fig. 1.

## 2.2 Analysis by the Curve Fitting Method

There are two methods of estimating formation temperature using mathematical models. One is a curve fitting technique by trial and error method, and the other is a non-linear least squares fitting method. In a curve fitting technique, the formation temperature can be obtained by superimposing a set of master curves, based on Equation (2), on observed data plotted at the same scale (refer to Fig. 2).

On the other hand, in a non-linear least squares fitting method, non-linear least squares method based upon Equation (3) is applied to obtain the formation temperature.

$$S=\sum_{i=1}^{n}\{BHTc(ti)-BHTo(ti)\}^2 \quad \cdots\cdots (3)$$

where BHTc(ti) is the calculated value from Equation (2), BHTo(ti) is the observed temperature data, and optimum values of Tf and Tm can be obtained by the mathematical inversion technique to minimize the value of S in Equation (3).

Features of a non-linear least squares fitting method, in comparison with curve fitting technique, are in its rapidity and objectivity. Therefore, we call this inverse method the curve fitting method. Fig. 3 shows an example of the non-linear fitting result.

# 3. ESTIMATION OF THE EQUILIBRIUM FORMATION TEMPERATURE AFTER DRILLING

## 3.1 Comparison of the Curve Fitting Method and the Horner-plot Method

The Horner-plot method was devised by Parasnis (1971), Dowdle and Cobb (1975), and Fertl and Winchmann (1977), and is defined by Equation (4).

$$BHT=Tf+C\times log\left(\frac{t}{t_s+t}\right) \quad \cdots\cdots (4)$$

*where,*

BHT : *Borehole temperature*
Tf : *Formation temperature*
C : *Constant*
$t$ : *Period after cessation of mud circulation*
$t_s$ : *Circulation period before the cessation*

In Equation (4), BHT becomes close to Tf asymptotically when t is infinite.

In order to evaluate the reliability of the curve fitting method, a comparison between the curve fitting method and the Horner-plot method has been made using temperature loggings during warm-up obtained in three wells at eight levels of depth in Hohi geothermal field in Kyushu. Shown in Table 1 are the data of comparison between Tfbuild, formation temperature estimated by the Horner-plot method, and Tffit, formation temperature estimated by the curve fitting method. In three wells temperature logging had taken place at 128, 122 and 113 days respectively after cessation of circulation, so these observed results are shown as Tfobs, assuming they can be approximated to an equi-

librium formation temperature.

According to this example, the average difference temperature among Tfbuild, Tffit and Tfobs was as follows.

a) Average error between Tffit and Tfobs: 5.5°C
b) Average error between Tfbuild and Tfobs: 7.9°C

Assuming that Tfobs is the equilibrium formation temperature, the curve fitting method is found to suit the estimation of the formation temperature accurately enough compared with the Horner-plot method. This is because that a linear part in the Horner-plot for temperature loggings during warm-up is considerably short.

3.2 Factors Underlying Estimation Precision on the Curve Fitting Method

Da-Xin (1986) pointed out the limits of the application of the fitting method because some parameters in Equation (2), such as thermal diffusivity K and effective radius R, should be assumed to obtain the equilibrium formation temperature and this would cause large errors.

Consequently, effective radius; R and thermal diffusivity; K are evaluated the effectiveness of estimation precision from below. Also method for thermal recovery loggings is examined.

(1) Effective radius; R

As shown in Fig. 1, Middleton's wellbore model seems to depart from an ideal cylindrical shape but this rectangular coordinates are better to describe the real geometrical configuration of the well, such as wash-out or caving of poorly consolidated formation.

Although other models, such as circular well proposed by Luikov (1968) or square well by Carslaw and Jaeger (1959), were derived and examined by Leblanc et al. (1981), Middleton's model would be appropriate if we use a half of bit size as an effective radius R as shown in Table 2.

(2) Thermal diffusivity; K

Four important physical quantities to be considered in the warm-up problem are thermal conductivity $\lambda$, specific heat Cp, density $\rho$, and thermal diffusivity K. These quantities are related by following equation:

$$K = \frac{\lambda}{\rho \times Cp} \quad \cdots\cdots (5)$$

*where,*
K : *Thermal diffusivity*
$\lambda$ : *Thermal conductivity*
Cp : *Specific heat*
$\rho$ : *Density*

There are three ways described below to determine the value of thermal diffusivity in applying fitting method.

a) To use a typical assumed value of K, as Middleton (1979) or Leblanc et al. (1981, 1982) did.
b) To use measured physical quantities using geological samples (cores or cuttings) to calculate the value of K.
c) To handle K, in combination with R, as an inversion parameter in non-linear least square method in Equation (3), as Da-Xin (1986) did.

While we adopted b) in the latest analysis, Leblanc et al. (1982) empirically proposed 0.0035 $cm^2/sec$ as the value for thermal diffusivity under the curve method.

Table 3 shows a comparison of estimated temperature between thermal diffusivity as calculated from core physical properties value and that as fixed at 0.0035 $cm^2/sec$ proposed by Leblanc.

Using thermal diffusivity as a fixed value is considered undesirable in terms of accuracy since thermal conductivity, among other rock physical properties, shows a wide range of values depending on the proportions of component minerals, the presence of metamorphosis, etc.

Knowledge about thermal properties is needed for accurate estimation of formation temperature, but it is rare that the core samples can be obtained in normal drilling process.

(3) Ratio of R and K; $\alpha$

We examined the ratio of R and K as $\alpha$ ($\alpha = R/\sqrt{K}$). 255 core samples acquired in Japanese geothermal wells were statically treated as

concluded in Table 4. We found that $\alpha$ is between 55.0 and 318 and between 79.3 and 459 in case of 8-1/2" bit hole and 12-1/4" bit hole, respectively.

Therefore, we decided to apply $\alpha$ instead of R and K in the curve fitting method and to treat $\alpha$ as one of the parameter of inversion. Then, if $\alpha$ of inversion result is not adequate, we should consider reliability of estimated formation temperature is quite low.

(4) Procedure of temperature loggings during warm-up

However, the temperature loggings during warm-up, used in verifying the curve fitting technique, were presupposed to be analyzed by the Horner-plot method. Therefore, taking the following points into consideration in logging procedure would further improve the accuracy in estimated temperature by the fitting method.

1) More data in short-period

The non-linear least squares fitting technique, different from the Horner-plot method, is a theoretical method of solution, so improved accuracy is expected to result from an increased number of data in principle even if they are short-period ones.

Incidentally, Table 5 shows a comparison of the estimated temperature obtained by the use of all temperature loggings during warm-up and that obtained by the use of only the first two data.

The average error, from the formation equilibrium temperature Tfobs is not very great for estimation results from short-period and only two data. Estimating with this degree of accuracy would be impossible when a similar estimation were made by the Horner-plot method.

2) Correction for time lags during logging

When estimating the formation temperature from short-period logging data, it is necessary to determine the shut-in time as accurately as possible.

Correction was made in the latest analysis, too, since the cable speed and direction of logging (up/down survey) were definite.

Incidentally, it turned out in Table 6 that an error of 3.9°C on the average would occur by whether time lags were taken into consideration or not.

3.3 Case Study

Based upon previous discussion, we have acquired a set of temperature loggings during warm-up for the curve fitting method.

(1) Method

After cessation of circulation of drilling mud, 14 times of temperature loggings were conducted for 72.5 hours. Depth of this well was 800 meters. Logging data and estimated formation temperatures by the curve fitting method were plotted in Fig. 4. Logging tool could not go down to the bottom of the well after 48.5 hours because of mud gelation due to the temperature of the well at the deeper part.

(2) Accuracy of the curve fitting method

1) Period

We evaluated the accuracy of the curve fitting method with the data acquired at the depth of 700 meters. As shown Table 7, 12 cases were examined. Since we did not have an exact formation temperature, we compared the temperature estimated using all data (Case 13) with the temperature estimated using less number and less recovery time data. Through this comparison,

a) the accuracy of the estimated formation temperature using 24.5 hours data is at most 5°C, and
b) using 18.5 hours data, the accuracy is at most 10°C.
c) Also $\alpha$ is stable in case we use 18.5 hours or more data.

This means the curve fitting method will be able to estimate the formation temperature more accurately than the Horner-plot method with short period data.

2) Number of data

24.5 hours data consists of nine data. Then we selected five data from nine data with several patterns as shown in Table 8. Case 2 is the most

similar to the temperature estimated by nine data. This notifies us of the importance of periodical logging.

To approve this, a similar test using 48 hours data, which consists of 12 data, was conducted. In this case, six data were selected from 12 data with several patterns. Then the importance of periodical logging in log scale was approved, although it is more preferable to use long-period data, if possible.

(3) Conclusion

The curve fitting method is a rather reliable and easy way to estimate the formation temperature with short-period temperature loggings during warm-up.

## 4. ESTIMATION OF EQUILIBRIUM TEMPERATURE WHILE DRILLING

### 4.1 Objectives

It is important to know the formation temperature in real time, if possible. Because the formation temperature is the most consequent parameter for geothermal reservoir and warm-up after cessation of drilling mud circulation.

In this section, at first, we confirm the limitation of the curve fitting method, then we propose to apply GEOTEMP2 using bottom hole temperature measured by MWD.

### 4.2 Limitation of the Curve Fitting Method

We showed it is possible to estimate the formation temperature by several sets of temperature loggings during warm-up till 24 hours after cessation of drilling mud circulation in previous section. In this case, the data of recovery temperature is not continuous. Therefore, we have examined estimation of formation temperature using continuous warm-up measurement data at a certain depth.

We used the temperature data acquired while fall-off test, instead of four hours continuous measurement data just after cessation of mud circulation for our test purpose. We used also 95 hours warm-up measurement data, then we estimated the formation temperature using four hours continuous data and 95 hours warm-up measurement data. Estimated temperatures are shown in Table 9.

We should conclude by the curve fitting method that even four hours continuous temperature data is not enough. We noticed we need totally new idea instead of the curve fitting method for temperature estimation while drilling or at least just after drilling.

### 4.3 Formation Temperature Estimation Using MWD Bottom Hole Data

(1) GEOTEMP2

GEOTEMP2 is a wellbore thermal simulator designed for geothermal well drilling and production problems.

GEOTEMP2 has plenty of functions. One of these is to compute mud temperature while drilling as results of numerical simulation, and this function requires the formation temperature for numerical simulation. However, MWD will give us bottom hole temperature and mud logging system will give us mud temperatures at surface, although we will not have the formation temperature.

We have developed a prototype of inverse program to compute the formation temperature using bottom hole temperature by MWD and mud temperatures by the mud logging system. Namely GEOTEMP2 is forward program for our prototype inverse program using non-linear least squares fitting method.

(2) Feasibility study

We use GEOTEMP2 as forward modeling, therefore we needed to know the sufficiency of the forward model; GEOTEMP2. Comparison between mud temperature at surface and simulated one in Fig. 5 and between bottom hole temperature measured by maximum thermometer and simulated one in Fig. 6.

In both cases, simulated temperatures were 2°C to 10°C lower than measured ones. Reasons of this are examined as follows:

a) GEOTEMP2 allows to use very simple formation temperature distribution.
b) Unit of computation is day, not hour or minute, therefore it is impossible to simulate actual drilling procedure.

(3) Future task

We are modifying GEOTEMP2 according to our test results as mentioned above and are going to apply inverse method on it. The new code we are developing now will be able to estimate the formation temperature even while drilling using MWD and mud logging data.

## 5. SUMMARY

For estimating the formation temperature from short-period such as 12 or 24 hours temperature loggings during warm-up, it has turned out that the curve fitting method is applicable as a simple and relatively reliable method. However, this method is essential when certain period (12 or 24 hours) data is available. Therefore, it is very useful for analysis of the temperature loggings during warm-up after cessation of mud circulation, not for while drilling.

Now for real time estimation of formation temperature while drilling, we are modifying GEOTEMP2 according to our tests results and are going to apply inversion scheme on it.

## ACKNOWLEDGEMENTS

We would like to express our appreciation to the New Energy and Industrial Technology Development Organization (NEDO) for allowing us to use some of the results and data obtained in the projects, "Development of techniques to control lost circulation in geothermal wells", which was conducted from Fiscal Year 1986 to Fiscal Year 1990, and "Development of MWD system for geothermal wells", which has been conducted sine Fiscal Year 1991 in the Sunshine Project of MITI, Japan.

## REFERENCES

Cao, S., Lerche, I., and Hermanrud, C. (1988), "Formation temperature estimation by inversion of borehole measurements," Geophysics, 53, 979-988.

Carslaw, H.S. and Jaeger, J.C. (1959), "Condition of heat in solids," Oxford University Press.

Chiba, M., Takasugi, S., Hachino, Y., and Muramatsu, S. (1988), "Estimating of equilibrium formation temperature by curve fitting method," Proceedings of the International Symposium on Geothermal Energy, 383-386.

Da-Xin, L. (1986), "Non-linear fitting method of finding equilibrium temperature from BHT data," Geothermics, 15, 657-664.

Dowdle, W.L. and Cobb, W.M. (1975), "Static formation temperature from well logs empirical method," J. Petrol. Tech., 27, 1326-1330.

Fertl, W.H. and Winchmann, P.A. (1997), "How to determine static BHT from well log data," World Oil, 183, 105-106.

Leblanc, Y., Pascoe, L.J., and Jones, F.W. (1981), "The temperature stabilization of a borehole," Geophysics, 46, 1301-1303.

Leblanc, Y., Lam, H.L., Pascoe, L.J., and Jones, F.W. (1982), "A comparison of two methods of estimating static formation temperature from well logs," Geophys. Prosp., 30, 346-357.

Luikov, A.V. (1968), "Analytical heat diffusion theory," Academic Press Inc.

Middleton, M.F. (1979), "A model for bottom-hole temperature stabilization," Geophysics, 44, 1458-1462.

Mondy, L.A. and Duda, L.E. (1984), "Advanced wellbore thermal simulator GEOTEMP2 user manual," Sandia Report, SAND-84-0857, 147pp.

Parasnis, D.S. (1971), "Temperature extrapolation to infinite time in geothermal measurement," Geophys. Prosp., 19, 612-614.

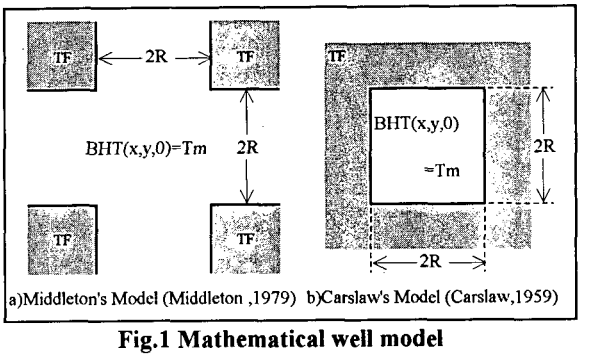


**Fig.1 Mathematical well model**

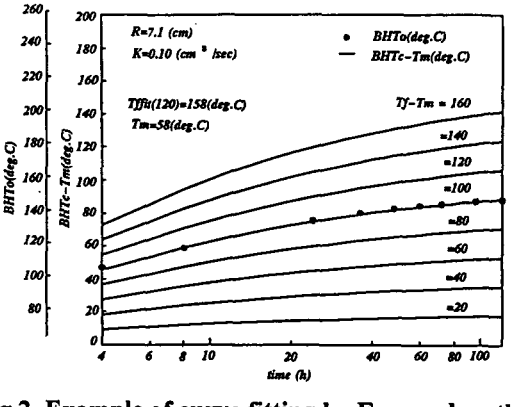


**Fig.2 Example of curve fitting by Forward method**

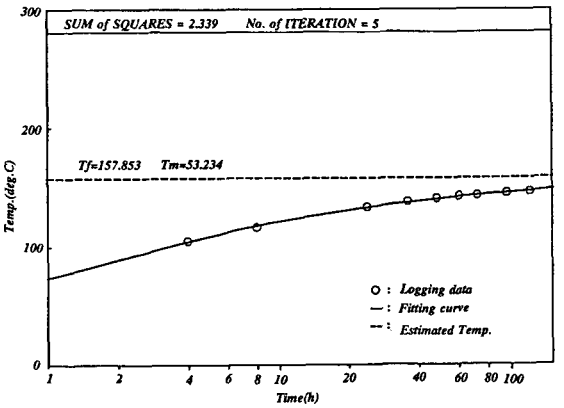


**Fig.3 Example of curve fitting by Invers method**

**Table 1 Comparision of estimated formation temperature(TF) between curve fifitting method and Horner Plot method**

| Well | depth (m) | Data No. | TFbuild (deg-C) | TFfit (deg-C) | TFobs (deg-C) |
|---|---|---|---|---|---|
| A | 700 | 7 | 209 | 188 | 190 |
| | 1,500 | | 198 | 182 | 189 |
| | 1,600 | | 193 | 180 | 185 |
| | 1,700 | | 187 | 176 | 183 |
| B | 1,400 | 6 | 167 | 154 | 170 |
| C | 2,600 | 5 | 250 | 251 | 255 |
| | 2,700 | | 254 | 261 | 262 |
| | 2,800 | | 259 | 269 | 267 |

**TFbuild ; Formation temperature estimated by Horner Plot**

**TFfit ; Formation temperature estimated by curve fitting method**

**TFobs ; Formation temperature measured by temperature logging**

**Table 2 Comparision of estimated formation temperature(TFfit) with different mathematical well model**

| Well | depth (m) | TFfit (deg-C) Middleton * Model | TFfit (deg-C) Carslaw Model | TFobs (deg-C) |
|---|---|---|---|---|
| A | 700 | 188 | 127 | 190 |
| | 1,500 | 182 | 146 | 189 |
| | 1,600 | 180 | 145 | 185 |
| | 1,700 | 176 | 144 | 183 |
| B | 1,400 | 154 | 141 | 170 |
| C | 2,600 | 251 | 230 | 255 |
| | 2,700 | 261 | 241 | 262 |
| | 2,800 | 269 | 253 | 267 |
| A.E. | | 5.5 (deg-C) | 34.3(deg-C) | |

**A.E. ; Averaged error of TFfit from TFobs**

**TFfit ; Formation temperature estimated by curve fitting method**

**TFobs ; Formation temperature measured by temperature logging**

*** Effective radius ; R is a half of bit size**

**Table 3 Effect of thermal diffusivity(K) on foramtion temperature estimation (TFfit)**

| Well | depth (m) | TFfit (deg-C) Measured Value of K | TFfit (deg-C) Fixed Value of K (K=0.0035) | TFobs (deg-C) |
|---|---|---|---|---|
| A | 700 | 188(K=0.0085) | 231 | 190 |
| | 1,500 | 182(K=0.0085) | 200 | 189 |
| | 1,600 | 180(K=0.0085) | 197 | 185 |
| | 1,700 | 176(K=0.0085) | 191 | 183 |
| B | 1,400 | 154(K=0.0259) | 163 | 170 |
| C | 2,600 | 251(K=0.0098) | 255 | 255 |
| | 2,700 | 261(K=0.0098) | 265 | 262 |
| | 2,800 | 264(K=0.0098) | 272 | 267 |
| A.E. | | 5.5 (deg-C) | 10.9(deg-C) | |

**A.E. ; Averaged error of TFfit from TFobs**

**TFfit ; Formation temperature estimated by curve fitting method**

**TFobs ; Formation temperature measured by temperature logging**

Table 4 Typical Thermal Conductivity( $\lambda$ ),Density ( $\rho$ ), Specific Heat( $Cp$ ) and Thermal Diffusivity( $K$ ) in Japanese geothermal wells

| | Number of Samples | Rang Min. | Rang Max. |
|---|---|---|---|
| $\lambda$ : Thermal Conductivity ($10^{-3}\times$cal/cm·sec·deg.C) | 255 | 1.0 | 10.0 |
| $\rho$ : Density ($g/cm^{-3}$) | 255 | 1.3 | 3.0 |
| $Cp$ : Specific Heat (cal/g·deg.C) | 18 | 0.2 | 0.24 |
| K : Thermal Diffusivity ($\times 10^{-2}$) | | 1.389 | 3.846 |

**Table 5 Effect of Number of data on formation temperature estimation(TFfit)**

| Well | depth (m) | TFfit (deg-C) Using all data | TFfit (deg-C) Using two data | TFobs (deg-C) |
|---|---|---|---|---|
| A | 700 | 188 (7 data) | 220 | 190 |
| | 1,500 | 182 (7 data) | 188 | 189 |
| | 1,600 | 180 (7 data) | 185 | 185 |
| | 1,700 | 176 (7 data) | 185 | 183 |
| B | 1,400 | 154 (6 data) | 147 | 170 |
| C | 2,600 | 251 (5 data) | 242 | 255 |
| | 2,700 | 261(5 data) | 251 | 262 |
| | 2,800 | 264 (5 data) | 268 | 267 |
| A.E. | | 5.5 (deg-C) | 10.1(deg-C) | |

**A.E. ; Averaged error of TFfit from TFobs**

**TFfit ; Formation temperature estimated by curve fitting method**

**TFobs ; Formation temperature measured by temperature logging**

**Table 6 Effect of exact period after cessation of mud circulation on formation temperature estimation(TFfit)**

| Well | depth (m) | TFfit (deg-C) Corrected | TFfit (deg-C) Non-Corrected | TFobs (deg-C) |
|---|---|---|---|---|
| A | 700 | 188(C.T.=1.16 h) | 186 | 190 |
| | 1,500 | 182(C.T.=2.5 h) | 177 | 189 |
| | 1,600 | 180(C.T.=2.67 h) | 174 | 185 |
| | 1,700 | 176(C.T.=2.83 h) | 171 | 183 |
| B | 1,400 | 154(C.T.=2.33 h) | 151 | 170 |
| C | 2,600 | 251(C.T.=4.33 h) | 246 | 255 |
| | 2,700 | 261(C.T.=4.5 h) | 256 | 262 |
| | 2,800 | 269(C.T.=4.67 h) | 265 | 267 |
| A.E. | | 5.5(deg-C) | 9.4(deg-C) | |

**TFfit ; Formation temperature estimated by curve fitting method**

**C.T. ; Corrected time**

**TFobs ; Formation temperature measured by temperature logging**

**A.E. ; Averaged Error of TFfit from TFobs**

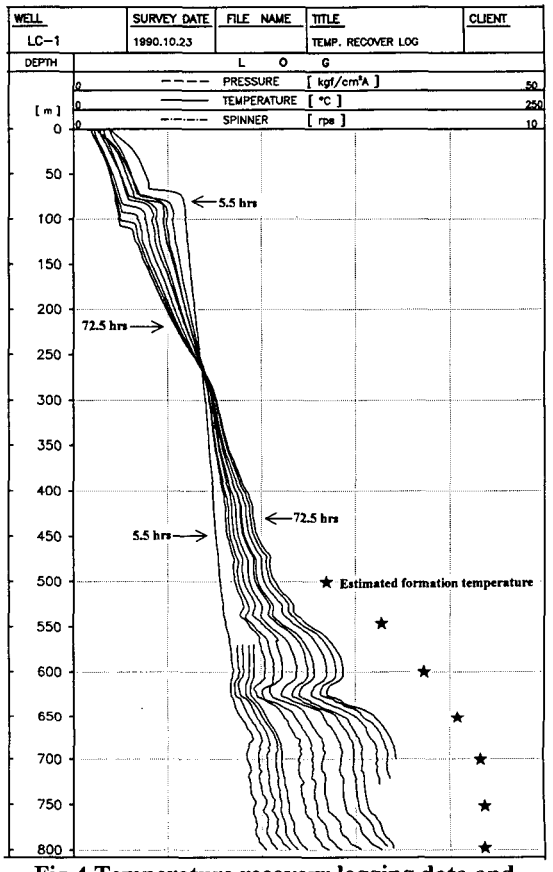


**Fig.4 Temperature recovery logging data and estimated formation temperature**

**Table 7 Effect of period after cessation of mud circulation on formation temperature estimation(TFfit) at 700m**

| time | Case1 | Case2 | Case3 | Case4 | Case5 | Case6 | Case7 | Case8 | Case9 | Case10 | Case11 | Case12 | Case13 |
|---|---|---|---|---|---|---|---|---|---|---|---|---|---|
| 5.5 h | Use | Use | Use | Use | Use | Use | Use | Use | Use | Use | Use | Use | Use |
| 6.5 h | Use | Use | Use | Use | Use | Use | Use | Use | Use | Use | Use | Use | Use |
| 7.5 h | | Use | Use | Use | Use | Use | Use | Use | Use | Use | Use | Use | Use |
| 8.5 h | | | Use | Use | Use | Use | Use | Use | Use | Use | Use | Use | Use |
| 9.5 h | | | | Use | Use | Use | Use | Use | Use | Use | Use | Use | Use |
| 12.5 h | | | | | Use | Use | Use | Use | Use | Use | Use | Use | Use |
| 15.5 h | | | | | | Use | Use | Use | Use | Use | Use | Use | Use |
| 18.5 h | | | | | | | Use | Use | Use | Use | Use | Use | Use |
| 24.5 h | | | | | | | | Use | Use | Use | Use | Use | Use |
| 30.5 h | | | | | | | | | Use | Use | Use | Use | Use |
| 36.5 h | | | | | | | | | | Use | Use | Use | Use |
| 48.5 h | | | | | | | | | | | Use | Use | Use |
| 60.5 h | | | | | | | | | | | | Use | Use |
| 72.5 h | | | | | | | | | | | | | Use |
| E.F.T. | 212.3 | 207.3 | 197.1 | 189.5 | 190.5 | 198 | 205.3 | 214.9 | 217.4 | 216 | 216 | 216 | 215.6 |
| delt E.F.T. | | -5 | -10.2 | -7.6 | 1 | 7.5 | 7.3 | 9.6 | 2.5 | -1.4 | 0 | 0 | -0.4 |
| Alpha | 160.70 | 160.70 | 161.00 | 160.70 | 164.10 | 158.70 | 137.40 | 120.50 | 101.40 | 101.20 | 112.4 | 129.30 | 120.50 |

E.F.T. ; Estimated Formation Temperature

delt E.F.T.=E.F.T.(i) - E.F.T.(i - 1)

Alpha=$R/(K)^{1/2}$

**Table 8 Effect of time interval on formation temperature estimation(TFfit) (Max. 24 hours)**

| Elapsed time | Case1 | Case2 | Case3 | Case4 | Case5 | Case6 | Case7 |
|---|---|---|---|---|---|---|---|
| 5.5 h | Use | Use | Use | | Use | Use | Use |
| 6.5 h | Use | | Use | | Use | Use | Use |
| 7.5 h | Use | Use | Use | | | Use | |
| 8.5 h | Use | | Use | | | | |
| 9.5 h | Use | Use | | Use | | | Use |
| 12.5 h | Use | | | Use | | | |
| 15.5 h | Use | Use | | Use | Use | | |
| 18.5 h | Use | | | Use | Use | Use | Use |
| 24.5 h | Use | Use | Use | Use | Use | Use | Use |
| data No. | 9 | 5 | 5 | 5 | 5 | 5 | 5 |
| E.F.T.(deg-C) | 214.9 | 216.2 | 208.8 | 228.9 | 220.2 | 210.2 | 209.9 |
| Alpha | 158.7 | 159.2 | 134.7 | 198.2 | 170.6 | 142.7 | 142 |

E.F.T. ; Estimated Formation Temperature
Alpha=R/(K) $^{1/2}$

**Table 9 Estimation of formation temperature(TFfit) using continuous data**

| Time | Case1 | Case2 | Case3 | Case4 | Case5 | Case6 | Case7 | Case8 |
|---|---|---|---|---|---|---|---|---|
| 0.0833 h | Use | Use | Use | Use | Use | Use | Use | Use |
| 0.1666 h | Use | Use | Use | Use | Use | Use | Use | Use |
| 0.25 h | Use | Use | Use | Use | Use | Use | Use | Use |
| 0.3333 h | Use | Use | Use | Use | Use | Use | Use | Use |
| 0.5 h | Use | Use | Use | Use | Use | Use | Use | Use |
| 1.0 h | | Use | Use | Use | Use | Use | Use | Use |
| 1.5 h | | | Use | Use | Use | Use | Use | Use |
| 2.0 h | | | | Use | Use | Use | Use | Use |
| 2.5 h | | | | | Use | Use | Use | Use |
| 3.0 h | | | | | | Use | Use | Use |
| 3.8 h | | | | | | | Use | Use |
| 96 h | | | | | | | | Use |
| E.F.T. | 171.1 | 298.4 | 363.6 | 383.3 | 361.1 | 344.5 | 330.9 | 298.2 |
| delt E.F.T. | | 127.3 | 65.2 | 19.7 | -22.2 | -16.6 | -13.6 | -32.7 |
| Alpha | 49.6 | 61.7 | 67.4 | 69.3 | 66.9 | 64.8 | 62.8 | 56.2 |

E.F.T. ; Estimated Formation Temperature
delt E.F.T.=E.F.T.(i) - E.F.T.(i - 1)
Alpha=R/(K) $^{1/2}$

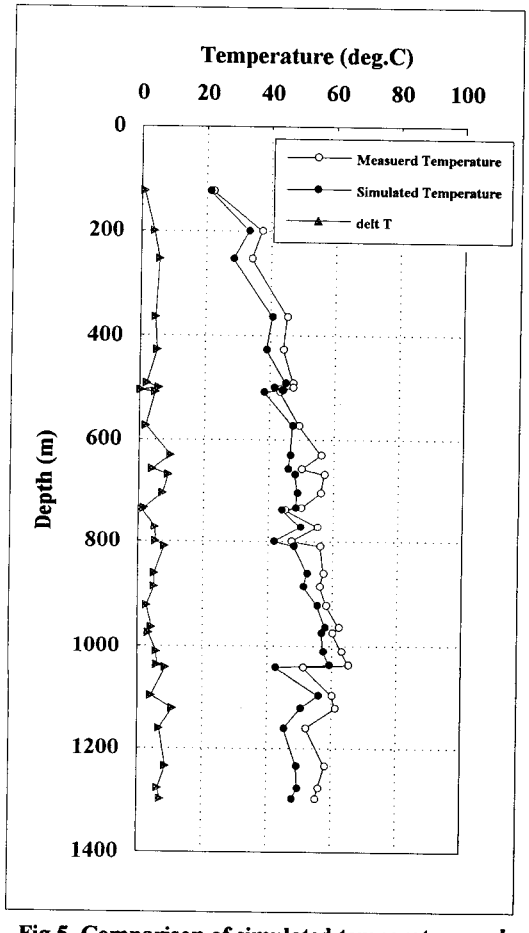


**Fig.5 Comparison of simulated temperature and measured mud temperature at surface while drilling**

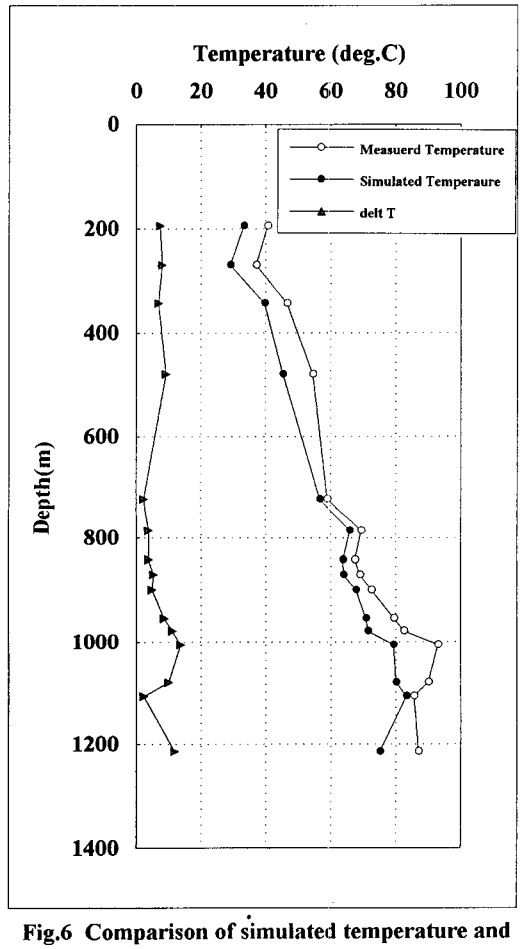


**Fig.6 Comparison of simulated temperature and bottom hole temperature measured by maximum thermometer while drilling**

PROCEEDINGS, Nineteenth Workshop on Geothermal Reservoir Engineering
Stanford University, Stanford, California, January 18-20, 1994
SGP-TR-147

# A STUDY OF PRODUCTION/INJECTION DATA FROM SLIM HOLES AND LARGE-DIAMETER PRODUCTION WELLS AT THE OGUNI GEOTHERMAL FIELD, JAPAN

S.K. Garg
S-Cubed
La Jolla, California, USA

Jim Combs
Geo Hills Associates
Los Altos Hills, California, USA

M. Abe
Electric Power Dev. Co., Ltd.
Tokyo, Japan

## ABSTRACT

Production and injection data from 11 slim holes and 10 large-diameter wells at the Oguni Geothermal Field, Japan, were examined in an effort to establish relationships (1) between productivity of large-diameter wells and slim holes, (2) between injectivity and productivity indices and (3) between productivity index and borehole diameter. The production data from Oguni boreholes imply that the mass production from large diameter wells may be estimated based on data from slim holes. Test data from both large- and small-diameter boreholes indicate that to first order the productivity and the injectivity indices are equal. Somewhat surprisingly, the productivity index was found to be a strong function of borehole diameter; the cause for this phenomenon is not understood at this time.

## 1. INTRODUCTION

Since a major impediment to the exploration for and assessment of new geothermal areas worldwide is the high cost of conventional rotary drilling, it would be desirable to be able to utilize low-cost slim holes ( 100 mm diameter) for geothermal exploration and definitive reservoir assessment. Garg and Combs (1993) presented a review of the publicly available Japanese data regarding slim holes. Slim holes have been successfully used in Japan (Garg and Combs, 1993) for (1) obtaining core for geological studies and delineating the subsurface stratigraphic structure, (2) characterizing the geothermal reservoir fluid state, and (3) as shutin observation boreholes in pressure interference tests. In order to establish the utility of slim holes for definitive reservoir assessment, it is also necessary to be able to predict the discharge characteristics of large-diameter wells based on injection/production tests on small-diameter slim holes. At present, there do not exist sufficient published data, either in Japan or elsewhere, to establish a statistically meaningful relationship between the injectivity/productivity of small-diameter slim holes and of large diameter production and/or injection wells.

The U.S. Department of Energy (DOE) through Sandia National Laboratories (Sandia) has initiated a research effort to demonstrate that slim holes can be used (1) to provide reliable geothermal reservoir parameter estimates comparable to those obtained from large-diameter wells, and (2) to predict the discharge behavior of large-diameter wells (Combs and Dunn, 1992). As part of its research program, DOE/Sandia plans to drill and test pairs of small-diameter slim holes with existing production wells in several geothermal fields in the western United States; the first of these tests was recently completed in mid-1993 at the Steamboat Hills Geothermal Field, Nevada. Because of fiscal constraints, it is unlikely that sufficient U.S. data will become available in the near future. Fortunately, the Japanese geothermal industry has had extensive experience in the use of slim holes for geothermal exploration and reservoir assessment. Most of the Japanese slim hole data are proprietary. However, assuming that data ownership issues can be resolved, the existing Japanese data in conjunction with planned field tests in the United States should help in establishing a statistically valid relationship between the injectivity/productivity of slim holes and of large-diameter wells.

The Oguni Geothermal Field, Kumamoto Prefecture, Kyushu, Japan is an attractive candidate for a case history on the use of slim holes in geothermal exploration and reservoir assessment. Since 1983, Electric Power Development Company, Ltd. (EPDC) has carried out an extensive exploration and reservoir assessment program in the area (Abe, 1992). As of mid-1993, EPDC had drilled and tested more than 20 boreholes ranging in depth from 500 to 2000 meters. In this paper, we examine data from 11 slim holes and 10 large-diameter wells at the Oguni Geothermal Field.

A brief overview of the Oguni Geothermal Field is presented in Section 2. This Section also lists the feed zone depths for all the 21 boreholes for which production and/or injection data are available. Injectivity indices and estimates of reservoir permeability-thickness product (kh) obtained from injection and fall-off data are discussed in Section 3. The discharge test data, productivity indices, and estimates of kh product given by pressure buildup data are presented in Section 4. Finally, in Section 5, we discuss the (1) variation of discharge rate, productivity index, and injectivity index with borehole diameter, (2) relationship between productivity and injectivity indices, and (3) kh determined from short-term injection and longer-term discharge tests.

## 2. OGUNI GEOTHERMAL FIELD

The Oguni and the Sugawara Geothermal Fields together comprise the northwestern Hohi geothermal region, Kumamoto and Oita Prefectures, Kyushu, Japan (see Figure 1). An area of numerous hot springs, it is approximately 40 km southwest of the coastal resort of Beppu, and some 20 km north of Mt. Aso, an active caldera. The New Energy and Industrial Technology Development Organization (NEDO) carried out a regional (200 $km^2$ area) exploration program in the Hohi area during the years 1979–1985; this work resulted in the identification of a highly permeable geothermal area in the northwestern Hohi area. EPDC initiated a geothermal exploration program in the Oguni area in 1983. The Oguni field is located at the northeast end of Kumamoto Prefecture; Oita Prefecture is to the north and northeast of the Oguni area. The Sugawara field, to the north of the Oguni area, is being surveyed by NEDO as a possible site for the demonstration of a binary power plant. Although the northern Hohi area has been subdivided into two separate geothermal fields (Oguni, Sugawara), the area constitutes a single hydrological unit.

The subsurface stratigraphic structure in the northern Hohi area is shown in Figure 2. The granite basement (not shown in Figure 2) is found at about –1000 m ASL in the Oguni area, and drops off steeply to the northeast (in the Sugawara area). The stratigraphic sequence above the basement consists of the Pliocene Taio formation, the late Pliocene/early Pleistocene Shishimuta formation (pre-Kusu group), the lower to middle Pleistocene Hohi and Kusu formations, and the upper Pleistocene Kuju formation. The Nogami mudstones (part of the Kusu group) and the Kuju volcanics appear to function as a caprock for the geothermal system. Based upon feedpoint locations, it appears that the Hohi formation and the upper part of the Shishimuta formation constitute the principal aquifers.

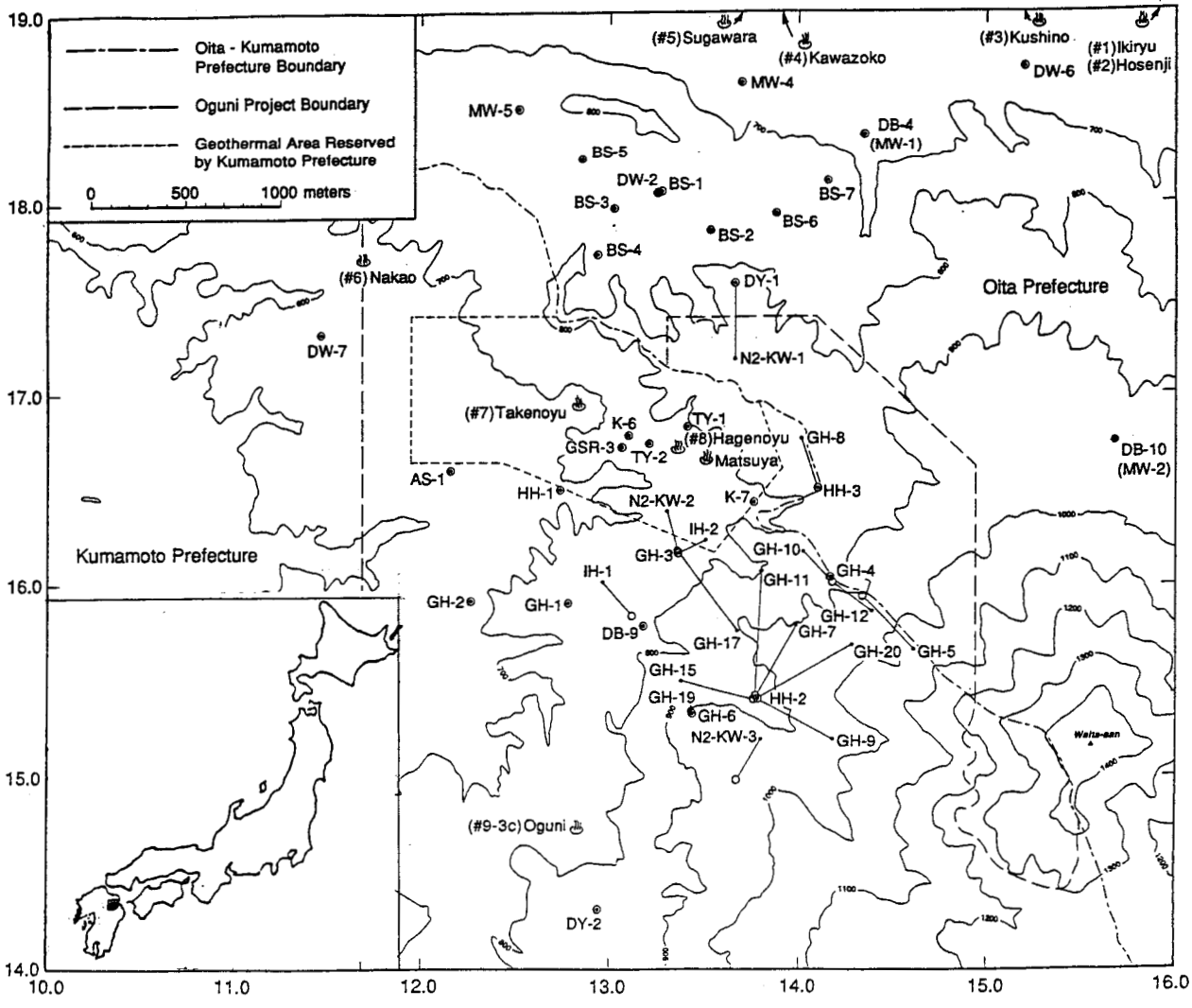


Figure 1. The northern Hohi geothermal area, Kyushu, Japan. The inset map of Japan (lower left hand corner) shows the location of the Hohi geothermal area (dark rectangle).

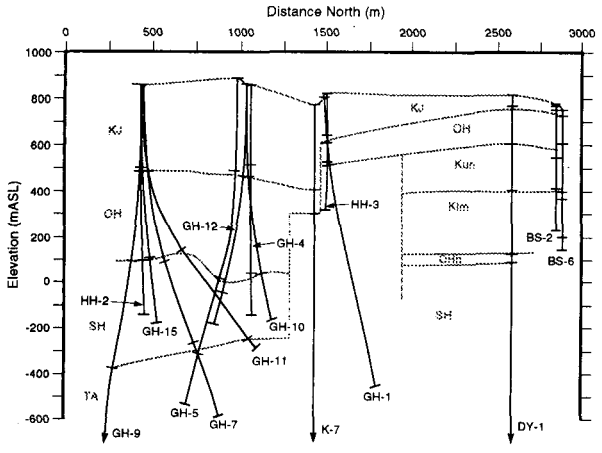


Figure 2. A north-south stratigraphic cross-section for the northern Hohi area. The following abbreviations are used for formation names: KJ (Kuju); Kun (Kusu/Nogami mudstone); Klm (Kusu/Machida lava); OH (Hohi); OHh (Hohi/Hatchobaru lava); SH (Shishimuta): TA (Taio).

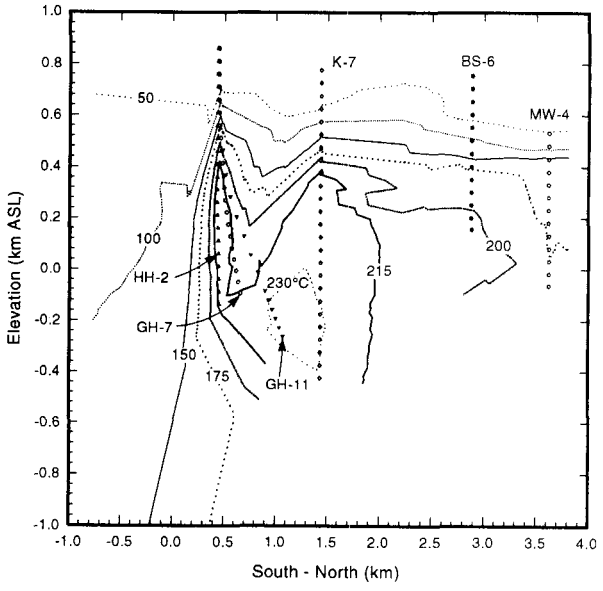


Figure 3. Subsurface temperature distribution along a south-north vertical plane in the northern Hohi area.

The feedzone pressures imply that the northern Hohi region consists of two pressure zones (a high pressure zone in the area of wells GH-15, GH-19, GH-6, HH-2, N2-KW-3 and DY-2; a low pressure zone in the central and northern parts of the field) which are in poor communication with each other. At present, the reasons for the existence of two different pressure zones are poorly understood. The maximum temperature (~240°C) in the area occurs near Oguni wells GH-4, GH-10, and GH-11 and Kumamoto Prefecture well K-7 (see Figure 3). Temperatures in the Sugawara field are significantly lower than those prevailing in the Oguni field. The northern Hohi area (excluding the Oguni high pressure zone) in its natural state is characterized by a vertical pressure gradient of 8.531 kPa/m (see Figure 4). This corresponds to a hydrostatic gradient at about 195°C, and implies upflow in regions of the geothermal reservoir where temperature exceeds 195°C. The mathematical fit to feedpoint pressures also implies that pressures decrease to the north; the pressure gradient is ~0.065 bars/km. Apparently, hot fluid is upwelling in the area of Oguni wells GH-4, GH-6, GH-10 and GH-11; this hot fluid then flows horizontally to the north. It is also worth noting here the Oguni geothermal reservoir fluid is single-phase liquid; the geothermal wells do not provide any direct evidence of a two-phase zone at depths greater than 300 meters in the Oguni field. The presence of a two-phase zone at shallow depths is, however, suggested by chemical data.

As part of its well drilling and testing program, EPDC has drilled both small-diameter core holes (9 GH and 3 HH series) and large-diameter production size wells (8 GH and 2 IH series); in addition, NEDO has drilled 3 small-diameter core holes (N2-KW-1, N2-KW-2 and N2-KW-3) in the Oguni area. With the exception of four core holes (GH-1, GH-2, HH-1 and HH-3), some production and/or injection data are available for all of the Oguni boreholes. Downhole pressure

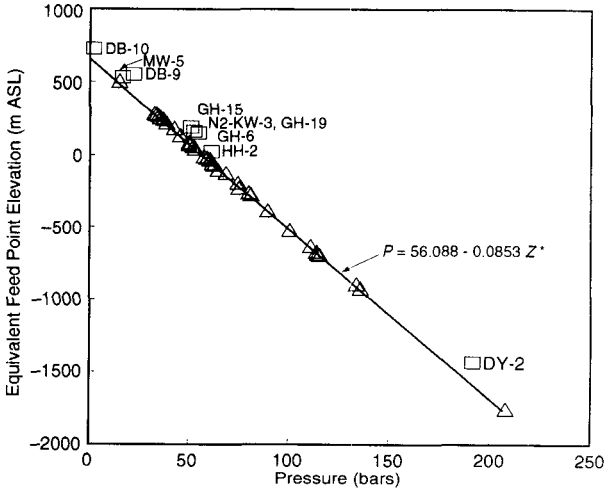


Figure 4. Correlation of pressure with equivalent feedpoint elevation of low-pressure zone wells (Δ). Also shown as □ are wells (DB-10, MW-5, DB-9, GH-15, N2-KW-3, GH-19, GH-6, HH-2, DY-2) not included in the pressure correlation.

measurements were made (1) during most of the injection tests and (2) for buildup after production tests. Pressure, temperature and spinner (PTS) surveys were run during production tests. In addition, repeat pressure and temperature (*i.e.*, heatup) surveys under shutin conditions were recorded in all of the Oguni boreholes. The available drilling (circulation loss, well completion, and geologic data) and downhole PTS surveys in flowing and shutin wells have been analyzed by the authors to obtain (1) feedzone depths and (2) feedzone pressures and temperatures. A list of Oguni boreholes for which some production (P) and/or injection (I) data are available is presented in Table 1. The feedzone

Table 1. List of Oguni boreholes with production or injection data.

| Well Name | Measured Depth (meters) | Vertical Depth (m TVD) | Feedzone Depth (m TVD) | Final Diameter (mm) | Downhole Flowing Temp (°C) | Production/ Injection Data |
|---|---|---|---|---|---|---|
| A. Low-Pressure Reservoir | | | | | | |
| GH-3 | 1500 | 1498 | 1030 | 79 | 214 | P |
| GH-4 | 1001 | 1001 | 900 | 76 | 234 | P |
| GH-5 | 1501 | 1421 | 1100 | 76 | 187 | P |
| GH-7 | 1547 | 1442 | 980/1400 | 98 | 219 | P |
| GH-8 | 1300 | 1255 | 1220 | 78 | 212 | P,I |
| GH-10 | 1063 | 1027 | 1010 | 159 | 241 | P,I |
| GH-11 | 1381 | 1143 | 1140 | 216 | 236 | P,I |
| GH-12 | 1100 | 1045 | 750 | 216 | 232 | P,I |
| GH-17 | 1505 | 1354 | 760 | 216 | — | I |
| GH-20 | 1790 | 1576 | 1560 | 216 | 241 | P,I |
| GH-21 | 810 | 810 | 650 | 216 | — | I |
| IH-1 | 900 | 810 | 590 | 159 | — | I |
| IH-2 | 650 | 616 | 550 | 216 | 226 | P,I |
| N2-KW-1 | 1000 | 898 | 860 | 76 | — | I |
| N2-KW-2 | 1000 | 978 | 860 | 76 | — | I |
| B. High-Pressure Reservoir | | | | | | |
| GH-6 | 1003 | 1003 | 770 | 76 | 215 | P |
| GH-9 | 1600 | 1481 | ? | 78 | — | I |
| GH-15 | 1190 | 1048 | 680 | 216 | Two-Phase | P,I |
| GH-19 | 773 | 773 | 750 | 216 | — | I |
| HH-2 | 1000 | 999 | 850 | 76 | Two-Phase | P |
| N2-KW-3 | 1350 | 1317 | 810 | 76 | 227 | P,I |

depth, final borehole diameter and downhole flowing temperature (production tests only) are also given in Table 1.

## 3. INJECTION TESTS

It is common practice at Oguni to conduct a short term (a few hours) injection test soon after the completion of a borehole. The injection test consists of injecting cold water into the borehole, and simultaneously recording pressure and temperature downhole at or near the principal feedzone for the borehole. (In a few cases, the pressure/temperature tool was placed substantially above the feedzone. Most of these measurements are dominated by thermal effects in the wellbore, and are not useful for inferring formation properties.) Measurements taken during a typical Oguni injection test are shown in Figure 5. After start of injection, the pressure rapidly rises and then slowly falls. The pressure rapidly falls after injection is terminated. The rapid fall off at shutin is not unusual, but the rise and subsequent fall in pressure which accompany injection need to be explained. Since the injection test was conducted right after borehole completion, it is likely that the fractures were still laden with cuttings at the time of the test. Injection tests presumably washed these cuttings away from the borehole. It is common practice in Iceland to "stimulate" a well by injection at maximum available rates. Strictly speaking, injection does not cause well stimulation in the usual sense; it merely accomplishes an effective washing of the borehole. Based on this interpretation, the three pressure falloffs for GH-11 in Figure 5 represent the real response to changes in injection rate; the pressure records during the injection phase for GH-11 (as well as most other Oguni wells) merely reflect the washing of the borehole.

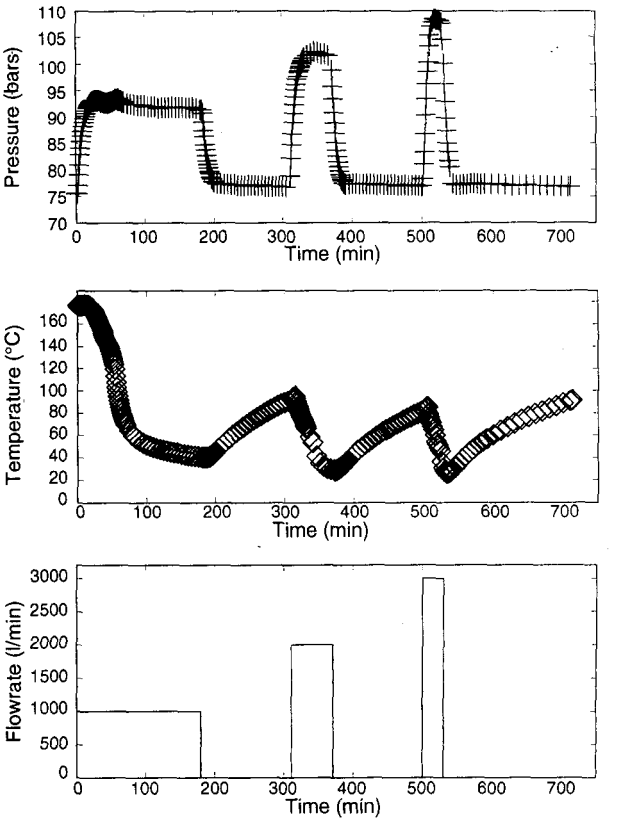


Figure 5. Downhole pressure and temperature (gauge depth = 1121 meters vertical depth) recorded during the injection test of well GH-11 on March 30, 1988.

The pressure fall-off data recorded after injection at 1000 kg/min (see Figure 5) are displayed in Figures 6a and 6b. At small shutin times, the pressure falls rather rapidly (Figure 6a); after a shutin time of about 15 minutes, the pressure fall off slows down considerably (Figures 6a and 6b). The slope of the late time pressure fall-off data ($m$ ~1.19 $10^5$ Pa/Cycle, Figure 6b) gives the following value for the formation permeability-thickness product (assuming $T$ ~225°C and dynamic viscosity $\mu$ ~ 1.2 × $10^{-4}$ Pa-s, $\rho$ = 834 kg/m$^3$):

$$kh = \frac{1.15M\mu}{2\pi m} \sim \frac{1.15 \times 1000 \times 1.2\,10^{-4}}{2\pi \times 60 \times 1.19\,10^{5} \times 834}$$

$$\sim 3.7\,10^{-12}\,\mathrm{m}^2 \sim 3.7\,\mathrm{darcy\text{-}m} \quad .$$

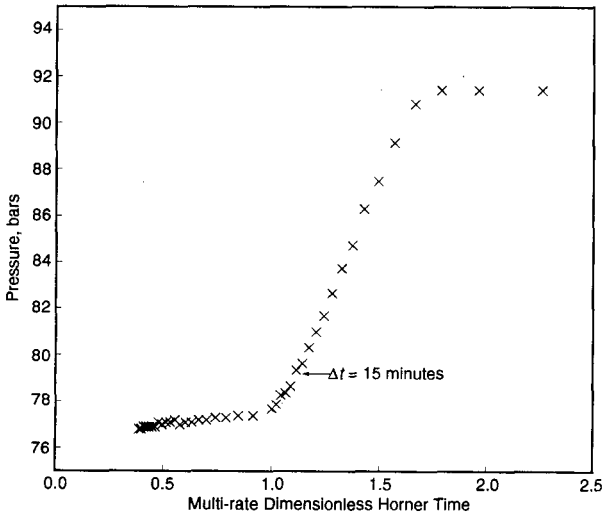


Figure 6a. Horner plot of pressure fall-off data no. 1 for well GH-11 (March 30, 1988).

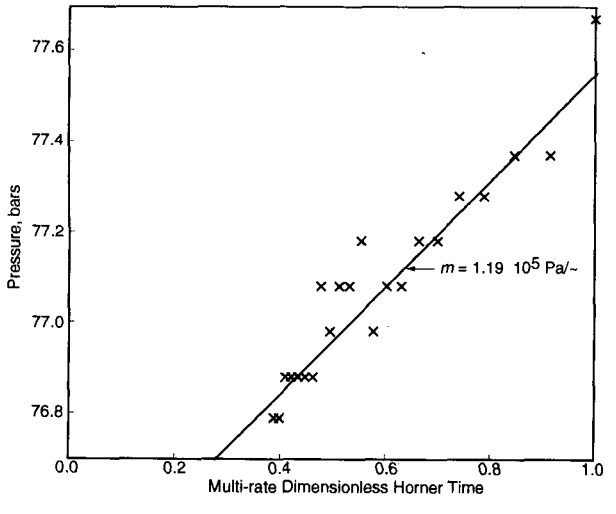


Figure 6b. Horner plot of pressure fall-off data no. 1 (late shutin time) for well GH-11 (March 30, 1988).

The pressure fall-off data from all the Oguni injection tests were analyzed in a similar manner. The kh values inferred from the injection tests are listed in Table 2.

Table 2. Permeability-thickness (kh) inferred from pressure fall-off (injection tests) and pressure buildup (discharge tests) data

| Well Name | Final Diameter (mm) | Production kh (darcy-m) | Injection* kh (darcy-m) |
|---|---|---|---|
| A. Low-Pressure Reservoir | | | |
| GH-3 | 79 | 0.44 | — |
| GH-4 | 76. | — | — |
| GH-5 | 76. | 4.5 | — |
| GH-7 | 98. | 1.3 | — |
| GH-8 | 78. | 29 | — |
| GH-10 | 159. | 92. | — |
| GH-11 | 216. | 83. | 6.9 |
| GH-12 | 216. | 32. | 5.1 |
| GH-17 | 216. | — | 0.14 |
| GH-20 | 216. | 55. | 6.1 |
| GH-21 | 216. | — | 14 |
| IH-1 | 159. | — | 0.73 |
| IH-2 | 216. | 44. | 25 |
| N2-KW-1 | 76. | — | 9.3 |
| N2-KW-2 | 76. | — | 0.58 |
| B. High-Pressure Reservoir | | | |
| GH-6 | 76. | — | — |
| GH-9 | 78. | — | 0.03 |
| GH-15 | 216. | 0.47 | 0.92 |
| GH-19 | 216. | — | — |
| HH-2 | 76. | — | — |
| N2-KW-3 | 76. | — | — |

* Average value obtained from the various fall-off tests for a borehole.

The injectivity index (II) is defined as follows:

$$(\mathrm{II}) = \frac{M}{P_f - P_i}$$

where $M$ is the mass rate of injection, $P_f$ is the flowing pressure and $P_i$ is the initial (or static) pressure. It was noted earlier that the flowing pressure $P_f$ was observed to fall in many Oguni injection tests; in such cases, the computed injectivity index represents a lower limit. The most reliable values of the injectivity index for the various Oguni boreholes are given in Table 3.

## 4. DISCHARGE TESTS

A borehole must be discharged to ascertain its productive capacity. A total of 8 small-diameter core holes and 6 large-diameter Oguni wells have been discharged at one time or another. As part of these discharge tests, the characteristic well output curves (*i.e.*, mass and enthalpy versus wellhead pressure) were also obtained. The output curve for well GH-20 is illustrated in Figure 7; the maximum well mass

Table 3. Productivity/injectivity indices of Oguni wells.

| Well Name | Final Diameter (mm) | Productivity Index (kg/s-bar) | Injectivity Index (kg/s-bar) |
|---|---|---|---|
| A. Low-Pressure Reservoir | | | |
| GH-3 | 79 | 0.53 | — |
| GH-4 | 76. | 1.44 | — |
| GH-5 | 76. | 1.19 | — |
| GH-7 | 98. | 1.05 | — |
| GH-8 | 78. | 1.01 | — |
| GH-10 | 159. | 3.88 | 3.39 |
| GH-11 | 216. | 5.65 | 1.53 |
| GH-12 | 216. | 5.77 | 5.12 |
| GH-17 | 216. | — | 0.46 |
| GH-20 | 216. | 15.2 | 7.82 |
| GH-21 | 216. | — | 12.1 |
| IH-1 | 159. | — | 0.84 |
| IH-2 | 216. | 11.9 | 33. |
| N2-KW-1 | 76. | — | 2.11 |
| N2-KW-2 | 76. | — | 0.86 |
| B. High-Pressure Reservoir | | | |
| GH-6 | 76. | 5.02 | — |
| GH-9 | 78. | — | 0.08 |
| GH-15 | 216. | 0.25 | 1.75 |
| GH-19 | 216. | — | 25.7 |
| HH-2 | 76. | 0.03 | — |
| N2-KW-3 | 76. | 3.85 | 5.85 |

Table 4. Measured and predicted discharge rates for Oguni boreholes.

| Well Name | Final Diameter (mm) | Measured Discharge (tons/hr) | Area Scaled Discharge† (tons/hr) | Scaled Maximum Discharge†† (tons/hr) |
|---|---|---|---|---|
| A. Low-Pressure Reservoir | | | | |
| GH-3 | 79 | 20 | 151 | 266 |
| GH-4 | 76 | 27 | 218 | 391 |
| GH-5 | 76 | 22 | 178 | 319 |
| GH-7 | 98 | 30 | 146 | 227 |
| GH-8 | 78 | 36 | 276 | 488 |
| GH-10 | 159 | 164 | 303 | 359 |
| Average (GH-3 to GH-8) | | | 194 | 338 |
| Average (GH-3 to GH-10) | | | 212 | 342 |
| GH-11 | 216 | 279 | | |
| GH-12 | 216 | 279 | | |
| GH-20 | 216 | 369 | | |
| IH-2 | 216 | 316 | | |
| Average (GH-11 to IH-2) | | 311 | | |
| B. High-Pressure Reservoir | | | | |
| GH-6 | 76 | 24 | 194 | 348 |
| GH-15 | 216 | 36* | | |
| HH-2 | 76 | 5* | 40 | 72 |
| N2-KW-3 | 76 | 28 | 226 | 406 |

† Area-Scaled Discharge Rate = Measured Discharge Rate × (216/well dia. in mm)$^2$

†† Scaled Maximum Discharge Rate = Measured Discharge Rate × (216/well dia. in mm)$^{2.56}$

* Two-Phase Flow

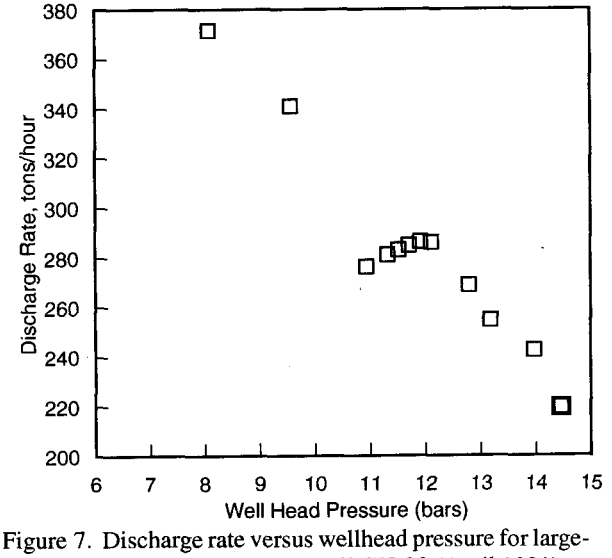


Figure 7. Discharge rate versus wellhead pressure for large-diameter production well GH-20 (April 1991).

discharge rate (~ 370 tons/hour) occurs at a wellhead pressure of ~ 8 bars. The maximum measured discharge rates for the various Oguni boreholes are given in Table 4.

Following the discharge tests (varying in duration from a few days to several months) pressure buildup was recorded by lowering a gauge (usually Kuster) into the borehole. Because of instrument limitations, it was in many cases necessary to pull (and reinsert) the gauge out of the hole after a few hours; this resulted in a gap in the pressure buildup record. A multi-rate Horner plot of pressure buildup data for well GH-20 is shown in Figure 8. The pressure buildup data in Figure 8 lie on a straightline; the slope of the straightline yields a permeability-thickness value of 55 darcy-meters for large-diameter production well GH-20. The kh values inferred from the pressure buildup data for the various Oguni boreholes are listed in Table 2.

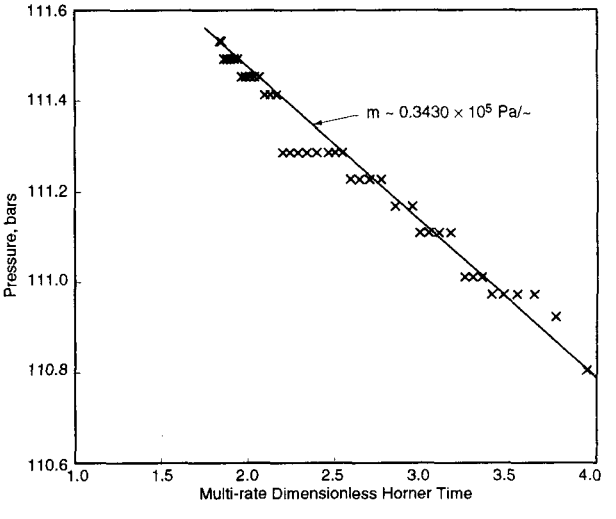


Figure 8. Multi-rate Horner plot of pressure buildup data for well GH-20 (04-27-91). Pressures were recorded at 1750 m MD (1542 m TVD) for 256 minutes following well shutin.

During all of the discharge tests, pressure and temperature (or pressure, temperature and spinner) surveys were also run. These pressure surveys are useful for estimating flowing feedzone pressures ($P_f$). Given $P_f$, stable feedzone pressure $P_i$, and mass discharge rate, the productivity index (PI) can be calculated from the following expression:

$$\mathrm{PI} = \frac{M}{P_i - P_f} \quad .$$

The computed values of PI for the Oguni boreholes are given in Table 3.

## 5. DISCUSSION AND CONCLUSIONS

EPDC has carried out several pressure interference tests in the Oguni Geothermal Field. Analyses of pressure interference data from the low-pressure zone wells indicate that the northern Hohi area has good permeability (100 to 250 darcy-meters). By comparison, pressure buildup data (see Table 2) from individual Oguni boreholes (low-pressure zone) yield kh values in the range 0.4 to 92 darcy-meters; interestingly, smaller kh values (Table 2) are generally associated with small-diameter boreholes. For large diameter wells, kh values inferred from buildup tests vary from 32 to 92 darcy-meters. In fractured reservoirs, interference tests commonly yield higher kh values than those given by pressure buildup tests. (An individual well intersects at most a few major fractures. These major fractures join the fracture network at some distance from the borehole. A pressure buildup test samples a smaller region of the reservoir than that investigated by an interference test.) In any case, the kh values inferred from pressure buildup tests (large-diameter wells) at Oguni are of the same order of magnitude as those given by interference tests. The kh values obtained from short-term injection tests range between 0.1 and 25 darcy-meters for all the low-pressure zone boreholes; the kh values for large-diameter wells (excluding well GH-17) vary from 5 to 25 darcy-meters. Clearly, the kh values derived from short-term injection tests (5 to 25 darcy-meters) are much smaller than those obtained from longer term discharge tests (32 to 92 darcy-meters). The explanation for the discrepancy in kh values is tied to the duration of the tests; the reservoir radius investigated during a well test is roughly proportional to the square root of time. In contrast with longer term discharge tests (days to months in duration), short term injection tests (a few hours) sample only the near well bore region. Thus, short term injection tests are likely to yield a lower bound on reservoir transmissivity.

Ignoring pressure transient effects, the flow resistance (or pressure losses) of the reservoir rocks can be represented by the productivity (or injectivity) index. Both the productivity and injectivity indices are available for only 7 of the Oguni boreholes (Table 3); these data are displayed in Figure 9. It is apparent from Figure 9 that to first order the productivity and injectivity indices for the Oguni boreholes are equal. The latter observation is at variance with the results of the classical porous-medium flow analyses (*e.g.*, Garg and

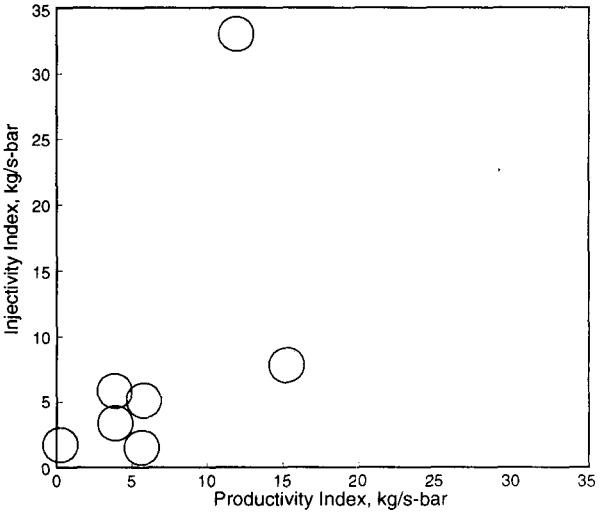


Figure 9. Productivity versus injectivity index for low-pressure reservoir boreholes, Oguni Geothermal Field.

Pritchett, 1990) which suggest that the injectivity index should be a strong function of the sand face injection temperature. Grant, *et al.* (1982), however, maintain that the classical analyses do not apply to geothermal systems which are mostly associated with fractured formations; and that injectivity is at least as great as productivity in discharge tests. The Oguni data are consistent with Grant, *et al.*'s viewpoint and imply that in the absence of productivity data, injectivity index may be used to characterize the flow resistance of the reservoir rocks.

Theoretical considerations (Pritchett, 1992) suggest that apart from any systematic difference associated with differences in drilling techniques (rotary versus core drilling), the productivity (or injectivity) index should exhibit only a weak dependence on borehole diameter. The available productivity/injectivity index data for low-pressure zone boreholes (see Table 3) are displayed in Figures 10a and 10b. Both the productivity and injectivity indices display a strong dependence on borehole diameter. At present, the exact cause for the latter phenomenon remains unknown.

To compare the fluid carrying capacity of boreholes of varying size, it is useful to introduce the "area-scaled discharge rate" $M^*$ as follows:

$$M^* = Mx\left(\frac{d}{d_o}\right)^2$$

where $M$ is the actual borehole discharge rate, and $d_o$ is the internal borehole diameter (mm). Based on numerical simulation of fluid flow in boreholes of varying diameters, Pritchett (1992) suggests that the maximum discharge rate will increase somewhat faster than the square of diameter.

$$M_{\max} = Mx\left(\frac{d}{d_o}\right)^{2+n}, \quad n \geq 0$$

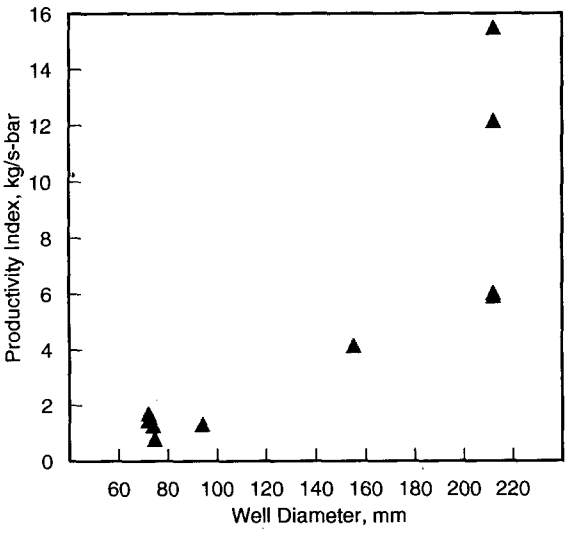


Figure 10a. Productivity index versus diameter for low-pressure reservoir boreholes, Oguni Geothermal Field.

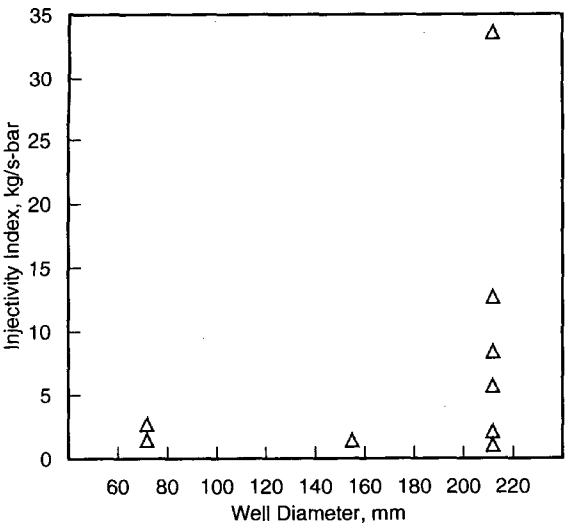


Figure 10b. Injectivity index versus diameter for low-pressure reservoir boreholes, Oguni Geothermal Field.

The exact value of $n$ will of course depend on the downhole conditions (*e.g.*, feedzone depth, flowing pressure and enthalpy, and gas content of fluid). For the conditions assumed by Pritchett (feedzone depth = 1500 meters, feedzone pressure = 80 bars, feedzone temperature = 250°C, single-phase liquid-water at feedzone, uniform wellbore diameter), $n$ is equal to 0.56. With the exception of two wells (GH-15 and HH-2) in the high pressure zone, all the Oguni boreholes have single-phase liquid conditions at their principal feedzones. On average, the Oguni feedzones are shallower and the feedzone temperatures are somewhat lower than that assumed by Pritchett (1992) for his computations.

Both the "area-scaled" and "scaled maximum ($n$ = 0.56)" discharge rates are given in Table 4. For the low-pressure zone large-diameter wells (GH-11, GH-12, GH-20 and IH-2), the average measured maximum discharge rate (311 tons/hour) is bracketed by the averaged "area-scaled" (194 tons/hour) and averaged "scaled maximum" (338 tons/hour) discharge rates. Despite differences between the conditions assumed by Pritchett (1992) and the actual conditions obtaining in the Oguni boreholes, it would appear that the "scaled maximum discharge rate" provides a reasonable prediction of the discharge performance of large-diameter wells.

In summary, it has been shown that the Oguni data are consistent with the premise that it should be possible to use small-diameter slim holes for definitive reservoir assessment, and for forecasting the discharge/injection performance of large-diameter production size wells. These conclusions must, however, be tested with data from a statistically significant collection of geothermal fields.

## 6. ACKNOWLEDGMENTS

We thank the management of the Electric Power Development Company for permission to use their unpublished proprietary data for this study. This work was supported under contract AG-4388 from Sandia National Laboratories.

## 7. REFERENCES

Abe, M., S. Kurishima, and Y. Mezaki (1992), "Drilling of Geothermal Well in the Onikobe Geothermal Field and Developing Oguni Geothermal Field," *Chinetsu, Vol. 29(1)*, p. 1-32.

Combs, J. and J.C. Dunn (1992), "Geothermal Exploration and Reservoir Assessment: The Need for a U.S. Department of Energy Slim-Hole Drilling R&D Program in the 1990s," *Geothermal Resources Council Bulletin, Vol. 21., No. 10*, pp. 329-337.

Garg, S.K. and J. Combs (1993), "Use of Slim Holes for Geothermal Exploration and Reservoir Assessment: A Preliminary Report on Japanese Experience," paper presented at *Eighteenth Workshop on Geothermal Reservoir Engineering*, Stanford University, California, January.

Garg, S.K. and J.W. Pritchett (1990), "Cold Water Injection into Single- and Two-Phase Geothermal Reservoirs," *Water Resources Research, Vol. 26*, pp. 331-338.

Grant, M.A., I.G. Donaldson, and P.F. Bixley (1982), Geothermal Reservoir Engineering, Academic Press, New York, p. 310.

Pritchett, J.W. (1992), "Preliminary Study of Discharge Characteristics of Slim Holes Compared to Production Wells in Liquid-Dominated Geothermal Reservoirs," Report No. SSS-TR-92-13133, S-Cubed, La Jolla, California, July, 48 pp.

PROCEEDINGS, Nineteenth Workshop on Geothermal Reservoir Engineering
Stanford University, Stanford, California, January 18-20, 1994
SGP-TR-147

# FLOW NEAR THE CRITICAL POINT: EXAMINATION OF SOME PRESSURE-ENTHALPY PATHS

Daniel O. Hayba[1] and Steven E. Ingebritsen[2]

[1]MS 959, U.S. Geological Survey, Reston, VA 22092
[2]MS 439, U.S. Geological Survey, Menlo Park, CA 94025

## ABSTRACT

Quantitative flow modeling of fluids at elevated temperatures and pressures has generally been limited to consideration of either single-phase flow or two-phase flow at conditions below the critical point of water. In this paper, we introduce a version of the GEOTHER model that can simulate both multiphase flow and flow above the critical point, and demonstrate its capabilities by simulating flow in the vicinity of the critical point. GEOTHER2 is a multiphase, finite-difference model that simulates three-dimensional flow of pure water and heat at temperatures ranging from 0° to 1,200°C and pressures ranging from 0.5 to 10,000 bars. The governing equations are expressions of mass and energy conservation that are posed in terms of pressure and enthalpy. A series of one-dimensional experiments indicates that permeability is a pivotal factor in determining pressure-enthalpy/temperature trajectories near the critical point. At low permeabilities ($\leq 10^{-18}$ m$^2$), heat transport by conduction dominates, and the trajectory defines a constant thermal gradient. At higher permeabilities ($\geq 10^{-16}$ m$^2$), advective heat transport dominates, and the pressure-enthalpy trajectory maintains a constant "flowing enthalpy".

## INTRODUCTION

Transport processes in magmatic-hydrothermal systems involve single- or two-phase flow of fluids at temperatures ranging from 0° to >1,000°C and pressures ranging up to several kilobars. The properties of water vary substantially over this P-T range, especially in the vicinity of the critical point, where some fluid properties exhibit extrema. Although these near-critical extrema may influence flow patterns in hydrothermal systems, computational difficulties have inhibited quantitative modeling of flow near the critical point. In this paper, we introduce an extended version of the computer program GEOTHER that is capable of simulating near-critical flow, and demonstrate this capability with some one-dimensional, steady-state experiments.

In the past, most users of geothermal models have had to choose between models for multiphase, pure-water (or water and gas) systems with a temperature range of about 0-350°C, and models for single-phase pure-water systems with a temperature range of about 0-1,000°C. Most of the multiphase, subcritical models were designed by reservoir-engineering groups to handle the range of conditions encountered in geothermal-reservoir development (e.g. TOUGH2: Pruess, 1991), whereas most of the single-phase, high-temperature models were developed by geoscience groups to examine heat transfer associated with cooling plutons (e.g. Norton and Knight, 1977; Cathles, 1977). Both types of models have generally assumed that the circulating fluid is pure water or water and noncondensible gas, although Battistelli and others (in press) recently presented a solute-transport algorithm for the TOUGH2 simulator.

One of the major obstacles to the development of a more complete geothermal model has been the radical variation in fluid properties near the critical point. For simulators that use pressure and temperature as dependent variables, the critical point poses particularly difficult problems. In P-T coordinates, the critical point is at the vertex of the vaporization curve and is a singularity in equations of state. For example, the partial derivatives of $\rho(P,T)$ diverge to positive and negative infinity, and $C_v(P,T)$ diverges to infinity (see, e.g., Johnson and Norton, 1991).

Multiphase models cannot use a pressure-temperature formulation because a P-T pair does not specify saturation. Some multiphase codes, such as TOUGH2 (Pruess, 1991), switch variables, solving for pressure and temperature in the single-phase region and pressure and saturation in the two-phase region. In developing the original version of GEOTHER, Faust and Mercer (1977, 1979a) took a different approach, choosing pressure and enthalpy as dependent variables because they uniquely specify the thermodynamic state of the fluid under both single-and two-phase conditions (fig. 1). This choice of variables greatly facilitated the extension of GEOTHER to supercritical conditions, because the pressure-enthalpy formulation eliminates singularities at the critical point.

## THE GEOTHER2 MODEL

GEOTHER2 is a three-dimensional, finite-difference model that can simulate both multiphase and supercritical flow of pure water and heat in a porous medium. This program is a descendent of the models developed at the U.S. Geological Survey by Faust and Mercer (1977, 1979a, 1979b, 1982). We have modified the 1982 version of the program by extending the temperature range to 0-1,200°C and the pressure range to 0.5-10,000 bars, modularizing the program architecture, adding provisions for spatial and temporal variation of porous-medium properties, automating the time-step control, making the convergence criteria more rigorous, and extensively revising the input and output formats. We have made only relatively minor changes to the mathematical model and

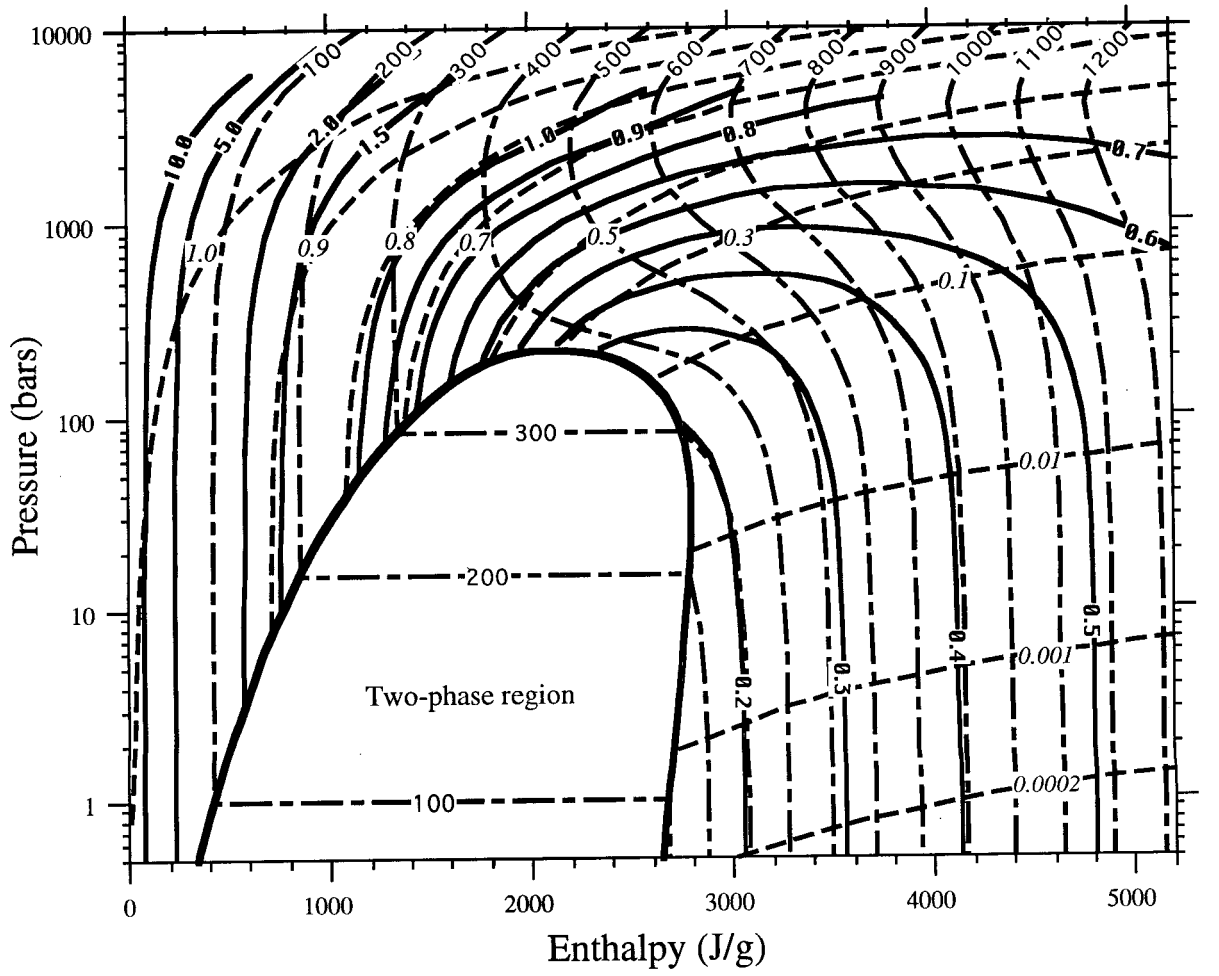


*Figure 1. Pressure-enthalpy diagram for pure water, showing contours of equal temperature, density, and viscosity. Saturated enthalpies of steam and liquid water define the boundaries of the two-phase region, and meet at the critical point (220.55 bars and 2086.0 J/g). Temperatures (*100*, long dashed lines) in °C; densities (0.02, short dashed lines) in g/cm$^3$; and viscosities (***0.2***, solid lines) in g/cm/sec x 10$^{-3}$.*

solution algorithm described by Faust and Mercer (1979a, 1979b, 1982). A complete documentation of GEOTHER2 is undergoing internal review at the U.S. Geological Survey. Ingebritsen (1986) and Hayba (1993) summarized earlier improvements to the Faust and Mercer (1982) version of GEOTHER, and Roberts and others (1987) described another extended version (to 1,000°C and 1 kbar) of the Faust and Mercer model that has not entered the public domain.

The governing equations for GEOTHER2 are expressions of mass and energy conservation, posed in terms of pressure and enthalpy:

$$\frac{\partial}{\partial t}\left[\phi(S_w\rho_w+(1-S_w)\rho_s)\right] - \nabla\cdot\left[\frac{\mathbf{k}k_{rs}\rho_s}{\mu_s}\cdot(\nabla P-\rho_s g\nabla D)\right] - \nabla\cdot\left[\frac{\mathbf{k}k_{rw}\rho_w}{\mu_w}\cdot(\nabla P-\rho_w g\nabla D)\right]-(R_s+R_w)=0 \qquad (1)$$

and

$$\frac{\partial}{\partial t}\left[\phi(S_w\rho_w H_w+(1-S_w)\rho_s H_s)+(1-\phi)\rho_r H_r\right] - \nabla\cdot\left[\frac{\mathbf{k}k_{rs}\rho_s H_s}{\mu_s}\cdot(\nabla P-\rho_s g\nabla D)\right] - \nabla\cdot\left[\frac{\mathbf{k}k_{rw}\rho_w H_w}{\mu_w}\cdot(\nabla P-\rho_w g\nabla D)\right] - \nabla\cdot\left[K_m T\right]-(R_s H_s+R_w H_w)=0 \qquad (2)$$

There are also several constitutive relations that complete the description of the system. Faust and Mercer (1979a) discuss these relations and various assumptions implicit in the governing equations. The more important assumptions are that a two-phase form of Darcy's Law is valid; capillary-pressure effects are negligible; rock and water are in thermal equilibrium; and heat transfer by dispersion and radiation are negligible.

The mass- and energy-balance equations are strongly coupled and highly nonlinear, because a number of the independent variables are functions of the dependent variables. The relative permeabilities, densities, and viscosities, in particular, vary widely with pressure and enthalpy. GEOTHER2 uses Newton-Raphson iteration to treat these nonlinear coefficients, and solves each vertical cross section of the finite-difference grid implicitly. For three-dimensional models, the solution technique is slice-successive overrelaxation embedded in the Newton-Raphson iteration. Convergence of the Newton-Raphson technique is determined by checking mass and energy balances for each finite-difference block.

The regression equations for fluid densities, viscosities, and temperature that were used in earlier versions of GEOTHER are accurate over the temperature range 10 - 300°C. We replaced these equations with an extended (0 - 1,200°C) lookup table that is interrogated by a bicubic interpolation routine. This method, which is accurate and relatively fast, provides values for density, viscosity, and temperature as well as the gradients of those values with respect to pressure and enthalpy. However, the table is large, containing approximately 4,500 grid points (P-H pairs), and requires about 2 Mbytes of space in binary form. The fluid density and temperature values in the lookup table are from the routines of Haar and others (1984), and the viscosity values are from the formulation by Watson and others (1980), which Sengers and Kamgar-Parsi (1984) re-evaluated using density values of Haar and others (1984). Although we applied the viscosity equation beyond its valid range (≤5 kbar and ≤900°C), we expect that the error introduced by this extrapolation is relatively modest. For the two-phase region, we use cubic splines to describe the saturated-water and saturated-steam curves. These splines provide values for the enthalpy, density, temperature, and viscosity of saturated liquid water and steam as functions of pressure.

Extending GEOTHER beyond the critical point created some problems with the definition of volumetric saturation and the liquid water/steam nomenclature. Above the critical point, the distinction between liquid and steam disappears, and the values assigned to the saturation variables become arbitrary. However, below the critical point, saturation is an important variable, and computational problems can arise in determining the average fluid properties for flow between super- and subcritical blocks. We enforced consistent averaging by treating supercritical blocks as though they contain two phases with identical properties (density, viscosity, saturation, and relative permeability).

## PREVIOUS WORK ON NEAR-CRITICAL FLOW

Norton and Knight (1977) were among the first to suggest that variations in fluid properties near the critical point of water may influence transport in magmatic-hydrothermal systems. They recognized that near-critical maxima in thermal expansivity and heat capacity nearly coincide with a minima in kinematic viscosity, thereby maximizing buoyancy forces and heat-transport capacity while minimizing viscous-drag forces. They further suggested that the near-critical extrema in fluid properties may control the overall style of fluid circulation, while noting that small differential pressure and temperature values would be required to adequately simulate the process, because the greatest variation in fluid properties occurs over a narrow P-T range. Johnson and Norton (1991) presented complete equations of state for pure water in the critical region and reiterated the importance of near-critical fluid properties to flow in hydrothermal systems, but did not simulate flow and transport.

Dunn and Hardee (1981) conducted laboratory experiments on heat-transfer enhancement in the vicinity of the critical point. Their experiments involved a heated platinum wire in the center of a cylindrical vessel filled with water-saturated silica sand. They applied constant current to the wire while maintaining the vessel wall at constant temperature. At pressures slightly above the critical point, they measured the energy required to establish a small temperature difference (~2°C) within the vessel. They suggested that their experimental results indicate near-critical heat-transfer rates as much as 70 times greater than conductive rates at ambient temperatures.

Cox and Pruess (1990), using an extended version of the TOUGH2 simulator, attempted to simulate the Dunn and Hardee (1981) experiments numerically, and found heat-

Table 1. Mass and energy fluxes from one-dimensional simulations in the vicinity of the critical point

| | Permeability ($m^2$) | Mass flux ($g/s/m^2$) | Energy flux ($W/m^2$) |
|---|---|---|---|
| Set 1. | Flow from 240.55 bars, 1886 J/g to 200.55 bars, 1886 J/g | | |
| | $10^{-20}$ | $4.0 \times 10^{-7}$ | $2.0 \times 10^{-2}$ |
| | $10^{-18}$ | $3.5 \times 10^{-5}$ | $8.4 \times 10^{-2}$ |
| | $10^{-16}$ | $3.5 \times 10^{-3}$ | 6.5 |
| | $10^{-14}$ | $3.5 \times 10^{-1}$ | $6.5 \times 10^{2}$ |
| Set 2. | Flow from 240.55 bars, 2086 J/g to 200.55 bars, 2086 J/g | | |
| | $10^{-20}$ | $3.6 \times 10^{-7}$ | $3.1 \times 10^{-2}$ |
| | $10^{-18}$ | $3.3 \times 10^{-5}$ | $9.7 \times 10^{-2}$ |
| | $10^{-16}$ | $3.2 \times 10^{-3}$ | 6.7 |
| | $10^{-14}$ | $3.2 \times 10^{-1}$ | $6.7 \times 10^{2}$ |
| Set 3. | Flow from 240.55 bars, 2286 J/g to 200.55 bars, 2286 J/g | | |
| | $10^{-20}$ | $2.7 \times 10^{-7}$ | $3.5 \times 10^{-2}$ |
| | $10^{-18}$ | $2.8 \times 10^{-5}$ | $1.0 \times 10^{-1}$ |
| | $10^{-16}$ | $2.8 \times 10^{-3}$ | 6.5 |
| | $10^{-14}$ | $2.8 \times 10^{-1}$ | $6.5 \times 10^{2}$ |
| Set 4. | Flow from 230.55 bars, 2086 J/g to 210.55 bars, 1786 J/g | | |
| | $10^{-20}$ | $2.9 \times 10^{-7}$ | $2.6 \times 10^{-2}$ |
| | $10^{-18}$ | $1.7 \times 10^{-5}$ | $5.8 \times 10^{-2}$ |
| | $10^{-16}$ | $1.6 \times 10^{-3}$ | 3.4 |
| | $10^{-14}$ | $1.6 \times 10^{-1}$ | $3.4 \times 10^{2}$ |
| Set 5. | Flow from 240.55 bars, 268 J/g to 200.55 bars, 1486 J/g | | |
| | $10^{-20}$ | $3.0 \times 10^{-7}$ | $1.6 \times 10^{-1}$ |
| | $10^{-18}$ | $2.8 \times 10^{-5}$ | $2.1 \times 10^{-1}$ |
| | $10^{-16}$ | $2.0 \times 10^{-3}$ | 5.4 |
| | $10^{-14}$ | $1.9 \times 10^{-1}$ | $5.2 \times 10^{2}$ |

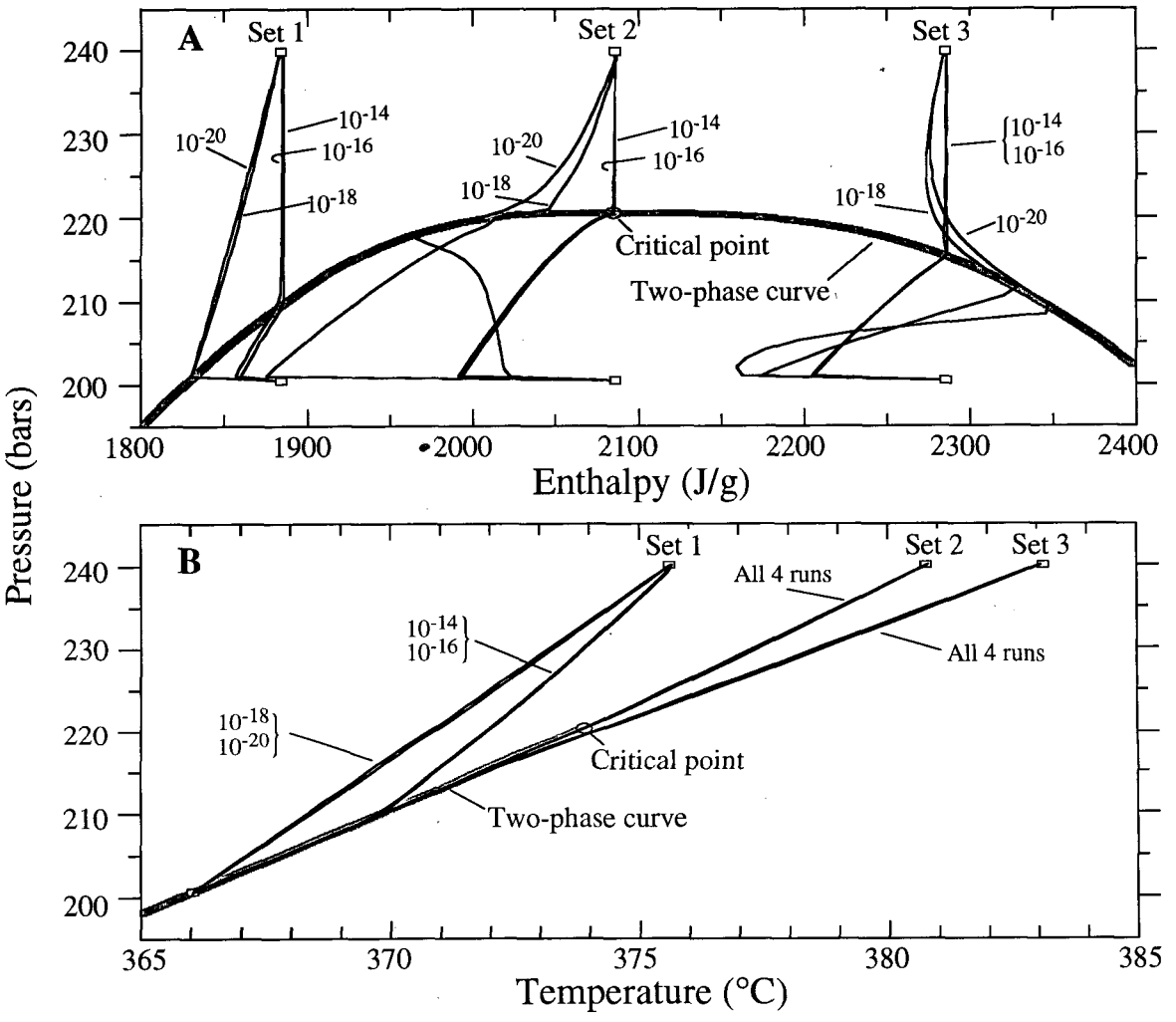


*Figure 2. A, Pressure-enthalpy and B, pressure-temperature trajectories for three sets of one-dimensional experiments in which both endpoints of the column were held at the same enthalpy (see table 1).*

transfer enhancement over a temperature range of about 40°C, whereas the numerical simulations and a Rayleigh Number analysis suggested large enhancements over only a 2-3°C temperature interval. We have not tried to simulate the Dunn and Hardee (1981) experiments, but we do have some preliminary results for a two-dimensional (10 m x 10 m) vertical slab with comparable permeability ($2x10^{-12}$ $m^2$), pressure (221 bars), and temperature difference (2°C). Our simulations show heat transfer enhancements of >100 for a narrow temperature interval bracketing the critical point.

## NEAR-CRITICAL PRESSURE-ENTHALPY PATHS

The numerical results from GEOTHER2 reported here illustrate some of the factors controlling fluid trajectories in the critical region. Our approach was to assign constant pressure and enthalpy values (table 1) at either end of a 1-km-long horizontal column divided into 25-m blocks. We varied the permeability of the column but held thermal conductivity constant at 2 W/m K. Arbitrary initial conditions were assigned to the interior of the column and equations (1) and (2) were solved iteratively until mass and energy fluxes reached a steady state, i.e., until mass and energy entering the high P-H end of the column equated with mass and energy exiting at the low P-H end. These one-dimensional experiments do not allow us to address the issue of enhanced convective heat transfer, but are a useful test case.

Figure 2 shows the results of three sets of experiments in which we assigned the same enthalpy values, but different pressure values, at either end of the column. Thus the endpoints define vertical lines in P-H coordinates. Within each set, differences in permeability cause the flow path to take different trajectories that are much more distinguishable in P-H coordinates (fig. 2A) than in P-T coordinates (fig. 2B). Each set involves a fixed pressure drop of 40 bars, and within each set mass and energy fluxes scale nearly linearly with permeability (table 1). The fluxes associated with the high-permeability ($\geq 10^{-16}$ $m^2$) experiments which pass through the critical point (table 1, set 2) do not appear to be significantly larger than the fluxes obtained in high-permeability experiments which bypass the critical point (table 1, sets 1 and 3). Constant P-H boundaries more tightly focused on the critical point may be needed to define any enhancements in transport.

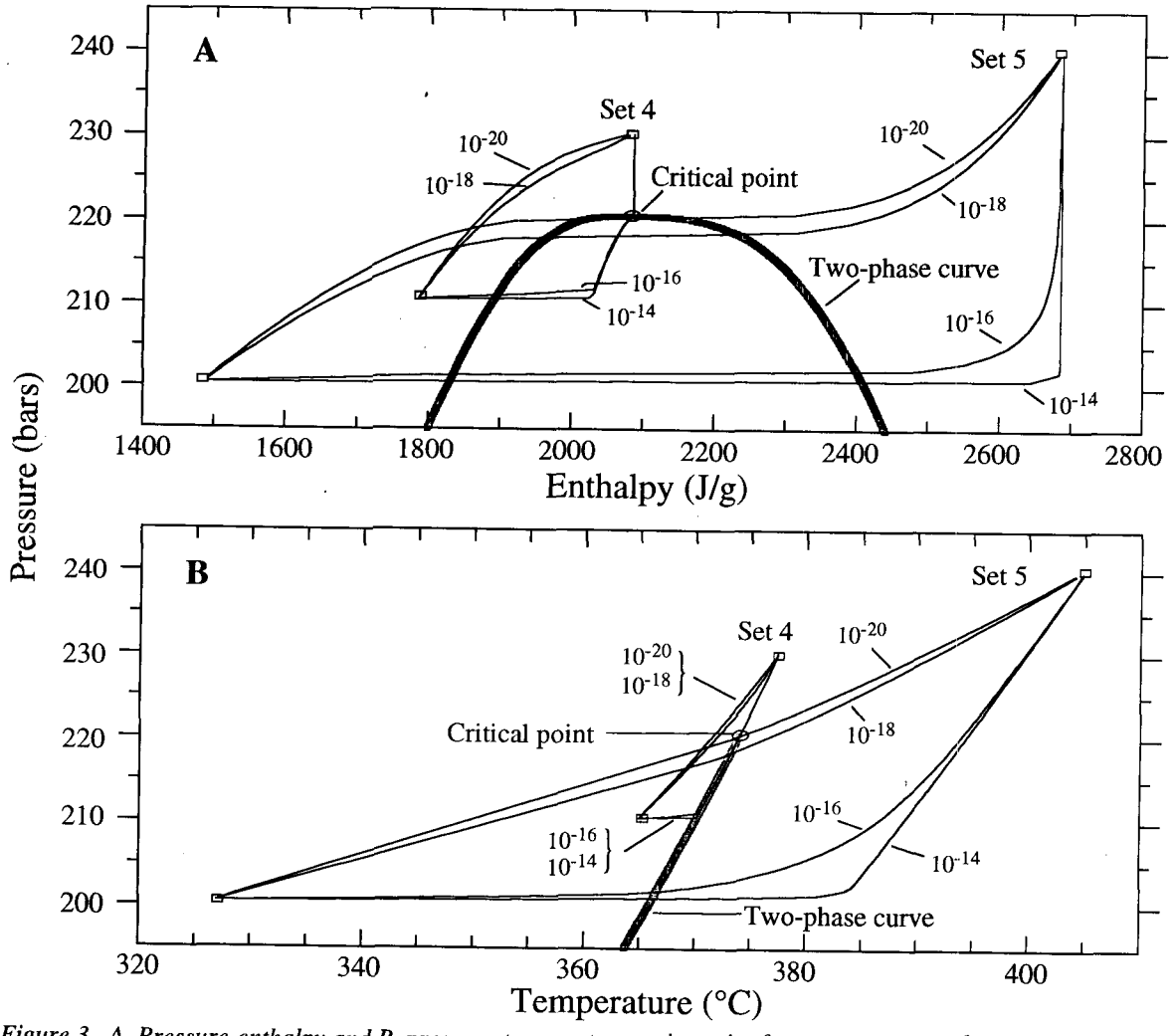


*Figure 3. A, Pressure-enthalpy and B, pressure-temperature trajectories for two sets of one-dimensional experiments in which the endpoints of the column were held at different pressures and enthalpies (see table 1).*

In other sets of experiments, designated sets 4 and 5 (fig. 3), we assigned different values of enthalpy and pressure at either end of the column, so that the end points define diagonals in P-H coordinates. In set 4, the high-permeability experiments intersect the critical point, whereas in set 5 the low-permeability runs do so. These two sets of experiments also highlight the importance of permeability in determining the trajectory of the flow path. Figure 4 shows the temperature gradient along the column for the set 4 experiments, and figure 5 shows the "flowing enthalpy", which is

$$H_{FLOWING} = \left(v_w \rho_w H_w + v_s \rho_s H_s\right) / \left(v_w \rho_w + v_s \rho_s\right) \quad (3)$$

In single-phase regions, flowing enthalpy is identical to the enthalpy of the fluid in place, but in the two-phase region the two enthalpy values are often significantly different.

At low permeabilities ($\leq 10^{-18}$ m$^2$), heat transport by conduction dominates, and the P-H and P-T trajectories (fig. 3) define a constant temperature gradient (fig. 4). At higher permeabilities ($\geq 10^{-16}$ m$^2$) advection dominates, and the cooling trajectories (fig. 3) reflect a nearly constant flowing enthalpy along the flow path (fig. 5). The transition from conduction- to advection-dominated transport seen at permeabilities between $10^{-18}$ m$^2$ and $10^{-16}$ m$^2$ is consistent with Norton and Knight's (1977) estimate. In the high-permeability cases, most of the variation in temperature gradient and flowing enthalpy occurs near the outflow boundary, where the lower enthalpy/temperature specified at that boundary must finally be accommodated. Analytical solutions for steady flow between constant-temperature boundaries (Bredehoeft and Papadopolous, 1965) predict similarly sharp variations for comparable flow rates. These sharp variations in enthalpy near the constant (H, P) outflow boundary disappeared when we reran these experiments with constant-flux outflow boundaries, specifying the mass fluxes determined from the runs with constant value boundaries (table 1). The results with constant-flux outflow boundaries were otherwise identical to the results with the constant (H,P) outflow boundaries.

In single-phase regions, the advection-dominated trajectories are essentially isoenthalpic (figs. 2 and 3). In the two-phase region, the flowing enthalpy is strongly

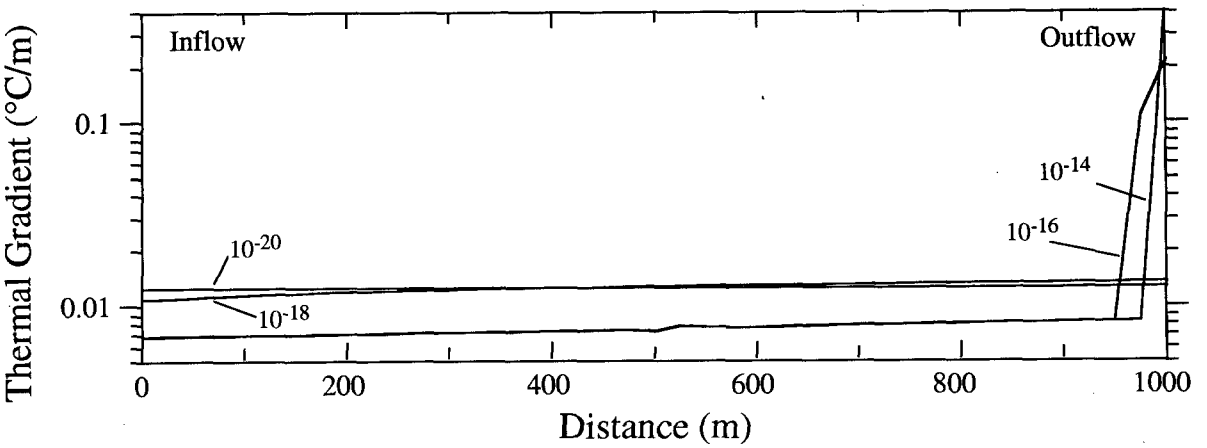


*Figure 4. Results from set 4 experiments, showing relation between temperature gradient and distance along column for selected permeability values. See figure 3 for associated pressure-enthalpy and pressure- temperature trajectories.*

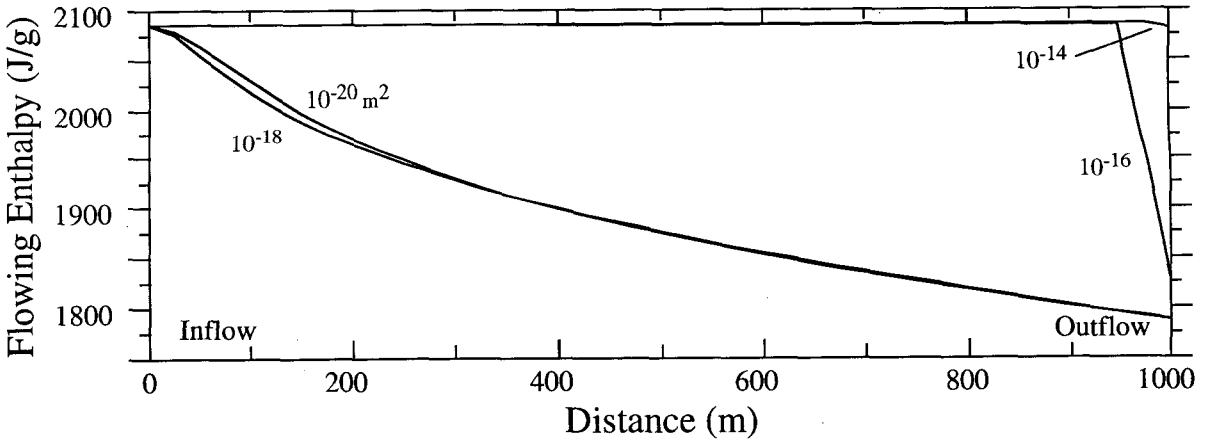


*Figure 5. Results from set 4 experiments, showing relation between flowing enthalpy and distance along column for selected permeability values. See figure 3 for associated pressure-enthalpy and pressure-temperature trajectories, and figure 4 for thermal gradients.*

dependent on the mobilities of the two phases; therefore, the choice of relative permeability functions affects the pressure-enthalpy trajectories. We used simple linear functions with no residual liquid or steam saturation to obtain the results shown here. Because advection-dominated pressure-enthalpy trajectories are dictated by the requirement of maintaining a constant flowing enthalpy, using different relative-permeability functions and/or non-zero residual saturations would change the trajectories of the high-permeability experiments through the two-phase region. In that sense, the particular trajectories shown in Figures 2 and 3 are arbitrary. However, the transition from variable to constant flowing enthalpy over a finite range of flowrates (fig. 5) should occur regardless of the relative-permeability functions used.

Useful extensions of this work might include 1) further sets of one-dimensional experiments that bring the constant pressure-enthalpy boundaries closer to the critical point (within 2°C); 2) simulations of the Dunn and Hardee (1981) experiments, with comparisons to the Cox and Pruess (1990) results; and 3) simulations of free convection within a vertical slab.

## SUMMARY

The geothermal-modeling program GEOTHER2 is capable of simulating both multiphase flow and flow beyond the critical point. Extending the program to supercritical conditions was relatively straightforward because the governing equations are written in terms of pressure and enthalpy, which eliminates singularities at the critical point. Sets of one-dimensional experiments indicate that permeability is an important factor in determining pressure - enthalpy/temperature trajectories: low-permeability trajectories define a constant temperature gradient, whereas high-permeability trajectories maintain a constant flowing enthalpy. Further two-dimensional tests are needed to investigate the influence of the critical point on convective heat transfer and overall fluid-flow patterns.

ACKNOWLEDGMENTS

We would like to thank Cliff Voss, Mike Sorey, James Bischoff and an anonymous reviewer for their thoughtful criticisms. Their comments, especially on our numerical results, greatly improved this manuscript.

NOTATION

$C_v$ = isochloric heat capacity
D = depth
g = gravitational acceleration
H = enthalpy
$\mathbf{k}$ = intrinsic permeability tensor
$K_m$ = medium thermal conductivity-thermal dispersion coefficient
$k_r$ = relative permeability ($0 \leq k_r \leq 1$)
P = pressure
R = mass source/sink flowrate
S = volumetric liquid saturation
T = temperature
t = time
$\phi$ = porosity
$\rho$ = density
$\mu$ = dynamic viscosity
$v$ = Darcian velocity (volumetric flowrate)

Subscripts
r refers to the porous medium (rock)
s refers to steam
w refers to liquid water

REFERENCES CITED

Battistelli, A., Calore, C., and Pruss, K., 1993, A fluid property module for the TOUGH2 simulator for saline brines and non-condensible gas: Eighteenth Stanford Geothermal Workshop, in press.

Bredehoeft, J.D., and Papadopolous, I.S., 1965, Rates of vertical ground water movement estimated from the Earth's thermal profile: Water Resources Research, v. 1, p. 325-328.

Cathles, L.M., 1977, An analysis of the cooling of intrusives by ground-water convection which includes boiling: Economic Geology, v. 72, p. 804-826.

Cox, B.L., and Pruess, Karsten, 1990, Numerical experiments on convective heat transfer in water-saturated porous media at near-critical conditions: Transport in Porous Media, v. 5, p. 299-323.

Dunn, J.C., and Hardee, H.C., 1981, Superconvecting geothermal zones: Journal of Volcanology and Geothermal Research, v. 11, p. 189-201.

Faust, C.R., and Mercer, J.W., 1977, Finite-difference model of two-dimensional, single- and two-phase heat transport in a porous medium-version I: U.S. Geological Survey Open-File Report 77-234, 84 p.

Faust, C.R., and Mercer, J.W., 1979a, Geothermal reservoir simulation 1. Mathematical models for liquid- and vapor- dominated hydrothermal systems: Water Resources Research, v. 15, p. 23-30.

Faust, C.R., and Mercer, J.W., 1979b, Geothermal reservoir simulation 2. Numerical solution techniques for liquid- and vapor-dominated hydrothermal systems: Water Resources Research, v. 15, p. 31-46.

Faust, C.R., and Mercer, J.W., 1982, Finite-difference model of three-dimensional, single- and two-phase heat transport in a porous medium, Scepter documentation and user's manual: Reston, Virginia, Geotrans, Inc., 73 p.

Haar, Lester, Gallagher, J.S., and Kell, G.S., 1984, NBS/NRC steam tables: thermodynamic and transport properties and computer programs for vapor and liquid states of water in SI units: New York, Hemisphere Publishing Corp., 320 p.

Hayba, D.O., 1993, Hydrologic modeling of the Creede epithermal ore-forming system, Colorado: Ph.D. thesis, University of Illinois, 186 p.

Ingebritsen, S.E., 1986, Vapor-dominated zones within hydrothermal convection systems: Evolution and natural state: Ph.D thesis, Stanford University, 179 p.

Johnson, J.W., and Norton, Denis, 1991, Critical phenomena in hydrothermal systems: state, thermodynamic, electrostatic, and transport properties of $H_2O$ in the critical region: American Journal of Science, v. 291, p. 541-648.

Norton, Denis, and Knight, J., 1977, Transport phenomena in hydrothermal systems: cooling plutons: American Journal of Science, v. 277, p. 937-981.

Press, W.H., Flannery, B.P., Teukolsky, S.A., and Vetterling, W.T., 1986, Numerical recipes: the art of scientific computing: New York, Cambridge University Press, 818 p.

Pruess, Karsten, 1991, TOUGH2-A general-purpose numerical simulator for multiphase fluid and heat flow: Lawrence Berkeley Laboratory Report LBL-29400, 102 p.

Roberts, P.J., Lewis, R.W., Carradori, G., and Peano, A., 1987, An extension of the thermodynamic domain of a geothermal reservoir simulator: Transport in Porous Media, v. 2, p. 397-420.

Sengers, J.V., and Kamgar-Parsi, B., 1984, Representative equations for the viscosity of water substance: Journal of Physical and Chemical Reference Data, v. 13, p. 185-205.

Watson, J.T.R., Basu, R.S., and Sengers, J.V., 1980, An improved representative equation for the dynamic viscosity of water substance: Journal of Physical and Chemical Reference Data, v. 9, p. 1,255-1,290.

PROCEEDINGS, Nineteenth Workshop on Geothermal Reservoir Engineering
Stanford University, Stanford, California, January 18-20, 1994
SGP-TR-147

# A MODEL OF LOCAL DISTRIBUTION OF SATURATION IN A FRACTURED LAYER, AND ITS APPLICATION

Yuichi NIIBORI and Tadashi CHIDA

Department of Resource Engineering,
Faculty of Engineering, Tohoku University
Sendai 980, Japan

## ABSTRACT

This paper describes a model of local distribution of liquid water (or steam) saturation in a fractured layer. The model, based on the Bernoulli trials as a probability density function of saturation, gives the following relation between the average value of the relative permeability for the water phase, $k_{rwa}$, and the arithmetical mean of saturation, $S_{wa}$:

$$k_{rwa}=S_{wa}^{m},$$

where $m$ is an index representing the non-uniformity of saturation ($1 \le m \le 4$). When $m=4$, the saturation is distributed uniformly. The proposed model also gives the average value for the relative permeability of the steam phase, $k_{rga}$, as follows:

$$k_{rga}=1-S_{wa}^{m}-2S_{wa}+2S_{wa}^{(2m+1)/3}.$$

These relations are applied to analysis of some experimental data already reported by the authors. Also, this presentation shows the validity of the Bernoulli trials as a density probability function of saturation in comparison with other kinds of such functions: the normal distribution, the triangle distribution and the beta distribution.

## INTRODUCTION

The relative permeability, $k_r$, plays an important role in analyzing two-phase flow through a porous medium, because $k_r$ determines the velocity of each phase, $v_i$, according to $v_i = -k_{ri} k \nabla p / \mu_i$, where $k$ is the absolute permeability (constant in time), $\mu$ is viscosity, $\nabla p$ is gradient of pressure and the subscript $i$ refers to phase of water (w) or steam (g). In general, $k_r$ is expressed by a function of water saturation, $S_w$ (Grant et al.,1982,p289). However, $S_w$ is not always distributed uniformly, even if the space considered in evaluating the value of $S_w$ is a unit of discrete region in the numerical analysis. Because a geothermal reservoir is composed of innumerable cracks. The authors have investigated about relative permeabilities (Niibori & Chida, 1989,1992,1994), for such flow system.

This presentation indicates a model of local distribution of $S_w$, using the Bernoulli trials as a probability density function of $S_w$. The model gives correlation equations between the relative permeabilities and the arithmetical mean of $S_w$ in the local distribution. Validity of the model is investigated through experimental data.

## MODELING SATURATION DISTRIBUTION

In the first place, let us consider a simple problem on local distribution of the saturation. Now assume that the two values of water saturation, $S_{w1}=0$ and $S_{w2}=1$ in the flow path 1 and 2, respectively, in a spatial region. Then, the average relative permeability, $k_{rwa}$, of liquid water phase (here in after, referred as water phase) in the region is calculated as follows:

$$k_{rwa}=(k_{rw1}+k_{rw2})/2=0.5, \quad (1)$$

where $k_{rw1}$ and $k_{rw2}$ are the relative permeabilities of the path 1 and 2, respectively. On the other hand, we have the following Corey's equation:

$$k_{rw}=S_w^4. \quad (2)$$

As the arithmetical mean of the path 1 and 2 is

$$S_{wa}=(S_{w1}+S_{w2})/2=0.5, \quad (3)$$

it is also possible to calculate the relative permeability, $k_{rw}$, by substituting $S_{wa}$ to Equation (2):

$$k_{rw}=0.5^4=0.0625. \quad (4)$$

Consequently, we have the two kinds of relative permeabilities, $k_{rwa}$ and $k_{rw}$, which are different from each other. This discrepancy suggests that the relation between relative permeabilities and saturation depends not only on the average of saturation but also its distribution, apparently.

To estimate the relative permeabilities considered local distribution of saturation, the saturation is assumed to be described by a suitable probability density function, $F(S_w)$, as shown in Figure 1. In general, we can assume that in a spatial region of several cm, as shown in Fig.1 (1), (2) and (3), Darcy's law and the concept of relative permeability (also, saturation) are established. On the contrary, in

a unit (e.g., Δx) of discrete region, whose size is about *10*m through *1*km in the numerical analysis, $S_w$ is not always distributed uniformly.

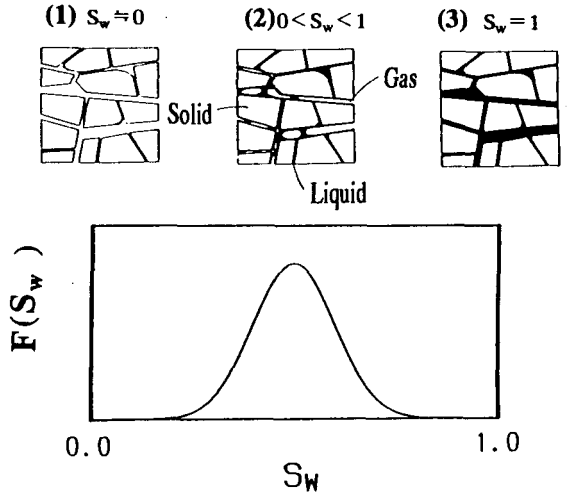


Figure 1 Illustration of Local Distribution of saturation.

Using such a probability density function, $F(S_w)$, Niibori & Chida (1989) defined the average, relative permeabilities, $k_{rwa}$ and $k_{rga}$, respectively, as follows:

$$k_{rwa} = \frac{\int_0^1 F(S_w) k_{rw} dS_w}{\int_0^1 F(S_w) dS_w} , \qquad (5)$$

$$k_{rga} = \frac{\int_0^1 F(S_w) k_{rg} dS_w}{\int_0^1 F(S_w) dS_w} . \qquad (6)$$

(here in after, $k_{rwa}$ and $k_{rga}$ are referred as the apparent relative permeability). Then the arithmetical mean of saturation is

$$S_{wa} = \frac{\int_0^1 F(S_w) S_w dS_w}{\int_0^1 F(S_w) dS_w} . \qquad (7)$$

As for $k_{rw}$ and $k_{rg}$ (not $k_{rwa}$ and $k_{rga}$), we use the empirical equations, Eq.(2) and the following equation, which have been widely used in geothermal reservoir analyses by; for example, Faust & Mercer (1979), Zyvoloski et al. (1980), Sorey et al. (1980), Pruess et al. (1983), O'Sullivan et al. (1985), Gudmundsson et al. (1986) and Niibori et al. (1987):

$$k_{rg} = (1 - S_w)^2 (1 - S_w^2), \qquad (8)$$

where $S_w$ is the normalized saturation (Aziz & Settari,1979,p.33) considering the residual saturations of water and gas phases in the strict sense.

Niibori & Chida (1992) investigated relationships between $k_{rg}$ and $S_{wa}$, assuming some kinds of probability density function of saturation, the Beta distribution, the triangle distribution, the normal distribution and the Bernoulli trials, because it is impossible to determine the probability density function a prior. The results suggest that the average relative permeabilities depend not on kind of such function, but on the arithmetical mean, the standard deviation, σ, and the skewness $\mu_3/\sigma^3$ of saturation as follows:

$$\sigma^2 = \frac{\int_0^1 F(S_w)(S_w - S_{wa})^2 dS_w}{\int_0^1 F(S_w) dS_w} , \qquad (9)$$

$$\mu_3 = \frac{\int_0^1 F(S_w)(S_w - S_{wa})^3 dS_w}{\int_0^1 F(S_w) dS_w} . \qquad (10)$$

For example, the apparent relative permeabilities based on the Beta distribution agree quit well with those on the Bernoulli trials, when the values of $S_{wa}$, σ and $\mu_3/\sigma^3$ each coincide with those of the Beta distribution. Such tendency is appeared, even if the probability function is described by any type function (the Beta distribution, the Normal distribution, the triangle distribution, and the Bernoulli trials).

Figure 2(a) displays the regions of $k_{rwa}$ and $k_{rga}$, given by the Beta distribution (with one peak), also comparing the experimental data already reported by Wyckoff & Botset (1936). In the same way, Figure 2(b) shows the regions given by the Bernoulli trials (representing a probability density function with two peaks). These figures suggest that some experimental data are accompanied with the saturation distribution with relatively small value of the standard deviation, because its maximum value for the Beta distribution is smaller than that for the Bernoulli trials under the condition of $0 \le S_w \le 1$.

The Bernoulli trials are composed of $S_{w1}$, $S_{w2}$ ($0 \le S_{w1} \le S_{w2} \le 1$) and $f$ (which is ratio of $S_{w2}$, thus the ratio of $S_{w1}$ is $1-f$), as shown in Figure 3. To derive correlation equations between $k_{rg}$ and $S_{wa}$ for the water- and the gas-phase, respectively, we assume such a distribution as Figure 4. This figure shows an illustration of the saturation distribution on the radial direction, considering the heat exchange surface locally in a fractured layer. In such a case, we assume the smaller saturation $S_{w1}$ to be zero, that is:

$$S_{w1} = 0, \qquad (11)$$

because the region, close to the heat exchange surface, is occupied with the steam-phase. On the other hand, when $S_{w2}$ is described as follows:

$$S_{w2} = S_{wa}^{(m-1)/3}, \qquad (12)$$

the model of local distribution of saturation gives

$$k_{rwa} = S_{wa}^{m}, \qquad (13)$$

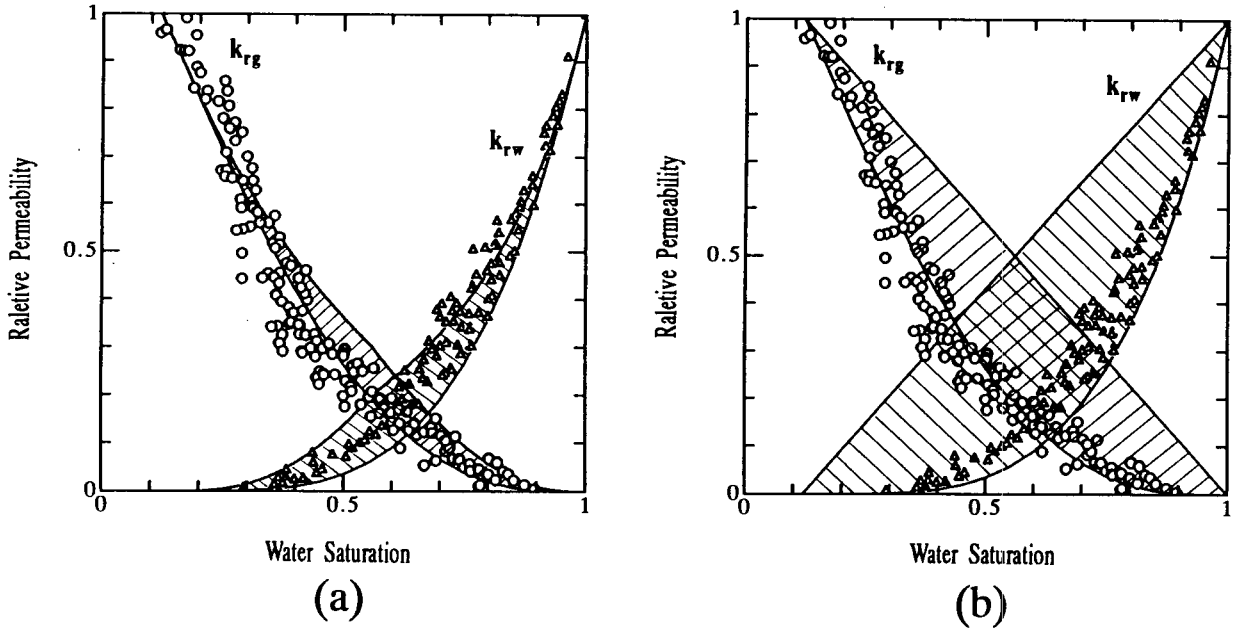


Figure 2 Application of the apparent relative permeability, based on (a)the Beta distribution and on (b) the Bernoulli trials, to the experimental data.

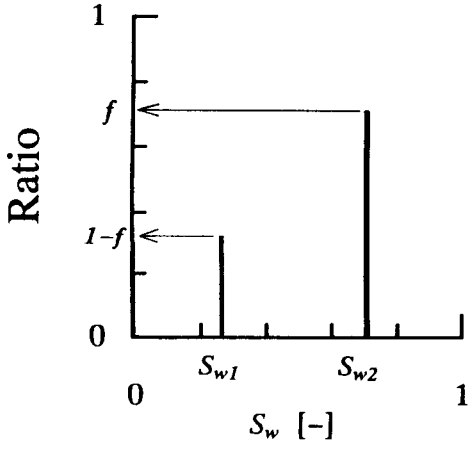


Figure 3 Illustration of the Bernoulli trials.

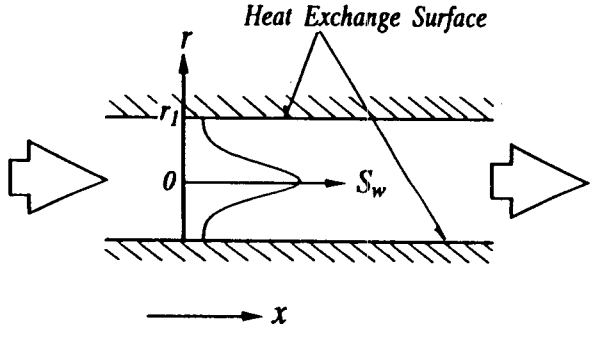


Figure 4 Modeling saturation distribution.

where $S_{wa}$ is the arithmetical mean of the water saturation. Then, the value of $f$ is described by

$$f = S_{wa}^{(4-m)/3}. \quad (14)$$

$m$ is an index representing the non-uniformity of saturation ($1 \leq m \leq 4$). When $m=4$, the saturation is distributed uniformly. The proposed model also gives the average value for the relative permeability of the steam phase, $k_{rga}$, as follows:

$$k_{rga} = 1 - S_{wa}^{\ m} - 2S_{wa} + 2S_{wa}^{(2m+1)/3}. \quad (15)$$

Figure 5 shows the relation between $S_{wa}$ and $k_{ra}$ for each $m$ (Fig.5(a) is for the water-phase, and Fig.5(b) is for the steam-phase.) From Figs.5(a) and (b), we can recognize that Eqs.(13) and (15), respectively, describe conveniently the regions of $k_{ra}$ indicated by Fig.2(b) for water- and steam-phase.

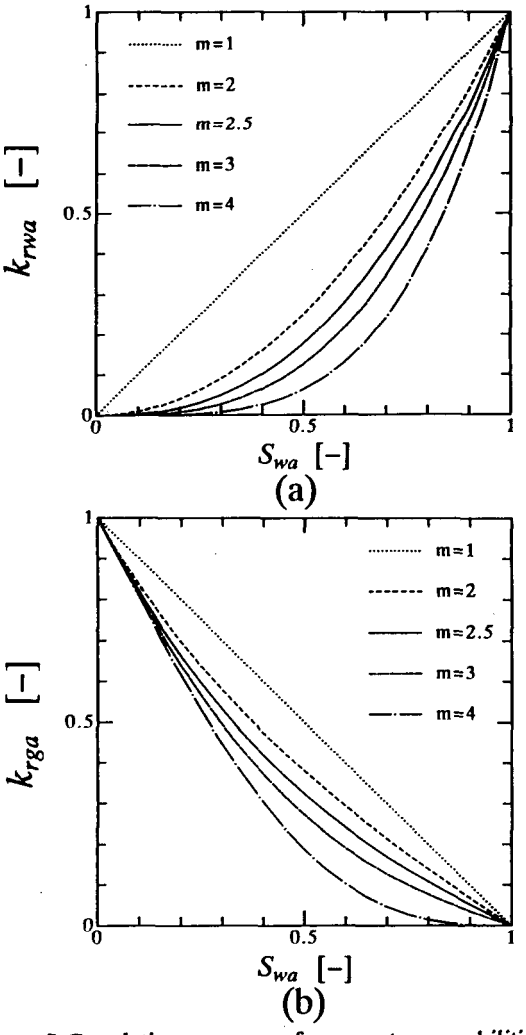


Figure 5 Correlation curves of apparent permeabilities to the arithmetical mean of saturation for (a) water-phase and (b) steam-phase.

## APPLICATION

### Experiments

The experiments are carried out by using a packed glass beads bed submerged horizontally in a thermostat at a temperature of more than 373K (Niibori et al., 1992). Figure 6 shows a schematic diagram of an experimental apparatus. Hydrostatic heads at the inlet and the outlet are fixed by overflows, respectively. Water is injected continuously into the bed under a constant pressure gradient and is heated from the surrounding, and part of the water vaporizes in the bed. When the temperature and the flow rates of steam and hot water attain to the steady state, $0.5 cm^3$ of ammonia water solution (about five volume percent of $NH_3$) is injected into the bed as a tracer. The tracer vaporizes in the bed, and ammonia gas flows out of the bed with steam. Then, the $NH_3$ content in the exit gas is measured by a gas chromatography every few minutes to evaluate the tracer response. Temperature in the bed is measured by thermocouples and an AD converter. Flow rates of water and steam at the outlet are also measured by a separator, a cooler and two electric balances. These data are stored to a magnetic disc through a personal computer every 15 seconds. Table 1 summarizes the experimental conditions.

Table 1 Experimental conditions

| | |
|---|---|
| *length of the packed bed* | *145mm, 290mm* |
| *Inner diameter of the bed* | *19mm* |
| *Average diameter of glass beads* | *0.3mm* |
| *Average porosity* | *0.36* [-] |
| *Temperature of thermostat* | *373K to 386K* |
| *Hydrostatic head difference* | *0.1mH2O, 0.2mH2O* |

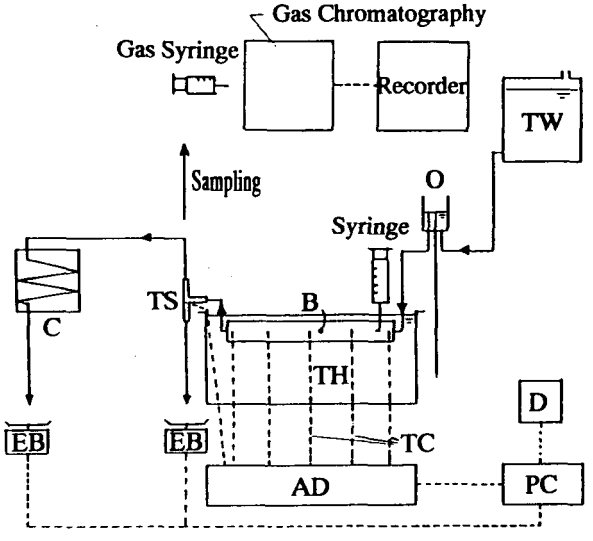


Figure 6 Schematic diagram of experimental apparatus. (C:cooler, B:packed bed, TW:water tank, TS:three-way tube, TH:thermostat, O:overflow, EB:electric balance, AD:A/D converter, D:disk unit, TC:thermocouples, PC:personal computer.)

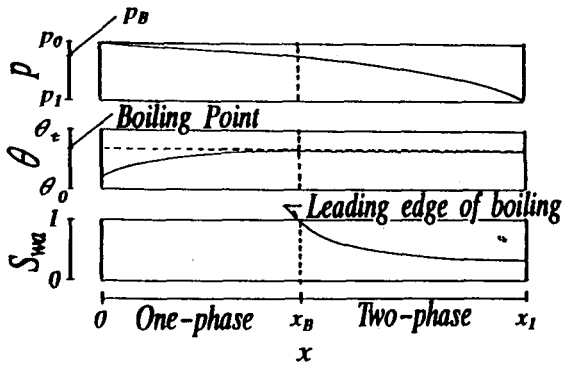


Figure 7 Illustration of numerical model.

## Numerical Model

Figure 7 shows an illustration of the mathematical model. In this figure, $x_B$ indicates the leading edge of boiling (that is, the position at which water phase starts to boil) in the water-steam flow system. Under the constant pressure gradient $(p_0-p_B)/x_B$, water in temperature of $\theta_0$ is injected into the bed submerged in the thermostat at a temperature $\theta_t$. When the water starts to boil at $x=x_B$ in the bed, the temperature of the steady state increases gradually in the region of $[0, x_B]$, and becomes the constant boiling point in $[x_B, x_1]$. Then, water saturation is equal to unity by the leading edge of boiling $x_B$. In the region of $[x_B, x_1]$, the saturation and the pressure are calculated by the following equations (Niibori et al.,1987, Niibori & Chida,1991):

$$\frac{\partial}{\partial X}\{(k_{rwa}+Mk_{rga})\frac{\partial P}{\partial X}\}=-G(\gamma-1)\ , \quad (16)$$

$$0=\frac{\partial}{\partial X}(k_{rwa}\frac{\partial P}{\partial X})\ , \quad (17)$$

where dimensionless variables, $X$, $G$, $\gamma$, $M$ and $P$ are defined as follows:

$$X=x/x_1,\ G=\{aU(\theta_t-\theta_f)x_1\}/(L_v\rho_w v_w^*),$$
$$M=\mu_w/\mu_g,\ \gamma=\rho_w/\rho_g,$$
$$P=\{k(p-p_1)\}/(\mu_w v_w^* x_1).$$

All symbols used in this paper are listed as nomenclature at the end. This paper applies the correlation equation of the apparent permeability, Eqs.(13) and (15) to Eqs.(16) and (17).

The boundary conditions are described by

$$P=1,\ S_{wa}=1,\ \ at\ X=0\ , \quad (18)$$

$$P=0,\ \frac{\partial S_{wa}}{\partial X}=0,\ \ at\ X=1\ . \quad (19)$$

In regard to the mass transfer, let us assume that:
(a)the tracer is injected into the water phase at the inlet;
(b)the tracer vaporizes into the steam phase by boiling;
(c)the mixing diffusion of the steam phase is ignored;
(d)the density and the viscosity of each phase, and the mixing diffusivity and the latent heat of the water phase are constant.
These assumptions give the following equations (Niibori et al.,1992):

$$(1-S_{wa})\frac{\partial C_g}{\partial T}=-\frac{\partial(V_gC_g)}{\partial X}+D_aC_w\ , \quad (20)$$

$$S_{wa}\frac{\partial C_w}{\partial T}=-\frac{\partial(V_wC_w)}{\partial X}+\frac{1}{P_e}\frac{\partial}{\partial X}S_{wa}\frac{\partial C_w}{\partial X}-D_aC_w\ . \quad (21)$$

Dimensionless variables used above are defined as follows:

$$C_w=c_w/c_w^*,\ C_g=y\rho/c_w^*,\ P_e=v_w^*x_1/E,$$
$$T=t/t^*,\ t^*=(x_1-x_B)\varepsilon/v_w^*,\ V_w=v_w/v_w^*,$$
$$V_g=v_g/v_w^*,\ D_a=K_{GT}t^*/\varepsilon,$$
$$X=(x-x_B)/(x_1-x_B),\ X_{IN}=-x_B/(x_1-x_B).$$

where $c_w^*$ is the concentration of the tracer at the inlet of the bed, $y$ is the fraction of the tracer in the gas phase, and $K_{TG}$ is the over-all mass transfer coefficient(Bird et al.,1960,p.654).

The boundary conditions are

$$V_wC_{w-}=V_wC_{w+}-\frac{1}{P_e}\frac{\partial C_w}{\partial X}\ ,\ at\ X=X_{IN}\ , \quad (22)$$

$$\frac{\partial C_w}{\partial X}=0,\ \frac{\partial C_g}{\partial X}=0\ ,\ at\ X=1\ , \quad (23)$$

where $C_{w-}$ is the tracer concentration at

$$X=\lim_{\delta\to 0}(X_{IN}-\delta)=X_{IN-}\ ,$$

and $C_{w+}$ is at

$$X=\lim_{\delta\to 0}(X_{IN}+\delta)=X_{IN+}\ ,$$

Eq.(22) is derived from the, so-called, closed vessel

assumption, which is available in a system which has larger back-mixing magnitude than that of the surrounding (Levenspiel, 1972, p.276).

The initial condition and the tracer injection are described by

$$T=0,\ C_w=0,\ C_g=0,\ in\ X_{IN}\leq X\leq 1, \tag{24}$$

$$0\leq T\leq T_{in},\ C_{w-}=1,\ at\ X=X_{IN}, \tag{25}$$

$$T<0,\ T_{in}<T,\ C_{w-}=0,\ at\ X=X_{IN}. \tag{26}$$

where $T_{in}$ is the injection time of tracer.

Comparisons with the experimental data

$m$, $x_B$, $G$, $D_a$ and $P_e$ are unknown parameters in the numerical model mentioned above. Of them, $m$ and $x_B$ are determined from the flow rate into the bed and the temperature data in the bed, respectively. The other parameters $G$, $D_a$ *and* $P_e$ are estimated as follows:

(a)The value $G$ is calculated from the steam flow rate $Q_g$ in the steady state, because the relationship between $G$ and $Q_g$ is expressed by

$$G=Q_g/Q_w^*, \tag{27}$$

(Niibori & Chida, 1992), where $Q_w^*$ is the characteristic flow rate, defined as follows:

$$Q_w^*=\pi r_{IN}^2 \rho_w v_w^*, \tag{28}$$

where $r_{IN}$ is the inner diameter of the bed, and $v_w^*$ is velocity of water phase, when the saturation is unity.

(b)The physical meaning of $D_a$ is the rate constant to describe the mass transfer of tracer from the water phase to the steam phase. The transfer rate is fast enough as compared with the rate through water or steam phase. Thus, the value can be basically assumed to be infinity in this paper. However, in the numerical analysis of the mathematical model, we must set $D_a$ large enough. Figure 8(a) shows the sensitivity of $D_a$ on the tracer response, where $W_{IN}$ is the dimensionless total amount of tracer, $C_g$ is the dimensionless concentration (the gas content in the steam phase) at the outlet, and $T$ is the dimensionless time. The sensitivity decreases, as the value of $D_a$ larger. When the $D_a$ is greater than *5*, the response does not depend on $D_a$. From these calculations, the value is assumed to be *10* in the numerical analysis. For reference, Figure 8(b) shows the time-change of $C_w$ at the outlet in the same way as Fig.8(a). Fig.8(b) denotes that the injected tracer almost moves from the water-phase to the steam phase in the bed for case of $D_a$ larger than *5*.

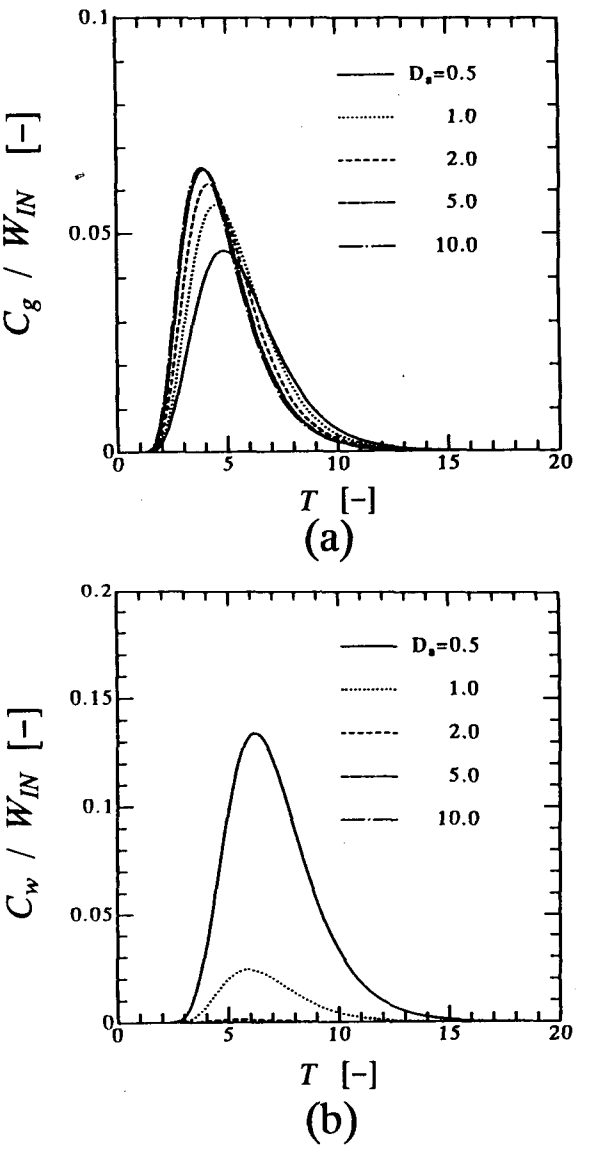


Figure 8 Sensitivity of the dimensionless, over-all mass transfer coefficient on (a)$C_g$ and (b)$C_w$ at the outlet.
*( $G = 2.5 \times 10^{-3}$, $P_e = 60$, $X_{IN} = -0.5$, $m = 4$ )*

(c)This paper determines the value of $P_e$ form the tracer response in a single-phase flow system of the bed. Figure 9 denotes the tracer responses without boiling of water. The experiment (Run No.C1) is carried out in room temperature, by using the same bed. The tracer is $2cm^3$ of KCl solution (about $7.5mol/m^3$), whose concentration at the outlet is estimated by the electronic conductivity. In Fig.9, the experiment data agree quite well with the calculation of $P_e$=*60*.

As mentioned above, all values of the parameters are evaluated in advance. Figure 10 indicates between $G$ and $m$, evaluated from the flow rate into the bed in the steady state. From this figure, we can recognize that the value of $m$ decreases from *4* to about *3*, as the value of $G$ increases.

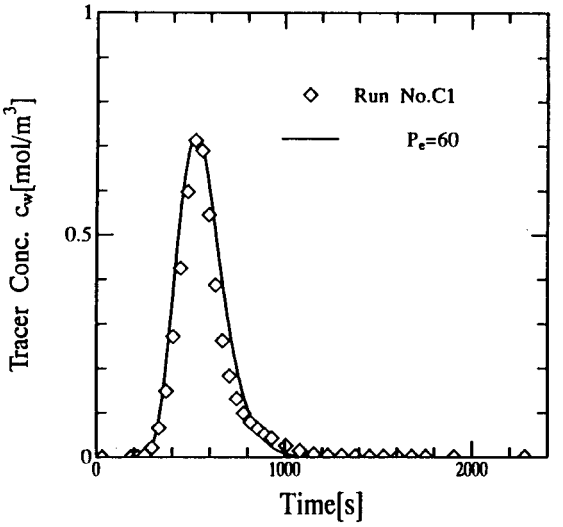


Figure 9 Evaluation of $P_e$.

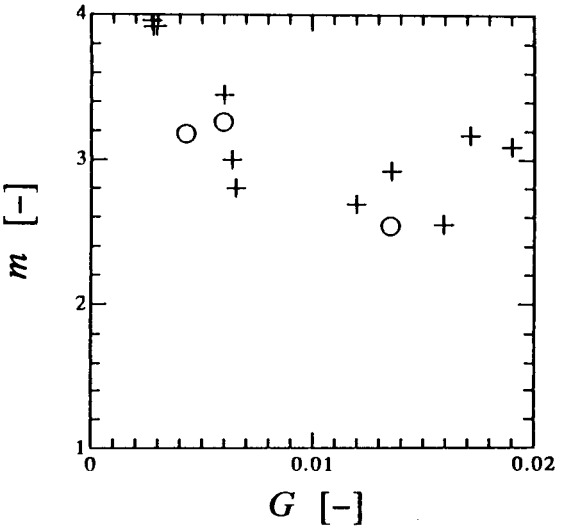


Figure 10 Relation between the dimensionless heat flow into the bed $G$ and the value of $m$ estimating the local distribution of saturation. (symbols o:290mm, +:145mm in length of the packed bed.)

Figure 11 shows an example of comparing the calculated results with the experiment data of tracer response. These data (Run No.31–33) are conducted at $m=3$ in Fig.10 ( $G = 6 \times 10^{-3}$ ). The calculated value for $m=3$ agrees well with the data. The fact confirm the validity of our model. If we refer to the calculated tracer responses for $m=2$, $m=3$, and $m=4$, it is clear that the mass transfer depends strongly on local distribution of $S_w$ in the bed. In the same way, Figure 12 shows the data (Run No.21–24) conducted at $m=4$ in Fig.10 ( $G = 3 \times 10^{-3}$ ). The calculated values for $m=4$ coincide with the data as well.

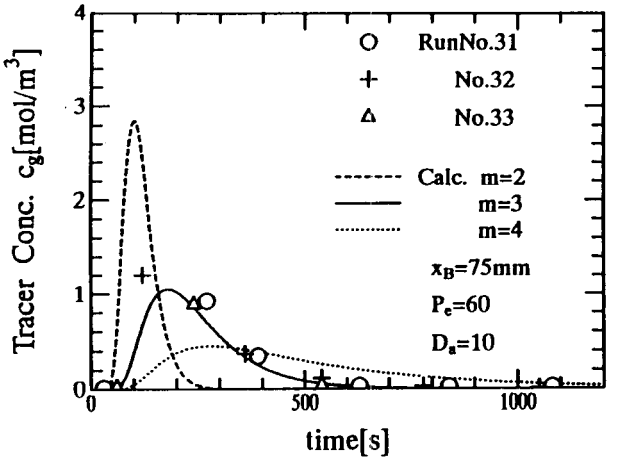


Figure 11 Comparisons of the calculated values with the experimental data conducted at m=3.

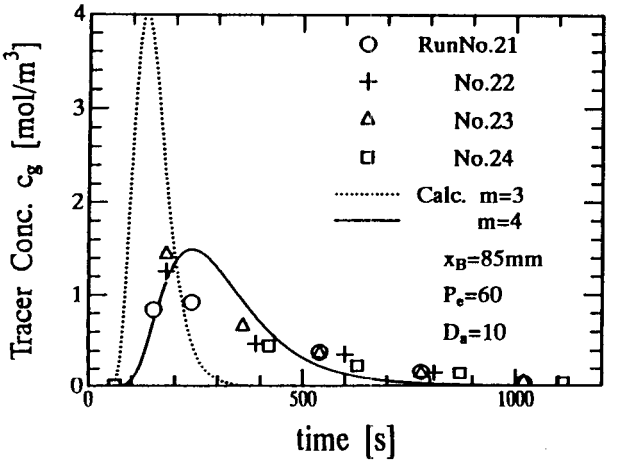


Figure 12 Comparisons of the calculated values with the experimental data conducted at m=4.

## CONCLUSION

We discussed a model of local distribution of saturation in a fractured layer, whose detail structure is not detected. The model, based on the Bernoulli trials as a probability density function of saturation, gives correlation equations of the apparent relative permeabilities to the arithmetical mean of saturation. The equations agrees quit well with the experimental results of mass transfer in water-steam flow with boiling in a permeable medium.

## NOMENCLATURE

$a$ : specific surface area [1/m]
$c$ : concentration of tracer [mol/m$^3$]
$c^*$ : concentration of tracer injected at inlet[mol/m$^3$]
$E^w$ : mixing diffusivity [m$^2$/s]
$k$ : permeability [m$^2$]
$K_{TG}$ : over-all mass transfer coefficient [s]
$k_r$ : relative permeability [-]
$k_{ra}$ : apparent relative permeability [-]
$L_v$ : latent heat [J/kg]
$p$ : pressure [Pa]
$Q$ : flow rate [kg/s]
$r_{IN}$ : inner diameter of the bed [m]
$S$ : saturation,ratio in volume [-]
$t$ : time [s]
$t^*$ : space time [s]
$U$ : over-all heat transfer coefficient [W/m$^2$ K]
$v$ : velocity [m/s]
$v_w^*$ : velocity of water phase, when the saturation is unity [m/s]
$W_{IN}$ : total amount of tracer [-]
$x$ : coordinate in flow direction [m]
$x_B$: leading edge of boiling (position at which water phase starts to vaporize in the bed [m]
$y$ : fraction of tracer gas [-]
$\theta$ : temperature [K]
$\mu$ : viscosity [Pa s]
$\rho$ : density [kg/m$^3$]
$\sigma$ : standard deviation [-]

Subscript
a : arithmetical mean
f : fluid
g : steam
t : thermostat
w : water
0 : inlet
1 : outlet

## REFERENCES


Aziz,K., and A.Settari (1979) *Petroleum Reservoir Simulation*, APPLIED SCIENCE PUBLISHERS LTD, London.

Bird,R.B., W.E.Stewart and E.N. Lightfoot (1960) *Transport Phenomena*, JOHN WILEY & SONS, Inc., New York.

Faust,C.R.and J.W.Mercer (1979) Geothermal Reservoir Simulation 2 :Numerical Solution Techniques for Liquid and Vapor-Dominated Hydrothermal Systems-, Water Resources Res.,15,31-46.

Grant,M., I.G.Donaldson, and P.F.Bixley (1982) *Geothermal Reservoir Engineering*, ACADEMIC PRESS, New York.

Gudmundsson,J.S.,A.J.Menzies and R.N.Horne (1986) Steamtube Relative Permeability Functions for Flashing Steam/Water Flow in Fractures, SPE Reservoir Eng., July, 1986, 371-377.

Levenspiel,O.(1972) Chemical Reaction Engineering, Second Edition, JOHN WILEY & SONS, Inc., New York.

Niibori,Y.,Y.Ogiwara and T.Chida (1987) Effects of Phase-Change on Water-Steam Flow through a Porous Medium, J. Geothermal Res. Soc. Jpn, 9(4), 271-284.

Niibori,Y, and T.Chida(1989) Estimations of Apparent Relative Permeabilities Considered Distribution of Saturation, J. Geothermal Res. Soc. Jpn,11(4), 251-268.

Niibori,Y. and T.Chida (1991) Effects of Heat Transfer on Water-Steam Flow Accompanied by Boiling in a Porous Medium, J.Geothermal Res. Soc. Jpn., 13(3), 157-166.

Niibori,Y. and T.Chida (1992) A Consideration on the correlation equation between average saturation and relative permeabilities, J. Geothermal Res. Soc. Jpn., 14(4), 323-339 (in Japanese).

Niibori,Y., A.Kounosu, and T.Chida (1992) Fundamental Study on Tracer Response Analysis for Water-Steam Flow Accompanied by Boiling in a Porous Medium, J.Geothermal Res., Soc., Jpn., 14(2), 129-144.

Niibori,Y. and T.Chida (1994) Estimation Equations of Relative Permeabilities Considered Saturation Distribution, J. Geothermal Res., Soc., Jpn., to be submitted (in Japanese).

O'Sullivan,M.J., G.S.Bodvarsson, K.Pruess and M.R.Blakeley (1985) Fluid and Heat Flow in Gas-Rich Geothermal Reservoir, Soc. Pet. Eng., J.,25, 215-226.

Pruess,K.(1983) Heat Transfer in Fractured Geothermal Reservoirs with Boiling, Water Resources Res.,19,201-208.

Sorey,M.L.,M.A.Grant and E.Braford (1980) Nonlinear Effects in Two-Phase Flow to Well in Geothermal Reservoir, Water Resour. Res., 16, 767-777.

Wyckoff,R.D. and H.G.Botset (1936) The Flow of Gas-Liquid Mixture through Unconsolidated Sands, Physics, 7, 325-345.

Zyvoloski, G.A. and M.J.O'Sullivan(1980) Simulation of a Gas-Dominated, Two-Phase Geothermal Reservoir, SPEJ,20, 52-58.

PROCEEDINGS, Nineteenth Workshop on Geothermal Reservoir Engineering
Stanford University, Stanford, California, January 18-20, 1994
SGP-TR-147

# Large-Scale Three-Dimensional Geothermal Reservoir Simulation on PCs

Emilio Antúnez, George Moridis, and Karsten Pruess

Earth Sciences Division, Lawrence Berkeley Laboratory
University of California, Berkeley, CA 94720

## ABSTRACT

TOUGH2, Lawrence Berkeley Laboratory's general purpose simulator for mass and heat flow and transport was enhanced with the addition of a set of preconditioned conjugate gradient solvers and ported to a PC. The code was applied to a number of large 3-D geothermal reservoir problems with up to 10,000 grid blocks. Four test problems were investigated. The first two involved a single-phase liquid system, and a two-phase system with regular Cartesian grids. The last two involved a two-phase field problem with irregular gridding with production from and injection into a single porosity reservoir, and a fractured reservoir.

The code modifications to TOUGH2 and its setup in the PC environment are described. Algorithms suitable for solving large matrices that are generally non-symmetric and non-positive definite are reviewed. Computational work per time step and CPU time requirements are reported as function of problem size.

The excessive execution time and storage requirements of the direct solver in TOUGH2 limits the size of manageable 3-D reservoir problems to a few hundred grid blocks. The conjugate gradient solvers significantly reduced the execution time and storage requirements making possible the execution of considerably larger problems (10,000+ grid blocks). It is concluded that the current PCs provide an economical platform for running large-scale geothermal field simulations that just a few years ago could only be executed on mainframe computers.

## INTRODUCTION

The introduction of computers have allowed practicing engineers and scientists to go beyond oversimplified analytical solutions (that certainly have their merits) to approximated semi-analytical or fully numerical solution of large and complex problems. Nevertheless, programmers and modelers very often find themselves saturating the capabilities of their hardware, demanding more memory, storage and processing speed. At the same time, software developers are continuously trying to exploit the capabilities of the current hardware, writing more efficient computer codes.

Prior to the mid '80s, the cost of more powerful machines used to grow exponentially as more memory, storage and processing speed were required. Fortunately, that trend has eased up as computer components started being mass-produced (lowering production cost) to satisfy the strongly emerging workstation and personal computer (PC) market. As workstations and PCs became more capable, it became more difficult to draw the line between them.

In geothermal engineering, computers have facilitated the analysis of processes that range from the simple movement of fluids through porous media (in which mass and energy balances have to be simultaneously accounted for) to the more complex problems in which heat pipes, non-condensable gases, salinity and chemical processes have to be included in the analysis.

Considering that current PCs have the same or more computational power than mainframes and minicomputers of a few years ago, it is not surprising that software that was developed for mainframes and minicomputers had started migrating towards the more cost-effective PC platforms. This has been the case with Lawrence Berkeley Laboratory's general purpose reservoir simulator TOUGH2 [Pruess, 1991].

TOUGH2 is a numerical simulation program for non-isothermal flows of multicomponent, multiphase fluids in porous and fracture media. This code has been widely applied in geothermal reservoir engineering, nuclear waste disposal, environmental restoration, and unsaturated groundwater hydrology.

TOUGH2 with its standard direct matrix solver and a package of three different preconditioned conjugate gradient (CG) solvers[1], were ported to a 486-66 MHz PC. These memory efficient and fast CG algorithms are analyzed and compared with the direct matrix solution.

## SOLVERS PACKAGE

VCG, a package of preconditioned conjugate gradient solvers, has been added to TOUGH2 to

[1] Conjugate Gradient solvers are algorithms for the iterative solution of large sets of linear equations.

complement its direct solver and significantly increase the size of problems tractable on personal computers. This package significantly decreases the execution time and memory requirements, and thus makes possible the simulation of much larger (in terms of number of equations) systems.

VCG was derived from the Sparse Linear Algebra Package (SLAP) Version 2.0 [Seager, 1988] developed for the solution of large sparse linear $N \times N$ systems

$$\mathbf{A} \cdot \mathbf{x} = \mathbf{b}$$

where $N$ is the order of the **A** matrix. SLAP is a collection of various conjugate gradient solvers, with two matrix preconditioning options: diagonal scaling (DS) and modified incomplete LU factorization (ILU).

In TOUGH2 the matrix **A** is a Jacobian with certain consistent characteristics. In systems with regular geometry, **A** has a known block structure with well defined sparsity patterns. In general, **A** matrices arising from TOUGH2 simulations (and geothermal reservoir engineering problems in particular) are non-symmetric with weak (or no) diagonal dominance. Although **A** can be positive definite in regular systems with homogeneous property distributions, in realistic heterogeneous large-scale simulations it usually is not, and ill-conditioning is expected . **A** being a Jacobian, its elements in a single row often vary by several orders of magnitude.

In TOUGH2 simulations of flow and transport through fractured media, the implementation of the "multiple interactive continua" (MINC) concept [Pruess, 1983] results in a large number of zeroes on the main diagonal of **A**, making pivoting impossible and resulting in very ill-conditioned matrices. It is evident that TOUGH2 simulations create matrices which are among the most challenging, with all the features that cause most iterative techniques to fail. This explains the heavy reliance of TOUGH2 on direct solvers in the past.

Extensive testing of the SLAP package in a variety of flow and transport problems identified the most promising conjugate gradient methods. The properties of the **A** matrix essentially precluded the use of DS preconditioning, a fact which was confirmed in the process of testing SLAP. Without exception, ILU preconditioning was far more effective and often the only possible option. Of the 15 methods available in SLAP, three were identified as the ones with the most potential. In terms of increasing robustness, these were the Bi-Conjugate Gradient (BCG) method, the Lanczos-type Bi-Conjugate Gradient Squared (BCGS) method, and the Generalized Minimum Residual (GMRES) method. In terms of the SLAP terminology, these methods corresponded to the subroutines DSLUBC, DSLUCS, and DSLUGM, respectively.

Fletcher [1976] proposed BCG for the solution of linear, but not necessarily positive definite or symmetric systems. Theoretical analysis of the properties of BCG indicates that as long as the recurrences in the method do not break down, it must converge in $m < N$ iterations. Although there is no guarantee of reduction of the quadratic functionals (i.e. that the recurrences will not break down or become unstable), in practice this is rare. If a good preconditioner is used, BCG is an effective method [Seager, 1988].

The BCGS [Sonneveld, 1989] method is related to the BCG, but it does not involve adjoint matrix-vector multiplications, requires half the computational work, and the expected convergence rate is about twice that of BCG. For a $N \times N$ problem, BCGS was theoretically shown to converge in at most $N$ steps. Seager [1988] reports that when BCG diverges, BCGS diverges twice as fast, and when BCG stagnates, BCGS is more likely to diverge. He also suggested using BCGS after first successfully applying BCG. However, in most TOUGH2 applications, this behavior was not observed. In addition, a non-monotonic reduction in the error of BCGS, with many local peaks (sometimes significant) in the convergence performance was seen. These local peaks are also observed in BCG, but they are usually smaller in magnitude.

The GMRES method of Saad and Schultz [1986] is a Lanczos-type extension of conjugate gradients for general non-symmetric systems which is expected to converge in $m < N$ steps for any non-singular matrix if truncation errors are not considered. It generates an orthonormal basis from the Krylov subspace

$$\mathbf{K}(m) = span\{\mathbf{r}_0, \mathbf{A}\mathbf{r}_0, \mathbf{A}^2\mathbf{r}_0, \mathbf{A}^3\mathbf{r}_0, ....., \mathbf{A}^{m-1}\mathbf{r}_0\},$$

where $\mathbf{r}_0 = \mathbf{b} - \mathbf{A}\mathbf{r}_0$ is the initial residual. Since storage requirements increase with $m$ and the number of multiplications with $m^2$, $m$ has to be much smaller than $N$. If the convergence criterion is not met within $m$ iterations, the iteration can be restarted using as an initial value of **x** the one obtained at the $m$-th iteration of the previous cycle. The GMRES used in the VCG package employs this approach. It was found that a $m$=20 to 30 is needed in most TOUGH2 simulations. Unsatisfactory performance is generally obtained for $m$<15, and it is usually pointless to use $m$>35 (since this probably indicates that GMRES may not be a good method for that particular problem). A unique feature of GMRES is that the residual norm is minimized at every iteration, i.e., the decrease in the error is monotonic.

In the VCG package the nomenclature of SLAP was maintained, but the structure and content of the subroutines was substantially modified. Most subroutines used in the SLAP structure were eliminated and large segments of the code were reprogrammed to take

advantage of the well-defined sparsity pattern of matrix A. This resulted in a compact code optimized for TOUGH2, which is substantially faster and lacks the modular structure of SLAP.

The standard TOUGH2 solver MA28 [Duff, 1977] uses a matrix storage scheme that is identical to the SLAP Triad Matrix Storage Format, and therefore remained unaltered in VCG. The ILU preconditioner was kept for use in simulations with irregular geometry. However, for simulations with regular geometry, using the known structure of the A matrix (determined by the integrated finite difference formulation of TOUGH2), an optimized Incomplete Block LU factorization (IBLU) preconditioner [Sonneveld, 1989] was developed. The IBLU preconditioner was based on an approach proposed by Meijerink [1983], and significantly sped up the convergence rate of the three methods compared to the ILU. Moreover, Sonneveld's [1989] observation that the IBLU factorization has the additional advantage of being less sensitive to special directions in the problem (e.g., the advection direction in the advection-diffusion equation, layering, etc.) was confirmed.

Storage requirements in VCG remained the same as in SLAP [Seager, 1988]. BCG and BCGS have the same requirements, while GMRES needs several times more memory. In terms of speed, our previous experience in a large number of TOUGH2 simulations indicates that BCGS is the fastest by a substantial margin, followed by BCG. GMRES is the slowest, but also the most robust, and managed to solve efficiently some of the most demanding problems. Contrary to Seager's [1988] observations, BCGS is the second most robust. Although one or two methods in the VCG package occasionally fails to converge successfully, no case where all three methods are unsuccessful in a TOUGH2 simulation has been encountered yet.

In the case of fractured systems (using the MINC approach) the large number of zeroes in the main diagonal resulted in a very poor convergence of the solution in all three CG solvers in VCG. The problems was alleviated by exchanging the zeroes in the main diagonal by a small number ($10^{-30}$). This approach resulted in no detectable effects on the accuracy of the solution and considerable improvement in processing speed.

## PCs SETUP AND REQUIREMENTS

The TOUGH2 code requires 64 bit arithmetic. When using a 32 bit machine (i.e., machines with 386, 486 or higher processor), it is necessary to modify the code to declare all variables REAL*8 (or DOUBLE PRECISION), and to comply with the FORTRAN77 ANSI X-3.9-1978 standards, also all floating point constants must be converted from E##.# to D##.# format. The processing speed of the code will depend on the machine being used.

The maximum size of computational grids will depend on the amount of extended memory (XMS) available on the machine[2]. A minimum configuration to run TOUGH2/PC would be a 386 PC equipped with 4 MB of RAM, an 80 MB hard drive and an optional (but recommended) numerical coprocessor (387). This configuration will allow to perform 3-D[3] simulations with grids of approximately 1,000 elements and 3,000 connections when using the VCG solvers; or approximately 500 elements and 1,500 connections using the standard version of TOUGH2/PC with the direct matrix solver (MA28).

The code testing presented here was conducted on a 486-DX2-66 MHz PC equipped with 32 MB of RAM and a 250 MB hard drive. This study was limited to grids with a maximum of 10,000 elements; however, this configuration can handle models with larger number of elements.

The code with a maximum grid size of 10,250 elements and 30,750 connections was compiled and linked using Version 5.0 of the Lahey Fortran Compiler for 32 bit machines. The resulting executable version required approximately 26 MB of disk space and the same amount of XMS RAM to run. Memory requirement for TOUGH2/PC with the CG solvers scales approximately linearly with problem size. Therefore, the amount of RAM required by a 3-D grid can be interpolated or extrapolated using the memory requirements for the 1,000 and 10,000 element grids. Hard disk space will depend on the amount of printout generated by the simulation run, which is a parameter controllable by the user. The largest model (10,000 elements), with printout at only the final time step, produced files requiring a total of approximately 6 MB of disk space.

## SOLVER'S TESTING PROCEDURE

The testing of the different solvers was conducted using two reservoir models, one with a regular Cartesian grid and the second with irregular gridding. Two cases were analyzed for each of the models, for a total of four simulation cases:

(1) a regular Cartesian grid with a single-phase liquid system,

(2) a regular Cartesian grid with a two-phase system,

(3) a two-phase field problem with irregular gridding with production from and injection into a single porosity reservoir, and

[2] Extended memory (XMS) is additional memory beyond the first MByte (MB) of random access memory (RAM). The first MB of RAM is usually occupied by the Disk Operating System (DOS), the 640 KB of DOS conventional memory and the Terminate and Stay Resident applications (TSR).

[3] 3-D simulations are the most memory demanding. 1-D and 2-D problems result in arrays of smaller size.

(4) a two-phase field problem with irregular gridding with production from and injection into a fractured reservoir.

The testing was based on the average time it took each algorithm to complete a Newtonian iteration, which consists of:

(a) Recalculating the terms of the Jacobian matrix that results from applying the mass and energy conservation equations at each grid element,

(b) Preconditioning (except for the direct solver MA28) and solving the matrix using VCG. The matrix solution provides the changes of all primary variables (pressure, temperature) for single-phase elements or (pressure, vapor saturation) for elements in two-phases, and

(c) recalculating all the secondary variables (density, internal energy, viscosity, relative permeabilities, capillary pressure, phase saturation, mass fractions of each component) for all the elements of the grid.

Each of the CG solvers performs "internal" iterations of the CG algorithm[4] (CG iterations) to a maximum specified by the user (usually 10% of the number of elements times the number of equations per element). A closure criterion of $10^{-6}$ was used in all three CG solvers.

## REGULAR CARTESIAN GRID MODELS

Five simulation models with different discretization were constructed, as shown in Table 1. The simulation models have an areal extent of 5 x 4 km (20 $km^2$) and a thickness of 1000 m, divided in ten layers of 100 m each (Fig. 1). All have a well producing at a constant rate of 30 kg/s in the sixth layer, an injection well operating at a rate of 30 kg/s in the third layer, and a 30 MW heat source at the bottom layer (layer 10). The wells are located at the node of the element closer to the points (500, 500, 550) for the producer and (4500, 3500, 250) for the injector. The heat source is distributed among the required elements to cover an area of $4x10^5$ $m^2$ (1000 m in x and 400 m in y) at the center of bottom layer (Fig. 1). All of the models were used to perform simulations for single-phase and two-phase conditions.

For the single-phase cases the initial conditions are 40 MPa and 280°C in all blocks; for the two-phase cases, 10 MPa and $S_g$=0.20 in all blocks. No-flow boundaries to mass and heat are employed. Relative permeabilities correspond to Corey's curves with residual saturations of liquid and steam equal to 0.3 and 0.05, respectively. Capillary pressures are neglected. Other relevant parameters are given in Table 2.

[4] Not to be confused with the Newtonian iterations which are external to the CG algorithm.

## IRREGULAR GRID - CERRO PRIETO MODEL

The Cerro Prieto geothermal field developed by the Comisión Federal de Electricidad (CFE), is located approximately 35 km south of Mexicali, Baja California, México. Since the beginning of the exploitation of Cerro Prieto in 1973, one of the most important operational problems that CFE has had to face was the handling of the waste brine [Hiriart and Gutiérrez Puente, 1992]. Up to date most of the brine is sent to evaporation ponds that presently cover an area of 18.6 $km^2$, Figure 2. An infiltration area west of the ponds is used during the winter, when the evaporation rate is significantly lower.

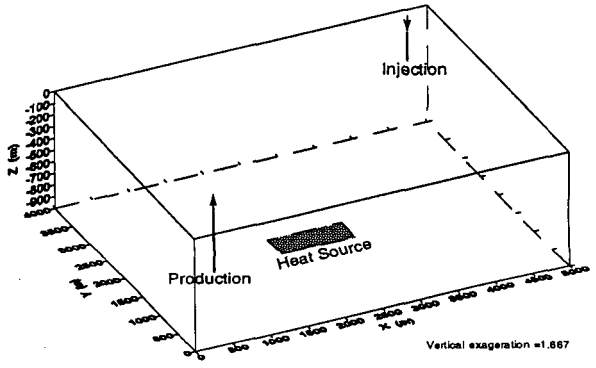


**Fig. 1: Characteristics of the Cartesian grid models**

**Table 1: Discretization of the Cartesian grids**

| Grid No. | Elements in x | Elements in y | Elements in z | Total number of elements |
|---|---|---|---|---|
| 1 | 5 | 10 | 10 | 500 |
| 2 | 10 | 10 | 10 | 1000 |
| 3 | 10 | 20 | 10 | 2000 |
| 4 | 25 | 20 | 10 | 5000 |
| 5 | 50 | 20 | 10 | 10000 |

**Table 2: Reservoir parameters for the Cartesian models**

| | | |
|---|---|---|
| rock density | 2650 | $kg/m^3$ |
| porosity | 3 | % |
| saturated thermal conductivity | 3.2 | W/m °C |
| rock specific heat | 1000 | J/kg °C |
| permeability | 200 | md |
| initial steam saturation | 0 | % |

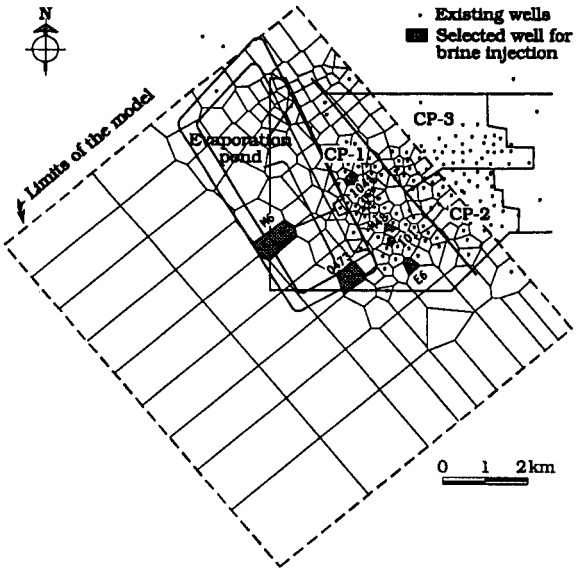


**Fig. 2: Cerro Prieto model. Characteristics of the irregular computational grid.**

Recently (1992-93), CFE started a series of cold brine (approximately at 20°C) injection tests, using brine from the evaporation ponds. The objective of these tests was to monitor the reservoir's response to the injection and to test the injectivity of different areas of CP1 in the western part of the field. CFE's final goal is to inject all the separated brine back into the system, to eliminate its surface disposal and, at the same time, provide pressure maintenance to the reservoir.

Under the DOE/CFE cooperative agreement on geothermal energy, a numerical model for CP1 was developed, using

data provided by CFE. The computational grid covering an area of 89 km$^2$, was defined based on the geological model of the field and the location and completion of the production and injection wells (Fig. 2).

In the vertical direction the model extends from the surface to 5,000 m depth, and is divided into six layers. All the layers have the same discretization and have 235 grid elements (Fig. 2), except layer five that has 47 additional blocks in the NE simulating the volume of the CP2, CP3 and CP4 areas. The numerical model has a total of 1457 elements and was developed as a single porosity model [Antúnez and Lippmann, 1992]. The model was calibrated with production and piezometric data, and was used to test several injection strategies.

For the Cerro Prieto model, the timing of the Newtonian iterations was conducted using the following scenario: Inject 3,500 t/h of 20°C brine evenly distributed between injection wells M-48, 101, 104, E-6, O-473 and M-6. Production wells will continue producing at a rate equal to that measured at the end of 1991 (for that year, the

**Table 3: Reservoir parameters for the Cerro Prieto model**

| | Single-Porosity | Double-Porosity |
|---|---|---|
| **Matrix properties** | | |
| density | 2000-2800 kg/m$^3$ | 2000-2800 kg/m$^3$ |
| porosity | 5-20 % | 15 % |
| saturated conductivity | 0.5-1.3 W/m °C | 0.5-1.3 W/m °C |
| specific heat | 600-2200 J/kg °C | 600-2200 J/kg °C |
| permeability | 0.1-100 md | 0.001-1 md |
| initial steam saturation | spatially variable | spatially variable |
| **Fracture domain properties** | | |
| rock grain density | | 2000-2800 kg/m$^3$ |
| porosity | | 1 % |
| rock specific heat | | 600-2200 J/kg °C |
| fracture spacing | | 50 m |
| permeability | | 0.1-6,000 md |
| initial steam saturation | | spatially variable |

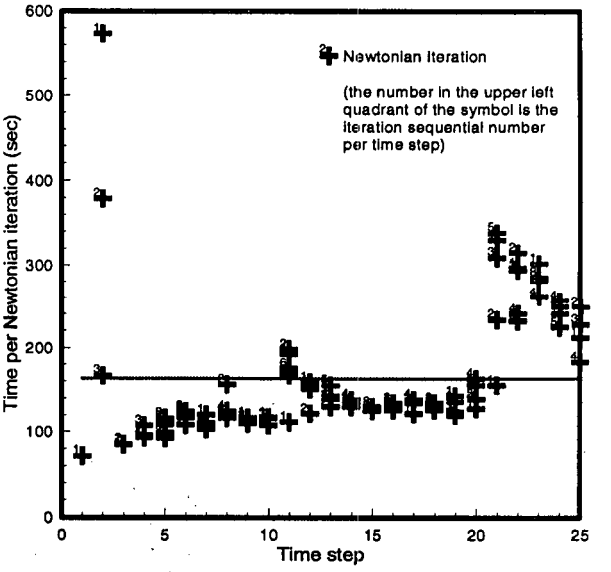


**Fig. 3: Timing of Newtonian iterations for a 10,000 element Cartesian grid using the Lanczos-type Bi-Conjugate Gradient Squared solver (Two-phase).**

average field production was 5,459 t/h of steam and 6,394 t/h of separated brine). Injection well locations are shown in Figure 2. The reservoir parameters used on the Cerro Prieto model are given in Table 3.

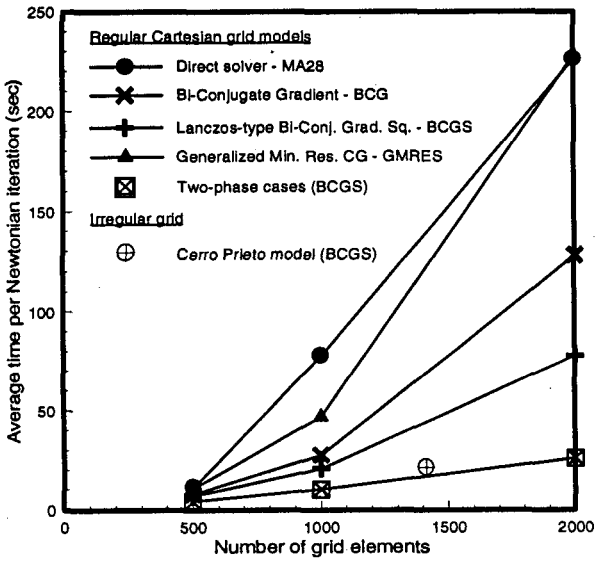


**Fig. 4: Timing of Newtonian iterations for each of the analyzed solvers as function of problem size. (Medium size grids)**

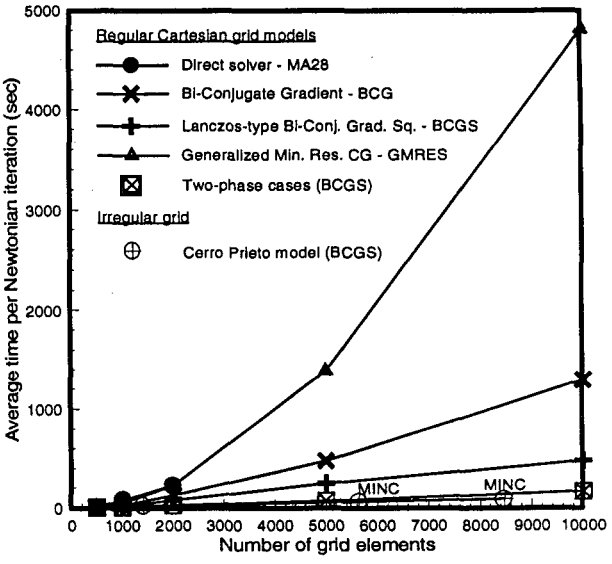


**Fig. 5: Timing of Newtonian iterations for each of the analyzed matrix solvers as function of problem size.**

## DISCUSSION OF RESULTS

All models were run for 25 time steps. An average of 3 to 4 Newtonian iterations were required to reach convergence in each time step. An example of this procedure is presented in Fig. 3. This figure shows the number of Newtonian iterations per time step. Each Newtonian iteration for a given time step is identified with a number on the upper left quadrant of the symbol. The straight line corresponds to the arithmetic average of all iterations. To compare the performance of the different solvers, the average timing of all Newtonian iterations per run was plotted against the number of elements in the grid. Timing data of the various solvers are presented in Figs. 4 and 5.

The upper four curves on Figs. 4 and 5 correspond to the single-phase Cartesian models matrix solvers. The top curve is for the direct matrix solver MA28 [Duff, 1977] which was the slowest but most robust of all the tested solvers. The mayor disadvantage of this solver is that it is not optimized to handle sparse matrices, therefore, its operation requires considerable amount of RAM. The 2000 element 3-D grid required approximately 21 MB of RAM compared to 4 MB for the 500 element case. An additional problem of the MA28 solver is that the dimensioning of the arrays for 3-D problems is rather obscure and most of the time trial and error is required to accommodate grids larger than 500 elements.

The second curve from the top in Figs. 4 and 5 corresponds to the GMRES CG solver with *incomplete Block LU* (IBLU) factorization preconditioning of the matrix [Meijerink, 1983; Sonneveld, 1989]. This algorithm is slower than the other two CG algorithms in the package. For the current problem settings it is as slow as MA28. Its main advantage, in geothermal problems, is that it needs significantly less memory than MA28, making possible 3-D simulations that the direct solver can not handle. This solver has the advantage of monotonic decline in the residual error from one CG iteration to the next

The third and fourth curves from the top in Figs. 4 and 5, correspond to the BCG, and to the BCGS, respectively. The BCG solver is the least robust of the three, but is faster than the GMRES solver. The BCGS solver was consistently the fastest of all solvers. From past experience it has been noticed that the decline of the residual error is not uniform and monotonic, and may exhibit strong oscillations. In previous tests with complex problems this method has not performed as well as the GMRES algorithm. However, it showed a solid performance in the cases tested here. In the remaining cases the BCGS solver was used. This solver was chosen on the basis of its performance efficiency.

The two-phase cases are presented in Figs. 4 and 5 by the curves with crossed out-squares. Execution times in these runs for the different grid sizes showed better performance than the similar single-phase cases.

The additional two test cases were conducted using the Cerro Prieto irregular grid model. Irregular grids may considerably increase the number of connections between contiguous elements; in this case, some elements have up to nine connections. The higher the number of connections, the denser the population of non-zero elements in the matrix. This specific case was not possible

to solve using MA28 since some of the connection-related arrays could not handle the Cerro Prieto mesh. However, this posed no problem to the conjugate gradient solvers with ILU preconditioner.

The timing per Newtonian iteration for the single-porosity, two-phase Cerro Prieto model using the BCGS solver is shown in Figs. 4 and 5. It is interesting to observe that the timing for this model almost falls on top of the corresponding line for the regular Cartesian grid models in two-phases.

The Cerro Prieto model was also used to compare execution times of a double-porosity formulation based on the MINC method [Pruess, 1983]. This method subdivides the elements in concentric shells. The external shell represents the fracture and is fully connected to fractures of neighboring elements. The internal shells represent the rock matrix and are connected to the fracture by means of single linear connections. For computational purposes, each of these shells or subdivisions of an element, becomes a new element of the Jacobian matrix to be inverted by the solvers. The linearity of the connection between matrix shells and between matrix and fracture add a large number of non-zero elements to the Jacobian matrix. The effectiveness of the ILU preconditioning is evident as only a very small increment in time is required for its solution when compared to the single-porosity case, as shown on Fig. 5 by the points labeled MINC.

Table 4 presents a summary of the results of testing the different solvers. Case 1 and 2 correspond to the Cartesian models for single and two-phase conditions. Cases 3 and 4 are for the two-phase conditions using an irregular grid with single and double porosity. The

**Table 4: Timing of the test runs for TOUGH2/PC with the solvers package**

Newtonian iteration tolerance = $1x10^{-5}$
Closure in CG solvers = $1x10^{-6}$

| Case | Grid size | Solver | Number of iterations | | | Time (sec) | | | | | Obsérvations |
|---|---|---|---|---|---|---|---|---|---|---|---|
| | | | Total[5] | Newtonian | Repeated due to convergence failure | per Newtonian iteration | Input | CPU | Total execution | Simulated | |
| 1 | 500 | MA28 | 96 | 71 | 0 | 10.84 | 4.07 | 791.31 | 795.38 | 7.1677E9 | Standard vers. |
| | | GMRES | 108 | 82 | 1 | 10.35 | 3.63 | 870.73 | 874.36 | 4.5053E9 | |
| | | BCG | 104 | 78 | 1 | 7.56 | 3.46 | 611.21 | 614.67 | 4.7101E9 | |
| | | BCGS | 97 | 71 | 1 | 6.79 | 3.46 | 518.06 | 521.52 | 4.7101E9 | |
| | 1,000 | MA28 | 96 | 71 | 0 | 77.57 | 9.12 | 5551.59 | 5560.71 | 19.660E9 | Standard vers. |
| | | GMRES | 126 | 97 | 4 | 46.78 | 8.08 | 4593.14 | 4601.22 | 4.0957E9 | |
| | | BCG | 103 | 75 | 3 | 27.45 | 7.74 | 2246.84 | 2254.58 | 6.9629E9 | |
| | | BCGS | 98 | 70 | 3 | 20.60 | 7.97 | 1726.42 | 1734.39 | 4.3005E9 | |
| | 2,000 | MA28 | 100 | 75 | 0 | 226.01 | 21.64 | 17041.46 | 17063.10 | 4.3005E9 | Standard vers. |
| | | GMRES | 144 | 113 | 6 | 227.88 | 19.55 | 25878.42 | 25897.97 | 1.2285E9 | |
| | | BCG | 112 | 82 | 5 | 127.92 | 19.06 | 11947.56 | 11966.62 | 1.3821E9 | |
| | | BCGS | 99 | 70 | 4 | 77.68 | 18.95 | 6655.65 | 6674.60 | 1.9453E9 | |
| | 5,000 | GMRES | 101 | 68 | 8 | 1381.20 | 80.57 | 94437.19 | 94517.76 | 1.7250E8 | |
| | | BCG | 106 | 75 | 6 | 471.38 | 79.20 | 48964.26 | 49043.46 | 5.5501E8 | |
| | | BCGS | 102 | 74 | 3 | 244.97 | 80.91 | 31499.60 | 31580.51 | 7.1650E8 | |
| | 10,000 | GMRES | 57 | 39 | 3 | 4803.00 | 261.83 | 187876.22 | 188138.1 | 4.1110E7 | 15 time steps |
| | | BCG | 109 | 77 | 7 | 1287.75 | 268.80 | 163326.51 | 163595.3 | 2.1730E8 | |
| | | BCGS | 97 | 64 | 8 | 472.05 | 269.85 | 106601.76 | 106871.6 | 3.3250E8 | |
| 2 | 500 | BCGS | 140 | 113 | 2 | 4.02 | 3.79 | 485.38 | 489.17 | 9.0900E7 | |
| | 1,000 | " | 122 | 97 | 0 | 10.00 | 7.85 | 1017.44 | 1025.29 | 9.0900E7 | |
| | 2,000 | " | 134 | 108 | 1 | 25.75 | 18.73 | 2910.39 | 2929.12 | 9.0900E7 | |
| | 5,000 | " | 132 | 107 | 0 | 69.95 | 82.77 | 7732.52 | 7815.29 | 3.8100E7 | |
| | 10,000 | " | 134 | 109 | 0 | 162.41 | 274.29 | 18203.14 | 18477.43 | 2.5300E7 | |
| 3 | 1,411 | BCGS | 145 | 117 | 3 | 21.20 | 33.51 | 2595.45 | 2628.96 | 4.8061E8 | |
| 4 | 5644 | BCGS | 194 | 154 | 15 | 55.56 | 114.85 | 10347.09 | 10461.94 | 4.1001E8 | 3 MINC shells |
| | 8466 | " | 179 | 142 | 12 | 85.53 | 169.94 | 16808.09 | 16978.13 | 4.1003E8 | 5 MINC shells |

[5] The total number of iterations includes one additional convergence iteration per prescribed time step, 25 in total. At each iteration convergence is checked and if convergence is satisfied a new time step is started.

reported total number of iterations are the sum of: a) the Newtonian iterations (external iterations); b) the repeated external iterations due to convergence failure (after nine Newtonian iterations without reaching convergence, the incremental time used in the current time step is divided by five and the iteration procedure for that time step is repeated); and c) the convergence iterations (iterations that do not need to call the solver since convergence has been attained) one per prescribed time step. The average timing per Newtonian iteration only includes the completed Newtonian iterations; convergence iterations are not considered in this column. The CPU time corresponds to execution time for all iterations Newtonian and non-Newtonian, plus the time to write the output files.

Time comparisons for the different cases indicates that of the three CG tested, the BCGS solver showed the best performance for the runs conducted with the models used in this study, followed by BCG, MA28 and GMRES. However, it is important to emphasize that iterative methods are problem specific. A solver that showed to be adequate for a given problem is not guaranteed to work with all problems. The GMRES solver was found to be the slowest of the three tested conjugate gradient solvers but in previous testing of some highly heterogeneous fluid and heat flow problems this solver was the only one that could converge. Testing of the solvers with an specific problem is strongly recommended to define which is the best for the task.

## CONCLUSIONS

- Lawrence Berkeley Laboratory's general purpose simulator TOUGH2 together with a set of three preconditioned conjugate gradient solvers has been transported to PC platforms and successfully tested.
- The tested conjugate gradient solvers significantly reduced the execution time and storage requirements making possible the execution of considerably larger problems (10,000+ grid blocks) on PCs.
- The Lanczos-type Bi-Conjugate Gradient Squared was found to be the fastest of all tested solvers. It is the best choice on the basis of its performance efficiency. Its computation time and memory requirements increased with problem size only slightly faster than linear.
- Memory requirements for TOUGH2/PC with the conjugate gradient solvers are approximately linear, therefore, the amount of random access memory required by a grid can be easily interpolated or extrapolated.
- This study demonstrates that the combination of the analyzed preconditioned conjugate gradient solvers and the current PCs (386 and higher) are a feasible, economical and efficient combination to conduct large-scale three-dimensional geothermal reservoir simulations that just a few years ago could only be executed on mainframe computers.

## ACKNOWLEDGMENTS

The authors want to express their gratitude to Marcelo Lippmann and Donald Mangold of LBL for reviewing this manuscript and for all their helpful suggestions. This work was supported by the Assistant Secretary for Energy Efficiency and Renewable Energy, Geothermal Division, of the U.S. Department of Energy under contract No. DE-AC03-76SF00098.

## REFERENCES

Antúnez, E., and Lippmann, M. (1993) Numerical Study of the Effects of Brine Injection on the CP1 Production Area of Cerro Prieto. Earth Sciences Division Annual Report 1992, Lawrence Berkeley Laboratory report LBID-33000, pp. 97-99

Duff, I. S. (1977) MA28 - A set of Fortran Subroutines for Sparse Unsymmetric Linear Equations, AERE Harwell Report R 8730.

Fletcher, R. (1976) Conjugate gradient methods for indefinite systems. Numerical Analysis, Lecture Notes in Mathematics 506, Springer-Verlag, New York. pp. 73-89.

Hiriart, G.L. and Gutiérrez, H.P. (1992) An Update of Cerro Prieto Geothermal Field, Twenty Years of Commercial Power. Geothermal Resources Council Bull. Sept/Oct, pp. 289-294.

Meijerink, J.A. (1983) Iterative methods for the solution of linear equations based on incomplete block factorization of the matrix. Paper SPE 12262, Proc. 7th SPE Symposium on Reservoir Simulation, San Francisco, CA, November 15-18, pp. 297-304.

Pruess, K. (1983) GMINC- A mesh generator for flow simulations in fractured reservoirs, Lawrence Berkeley Laboratory report LBID-15227.

Pruess, K. (1991) *TOUGH2* - A General-Purpose Numerical Simulator for Multiphase Fluid and Heat Flow, Lawrence Berkeley Laboratory report LBL-29400.

Saad, Y. and Schultz, M.H. (1986) GMRES: A generalized minimal residual algorithm for solving nonsymmetric linear systems. SIAM J. Sci. Stat. Comput., Vol. 7, No. 3, pp. 856-869.

Seager, M.K. (1988) A SLAP for the Masses. Paper presented at "Methods & Algorithms for PDE's on Advanced Processors", Austin, TX, Oct 17-18, 1988, Lawrence Livermore National Laboratory report UCRL-100195.

Sonneveld, P. (1989) CGS, A fast Lanczos-type solver for nonsymmetric linear systems. SIAM J. Sci. Stat. Comput., Vol. 10, No. 1, pp. 36-52.

PROCEEDINGS, Nineteenth Workshop on Geothermal Reservoir Engineering
Stanford University, Stanford, California, January 18-20, 1994
SGP-TR-147

# A STUDY OF VAPOR-LIQUID FLOW IN POROUS MEDIA

Cengiz Satik and Yanis C. Yortsos

Petroleum Engineering Program
Department of Chemical Engineering
University of Southern California
Los Angeles, CA 90089-1211

## ABSTRACT

We study the heat transfer-driven liquid-to-vapor phase change in single-component systems in porous media by using pore network models and flow visualization experiments. Experiments using glass micromodels were conducted. The flow visualization allowed us to define the rules for the numerical pore network model. A numerical pore network model is developed for vapor-liquid displacement where fluid flow, heat transfer and capillarity are included at the pore level. We examine the growth process at two different boundary conditions.

## INTRODUCTION

Vapor-liquid flow in porous media, driven by temperature and pressure gradients, is involved in a wide variety of processes, such as geothermal systems [9, 8, 1], solution gas-drive oil reservoirs [10], thermal oil recovery [5], nuclear waste disposal [3], porous heat pipes [4], boiling [2] and drying [7] These processes share common aspects, such as phase change and its interplay with fluid flow, heat (or mass) transfer and capillarity.

As in other flow processes in porous media, vapor-liquid flows can be described at three different levels: the pore level, where the emphasis is on the mechanisms of nucleation and local interface growth; the pore network level, where the collective action of an ensemble of interacting pores is considered; and the macroscopic or continuum level, where information of the average behavior only is relevant. In the past, the overwhelming majority of theoretical and experimental studies have addressed the continuum level. Continuum approaches make use of Darcy's law extended to multi-phase flow with saturation-dependent relative permeabilities and capillary pressure functions (borrowed from isothermal, immiscible displacement processes) which assume capillary control at the pore level (low Capillary and Bond numbers). These approaches ignore the underlying pore micro structure and require restrictions on scale-dependent viscous and gravity forces. Due to these limitations, continuum approaches may not be fully adequate to describe these vapor-liquid flows. To obtain a better understanding of the process over a very large range of operating conditions, a microscopic approach in which the pore microstructure is acknowledged must be used. A network model approach, in which the porous medium is represented as a two- or three-dimensional network of interconnected simple geometrical shapes of pores (pore bodies or throats), is one such approach that can capture many important details.

To understand key features of heat transfer-driven bubble growth in porous media, we have developed experimental and numerical pore level models. We consider the application of glass micromodels to visualize pore level mechanisms such as nucleation, phase change and phase growth during vapor-liquid flow in porous media.

This paper is organized as follows: First, we discuss our experimental results. Next, we shall describe the numerical pore network model. Finally, we examine its application to two different cases.

## EXPERIMENTS

Visualization experiments for boiling and bubble growth in micromodels were carried out to get a better understanding of the phenomena occurring at the microscopic pore level [6].

During one of our visualization experiments, using a microscope, we observed the vapor phase growth in a pore body, following a nucleation event. Shown in Figure 1 are snapshots for the consecutive stages of this event. The time elapsed from the first snapshot to the last is two minutes and ten seconds. Vapor phase first formed on the pore wall at the onset of a nucleation event and it was followed by growth of vapor phase due to the continuous phase change occurring at the liquid-vapor interface. Note that the shape of the microscopic bubble is circular (Figure 1a and b) until it

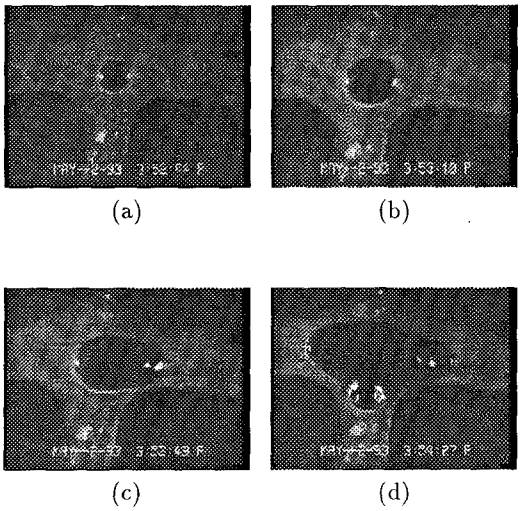

(a) (b) (c) (d)

Figure 1: Observation of vapor phase growth in a pore body, following a nucleation event.

encounters the effects of constraining pore geometry. When this happens, the bubble elongates in the pore body (Figure 1c ) and the growth process continues to completely fill the entire pore body (Figure 1d).

Following nucleation, growth of the bubble continues until the pore body is completely filled with vapor phase. When this is completed, bubble cannot grow because of the capillary pressure barrier induced by the constraining pore walls. During this stage, since the volume does not change significantly, the pressure in the vapor phase increases due to the continuous phase change at the liquid-vapor interfaces. We refer this stage as "pressurization step". This stage continues until the capillary pressure barrier is exceeded, which occurs when the difference between the pressures in the vapor and the surrounding liquid phases becomes equal to the capillary pressure. When this condition is achieved, an immediate jump of the interface takes place from one pore body to another. The next stage is a "pore-filling step", during which bubble growth continues until full occupancy is achieved in all pore bodies. During a bubble growth process, these two stages are repeated continuously.

Figure 2 shows a bubble growth pattern obtained during one experiment. As shown in this figure, bubble growth patterns obtained are ramified and not compact, contrary to the growth in the bulk. These patterns reflect the underlying pore microstructure.

## PORE NETWORK MODEL

To describe bubble growth in a porous medium, we used a pore network model by representing the

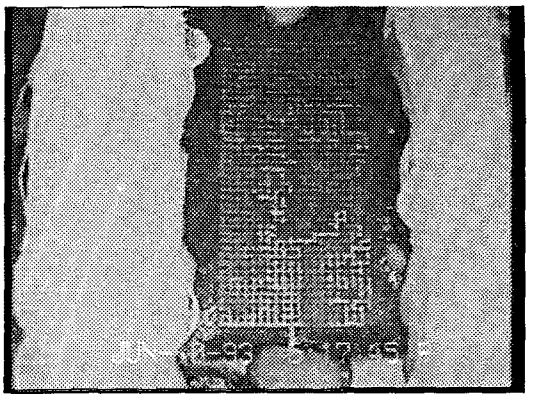

Figure 2: Bubble growth pattern in a horizontal pore network.

porous medium as an equivalent two-dimensional network of interconnected pore bodies and pore throats randomly distributed according to a uniform distribution. We consider growth from a single vapor bubble in a horizontal porous medium of finite size by allowing only one nucleation event to take place at a given location. Details of the model are given in [6]

We examine two different cases: (i) Bubble growth with a uniform superheat imposed initially and (ii) Bubble growth with a prescribed heat flux at one boundary. In the first case, the pore space is completely filled with a superheated liquid. Initial temperatures in the liquid and solid of the porous medium are spatially constant and at the same temperature value. The geometry of the porous medium is square and all four boundaries are open to a constant (atmospheric) pressure. The pressure in the liquid-occupied pore space is initially constant and at atmospheric pressure. In the second case, the geometry of the medium is rectangular. A heat flux is imposed on one side of the medium. No-heat flux boundary conditions are imposed at the remaining boundaries. A constant pressure (atmospheric) boundary condition is imposed on the left-hand side boundary, while no-flux boundary conditions are imposed on all other boundaries of the medium. The initial nucleation site is located at the center of the medium in the first case and at the center of the side where the heat flux is imposed in the second case.

## BUBBLE GROWTH IN A UNIFORM INITIAL SUPERHEAT

In the model, we used a square lattice (31x31). Throat (bond) sizes were randomly assigned from a uniform distribution, while pore body (site) sizes were kept constant. Initial temperature and pressure were set to 104.44 °C and $1.0133 \times 10^5$ N/m$^2$,

respectively, and the amount of the superheat imposed was 4.4 °C. Other typical parameters used are shown in Table 1. In the table $\rho_l$, $C_{pl}$, $\lambda_l$, $\mu_l$, $L_v$, $\gamma$, $\rho_v$, $\rho_s$, $C_{ps}$, $\lambda_s$, $d^*$, $d^*_{tf}$, $M$, $L_b$, $R^*_b$ and $R^*_s$, are liquid density, specific heat, thermal conductivity and viscosity, latent heat, interfacial tension, vapor density, solid density, specific heat and thermal conductivity, dimensionless parameters for solid-to-liquid and solid-to-thin liquid film heat transfer coupling, molecular weight, bond length, average bond and pore body sizes, respectively.

Fluid distributions at two different stages of bubble growth for the typical parameters given in Table 1 are shown in Figure 3. Corresponding time values for these stages are 2.45 and 7.42 seconds, respectively. Many other simulation results with different parameter values and larger network sizes showed that the time spend to reach the final stage is in fact very small (order of a few seconds), implying that heat transfer driven bubble growth of this type is very fast process. In the Figure, white or black colors represent liquid only or vapor only occupancy, respectively, while gray color denotes partial liquid occupancy. The growth regime for the first stage is of percolation type, during which the two steps (pressurization and pore-filling steps) discussed above follow one another and penetration of single interface occurs at the end of each pressurization step with no further interface penetration until it ends. Both fluid distributions shown in the Figure are at the end of a pore-filling step. Therefore, for the first stage, pore bodies are occupied with either vapor- or liquid-only. However, in a regime other than percolation, penetration of multiple interfaces may occur during both pressurization and pore filling steps, hence some of the pore bodies may be partially liquid-occupied, as shown in Figure 3b.

Table 1: Typical parameter values.

| | | |
|---|---|---|
| $\rho_l$ | = | 960.85 kg/m$^3$ |
| $C_{pl}$ | = | $4.2092 * 10^3$ J/kg − K |
| $\lambda_l$ | = | 0.6808 W/m − K |
| $\mu_l$ | = | $2.4799 * 10^{-4}$ N − s/m$^2$ |
| $L_v$ | = | $2.2568 * 10^6$ J/kg |
| $\gamma$ | = | 0.0584 N/m |
| $\rho_v$ | = | 0.5886 kg/m$^3$ |
| $\rho_s$ | = | 2082.40 kg/m$^3$ |
| $C_{ps}$ | = | $8.3732 * 10^2$ J/kg − K |
| $\lambda_s$ | = | 6.808 W/m − K |
| $d^*$ | = | 1 |
| $d^*_{tf}$ | = | 0.01 |
| $M$ | = | 18 kmol/kg |
| $L_b$ | = | 1320 $\mu$m |
| $R^*_b$ | = | 450 $\mu$m |
| $R^*_s$ | = | 601 $\mu$m |

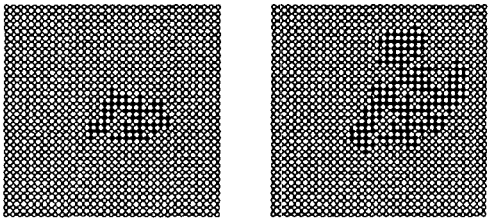

(a) (b)

Figure 3: Fluid distributions at two stages of bubble growth in a uniform initial superheat.

Fluid temperature and pressure and solid temperature distributions corresponding the stages examined above are shown in Figures 4, 5 and 6, respectively. In the Figures, black or white colors denote maximum or minimum values, respectively. As described above, all pore bodies in the network are initially filled with a superheated liquid and initial temperatures in both pore bodies and solid are spatially constant. At the completion of a nucleation event, bubble growth process begins and a liquid-to-vapor temperature gradient forms since the vapor is at the saturation temperature which is lower than the surrounding liquid temperatures. With the existence of such gradient, heat transfer (both conduction and convection) takes place towards the bubble and this drives the phase change process at all liquid-vapor interfaces, resulting to the growth of the bubble. The fluid temperatures in Figure 4 show a good agreement with the above argument. In the Figure, fluid temperatures are constant in the liquid-occupied pore space except in a boundary layer where liquid-to-vapor temperature gradient exist. However, for this particular parameter values, a very sharp gradient is observed.

Solid temperatures, shown in Figure 5, are coupled with liquid temperatures. The measure of coupling between the two fields is provided by a dimensionless parameter $d^*$. The thermal interaction between solid and liquid increases as $d^*$ increases. We also allow another coupling between the solid and vapor-occupied pore space to account for possible thin liquid films by defining a parameter $d^*_{tf}$. Solid temperature fields shown in the Figure are almost uniform with maximum and minimum values of 104.44 and 104.39 °C, respectively. Due to the coupling with fluid temperatures, a very small gradient, similar to the liquid-to-vapor temperature gradient in the pore space, is present.

Finally, fluid pressure distributions in Figure 6 shows that the highest pressure is in the bubble while lower pressures are in the liquid indicating the displacement of liquid by vapor. This is expected because the total increase in vapor volume

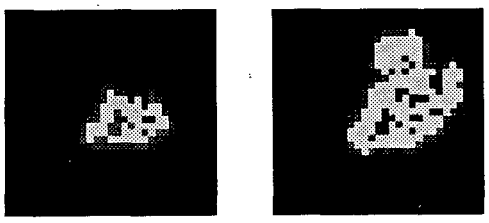

(a) (b)

Figure 4: Fluid temperature distributions at two stages of bubble growth in a uniform initial superheat.

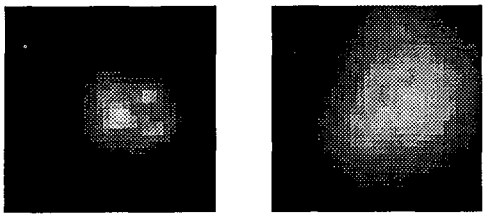

(a) (b)

Figure 5: Solid temperature distributions at two stages of bubble growth in a uniform initial superheat.

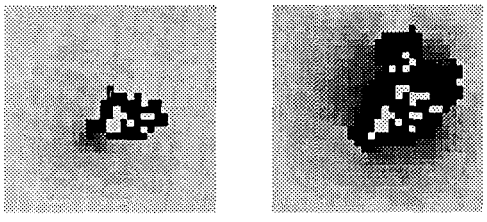

(a) (b)

Figure 6: Fluid pressure distributions at two stages of bubble growth in a uniform initial superheat.

due to phase change is significantly larger than the actual volume of liquid evaporated since the ratio of liquid and vapor densities is very large ($O(10^3)$).

## BUBBLE GROWTH WITH A PRESCRIBED HEAT FLUX

To model this process, we used a square lattice (21x42) network with the same bond and site distributions as in the previous case. Now, initial liquid and solid temperatures are the same, while a heat flux ($q_h$) is imposed over the first column of the network which represents the solid part of the porous medium. Initial liquid temperature and pressure were set to 100 °C and $1.0133 \times 10^5$ N/m$^2$, respectively. The initial nucleation site was arbitrarily located at the node (11,1). Onset of nucleation takes place when the temperature of the node (11,1) reaches the nucleation temperature. Fluid and Solid temperature fields at two different stages of bubble growth for typical parameters given in Table 1 are are shown in Figures 7 and 8. For this particular run, the onset of nucleation took place at 39.673 second and corresponding time values for these stages are 52.99 and 60.80 seconds, respectively. As in the previous case, fast growth dynamics are also observed. The important difference between this and the previous case is the existence of a prescribed heat flux in the solid temperature field. This heat flux generates a temperature gradient along the solid body of the porous medium, while another gradient also forms in the fluid since both are coupled (Figures 7 and 8). As a result, the liquid phase in the pore spaces become superheated, providing a driving force for bubble growth. The magnitude of the superheat increases as the heat flux is imposed. As in the previous case, liquid-to-vapor gradient also exist in the liquid temperatures since it is a requirement for the bubble growth process. Fluid pressure fields are similar to the ones obtained in the previous case.

## CONCLUSIONS

In this paper, we discussed the visualization of boiling and bubble growth in pore networks and presented a pore network model that describes bubble growth in porous media due to a temperature supersaturation. Visualization experiments for boiling in horizontal glass micromodels were conducted. We observed the growth of a micro-

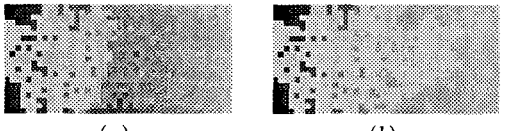

(a) (b)

Figure 7: Fluid temperature fields at two stages of bubble growth with a prescribed heat flux.

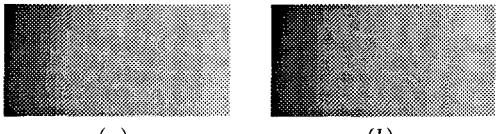

(a) (b)

Figure 8: Solid temperature fields at two stages of bubble growth with a prescribed heat flux.

scopic bubble formed at the onset of a nucleation event. We found that, during bubble growth process, two stages are repeatedly followed: pore-filling and pressurization stages. During the pore-filling stage, the vapor phase is filling a pore body while the liquid is being discharged. During the pressurization stage, the occupancy of all vapor-occupied pore bodies is complete and bubble volume does not change significantly due to the capillary pressure barrier, thus the mass generated at the liquid-vapor interfaces due to the phase change increases the vapor pressure until the capillary pressure barrier is exceeded. When this condition is achieved, a sudden jump of the interface occurs. Contrary to the growth in the bulk, bubble growth patterns in pore networks are ramified and not compact.

The numerical model accounts for fluid flow, heat transfer and capillarity. We have analyzed two different types of bubble growth: (i) Bubble growth with a uniform superheat initially imposed, and (ii) Bubble growth with a constant heat flux imposed. In both cases, the final stages of the growth are reached at very small time values (order of a few second), indicating fast growth. During the bubble growth process, a liquid-to-vapor temperature gradient exist in the fluid temperature fields and this gradient drives the growth. Due to the coupling between liquid and solid temperatures, a similar gradient also exists in the solid temperature fields.

## ACKNOWLEDGEMENTS

This work was partly supported by DOE contract DE-FG22-90BC14600, the contribution of which is gratefully acknowledged.

## References

[1] N.E. Bixler and C.R. Carrigan. Enhanced heat transfer in partiallly-saturated hydrothermal systems. *Geophysical Res. Letters*, 13:42–45, 1986.

[2] K. Cornwell, B.G. Nair, and T.D. Patten. Observation of boiling in porous media. *J. Heat Mass Transfer*, 19:236–238, 1976.

[3] C. Doughty and K. Pruess. A semianalytical solution for heat-pipe effects near high-level nuclear waste packages burried in partially saturated geological media. *Int. J. Heat Mass Transfer*, 31:79–90, 1988.

[4] Y. Ogniewicz and C.L. Tien. Porous heat pipe. in *Heat Transfer, Thermal Control and Heat Pipes*,(Edited by W.B. Olstad), 70, Progress in Astronautics (Series Editor M. Summerfield) 329-345, AIAA, New York. Presented as paper 79-1093, AIAA 14th Thermophysics Conf., Orlando, Florida, June 1979.

[5] M. Prats. *Thermal Recovery.* SPE Monograph, Dallas, Texas, 1982.

[6] C. Satik. Studies in vapor-liquid flow in porous media. Ph. D. Thesis, May 1994, University of Southern California, Los Angeles, California.

[7] T.M. Shaw. Drying as an immiscible displacement with fluid counterflow. *Phys. Rev. Lett.*, 59:1671, 1987.

[8] C.H. Sondergeld and L. Turcotte. An experimental study of two phase convection in a porous medium with application to geological problems. *J. Geophys. Res.*, 82:2045–2053, 1977.

[9] D.E. White, L.J. Muffler, and A.H. Truesdell. Vapor-dominated hydrothermal systems compared with hot-water systems. *Econ. Geol.*, 66(1):75–97, 1971.

[10] Y.C. Yortsos and M. Parlar. Phase change in porous media: Application to solution gas drive. Paper SPE 19697 presented at the 64th Annual Technical Conf. and Exhibition of SPE, San Antonio, Texas,Oct. 8-11, 1989.

PROCEEDINGS, Nineteenth Workshop on Geothermal Reservoir Engineering
Stanford University, Stanford, California, January 18-20, 1994
SGP-TR-147

# SUMMARY OF RECENT FLOW TESTING OF THE FENTON HILL HDR RESERVOIR

Donald W. Brown

Los Alamos National Laboratory
Earth and Environmental Sciences Division
Los Alamos, New Mexico 87545

## Abstract

Through May of 1993, a sequence of reservoir flow tests has been conducted at our Fenton Hill Hot Dry Rock (HDR) test site as part of the Long-Term Flow Testing (LTFT) program. This testing, which extended over an aggregate period of about 8 months, has demonstrated several significant features concerning HDR reservoirs that taken together reflect very positively on the future development of the HDR concept into a viable commercial reality.

Of most significance is the demonstrated self-regulating nature of the flow through such a reservoir. Both temperature and tracer data indicate that the flow, rather than concentrating in a few potential direct flow paths, progressively shifted towards more indirect flow paths as the test proceeded. This self-regulating mechanism may be related to the strongly temperature-dependent viscosity of water.

Measurements have shown that the reservoir flow impedance is concentrated in the near-wellbore region surrounding the production well. This situation may well be a blessing in disguise since this suggests that the distance between injection and production wells can be significantly increased, with a greatly enhanced access to fractured hot rock, without an undue impedance penalty. However, since the multiply interconnected joints within the HDR reservoir are held open by fluid pressure (pressure-propping), a higher mean reservoir pressure is the obvious path to increased productivity while still retaining the distributed nature of the flow.

Other significant observations include a very small rate of reservoir water loss that was still declining at the end of the flow testing, and a set of temperature measurements in the production well that show no significant temperature drawdown during the period of testing.

## Introduction

The long-term flow testing of the Phase II Hot Dry Rock (HDR) reservoir at Fenton Hill began in early April 1992 and extended through May 1993. During this period of testing, as shown in Figure 1, there were two intervals of near-steady-state operation referred to as the first (16-week) and second (8-week) phases of the Long-Term Flow Test (LTFT). This testing was generally conducted at an injection pressure of 3960 psi (close to the pressure which would cause renewed reservoir growth) and at a production backpressure of 1400 psi. Between these two phases of the LTFT, there was a 6-week period of lower-rate flow testing referred to as the Interim Flow Test (IFT) and two months of testing in November and December of 1992 where the reservoir was operated at even higher backpressure conditions. Finally, in May of 1993, a brief series of cyclic flow tests was conducted.

What follows is a summary of the results of the recent flow testing of the Fenton Hill HDR reservoir, emphasizing the four different steady-state operating conditions that were established during the last 5 months of 1992. Then, the remainder of the paper is devoted to an extended set of conclusions that focus on the significant features of this particular HDR reservoir that have been determined during the flow testing, and their significance for the future development of the HDR concept.

## Steady-State Flow Performance

Near the end of each phase of significant reservoir testing, a 1- to 8-day period of time was selected as representative of steady-state operation under each specific set of conditions. These were as follows:

| | |
|---|---|
| (1) LTFT, first phase | July 21-29, 1992 |
| (2) IFT | September 29, 1992 |
| (3) 1800 psi backpressure | December 27, 1992 |
| (4) 2200 psi backpressure | December 10, 1992 |
| (5) LTFT, second phase | April 12-15, 1993 |

However, since the reservoir flow conditions existing near the end of the second phase of the LTFT were nearly identical to those near the end of the first phase of the LTFT (as discussed later), only the first four reservoir operating conditions will be considered at this point. In Table I, these four sets of pressure/flow conditions, referred to as Operating Points 1, 2, 3, and 4, correspond to the numbers in parenthesis given above.

A review of these four sets of steady-state test data shows that we operated the Fenton Hill HDR reservoir at two different surface injection pressures -- 3960 psi and 3240 psi, but at the same backpressure of 1400 psi; and at three different levels of production backpressure -- 1400 psi, 1800

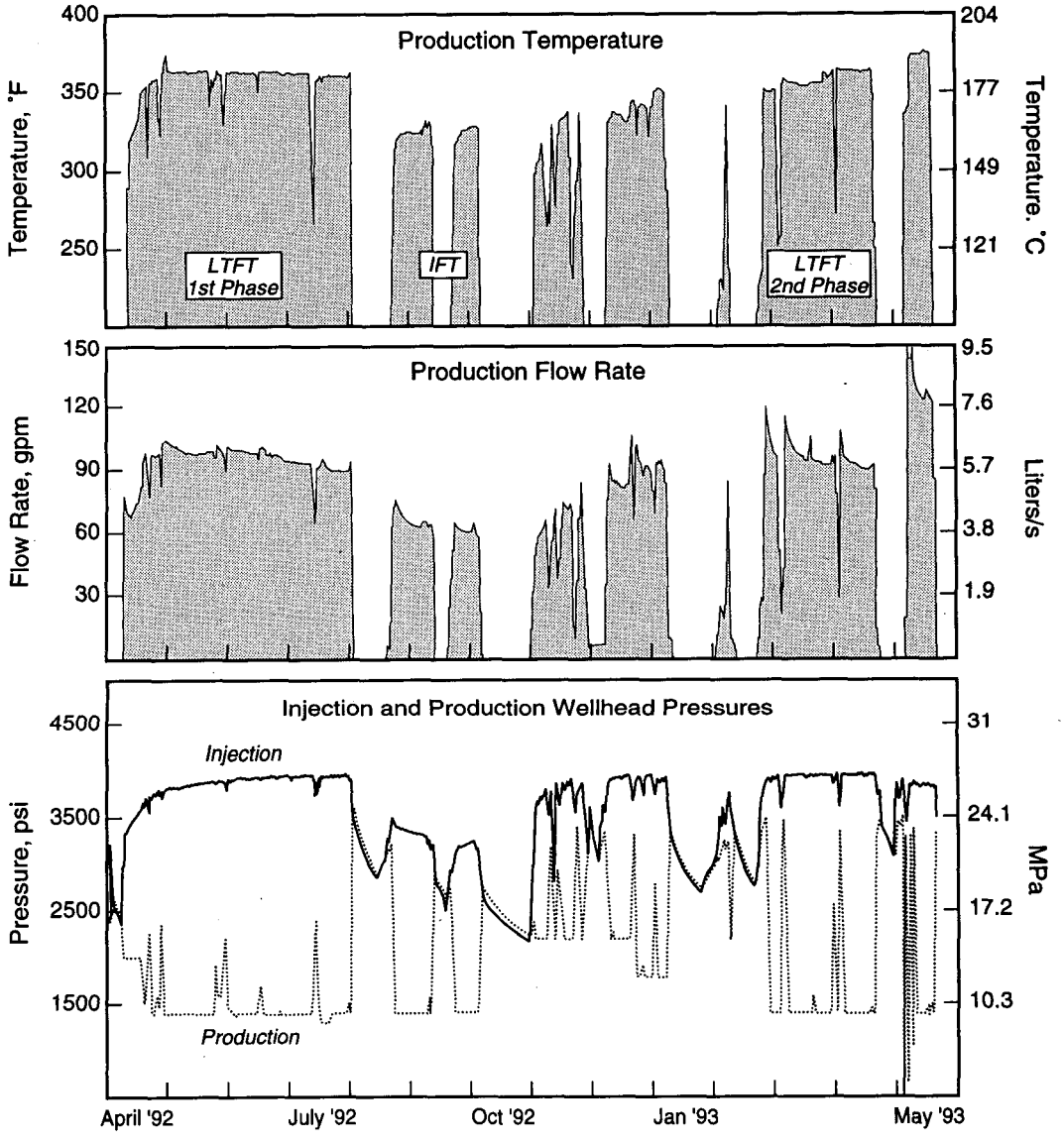


Figure 1. Fenton Hill Reservoir Operating Conditions from April 1992 to May 1993.

Table I
Steady–State Operating Conditions at Fenton Hill

| Operating Point | 1 | 2 | 3 | 4 |
|---|---|---|---|---|
| *Surface Inlet Conditions* | | | | |
| Pressure, psi | 3958 | 3243 | 3962 | 3963 |
| Flow Rate, gpm | 107.1 | 68.8 | 113.1 | 116.2 |
| Temperature, °C | 19 | 18.5 | 17.5 | 17.5 |
| *Surface Outlet Conditions* | | | | |
| Pressure, psi | 1401 | 1399 | 1798 | 2201 |
| Flow Rate, gpm | 89.7 | 61.1 | 90.5 | 84.6 |
| Temperature, °C | 183 | 165 | 183 | 177 |
| *Reservoir Pressure Drop* | | | | |
| Apparent, psi | 2557 | 1844 | 2164 | 1762 |
| Buoyant Drive, psi | +719 | +664 | +709 | +686 |
| Corrected for Buoyancy | 3276 | 2608 | 2873 | 2448 |

psi and 2200 psi, but at the same injection pressure of about 3960 psi.

Point 2, representing the IFT, indicates that at about 2/3 of the LTFT injection rate (68.8 gpm vs. 107.1 gpm), the injection pressure could be maintained at only about 3240 psi, a drop of 18% from the LTFT injection pressure of 3960 psi. Points 1, 3 and 4 show that there is a broad maximum in the production flow rate between 1400 and 1800 psi, with the rate dropping by about 6.5% as the backpressure is further increased to 2200 psi. These steady-state data are currently being used to validate the coupled flow/displacement discrete-element reservoir model (GEOCRACK) being developed by Prof. Dan Swenson and his team at Kansas State University (KSU). A coupled heat transfer solution has recently been added to this finite-element model, which will be reported on in the near future.

### Comparison of the Two Phases of the LTFT

Table II presents the steady-state operating data for the two phases of the LTFT shown in Figure 1.

Table II
Comparison of Reservoir Performance Between the Two Phases of the Long–Term Flow Test

| Measured Performance | July 21-29, 1992 | April 12-15, 1993 |
|---|---|---|
| *Injection Conditions* | | |
| Flow Rate, gpm (l/s) | 107.1 (6.76) | 103.0 (6.50) |
| Pressure, psi (MPa) | 3958 (27.29) | 3965 (27.34) |
| *Production Conditions* | | |
| Flow Rate, gpm (l/s) | 89.7 (5.66) | 90.5 (5.71) |
| Backpressure, psi (MPa) | 1401 (9.66) | 1400 (9.65) |
| Temperature, °C | 183 | 184 |
| *Peripheral Water Loss* | | |
| Rate, gpm (l/s) | 12.5 (0.79) | 7.3 (0.46) |
| Percent | 11.7 | 7.0 |

Of most significance is the repeatability of the operating data between these two phases of the LTFT, separated in time by almost 9 months. Except for a reduction in the rate of water loss from 12.5 gpm to 7.3 gpm, which is reflected in a concomitant reduction in the injection flow rate, the two sets of operating data are remarkably similar. Further, it should be noted that the surface production temperature, within the accuracy of the measuring system, remained constant during this time reflecting the fact that for this limited period of flow testing, there was no drawdown in the reservoir production temperature. However, how long this situation would have continued if the long-term flow testing had not been terminated is pure conjecture in light of an unknown effective reservoir volume and joint spacing for heat transfer.

### Self-Regulating Nature of the Flow Through HDR Reservoirs

The most significant observation that has been made during the recent testing at Fenton Hill is the self-regulating nature of the flow through the pressure-dilated (i.e., pressure-propped) HDR reservoir. With time, the flow tends to progressively concentrate in the more indirect flow paths at the expense of the more direct flow paths. That is, the flow tends to become more distributed with time rather than becoming more concentrated in a few direct flow paths. This observation is based on both tracer and borehole temperature data obtained during the recent long-term flow testing of the Fenton Hill reservoir.

Figure 2 shows the dye tracer response for three times during the flow testing: Early and late during the first phase of the LTFT and late during the second phase of the LTFT. As shown, the first arrival of the tracer in April 1992 took about 3-1/2 hours. The delay in tracer arrival then increased in subsequent tests to a final value of about 5

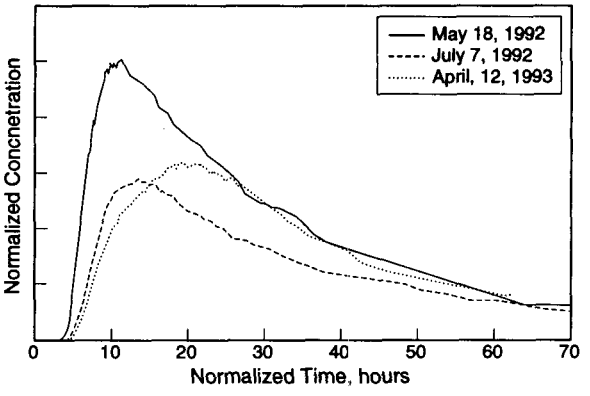


Figure 2. Recovery of Fluorescein Dye Tracer on Three Occasions During the LTFT.

hours. This suggests that the most direct flow paths were being somewhat closed off with time. A corollary observation is the peak in the tracer arrival, which was progressively delayed in time as the testing proceeded. This delay would imply that the flow was becoming more diffuse with time, with the flow tending to concentrate in the more indirect flow paths.

The production interval temperature data given in Figure 3 and Table III chart the redistribution of the flow and temperature in this part of the reservoir as the testing proceeded. The most significant change occurred in the deepest flowing joint in the production interval -- at point A -- where the temperature decreased by 3°C over a period of 8 months. However, the mixed-mean production-interval outlet temperature at point D varied only slightly, and within the error of the measuring system. The strong inference is that while the flow through Joint A was being cooled, it was also being impeded; otherwise the mixed-mean temperature at point D would have shown a corresponding cooling. Preliminary analyses by members of the KSU team would suggest that this self-regulating phenomenon is associated with the almost order-of-magnitude decrease in the viscosity of water between ambient and reservoir temperature conditions.

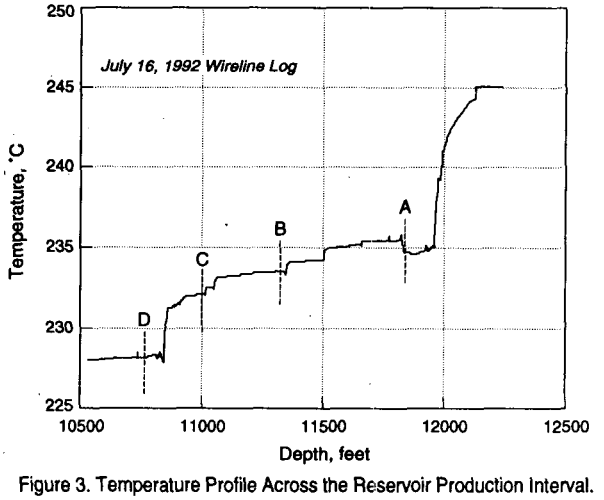


Figure 3. Temperature Profile Across the Reservoir Production Interval.

Table III
Comparison of Fluid Temperatures at Four Specific Points Across the EE-2A Production Interval

| | 7/16/92 Log | 9/29/92 Log | 3/16/93 Log |
|---|---|---|---|
| *Point A* (11,840 ft) | 234.5°C | 233.9°C | 231.5°C |
| *Point B* (11,320 ft) | 233.4°C | 232.9°C | 232.4°C |
| *Point C* (10,990 ft) | 232.0°C | 231.7°C | 231.5°C |
| *Point D* (10,750 ft) | 228.2°C | 228.1°C | 227.8°C |

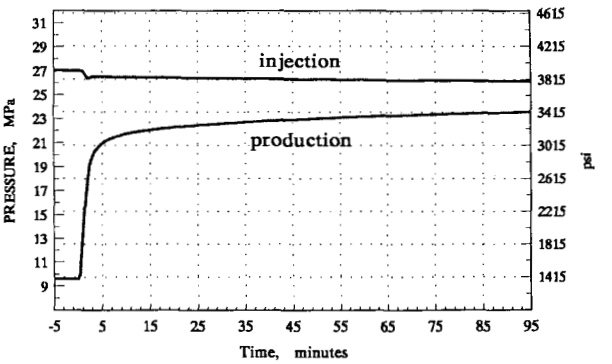


Figure 4. Wellhead Shut-in Pressure Responses.

### Flow Impedance Implications from Test Data and Modeling Results

Numerous shut-ins of the reservoir have shown that the flow impedance is concentrated in the vicinity of the production wellbore. For instance, Figure 4 shows the pressure response for 94 minutes following the shut-in of the injection and production flow at the end of the first phase of the LTFT. As can be seen, after 5 minutes of shut-in, the pressure had risen very markedly at the production well while the corresponding injection pressure had dropped only slightly. This pressure behavior would suggest that the reservoir flow impedance is much greater around the production well than in the body of the reservoir. It appears that the reservoir is very well manifolded to the injection well due to the cooling-induced dilation of the joints connecting the injection interval to the body of the reservoir. Numerical modeling of the reservoir by the KSU team shows that this impedance concentration may actually be to our advantage. Figure 5 shows the computed difference in the reservoir pressure profiles for wellbore separation distances of 200 m and 400 m. For only a small decrease in flow rate (from 100 gpm to 84 gpm), the accessible region of fractured hot rock is greatly increased -- probably by almost a factor of four.

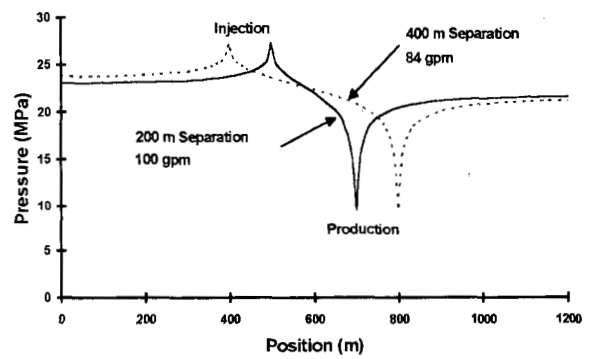


Figure 5. Pressure Profiles for Two Wellbore Spacings.

PROCEEDINGS, Nineteenth Workshop on Geothermal Reservoir Engineering
Stanford University, Stanford, California, January 18-20, 1994
SGP-TR-147

# TESTS FOR RESISTIVITY BOUNDARY CHANGES AT OHAAKI NEW ZEALAND

G F Risk

Institute of Geological and Nuclear Sciences Ltd
P O Box 1320, Wellington, New Zealand

## ABSTRACT

Close-spaced resistivity measurements along ten traverse lines crossing the resistivity boundary of the Ohaaki Geothermal Field, New Zealand, were first measured in 1975 and remeasured in 1992. The 1992 resistivity profiles were similar in shape to the original ones. On both occasions very sharp resistivity boundaries were delineated along the southern and southwestern edges of the field where apparent resistivity rises sharply over a horizontal distance of a few hundred metres from 2-5 ohm m on the inside of the field to 20-50 ohm m on the outside. On two of the southern lines the resistivity boundary appears to have moved outwards by about 100 m, which may be caused by southward movement of reinjected waste water from nearby drillholes. On the other southern lines the outward movement appears to be less than about 25 m, which is the limit of resolution of the survey.

Over the 17 year interval apparent resistivity values have dropped slightly at most measurement sites. The decrease is more pronounced on the inside of the field boundary where apparent resistivities have declined by up to about 40 percent. Some of this decrease is attributed to reinjection of conductive waste water near the field boundary causing a drop in ground resistivity. Part of this change may be due to calibration errors and measurement difficulties, including the disturbing effects of the new drillholes, steam pipes and an earthing mat that have been installed since 1975.

## INTRODUCTION

As part of the exploration phase in the development of the Ohaaki Geothermal Field, New Zealand, a resistivity survey was made in 1975/76 (Risk et al, 1977) using close-spaced measurement points which had been accurately located relative to permanent benchmarks. Measurements along 10 of these lines in the south and west of the field (which had originally been measured in November-December 1975) were repeated in November 1992, 17-year years later. The aim was to determine whether the resistivity boundary zone had moved and whether any changes could be detected resulting from exploitation of the field since the commissioning of the Ohaaki Power Station in 1989. A preliminary account of this work is given in Risk (1993).

An experiment for monitoring resistivity variations in the Cerro Prieto Geothermal Field was done over a 2.5 year interval by Wilt and Goldstein (1984). They used an in-line dipole-dipole array with electrodes 1 km apart. They found a rather complex pattern of resistivity changes whose dominant feature was an annual 5 percent increase in resistivity over the production zone of the field which they attributed to dilution of reservoir fluids.

## FIELD MEASUREMENTS

The transmitter and receiver sites for the part of the original survey that was repeated are shown in Figure 1. Points T1 and T2 show the locations of the current electrodes forming the transmitter; T1 is near the centre of the field, and T2 is about 2 km south of the southern boundary of the field. The transmitter location was kept constant throughout each of the surveys.

In 1992, measurements of the signal strength were made at receiver sites spaced at 50 m intervals along the lines B, C, D, E, F, G, J, K, L, N (see Fig. 1). These lines were the same (to within about 10 m) as those used in 1975, except for lines J and L which had to be moved because of the construction of the Power Station and associated facilities. The scope of the remeasurement project was insufficient to allow remeasurement of the lines to the north and east of the field, or to repeat the 1975 measurements made using the current electrode pairs T1-T3 (north-west) and T1-T4 (east).

Although the layout and method for making the measurements in 1992 was the same as used in 1975, completely different instruments were used for both transmitter and receiver. The accuracy of calibration of all the instruments is hard to assess, but it is expected that the apparent resistivities have been measured to within about 5 percent on each occasion. Thus, measured apparent resistivity differences greater than about 10 percent should represent real changes.

## RESISTIVITIES

Both the 1975 and 1992 field data (currents, electric field strengths, geometric data, etc) were analysed using the same standard programs to obtain apparent resistivities at each receiver site. Figures 2 and 3 show plots of apparent resistivity versus horizontal distance from the centre of the field for eight of the ten lines.

The left of each plot corresponds to the inside of the field where the apparent resistivities are smallest (2 - 5 ohm m). Although the lines traverse only a few hundred metres into the field, measurements from other resistivity surveys (Risk et al 1970) show that a low resistivity anomaly of nearly constant value continues right across the Ohaaki Field. The resistivity boundary zone for each line is thus definable as the zone at the edge of the field over which the apparent resistivity increases above this average 'inside' level to a nearly constant larger value typifying the outside of the field. On most of the lines the apparent resistivity increases by an order of magnitude across the boundary zone and levels off on the outside of the field at values of the order of 20 - 50 ohm m.

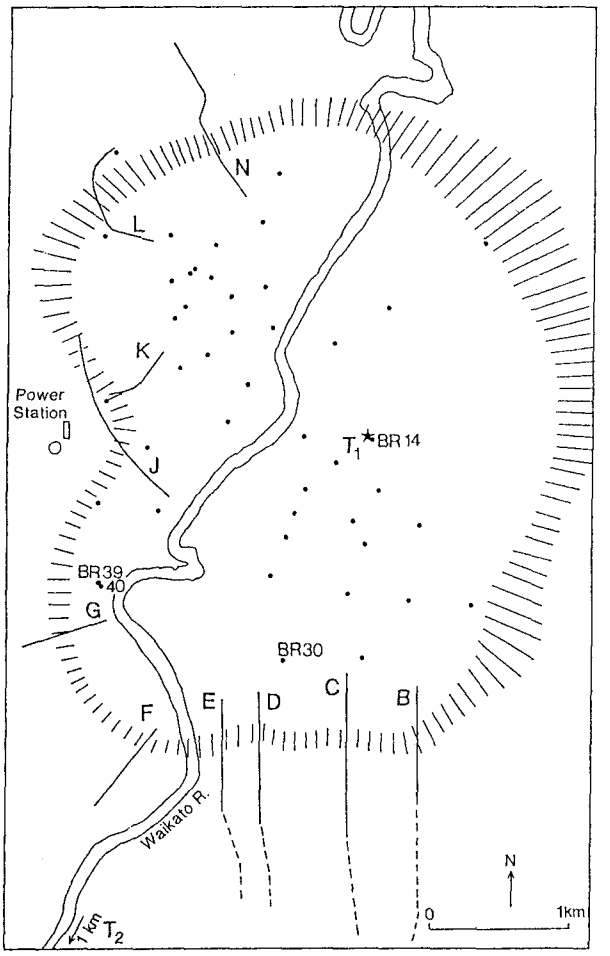


Fig. 1: Layout of multiple-source bipole-dipole array at Ohaaki. $T_1$ and $T_2$ are current electrodes. Measurements with receiver array were made along lines B, C, .. N, at 50 m intervals. Dots show drillholes.

Experiments in 1973-75 showed that some arrangements of the current electrodes allow a clearer definition of the resistivity boundary zone than others. The best electrode arrangement was found to be similar to the Schlumberger layout for which the receiver sites are near the mid-point of the two current electrodes. Thus, for the repeated part of the survey using current electrodes T1 and T2, clearest definition of the boundary was found, as expected, across the southwestern sector.

### Lines B and C

Over the southern parts of these lines (Fig. 2) very little change was found between the resistivities measured in 1975 and 1992. The sharp rise in apparent resistivity over the boundary zone occurs in the same place (to within about 25 m). Thus, there has been no detectable horizontal movement of the resistivity boundary. However, on the inside of the field apparent resistivities in 1992 were significantly smaller (by up to 40 percent) than in 1975.

### Lines D and E

These lines are close together and cover a small region studied in detail by separate resistivity and magnetic surveys in June 1973 (Risk, 1981). In both 1973 and 1975 the resistivity measurements near the boundary zone exhibited some unusual charateristics (i.e. electric transients, anomolous electric field directions and fine structure of the resistivity pattern). However, these unusual characteristics were no longer present in the 1992 resurvey.

Comparison of the 1975 and 1992 data shows that, in the zone where the unusual fine structure had been found in 1973 and 1975, the apparent resistivities are much smaller now (ca. 3 ohm m, Fig 2). Thus, the inside edge of the resistivity boundary appears to have moved south by about 100 m. The anomalous zone now appears to contain low resistivity material. The suggested explanation is that this region has recently been flooded with geothermal water.

### Lines F and G

For these lines in the southwest corner of the field, the curves show large, sharp steps in resistivity across the resistivity boundary. The 1992 curves are similar in shape to the 1975 ones, but are slightly offset, implying that the 1992 resistivities are about 10 - 20 percent smaller than the 1975 values. The boundary appears to have moved southwards by a small amount (up to 20 m), but as this is about the same as the resolution of the survey, the movement is not certain. Near the outside of

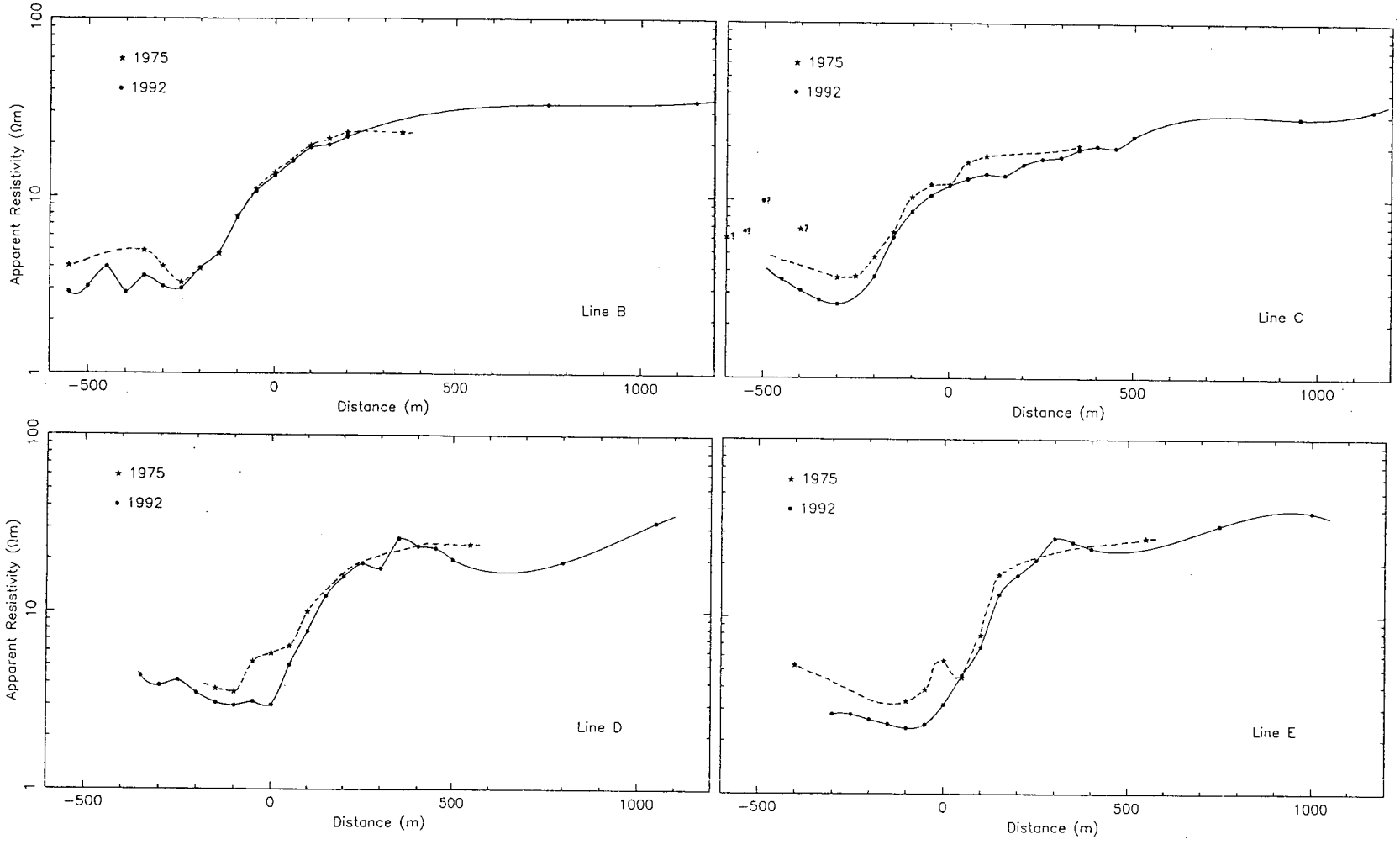


Figure 2: Apparent resistivities measured along lines B, C, D and E in 1975 and 1992. Centre of Field is at left.

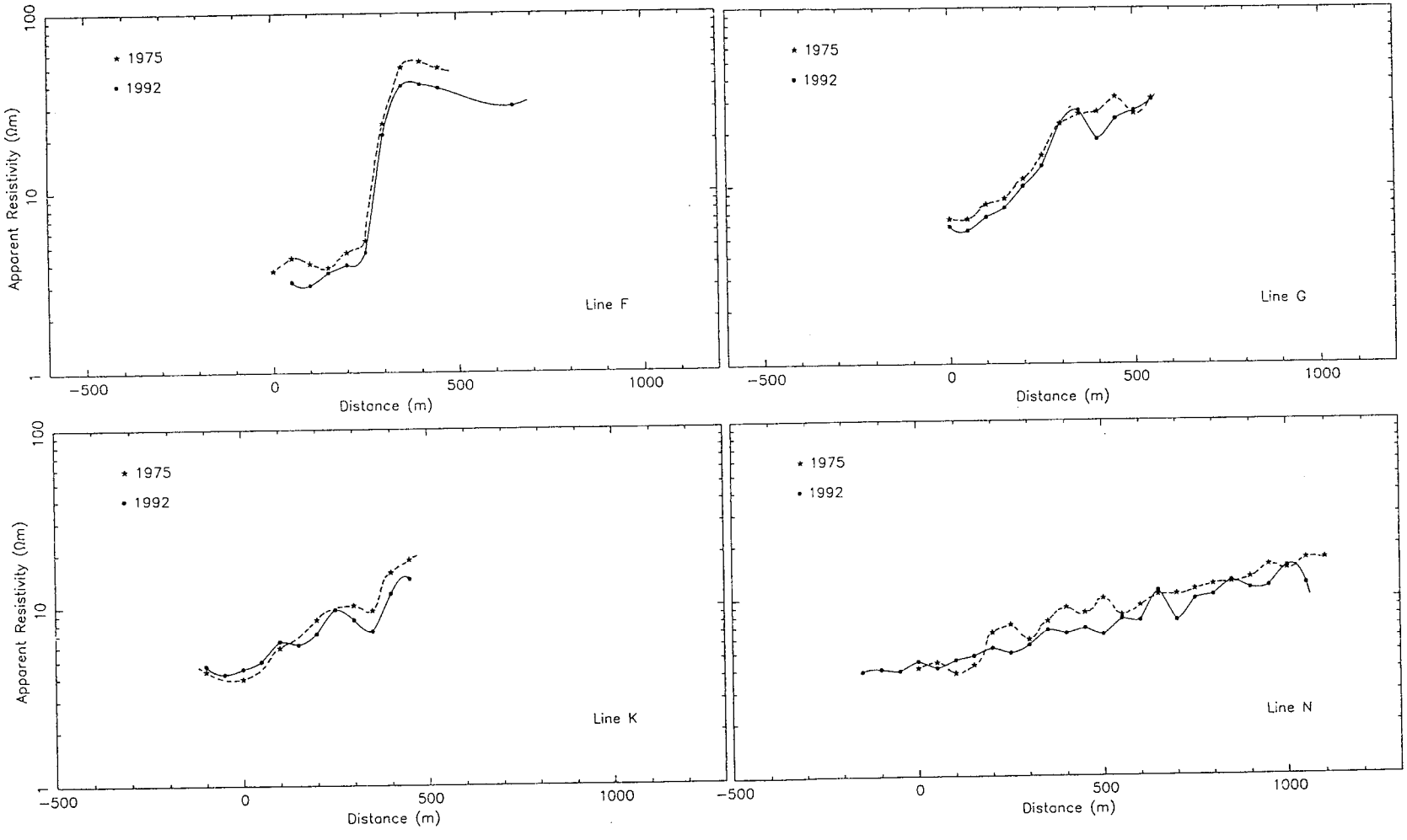


Figure 3: Apparent resistivities measured along lines F, G, K and N in 1975 and 1992. Centre of Field is at left.

line G, the 1992 measurements are disturbed by the presence of the shallow well BRM9, which was not there in 1975.

### Line J

Since the original line J (1975) could not be remeasured because it now runs through the Power Station, a new line J, further north, was measured in 1992. The measurements were found to be very irregular. This is attributed to disturbances caused by the presence of the earth mat at the Power Station, the network of pipes, and other grounded conductive structures near the line.

### Lines K and L

Lines K and L also lie close to the Power Station (Fig. 1). The apparent resistivity curves from line K (Fig. 3) for 1975 and 1992 have similar shapes, but the 1992 curve does not rise as steeply as that for 1975. The differences are more likely to be due to the disturbing effects of conductors associated with the Power Station than to movement of the boundary. Results from Line L are similar.

### Line N

Signal levels were smaller on line N and it was difficult to lay out the 50m x 50m receiver array because of the scrub and blackberry on both sides of the line. This appears to have caused larger-than-usual measurement errors on both surveys and accounts for the scatter of data. On average, the 1992 data are about 20 percent smaller than the 1975 data, and the curves have similar shapes suggesting little change of the resistivity boundary since 1975. However, on line N the resistivity boundary zone is not well delineated by either survey. This appears to be because the (T1-T2) transmitter orientation is not appropriate for this line.

## COMPUTER MODELING

The nearly circular shape of the Ohaaki Geothermal Field as well as the geometric arrangement of electrodes, with one electrode at the centre and the other well outside the field, makes this problem well suited to computer modeling analysis using axially symmetric models (Bibby 1978). With this kind of modeling, the field is simulated as a stack of (up to 100) concentric annular shaped rings. An example of such a theoretical model is given in Figure 4a which shows a radial cross-section. The centre of the field is at the left-hand side, with the boundary of the field at ca. 2 km from the centre.

This model tests the basic premise underlying the use of this resistivity resurveying method; i.e. whether it is possible to detect lateral movements of a vertical resistivity boundary. The model simulates boundary movements and assesses the resulting effects on the apparent resistivity profiles. This is illustrated in Figure 4. Model (i) has the (vertical) boundary in its initial position, while in models (ii), and (iii) it has been moved, respectively 100m and 200m, away from the centre of the field. Corresponding outward movements of the theoretical apparent resistivity curves can be seen, verifying the viability of the method (Fig. 4b).

Other more complex models were also run. These included sloping boundaries and simulating a gradual increase in resistivity across the boundary zone. Various different resistivity-depth profiles were also investigated. This work indicates that shallow structures dominate the apparent resistivity pattern and that many alternative resistivity structures are possible. Thin deeply buried formations are unlikely to be detected.

## DISCUSSION

The eight resistivity profiles remeasured at the same sites in 1992 are all similar in shape to those of the original survey in 1975. Sharp steps of an order of magnitude in apparent resistivity were found on both occasions in the south and south-west of the field. This degree of repeatability suggests that the Schlumberger-like electrode arrangement is appropriate for monitoring the resistivity boundary. The pattern of changes is simpler than that found at Cerro Prieto with the in-line dipole-dipole array (Wilt and Goldstein 1984).

The modeling shows that any large-scale lateral movement of the boundary of the hydrothermal reservoir is expected to be reflected as a movement in the place where the sharpest rise in apparent resistivity occurs. The lines in the south and south-west of the field show sharp resistivity boundaries for which lateral movements of more than 20 - 50 m should have shown up. Such movements between 1975 and 1992 were detected on only lines D and E where the resistivity boundary appears to have moved outwards by about 100m. However, very little outward movement is evident on lines F and G.

In the south of the Ohaaki Field, most of the reinjection of waste water has been into drillholes BR39 and BR40, with a smaller amount going into BR30 (Fig. 1). Since the temperature of this water is about 145 - 150C with chloride concentrations of about 1500 mg/kg, the resistivity of the water would be about 0.5 ohm m. The water is mostly injected into the Broadlands Rhyolite formation at about 500 m depth, and some of it appears to flow south across the resistivity boundary. This probably explains the small southward movement of the resistivity boundary on lines D and E. However, it is not consistent with the lack of any significant southward movement in the resistivity patterns on lines F and G, which are closer to the main injectors (BR39, BR40). Possible explanations are that the reinjected water is flowing outward in thin aquifers, too deep to give an unambiguous apparent resistivity change or that there has been insufficient time for the effects to show up.

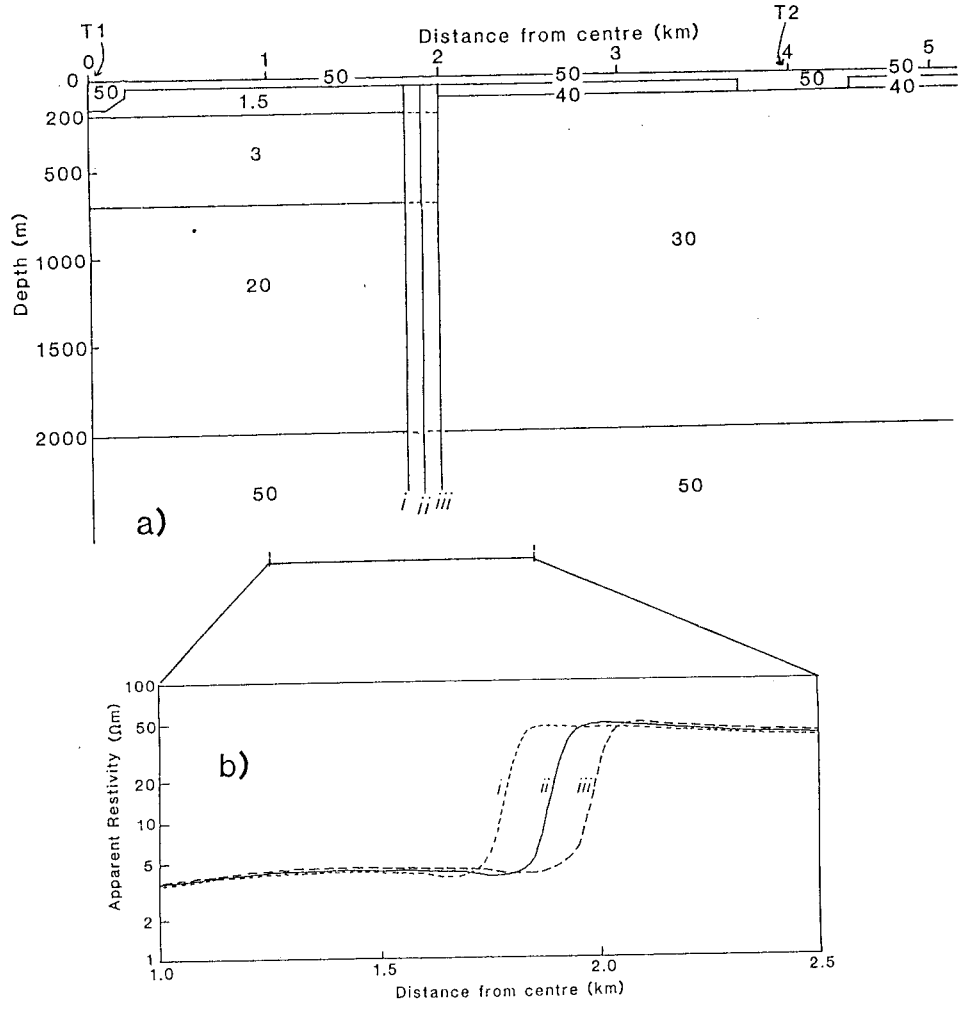


Figure 4: a) Section along a radius of axially symmetric resistivity models of Ohaaki Geothermal Field. Models have vertical boundaries at the edge of the field at distances from the centre of:
(i) 1.8 km, (ii) 1.9 km, (iii) 2.0 km.
b) Apparent resistivity curves for models (i) (ii) and (iii).

Over the 17 years between 1975 and 1992 apparent resistivity values have dropped in most places. The decrease is more pronounced on the inside of the field where apparent resistivities have declined by up to about 40 percent. A large part of this drop is thought to be caused by the redistribution of the conductive reservoir fluids which are being extracted from the centre of the field and reinjected near the southwest edge. This would raise the watertable in the boundary region and decrease the formation resistivity over the south of the field.

However, other causes for the resistivity drop are possible. Calibration and measurement errors may account for up to 10 percent of the drop. There has also been a major change, between the surveys, in the number of drillholes in the field and in the installation of steam pipes and other metal structures at the surface. The new pipework near electrode T1 would be expected to affect the measurements. The biggest change here is that nearby drillhole BR14 is now connected by steam pipes to the other neighbouring bores. A low resistance was measured between electrode T1 and BR14. Thus, in 1992 but not in 1975, some of the current will have entered the ground through bores BR43 and BR44. This increases the effective size of the electrode. The implications of these effects have not yet been fully examined.

## ACKNOWLEDGEMENTS

This work was funded by grants from The NZ Foundation for Research, Science and Technology and the Electricity Corporation of NZ. Fieldwork in 1992 was undertaken by the author, S L Bennie, D J Graham, D E Keen, and R R Reeves.

## REFERENCES

Bibby, H.M., 1978: Direct current resistivity modeling for axially symmetric bodies using the finite element method, Geophysics, 43, 550-562.

Risk, G.F., 1981: Induced polarisation (IP) in the Broadlands Geothermal Field, Proceedings 3rd NZ Geothermal Workshop, University of Auckland, 43-48.

Risk, G.F., 1993: Resurvey of resistivity boundary of Ohaaki Geothermal Field, 1975-92. Proceedings 15th NZ Geothermal Workshop, University of Auckland, 195-200.

Risk, G.F., Macdonald, W.J.P., Dawson, G.B. 1970: DC Resistivity Surveys of the Broadlands Geothermal region, New Zealand. Geothermics Special Issue 2(2): 287-94.

Risk, G.F., Groth, M.J., Rayner, H.H., Dawson, G.B., Bibby, H.M., Macdonald, W.J.P., Hewson, C.A.Y. 1977: The Resistivity Boundary of the Broadlands Geothermal Field. Geophysics Division Technical Report No 123, DSIR, Wellington, 42p.

Wilt, M.J., Goldstein, N.E., 1984: Interpretation of monitoring resistivity data at Cerro Prieto. Geothermics 13, 13-25.

PROCEEDINGS, Nineteenth Workshop on Geothermal Reservoir Engineering
Stanford University, Stanford, California, January 18-20, 1994
SGP-TR-147

# GEOLOGICAL CONTROL ON THE RESERVOIR CHARACTERISTICS OF OLKARIA WEST GEOTHERMAL FIELD, KENYA.

**Peter A. Omenda,**

**The Kenya Power Co. Ltd., P. O. Box 785,
Naivasha, KENYA.**

## ABSTRACT

The reservoir of the West Olkaria Geothermal Field is hosted within tuffs and the reservoir fluid is characterized by higher concentrations of reservoir $CO_2$ (10,000-100,000 mg/kg) but lower chloride concentrations of about 200 mg/kg than the East and North East Fields. The West Field is in the outflow and main recharge area of the Olkaria geothermal system.

Permeability is generally low in the West Field and its distribution is strongly controlled by the structures. Fault zones show higher permeability with wells drilled within the structures having larger total mass outputs. However, N-S and NW-SE faults are mainly channels for cold water downflow into the reservoir. Well feeder zones occur mostly at lava-tuff contacts; within fractured lava flows and at the contacts of intrusives and host rocks.

## INTRODUCTION

The Olkaria Geothermal area is located at about $0^o$ 54'S and $36^o$ 20'E in the Central Rift Valley of Kenya at an elevation of about 2000 m.a.s.l.. The Geothermal area has an aerial extent of more than 100 $km^2$ and has been divided into four fields for ease of development and management, namely; East, North-East, Central and West Fields (Figure 1). The East Field has been generating electricity since 1981 with an installed capacity of 45 $MW_e$. Production drilling has been completed in the NE Field for a 64 $MW_e$ power plant that is expected to be operational by 1996.

The Central and West Fields are still under exploration and eight wells have been drilled in the West Field and two in the Central Field. Out of the eight wells drilled in the West Field, only five could sustain discharge, namely; OW-301, OW-306, OW-305, OW-304D and OW-401. Well OW-304D discharged for 168 days before ceasing production due to calcite scaling. Well OW-307 discharged low enthalpy fluid on vertical discharge test only while well OW-601 could not discharge due to very low permeability but the bottomhole temperature is more than $294^oC$.

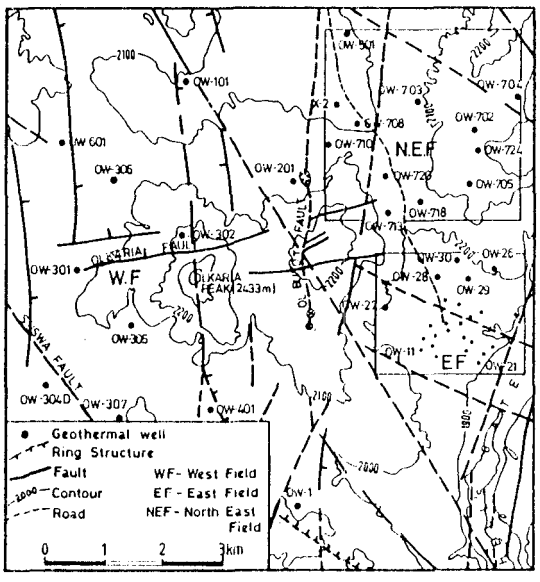


**Figure 1.** Structural Map of Olkaria Geothermal Field showing well sites

## GEOLOGY

The geology of the Olkaria Geothermal area generally shows a division into two based on lithostratigraphy, namely; eastern and western. The eastern section includes; the East, North-East and Central Fields while the western sector has only the West Field. The dividing line between the two sectors is along the N-S Olkaria Fracture (Fault) that passes through the Olkaria hill (Figure 1).

A caldera association has been suggested for the Olkaria geothermal system with the main western collapse margin possibly passing through Olkaria hill but some other workers put it further to the west. Olkaria geothermal system is closely associated with Quaternary volcanism and surface geology is dominated by unconsolidated ashes and comenditic rhyolites, some of which form domes.

The field, being close to the western rift scarps, has major normal east dipping faults that are characterized by N-S and NW-SE trends. Some of these faults are still active and reach the deep levels to tap magma, eg., Ololbutot lava flow. Other

structures also occur, for instance, the Olkaria fault that traverses the Olkaria geothermal area in an ENE-WSW trend is the most important.

The subsurface geology of the Western sector is dominated by semi-welded thick tuffaceous rocks and minor trachytes, rhyolites and basalts. The zone above about 1600 m.a.s.l. is composed of rhyolites, trachytes and unwelded tuffs. Ashes occur on the surface but are underlain by rhyolitic lavas and trachytes. The zone at about 1600 m.a.s.l is interpreted to be a major disconformity in the whole of Olkaria geothermal area and the rocks above it are considered to be of Quaternary age while those below are of Tertiary age. In the eastern fields, the upper zone is underlain by basaltic lava flows that are considered the cap-rock to the geothermal system but none has been identified in the West Field.

Tuff is the main rock in the zone below 1600 m.a.s.l but rhyolites, trachytes, minor basalts and trachy-basalts occur. The tuff is the main reservoir rock for the West Field while the zone above 1600 m.a.s.l., that is largely composed of rhyolites, tuffs and trachytes is cased off in most wells. Dioritic intrusives have been intersected by some wells drilled close to known fault zones. By comparison, the East, North-East and Central fields have the reservoir within trachytes (Figure 2).

## GEOCHEMISTRY

Most wells in the West Field show different reservoir fluid characteristics from those in the East and North-East Fields (Table 2). These characteristics include high reservoir $CO_2$ content (10,000 - 100,000 mg/kg) but low Cl values ($\leq$300 mg/kg) implying that the reservoir is of bicarbonate type. By comparison, the fluid chemistry in the North-East and East Fields have chloride and reservoir $CO_2$ concentrations of more than 300 mg/kg and less than 1000 mg/kg respectively.

A plot on the $Cl\text{-}SO_4\text{-}HCO_3$ diagram (Figure 3) indicates that the fluid in West Field is largely of bicarbonate composition except for well OW-401 which is of mixed chloride-bicarbonate and OW-305 that is of chloride composition. Interpretation of the deep fluid chemistry based on chloride - enthalpy diagram (Figure 4) indicates that there is variable degree of mixing of the reservoir fluid westward with well OW-304D, having chloride concentration of less than 70 mg/kg, being the most diluted. The diluent is both steam heated and cool ground waters.

Hydrothermal mineralogy indicates an abundance of calcite in the reservoir and it occurs in veins where it is the last phase of deposition. The other secondary minerals in the reservoir include; illite, chlorite, vermiculite, gypsum/anhydrite and rarely epidote. On the whole, the mineralogy indicates less than neutral pH conditions in the reservoir.

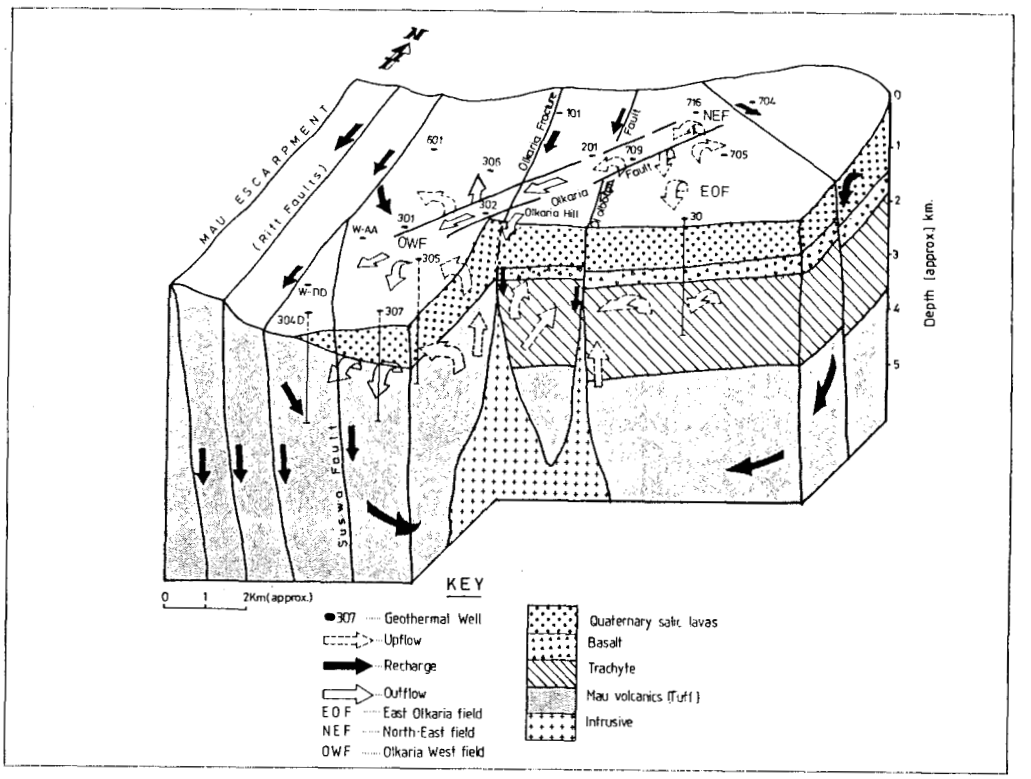


**Figure 2.** Structure and fluid flow patterns in Olkaria Geothermal Field.

**TABLE 1 TOTAL DISCHARGE CHEMISTRY FOR OLKARIA WEST WELLS (mg/kg)**

| WELL | Li | Na | K | Mg | Ca | F | Cl | $SO_4$ | $SiO_2$ | B | $CO_2$ | $H_2S$ |
|---|---|---|---|---|---|---|---|---|---|---|---|---|
| **OW-101** | 2.2 | 498 | 84 | 0.12 | - | 20 | 233 | 9 | 452 | 8.1 | 13364 | 18 |
| | 0.4 | 474 | 82 | 0.06 | 0.6 | 19 | 214 | 8 | 465 | - | 9074 | 23 |
| **OW-201** | 0.7 | 255 | 27 | - | - | 22 | 260 | 15 | 189 | - | 915 | 50 |
| | 0.7 | 641 | 63 | 0.06 | 0.5 | 61 | 599 | 30 | 373 | - | 864 | 21 |
| **OW-301** | 2.4 | 923 | 138 | 0.23 | 1.5 | 42 | 102 | 93 | 333 | - | 24742 | 50 |
| | 1.4 | 1090 | 129 | 0.11 | 0.6 | 65 | 175 | 53 | 333 | 10.2 | 19064 | 1140 |
| **OW-304** | 0.9 | 1339 | 84 | 0.00 | 0.0 | - | 57 | 113 | 280 | 2.0 | 111520 | 23 |
| | 0.9 | 255 | 42 | 0.00 | 1.4 | 38 | 49 | 101 | 262 | 3.9 | 26581 | 9 |
| **OW-305** | 1.6 | 324 | 63 | 0.00 | 0.0 | 32 | 386 | 19 | 471 | 1.4 | 2186 | 91 |
| | 1.4 | 379 | 71 | 0.00 | 0.0 | 30 | 392 | 40 | 483 | 1.6 | 2414 | 89 |
| **OW-306** | 0.8 | 782 | 89 | 0.00 | 0.0 | - | 174 | 69 | 442 | 3.8 | 13504 | 108 |
| | 0.9 | 503 | 21 | 0.00 | 0.1 | 29 | 184 | - | 433 | 4.3 | 14517 | 16 |
| **OW-307** | 1.6 | 684 | 57 | 0.00 | 0.0 | - | 84 | 155 | 159 | 3.5 | 1028 | 0 |
| **OW-401** | 0.8 | 418 | 59 | 0.15 | 0.8 | 14 | 343 | 12 | 385 | | 1972 | 12 |
| | 0.7 | 419 | 61 | 0.03 | 0.3 | 12 | 360 | 12 | 408 | | 2181 | 10 |

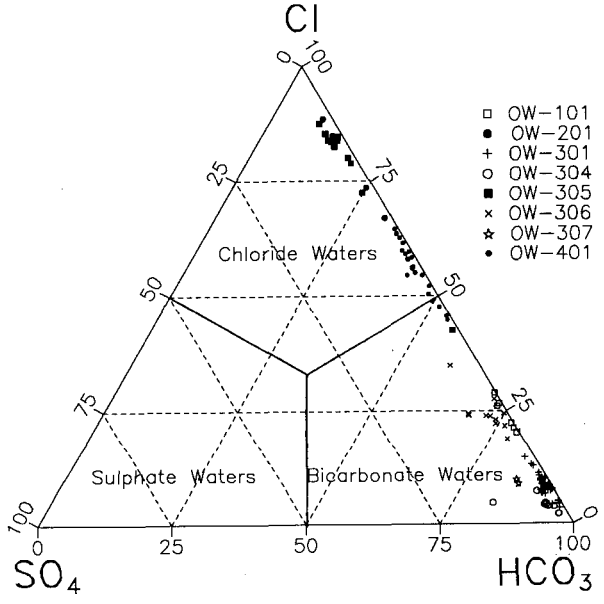


**Figure 3.** Ternary Diagram of Cl-$SO_4$-$HCO_3$

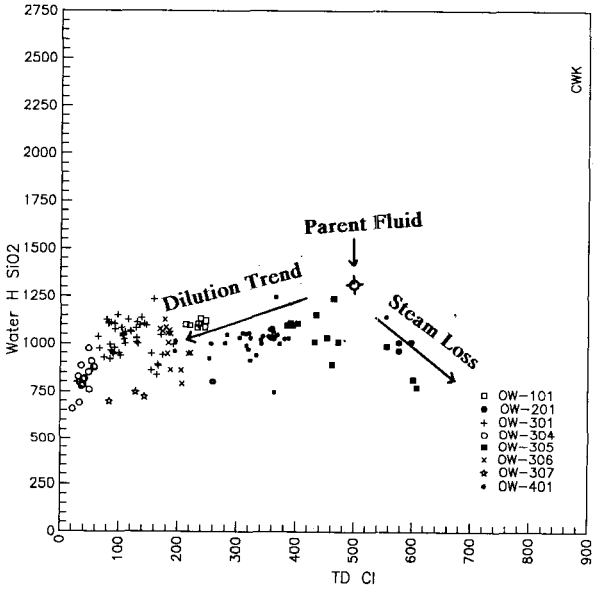


**Figure 4.** Chloride - Enthalpy Diagram

## HYDROGEOLOGY

Hydrological structure of the Olkaria geothermal system is controlled by the following: Mau catchment area to the west; Lake Naivasha at about 5 km to the north and fault structures. The Mau escarpment is considered to be the main recharge area for the geothermal system and the recharge paths are the NW-SE, east dipping rift faults (Figure 2). N-S faults are common in the axial region of the rift and in the Olkaria area, they channel cool waters into the system (Ogoso-Odongo, 1986). Stable isotope studies of the Lake Naivasha water and some geothermal wells drilled close to the N-S faults / fractures indicate comparable isotopic composition between the two waters (Ojiambo and Lyons, 1993) and this shows that the hydrologic gradient in the area is southward and that the N-S faults are important in the transmission of cold water.

The ENE-WSW trending Olkaria fault is considered the most important structure in the whole of Olkaria geothermal area in terms of resource exploitation. The fault zone transects the North-East, Central and West Fields. The upflow of the North-East Field has

been associated with the structure (Ambusso and Ouma, 1991) and it is also possible that the structure could be channeling the outflow westward and hence the high concentration of $CO_2$ in the West Field. It is also possible that some $CO_2$ could be of deep magmatic source discharging through the deep seated rift faults. Such discharges occur in many places along the major rift faults.

Permeability, as indicated by water loss test and heating profiles, is generally low in the West Field and this is due to the abundance of tuffs as the reservoir rock. Though tuffs have good primary permeability, this is often reduced on alteration to clays.

Most important permeability intersected by wells is associated with lithostratigraphic contacts between lavas and tuffs. The lava units are also better transmitters of fluid than tuffs and this can be related to their brittle nature that allows for open fractures that are not possible with tuffs. Some permeability is also associated with dykes as in well OW-304D but in this part of the field, they channel cool fluids into the reservoir (Figure 5).

## DISCUSSION

The Olkaria West Field is largely located within an outflow structure of a system located under Olkaria hill and possibly further to the east. This is shown by the high bicarbonate and low chloride content of the reservoir fluid encountered by most of the wells, except OW-305. Clay analysis of samples from well OW-304D shows that the well has some cold feed zones at depths below 1200 m.a.s.l. (Figure 5). Inter-planar spacing (d) value of more than 16 Å indicate the presence of hydrothermal smectite that is stable at temperatures less than 150 °C thus the coincident zones in the well are interpreted to be cool inflow points. Correlation with lithology in well OW-304D shows that most of the cool inflow points coincide with trachy-basaltic layers which are interpreted to be dioritic intrusives that were injected through N-S faults. Downhole temperature profiles, however, do not show the cool (150 °C) fluid inflow zones in form of temperature inversion (Figure 6). This can be attributed to the fact that these zones may not be the main producers. The well is therefore, considered to define a SW boundary to the system and is possibly within the recharge area. The northern boundary of the system is still uncertain since high temperatures occur in well OW-601 though the well is none-productive.

The other boundaries of the field are defined by downhole temperature inversions that have been observed in some wells, namely; OW-307, OW-401 and OW-302. The southern extent is defined by wells, OW-401 and OW-307 while wells OW-302 marks an eastern boundary. Wells OW-401, OW-101 and OW-302 were drilled within a N-S fault zone and the lower temperatures observed are possibly due to cold water movement through the fault. The importance of fault permeability is indicated by higher total mass output in wells drilled within known fault zones (Figure 1 and Table 2).

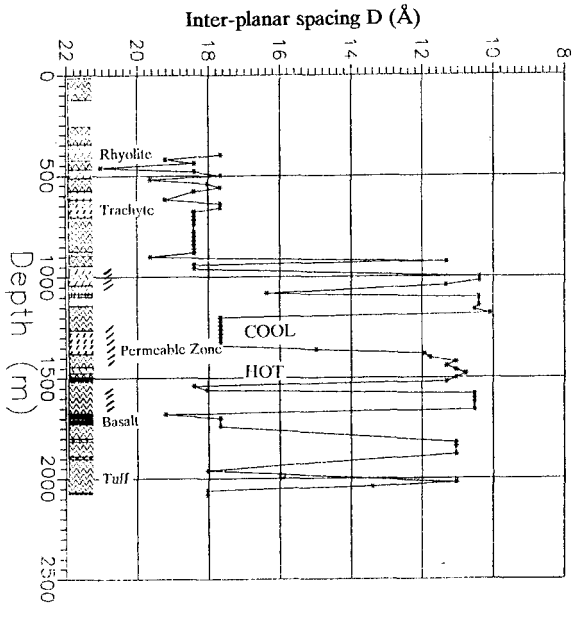


**Figure 5.** Clay data analysis of well OW-304D

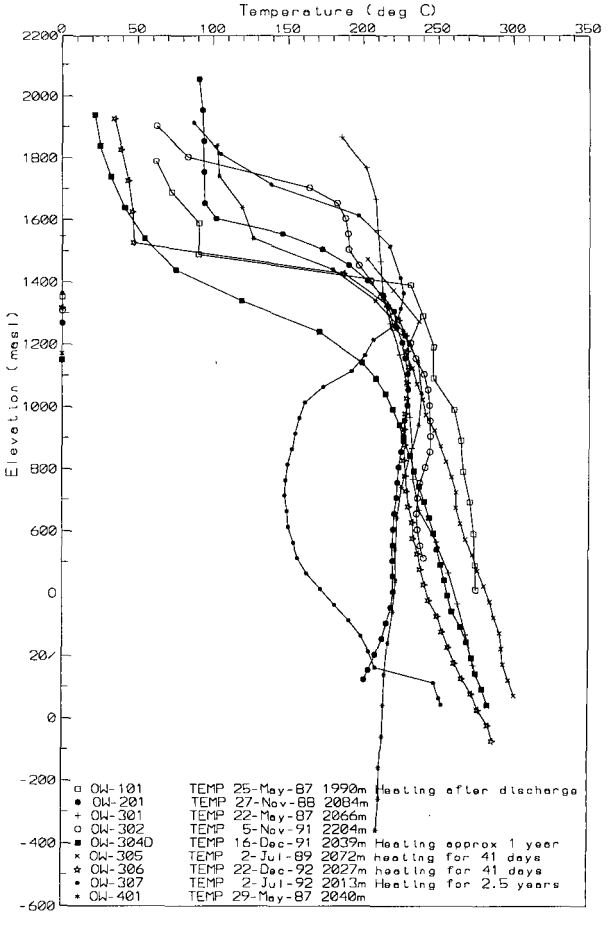


**Figure 6.** Temperature profiles of Olkaria West wells

**Table 2. Summary of the Well Properties**
(After Ouma, 1993)

| Well | KH dm | Inject. kg/s/ba | Enthal kJ/kg | Mass kg/s | Power ($MW_e$) |
|---|---|---|---|---|---|
| 101 | 5.0 | 5.0 | 1060 | 16.0 | 1.2 |
| 201 | 3.1 | 1.7 | 1050 | 35.0 | 1.5 |
| 301 | 4.2 | 4.4 | 1600 | 27.9 | 5.0 |
| 302 | 4.4 | 1.9 | 1140 | - | |
| 305 | 2.2 | 7.8 | 2085 | 5.8 | 1.7 |
| 306 | - | - | 1037 | 12.9 | 1.2 |
| 307 | - | - | - | - | - |
| 401 | 2.8 | 0.9 | 1030 | 21.0 | 1.6 |
| 601 | - | - | - | - | - |
| 304D | - | - | - | - | - |

The resource area in the West Field is about 6 $km^2$, however, its exploitation will require some techniques of handling calcite scaling in the wellbore and reservoir. Using estimates of power generation of 11 $MW_e/km^2$ obtained by reservoir simulation studies of the East Field (Bodvarsson and Pruess, 1988), about 66 $MW_e$ can be produced from the field for 25 years. However, the high $CO_2$ concentration may hinder its realization due to calcite scaling that is expected to occur both in the reservoir and bore of most wells.

## CONCLUSIONS

1. Most areas of the west field are in an outflow structure and calcite scaling is expected to occur both in the reservoir and well bore.

2. The western sector of the field is in the main recharge area of the Olkaria geothermal system.

3. Permeability is associated with lithostratigraphic contacts, fractured lava units and fault zones.

4. About 66 $MW_e$ can be generated for 25 years in the field.


## ACKNOWLEDGEMENT

I thank the management of Kenya Power Company Ltd. for allowing me to publish this paper.


## REFERENCES


Ambusso, W. J. and Ouma, P. A. (1991), "Thermodynamic and permeability structure of Olkaria North-East Field: the Olkaria fault", Geothermal Resources Council Transactions Vol. 15 pp 237-242.

Bodvarsson, S. G. and Pruess, K. (1988), "Numerical Simulation Studies of the Olkaria Geothermal Field", Report prepared for KPC Ltd. Restricted.

Ojiambo, B. S. and Lyons, W. B. (1993), "Stable Isotope composition of Olkaria Geothermal Field fluids, Kenya. Geothermal Resources Council Transactions, V. 17 pp 149-154.

Ogoso-Odongo, M. E., (1986), "Geology of the Olkaria Geothermal Field", Geothermics Vol. 15 No. 5/6 pp 741 - 748.

Ouma, P. A. (1993), "Analysis of Well Test Data for Olkaria West Field and Preliminary Assessment of its Power potential", Proceed. 15 Th. NZ Geoth. Workshop p 331-336.

PROCEEDINGS, Nineteenth Workshop on Geothermal Reservoir Engineering
Stanford University, Stanford, California, January 18-20, 1994
SGP-TR-147

# Use of Slim Holes for Reservoir Evaluation at the Steamboat Hills Geothermal Field, Nevada, U.S.A.

Jim Combs
Geo Hills Associates, Los Altos Hills, California 94022

Colin Goranson
Geological Engineering Consultant, Richmond, California 94805

## ABSTRACT

Three slim holes were drilled at the Steamboat Hills Geothermal Field in northwestern Nevada about 15 km south of Reno. The slim holes were drilled to investigate the geologic conditions, thermal regime and productive characteristics of the geothermal system. They were completed through a geologic sequence consisting of alluvium cemented by geothermal fluids, volcaniclastic materials, and granodiorite. Numerous fractures, mostly sealed, were encountered throughout the drilled depth; however, several open fractures in the granodiorite, dipping between 65 and 90°, had apertures up to 13 mm in width. The depths of the slim holes vary from 262 to 277 m with open-hole diameters of 76 mm. Pressure and temperature logs gave bottom-hole temperatures ranging from 163 to 166° C. During injection testing, downhole pressures were measured using capillary tubing with a surface quartz transducer while temperatures were measured with a Kuster temperature tool located below the capillary tubing pressure chamber. No pressure increase was measured at reservoir depths in any of the three slim holes while injecting 11 kg/s of 29°C water indicating a very high permeability in the geothermal reservoir. These injection test results suggested that productive geothermal fluids could be found at depths sufficient for well pumping equipment and at temperatures needed for electrical power production using binary-type conversion technology.

## INTRODUCTION

The Steamboat Springs Geothermal Area was classified as a Known Geothermal Resource Area ("KGRA") by the United States Geological Survey. The KGRA is located about 15 km south of Reno, Nevada along side of Highway 395 (see, Figure 1). Commercial geothermal development in the Steamboat Springs area began in the early 1900's. Initial development used geothermal fluids from hot spring discharge for heated baths and swimming pools. Wells were drilled beginning in the 1920's in order to obtain more reliable supplies of geothermal fluids. The first geothermal well was drilled in 1920, located at a site about one mile south of the Far West Capital, Inc. ("FWC") geothermal electric power development area. Additional wells located at the Steamboat Spa, just across Highway 395 to the south of the FWC development area, were drilled in the late 1930's through the late 1980's. Several of the Steamboat Spa wells are still in use.

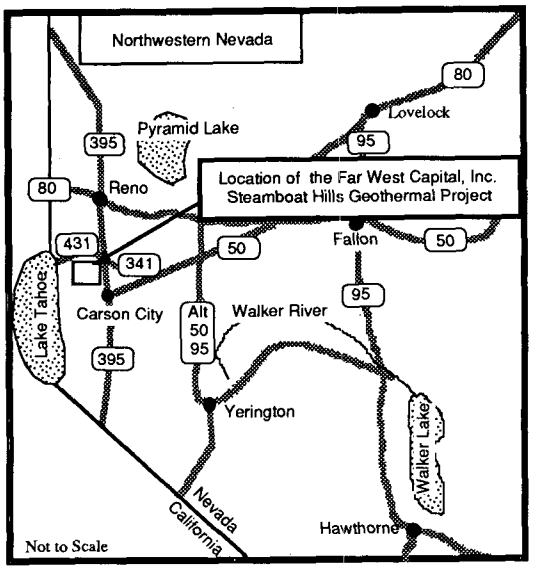


**Figure 1.** Location map of the Steamboat Hills Geothermal Field, Nevada.

Geothermal investigators from the United States Geological Survey, principally Donald E. White (1967, 1968), have conducted scientific studies of the Steamboat Springs geothermal area beginning in 1945 and continuing through the 1960's and 1970's (Thompson and White, 1964; White, et al., 1964; Silberman, et al., 1979) into the 1990's (Janik and Mariner, 1993). The early exploration efforts consisted of drilling small-diameter auger holes to depths of 4 m and core holes to depths up to 209 m. These shallow holes were completed to assist in defining the hydrogeologic characteristics of the geothermal hot spring system. Temperature versus depth, water level, fluid chemistry and geological data were obtained from the boreholes. Based on his interpretation of the data, White (1973) suggested that the Steamboat Springs hot-water system did not have adequate volume, temperature, or permeability to maintain commercial production of electricity.

Nevertheless, Gulf Oil Company and Phillips Petroleum Company began a joint geothermal drilling project in the late 1970's through the 1980's. About 25 shallow thermal gradient holes were drilled during this period. Additionally, 14 intermediate-depth stratigraphic test holes were drilled in the Steamboat area. Two large-

diameter geothermal production wells were drilled in 1979 and 1980. In the mid-1980's, Chevron Geothermal Company acquired the Phillips Petroleum interests in the Steamboat area and Yankee Caithness Joint Venture ("YCJV") acquired the Gulf interests. Caithness Power, Inc. ("CPI") and YCJV acquired the Chevron interest in Steamboat. CPI drilled two additional geothermal production wells southwest of the FWC acreage in the mid-1980's. A 12 $MW_{net}$ single flash steam geothermal power plant began operations in 1988. The CPI power plant operations have produced over 20 billion liters of geothermal fluid to date and about 17 billion liters of the fluid have been injected into the geothermal reservoir below the CPI leases (Goranson, et al., 1990).

During the 1980's, Geothermal Development Associates ("GDA") acquired Sierra Pacific Power Company ("SPPCo") leases that are now a portion of the FWC Steamboat Hills lease area. FWC has geothermal mineral leases on approximately 202 hectares. Three geothermal production and three injection wells were drilled by GDA on the SPPCo leases. Commercial production of electricity was commenced at Steamboat Hills in 1987 at which time a small 5 $MW_{net}$ power plant, Steamboat #1 ("SB#1") was completed, certified and owned by a public partnership formed by FWC. SB#1 began selling electricity to the local public utility, SPPCo. SB#1 consisted of seven air-cooled binary-type Ormat Energy Converter Units utilizing the geothermal fluids to heat the working fluid, n-pentane, a hydrocarbon used to operate the turbines. FWC took over geothermal operations of the SB#1 power plant in the latter portion of 1990. An additional 1.7 $MW_{net}$ unit, Steamboat #1A ("SB#1A"), was added at a later date. These units have been continually operating with the use of geothermal fluids since 1987. To date over 39 billion liters of geothermal fluid have been produced for power plant operations and 33 billion liters have been injected (Goranson, et al., 1991).

In January 1991, FWC entered into two power sales contracts with SPPCo each for 12 $MW_{net}$ electricity capacity to be supplied from two proposed new power plants, Steamboat #2 and #3 ("SB#2/3"), to be situated contiguous and to the east and south of the site of SB#1 and SB#1A. FWC assigned approximately 50 hectares of its Towne geothermal lease for this project (Figure 2).

The slim-hole drilling program was designed to determine whether productive geothermal fluids could be found at depths sufficient for well pumping equipment and at temperatures needed for electrical power production at SB#2/3 utilizing air-cooled, binary-type, turbine-generator units.

## PROGRAM DESCRIPTION

Since the major cost of geothermal exploration in fractured volcanic and igneous areas is the high cost associated with conventional rotary drilling, it would be desirable to use low-cost slim holes with diameters less that 100 mm for exploration and definitive reservoir assessment (Combs and Dunn, 1992). While the drilling of slim holes for geothermal exploration and initial reservoir evaluation is common in several countries (Garg and Combs, 1993), the technique has not been widely used in the United States before the present program.

The three slim holes (TH#1, #2, and #3) reported on in the present paper were drilled and injection tested during 1991 to investigate the geological conditions, thermal regime, and productive characteristics of the geothermal system in the northeastern portion of the Steamboat Hills hot-water system. The slim-hole locations (Figure 2) were chosen to investigate the subsurface conditions along a series of northwest trending surface lineaments noted in surface geologic investigations and on air photos (van de Kamp, 1991).

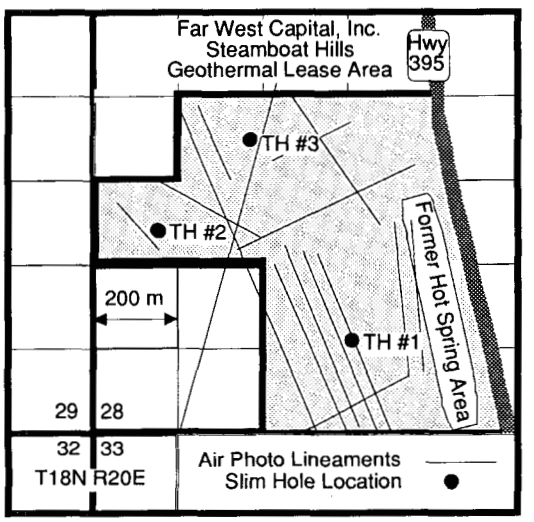


**Figure 2.** Map of FWC Towne lease showing surface lineaments and locations of the slim holes.

A Longyear vertical mounted core rig was used to drill the slim holes. Since it was known from the drilling of production and injection wells on the offset acreage that the subsurface would consist primarily of fractured granodiorite, the core rig was chosen to be able to obtain geological samples from the productive intervals (something that had not been possible on the existing geothermal wells in the area that had been rotary drilled). Furthermore, the slim-hole core rig was selected for its ability to drill under loss of circulation conditions while still obtaining geologic samples.

The depths and completion programs for the slim hole were designed to test the fracture sets in subsurface between the depths of 200 m to 300 m. The slim holes were cased to about 200m in order to eliminate interzonal flow from the fractures above this depth. If the deeper fracture sets found in the area are productive, it would allow for well pumps to be set to depths greater than 200 m, possibly to depths of 225 m. This would allow the geothermal production wells to be pumped at flow rates higher that existing wells in the area and allow spacing between wells to be less than with existing ones.

## GEOLOGICAL AND STRUCTURAL SETTING

A detailed description of the geology, hydrology, and hydrothermal alteration is beyond the scope of this paper, but a general description of the geology and

structure of the Steamboat Hills geothermal area is provided based on the work of van de Kamp (1991). The geology of the Steamboat Springs area was mapped in detail by Thompson and White (1964) and their work forms the basis for the geological evaluation of the geothermal system under the FWC leases in the northeastern Steamboat Hills area. The geothermal system covers about 6.5 $km^2$ and includes hot springs and numerous fumaroles associated with siliceous sinter terraces.

The oldest rock unit present in the northeast Steamboat Hills is the granodiorite of Jurassic-Cretaceous age (estimated as 150 to 80 mya). Younger sediments, volcanic rocks and alluvial deposits overlie the granodiorite. The granodiorite underlies the FWC leases and is penetrated by several geothermal wells. It ranges from very fine to coarse-grained and generally shows little internal structure other than faults, fractures, and joints. Quartz veins as well as aplite and pegmatite dikes are found within the granodiorite. In outcrop, it is apparent that there has been fracturing and faulting in the granodiorite.

An unconformity between the granodiorite and the overlying Miocene Alta Formation represents a time hiatus of about 60 my. The hiatus represents the late Cretaceous and early Tertiary Laramide uplift and erosion event which removed several kilometers thickness of older metamorphic rocks into which the granodiorite was intruded to expose the granodiorite. These volcanic units represent volcanic activity which accompanies the Oligocene-Miocene tectonic extension and faulting in the Basin and Range Province, which began about 17 mya (Stewart, 1980). In the FWC lease area, these volcanics and volcaniclastic sediments are up to 150 m thick. The Alta Formation is an early to mid-Miocene soda trachyte occurring mostly as lava flows and pyroclastics. The Kate Peak Formation, overlying the Alta Formation, is late Miocene to Pliocene age and is composed of andesitic volcanic flows and tuff-breccias up to several tens of meters thick.

Above the Tertiary volcanics, there is an erosional unconformity representing late Pliocene and Pleistocene uplift and erosion. This event caused erosion of volcanics and granodiorite toward the south. Alluvium now covers the erosionally thinned volcanics and granodiorite southward across the FWC lease area. The alluvial deposits range up to 100 m thick and over much of the area are cemented by silica deposited from Pleistocene to Recent hot springs which flowed from fractures in the underlying bedrock. Additionally, there are common silica sinter deposits overlying the alluvium in areas where hot springs flowed to the surface. Silberman, et al. (1979) provide data suggesting that the Steamboat Hills hydrothermal system has been active, probably intermittently, for the last 2.5 my. Faulting appears to be the principal structural control for subsurface fluid flow. Thermal fluids are meteoric in origin, and the heat source is believed to be a slowly cooling, shallow intrusive body, possible of rhyolitic composition.

The northeastern Steamboat Hills which is part of the larger Steamboat Hills structural block was uplifted relative to areas to the east, north, and west in late Tertiary and Recent times. The uplift is bounded by steep dipping north-northeast and east-northeast trending normal faults with displacement of tens to hundreds of meters or more. Bedding strikes range from northeast to northwest, while measured dips range from 45° to 90°. Cenozoic warping and block faulting are responsible for the present mountainous topography. At least three systems of faulting have been recognized in the Steamboat Hills (Figure 2). One set strikes northeast, parallel to the axis of the Steamboat Hills. A second set, essentially at right angles to the first, strikes northwest. The third set of faults strike north-northeast and are prominent on the sinter terrace of the dormant hot springs. In the distant past, this fault zone issued geothermal fluids to the surface where active hot springs and silica sinter precipitation occurred, similar to the modern situation at the Steamboat Hot Springs located to the east of the FWC leases.

## DRILLING AND COMPLETION DATA

Each of the slim holes was drilled through a sequence of alluvium and sinter, volcaniclastic materials, and granodiorite (Figure 3). The final completion of the slim holes consisted of a surface casing of 114 mm diameter, an intermediate casing of 89 mm diameter, and a 70 mm open-hole section to total depth. For each of the slim holes, a 101 mm hole was drilled and cored to about 30 m and was then opened to 190 mm with a tricone bit. Only partial core recovery occurred above about 30 m in each of the slim holes. After coring to depths ranging from 30 m in TH#1 and TH#2 and to 49 m in TH#3, a 114 mm-diameter, schedule 40, steel threaded pipe was set and cemented to surface. A 140-mm Hydril blowout preventor with a 122-mm gate valve located below the BOP was used for well control.

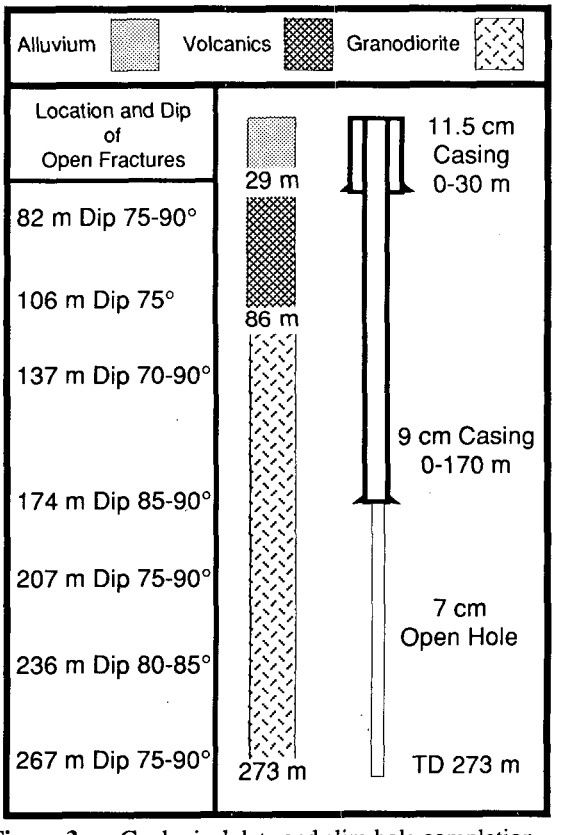


**Figure 3.** Geological data and slim hole completion for TH#1.

The slim holes were originally planned to have only a 114-mm casing set to about 30 m and then completion with a 101-mm (HQ size) open-hole to total depth. However, due to numerous open fractures being encountered between 82 m and 152 m in TH#1, it was decided to set an intermediate casing of 89-mm diameter to about 175 m. Casing to this depth would allow for an injection test to be performed on open fractures encountered below 175 m. The depth of the intermediate casing was 169 m in TH#1, 183 m in TH#2, and 201 m in TH#3. Only partial returns were obtained during cementing of the casing.

After setting the 89-mm casing, partial to complete loss of circulation was encountered after drilling out into the granodiorite. The slim holes were drilled using a 74-mm (NQ size) core bit to total depths of 272 m in TH#1, 262 m in TH#2, and 277 m in TH#3. Essentially 100% core recovery was obtained through the lower section of each of the slim holes. The slim holes were drilled during the time period of 12 July to 10 August 1991 and completed in 10 to 11.5 days with average drilling rates of 1.8 to 2.4 meters per hour and at a cost of approximately $280 per meter.

## SUBSURFACE GEOLOGICAL DATA

Data from geothermal wells drilled in the area indicate that productive geothermal horizons lie below depths of about 125 m in fractured volcanics and granodiorite. The shallow alluvium has been cemented and hydrologically sealed. Granodiorite situated below the shallow alluvium is fractured and also sealed with silicic and carbonaceous materials to depths less than 150 m. To the north of the FWC leases, subsurface data suggest that a hydrologic boundary exists.

The generalized subsurface geological information for the three slim holes is summarized in Table 1. Pleistocene and Holocene alluvium and siliceous sinter deposits make up the geological section from the surface to the underlying volcanics. Much of the alluvium is cemented and/or replaced by silica as vuggy, layered sinter and solid, cherty texture deposits. Measured dips of the layers are 0° to 40° with most in the 5° to 15° range. The sinter is generally hard and granular to glassy in texture with eroded and re-cemented sinter fragments being common.

Gray and gray-green pyroclastic (volcaniclastic) deposits of the Miocene-Pliocene Kate Peak Formation make up the next sequence in the subsurface column. The rocks are generally hard and competent, but there are short intervals of rocks severely altered to clays. These pyroclastic deposits are thin to thick bedded with measured dips of 5° to 40°, many dips are 20° to 30°. There is a sharp, but non-faulted, contact with the slightly weathered granodiorite below.

The upper one-half to one meter of the Cretaceous granodiorite is brown-red, hard, silica-cemented rock, apparently weathered prior to deposition of the overlying Kate Peak Formation. A fine to medium grained granodiorite is the major portion of the rocks penetrated by the slim holes. The granodiorite has no intrinsic permeability, nor is there any appreciable rock matrix porosity. The granodiorite has essentially no fluid storage capacity and all fluid flow within the granodiorite is confined to fractures. The rock is generally hard and only slightly altered to chlorite and clay minerals with abundant minute pyrite crystals. Apparently there was an early stage of chloritic alteration and fracturing in the granodiorite followed much later by fracturing related to geothermal processes. In the later stage of fracturing, there was also chloritic alteration plus filling of fractures with calcite, chlorite, silica, and minor amounts of heavy-metal mineralization.

**Table 1.** Summary geological data from the slim holes.

| Slim Hole Name | Depth Interval (m) | Rock Type |
|---|---|---|
| TH#1 | 0-29 | Alluvium and Sinter |
| | 29-86 | Volcanics |
| | 86-272 | Granodiorite |
| TH#2 | 0-21 | Alluvium and Sinter |
| | 21-59 | Volcanics |
| | 59-262 | Granodiorite |
| TH#3 | 0-17 | Alluvium and Sinter |
| | 17-138 | Volcanics |
| | 138-277 | Granodiorite |

## FRACTURE DATA

Numerous fractures were encountered throughout the drilled depth of all of the slim holes. There are fractures in both the volcanics and the granodiorite portion of the slim holes. Most of the fractures are cemented tight with calcite and silica and are thus ineffective for fluid transmission. However, significant open fractures, which occur in the same subsurface intervals as loss of circulation, were found at several depths. For example, the depth intervals and dip of the open fracture zones in slim hole TH#3 are presented in Table 2.

**Table 2.** Depth interval and dip of the open fracture zones in slim hole TH#3.

| Depth Interval (m) | Dip (degrees) |
|---|---|
| 152 | 55 |
| 155 | 55-60 |
| 219 | 75 |
| 222 | 75 |
| 232-234 | 72-90 |
| 242-243 | 80-90 |
| 273-274 | 65 |

The data clearly indicate that the open fracture zones are steeply dipping in TH#3. This is also the case for the other two slim holes, TH#1 (see Figure 3) and TH#2. The open fractures range from 1.3 mm to 130 mm in width with calcite and/or silica lining the walls so that the actual open width of the fractures vary between 1.3 mm and 13 mm wide and up to 150 mm in length. Open fractures of this size can provide permeability necessary for subsurface geothermal fluid movement within the granodiorite. Adjacent and parallel to some of these steeply dipping fractures are 50 to 150 mm wide protomylonites indicative of shearing. Dips of the open fractures vary between 65° to 90°. The direction of fracture dip and strike is essentially unknown. However, surface geological mapping and structural information suggest an easterly dip and a north to northwest strike (van de Kamp, 1991). The recovery of cores has allowed for a much

better understanding of the nature of the geothermal reservoir system.

## TESTING OPERATIONS

The slim holes were first logged for downhole temperature and pressure about 2 or 3 days after drilling was completed. A few days after these initial downhole temperature and pressure logs were run, an injection test was carried out to determine the productivity of the fractures located in the open-hole section in each of the slim hole.

Downhole pressures were measured with capillary tubing attached to a surface quartz transducer. Temperatures were measured with a Kuster temperature tool with a 38-204°C temperature range located below the capillary tubing pressure chamber. Surface wellhead pressure was measured with a 2.1 MPa pressure gauge. Capillary tubing pressure was measured with a 6.2 MPa quartz transducer. The injection pump consisted of a Gardner Denver 5 x 6 duplex mud pump. Injection rate was measured by counting strokes on the duplex pump and by measuring the water level in the 2.4 m x 2.4 m x 12 m long Baker tank used for test water storage.

During the injection testing, fluids at a temperature of 29°C were pumped into the open-hole section of the slim holes at a rate of 11 kg/s for about two hours. The original injection test program for each of the slim holes called for the pressure and temperature tools to be set about 250 m depth; however, as discussed below, this was not possible in TH#1.

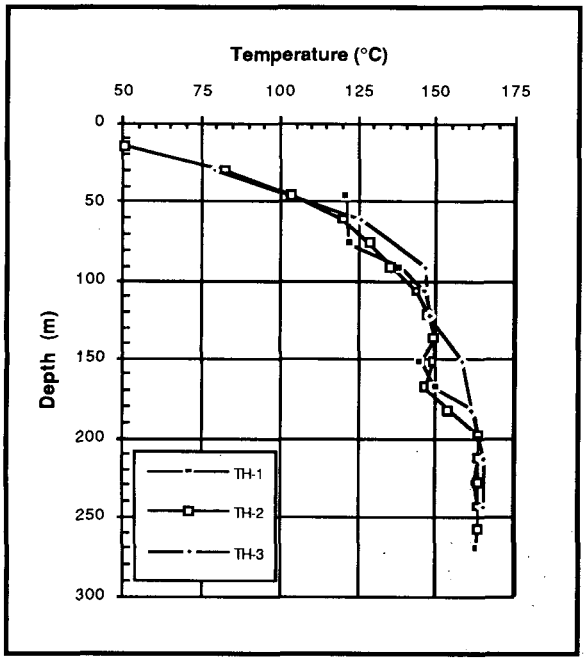


**Figure 4.** Temperature-depth curves for the three slim holes at Steamboat Hills Geothermal Field.

## RESULTS AND DISCUSSION

The maximum downhole temperature in TH#1 was 163°C, 164°C in TH#2, and 166°C in TH#3. However, since the temperatures were measured about 2 or 3 days after drilling was completed, thermal equilibrium would not have been attained. Furthermore, as will be seen from the discussion below and from the shape of the temperature-depth curves (Figure 4), the interzonal flow and mixing of fluids caused by drilling the boreholes have essentially made it impossible to determine the in situ subsurface temperatures. In other words, the actual temperature of fractures below approximately 175 m can not be determined due to the wellbore fluid circulation induced by the open-hole section of the borehole.

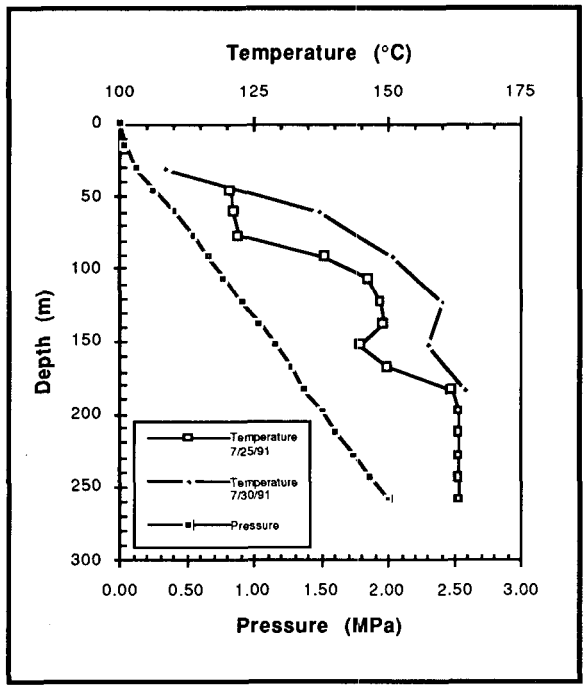


**Figure 5.** Pressure and temperature versus depth for slim hole TH#1.

Downhole temperature data from large-diameter geothermal production wells in the area suggest that Downhole quasi-equilibrium temperatures will be at a minimum of between 168°C to 171°C. However, chemical geothermometry data from fluid samples taken from the now non-flowing hot springs and from the nearby geothermal production wells of CPI indicate that temperatures as high as 200°C may be encountered in the area (Janik and Mariner, 1993).

The downhole pressure measurements indicate that a single phase hot-water reservoir was encountered in the subsurface between about 60 and 275 m in each of the slim holes. Based on the pressure data, the water level in TH#1 is at 10 m, 9 m in TH#2, and 11 m in TH#3.

The TH#1 slim hole was first logged for downhole temperature and pressure on 25 July 1991. The temperature-depth data are shown in Figure 5; however, the pressure tool failed to operate properly. The data show an isothermal zone between 175 m and 272 m. This isothermal condition (and the injection test data) indicates that fluid is circulating between open fractures, using the wellbore of the slim hole as a flow path.

During the injection test on TH#1, the downhole equipment would not readily pass 186 m. The geological data indicates that a short clay interval exists at this depth. Since there was a possible risk of losing the equipment if this zone was traversed, it was decided to choose this depth as the maximum depth for logging during the injection test. The data obtained during the injection test are presented in Table 3. No wellhead pressure was observed during injection at a rate of 11 kg/s with 29°C fluid. The downhole temperature data show that the slim hole was accepting fluid below the 186-m depth since the temperature cooled to approximately 38°C at 186 m.

**Table 3.** Time, pressure, temperature, and injection rate data during testing of TH#1.

| Time (min) | Press @ 186m (MPa) | Temp @ 186m (°C) | Inj Rate (kg/sec) | Comments |
|---|---|---|---|---|
| 0 | 1.59 | 164 | 0 | |
| 5 | 1.59 | 164 | 0 | |
| 10 | 1.59 | 60 | 6.3 | Start Injection |
| 15 | 1.49 | 49 | 6.3 | |
| 20 | 1.45 | 149 | 0 | Stop Injection Change Rate |
| 25 | 1.63 | 157 | 0 | Purge Tubing |
| 30 | 1.59 | 43 | 11 | Start Injection |
| 35 | 1.58 | 38 | 11 | |
| 40 | 1.57 | 38 | 11 | |
| 45 | 1.56 | 38 | 11 | |
| 50 | 1.56 | 38 | 11 | |
| 55 | 1.56 | 38 | 11 | |
| 60 | 1.56 | 38 | 11 | |
| 65 | 1.56 | 38 | 11 | |
| 70 | 1.56 | 38 | 11 | |
| 75 | 1.56 | 38 | 11 | |
| 80 | 1.55 | 38 | 11 | |
| 85 | 1.55 | 38 | 11 | |
| 90 | 1.55 | 38 | 11 | |
| 95 | 1.80 | 33 | 11 | Purge Tubing |
| 100 | 1.60 | 38 | 11 | |
| 105 | 1.60 | 38 | 11 | |
| 110 | 1.60 | 38 | 11 | |
| 115 | 1.60 | 38 | 11 | |
| 120 | 1.60 | 38 | 11 | Stop Injection |
| 125 | 1.60 | 82 | 0 | |
| 130 | 1.60 | 149 | 0 | |
| 135 | 1.60 | 161 | 0 | |
| 140 | 0.085 | | 0 | Atm Reading |

The pressure data from TH#1 shows that there was no pressure increase at 186 m due to injection of 11 kg/s. However, the fact that fluid was exiting the slim hole below the pressure measurement point hampers the data interpretation. The analysis is not straight forward due to the fact that the density of the injected water is greater than the density of fluid in the wellbore and reservoir below 186 m. In addition, frictional fluid pressure losses develop due to the fluid flow between the 186-m depth of pressure measurement and the point that fluid exits the wellbore. There are three competing pressure changes due to the flow of injected fluid below the 186-m pressure measurement point; specifically, (1) pressure increase due to frictional fluid flow, (2) pressure increase due to fluid flow into the reservoir system, and (3) pressure decrease due to the difference in injected fluid density versus wellbore and reservoir fluid density. The pressure change that is of interest for this analysis is the increase in pressure due to fluid flow into the fractures in the geothermal reservoir.

The frictional pressure losses and the density induced pressure decreases can be readily calculated. Using the parameters measured in the injection test and assuming that fluid is exiting the slim hole at the 262-m depth, which is a reasonable assumption based on the temperature data showing fluid flow between fractures located at 175 m to 262 m, the decrease in pressure due to density differences is determined to be about minus 0.066 MPa. Then, calculating the Reynolds Number of approximately 190,000 which implies for rough pipe a friction factor of about 0.019, the pressure change due to frictional fluid flow is about plus 0.066 MPa. This analysis indicated that the decrease in pressure due to density changes and the increase in pressure measured at 186 m from frictional losses will offset each other. The fact that there was no pressure increase measured at 186 m (see, Table 3) suggests that there were no increases in pressure due to flow of injected fluid into the reservoir system. Assuming the resolution of the pressure measurement device is 0.007 MPa yields a calculation of the minimum reservoir permeability on the order of 1,200 darcy-meters. This suggests, essentially, infinite permeability; however, the actual zones that fluid exited the wellbore are unknown. It suffices to say that the geothermal reservoir in the vicinity of slim hole TH#1 has a very high permeability.

Another significant technical point is the behavior of the wellbore temperature during the injection test (see, Table 3). Injection started at a rate of 6.3 kg/s, however, injection was stopped for ten minutes to adjust the pump setting, and injection was then resumed at 11 kg/s. The temperature increased immediately after stopping the injection flow. In addition, at the end of the test, the slim hole recovered to its initial temperature immediately after cessation of injection. This indicates that fluid is flowing from fractured intervals above 186 m and exiting below 186 m. The temperature survey data show that the slim hole is isothermal to the bottom of the hole. This suggests that fluid does enter from approximately 175 m and exits through fractures at the bottom of the slim hole.

The temperature-depth data from slim hole TH#2 (see, Figure 4) show an isothermal zone between 213 m and 262 m, suggesting that there is fluid flow between the fractures intersected by the wellbore. The data obtained during the injection test are presented in Figure 6. No wellhead pressure was observed while injecting 29°C fluid at 11 kg/s. The temperature at 259 m was reduced from 164°C to about 66°C during the injection test. It is not clear whether these data indicate that only a portion of injected fluid was flowing into fracture zones located below 259 m or if mixing of injected and down-flowing fluid from the 216-m fracture interval was occurring. Mixing of injected fluid with fluid from the 216-m zone in TH#2 is the most likely cause of the observed temperature data. If we assume that all of the injected fluid was exiting the wellbore below 259 m, a heat balance calculation indicates that approximately 3.8 kg/s of 166°C fluid from the fracture zone located at a depth of 216 m is flowing down the wellbore with the injected fluid. This is a significant volume of fluid

circulating within the wellbore. The implication of this information is that there exists a large influx of fluid into the geothermal system. However, the calculation is sensitive to the actual volume of fluid exiting out the bottom of the slim hole, and this volume can only be estimated. In any case, the data suggest that productive fractures exist to the bottom of slim hole TH#2. Furthermore, the pressure data show that there was no pressure increase at 259 m due to injection of 11 kg/s of fluid, indicating that slim hole TH#2 encountered highly productive fractures. Thus, the reservoir in the vicinity of TH#2 has a very high permeability. The productive capacity of this portion of the FWC lease is as high as that found near slim hole TH#1, located in the southern portion of the lease. The overall productive capacity for geothermal fluids in this area is substantial.

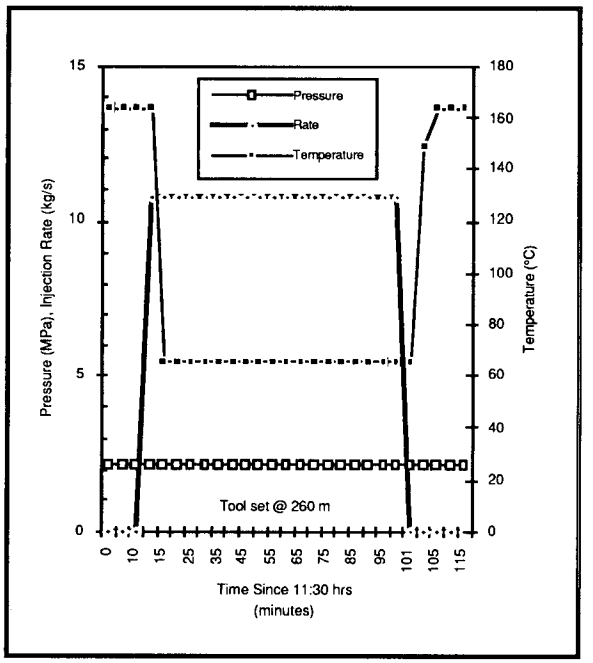


**Figure 6.** Downhole pressure and temperature as well as injection rate data versus time while testing of TH#2.

The temperature-depth data from slim hole TH#3 (see, Figure 4) show an isothermal zone between 213 and 251 m, which, although the total depth of TH#3 is 277 m, 251 m is the maximum depth the slim hole was surveyed. During the downhole survey, the temperature equipment would not readily pass the 251-m depth. From the thermal data, it is not clear whether this slim hole has fluid flow between the fractures intersected by the wellbore. The data obtained during the injection test are presented in Table 4. No wellhead pressure was observed while injecting 29°C fluid at 11 kg/s. The temperature at 251 m was not reduced during the injection test. These data indicate that injected fluid was not exiting the bottom of the well. Based on the geological data from this slim hole, it is postulated that fluid is exiting the wellbore between 213 and 244 m. The pressure data show that there was essentially no pressure increase at 251 m due to injection of 11 kg/s of fluid at a temperature of 29°C, indicating that this area also has a very high permeability.

**Table 4.** Time, pressure, temperature, and injection rate data during testing of TH#3.

| Time (min) | Press @ 251m (MPa) | Temp @ 251m (°C) | Inj Rate (kg/sec) | Comments |
|---|---|---|---|---|
| 0 | 2.25 | 166 | 0 | |
| 5 | 2.24 | 166 | 0 | |
| 9.9 | 2.24 | 166 | 0 | |
| 10 | 2.24 | 166 | 11 | Start Injection |
| 15 | 2.22 | 166 | 11 | |
| 20 | 2.22 | 166 | 11 | |
| 25 | 2.40 | 166 | 11 | Purge Tubing |
| 30 | 2.23 | 166 | 11 | |
| 35 | 2.23 | 166 | 11 | |
| 40 | 2.23 | 166 | 11 | |
| 45 | 2.23 | 166 | 11 | |
| 50 | 2.23 | 166 | 11 | |
| 55 | 2.23 | 166 | 11 | |
| 60 | 2.23 | 166 | 11 | |
| 65 | 2.24 | 166 | 11 | |
| 70 | 2.27 | 166 | 11 | Purge Tubing |
| 75 | 2.23 | 166 | 11 | |
| 80 | 2.24 | 166 | 11 | |
| 85 | 2.23 | 166 | 11 | |
| 90 | 2.22 | 166 | 11 | |
| 95 | 2.27 | 166 | 11 | Purge Tubing |
| 100 | 2.24 | 166 | 11 | |
| 101 | 2.24 | 166 | 0 | Stop Injection |
| 102 | 2.24 | 166 | 0 | |
| 105 | 2.24 | 166 | 0 | |
| 110 | 2.24 | 166 | 0 | |
| 115 | 2.24 | 166 | 0 | |

## CONCLUSIONS

Slim holes have been successfully used at the Steamboat Hills Geothermal Field (1) for drilling to targeted depths in fractured volcanic and igneous rocks with partial to complete loss of circulation, (2) to obtain core for geological studies and delineation of the subsurface stratigraphic structure, (3) for characterizing the geothermal reservoir fluid state, and (4) to determine the fracture permeability and productive capacity of the geothermal reservoir in the vicinity of the slim hole.

The data from the injection tests on the three slim holes at Steamboat Hills support the premise that it is possible to obtain a definitive reservoir assessment and forecast the discharge and injection performance of large-diameter production size geothermal wells from slim hole data.

The drilling and testing of the three slim holes has yielded much insight into the geothermal system in the northeast Steamboat Hills. The slim-hole drilling program was designed to determine whether productive geothermal fluids could be found at depths sufficient for well pumping equipment and at temperatures needed for power production. The deeper (173 m to 277 m) fracture sets found in the area of the FWC leases will allow for well pumps to set to depths greater than 200 m, possibly to depth in excess of 225 m.

This will allow the geothermal production wells to be pumped at flow rates higher than existing wells in the area and allow spacing between wells to be less than with existing wells. Based on all of the available data obtained to date, the reservoir should easily supply fluid in sufficient quantities at temperatures necessary for the development of a 30 MW geothermal power project.

## ACKNOWLEDGMENTS

We thank the management of Far West Capital, Inc. for permission to use their unpublished proprietary data for this study. This work was partially supported through Geo Hills Associates under Contract AA-7144 from Sandia National Laboratories.

## REFERENCES

Combs, J. and J.C. Dunn (1992), "Geothermal Exploration and Reservoir Assessment: The Need for a U.S. Department of Energy Slim-Hole Drilling R&D Program in the 1990s," *Geothermal Resources Council Bull.*, v. 21, no. 10, pp. 329-337.

Garg, S.K. and J. Combs (1993), "Use of Slim Holes for Geothermal Exploration and Reservoir Assessment: A Preliminary Report on Japanese Experience," *Proceedings Eighteenth Workshop on Geothermal Reservoir Engineering*, Stanford University, Stanford, California, 26-28 January, 7pp., in press.

Goranson, C., P. van de Kamp, and T. DeLong (1990), "Geothermal Injection and Monitoring Program History at the Caithness Power, Inc. Flash Steam Power Plant Steamboat Springs," Nevada: *Proceedings of the Symposium on Subsurface Injection of Geothermal Fluids*, Santa Rosa, CA , 29-30 October, pp. 101-124.

Goranson, C., P. van de Kamp, and E. Call (1991), "Summary and Interpretation of Six Years of Groundwater Monitoring Data at the SB GEO, Inc. Geothermal Power Plant Steamboat Springs," NV: *Proceedings of the Underground Injection Practices Council Meeting*, Reno, NV, 28-31 July, pp. 77-94.

Janik, C.J., and R.H. Mariner (1993), "Geochemical Investigation of Hydrothermal Systems and Geochemical Aspects of Geothermal Reservoir Depletion," in *Geothermal Reservoir Technology Research Program Abstracts of Selected Research Projects*, edited by M. R. Reed, U. S. Dept. of Energy, March, 1993, Washington, D.C., pp. 75-76.

Silberman, M.L., D.E. White, T.E.C. Keith, and R.D. Docker (1979), "Duration of Hydrothermal Activity at Steamboat Springs, Nevada, from Ages of Spatially Associated Volcanic Rocks," *U. S. Geol. Survey Prof. Paper 458-D*, 14pp.

Stewart, J.H. (1980), "Geology of Nevada," *Nevada Bureau Mines & Geology Special Publication 4*, 139pp.

Thompson, G.A., and D.E. White (1964), "Regional Geology of the Steamboat Springs area, Washoe County, Nevada," *U.S. Geol. Survey Prof. Paper 458-A*, 52pp.

van de Kamp, P.C. (1991), "Geothermal Geology of the Northern Steamboat Hills, Nevada," report submitted to Far West Capital, Inc., Salt Lake City, Utah, August, 5pp and 9 plates.

White, D.E. (1967), "Some Principles of Geyser Activity, Mainly from Steamboat Springs, Nevada," *American Journal Science*, v. 265, pp. 641-648.

White, D.E. (1968), "Hydrology, Activity, and Heat Flow of the Steamboat Springs Thermal System, Washoe County, Nevada," *U.S. Geol. Survey Prof. Paper 458-C*, 109pp.

White, D.E. (1973), "Characteristics of Geothermal Resources," in *Geothermal Energy: Resources, Production, Stimulation*, ed by P. Kruger and C. Otte, Stanford University Press, Stanford, CA, pp. 69-94.

White, D.E., G.A. Thompson, and G.A. Sanberg (1964), "Rocks, Structure, and Geologic History of the Steamboat Springs Thermal Area, Washoe County, Nevada," *U.S. Geol. Survey Prof. Paper 458-B*, 63pp.

PROCEEDINGS, Nineteenth Workshop on Geothermal Reservoir Engineering
Stanford University, Stanford, California, January 18-20, 1994
SGP-TR-147

# HEAT TRANSFER PROCESSES DURING LOW OR HIGH ENTHALPY FLUID INJECTION INTO NATURALLY FRACTURED RESERVOIRS

Fernando Ascencio Cendejas (†) and Jesús Rivera Rodríguez (‡)
(†) Gerencia de Proyectos Geotermoeléctricos. CFE., UNAM.
Apartado Postal 31-C. Morelia, Mich., MEXICO. CP 58290.
(‡) División de Estudios de Posgrado. UNAM. MEXICO, D.F.

## ABSTRACT

Disposal of hot separated brine by means of reinjection within the limits of the geothermal reservoir is, at present, a problem that remains to be solved. Possible thermal, as well as chemical contamination of the resources present key questions that have to be appropiately answered before a reinjection project is actually implemented in the field. This paper focusses on the basic heat-transfer process that takes place when a relatively cold brine is injected back into the naturally fractured hot geothermal reservoir after steam has been separated at the surface. The mathematical description of this process considers that rock matrix blocks behaves as uniformly distributed heat sources, meanwhile heat transfer between matrix blocks and the fluid contained in the fractures takes place under pseudo-steady state conditions with the main temperature drop occurring in the rock-matrix blocks interphase.

Analytical solutions describing the thermal front speed of propagation are presented. Discussion on the effect of several variables affecting the thermal front speed of propagation is included, stressing the importance that a proper "in-situ" determination of the effective heat transfer area at the rock-fluid interphase has on the whole process. Solutions are also presented as a type-curve that can be practically used to estimate useful parameters involved in heat transfer phenomena during cold fluid reinjection in naturally fractured geothermal systems.

## INTRODUCTION

Reinjection of separated brine in geothermal fields is currently a subject of major concern in current projects under development around the world ( *Pruess* and *Bodvarsson* [1984], *Horne* [1985], *Rivera*, [1991]). It has been long recognized that although replineshment of extracted fluids by means of reinjection could have positive aspects on the long-term behavior of a project, such as providing support to declining reservoir pressures, and to enhance total heat recovery from the resource, while reducing subsidence, some negative aspects that could also be present, should be taken into account. Among these negative aspects, premature injected cold water breakthrough into productive wells due to the presence of fast-circulation paths, established through highly permeable natural fractures are the subject of major concern among natural resources developers. These fast-circulation conduits originates a poor secondary heat-mining from hot reservoir rock from colder injected fluids. When cold water is injected into the productive formations a hydrodynamic front between the undisturbed reservoir fluid and the one injected originates. This front moves away from the injection well as time proceeds, capturing some heat coming from mixing with the fluid *in situ*, as well as from heat transfered from hot rock. This originates a second front called "the thermal front", that moves some distance behind the hydrodynamic front. The distance between both fronts depends on several factors such as travel time through the system, effective rock surface area avalaible for heat transfer between injected fluids and rock matrix, system geometry, microscopic fluid velocity, etc.

As it could be easyly inferred from the discussion above, the complex flow patterns and velocity fields generated by injected fluids through a geothermal reservoir, present a challange to the reservoir engineer in charge of performing a forecast of energy recovery from the resource and its distribution through the life of the project. Besides the problem of reservoir characterization to locate the position of fast circulation paths, the proper definition and understanding of the heat transfer processes that govern heat mining from hot reservoir rock by means of colder fluids circulating through the fracture system is of prime importance ( *Bodvarsson et al* [1985], *Bodvarsson and Stefansson* [1989]). This paper presents an analytic solution to this heat transfer problem.

The approach followed in this paper to study the heat transfer processes described above, assumes that fluid flow takes place only through the fracture network. Two basic models could be used to describe this flow problem; the first model considers the fracture network as a series of parallel-horizontal fractures alternated with matrix layers, *Kazemy* [1969], while the second one assumes that matrix blocks are completely surrounded by fractures (*Barenblatt and Zheltov* [1960], *Warren and Root* [1963]). Previous papers dealing with heat transfer during cold fluid injection into hot-fractured systems have used the first model (*Bodvarsson and Tsang* [1982], *Gringarten, Witherspoon and Onishi* [1975]). This paper instead uses the second model, where the hot matrix blocks are considered as uniformly distributed heat sources through the fractured media. *Bodvarsson and Lai* [1982] considered a similar model in their study.

# MATHEMATICAL MODEL

The basic equation for heat transfer in a fluid flowing radially away from the injection well through an infinite naturally fractured medium, where the flow conduits are provided by the fractures network is given by the energy conservation equation:

$$\phi\rho_f c_f \frac{\partial T_f}{\partial t} = -\phi\rho_f c_f v_R \frac{\partial T_f}{\partial r} + \kappa_f \nabla^2 T_f + q^* \quad (1)$$

where $T_f$ is the fluid temperature, $v_R$ is the microscopic radial fluid velocity, $\phi_f$ is the fracture porosity and $\rho_f$, $c_f$, and $\kappa_f$ are the fluid density, specific heat, and conductivity, respectively.

Considering that flow within the fracture network involves relatively small temperature gradients $\nabla T$, then the second term on the right hand side of Eq. 1 can be neglected compared with the convective term. Thus, Eq. 1 can be expressed as:

$$\phi_f\rho_f c_f \frac{\partial T_f}{\partial t} + \phi_f\rho_f c_f v_R \frac{\partial T_f}{\partial r} - q^* = 0 \quad (2)$$

From Eq. 2, it is easily seem that the first term on the left hand side is the energy accumulated in the fluid contained in the fracture network; while the second term contemplates the heat transfered by convection, and the third term represents the heat interchanged between matrix rock and fluids, with matrix blocks considered as a uniformly distributed heat source throughout the fractured medium. The main assumptions implicit in Eq. 2 are:

1. The system is made up of two homogenous and isotropic media (the fracture network and the matrix system) coupled together, Fig. 1.
2. The system is of infinite extent in the radial coordinate.
3. Fluid and rock physical and thermal properties are constant.
4. Conduction heat transfer in the fluid within the fracture network is negligible.
5. Heat losses in the vertical direction are zero.
6. Matrix blocks are impermeable, so that fluid flow takes place only throughout the fracture network.
7. Mass transfer between rock matrix and fluid is negligible.
8. There is no resistance to heat flow at the rock-fluid interphase.

9. Fluid flow within the fracture network is assumed to occur under steady-state conditions, so that for an incompresible fluid the following relationship holds:

$$r\phi_f v_R = q_{in}/2\pi h = const. \quad (3)$$

where $q_{in}$ is the volumetric fluid injection rate and $h$ is the formation thickness.

To completely describe the boundary value problem given by Eq. 2, the following initial and boundary conditions are considered:

$$\text{For } t \leq 0 \text{ and } 0 \leq r < \infty : \; T_f = T_{f0} \quad (4)$$

$$\text{For } t > 0 \text{ and } r = 0 : \; T_f = T_{fin} \quad (5)$$

where $T_{f0}$ is the initial fluid temperature and $T_{fin}$ is the injection fluid temperature.

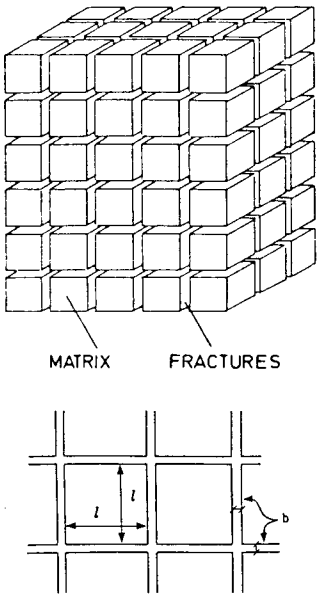


**Figure 1: Idealised fractured reservoir: Warren-Root model.**

**Heat transfered between fluid and matrix rock, $q^*$.**

Assuming that matrix blocks act as heat sources uniformly distributed, so that they liberate heat to the surrounding colder fluid under a pseudo-steady state process, then by performing an energy balance on the system the following expression can be obtained:

$$(1-\phi_f)\rho_r c_r \frac{\partial T_r}{\partial t} = -A_{HTb}(k_r/l)[T_r - T_f] \quad (6)$$

where $l$ is a characteristic length for the matrix blocks, $A_{HTb}$ is the effective block heat transfer area per unit volume, and $\kappa_r, \rho_r, c_r$ are the rock thermal conductivity, density, and heat capacity, respectively.

Considering that the whole system is initially under thermal equilibrium conditions, i.e.:

$$\text{For } t \leq 0 : T_r = T_{r0} = T_{f0} \quad (7)$$

and defininig

$$\Delta T_r = T_{r0} - T_r \quad (8)$$

where $T_{r0}$ is the initial rock temperature. Then, the solution to Eq. 6 is:

$$\Delta T_r = \Delta T_f \Big[1 - \exp\Big(-\frac{A_{HTb}(k_r/l)}{(1-\phi_f)\rho_r c_r}t\Big)\Big] \quad (9)$$

where

$$\Delta T_f = T_{f0} - T_f. \quad (10)$$

From Eq. 9, the heat flux liberated from the matrix blocks due to a unit temperature drop at the rock-fluid interphase is given by:

$$Q_1 = A_{HTb}(k_r/l)\exp\Big(-\frac{A_{HTb}(k_r/l)}{(1-\phi_f)\rho_r c_r}t\Big) \quad (11)$$

Since temperature at the rock-fluid interphase is changing continuosly with time, the heat flow transfered from rock matrix to the fluid can be adequately expressed by means of a convolution type of integral as follows:

$$q^{*} = A_{HTb}\cdot(k_r/l)\int_0^{t_D}\frac{\partial\Delta T_f(t)}{\partial\tau}\cdot$$

$$\exp\Big(-\frac{A_{HTb}(k_r/l)}{(1-\phi_f)\rho_r c_r}(t-\tau)\Big)d\tau \tag{12}$$

Finally, substituting Eq. 12 into Eq. 2 and using the temperature difference defined by Eq. 10, Eq. 2 can be expressed as:

$$\phi_f\rho_f c_f\frac{\partial\Delta T_f}{\partial t}+\phi_f\rho_f c_f v_R\frac{\Delta T_f}{\partial r}+A_{HTb}(k_r/l)\cdot$$

$$\int_0^{t_D}\frac{\partial\Delta T_f(t)}{\partial\tau}\exp\Big(-\frac{A_{HTb}(k_r/l)}{(1-\phi_f)\rho_r c_r}(t-\tau)\Big)d\tau=0 \tag{13}$$

Therefore, the heat transfer problem is defined by means of Eq. 13 with initial and boundary conditions given by:

$$\text{For } t\le 0 \text{ and } 0\le r<\infty:\ \Delta T_f=0 \tag{14}$$

$$\text{For } t>0 \text{ and } r=0:\ \Delta T_f=T_{f0}-T_{fin} \tag{15}$$

# DIMENSIONLESS FORMULATION

The boundary-value problem given by Eqs. 13 through 15 can be expressed in dimensionless form by means of the following definitions:

$$T_D=\frac{T_{f0}-T_f}{T_{f0}-T_{fin}} \tag{16}$$

$$t_D=\frac{A_{HTb}(k_r/l)}{(1-\phi_f)\rho_r c_r}t \tag{17}$$

$$r_D=A_{HTb}r \tag{18}$$

$$\mathrm{Pe}=\frac{2\pi(k_r/l)h}{A_{HTb}\rho_f c_f q_{in}} \tag{19}$$

$$\Theta=\frac{\phi_f}{(1-\phi_f)}\cdot\frac{\rho_f c_f}{\rho_r c_r}. \tag{20}$$

Introducing definitions (16) through (20) into Eqs. 13 through 15, they can be expressed as:

$$\Theta\frac{\partial T_{Df}}{\partial t_D}+\int_0^{t_D}\frac{\partial T_{Df}(t_D)}{\partial\tau}\exp\Big(-(t_D-\tau)\Big)d\tau+$$

$$\frac{1}{\mathrm{Pe}}\frac{1}{r_D}\frac{\partial T_{Df}}{\partial r_D}=0 \tag{21}$$

$$\text{For } t_D\le 0 \text{ and } 0\le r_D<\infty:\ T_{Df}(r_D,0)=0 \tag{22}$$

$$\text{For } t_D>0 \text{ and } r_D=0:\ T_{Df}(0,t_D)=1 \tag{23}$$

# ANALYTIC SOLUTION

Solution to Eqs. 21 through 23 in Laplace's space is given as:

$$\overline{T}_{Df}=\frac{1}{\mathrm{s}}\exp\Big(-\frac{1}{2}(\Theta+\frac{1}{\mathrm{s}+1})\mathrm{Pe}\ r_D^2\ \mathrm{s}\Big) \tag{24}$$

The inverse transformation of Eq. 24 gives, *Luke* [1962]:

$$T_{Df}(r_D,t_D)=\mathbf{J}\Big(,t_D-\frac{1}{2}\Theta\mathrm{Pe}\ r_D^2\Big)\cdot$$

$$\mathbf{U}(t_D-\frac{1}{2}\Theta\mathrm{Pe}\ r_D^2) \tag{25}$$

where

$$\mathbf{U}(t_D-\frac{1}{2}\Theta\mathrm{Pe}\ r_D^2)=\begin{cases}0, & \text{for } t_D-\frac{1}{2}\Theta\mathrm{Pe}\ r_D^2\le 0\\ 1, & \text{for } t_D-\frac{1}{2}\Theta\mathrm{Pe}\ r_D^2>1\end{cases} \tag{26}$$

$$\mathbf{J}(\chi,\tau)=\begin{cases}\exp[-(\chi+\tau)]\sum_{\mathrm{k}=0}^{\infty}\Big(\sqrt{\frac{\tau}{\chi}}\Big)^{\mathrm{k}}\mathrm{I_k}\big(2\sqrt{\chi\tau}\big)\\ \qquad\text{if } \sqrt{\frac{\tau}{\chi}}\le 1\\ 1-\exp[-(\chi+\tau)]\sum_{\mathrm{k}=0}^{\infty}\Big(\sqrt{\frac{\tau}{\chi}}\Big)^{-\mathrm{k}}\mathrm{I_k}\big(2\sqrt{\chi\tau}\big)\\ \qquad\text{if } \sqrt{\frac{\tau}{\chi}}\ge 1\end{cases} \tag{27}$$

where $\mathrm{I_k}$ is the modified Bessel Function of order $k$.

Eq. 25 gives at complete description of temperature changes in the injected fluid while flowing through the fractured system, subjected to the restrictions given by Eqs. 22 and 23 and to assumptions (1) through (8). A similar solution was previously reported by *Rodríguez* [1988] for the problem of linear oil displacement by water injection in fractured reservoirs.

## LIMITING SOLUTIONS

Limiting approximate expressions of Eq. 25 can be obtained for early, late and intermediate times as follows:

1. *Early times.* From Eq. 24, at early times ($s \rightarrow \infty$); Eq. 24 can be expressed as:

$$\overline{T}_{Df} = \frac{1}{s}\exp\left(-\frac{1}{2}\Theta \mathrm{Pe}\, r_D^2\, s\right) \qquad (28)$$

The inverse transformation of this equation is:

$$T_{Df} = \mathbf{U}\left(t_D - \frac{1}{2}\Theta \mathrm{Pe}\, r_D^2\right) \qquad (29)$$

2. *Late times.* From Eq. 24, at large times $s \rightarrow 0$; hence, Eq. 24 can be written as:

$$\overline{T}_{Df} = \frac{1}{s}\exp\left(-\frac{1}{2}(\Theta+1)\mathrm{Pe}\, r_D^2\, s\right) \qquad (30)$$

The inverse transformation of this equation is:

$$T_{Df} = \mathbf{U}\left(t_D - \frac{1}{2}(\Theta+1)\mathrm{Pe}\, r_D^2\right) \qquad (31)$$

3. *Intermediate times.* Expanding the exponential function in series and keeping only the first two terms of such expansion, i.e., $e^x \approx 1 + x$, then Eq. 25 can be approximate for intermediate times as:

$$T_{Df} = \left[1 - \frac{1}{2}\mathrm{Pe}\, r_D^2 \exp\left(-\left(t_D - \frac{1}{2}\Theta \mathrm{Pe}\, r_D^2\right)\right)\right] \cdot \mathbf{U}\left(t_D - \frac{1}{2}\Theta \mathrm{Pe}\, r_D^2\right) \qquad (32)$$

## TYPE CURVE DEVELOPMENT

Evaluating Eq. 25, with parameters defined by means of Eqs. 26 and 27, and taking into account the dimensionless parameters given in Eqs. 16 through 20, the type-curve shown in Fig. 2 was developed. As shown in this figure, a family of curves results when $\frac{1}{2}\mathrm{Pe}\, r_D^2$ *vs.* $t_D$, with $\Theta$ as a parameter, is plotted. Fig 2 shows the radial dimensionless distance that the thermal front has traveled through the fractured medium from the injection well, as dimensionless time proceeds, for several values of $\Theta$. The parameter $\Theta$, as defined by Eq. 20 represents the ratio of the block size to the fracture apertures, which can also be considered as the ratio of the thermal energy contained in the fluid to that stored in the matrix rock. On the other hand, the thermal front is taken as the locus of points where temperature has dropped to a certain fraction of the difference between initial reservoir and injection temperature, as previously defined by *Pruess and Bodvarsson* [1984]:

$$T_f = T_{in} + f(T_0 - T_{in}) \qquad (33)$$

where $f$ is taken as 0.75, as suggested by these authors, for a non-symmetrical front.

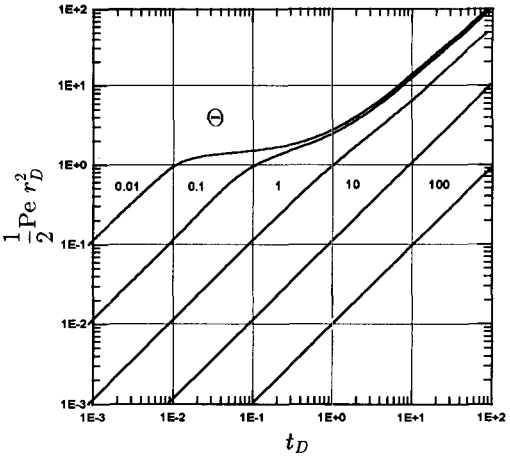


**Figure 2: Type-curve for the thermal front movement in fractured reservoir.**

From Fig. 2, it is apparent that for values of $\Theta < 5$, the thermal front shows two parallel linear portions at early and late times, connected by a transition zone at intermediate times. For $\Theta > 5$ a linear relationship holds for all $t_D$. The early straight line corresponds to the behavior exhibited by the fluid once it enters the fracture network, before it can experience any effect of heat transfered from the surrounding hot matrix blocks. After some time, and depending on the magnitud of $\Theta$, the heat transfered from the matrix blocks start to show up, producing a bending on the curve, which is shown in Fig. 2 as the transition period. The length of this transition zone decreases as $\Theta$ increases. Later on, a condition of instantaneous thermal equilibrium between the injected fluid and the rock is reached, which shows in Fig. 2 as the second straight line portion of each curve. It is clear from this figure that for $\Theta > 5$ no transition zone occurs; therefore, instantaneous thermal equilibrium conditions are reached within the system. *Bodvarsson and Tsang* [1982] and *Bodvarsson and Lai* [1982] presented type-curves similar to Fig. 2 for layered and cube-type fractured systems, respectively, although their dimensionless parameters definitions are different to those given in this paper and, on the other hand, they assumed transient heat flow conditions between matrix and fractured systems, while the present paper assumes pseudo-steady state heat transfer conditions.

For early times and from Eq. 29, the thermal front will move according to the expression:

$$r_{TF}^2 = \frac{q_{in} t}{\pi H \phi_f} \tag{34}$$

For late times, the thermal front will move according to:

$$r_{TF}^2 = \frac{\rho_f c_f q_{in} t}{\pi H [\phi_f \rho_f c_f + (1-\phi_f)\rho_r c_r]} \tag{35}$$

It should be pointed out that Eq. 35 is usually mentioned in the literature when instantaneous thermal equilibrium conditions are assumed.

At intermediate times, from Eq. 32, the temperature at the transition zone is given by:

$$T_{Df} = \Big(1 - \frac{\pi (k_r/l) h A_{HTb} r^2}{q_{in} c_f \rho_f}\Big) \cdot$$

$$\exp\Big(-(t_D - \frac{1}{2}\Theta \mathrm{Pe}\ r_D^2)\Big)\mathbf{U}\Big(t_D - \frac{1}{2}\Theta \mathrm{Pe}\ r_D^2\Big) \tag{36}$$

From Eqs. 34 and 36, the start of the transition zone is given by:

$$t_D \approx \frac{3}{4}\Theta \tag{37}$$

$$\frac{1}{2}\mathrm{Pe}\ r_D^2 \approx \frac{3}{4} \tag{38}$$

From Fig. 2, it is apparent that independently from the value of $\Theta$, instantaneous thermal equilibrium conditions are reached for:

$$t_{Dte} \geq 10 \tag{39}$$

$$\frac{1}{2}\mathrm{Pe}\ r_{Dte}^2 \geq 10 \tag{40}$$

Expressing these Eqs. in terms of real variables:

$$t_{te} = \frac{10\ (1-\phi_f)\rho_r c_r (l/A_{HTb})}{k_r} \tag{41}$$

$$r_{te} = \left(\frac{10\ \rho_f c_f q_{in} (l/A_{HTb})}{\pi h k_r}\right)^{1/2} \tag{42}$$

Eqs. 41 and 42 can be used to estimated the time and length required for reaching instantaneous thermal conditions in a given reinjection field project.

# EXAMPLES

To illustrate the application of Eqs. 41 and 42, let's considerer two hypothetical cases:

1. Assuming a fractured system made up of cubic elements with lenght of $0.5m$, and by using the additional data given in Table 1, the following results can be obtained:

$$t_{te} = 6.5 \; days$$

$$r_{te} = 9.14 \; m$$

2. Assuming a fractured system composed by cubic elements with lenght of $0.25m$, and using data from Table 1, the following results can be obtained:

$$t_{te} = 1.63 \; days$$

$$r_{te} = 4.6 \; m$$

**TABLE 1. PARAMETERS USED IN EXAMPLES.**

| | |
|---|---|
| Volumetric rate (water), $q_{in}$, $m^3/s$ | 0.03 |
| Thickness, $h$, $m$ | 100. |
| Porosity, $\phi_f$ | 0.01 |
| Fluid density, $\rho_f$, $kg/m^3$ | 1000. |
| Rock density, $\rho_r$, $kg/m^3$ | 2700. |
| Fluid heat capacity, $c_f$, $J/kg\ ^\circ C$ | 4200. |
| Rock heat capacity, $c_r$, $J/kg\ ^\circ C$ | 1000. |
| Thermal conductivity, $k_r$, $J/m\ s^\circ C$ | 2. |

These examples illustrates the great effect that the effective area for heat transfer , $A_{HTb}$, and the block size have on the time required for the injected fluid to reach thermal equilibrium conditions with the surrounding rock.

# CONCLUSIONS

A mathematical model has been proposed to study the behavior of thermal front propagation during cold fluid injection into a hot naturally fractured system. Based upon results obtained from this study, the following conclusions can be withdrawn:

1. A mathematical model for studying the heat transfer processes occurring when cold fluids are injected into hot fractured formations has been proposed. This model considers matrix blocks as uniformly distributed heat sources, with heat transfer to the fluid taking place under pseudo-steady state conditions.

2. A type-curve has been developed to describe the heat transfer processes taking place within the fractured system, for different values of the parameter $\Theta$.

3. Expressions to calculate the position of thermal fronts at early, intermediate, and late times were developed.

4. From the parameters included in the dimensionless groups considered in this paper, the ratio of block size to the effective heat transfer area showed the greatest effect on the heat transfered between matrix blocks and the fluid.

5. Additional work has still to be performed to extend the results presented in this paper.

# NOMENCLATURE

$A_{HTb}$ Heat transfer area per unit bulk volume.

$k$ Thermal conductivity.

$c$ Specific heat.

$h$ Thickness of producing formation.

$q$ Volumetric rate.

$Q$ Heat flux.

$v$ Microscopic velocity.

$l$ Characteristic length.

$s$ Laplace's space parameter.

Pe Peclet number.

$t$ Time.

$T$ Temperature.

$w_i$ Mass flow rate.

$\rho$ Density.

$\phi_f$ Porosity.

**Subscripts:**

0 initial

$in$ injection

$r$ rock

$f$ fluid,fracture

$te$ thermal equilibrium

$R$ radial

$TF$ thermal front

**Special functions:**

$I_k(x)$ Modified Bessel function of order k.

$U(t-\tau)$ Unit step function.

# REFERENCES


Barenblatt,G.I. and Zheltov, Yu. P. (1960): *Fundamental Equations of Filtration of Homogeneous Liquids in Fissured Rocks.* Soviet Physics Dodlady. Vol.5, 522-525.

Bodvarsson, G.S. and Tsang,C.F. (1982):*Injection and Thermal Breakthrough in Fractured Geothermal Reservoir.* Journal of Geophisical Research. Vol.87, B2, p 1031.

Bodvarsson,G.S., Pruess, K., and O'Sullivan, M.J. (1985): *Injection and Energy Recovery in Fractured Geothermal Reservoirs.* Soc. Pet. Eng. Jour. April, pp 303-312.

Bodvarsson,G.S., and Stefansson,V. (1989): *Some Theoretical and Field Aspects of Reinjection in Geothermal Reservoirs.* Water Res. Res., Vol.25,No.6, 1235-1248.

Bodvarsson,G.S., and Lai,C.H. (1982):*Studies of Injection into Naturally Fractured Reservoirs.* Trans. Geoth. Resources Council.

Gringarten,A.C., Witherspoon,P.A. y Onishi, Y (1975):*Theory of Heat Extraction from Fractured Hot Dry Rock.* Journal of Geophysical Research. Vol.80, No.8.

Horne,R.N. (1985):*Reservoir Engineering Aspects of Reinjection.* Geothermics, Vol.14, No.2/3 449-457.

Kazemi,H. (1969):*Pressure Transient Analysis of Naturally Fractured Reservoirs with Uniform Fracture Distribution.* Soc. Pet. Eng. J. (Dec.) 451-462. Trans. AIME, 246.

Luke, Y.L. (1962):*Integral of Bessel Functions.* McGraw-Hill Book Co. Inc., New York.

Pruess,K., and Bodvarsson,G.S. (1984) :*Thermal Effects of Reinjection in Geothermal Reservoir with Major Vertical Fractures.* Jour. Pet. Tech (Sept.).

Rivera,R.J. (1991): *Reinjection in Geothermal Fields Under Explotation Stage-Experiences and Perspectives.* Proceedings UN/DTCD-OLADE Workshop on Evaluation of Environmental Impact, Natural Ricks and Reinjection in Geothermal Areas. Quito, Ecuador. Nov.

Rodríguez de la Garza, F.(1988):*Modelo Analítico del Desplazamiento Lineal de Aceite por Inyección de Agua en Yacimientos Fracturados.* Ingeniería Petrolera, (Junio) 20-26.

Warren, J.E. and Root, P.J. (1963):*The Behavior of Naturally Fractured Reservoirs.* Soc. Pet. Eng. J. (Sept.) 245-255. Trans. AIME, Vol. 228.

PROCEEDINGS, Nineteenth Workshop on Geothermal Reservoir Engineering
Stanford University, Stanford, California, January 18-20, 1994
SGP-TR-147

# COMPUTER PROGRAM TO ANALYZE MULTIPASS PRESSURE-TEMPERATURE-SPINNER SURVEYS

Paul Spielman
Reservoir Engineer

California Energy Company, Inc.
900 N. Heritage, Bldg. D
Ridgecrest CA 93555

## ABSTRACT

A computer program has been developed to analyze multipass pressure-temperature-spinner surveys and summarize the data in graphical form on two plots: (1) an overlay of spinner passes along with a fluid velocity profile calculated from the spinner and (2) an overlay of pressure, pressure gradient, and temperature profiles from each pass. The program has been written using SmartWare II Software. Fluid velocity is calculated for each data point using a cross-plot of tool speed and spinner counts to account for changing flow conditions in the wellbore. The program has been used successfully to analyze spinner surveys run in geothermal wells with two-phase flashing flow.

## INTRODUCTION

Flowing pressure-temperature-spinner (PTS) surveys are run in geothermal production wells to identify production zones. The spinner is a wireline tool with a small propeller that spins when fluid flows past the tool. Revolutions of the propeller in a fixed period are counted and recorded at the surface. Commonly, one continuous pass over the length of the wellbore is made at a constant speed, and then stationary stops may be made at locations between inflow zones. Spinner counts are proportional to the velocity of fluid in the wellbore, provided fluid density is constant. If wellbore diameter is constant, then the difference of spinner counts above and below an inflow zone is proportional to the production rate from the zone. This method works in geothermal wells that produce a single phase liquid, provided the water does not flash to steam in the producing interval of the well. Other factors that can complicate spinner interpretation are: uneven borehole size, thief zones, surging flow, and flow reversals.

Flowing PTS surveys are run frequently in production wells in the Coso Geothermal Field to identify the best depth for injection of an inhibitor to prevent calcium carbonate scale. The pressure data from a PTS survey can be used to determine the depth at which geothermal fluids begin flashing to steam in the wellbore. In general, it is desirable to inject scale inhibitor below the flash depth, because calcium carbonate scale often forms when geothermal fluids flash to steam. However, in some wells the flash depth is at or below the deepest inflow. In other wells, thief zones may draw off fluids coming from deeper producing zones, or they may cause downflow of fluids from shallower producing zones. In such cases, inhibitor injected below the flash depth may not be carried up the wellbore where it is needed to prevent scale. The spinner data from a PTS survey is then critical to determine the velocity and the direction of fluid flow so that the inhibitor tube can be installed at the optimal depth.

All the complicating factors for spinner interpretation listed in the above discussion have been seen in one or more production wells in the Coso Geothermal Field. The frequency of PTS surveys and the interpretation difficulties prompted development of a computer program to analyze the surveys and produce a graphical output that summarizes all of the data on two graphs. The automated interpretation has also been useful for diagnosing mechanical problems in production and injection wells.

## MULTIPASS PTS SURVEYS

Multipass PTS surveys are usually run in wells at Coso because the single-pass survey described in the introduction is inadequate to resolve complicated flow situations. Four passes of the PTS tool are made through the completion interval of the well at different cable speeds. (The completion interval is the slotted portion of the production liner.) Usually one down-pass at 200 feet per minute (fpm) is made from the surface to the bottom of the well. Then an up-pass is made, at 200 fpm, from the bottom to the top of the production interval. Two more passes over the production interval are made at 100 fpm, down and up. The four spinner passes allow tool response to be calibrated for each location in the wellbore so that fluid velocity can be calculated as fluid density changes above the flash depth. Multiple passes of pressure, temperature, and spinner are also useful for identifying tool glitches, surging, and transient effects.

The spinner response is calibrated by a crossplot of spinner counts versus cable speed, with up passes having a negative cable speed. (Figure 1, See reference 2 for a derivation of the crossplot method.) Ideally the points plot in a straight line, and the spinner response is the slope of the line that goes through the points. If the tool moves at the same speed as the fluid, spinner counts will be zero, so fluid velocity is equal to the cable speed where the

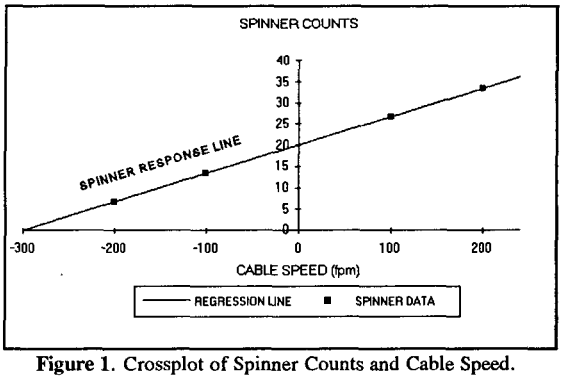


**Figure 1.** Crossplot of Spinner Counts and Cable Speed.

spinner response line intercepts the cable speed axis. In wells with single phase flow, there are usually several intervals of constant fluid velocity, separated by production zones and borehole diameter changes. Several crossplots, one for each interval, can be constructed by hand. However, flashing flow in a geothermal well causes velocity to increase continuously as it flows up the wellbore, and intervals of constant velocity do not exist above the flash point. The best way to view spinner data from a geothermal production well with a deep flash depth is as a continuous velocity profile. This requires many crossplots to determine spinner response as the two-phase fluid density changes. The crossplot process can be automated by a computer program and summarized graphically along with the pressure and temperature profiles.

The data in Figure 1 would be produced by an ideal frictionless spinner in an ideal nonviscous fluid. Real spinners deviate from the straight line of Figure 1 in several subtle ways. There is a threshold fluid velocity below which the spinner counts are zero. Two-phase flow will cause a nonlinear response at low spinner count rates due to liquid hold-up. (Liquid hold-up refers to the difference between liquid velocity and gas velocity in two-phase flow.) Because of viscosity effects, the actual fluid velocity is slightly offset from the intercept of the spinner response line and the cable speed axis. When the fluid velocity reverses direction relative to the tool, the spinner response curve will have a slightly different slope. For the analysis of spinner surveys from geothermal production wells, the nonlinear effects can usually be ignored because velocities are high and instabilities in two-phase flow cause variations that are much larger than the nonlinearities of the tool response. The exception would be for spinner measurements that are below the flash depth and below all major entries, where flow is single phase and fluid velocity is low.

## AUTOMATED ANALYSIS METHOD

The PTS survey analysis program reads the PTS survey data into a spreadsheet, analyzes the data, and prints out two plots that summarize the raw data and the results of the analysis. Operator input is required at several steps in the process to adjust for variations in the data, to make analysis decisions, and to produce the most useful output. The spinner analysis is programmed in SmartWare II Software because SmartWare provides a compiled programming language for rapid calculations and high quality graphical output controlled by the program.

The PTS survey data is read from floppy disks provided by the survey company. The data can be in ASCII text or spreadsheet format. The best analysis is produced if pressure, temperature, spinner counts, and cable speed (or time of measurement) are available at each depth for each pass. A static pressure and temperature survey can also be included for reference. However, the minimum data required for a spinner analysis are depth, spinner counts and an average cable speed for each pass. As the data is read, it is filtered to remove sections where the tool slowed down, reversed direction or sped up. A pressure gradient is calculated from depth and pressure differences over an interval above and below the data point. The differences between passes of the average cable speeds divided by the differences of the average spinner counts, over several intervals, are calculated and the median is used as a starting estimate for the spinner response slope calculation.

To process the data in the spreadsheet, the measurement points for all the passes are sorted by depth, and calculation of fluid velocity starts with the deepest data point. The fluid velocity for the deepest data point is calculated using the spinner response slope estimated during data input. Fluid velocity ($VA$) is equal to the spinner response slope ($BA$) times the spinner counts ($SP$) minus the cable speed ($CS$).

$$VA = BA * SP - CS \tag{1}$$

Spinner response slope ($BA$) in this analysis is defined as $\Delta$cable speed/$\Delta$spinner counts. Then the next data point is analyzed. The spinner response slope can be calculated when there is data from more than one pass. A least squares linear regression of the data points (one data point from each pass) provides fluid velocity and spinner response slope using: sum of spinner counts ($SSP$), sum of cable speed times spinner counts ($SCSP$), sum of cable speeds ($SCS$), sum of spinner counts squared ($SSP2$), and number of data points summed ($N$).

$$VA = \frac{SSP * SCSP - SCS * SSP2}{N * SSP2 - SSP^2}$$

$$BA = \frac{SCS + N * VA}{SSP} \tag{2}$$

Each data point in the crossplot is replaced when a new data point for that pass is read. The calculated slope is averaged with previous slopes to adjust the spinner response as the analysis proceeds up the wellbore.

The crossplot is also used to set the sign of the spinner counts and to check the validity of the data. Most spinner surveys do not record the direction of spin but this can be determined from the crossplot. Figure 2 shows the crossplot that results when there is no fluid movement. Spinner counts going up hole are the same as spinner counts going downhole at the same speed. To

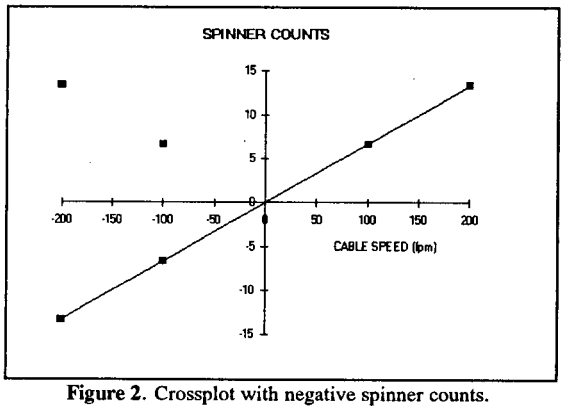


**Figure 2.** Crossplot with negative spinner counts.

form a straight line, the spinner counts must be negative for cable speeds of -100 and -200 fpm. When fluid velocities are low, spinner counts can be negative on up passes. When fluid movement is downward, as in an injection well, spinner counts can also be negative on down passes. When a data point is read, its sign is checked with a crossplot of the data points from the other three passes. The data point is given a positive or negative sign depending on which fits the crossplot best. If the fit is within data quality criteria, another crossplot is made using all four passes. The resulting fluid velocity is recorded, and the spinner response slope is averaged with the previous slope.

When all of the spinner data has been processed, a menu allows the operator to choose from several tasks that allow the results to be viewed, modified, or recalculated.

- A plot of pressure, pressure gradient, and temperature profiles can be viewed.
- A plot of spinner counts and fluid velocity profiles can be viewed.
- The pressure-temperature plot and spinner-fluid velocity plot can be printed in color or black and white.
- Wellbore data can be input to place a wellbore flow area profile on the spinner plot.
- A symbol can be placed at the depth of mud loss zones, steam entries, or altered zones.
- A footnote can be entered to print at the bottom of the plots.
- Adjustments to the spinner interpretation can be made.
- The fluid velocity can be recalculated using the adjustments.
- Sign of the spinner counts can be set manually.
- Spikes in the pressure and temperature data can be deleted.
- Plot scales can be modified.

The adjustments to the spinner interpretation allow the operator to compensate for many flow situations and poor data quality.

- The initial guess for the slope of the spinner response line can be changed.
- The number of slopes to average together can be increased to stabilize the slope of the spinner response line or decreased to allow more variation.
- The tolerance for slope data quality control can be tightened or loosened.
- A depth can be entered to exclude distant data from the crossplot.
- The tolerance for spinner counts data quality control can be tightened or loosened.
- Minimum counts can be set to eliminate small or zero spinner counts that are below the spin threshold.
- Maximum counts can be entered to eliminate spurious data.
- The spinner default sign, for data where a crossplot is not available, can be set to positive for production wells and negative for injection wells.
- The sign can also be set positive or negative for all spinner data, it can be set to use the previous sign for the same pass, or it can be left unchanged so that spinner signs set manually will not change.

## EXAMPLE SURVEYS

This program has been used to analyze 137 PTS surveys from 58 different production and injection wells from late 1991 through the end of 1993. Most of the surveys provided useful information and many provided insight into the flow mechanics of geothermal wells. The program allowed extraction of necessary information from surveys with poor data quality. Some peculiar phenomena have been observed that might be blamed on tool malfunction, except that they occur in similar situations in more than one well. The following six example plots illustrate the most important flow patterns observed at Coso.

The PTS survey from Well 1 is typical of surveys run in Coso production wells (Figure 3). One major inflow at 3200 feet is represented by a step-increase in fluid velocity. This is in single-phase liquid as indicated by the pressure gradient of 330 psi/1000ft. Moving up the wellbore, the pressure gradient begins to decline, indicating that the flash depth is at 3050 feet. Fluid velocity decreases slightly just above the flash depth and then steadily increases while pressure, pressure gradient, and temperature decrease up to the top of the liner at 1200 feet. The increase in flow area above the liner top allows fluid velocity and pressure gradient to drop. Then the increasing velocity and decreasing pressure and temperature continue to the wellhead. The slow zone just above the flash depth has been seen on surveys in many wells, even when the flash occurs in blank pipe. Liquid hold-up in deviated wellbores is thought to be the cause of the slow zone. The spinner tool lies in the slower moving liquid on the low side of the wellbore while the small amount of steam flows along the high side of the wellbore at a higher velocity. Flash fraction and velocity increase farther up and greater turbulence causes the velocity to become uniform across the wellbore.

Well 2 has flashing fluid to the bottom of the wellbore (Figure 4). The pressure gradient is 210 psi/1000ft at the bottom of the well and is less than the liquid gradient of 330 psi/1000ft as seen in Well 1. There are three production zones represented by fluid

velocity increases at ~3000 feet, ~2650 feet, and ~2150 feet. The static pressure profile shows that static liquid level is at 2800 feet so the reservoir is two-phase or vapor dominated at 2650 and 2150 feet. Production from the two-phase or vapor dominated portion of the reservoir is unlikely to cause scale in the wellbore. However, the entry at 3000 feet produces from a liquid zone, so there is a potential for scaling. The scale will tend to form in the formation, where the flash occurs. We can only hope that it is deep in the formation where it will not reduce productivity. If the productivity of the well declines and there is no scale in the wellbore, an acid job will be performed to remove the calcium carbonate scale from the formation. The overlay of the four spinner passes shows how the slope of the spinner response line can change. The spread of the spinner passes is 50 counts below 2500 feet, but above 2000 feet the spread is only 30 counts. The cable speeds were constant so the change in the spread of spinner counts indicates a change in the slope of the spinner response line.

The flash depth in Well 3 is below the major entries (Figure 5). Single-phase liquid up to 5600 feet is indicated by a pressure gradient of 330 psi/1000ft. Flashing flow is represented by the declining pressure gradient above 5600 feet. The fluid velocity profile indicates a small upflow from 6500 feet and major production zones at 4900 feet and 4100 feet. From the flash depth at 5600 feet up to 4900 feet, the spinner profiles are irregular but the peaks and valleys repeat on all four passes. The irregular spinner profile is typical of flashing flow, and the repeat of irregularities has been seen on many wells including Well 2, Well 4 and Well 6. This phenomenon may be due to washouts but, it occurs most often in the two-phase region, so it may be a characteristic of two-phase flow. Scale inhibitor can be injected below the flash depth in this well because there is some upflow, but the well must be watched to make sure that the inhibitor continues to be carried uphole.

There are two flash depths in Well 4 (Figure 6). The pressure gradient is ~320 psi/1000ft up to 4900 feet where it begins to drop off indicating flash. At 4650 feet a cooler inflow, represented by a step down on the temperature profile, raises the pressure gradient back up to 320 psi/1000ft. At 4400 feet it drops off again, indicating another flash depth. The fluid velocity calculated from the spinner survey indicates an inflow at 5500 feet. Then the velocity drops off at 5000 feet, probably due to flashing at that depth. There is a very small increase at 4650 feet where the temperature profile indicates an inflow, and then velocity increases above 4400 feet. The double flash zones have been seen on several surveys run in this well.

Production from Well 5 is disturbed by severe surging (Figure 7). The surges are most evident on the pressure gradient profiles as large spikes at periodic intervals. The overlay of pressure and temperature profiles shows variations that are due to the surging, and the four spinner passes do not line up parallel as they do in stable wells. The flash depth is at 4600 feet, as indicated by a decline in pressure gradient above that depth. The fluid velocity profile shows a small flow from near bottom and a significant inflow at 6050 feet. There is a slow zone at 4500 feet, probably due to the flash at that depth. Another production zone is indicated at 4400 feet where the fluid velocity increases again. Scale inhibition in this well was complicated by the surges, which diluted the inhibitor below the necessary dosage.

Well 6 had a downflow and thief zone when this survey was run (Figure 8). The downflow is represented by a negative fluid velocity from 3000 to 2600 feet. The flash depth is at 2900 feet, as indicated by a decline in pressure gradient above that depth. The fluid velocity indicates flow from near the bottom of the well that continues up to 3100 feet where it drops off to zero and then goes negative up to 2600 feet. The fluid velocity jumps up at 2600 feet and, except for a dip at 2400 feet, continues to increase up the wellbore. Scale inhibition in this well was not successful because inhibitor injected below the flash depth was lost to the thief zone. A workover was performed to plug the thief zone with cement and subsequent surveys did not show a downflow.

## CONCLUSION

Multipass PTS surveys, analyzed with the aid of a computer program, have provided much useful information on wells in the Coso Geothermal Field. The results of PTS survey interpretations have been valuable in choosing depths at which to hang tubing for the inhibition of calcium carbonate scale. The surveys have some interesting characteristics that have not been investigated in depth but may be due to two-phase flow effects. Refinement of the PTS survey analysis methods, such as accounting for nonlinear effects, could improve the accuracy of the results. Other methods of investigating wellbore flow can clarify some ambiguities of PTS surveys. Dye tracer has been injected down the inhibitor injection tubes at Coso to measure the quantity and timing of returns to the surface. It is planned to summarize the results of the dye tracer testing in a subsequent paper.

## ACKNOWLEDGEMENTS

I want to thank the management of California Energy Company, Inc.(CECI) for providing the resources necessary to develop the multipass PTS survey analysis program and for permission to publish this paper. Thanks are also due to Mark Tibbs of CECI for coordinating the field operations and to Tom Bradley of Flo-Log, Inc. for running the multipass PTS surveys and providing the data in the required format.

## REFERENCES

1. Dresser Atlas, *Interpretive Methods for Production Well Logs*, Third Edition, 1982.

2. Peebler, Bob, *Multipass Interpretation of the Full Bore Spinner*, Schlumberger Well Services, 1982.

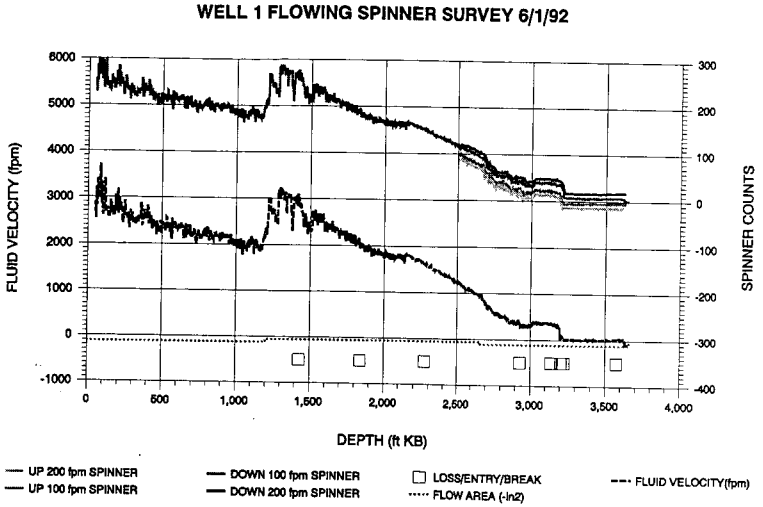


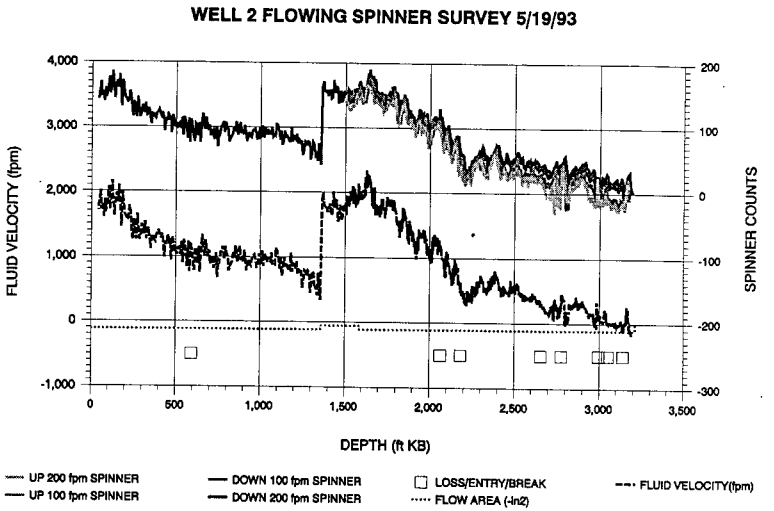


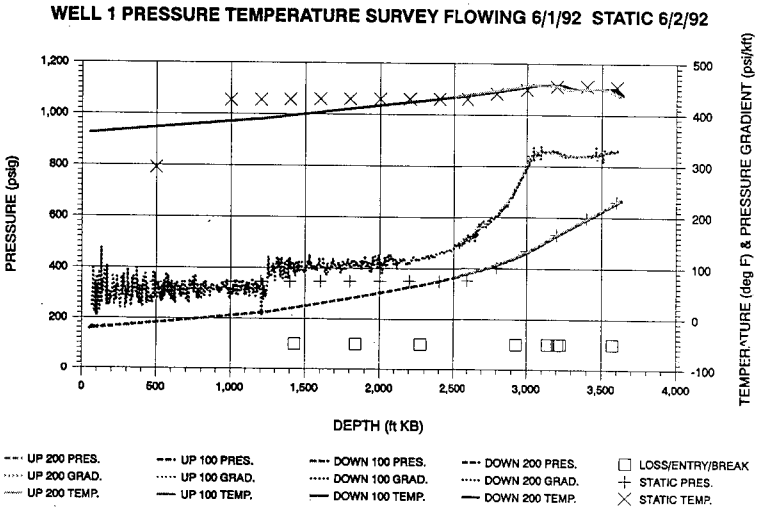


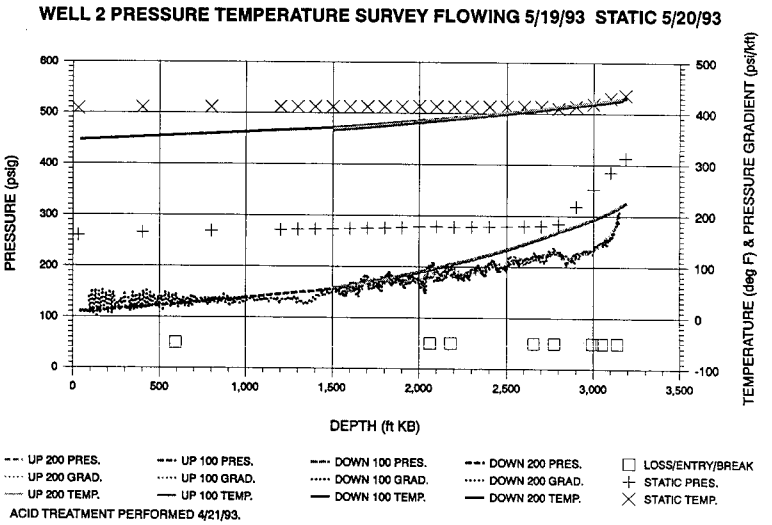


**Figure 3.** Pressure-Temperature-Spinner Survey from Well 1.

**Figure 4.** Pressure-Temperature-Spinner Survey from Well 2.

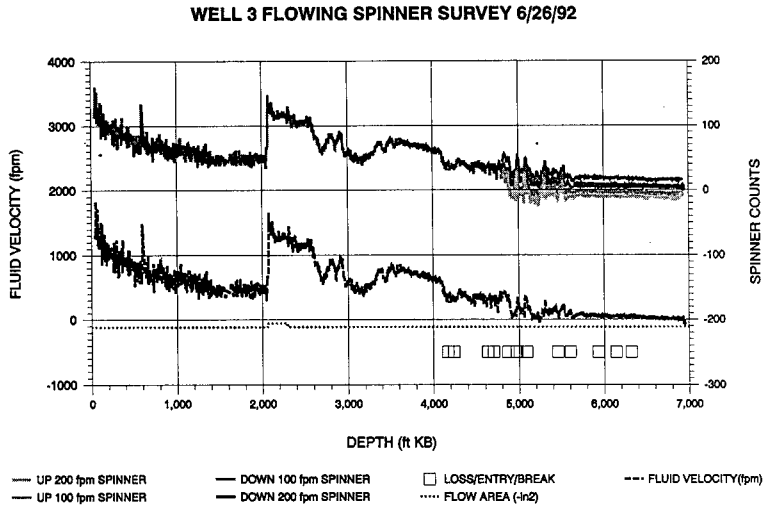


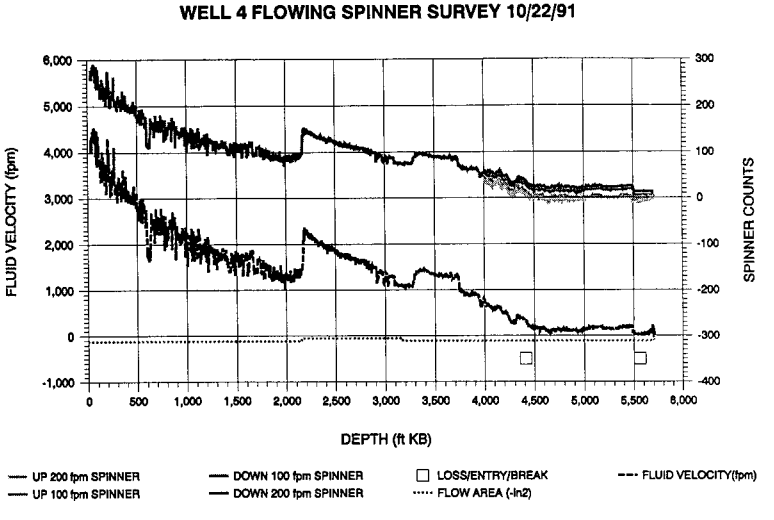


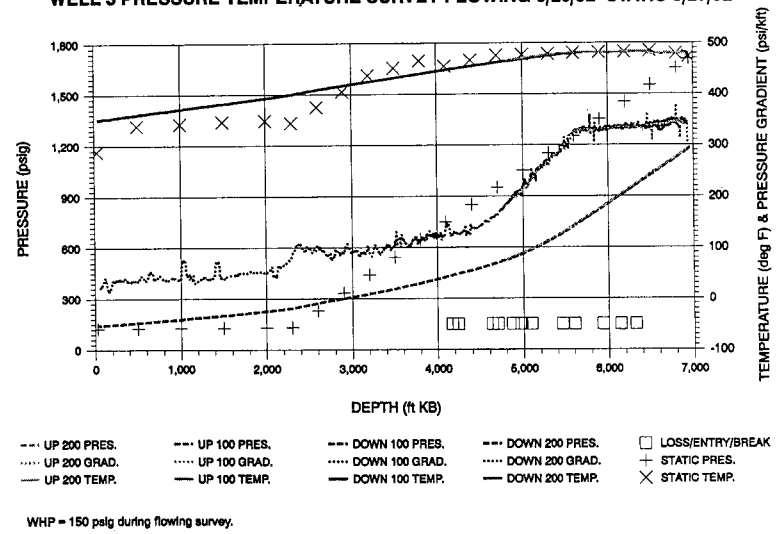


**Figure 5.** Pressure-Temperature-Spinner Survey from Well 3.

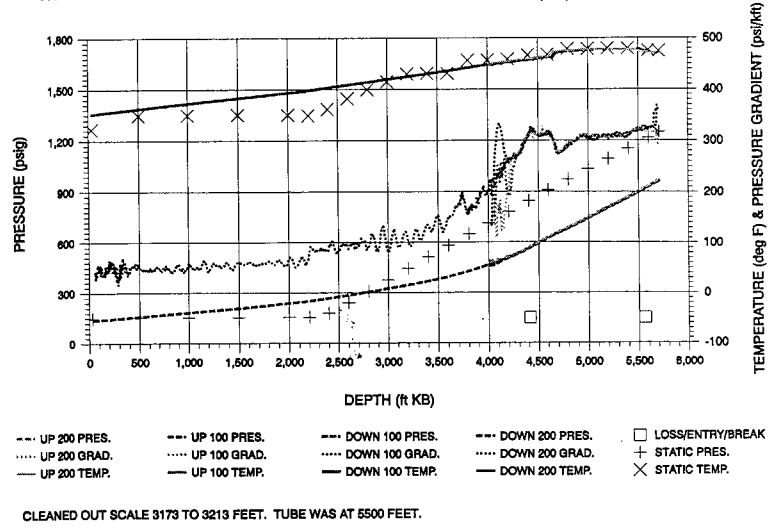


**Figure 6.** Pressure-Temperature-Spinner Survey from Well 4.

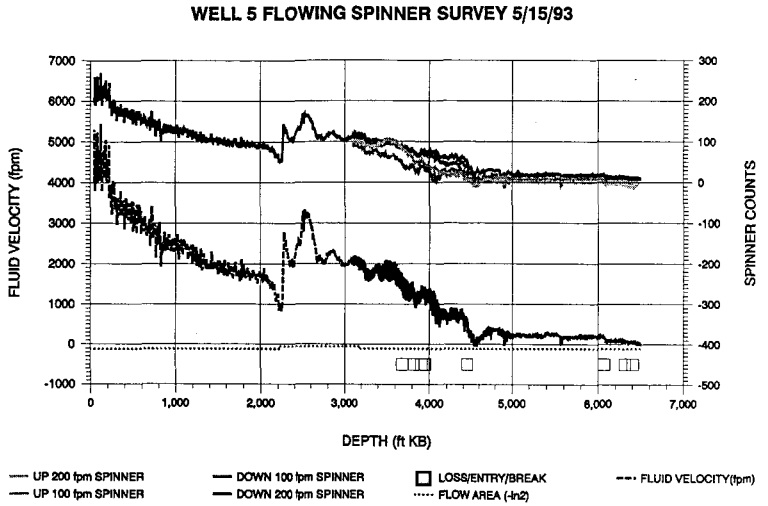


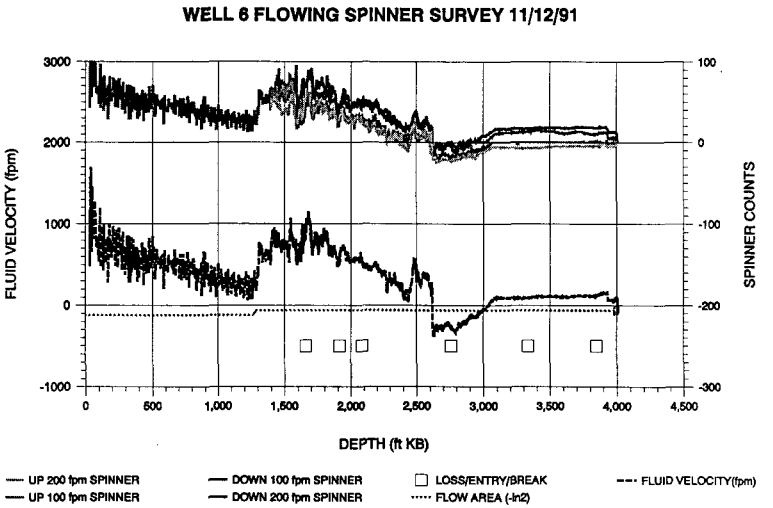


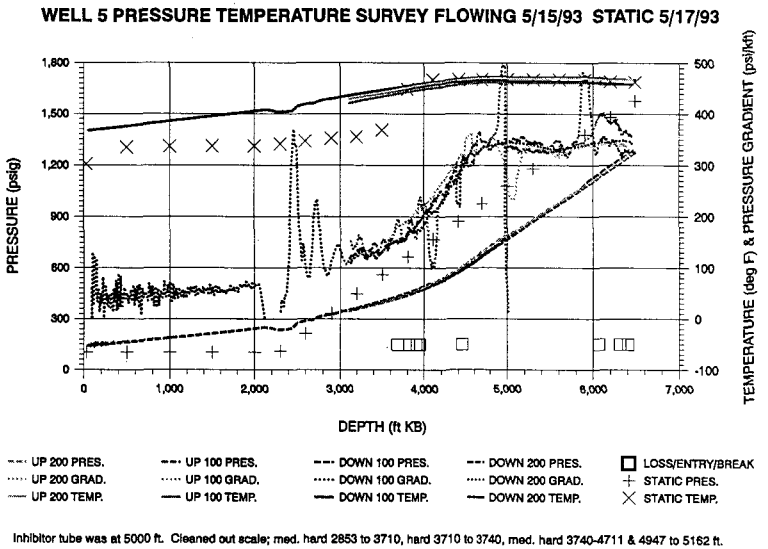


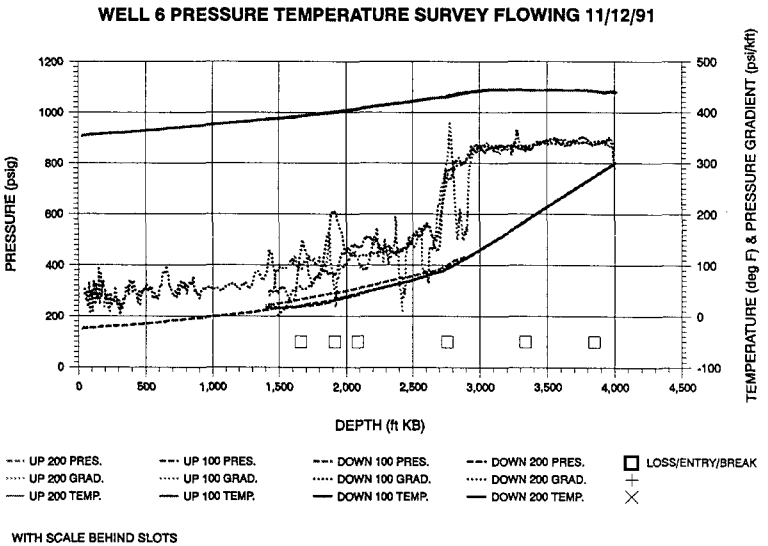


**Figure 7.** Pressure-Temperature-Spinner Survey from Well 5.

**Figure 8.** Pressure-Temperature-Spinner Survey from Well 6.

PROCEEDINGS, Nineteenth Workshop on Geothermal Reservoir Engineering
Stanford University, Stanford, California, January 18-20, 1994
SGP-TR-147

# RESULTS OF INJECTION AND TRACER TESTS IN OLKARIA EAST GEOTHERMAL FIELD.

Willis J Ambusso

Kenya Power Company Ltd, P.O Box 785
Naivasha, Kenya.

## ABSTRACT

This paper presents results of a six month Injection and Tracer test done in Olkaria East Geothermal Field. The Injection tests show that commencement of injection prior to onset of large drawdown in the reservoir leads to greater sustenance of well production and can reduce well cycling which is a common feature of wells in Olkaria East Field. For cases where injection is started after some drawdown has occurred in the reservoir, injection while leading to improvement of well output can also lead to increase in well cycling which is a non desirable side effect. Tracer tests reveal slow rate of fluid migration (< 5 m/hr). However estimates of the cumulative tracer returns over the period of injection is at least 31 % which is large and reveals the danger of late time thermal drawdown and possible loss of production. It is shown in the discussion that the two sets of results are consistent with a reservoir where high permeability occurs along contact surfaces which act as horizontal "fractures" while the formations between the "fractures" have low permeability. This type of fracture system will lead to channeled flow of injected fluid and therefore greater thermal depletion along the fractures while formations further from the fracture would still be at higher temperature. In an attempt to try and achieve a more uniform thermal depletion in the reservoir, it is proposed that continuous injection be done for short periods ( ~ 2 years) and this be followed by recovery periods of the nearly the same length of time before resumption of injection again.

## INTRODUCTION.

A joint Injection and Tracer test was done in Olkaria East Field between April and September 1993 to determine the effect of injection on the performance of production wells and to evaluate the possibility of implementing long term injection programmes in the field. This sector of Olkaria field has been exploited for power generation for over ten years now and most parts of the field have experienced pressure drawdown of about ten (10) bars. This has lead to the enlargement of an originally thin steam dominated zone in the upper part of the reservoir and to development of two phase conditions in the lower sections. Total steam production from the entire field has declined at an average rate of 4-5 % per year while most wells have also experienced an enthalpy rise over this period with a number of wells in the field center discharging saturated and slightly superheated steam (Ambusso and Karingithi,1993). Temperature changes in the field center have dropped by between 5 and 15$^0$C as deduced from short shut-in tests and regular downhole surveys. Because of this injection is considered an attractive way of extracting the high energy reserves in the reservoir and has the possibility of restoring some of the lost production or at least reducing the rate of decline in steam production. The tests discussed in this paper were aimed at determining a suitable injection strategy that would lead to efficient extraction and utilization of the energy reserves while avoiding some of the detrimental effects that have been reported in several injection projects worldwide.

Though it is intended that injection be done in parts close to the field center where largest drawdown have been experienced, no wells were immediately available there and OW-3 which is a non-commercial well to the south west of the field was selected as an injector well. This well has been used for pressure monitoring in the field and is known to be in communication with the reservoir having itself experienced a pressure drop of about twelve (12) bars. A number of production wells are within a few hundred meters of this well and it was therefore considered suitable for the preliminary tests. Fig 1 shows a layout of the wells in the field.

## TEST DESCRIPTION.

A total of 413542 cubic meters of water at ambient conditions (18$^0$C) was injected over the period of the test which in all took 172 days giving an average injection rate of about 100 cubic meters per hour. The total amount of water injected during the test is almost twice the amount of steam withdrawn per month from the whole field while the average injection rate is close to half the mass withdrawal rate by the wells around OW-3.

As a method of evaluating effects of injected fluid on the production wells all output parameters of the wells around OW-3 were continuously monitored during the period of injection and shortly after to asses the rate of return to normal after stoppage of injection. The parameters selected for this purpose were steam and water flowrates, and discharge enthalpy. The overall variation of the three parameters with time (cycling) also formed an important part of the tests. Due to fluctuation in well output for most wells it was found necessary to compute average values from data collected in five (5) minute intervals for 2 to 3 hours

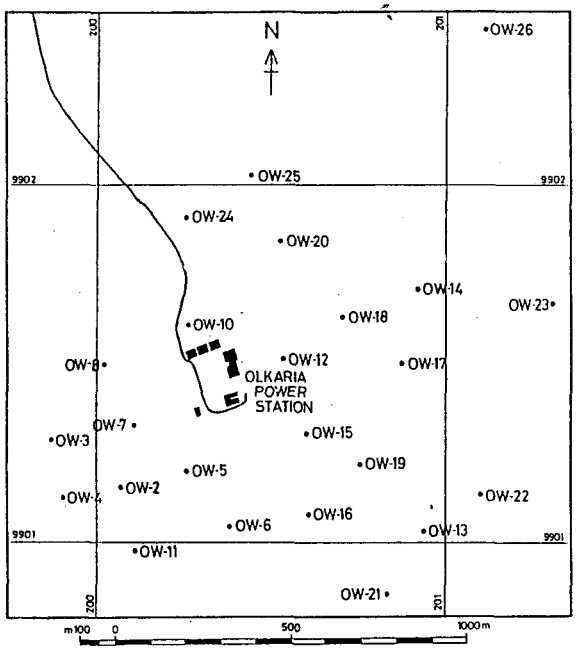


Fig.1 Well sites

either once a week or once a fortnight. These values were then plotted against time and changes noted. For wells with steady flowrates daily spot readings were found to be sufficient. For wells connected to the power plant steam flow was determined from pressure drop across orifice plates on the steam line. The pressure drop across the orifice plates was also recorded on charts that were fixed on the steam line which also indicated variations in steam flow. Water flow was measured by a weir-box and corrected for flushing to the atmosphere. One well, OW-4 which shares a production separator with OW-2 and with which it produces alternately was blowing to atmosphere and the James lip pressure method was used for output computations.

For the Tracer test Fluorescein Sodium a chemical that is known to undergo thermal degradation at elevated temperatures was used. However this degradation is known to take place exponentially (Adams and Davies, 1991) and large amount of the tracer was used so as to compensate for the effects of temperature. One hundred and twenty five (125) Kilograms of the tracer was introduced in OW-3 after forty five (45) days of injection. This was done over a 1¼ hour period with the water flow stopped and therefore effectively represents a slug. A multipurpose Perkin-Elmer florimeter with a sensitivity of $10^{-14}$ mole/ liter was used to detect the tracer in brine samples. However the lowest sensitivity had to be raised to $10^{-9}$ mole/liter as a number of wells had background fluorescence at this level presumably due to fine suspensions.

Three samples per day were collected and analysed during the first month after introducing the tracer. The frequency was later reduced to one sample per day for the next two months. For all wells samples were collected from the weir-box except OW-8 which shares a separator with OW-7. Samples for OW-8 were collected from the two phase line. For OW-7 which was blowing through the well silencer and not connected to the plant it was not possible to determine independent tracer level as the water flow at the weirbox was for the two wells (with OW-8). It was however still possible to determine the first arrival time as Fluorescein was detected first at the weir-box while the tracer was detected in samples from the two phase line at a later time.

Due to strong tracer returns and notable changes in well output for a number of wells during the injection period, it was decided in the course of the tests to determine changes in brine chemistry as these were likely to show dilution trends with time. The comparatively inert and easy to analyze chloride was selected and it's concentration was determined alongside the Fluorescein. This data as shown below proved useful in tracing the fluid returns as two wells OW-2 and OW-4 showed what seemed to be clear dilution trends.

Pressure Transient tests that were planned to be done at various stages of injection were abandoned due to difficulty in maintaining steady injection rates. However regular downhole surveys were done throughout the injection period and shortly after. Temperature information from these surveys did prove useful for purposes of identifying water loss zones. These profiles also provided a suitable method for evaluating the extent of thermal depletion as the injection well being the point of cold water entry should basically represent the extreme case as far as heat extraction by the injected fluid is concerned and temperature recovery trends are important in this aspect.

## RESULTS

Results are presented for those wells that did show changes in output that can be attributed to injection and those that did receive significant amount of the tracer. This is done separately for injection and tracer tests before the two sets of results are integrated into one and the overall conclusion from the two sets discussed in the next section.

### Injection tests

OW-2 which is 216.7 meters from OW-3 was the first well to show change in output parameters which occurred within the first month of injection. The water flow which hitherto had only small fluctuations started having surges which exceeded ten (10) tonnes/ hour an amount that was nearly twice the highest recorded water flowrate over the past three years. The surges increased both in magnitude and frequency throughout the injection period. These surges in water flow were accompanied with reduction in steam flow. Figures 2 shows daily water readings for OW-2 during the injection period. It is clear from the graph that the surges increased throughout the injection period.

Figure 3 shows the average steam and water flow for OW-2 from monitoring data collected every fortnight. The figure shows that the average water flow increased progressively throughout the injection period before falling gradually shortly after injection

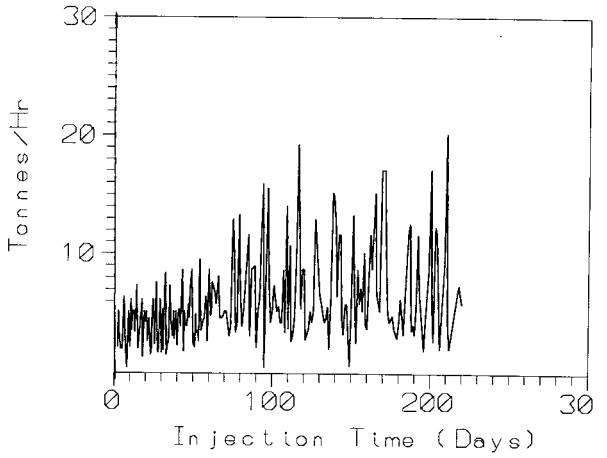


Fig.2 OW-2 Daily Water Flow

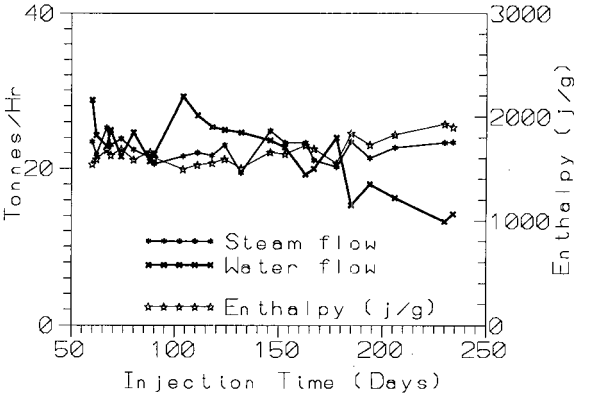


Fig.4 OW-4 Average Output Values

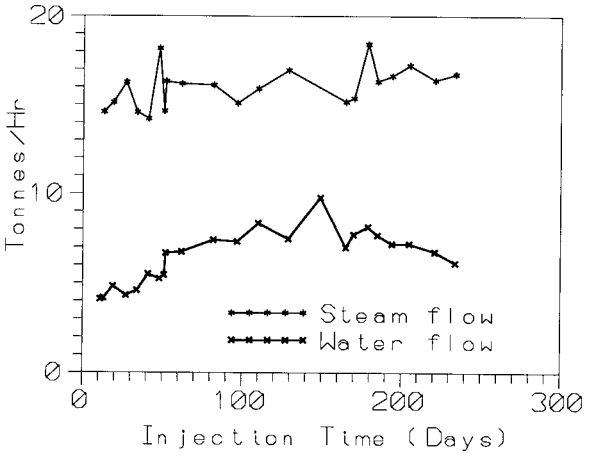


Fig.3 OW-2 Average Output Values

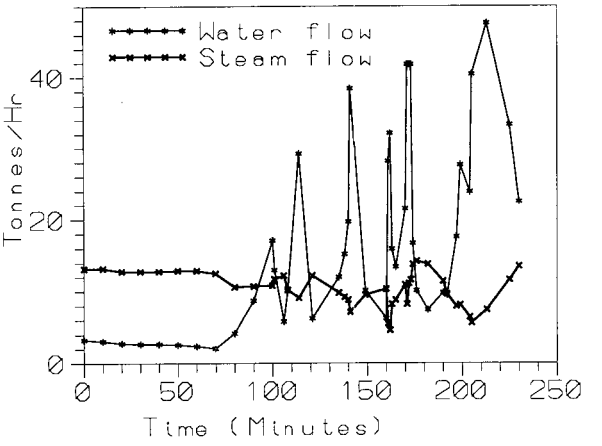


Fig.5 Ow-4 Output in 1988

was stopped. The surges in water flow did not show any reduced frequency but the highest readings were subsequently lower than those recorded during the injection time. The steam flow on the other hand remained unchanged during the injection period. This shows that the main effect of injection is to cause an increase in water flow.

Figure 4 shows average steam and water flow, and enthalpy for OW-4 during the injection period and shortly after. This well is 185 meters from OW-3 and was only opened for discharge through the atmospheric silencer with injection in progress. The figure shows that steam and water flow were unchanged throughout the injection period' but the water flow dropped after injection was stopped. This is also reflected in the increase in enthalpy after injection. This behavior shows that as in the case of OW-2 the injected water goes largely to increase the water flow. Another notable feature of this well over the injection period was the reduction in cyclicity. This well is known from previous discharge tests to be cyclic with periodic variations in water flow. However during the injection period there was notable stability in all output parameters which in all cases were higher than those recorded during the earlier tests. Figure 5 and 6 show steam and water flow over monitoring periods during discharge tests in 1988 and during the

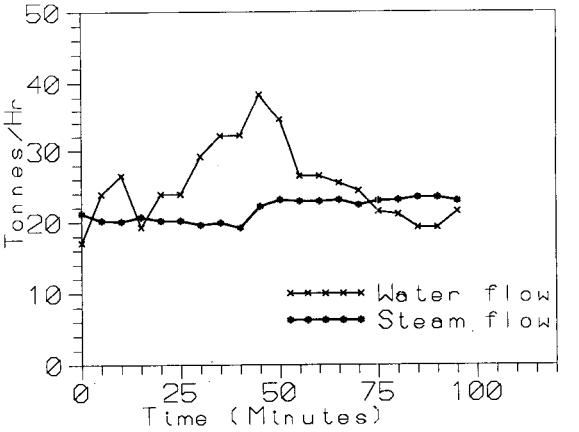


Fig.6 OW-4 Ouput during injection (118 days of injection)

just concluded injection tests respectively. In both cases the lip pressure pipe was 5 inches. The increased production and higher stability show that the well output was boosted by the injected fluid.

Figure 7 shows daily water flow for OW-11 which is 438 m from OW-3. The initial increase in water flow

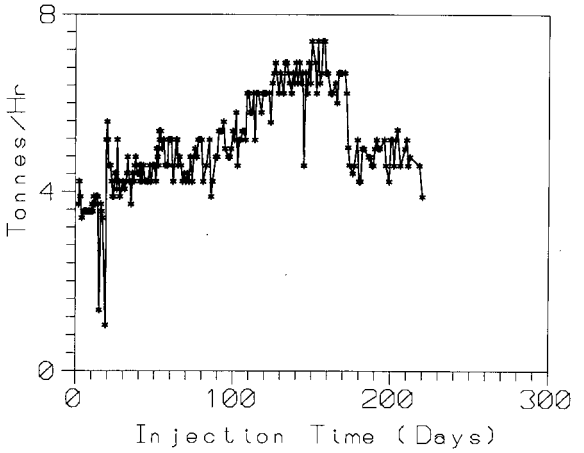


Fig.7 OW-11 Water Flow (T/Hr)

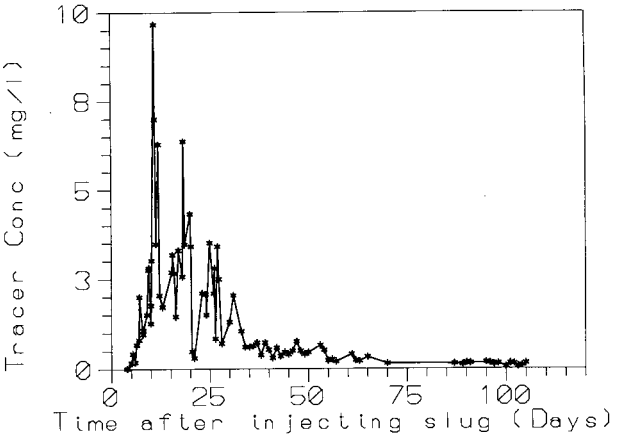


Fig.8 Tracer Profile for OW-4

after 20 days is due to weir-box cleaning and is therefore not real. There is a systematic increase in water flow after about ninety (90) days of injection before the flow stabilizes about a month later. Steam flow over this period was constant and no changes in flowrate or cycling as in the case of OW-2 was observed. This increase in flow can only be attributed to return of the injected fluid. This late increase in water flow is followed by a rapid and almost immediate decline in water flow after injection.

No other wells showed changes in output due to injection. Most notable among these wells is OW-5 which being 374 meters from the injection well is closer than OW-11 which had did show significant increase in water flow. This negative result has to do with the shallow depth of the well (901 meters) and is discused below.

**Tracer tests.**

Tracer return profile for OW-4 is shown on figure 8 while figure 9 shows profiles for OW-2 and OW-7(& OW-8). The strongest tracer return was recorded in OW-4 whose tracer concentration at the peaks was five hundred times higher than those for OW-2 and OW-7 and the strong green colour of the Fluorescein Sodium was visible at the weir-box during most of the test period. The first arrival times are 106 hours for OW-2, 88 hours for OW-4 and 98 hours for OW-7. The tracer speeds from these arrival times are 2 meters per hour for OW-2 and 2.1 meters per hour for OW-4 and OW-7. These tracer speeds are moderate as compared to speeds reported for other fields in the world.

The tracer return profile for OW-2 does not have the classical build up to the peak as for OW-4 but still does have a number of important interpretive features. However given the strong effects of injection reported above a stronger tracer return should have been expected. That this was not so does show that the tracer could have suffered thermal degradation and stronger tracer returns should been observed otherwise. However taken as it is the short return time and the extended peak show the existence of short circuit paths between the well and OW-3 and that there is substantial mixing along the path respectively. The obvious tail does show that there is tracer

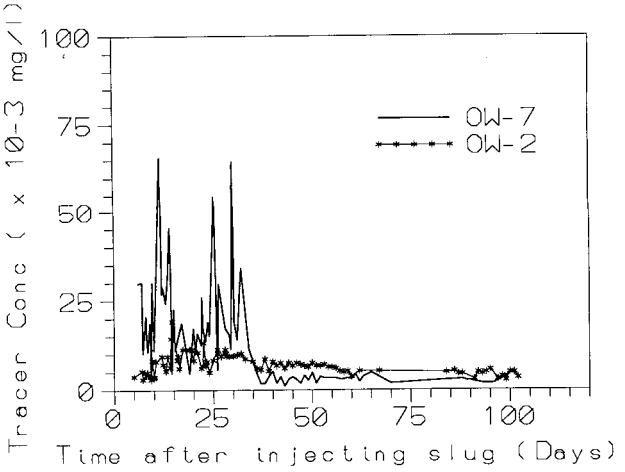


Fig.9 Tracer Profile

dispersion/retention along the return path. This shows that the fracture(s) transmitting the fluid is (are) small and that the formation does have high permeability. Only 120 grammes of the tracer or .1 % of the total injected tracer was recovered in this well over a period of about 100 days.

For OW-4 three classical peaks in a declining manner were observed and a tail at lower concentration was observed after the last peak. The profile shows that there are several return paths between this well and OW-3. However the lower tracer concentration at the tail shows that only a small proportion of the tracer is either dispersed or retained as most of the tracer returned during the peaks. Further more the tracer build to the first peak after first arrival takes along time while the peaks are rather sharp. These return characteristics do show greater tracer spread rather than mixing as the later property would lead to a prolonged or extended peak. The low tracer concentration at the tail does indicate lower formation permeability as otherwise a significant level of tracer should have been retained. 38 kgs or 30 % of the total tracer injected was recovered in this well over a period of about 100 days. This amount of tracer is large and indicates large injection fluid returns and does show the potential for rapid thermal depletion even though

tracer speeds were low.

The return profile for OW-7 is very fluctuative. This variation was because the water flow at the weir-box was combined with that from OW-8 a well with a variable water flow and only had low levels of tracer at a latter time. The total, amount of tracer recovered from this well was estimated to be 160 grammes.

## Chloride

Figure 10 shows the daily weir-box chloride concentration for OW-2 and OW-4 the two wells that showed chloride change during injection. The dilution trends are different as OW-2 shows a gradual linear dilution trend while OW-4 shows a 'step' change in chloride concentration. The former shows that there was a gradual increase in the proportion of injected fluid in the final discharge throughout the injection period while the step change observed for OW-4 shows that the proportion of injected fluid in the final discharge remained constant throughout the injection period. The trend shown by OW-2 is reminiscent of a diffusion type process such as would occur in gradual temperature decline as observed in cases of fluid transmission through a fracture at high temperature with heat being transferred to the fracture conductively. This trend is suggestive of fracture-matrix interaction where there is fluid contribution from the matrix to the fracture with the fluid from the matrix either diminishing continuously or itself undergoing dilution. For the case of OW-4 the step change does show absence of continuous fluid contribution by the matrix and possibly existence of different return paths for the injected and resident reservoir fluid to the production well. This could also imply that mixing of the two species of fluid occurs near the production well.

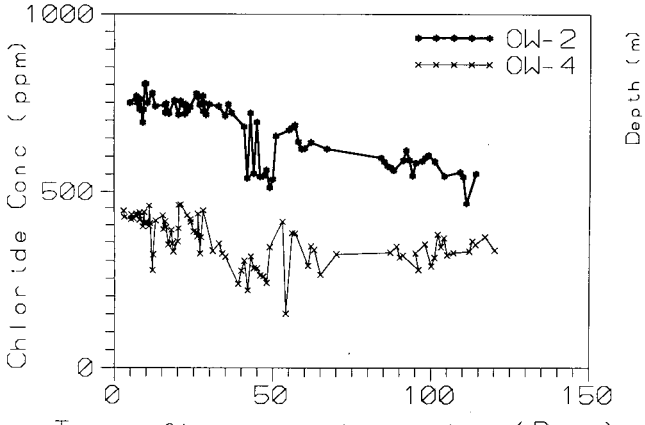


Fig.10 Chloride (OW-2 and OW-4)

It is possible to estimate the proportion of injected fluid in the final discharge in both cases by assuming simple single stage mixing between the injected fluid whose chloride concentration was about 95 ppm and the liquid phase of the resident reservoir fluid. These estimates give the proportion of injected fluid in the total discharge as 3.5 % and 18 % for OW-2 and OW-4 respectively. Further refinements taking into account the chloride variation in the field, fracture and other formation properties need to be applied to this data to obtain more reliable estimates of proportion of injected fluid in the final discharge from this data.

## Down hole surveys.

Figure 11 shows temperature profiles taken in OW-3 during the injection tests and shortly after. Also included is a profile taken in the well before injection. The profiles during injection show high temperature readings ($35^0$ C) and implies that the upper parts of the well could have been discharging during injection. This is supported by the profiles taken after injection which show rapid recovery of the upper parts of the well. The main parts of water loss from the profiles were below 850 m depth. This deep level of water entry explains partially the negative results observed in OW-5 whose total depth is only 910 meters. The temperature recovery even for parts that are within the main loss zones is significant and does show that the effect of injection in the reservoir parts beyond OW-3 are less than those in the well.

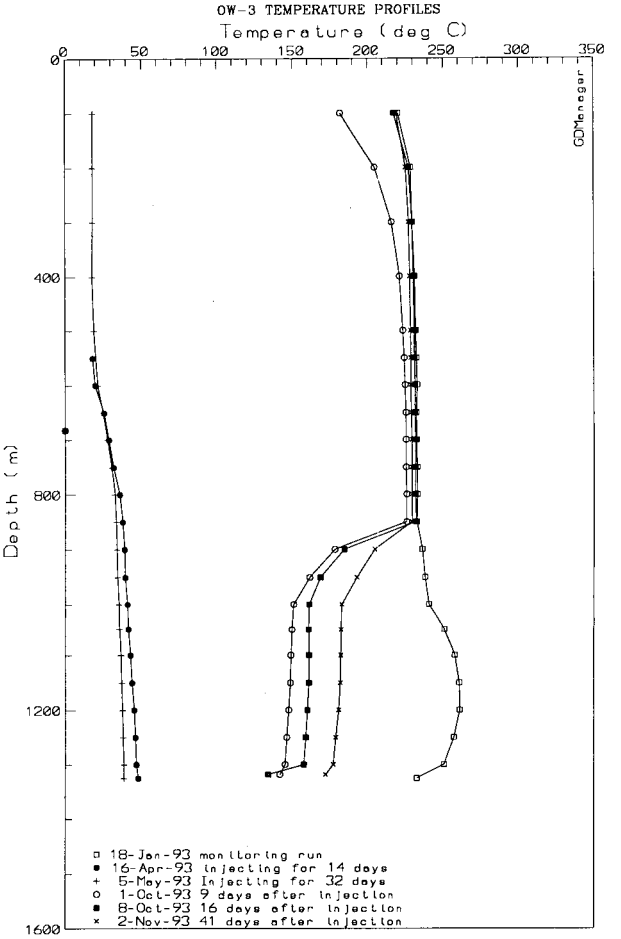


Fig.11

## DISCUSSION

The results of injection and tracer tests show that the principal directions of fluid migration is southwards with smaller proportions migrating to the north. These are the directions of low pressure potential as these zones have undergone depletion due to production. It

however does seem necessary to invoke a high permeability channel between OW-4 and the injection well given the high level of tracer return in the well. The most important part of the tests are the results of injection tests as these show directly the effect of injected fluid on well performance. However there are some aspects of the tracer tests that have important bearing on the reservoir structure and these are evaluated first before making an assessment of injection strategy.

For all the wells where tracer returns were recorded the tracer speeds were low. However the total tracer returns are large being at least 31% of the injected tracer for all wells. Another aspect of the tracer profiles is the sharp peaks seen in OW-4 that show less mixing of the fluid but a gradual build up to the peak indicates tracer spread. A fracture characteristic that adequately accounts for these features is one where large horizontal fractures are the ones transmitting fluid while the surrounding formations have low permeability. Such fractures would give low tracer speeds due to their large size and fluid flow in them would be radial and speed should decrease inversely with distance. The returns would still be large as the injected fluid would nearly all be transmitted to the production wells. This is supported by the geological structure of the wells which show nearly similar lithologies of the wells (Noble and Ojiambo,1976). This structure is the cause of the mainly lateral permeability known to exist in this part of the Field.

As for the effects of the injected fluid on well performance the most significant was the increase in water flow. Except for OW-4 (see next paragraph), for the other wells steam flow was not affected by the injection and does show that only the mobility of the liquid phase was increased by injection. That steam is unaffected by injection could be because of the two phase nature of the reservoir where pressure is governed by temperature which changes very slowly even on injection. However it is possible some of the injected could have been boiled and returned as steam. It would be difficult to increase the steam flow as significant proportion of the injected fluid would have to boil so as to increase the pressure and steam phase mobility in the reservoir. This can be achieved to some extent in the field center which is steam dominated and a higher proportion of the injected fluid could be boiled. Higher Injection temperature would lead to better results.

For OW-4 the effect of injection was not only an increase in total flow but also low cycling compared to what was seen in the well during discharge tests. The steam flow during this period was also higher than those during the tests. This does show that production was sustained as the well was able to maintain production most of the time. There also seems to be an advantage in opening the well with injection in progress as the zone around the well was still at a higher pressure potential. Thus the injected fluid goes to sustain the fluid flow rather than first restore then sustain flow as was the case for the other wells. This indeed seems to be the case with OW-2 where increase in instability was noted. This can be attributed to premature return of injected fluid and could be reduced by injecting at higher temperature.

The recovery trends after injection do show that the effects of injection are reversible provided the injection periods are short. This is true for the production trends in OW-2 and OW-4 and in the injection well itself where temperature measurements have shown significant recovery. However due to channeled flow along fractures, thermal depletion along the return path can still be large while formations beyond the fractures could still be at high temperature. This non uniform extraction of heat along the fractures can lead to enthalpy reduction and loss in output. Allowing for a recovery time as was done for the above tests will lead to better redistribution of heat from the hotter formation to the cooler fractures. This will lead to more uniform heat extraction without risking loss of production. Further tests will be necessary to establish the safe lengths of injection and recovery that will be applied. However in the central parts of the field longer periods of injection could be used as there are several production wells.

## CONCLUSION.

From the foregoing results and discussions injection into OW-3 is feasible and the effects of injection over short periods on well output do not show severe thermal degradation. The advantage of increased well output for OW-4 and reduced cycling do outweigh the small disadvantage of increased cycling seen in OW-2. Further more the cycling does not lead to loss in steam production and could be reduced by injecting water at higher temperature. The results also show that injecting in the field center which is steam dominated could lead to better results. However as in the case OW-3 continuous injection should be over short periods and be followed with 'recovery' periods for about the same length of time before resumption of injection again.

References

Adams M.C and J Davis, 1991 "Kinetics of Fluorescein Decay and it's Application as a Geothermal Tracer". Geothermics Vol. 20 1991.

Ambusso W.J and C.W Karingithi, 1993 "Response of Olkaria East Geothermal Field to Production". GRC Vol.17

Noble J.W and S.B Ojiambo,1976 " Geothermal Exploration in Kenya". KPC Report.

Horne R.N,1982 "Geothermal Reinjection Experience in Japan". JPT Vol 34.

PROCEEDINGS, Nineteenth Workshop on Geothermal Reservoir Engineering
Stanford University, Stanford, California, January 18-20, 1994
SGP-TR-147

# On the Interpretation of Tracer Experiments

Ibrahim Kocabas
Suleyman Demirel University, Isparta, Turkiye

Roland N. Horne
Stanford University

William E. Brigham
Stanford University

## Abstract

Recently, two new developments appeared in the literature on modelling flow and transport in heterogeneous systems. The first one is the use of two different concentration variables namely, the resident and flux concentrations, in tracer studies. The second one involves representing the heterogeneity by means of a frequency disribution function for immobile phase size. Based on these developments, this work involves a classification of the solutions of transport equation in heterogeneous systems. It also demonstrates interpretation of tracer experiments in such systems.

Distinguishing between the resident and flux concentration variables prevents the inconsistencies between theoretical solutions and actual conditions of experiments and hence, allows correct interpretation of tracer return profiles. Representing heterogeneities by means of frequency distribution functions allows representing matrix blocks of various sizes likely to exist in a fractured reservoir.

## 1 Introduction

Convection-dispersion equation has been the most commonly used model of transport in porous media. Common experience, as summarized by Parker and van Genuchten[1], is that in cases of media with low apparent dispersivities, experiments yielded fairly symmetrical tracer return profiles and solutions of this model matched the observed profiles well. However, in cases of media with large variations in pore water velocities caused by preferential flow paths, experiments yielded asymmetrical tracer return profiles. An apparent cause of this is that some part of pore space could be bypassed resulting in different flux and resident concentrations.

As a result, need arised for re-evaluating the applicability of convection-dispersion model for heterogeneous media. This re-evaluation indicated that some of the limitations come from the failure to distinguish between the resident and the flux concentrations.

Failure to distinguish between these two types of concentrations leads to use of solutions inconsistent with the actual conditions. This point has first been shown by Brigham[2], then Kreft and Zuber[3] classified solutions of convection-dispersion equation in terms of these concentration variables and others followed them.

Modelling flow and transport in heterogeneous media depends on the scale of flow and varies from employing a single fracture located in a porous matrix to considering the entire medium as a single continuum representing the characteristics of both fractures and porous matrix blocks[4].

One of the two recent developments in modelling transport in heterogeneous media is use of frequency distribution functions for the size distribution of matrix blocks [5, 6]. Another development in modelling such systems is representation of the fracture transport equations of the far field approach by a single standard equation by using block geometry functions[7], BGFs.

## 2 Theoretical Developments

In the following, the above mentioned two new developments are combined to develop solutions to equations of transport in heterogeneous media. The standard equation of transport is nondimensionalized to be made independent of scale. Then, the solutions were classified with regard to the distinction between the resident and flux concentrations.

### 2.1 Two Concentration Variables in Tracer Studies

A variable of a system is defined as a characteristic which acquires different numerical values at different times. A parameter, on the other hand, is defined as a quantity characterizing the physical processes acting upon the variable and remaining constant in time[8]. In tracer studies, the use of two different variables, namely resident and flux concentrations, has been equally common.

In development of mathematical equations, the resident concentration, $C_R$, defined as the amount of tracer per unit volume of the system at a given instant, has always been taken as the variable of the system. In experiments, on the other hand, the flux concentration, $C_F$, defined as the ratio of the tracer flux to the volumetric flux, has been the most commonly measured quantity. As a result, tracer return profiles have been plotted mostly by using the flux concentration as the output variable. These two concentrations differ whenever the system is dispersive and there is a concentration gradient. In a dispersive system the flux and the resident concentration variables are related by:

$$C_F = C_R - \frac{1}{P_e}\frac{\partial C_R}{\partial x_D} \tag{1}$$

where $x_D$ is the dimensionless distance and $P_e$ is the Peclet number. Eq. 1 serves for finding $C_F$ whenever the theoretical form of $C_R$ is known, or vice versa.

Based on $C_R$, the equation of transport in a one-dimensional linear system is:

$$\mathcal{L}C_R = q_D \tag{2}$$

where $q_D$ is a dimensionless source function, and the linear operator $\mathcal{L}$ is:

$$\mathcal{L} = \frac{1}{P_e}\frac{\partial^2}{\partial x^2_D} - \frac{\partial}{\partial x_D} - \frac{\partial}{\partial t_D} \tag{3}$$

where $t_D$ is the dimensionless time:

$$t_D = \frac{ut}{L} \tag{4}$$

Normally, one would solve Eq.2 for $C_R$, and then find the expression for $C_F$ by using Eq.1. However, whenever $q_D$ is a linear function of $C_R$, it is also possible to solve Eq.2 for $C_F$ directly as explained below.

Differentiating Eq.2 with respect to $x_D$ yields:

$$\frac{\partial}{\partial x_D}\mathcal{L}C_R = \frac{\partial q_D}{\partial x_D} \tag{5}$$

Since the solution is required to be continuous in $x_D$ the differentiation can be carried inside the operator:

$$\mathcal{L}\frac{\partial C_R}{\partial x_D} = \frac{\partial q_D}{\partial x_D} \tag{6}$$

Eq.6 states that if the source term $q_D$ is a linear function of $C_R$, the partial derivative of $C_R$ with respect to $x_D$ is also a solution of Eq.2. Similarly, partial derivatives of any order with respect to either of $x_D$ or $t_D$ yield the same result[9]. In addition, according to the superposition principle, a linear combination of two solutions must also be a solution. Based on this principle, the following particular relation is important:

$$\mathcal{L}\{C_R - \frac{1}{P_e}\frac{\partial C_R}{\partial x_D}\} = q_D - \frac{1}{P_e}\frac{\partial q_D}{\partial x_D} \tag{7}$$

Expressing Eq.7 in terms of $C_F$:

$$\mathcal{L}C_F = q_F \tag{8}$$

Eq.8 states that when the dependent variable $C_R$ of Eq.2 is transformed to $C_F$, the form of Eq.2 remains the same. Consequently, it is possible to solve Eq.2 for $C_F$ directly by specifying the initial and boundary conditions properly. Unless a distinction is made between these two concentration variables, material balance errors will occur due to incorrect use of solutions. Such conclusions were also arrived at earlier by several researchers[1, 2, 3] who mostly used the classical convection-dispersion equation and actually performed a dependent variable transformation to show that Eq.2 is also satisfied by $C_F$. The method employed here, however, is more general and in the following section it will be applied to heterogeneous medium models.

## 2.2 Modelling Heterogeneous Systems

The classical convection-dispersion equation represents only one of the various approaches in modelling the transport in heterogeneous media. Therefore, it is desirable to generalize classification of solutions to dispersive models by constructing a similar table of solutions for heterogeneous medium models.

A heterogeneous system is characterized by preferential flow paths due to dead end pores, aggregates, fissures, fractures, layering, and so on. Tracer transport in heterogeneous porous media may be modelled in four ways[4] namely, the very near field, the near field, the far field, and he very far field. Names of these various approaches are related to the scale of heterogeneities with respect to the scale of flow.

The very near field is usually conceptualized as a fracture located in a porous matrix. Flow is assumed to occur in the fracture only. The reservoir fluid occupying the pores of the matrix is considered to be virtually immobile. The exchange of tracer between fracture and matrix occurs by molecular diffusion. Tracer concentrations across the fracture are equalized before any significant effect of the convection appears. Within the matrix, diffusive transport is assumed to occur only perpendicular to the flow direction in the fracture.

In the near field, tracer transport in a set of well defined preferential flow paths is considered. When a deterministic approach is chosen the transport equations are identical to equations of the very near field approach.

In the far field approach, tracer transport is modelled by using two superposed continua, a mobile phase composed of a network of preferential flow paths, and

an immobile phase representing the rest of the system. Immobile phase is assumed to act as a distributed source in mobile phase. Transfer from mobile to immobile phase may be assumed proportional to the difference between average concentrations of the two phases[10]. Alternatively, a diffusive transport may be assumed between mobile and immobile phases[11]. If a diffusive transport is considered between the two phases, a geometry and a size are assigned to the immobile phase. Superposition of multiple continua is required due to existence of different geometries or differing sizes of the same geometry.

A natural extension of multiple source terms is to assume the immobile phase size as a distribution function. This concept, which is one of the new developments in this field, has been successfully applied for fluid flow in porous media where the heat equation applies[5, 6].

Finally, the very far field approach is employed where the scale of flow is far greater than the scale of heterogeneities. In this approach the entire medium is treated as a single continuum representing characteristics of both mobile and immobile phases and no source term exists in the transport equation.

Except for the very far field approach, two coupled one-dimensional equations are used to represent the transport in heterogeneous systems. The dimensionless one-dimensional equation of the transport in mobile phase is given by Eq.2. Writing it in an open form, one obtains:

$$\frac{1}{P_e}\frac{\partial^2 C}{\partial x^2{}_D} - \frac{\partial C}{\partial x_D} - \mathrm{q_D} - \frac{\partial C}{\partial t_D} = 0 \qquad (9)$$

Also the nondimensionalized equation of transport in immobile phase is in the form of either:

$$\frac{1}{P_{im}}\nabla^2{}_D C_m = \frac{\partial C_m}{\partial t_D} \qquad (10)$$

or:

$$K_D \frac{\partial C_m}{\partial t_D} = (C - C_m) \qquad (11)$$

where

$$P_{im} = \frac{a^2 u}{D_m L} \qquad (12)$$

$$K_D = \frac{u}{KL} \qquad (13)$$

While Eq.10 is valid for a diffusive transfer between the two phases, Eq.11 is used when the transfer is assumed to be proportional to the average concentration difference between them. Equations 9 and 10 are coupled by using the continuity of the flux and concentration across the interface of mobile and immobile phases. Hence, the following relations holds:

$$C_R = C_m \quad on \quad \Gamma_D \qquad (14)$$

$$q_D = \frac{1}{\sqrt{P_t P_{im}}}\langle\frac{\partial C_m}{\partial \eta_D}\rangle_{\Gamma_D} \qquad (15)$$

where

$$P_t = \frac{(\frac{V_{fp}}{\phi A_m})^2 u}{D_m L} \qquad (16)$$

Equations 9 and 11, on the other hand, are coupled through the relation:

$$q_D = \omega \frac{\partial C_m}{\partial t_D} \qquad (17)$$

where $\omega$ is the ratio of the mobile phase fraction of the total pore space to the immobile phase fraction.

The presence of multiple blocks in immobile phase for the far field approach is treated as follows. Rearranging Eq.15 gives:

$$q_D = \frac{\sqrt{P_{im}}}{\sqrt{P_t}}\frac{1}{P_{im}}\langle\frac{\partial C_m}{\partial \eta_D}\rangle_{\Gamma_D} \qquad (18)$$

For a finite diffusive transport medium $\sqrt{P_{im}/P_t}$ is equal to the pore volume ratio, $V_{mp}/V_{fp}$. Keeping this ratio constant, that is if pore volume of immobile phase increases pore volume of mobile phase increases at the same rate or vice versa, means employing a distributed approach. That means the immobile phase is uniformly distributed within the mobile phase and pore volume ratios will be equal to $\omega$. If there are blocks of various size uniformly distributed in the field, the source term has to account for that distribution. Considering the block size is a continuous variable and the relative frequency density of blocks of size a in all blocks is $f_i(a)$, the expected total contribution is:

$$q_{DT} = \omega \int_{a_{min}}^{a_{max}} \frac{f_i(a)}{P_{im}}\langle\frac{\partial C_m}{\partial \eta_D}\rangle_{\Gamma_D} da \qquad (19)$$

where

$$\int_{a_{min}}^{a_{max}} f_i(a) da = 1 \qquad (20)$$

At this point it should be pointed out that all of the parameters of Eq.9 are based on the mobile phase characteristics, so that any difference between the solutions of various approaches will result only due to the source term $q_D$. Thus, for a comparision of solutions, observing the differences in the source term $q_D$ will suffice.

Regardless of the approach of modelling and the type of transfer between the two phases, the source term in Eq.9 defined by either of equations 15 and 17, may be expressed as:

$$q_D = \int_0^{t_D} \frac{\partial C}{\partial \tau}\, \mathrm{q_{uD}}(t_D - \tau)\, d\tau \qquad (21)$$

where $q_{uD}$ is the flux across the interface between the two phases for $C_m$ being equal to unity at the in-

terface, instead of $C$. Eq.21 is based on the well known convolution principle used mostly for deriving solutions of heat equation for a variable surface condition[9, 12].

Similarly, if $q_D$ is defined by Eq.11, it may also be expressed as Eq.21. However, in this case $q_{uD}$ will be:

$$q_{uD} = \frac{\omega}{K_D} \exp(-\frac{t}{K_D}) \qquad (22)$$

Eq.21 shows that the source term is a linear function of $C$ for all heterogeneous medium models discussed above. Consequently, the discussion on the $C_R$ and $C_F$ variables in the prevoius section, applies for heterogeneous medium models as well.

In summary, Eq.9 is also satisfied by $C_F$ for all heterogeneous medium models. The corresponding dependent variable of the immobile phase transport equation namely, $C_{mF}$ could satisfy both Eq.10 and Eq.11. As in the case of $C$ and $C_m$, $C_F$ and $C_{mF}$ are also correlated by the same relation[13] namely:

$$C_{mF} = C_m - \frac{1}{P_e} \frac{\partial C_m}{\partial x_D} \qquad (23)$$

Consequently, Eq.9 coupled with either Eq.10 or Eq.11 can be solved directly for $C_F$ as well as for $C_m$.

Finally, if the source term is a nonlinear function of $C_R$, none of the functions derived by using linear combinations of $C_R$ and its derivatives satisfy Eq. 9. In such a case, however, $C_F$ does not loose its physical meaning but can only be found from the theoretical expression for $C_R$ by using Eq. 1.

# 3 Classification of Solutions

If both concentration variables $C_R$ and $C_F$ satisfy the same equation, initial and boundary conditions determine whether the solution is in terms of $C_R$ or $C_F$. In solving mathematical equations, Brigham[2] explained the proper specification of the initial and boundary conditions based on these two concentration variables. Later, Kreft and Zuber[3] provided a classification of the solutions to the convection-dispersion equation and the transformations linking the solutions.

Based on the above discussion, solutions of Eq.9 may also be classified with respect to the modes of injection and detection of tracer. However, a complete set of solutions of Eq.9, of which the instantaneous injection solutions are given in Table 1, is mostly of academic interest. The continuous injection solutions could be obtained by multiplying the instantaneous injection solutions by $1/s$. The $C_{RR}$ and $C_{RF}$ solutions in Table 1 seem to be presented first in this work. In addition, $C_{FR}$ solution appeared in an earlier work[14], seem to be never used in interpretation of tracer return profiles. Nevertheless, such a classification would serve for understanding the physical meaning of $C_{FF}$ solution, which corresponds to an injection into the fluid stream entering the system and measuring the concentration of outflowing fluid at the outlet boundary.

If, for example, one were to inject the tracer into the inflowing stream and measure the concentration within the system at an instant at the outlet boundary, one then would have to use the $C_{FR}$ solution.

Since most of the tracer return profiles obtained from experiments are plotted in $C_{FF}$ variable, the theoretical $C_{FF}$ solutions of various heterogeneous medium models will be compared in the following.

# 4 Theoretical Return Profiles

Fig.1 shows the tracer return profiles resulting from various heterogeneities leading to different dominant transport mechanisms represented by the solutions in Table 2.

The line 1 represents the limiting case of the pure convective transport. The curves 2 and 3 represent a convective and a diffusive transport, the latter of which takes place perpendicular to the direction of flow. The difference between them results from the extent of diffusive transport medium which is infinite for line 2 and finite for line 3. Since there is no dispersion the tracer breakthrough will occur only after the convective fluid flow breakthrough. The degree of diffusive transport will determine the slope of the profile. If there are only the convective and dispersive transports mechanisms in mobile phase, the resulting figure will be similar to line 4. In this case the whole shape is affected by the dispersive transport only. The spreading of the transition zone is direcly proportional to the dispersivity of the system. Finally, the presence of all three mechanisms namely, convective, dispersive and diffusive transports yield the curves 5 and 6. The difference between these two curves also results from the extents of their diffusive transport media. The early part of the breakthrough curve will be determined mostly by the dispersive transport. The part after the convective breakthrough time will be controlled by the diffusive transport.

As mentioned earlier, the parameters are based on the mobile phase pore volume so that the solutions for all approaches could be compared. The commonly employed method of basing the parameters on the total pore volume is unable to give a way of respresenting the very near field with an infinite diffusive transport medium.

One may wish to study various alternatives in the far field approach, in addition to these fundamental models. These alternatives are defined according to the type of transfer between the two phases, geometry of the immobile phase, and discrete and continuous size distribution for multiple blocks in immobile phase.

An effective way of investigating these alternatives is a study of the behavior of block geometry functions, BGFs. The BGF may be defined as the Laplace transform of the transport rate per unit capacity of matrix block for a unit concentration at the surface of the block. The BGF is also called as effectiveness factor[15] or outflow function[16] depending on the area of study.

The Laplace transform of the source term in Eq.9 is a product of the Laplace transforms of the two terms inside the integral in Eq.21, one of which is $q_{uD}$. Therefore, by definition, for a finite immobile phase volume, the Laplace transform of $q_{uD}$ will be a product of $V_{mp}/V_{fp}$ and BGF. Hence, any difference between these alternatives will come from the difference between their BGFs.

The behavior of BGFs of principal geometries given in Table 3 were studied earlier by several authors[7, 15, 16] whose findings may be summarized as follows. Choosing their characteristic dimension as the ratio of the block volume to the surface area one may express the BGFs of basic geometries as a function of a single parameter $\Lambda$, given by:

$$\Lambda = \sqrt{sP_{im}} \tag{24}$$

As long as volume to surface ratios of the blocks are equal BGFs of basic geometries follow one another quite closely, Fig. 2. It can also be seen that for large and small values of $\Lambda$, all curves collapses to a single curve. Therefore, one expects that the solutions would depend on the geometry only slightly.

A further point in the investigation of BGFs is the determination of the behaviors of BGFs of multiple blocks. Multiple blocks case also presents several alternatives due to the distribution type of block size. Here, however, only BGFs of uniform (rectangular) continuous size distribution will be considered. Fig.3 shows BGFs of uniform continuous size distributions for the immobile phase with respect to that of a single block having a size equal to the mean of the distribution. There are three important findings: First, for an observable variation of a multiple block BGF from that of a single block, the ratio of the minimum block size to the maximum block size, $\theta_{min}$, must be at most 0.1. Second, the differences occur only for large $\Lambda$ which corresponds to early time and large block sizes. This is the major difference between the geometrical effect and distribution effect. Finally, for $\theta_{min}$ greater than 0.01 and $\Lambda$ less than 100, the difference between BGFs appears to be logarithmically proportional to $\theta_{min}$. As a result, it seems reasonable to represent the multiple blocks with a single block of size equivalent to their mean size.

However, we need to justify that small differences in BGFs do not give rise to large differences in the complete solution. Also, we have to show that the process of inverting the Laplace transform does not enhance such differences.

The upper curves in Fig.4 shows that for the immobile phase fraction being smaller than that of the mobile phase the solutions are indeed very closely follow each other. However, as the immobile phase fraction grows close to the mobile phase fraction both geometry and presence of multiple immobile phases lead to considerable differences in solutions of these alternatives, as shown in the lower curves in Fig.4.

The higher the value of BGF the greater the diffusion rate and hence the lower the concentration values in mobile phase. This could be observed from curves of BGF and the corresponding $C_{FF}$ solution curves.

# 5 Interpretation Methods

The best way of interpreting the tracer return profiles may be employing a nonlinear curve fitting method[17]. Such a method could give fast and efficient results.

Efficiency of this method depends on first using the right theoretical model and then choosing the parameters independent of each other. In addition, close initial estimates of parameters to their true values speeds convergence. Choosing the theoretical model and providing good initial estimates are considerably dependent upon the experience of the user.

Among heterogeneous medium models the far field approach solutions have the most number of parameters. These parameters are four characteristic times, $t_d$, $t_w$, $t_t$, and $t_m$ corresponding respectively to four mechanisms, convection and dispersion in mobile phase, interaction between the two phases and diffusion in immobile phase. Since these parameters affect different segments of tracer return profiles they are unlikely to be correlated[18]. Therefore, the nonlinear regression method should work satisfactorily with these parameters. They relate to other parameters by:

$$t_d = \frac{L^2}{D} \tag{25}$$

$$t_w = \frac{L}{u} \tag{26}$$

$$t_t = \frac{(\frac{A}{\phi V_f})^2}{D_m} \tag{27}$$

and

$$t_m = \frac{a^2}{D_m} \tag{28}$$

If only a convective and dispersive transport is assumed, the source term in Eq.9 becomes zero and there remains only two parameters whose initial estimates may be obtained by[19]:

$$t_w \cong 2t_p - t_b \tag{29}$$

and

$$t_d = \frac{6t_w^2 t_p}{t_w^2 - t_p^2} \tag{30}$$

The model based only on a convective and diffusive transport has also two parameters, $t_w$ and $t_t$, that may initially be estimated as:

$$t_w \cong t_b \tag{31}$$

$$t_t = (t_p - t_w)\frac{3}{2t_w^2} \tag{32}$$

For the far field approach solutions which include all three mechanisms of transport, the parameter $t_w$ should be assigned an initial value which is slightly smaller than $t_p$. The initial estimate of the characteristic time for dispersion, $t_d$ may be:

$$t_d \cong \left[t_d(\frac{t_w}{t_p})^2\right] \tag{33}$$

where the terms in the bracket refers to values obtained from equations 29 and 30.

The parameter $t_t$ is again given by Eq.32. Finally, $t_m$ should be based on the value of $t_t$ and the tailing of tracer return profile. A pronounced tailing indicates $t_t$ and $t_m$ values are close. Little tailing, on the other hand, means a $t_m$ value at least ten times smaller than that of $t_t$.

As an example, a model generated data set was mached by a regression procedure, Fig.5, whose generated, initially estimated and regressed parameter values are given in Table 4. Fig.5 and Table 4 together show that matching of the return profile and parameter estimation results are excellent. Even if one were to use initial estimates much different than the true values, the parameter values would still have converged. However, in such a case the regression procedure takes more iteration steps.

# 6 Conclusions

A distinction is necessary between the resident and flux concentrations to prevent material balance errors and incorrect interpretation of tracer return profiles resulting from employing solutions inconsistent with the actual conditions of experiments. Therefore, the classification of the solutions of classical convection dispersion model in terms of these two concentration variables is extended to include those of heterogeneous system models as well. Such a classification provides an insight into the physical meaning of solutions and help choosing the right theoretical model when interpreting an experimental tracer return profile.

Earlier works studying the influence of immobile phase geometry have shown that principal geometries yield similar block geometry function, BGF, curves. This work showed that size distribution of immobile phase also gives similar BGF curves to the BGF curve of their mean size. This particularly true for intermadiate to late times.

The questions of whether the small differences in BGFs give rise to larger differences in the complete solution or whether these differences are enhanced by the Laplace transform inversion process were also investigated. It was found that differences in BGFs yield significant differences in solutions only if the immobile phase fraction is close to or larger than that of the mobile phase.

In the interpretation of tracer return profiles use of a nonlinear regression technique is recommended. Providing close initial estimates of the parameters, which greatly speeds convergence, depends on experience of the user about the field. However, one may also use the provided formulae based on distinctive features of the experimental tracer return profiles.

# 7 Nomenclature

- $a$ = volume to area ratio of a matrix block
- $A$ = interface area between mobile and immobile phases
- $B$ = block geometry function
- $C$ = mobile phase concentration
- $C_m$ = immobile phase concentration
- $D$ = longitudinal dispersion coefficient
- $D_m$ = diffusion coefficient in immobile phase
- $f_i$ = relative frequency density function of immobile phase blocks
- $K$ = mass transfer coefficient
- $L$ = characteristic length of flow system
- $P_e$ = longitudinal Peclet number of mobile phase
- $P_{im}$ = Peclet number of immobile phase
- $P_t$ = transverse Peclet number of mobile phase
- $q$ = a source/sink in the system (amount of tracer generated/lost per unit volume of the mobile phase per unit time)
- $s$ = Laplace transform variable
- $t$ = time variable of the transport equations
- $t_b$ = tracer breakthrough time
- $t_d$ = characteristic time for dispersion
- $t_m$ = characteristic time for diffusion
- $t_t$ = characteristic time for interaction between two phases
- $t_p$ = peak arrival time of a tracer slug
- $t_w$ = breakthrough time of the convective front
- $u$ = flow velocity
- $x$ = space variable along the flow direction
- $V_{mp}$ = pore volume of immobile phase
- $V_{fp}$ = pore volume of mobile phase

$y$ = space variable perpendicular to the flow direction
$\delta$ = Dirac delta function
$\phi$ = matrix porosity
$\eta$ = space variable of diffusive transport domain
$\theta_{min}$= the ratio of the smallest block size to largest block size
$\tau$ = time convolution variable
$\lambda$ = ratio of a block to the largest block size
$\Lambda$ = block geometry function parameter
$\nabla$ = gradient operator
$\mathcal{L}$ = linear Operator

*subsrcipts*

$D$ = dimensionless
$F$ = flux
$mb$ = multiple block
$R$ = resident
$sb$ = single block
$u$ = for a unit concentration at the boundary
min = minimum
max = maximum

*superscripts*

$-$ = indicates Laplace transformation
$'$ = indicates derivative

# References


[1] Parker, J. C. and van Genuchten M. Th.: "Flux-Averaged and Volume-Averaged Concentrations in Continuum Approaches to Solute Transport," *Water Resour. Res.* (1984a), *20* 7, 866-872.

[2] Brigham, W. E.: "Mixing Equations in Short Laboratory Cores," *Soc. Pet. Eng. J.,* (1974), *14,* 91-99.

[3] Kreft, A. and Zuber, A.: "On the Physical Meaning of the Dispersion Equation and its Solutions for Different Initial and Boundary Conditions," *Chem. Eng. Sci.* 33, (1978), *33,* 1471-1480.

[4] Bear, J. and Berkowitz, B: " Groundwater Flow and Pollution in Fractured Aquifers," *Developments in Hydraulic Engineering, Vol. 4* , P. Novak (Editor), Elsevier, London, (1987), 175-235.

[5] Cinco-Ley, H., et. al. : " The Pressure Transient Behavior For Naturally Fractured Reservoirs with Multiple Block Size," *SPE 14168,* presented at the 60th Fall Technical Conference held in, Las Vegas, NV,Sept., (1985).

[6] Katsunori, F. : " Rate Decline Analysis for Naturally Fractured Reservoirs," Masters Report, Stanford University, (1989).

[7] Barker, J. A. : "Block Geometry Functions Characterizing Transport in Densely Fissured Media," *J. Hydrol.,* (1985), *7,* 263-279.

[8] Clark, R. T.: "A Review of Some Mathematical Models Used in Hydrology with Observations on Their Calibration and Use," *J. Hydr.,* (1973), *19,* 1-20.

[9] Carslaw, H. S. and Jeager, J. C.: *Conduction of Heat in Solids,* Clarendon Press, Oxford, (1986), 75-77.

[10] Coats, K. H. and Smith, B. D. : "Dead-end Pore Volume and Dispersion in Porous Media," *Soc. Pet. Eng. J., Trans. AIME, 231,* (March 1964), 73-84.

[11] Passioura, J. B.: "Hydrodynamic Dispersion in Aggregated Media: I. Theory," *Soil Sci.,* (1971a), *3,* 6, 339-344.

[12] de Swaan, O. A.: " Analytical Solution for Determining Naturally Fractured Reservoir Properties by Well Testing," *Soc. Pet. Eng. J.,* (June, 1976)

[13] Baker,L. E.: "Effects of Dispersion and Dead-End Pore Volume in Miscible Flooding," *Soc. Pet. Eng. J.,* (June 1977), 219-227.

[14] Correa, A. C., Pande, K. K., Ramey, H. J. Jr. and Brigham, W. E.: "Prediction and Interpretation of Miscible Displacement Using a Transverse matrix Dispersion Model," *SPE 16704,* (Sep. 1987).

[15] Aris, H. : " On the Shape Factors for Irregular Particles-I," *Chem. Eng. Sci., vol. 6* (1957), 262-268.

[16] de Swaan, O. A.: " Influence of Shape and Skin of Matrix-Blocks on Pressure Transients in Naturally Fractured Reservoirs," *SPE 15637,* Presented at the 61st Technical Conference held in, New Orleans, LA, (Oct.,1986).

[17] Rosa, A. J. and Horne, R. N. : " Automated Type-Curve Matching in Well Test Analysis Using Laplace Space Determination of Parameter Gradients," *SPE 12131,* presented at the 1983 SPE Annual Meeting held in, San Fransisco, CA, (Oct.,1983).

[18] De Smedt, F., Wierenga, P. J. and Van der Beken, A.: *Theoretical and Experimental Study of Solute Movement Through Porous Media with Mobile and Immobile Water,* Vrije Universtait Brussel, Brussel, (1981).

[19] Bullivant, D. P.: "Tracer Testing of Geothermal Reservoirs," Ph.D. Thesis, Department of Theoretical and Applied Mechanics, School of Engineering, University of Auckland, Auckland, New Zealand, (1988).

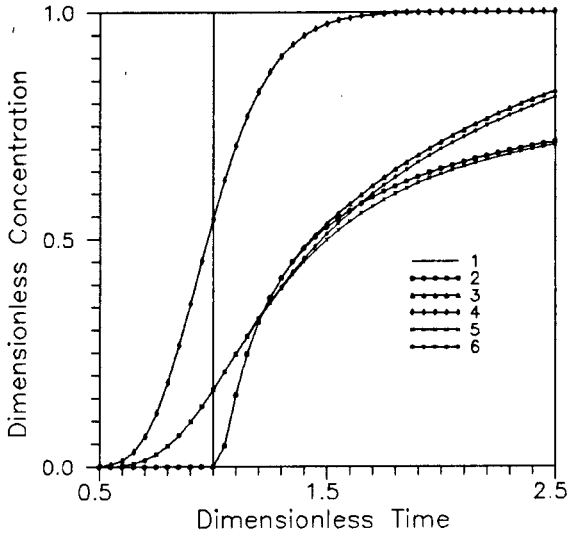


Figure 1: Theoretical Tracer Return Profiles of Fundamental Models

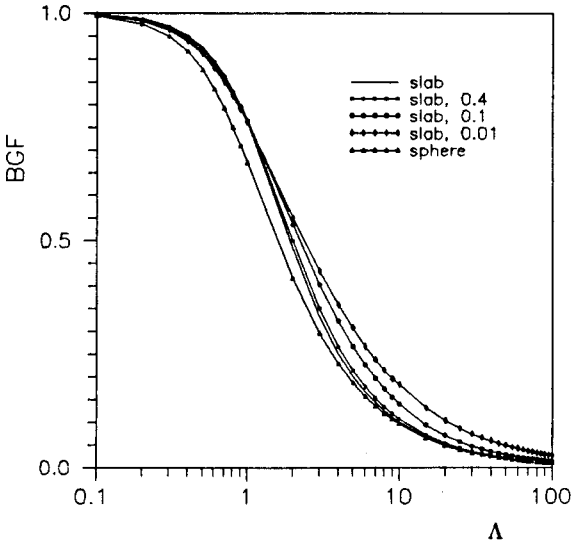


Figure 3: BGFs for Uniform Frequency Distribution

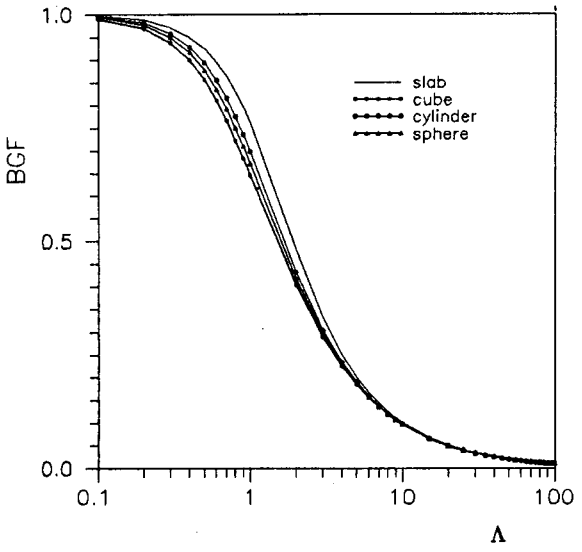


Figure 2: BGFs for Principal Geometries, [after Barker 1985]

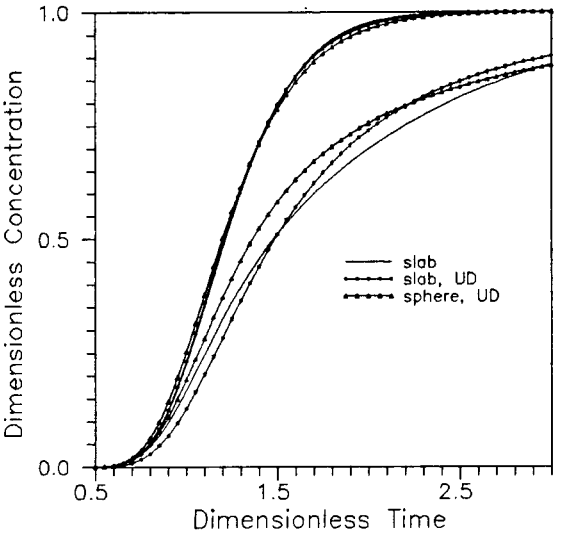


Figure 4: Tracer Return Profiles for Various Immobile Phase Geometries and Distributions

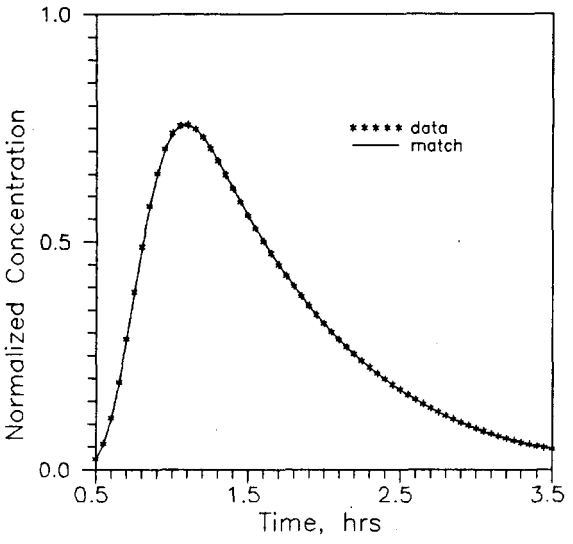


Figure 5: Matching a Data Set by Nonlinear Regression Method

| IC & BC | Solution |
|---|---|
| $C(x_D,0) = \delta(x_D)$, $C_m(x_D,y_D,0) = 0$<br>$\lim_{x_D\to-\infty} C(x_D,t_D) = 0$<br>$\lim_{x_D\to\infty} C(x_D,t_D) = 0$<br>$C(x_D,t_D) = C_m(x_D,0,t_D)$<br>$2^{nd}$ BC for $C_m$ | $\overline{C}_{RR} = \frac{2}{\gamma(s)} \exp\left[(1-\gamma(s))\frac{P_e\lvert x_D\rvert}{2}\right]$ |
| $C(x_D,0) = (\delta(x_D) - \frac{1}{P_e}\delta'(x_D))$<br>$C_m(x_D,y_D,0) = 0$<br>$\lim_{x_D\to\mp\infty} C(x_D,t_D) = 0$<br>$C(x_D,t_D) = C_m(x_D,0,t_D)$<br>$2^{nd}$ BC for $C_m$ | $\overline{C}_{RF} = \frac{1+\gamma(s)}{2\gamma(s)} \exp\left[(1-\gamma(s))\frac{P_e x_D}{2}\right]$ |
| $C(x_D,0) = C_m(x_D,y_D,0) = 0$<br>$[C - \frac{1}{P_e}\frac{\partial C}{\partial x_D}]_{x_D=0} = \delta(t_D)$<br>$\lim_{x_D\to\infty} C(x_D,t_D) = 0$<br>$C(x_D,t_D) = C_m(x_D,0,t_D)$<br>$2^{nd}$ BC for $C_m$ | $\overline{C}_{FR} = \frac{2}{1+\gamma(s)} \exp\left[(1-\gamma(s))\frac{P_e x_D}{2}\right]$ |
| $C(x_D,0) = C_m(x_D,y_D,0) = 0$<br>$C(0,t_D) = \delta(t_D)$<br>$\lim_{x_D\to\infty} C(x_D,t_D) = 0$<br>$C(x_D,t_D) = C_m(x_D,0,t_D)$<br>$2^{nd}$ BC for $C_m$ | $\overline{C}_{FF} = \exp\left[(1-\gamma(s))\frac{P_e x_D}{2}\right]$ |
| *where* $\gamma(s) = \sqrt{1+\frac{4s}{P_e}(1-\overline{q}_{uD}(s))}$, and<br>$2^{nd}$ BC of $C_m$ and hence $\overline{q}_{uD}(s)$ depends on the modelling approach | |

Table 1: Instantaneous injection solutions of heterogeneous medium models

| Mechanisms | Solution |
|---|---|
| Convection & Diffusion | $C_{D_{sf}} = \frac{1}{s}\exp\left(-s-\sqrt{s/P_t}\right)$ |
| | $C_{D_{pf}} = \frac{1}{s}\exp\left(-s-\sqrt{s/P_t\ tanh\sqrt{sP_{im}}}\right)$ |
| Convection & Dispersion | $C_D = \frac{1}{s}\exp\left[\left(1-\sqrt{1+4s/P_e}\right)P_e/2\right]$ |
| Convection Dispersion & Diffusion | $C_{D_{sf}} = \frac{1}{s}\exp\left[\left(1-\sqrt{1+4(s+\sqrt{s/P_t})/P_e}\right)P_e/2\right]$ |
| | $C_{D_{pf}} = \frac{1}{s}\exp\left[\left(1-\sqrt{1+4(s+\sqrt{s/P_t\ tanh\sqrt{sP_{im}}})/P_e}\right)P_e/2\right]$ |
| | $C_{D_{sb}} = \frac{1}{s}\exp\left[\left(1-\sqrt{1+4s(1+\omega B_{sb}(\Lambda))/P_e}\right)P_e/2\right]$ |
| | $C_{D_{mb}} = \frac{1}{s}\exp\left[\left(1-\sqrt{1+4s(1+\omega B_{mb}(\Lambda))/P_e}\right)P_e/2\right]$ |

Table 2: Solutions of Fundamental Transport Models

| | Geometry | Block Geometry Function, $B(\Lambda)$ |
|---|---|---|
| Single Block Size | Slab | $tanh(\Lambda)/\Lambda$ |
| | clinder | $I_1(2\Lambda)/(\Lambda I_0(2\Lambda))$ |
| | sphere | $coth(3\Lambda)/\Lambda - 1/(3\Lambda^2)$ |
| | cube | $512/\pi^6 \sum_{i=1}^{\infty}\sum_{j=1}^{\infty}\sum_{k=1}^{\infty}\left[\alpha_{ijk}/(\alpha_{ijk}+\Lambda^2)\right]/(ijk)^2$ <br> $where\ \ \alpha_{ijk} = (\pi/6)^2(i^2+j^2+k^2)\ \ i,j,k\ \ odd\ \ integers$ |
| Multiple Block Size | slab, uniform distribution | $1/(1-\lambda_{min})\int_{\lambda_{min}}^{1} tanh(\Lambda_{max}\lambda)/(\Lambda_{max}\lambda)\ d\lambda$ <br> $where\ \ \lambda = a/a_{max}\ \ and\ \ \Lambda_{max} = \sqrt{s(P_{im})_{max}}$ |

Table 3: Block Geometry Functions for Principal Geometries [after Aris,1957 and Barker 1985

| parameter | generator value | initial estimate | regressed value |
|---|---|---|---|
| $t_d$ | 30.0 | 26.5 | 30.0 |
| $t_w$ | 1.0 | 0.9 | 1.0 |
| $t_m$ | 2.5 | 2.08 | 2.5 |
| $t_{im}$ | 1.0 | 1.5 | 1.0 |

Table 4: The Parameter Values of Regression Shown in Fig. 5.

PROCEEDINGS, Nineteenth Workshop on Geothermal Reservoir Engineering
Stanford University, Stanford, California, January 18-20, 1994
SGP-TR-147

# NUMERICAL SIMULATION OF THE MORI GEOTHERMAL FIELD, JAPAN

Yukihiro Sakagawa[*1], Masahiro Takahashi[*1], Mineyuki Hanano[*1],
Tsuneo Ishido[*2] and Nobuhiro Demboya[*3]

[*1] Japan Metals and Chemicals Co., Ltd., Takizawa-mura, Iwate 020-01, Japan
[*2] Geological Survey of Japan, Tsukuba, Ibaraki 305, Japan
[*3] New Energy and Industrial Technology Development Organization, Toshima-ku, Tokyo 170, Japan
(now at Electric Power Development Co., Ltd., Chuo-ku, Tokyo 106, Japan)

## ABSTRACT

A numerical study of the Mori geothermal field which consisted of a series of three-dimensional natural state modeling and history matching was carried out with porous models. Finally satisfactory fits both on temperature and pressure of the natural state and on pressure history caused by exploitation were obtained. The results indicate that the deep hot water ascends mainly through the fractures near the caldera wall and the fractures confined to some lithofaces, and some of the ascending hot water flows to the west from the caldera. A sketch of the geological structure, the way of making up the initial numerical model, the way of concluding free parameters, and results of calculations of natural state modeling and history matching for the best numerical model are presented.

## INTRODUCTION

New Energy and Industrial Technology Development Organization (NEDO) started "the Development of Geothermal Reservoir Evaluation Technology Project" to develop the technology to analyze mass and heat transport in geothermal reservoirs, to predict the well production and to evaluate the optimum output power for the optimum geothermal development (e.g. Kitamura et al., 1988; Kawano et al., 1989).

As a part of the NEDO's project, this study was carried out to analyze the fluid flow and heat transport in the Mori geothermal field, Japan for the purposes of acquiring knowledge on structure of the geothermal system and of developing a reservoir model which reproduces the natural state and the reservoir behavior after the exploitation of the field to help the development of the field.

The Mori geothermal field is a liquid-dominated geothermal field located at the Nigorikawa Basin in the north Japan (Fig.1). In this field, the Mori geothermal power station (50 MWe) has been in operation since 1982 by Hokkaido Electric Power Inc. where Dohnan Geothermal Energy Co., Ltd., a subsidiary of Japan Metals and Chemicals Co., Ltd., is a steam supplier.

The geological structure of the field consists of the Pre-Tertiary Kamiiso Group, the Neogene Ebiyagawa Formation which unconformably overlies the Kamiiso Group and Quaternary caldera fill deposits composed of pyroclastics by caldera eruption, lake deposits, and andesite intrusions, as shown in Fig.2 (e.g., Sato, 1988; Ando et al., 1992; Kurozumi and Doi, 1993). The shape of the caldera has been confirmed by drilling and the three-dimensional gravity analysis (Kondo et al., 1993). The geothermal fluid is formed by simple mixing of heated meteoric water with deep hot water, with the latter having a large component of magmatic and/or altered sea water (e.g., Yoshida, 1991; Sato et al., 1992) . Fractures near the caldera wall and fractures confined to some lithofaces in the Ebiyagawa Formation and the Kamiiso Group are regarded as main conduits of hot up flow (Akazawa et al., 1993).

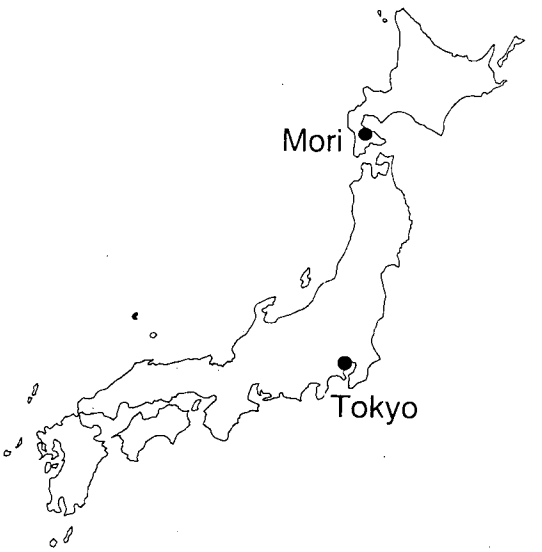


Fig.1 Location of the Mori geothermal field

In this study, three-dimensional natural state modeling, history matching, and prediction were carried out with porous models. The study proceeded on aiming at good matches both about temperature and pressure distribution of natural state and about reservoir pressure history measured in wells, with a single model. In this study we used SING-II, one of the NEDO's reservoir simulators, which is capable of analyzing three-dimensional transient mass and heat transport in porous or fractured media (e.g. Tsutsui et al., 1991).

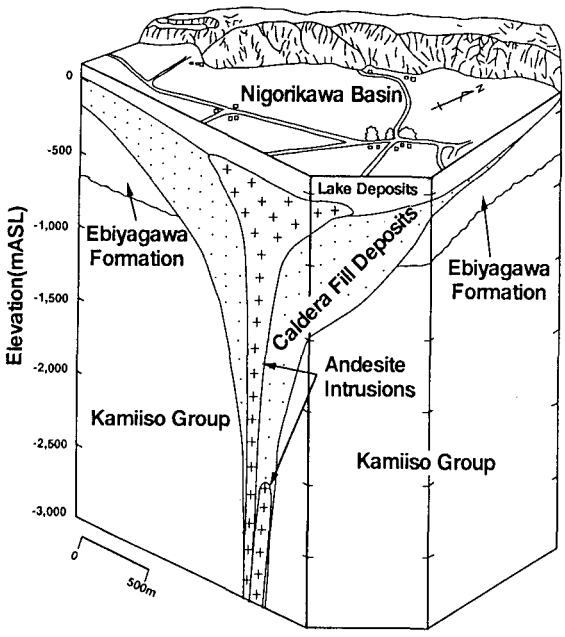


Fig.2 Schematic geological structure of the Mori field (modified from Kurozumi and Doi, 1993)

## STUDY AREA AND GRID GEOMETRY

Since the horizontal shape of the caldera wall which makes the main conduit of fluid flow is rectangular in the depth, and the direction of its major axis is northeast–southwest, the grids were directed to northeast–southwest. The horizontal study area was 11.4km along northeast–southwest and 11.3km along northwest–southeast, and was divided into 14 x 14 grids (Fig.3). This area covers the Nigorikawa Basin and the mountainous area around the Nigorikawa Basin. It also includes wide area west of the Nigorikawa Basin, such as the Kaminoyu and Santai area, since the hydrothermal system of the Mori field was thought to extend mainly to the west (Kato and Takahashi, 1993). This extension of the hydrothermal system to the west was inferred from the facts that the hot area, centered on the caldera, extends to the west and that the reservoir pressure of the Kaminoyu and Santai area located in the west of the basin is essentially the same as that in the Mori field as shown in Fig.11.

The vertical study area was 3,900 m, from 100 mASL which is the approximate elevation of the ground surface of the Nigorikawa Basin to −3800 mASL. It was divided into 19 layers (Fig.4) to express the fractures confined to the upper part of limestone and chert in the Kamiiso Group, since a core fracture study shows that the deep fluid flows laterally in the fractures confined to the upper part of limestone and chert in the Kamiiso Group (Akazawa et al., 1993).

## ROCK PROPERTIES

The values of porosity, rock density, thermal conductivity of rock, heat capacity of rock, and the values of permeability imposed to an initial model were given to each geological structure element or lithoface. The porosity was decided based on the analysis result of the electric log by the Archie's equation (Sunshine Project Promotion Headquarters, 1980). The rock density and thermal conductivity of rock were decided based on the core data; rock density ranges from about 2,300 to about 2,700 kg/m$^3$, and thermal conductivity about 1.4 to about 4.5 W/m·K. The heat capacity of rock was decided as 1,130 J/kg·K all over the area.

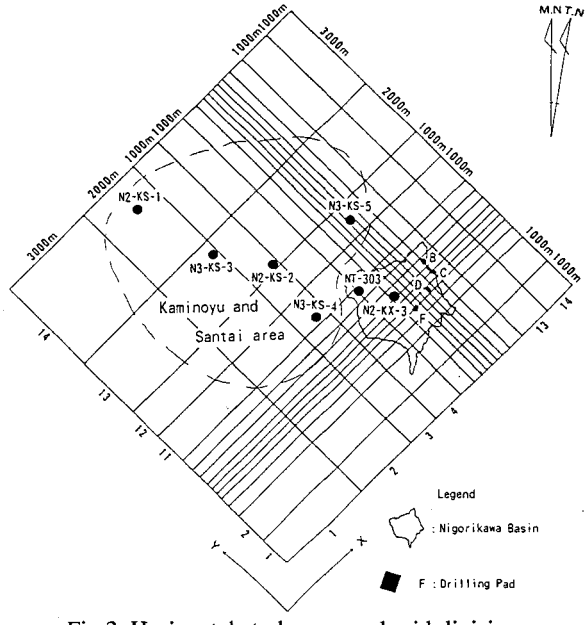


Fig.3 Horizontal study area and grid division

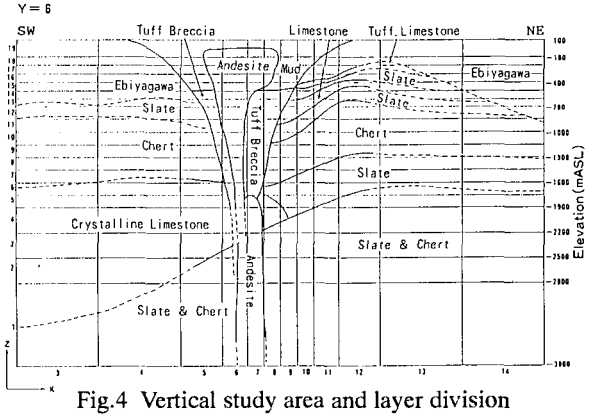


Fig.4 Vertical study area and layer division

With respect to the distribution of permeability given to the initial model, the geological structure was classified to some lithofaces, domains in which the fractures dominate, caldera wall and others, based on the results of such as chemical analysis of fluid, temperature profiles in wells and the results of core fracture study. The permeability of each grid was then decided by its class (e.g. horizontal permeability of the grids classified to Ebiyagawa Formation is $10^{-15}$m$^2$ everywhere).

## BOUNDARY AND INITIAL CONDITIONS

The top boundary was opened with respect to mass and heat flow. To permit the fluid flow we imposed a pressure distribution to the boundary surface. The pressure distribution was set heterogeneous; the boundary which has the higher elevation of the ground surface has the greater boundary pressure to account for the effect of the

mountainous area around the Nigorikawa Basin. With the homogeneous boundary pressure distribution, low temperature area in the shallow part of the southern basin was not reproduced. To permit conductive heat flow at the top boundary, we extracted heat from the each upper-most grid. The extracted heat was adjusted automatically all the time to maintain the initial temperature of the upper-most grids. The temperature of each upper-most grid was decided with reference to results of temperature logs in static wells and temperature distribution of the one meter depth which was reported by Urakami and Nishida (1977).

With respect to the bottom boundary, conductive heat flux was imposed on the bottom surface as heat supply but was closed to mass flow. However, constant rate mass input was imposed to some grids in the lower-most layer to represent up-flow of the deep hot recharge. Location and amount of the mass input are described later. The conductive heat flux at the bottom boundary was set to be 0.2 $W/m^2$ except up-flow zone of the deep recharge. This value is based on the initial temperature gradient of the model.

Side boundaries were closed to conductive heat flow and mass flow. Theoretically, there is no geothermal field with all of the side boundaries wholly closed, so that side boundaries are open though their boundary permeability is very small (e.g. order of $10^{-18}$ $m^2$). However, boundary conditions should not be sensitive to the result of simulation, if actual distributions of pressure or mass flux at the boundary can not be concluded. Therefore closed boundary conditions is thought to work well. This is the reason why we chose closed side boundary conditions.

The initial temperature distribution for the natural state modeling is linear for depth and laterally uniform; 20 °C at the top surface and 290 °C at the bottom surface. The bottom temperature is based on the hottest fluid temperature measured in one of the deepest production wells of the field. The initial pressure of each layer for the natural state modeling is hydrostatic with the uniform pressure distribution of 2.5 bars at the top surface (100 mASL).

## RECHARGE GRIDS

At the first run of the natural state modeling, only one recharge grid was set in the lower-most layer just under the predominant producers since the feed points of them are located at almost the same point laterally. But with this recharge grid, the calculated hot area on each layer was laterally different from the measured one, so we shifted the recharge grid to cancel this gap. Moreover, only a small part of the depth of the system was warmed up with one recharge grid, so that an extreme amount of energy supply to the system was required to warm up the whole system. Thus, we made the recharge grids one of the free parameters, and we employed plural recharge grids laterally apart from its location of the initial model. Finally, the location of the recharge grids was concluded with X of 6 to 10, Y of 5 to 7 in the lower-most layer.

## RECHARGE RATE

At the first run of the natural state modeling, the recharge rate of the deep hot water was set to be 13 kg/s which is equal to the total flow rate of hot springs through the ground surface of entire study area reported by Fukutomi et al. (1963). However, the result was not warm enough and temperature distribution of the natural state was not reproduced. Then we used 35 kg/s as the recharge rate based on the following analysis of the temperature profile of the well NT-303 located at the west of the Mori field (Fig.3).

The volume flux of steady state ascending flow in homogeneous half-infinite porous medium is obtained from the vertical temperature profile in the medium, when the hot water ascends homogeneously and one dimensionally from the infinite depth to the ground surface on which the temperature is kept constant. According to Turcotte and Schubert (1982, p.401), the temperature T (K) of the depth y (m) is

$$T=T_r-(T_r-T_o)\cdot\exp((\rho cv/\lambda)\cdot y) \qquad (1)$$

where $T_r$(K) is the temperature of the infinite depth, $T_o$(K) is the temperature at the ground surface, $\rho$(kg/$m^3$) is the density of fluid, c(J/kg·K) is the isobaric specific heat capacity of fluid, $\lambda$(W/m·K) is the thermal conductivity, and v($m^3$/s·$m^2$) is the volume flux of the ascending flow.
Equation (1) can be reduced to

$$\log(T_r-T)=(\rho cv\cdot\log(e)/\lambda)\cdot y+\log(T_r-T_o) \qquad (2)$$

Thus, when the appropriate $T_r$ is found, the relation of y and $\log(T_r-T)$ becomes linear, so that the volume flux of the ascending flow v can be calculated from the gradient of the graph.

All of the static temperature profiles of wells in the Mori field were investigated, and the profile of the well NT-303 was found to show the typical pattern of one dimensional ascending flow. Fig.5 shows the relation of the true vertical depth and $\log(T_r-T)$ for NT-303 with the tentative temperature of the infinite depth $T_r$ of 230 °C (503 K). As the gradient of the linear part of the graph is -980 m/log-cycle, the volume flux of the ascending flow is 9.3 x $10^{-10}$ $m^3$/s·$m^2$, where $\rho$, c and $\lambda$ are 919 kg/$m^3$, 4.18 x $10^3$ J/kg·K, and 1.52 W/m·K, respectively.

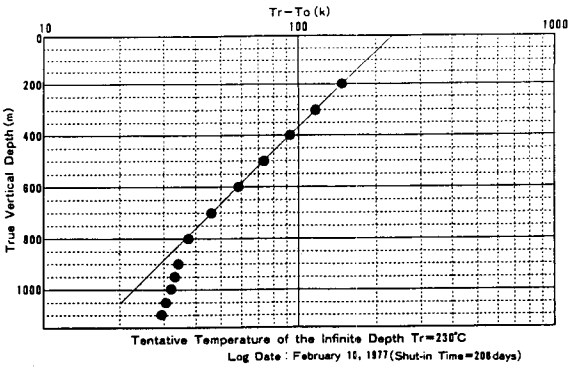

Fig.5 Analysis of the temperature profile of NT-303

Although this value was obtained by the analysis for the shallow part of NT-303, this value is regarded as the mean value of the whole study area because the well is located somewhat apart from the hottest part of the reservoir (Fig.9). The approximate flow rate of the hot water from the depth of the reservoir is obtained by multiplying this value by the area of the ascending flow. Since the domain of the ascending flow of the

hydrothermal convection in the Mori field is supposed to be about 6,300m x 6,400m ($4.03 \times 10^7$ $m^2$ ; A ), the mass rate of the ascending flow vρA is 34.5 kg/s. Therefore the recharge rate in the lower-most layer was finally decided as 35 kg/s. With respect to the temperature of the recharge, we employed 290 °C which is identical to the initial bottom-boundary temperature.

## PERMEABILITY DISTRIBUTION

As described above, permeability distribution was firstly given in some classes based on the geological information. The permeability values were then adjusted to obtain a good fit basically as free parameters with the reference of the results of the natural state modeling and the history matching accounting for the results of pressure monitoring and pressure transient tests. The essential points to decide the permeability distribution are as follows.

(1) Permeability of the shallow grids in the mountainous region around the basin (grids which represent the Ebiyagawa Formation ; X=1 to 4, 13, 14, or Y=1, 2, 11 to 14) were reduced by one order of magnitude than their initial values. Since the pressure at the top boundary was specified taking into account the elevation of the ground surface, high pressure was given to the top boundary corresponding to the mountainous region as described above, so that the meteoric water is inclined to come down to the system. Therefore the permeability of the grids corresponding to the shallow part of the mountainous region around the basin had to be reduced to reduce the cold down flux and to warm up the entire system appropriately with a moderate heat input.

(2) Caldera fill deposits were divided into the shallow part with high permeability and the deep part with low permeability. Also, the concept of the shallow ground water aquifer was introduced. The cool part in the shallow portion of the southern basin was reproduced only with this shallow ground water aquifer. There exists small lateral gradient in the top boundary pressure given in the basin, since its pressure is high at the southern part and its pressure is low at the northern part due to the topographic gradient. Because of this lateral pressure gradient and high permeability of the aquifer, lateral cold water flow is induced and this makes the shallow part cool, while the low permeability below the aquifer guards all the other part against cooling by avoiding descent of the cold water to the deeper part of the system. This concept of the shallow ground water aquifer is supported by the fact that the cool part in the shallow portion of the southern basin was certified by wells mainly drilled in the F pad near the center of the basin as shown in the profile of measured temperatures of the well NF-2 in Fig.8. This concept is also supported by the fact that the temperature in the cool part proved by a well for water level monitoring in the southern basin and a test well in the southeastern basin is 10 to 12 °C which is lower by several tens degrees compared with temperature of the shallow ground water aquifer in other part of the basin (from the internal data of Dohnan Geothermal Energy Co., Ltd., 1992).

(3) The permeability values of caldera wall were adjusted according to the sizes of the relevant grids. If two grids of different size are considered for the caldera wall, and if they have the same permeability, the larger one has the higher transmissibility than the other in calculation. Thus, in deciding the permeability values of the grids which represent the caldera wall, we employed lower permeability for larger grids and higher permeability for smaller grids.

Fig.6 shows the final permeability distribution. Symbols in the figure denote the permeability class of each grid. For example, the deeper part of the caldera wall denoted by "W1" was given very large permeability of horizontally $1{,}000 \times 10^{-15}$ $m^2$ and vertically $100 \times 10^{-15}$ $m^2$, while the Ebiyagawa Formation denoted by "Eb" was given relatively small permeability of horizontally $1 \times 10^{-15}$ $m^2$ and vertically $0.1 \times 10^{-15}$ $m^2$. Roughly speaking, the up flow zone of the deep recharge ("Up"; horizontally $10 \times 10^{-15}$ $m^2$ and vertically $100 \times 10^{-15}$ $m^2$), the deeper part of the caldera wall and the ground water aquifer ("Rs"; horizontally $4{,}000 \times 10^{-15}$ $m^2$ and vertically $4{,}000 \times 10^{-15}$ $m^2$) were given large permeability, and the deeper part of the caldera fill deposits ("Tf" and "An1"; horizontally $0.1 \times 10^{-15}$ $m^2$ and vertically $0.01 \times 10^{-15}$ $m^2$), the shallower part of the caldera wall ("W2"; horizontally $1 \times 10^{-15}$ $m^2$ and vertically $0.1 \times 10^{-15}$ $m^2$) and the Ebiyagawa Formation were given small permeability.

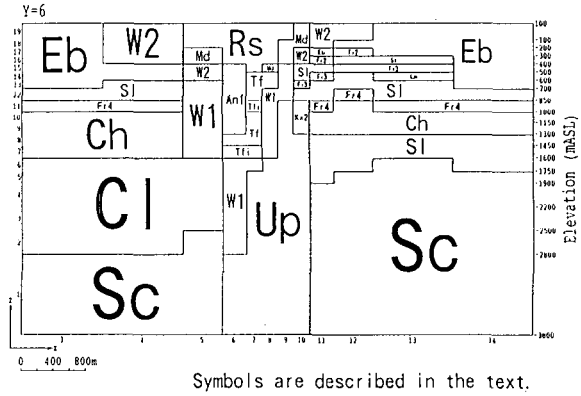


Symbols are described in the text.

Fig.6 Permeability distribution

## RESULTS OF THE NATURAL STATE MODELING

The duration of the calculation was 20,000 years. This duration is regarded as reasonable since the volcanic activity which formed the caldera took place about 12,000 to 20,000 years ago, although the older volcanic activities also seems to have occurred (Sato, 1988). The flow of mass and heat approached steady state at the end of the run (Fig.7).

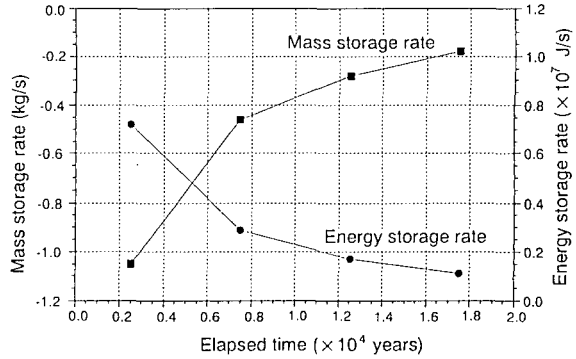


Fig.7 Change of mass and energy storage rate

The results of the natural state modeling were fitted to temperature profiles in wells and reservoir pressure measured before the exploitation in the Mori field. Fig.8 shows some of the temperature fits for the best model. Although the well N3-KS-4 was drilled after the start of exploitation, the well was thought to maintain its initial temperature because of distance from the Nigorikawa Basin. The calculated temperatures in Fig.8 are the temperatures of the grids in which the wells penetrate, and the minimum and maximum temperatures among the horizontally neighboring grids. The figure shows good fits in general. Especially the cool portion in the shallow southern part of the basin is clearly reproduced for the wells in the F pad. The temperature profiles of the wells NT-303 and N3-KS-4 which are drilled in the west part of the study area are also reproduced well. Thus, the lateral flow of the deep hot water to the west is well reproduced suggesting that the idea of the lateral flow towards west is feasible.

Fig.9 and Fig.10 show the calculated temperature distribution in plans and sections respectively. The figures show the extension of the hydrothermal system to the west. The cool part in the shallow portion of the southern basin is also shown in the figures.

Fig.11 shows the fit about the pressure distribution. The figure shows that the model well reproduced the pressure distribution of both the Mori field and the Kaminoyu and Santai area. This result also supports the idea of the lateral flow towards west. This result indicates that the average temperature of the whole study area is realistic enough. Therefore, the amount of the mass input and the conductive heat flux imposed to the deepest part of the study area are reasonable.

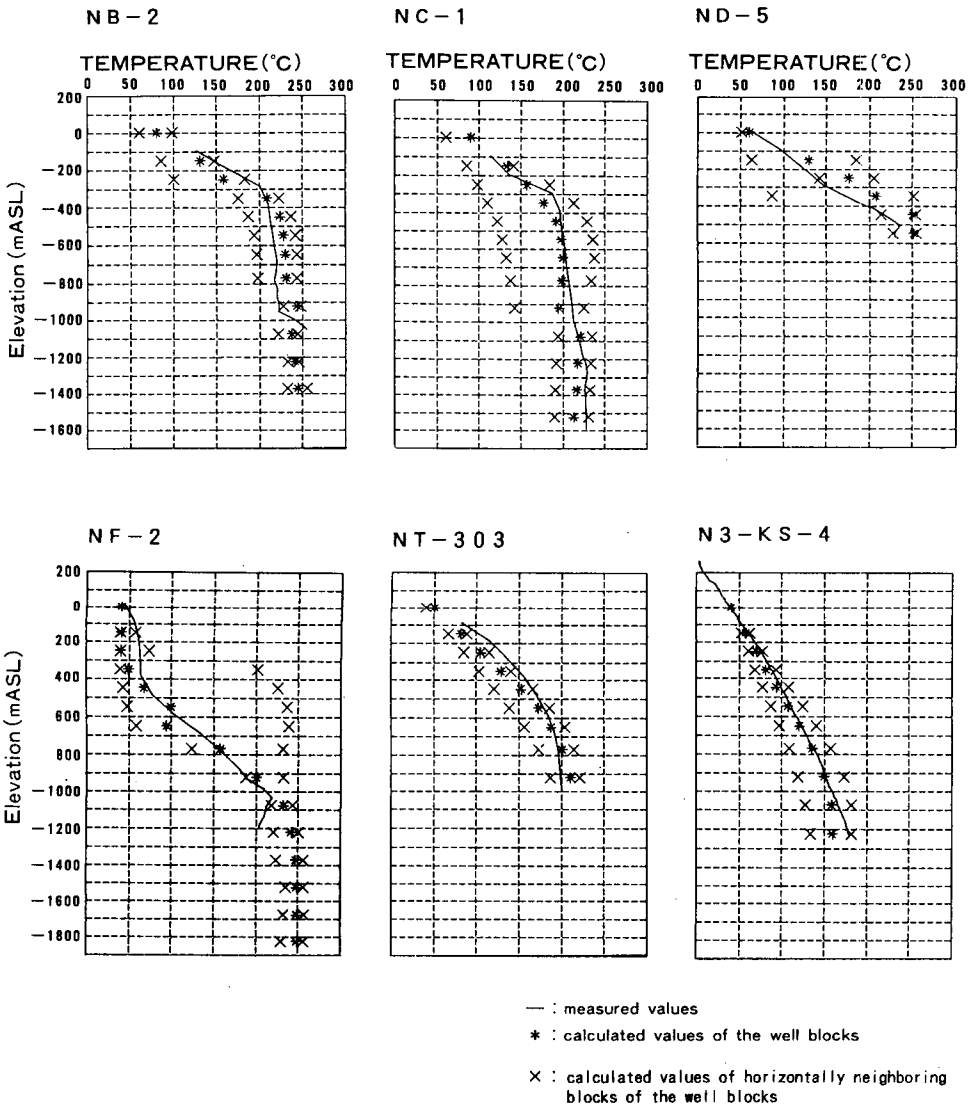


Fig.8 Some of the fits about the temperature profile of wells

## RESULTS OF THE HISTORY MATCHING

Fig.12 shows some of the fits about pressure history. The calculated values in the figure were converted from the grid center depth to the depth of the feed point of the well using the temperature and the pressure of the grid. Two kinds of the measured values were used ; the results of the pressure logging in the static wells and the continuous observation of the pressure in the wells with the capillary tubes. The pressure values in the wells from the continuous observation with the capillary tubes were converted to the depth of the feed point using the temperatures and the pressures in the well. The figure shows that the fits of the pressure history are quite well.

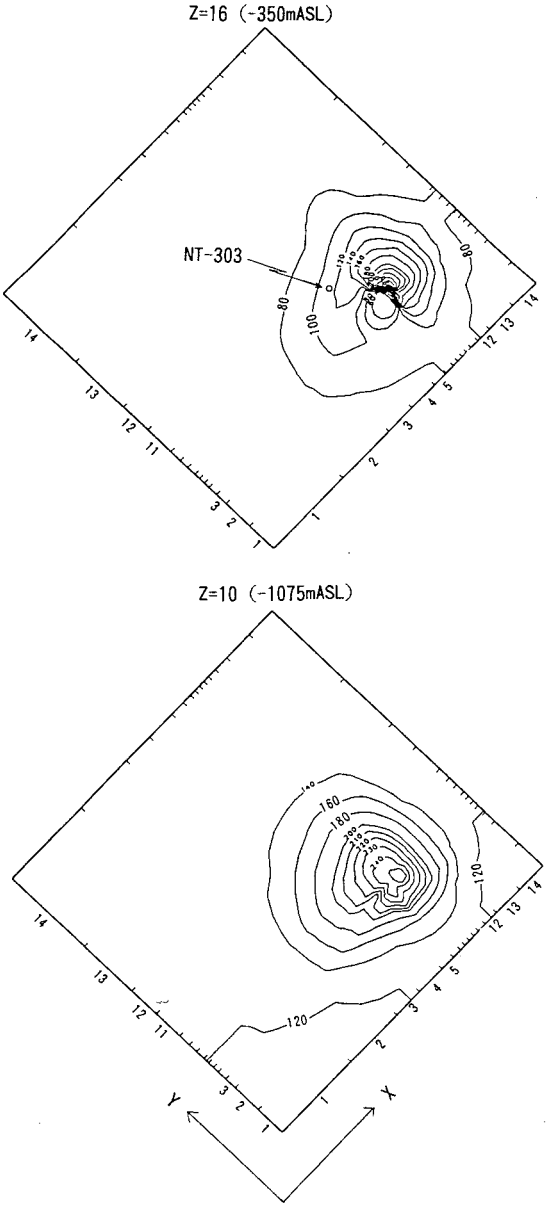


• Fig.9 Calculated temperature distribution (plan)

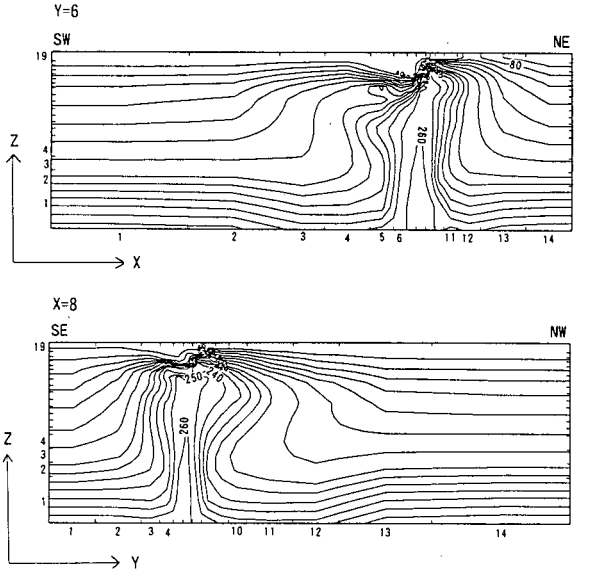


Fig.10 Calculated temperature distribution (vertical section)

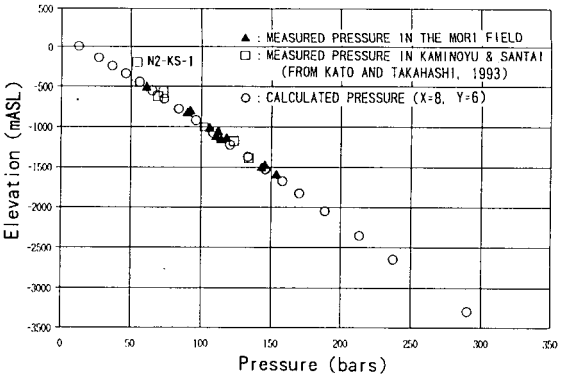


Fig.11 Fit about the pressure distribution

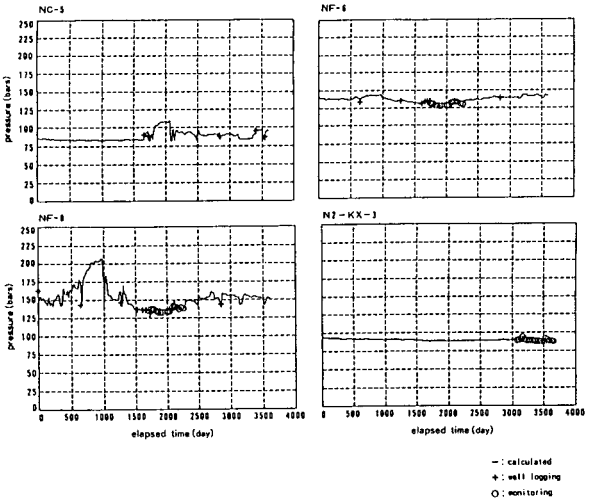


Fig.12 Some of the fits about the pressure history

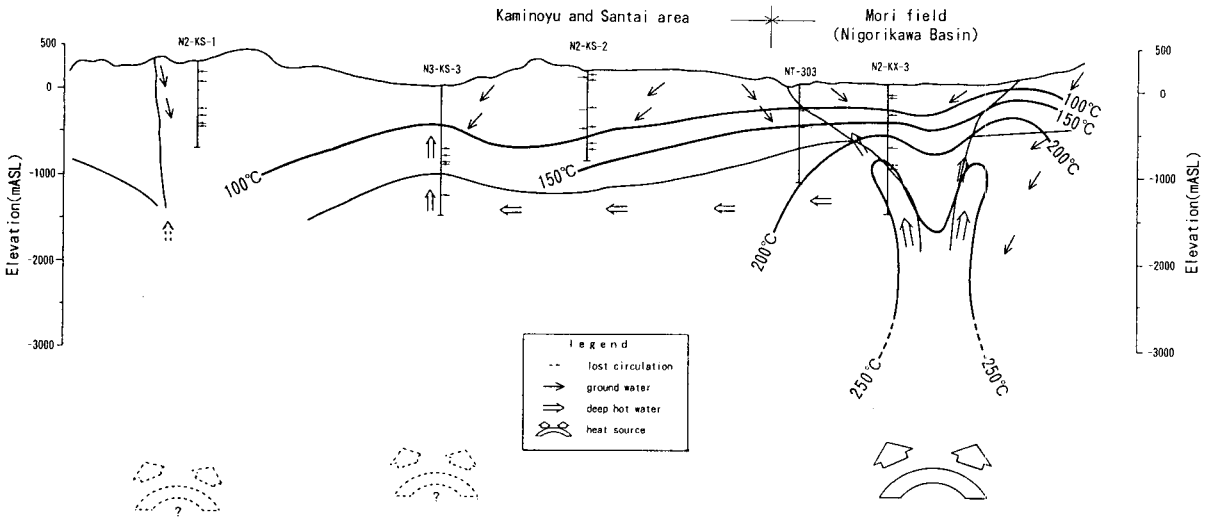


Fig.13 Conceptual model of schematic hydrothermal system of the Mori field and the Kaminoyu and Santai area (Kato and Takahashi, 1993; internal data of Dohnan Geothermal Energy Co., Ltd., 1992)

## HYDROTHERMAL SYSTEM OF THE MORI FIELD

Based on the results of this study, we present a conceptual model of the hydrothermal system of the Mori geothermal field and the Kaminoyu and Santai area (Fig.13). The deep hot water of the Mori field consists of the meteoric water and the magmatic and/or altered sea water. It ascends from the depth of the Nigorikawa Basin and flows in the wide area including the Kaminoyu and Santai area. Some of the ascending fluid flows to the west in the Kamiiso Group because of the low permeability of the Ebiyagawa Formation overlying the Kamiiso Group (c.f. Fig.4). Also, because the permeability of the deeper part of the caldera fill deposits is low compared with that of the shallower part, the ground water does not descend so much and does not cool down the entire field. The up flow zone of the deep recharge had been thought to be rather small based on the distribution of the feed points of the predominant producers before this study, while now it has been found to be larger through this study. In this field, the reinjected water returned to the producers at the early periods of exploitation because of the short distances between producers and injectors. Thus, the distances have been enlarged to reduce the rate of return of reinjected water. Therefore, the possibility of the larger area of the up flow is an important implication to the future development of the Mori field.

## CONCLUSIONS

The numerical model constructed in this study was proved to reproduce the temperature and pressure in the natural state and also the pressure change after the start of exploitation. Therefore the conceptual model that the deep hot water ascends mainly through the fractures near the caldera wall and the fractures confined to the upper part of limestone and chert in the Kamiiso Group, and some of the ascending hot water flows to the west from the caldera, was proved feasible. Also the concept of the shallow ground water aquifer was proved to well reproduce the cool part in the shallow portion of the southern basin.

## ACKNOWLEDGEMENTS

This study was a part of the project "the Development of Geothermal Reservoir Evaluation Technology" assigned to Japan Metals and Chemicals Co., Ltd. (JMC) by New Energy and Industrial Technology Development Organization (NEDO). The authors sincerely thank NEDO and all members of the advisory committee for the project and for the sectional meeting about the Mori field for their support and suggestions. The authors thank NEDO for providing the data of the Kaminoyu and Santai area. The authors also thank NEDO, JMC and Dohnan Geothermal Energy Co., Ltd. for their permission to publish this paper.

## REFERENCES

Akazawa, T., Kurozumi, H., Komatsu, R. and Demboya, N. (1993) Characteristics of Fractures in the Mori Geothermal Field. *Abstr. with Progr., Annual Meeting, Geothermal Research Society of Japan*, A7 (in Japanese).

Ando, S., Kurozumi, H., Komatsu, R. (1992) Structure and Caldera-fill Deposits of Nigorikawa Caldera. *Abstr., 29th International Geological Congress*, Vol.2, p.480.

Fukutomi, T., Fujiki, T., Sugawa, A., Ohtani, K., Wada, A. and Tokunaga, E. (1963) On the Hot Springs of Nigorikawa in Southern Hokkaido. *Geophys. Bull. Hokkaido University*, Vol.10, p.61-76 (in Japanese with English abstract).

Kato, H. and Takahashi, T. (1993) Hydrothermal System in the West of Nigorikawa Geothermal Field. *Abstr. with Progr., Annual Meeting, Geothermal Research Society of Japan*, A3 (in Japanese).

Kawano, Y., Maki, H., Ishido, T. and Kubota, Y. (1989) NEDO's Project on Geothermal Reservoir Engineering : A Reservoir Engineering Study of the Sumikawa Geothermal Field, Japan. *Proc., 14th Workshop on Geothermal Reservoir Engineering, Stanford University*, pp.55-59.

Kitamura, H., Ishido, T., Miyazaki, S., Abe, I. and Nobumoto, R. (1988) NEDO's Project on Geothermal Reservoir Engineering – A Reservoir Engineering Study of the Kirishima Field, Japan. *Proc., 13th Workshop on Geothermal Reservoir Engineering, Stanford University*, pp.47–51.

Kondo, T., Komatsu, R., Kurozumi, H. and Hanano, M. (1993) A Three–Dimensional Gravity Analysis at the Mori Geothermal Field, Hokkaido, Japan. *Proc., 88th Society of Exploration Geophysicists of Japan Conference*, p.490–495 (in Japanese).

Kurozumi, H. and Doi, N. (1993) Inner Structure of the Nigorikawa Caldera, *Progr. and Abstr., Volcanological Society of Japan*, No.2, p.14 (in Japanese).

Sato, K. (1988) Mori Geothermal Power Plant. *Geothermal Fields and Geothermal Power Plants in Japan, International Symposium on Geothermal Energy, Kumamoto and Beppu, Japan*, p.21–25.

Sato, K., Kasai, K. and Demboya, N. (1992) Isotopic Geochemistry in the Mori Geothermal Field. *Abstr. with Progr., Annual Meeting, Geothermal Research Society of Japan*, B7 (in Japanese).

Sunshine Project Promotion Headquarters (1980) Studies on Physicochemical Mechanism of Hot Water Injection. *Agency of Industrial Science and Technology, Ministry of International Trade and Industry*, pp.185 (in Japanese).

Tsutsui, M., Demboya, N., Nakai, Y., Oikawa, Y. and Ishido, T. (1991) Development of Three–Dimensional Unsteady Geothermal Reservoir Simulator, SING. *Abstr. with Progr., Annual Meeting, Geothermal Research Society of Japan*, P7 (in Japanese).

Turcotte, D.L. and Schubert, G. (1982) *Geodynamics*, Wiley, pp.450.

Urakami, K. and Nishida, Y. (1977) Heat Discharge Measurement and Geophysical Prospecting at Nigorikawa Basin, Northern Part of Komagatake. *Bull. Geol. Surv. Japan*, Vol.28, p.1–20 (in Japanese with English abstract).

Yoshida, Y. (1991) Geochemistry of the Nigorikawa Geothermal System, southeast Hokkaido, Japan. *Geochemical Journal*, Vol.25, p.203–222.

PROCEEDINGS, Nineteenth Workshop on Geothermal Reservoir Engineering
Stanford University, Stanford, California, January 18-20, 1994
SGP-TR-147

# REAL-TIME AND POST-FRAC' 3-D ANALYSIS OF HYDRAULIC FRACTURE TREATMENTS IN GEOTHERMAL RESERVOIRS

*C.A. Wright and J.J. Tanigawa, Pinnacle Technologies Inc.; Masami Hyodo and Shinji Takasugi, Geothermal Energy Research and Development Co., Ltd.*

## ABSTRACT

Economic power production from Hot Dry Rock (HDR) requires the establishment of an efficient circulation system between wellbores in reservoir rock with extremely low matrix permeability. Hydraulic fracturing is employed to establish the necessary circulation system. Hydraulic fracturing has also been performed to increase production from hydrothermal reservoirs by enhancing the communication with the reservoir's natural fracture system. Optimal implementation of these hydraulic fracturing applications, as with any engineering application, requires the use of credible physical models and the reconciliation of the physical models with treatment data gathered in the field. Analysis of the collected data has shown that 2-D models and 'conventional' 3-D models of the hydraulic fracturing process apply very poorly to hydraulic fracturing in geothermal reservoirs. Engineering decisions based on these more 'conventional' fracture modeling techniques lead to serious errors in predicting the performance of hydraulic fracture treatments. These errors can lead to inappropriate fracture treatment design as well as grave errors in well placement for hydrothermal reservoirs or HDR reservoirs.

This paper outlines the reasons why conventional modeling approaches fall short, and what types of physical models are needed to credibly estimate created hydraulic fracture geometry. The methodology of analyzing actual measured fracture treatment data and matching the observed net fracturing pressure (in real-time as well as after the treatment) is demonstrated at two separate field sites. Results from an extensive Acoustic Emission (AE) fracture diagnostic survey are also presented for the first case study as an independent measure of the actual created hydraulic fracture geometry.

## INTRODUCTION

Hydraulic fracture stimulation has been extensively employed for nearly fifty years by the petroleum industry as a technique to increase an individual wellbore's contact, or communication, with reservoir rocks. Hydraulic fracture stimulation is achieved by injecting fluid into reservoir rocks at rates and pressures (above in-situ reservoir confining stress) sufficient to part and hydraulically propagate fractures in the reservoir rock. A schematic of the process and equipment necessary for a hydraulic fracture stimulation is shown in Figure 1 (from Ref. 1). The retained hydraulic conductivity of the generated fractures (which are often held open by pumping particulates known as 'proppant') increases the cross-sectional area over which a wellbore contacts reservoir rock, therefore, allowing significantly enhanced fluid production rates compared to those achievable with an unstimulated wellbore.

Hydrothermal reservoirs offer the same opportunity as oil and gas reservoirs to enhance production from a wellbore by employing hydraulic fracture stimulation. In contrast, however, to conventional oil and gas reservoirs where production rates are (predominantly) controlled by the reservoir (matrix) permeability, hydrothermal reservoir fluid production rates are typically controlled by the conductivity of the natural fracture system intersected by the wellbore. Prolific wells usually intersect highly conductive and interconnected natural fracture networks. Often, adjacent wells may be far less prolific producers simply because they lack the connection at the wellbore to the nearby natural fracture systems. Significant productivity enhancement can often be achieved by establishing the necessary communication with nearby natural fracture systems through hydraulic fracture stimulation (Refs. 2 - 3).

Hydraulic fracture stimulation plays an indispensable role in the extraction of heat from Hot Dry Rock (HDR) reservoirs (Refs 4 - 7). The tremendous resource base of HDR reservoirs versus conventional hydrothermal reservoirs makes efficient HDR production technology of global importance. Heat extraction from HDR reservoirs is the result of circulating water from an injection wellbore through an artificially created fracture system and out a production wellbore(s). Efficient energy production depends not only on achieving effective hydraulic fracture stimulation of a large volume of reservoir rock, but also on possessing the modeling and diagnostic capability required to optimally design hydraulic fracture stimulations and to reliably estimate the created geometry and dimensions of the induced hydraulic fracture systems.

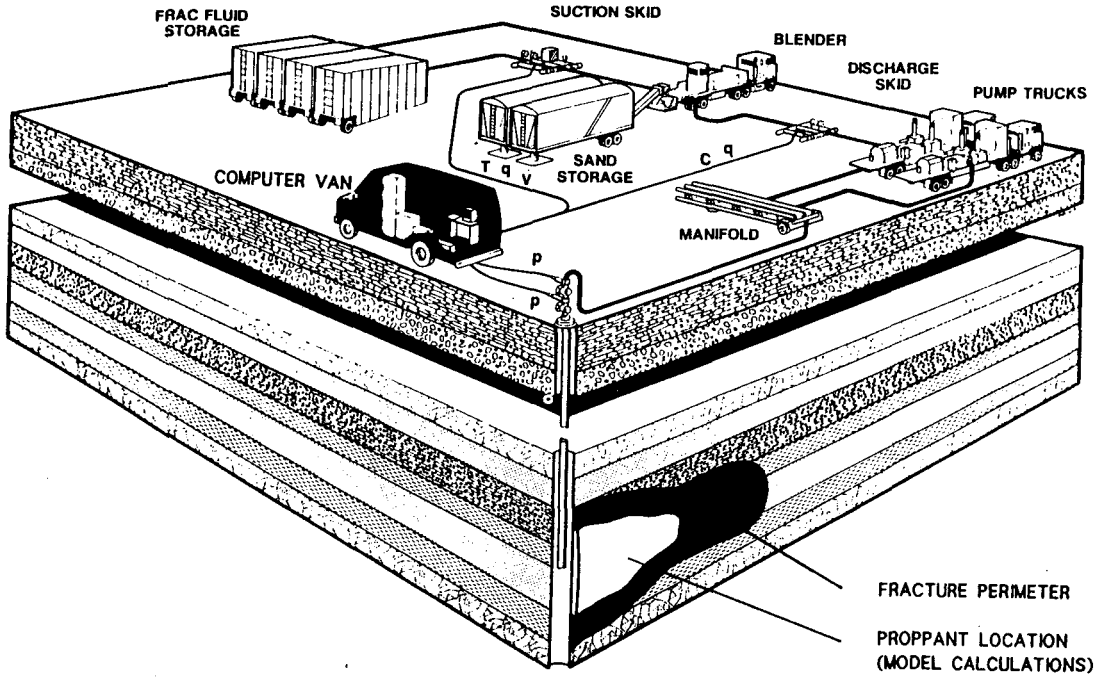


**Figure 1: Isometric View of the Hydraulic Fracturing Process Including Surface Equipment and Generalized Created Hydraulic Fracture**

This paper outlines some of the basic concepts behind hydraulic fracturing and briefly overviews the current modeling approaches. Detailed analysis of measured field data has shown that industry two-dimensional models and 'conventional' three-dimensional models of the hydraulic fracturing process apply very poorly to hydraulic fracturing in geothermal reservoirs. However, an enhanced three-dimensional fracture modeling system is described which contains real-time data acquisition and complex fracture modeling capabilities that more realistically represent fracturing in geothermal reservoirs. Finally, two case studies of hydraulic fracturing applications -- one in an HDR reservoir and the other in a (nominally) hydrothermal reservoir -- are presented with detailed analysis of collected treatment data and comparison with independent fracture diagnostic data. The final section presents a summary of conclusions.

## MODELING OF HYDRAULIC FRACTURES

Early fracture models (Refs 8, 9), which are still in all-too-common use today, simply assumed that the height of the fracture was known and that only the length and width needed to be calculated. Various height assumptions were made, with those of the reservoir 'pay-zone' height and perforated (or open-hole) interval being the most common. Despite their lack of physical realism, two-dimensional models, due to their physical simplicity, are still by far the most widely used tools today for designing and evaluating hydraulic fracture treatments. Constant height fracture models invariably overestimate the predicted fracture lengths, by as much as a factor of 10 or more. A more physically realistic (for most applications) two-dimensional fracture model is provided by the assumption of radial fracture geometry, where the two independent fracture dimensions become fracture radius and width. While the geometric assumption of a radial fracture may approximate reality for most hydraulic fracture stimulations of geothermal reservoirs which typically lack the necessary 'barriers' for fracture height containment, the typical fracture dimensions predicted by simple radial fracture models vastly overestimate the actual created fracture radius (the reasons for this are discussed below). 'Conventional' three-dimensional fracture modeling allows the incorporation of variations in reservoir stress, modulus, and (sometimes) permeability into the fracture modeling process. While this three-dimensional enhancement is necessary, the 'conventional' three-dimensional modeling assumptions of (1) the applicability of Linear-Elastic Fracture Mechanics (LEFM) and (2) the generation of a single planar fracture, prevent credible results from being obtained using such modeling approaches (Refs 10, 11).

Over the last decade a focused research effort, primarily sponsored by the U.S. Gas Research Institute, has striven to acquire the field and laboratory data necessary for the development of more realistic three-dimensional hydraulic fracture models. This research resulted in a commercially available hydraulic fracture modeling system called FRACPRO (Refs 12-13). The initial

effort focused on comparing carefully collected field data-sets from dozens of actual hydraulic fracture stimulations to the predictions from then state-of-the-art 'conventional' three-dimensional fracturing simulators. Model agreement with field data-sets was found to be very poor. A host of mechanisms, which were not previously accounted for, were found to often play dominant roles in hydraulic fracture growth, including; non-linear rock behavior near the fracture tip; fracture containment due to permeability barriers; proppant convection; near-wellbore fracture tortuosity; and the simultaneous propagation of multiple hydraulic fractures. The FRACPRO models are generalized and modular 'lumped' parameter three-dimensional models. This type of model formulation allows for the (approximate) handling of the complex fracture mechanisms mentioned above and, therefore, allows more realistic estimates of created fracture geometry (Ref 14).

The specific models contained in FRACPRO are three-dimensional, in that spatial variations in reservoir stress, permeability, modulus, pressure, and flow distribution are taken into account. However, the models are 'lumped parameter' and do not calculate the variations at specific points within the fracture: instead, the effects are integrated into (functional) coefficients of the governing differential equations, greatly simplifying the calculation of the fracture dimensions. The system can therefore run much faster than real time, as required for pressure history-matching on-site. The (functional) coefficients necessary to calculate the spatial variations are calculated from a full three-dimensional model and checked against experimental laboratory and field test data. It is through these (functional) coefficients that the complex fracture mechanisms (e.g. near-tip non-linear rock behavior, permeability barriers, etc.) are handled in the FRACPRO models.

When modeling hydraulic fracture stimulations in geothermal reservoirs, or any other reservoir which has significant natural fracturing, it is essential to consider the role natural fractures play in the evolution of induced hydraulic fractures. Fracture initiation from an open hole interval (or perforation) always takes place at points of pre-existing cracks with the greatest hydraulic conductivity. Wellbores which intersect swarms of natural fractures tend to initiate swarms of hydraulic fractures upon stimulation. The combined generality and relative simplicity of the FRACPRO models allows, at least to first order, the modeling of multiple hydraulic fractures growing simultaneously. Input assumptions must be made on the number of fractures growing (this can vary with time) and whether the individual fractures are competing for opening space, and/or access to the reservoir for fluid leak-off, or whether the fractures are growing independently and don't "feel" the effects of the other fractures. A time-history of the number of the fractures taking fluid, competing for opening space, and leaking fluid is entered into the model and a simulation is run modeling the mechanical effects of the multiple fractures and the resulting fracture dimensions, pressures, etc. are calculated. As with any history-matching process, iteration is required to find which assumptions best match the observed fracturing pressure response. Care must be taken to justify the assumption of the simultaneous propagation of multiple fractures over the mechanically simpler assumption of the propagation of a single hydraulic fracture.

Input assumptions are often influenced from direct knowledge of a wellbore's reservoir contact from observed zones of lost circulation during drilling; core data; or borehole imaging log data. Since FRACPRO does not know the orientation of the in-situ stress field or the orientation of the existing natural fractures and micro-cracks, it simply assumes that fractures are created in the plane perpendicular to the least principle stress direction. FRACPRO's generated fracture profiles and opening (width) profiles are *approximations of the overall* created hydraulic fractures. Borehole imaging and other logs, in contrast, can be used to attempt to get a more detailed view of the fracture(s) at the *point of intersection with the wellbore.* These are very different, but complimentary, views of the same phenomenon.

The actual complexity of the created fracture(s) is certainly greater than that captured in FRACPRO, as is the case in all engineering modeling. The goal of FRACPRO is to determine the aerial penetration (radius or length); the geometry (i.e. is the fracture roughly radial or do stress or permeability barriers significantly contain or elongate the fracture(s)?); the complexity (i.e. are there likely to be multiple created hydraulic fractures?); and the opening width(s) of the created hydraulic fracture(s).

## REAL-TIME FRACTURE ANALYSIS

Real-time analysis requires an on-site PC (80386/486) with appropriate data acquisition and modeling software (FRACPRO, in this case) and measured treatment data (injection rates, pressures, fluid properties, etc.) in digital format. Digital treatment data can usually be acquired directly from the pumping service company or from on-site data acquisition hardware. A schematic of this set-up is shown in Figure 2.

To achieve confidence in the predictions of any hydraulic fracture simulator requires that the net fracturing pressure (fracturing fluid pressure above formation closure stress) predicted by the model match the observed net fracturing pressure of the treatment. In fact, the two-dimensional and 'conventional' three-dimensional fracturing models discussed earlier can often be dismissed based on their complete inability to match observed net fracturing pressures. The

determination of observed net fracturing pressure requires accurate knowledge of the bottomhole pressure, $P_{bottomhole}$, during the pumping of the fracturing treatment. Bottomhole pressure, when not measured directly, can be calculated using the following formula:

$$P_{bottomhole} = P_{surface} + P_{head} - P_{friction} \quad (1)$$

$P_{surface}$ is the treating pressure measured at the surface; $P_{head}$ is the hydrostatic head, or weight, of the fluid in the wellbore; and $P_{friction}$ is the head-loss due to friction in the pipe. Once bottomhole pressure is known, the net fracturing pressure can be calculated by subtracting the closure stress and any pressure loss due to perf and/or near-wellbore friction, $P_{perf/near\text{-}wellbore}$, from the bottomhole pressure:

$$P_{net} = P_{bottomhole} - P_{closure} - P_{perf/near\text{-}wellbore}, \quad (2)$$

Frictional losses in the wellbore and/or the perf/near-wellbore region, the major unknowns in the equations above, are very difficult to *predict*, but they are relatively simple to *measure* using abrupt flow-rate changes and shut-ins.

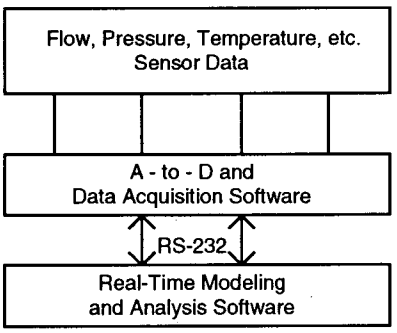


**Figure 2: Schematic of Real-time Data Acquisition and Fracturing Analysis**

FRACPRO uses the measured flow rate, fluid rheology, proppant concentration and reservoir description to predict the net fracture pressure. This predicted net pressure can be compared, in a history-matching process, to the 'observed' value of net pressure described in Equation (2). Unknown or uncertain reservoir properties upon which the pressure response (and therefore, fracture growth) depends can be changed and the simulator re-run until the observed and predicted net pressures match. A good match of net pressures will result in a good estimation of fracture extent and proppant placement. Obviously, the more accurately bottomhole pressure and closure stress are known, the more precisely the true net pressure in the fracture can be calculated, and the more precise will be the fracture-geometry predictions.

## CASE STUDY 1: HDR-1 WELL, JAPAN

The HDR-1 well is located at the Hijiori Hot Dry Rock Test Site, in central Honshu Island, Japan. This well is a part of the New Energy and Industrial Technology Development Organization's (NEDO) and the Geothermal Energy Research and Development Company's (GERD) effort to develop fundamental technologies in Hot Dry Rock geothermal reservoirs (Ref 15). As with typical HDR reservoirs, the pre-existing natural fracture system at the Hijiori site does not nearly provide adequate reservoir communication and, therefore, must be fracture stimulated to achieve the necessary rates of heat extraction. In July 1992, HDR-1 was hydraulically fractured (without proppant) to create an artificial reservoir between injection and production wells in the Hijiori deep reservoir.

The treatment included a pre-frac' test, a massive main fracture stimulation, followed by two post-frac' tests. The purpose of the pre and post pump-in tests was to ascertain the value of reservoir closure stress (243 KSC) and the value of reservoir leak-off coefficient (approx. $2.0\times10^{-4}\,ft/\sqrt{min}$) for the Hijiori deep reservoir, and to evaluate the effectiveness of the main hydraulic fracture treatment. The main fracture treatment consisted of 2,110 $m^3$ of fresh water pumped at an average rate of 3,600 l/min The collected treatment data was analyzed by matching the net fracturing pressures in real-time using the FRACPRO system. Core derived reservoir mechanical properties and log derived natural fracture descriptions were incorporated in the analysis. Figure 3 illustrates the observed net pressure to simulated net pressure match.

As Figure 3 illustrates, the character and the level of observed net pressure was matched during the injection period. Oscillations in the observed net pressure are the result of rapidly changing wellbore friction (not actual changes in net fracturing pressure) due to sporadic addition of friction reducer. The difference in the rate of pressure decline (between observed net pressure and modeled net pressure) after the end of pumping was due to flow-back of the injected fluid. The post-treatment flowback made the observed net pressure appear to fall much faster than it would have fallen if the well were shut-in after the stimulation. Therefore, the correct value for fluid leak-off coefficient was inferred from the pre- and post-frac' tests.

This net pressure match concluded that a fracture radius of 145 meters (476 ft) and a maximum total hydraulic fracture width of 40 mm (1.57 inches) was achieved (Ref 16). Modeling also deduced that the width was divided among roughly 18 'equivalent' multiple, near-parallel, fractures. Since no significant barriers to fracture growth were known to exist at the Hijiori test site, the modeled fracture geometry is radial in nature. The radial shape of the hydraulic fracture was verified

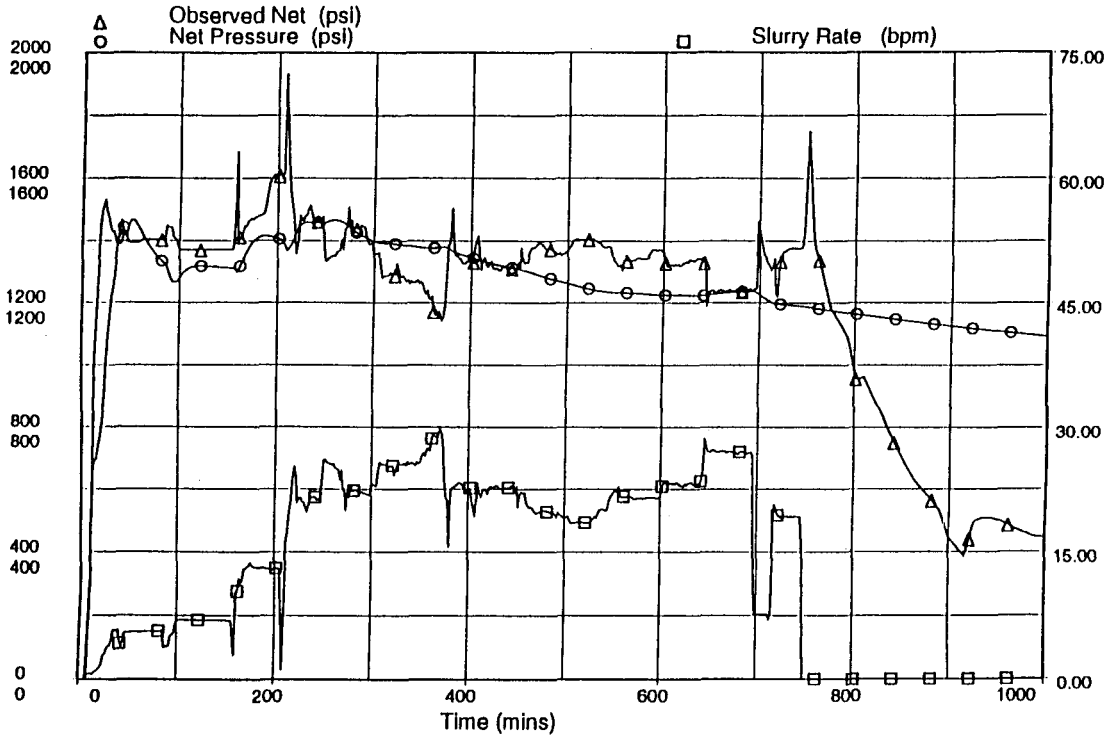


**Figure 3: Net Pressure Match for HDR-1 Main Fracture Treatment**

by the Acoustic Emission (AE) fracture diagnostics that were performed on the HDR-1 main fracture. Figure 4 shows three map views of the locations of the recorded high quality AE events.

The HDR-1 main fracture treatment was also analyzed using two more traditional fracture models -- the two-dimensional PKN fracture model and a 'conventional' three-dimensional fracture model. These results are shown in Table 1.

As Table 1 illustrates, the other two fracture models predict a far greater fracture radius than that predicted by the FRACPRO model (or observed by the AE diagnostics). In addition, the other models predict net fracture pressures that are more than an order of magnitude lower than the observed net fracture pressure, casting doubt on their predicted fracture dimensions even before the AE results were known. FRACPRO's ability to match the observed net pressure response and account for complex hydraulic fracture mechanisms results in an estimated fracture size and geometry that roughly match the observed AE results, but at a fraction of the cost of an AE survey.

Since the creation of an artificial reservoir is crucial to any HDR system, realistically modeling the created fracture's dimensions (i.e., reservoir size) is of paramount importance. If unrealistic fracture dimensions are estimated, injectors and producers can be drilled too far apart yielding economically disastrous results.

## CASE STUDY 2: TG-2 WELL, JAPAN

The TG-2 well, located in the Iwate Prefecture Japan, was drilled *within* 300 meters of the Matsukawa Hydrothermal Reservoir (the exact distance was not known) and was a part of NEDO's "Technology for Increasing Geothermal Energy Recovery Project". A series of injection tests were performed in January and September of 1992, prior to the November 1992

**Table 1: Comparison of Three Fracture Simulators to Actual Acoustic Emission Data**

| SOURCE | FRACTURE RADIUS (METERS) | NET PRESSURE AT SHUT-IN (KSC) [1] |
|---|---|---|
| PKN Model | 900 [2] | 7 |
| Conventional 3-D | 640 | 2 |
| FRACPRO | 145 | 90 |
| *AE Results* | *150-200* | |

NOTE: 1. Observed Net Pressure was 90 KSC
2. Fracture Length assuming height equal to open hole interval (55 m)

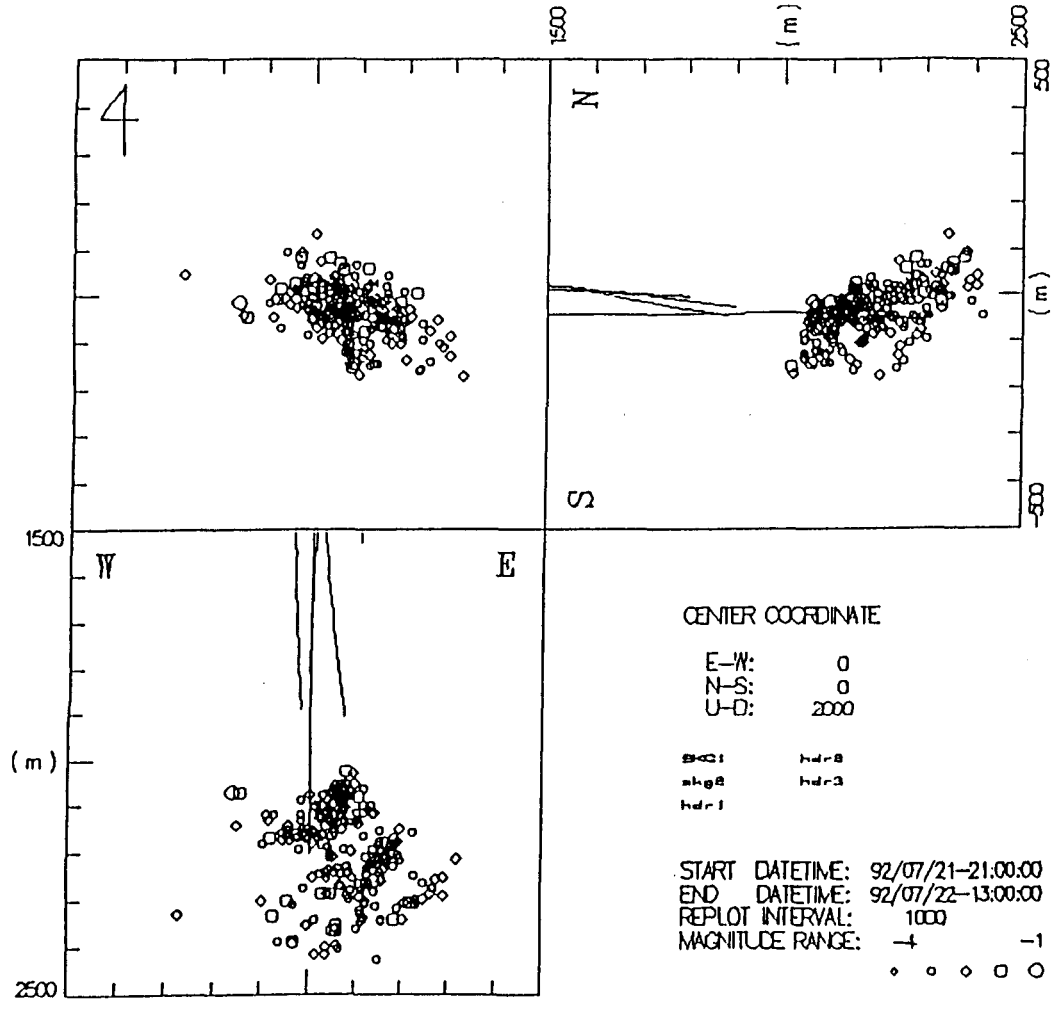


**Figure 4: Epicenter Plot of AE Results from HDR-1 Main Fracture Treatment**

massive fracture treatment, to test different fracturing fluids (water proved to be the economic choice) and to characterize reservoir properties like formation closure stress, fluid leak-off, natural fracture induced growth of multiple hydraulic fractures, and reservoir mechanical properties (Refs 17-22). The (original) goal of the massive stimulation was to create a hydraulic fracture extending from the TG-2's open hole wellbore section (710-1,298 m depth) to the Matsukawa reservoir. In this way, the hydraulic fracture would communicate with the hydrothermal reservoir and produce its steam and hot water. The results from the initial injection tests raised serious doubts about the ability to feasibly generate a fracture radius significantly greater than 100 meters in this reservoir.

FRACPRO was utilized to collect data and analyze all injections in both real-time and after the stimulation. The massive hydraulic fracture consisted of 4,352 $m^3$ of fresh water pumped at approximately 4,000 l/min. A series of four 30 minute shut-ins were scheduled throughout the treatment to monitor the reservoir 'permeability' (from interpreting pressure decline data) contacted by the created hydraulic fractures. Since the Matsukawa reservoir has a permeability ten to thousands of times greater than the rock immediately surrounding TG-2, a dramatically higher leak-off would result if the fracture extended into the Matsukawa reservoir. Figure 5 shows the match of modeled net pressure to observed net pressure.

Careful matching of the pressure decline during all five shut-ins (including the period after pumping) indicated that the hydraulic fractures did appear to contact reservoir of enhanced permeability as the treatment progressed -- but the inferred increase in reservoir permeability was a relatively modest factor of 2.5 greater than the rock surrounding TG-2. Thus, communication with the Matsukawa reservoir was not well established.

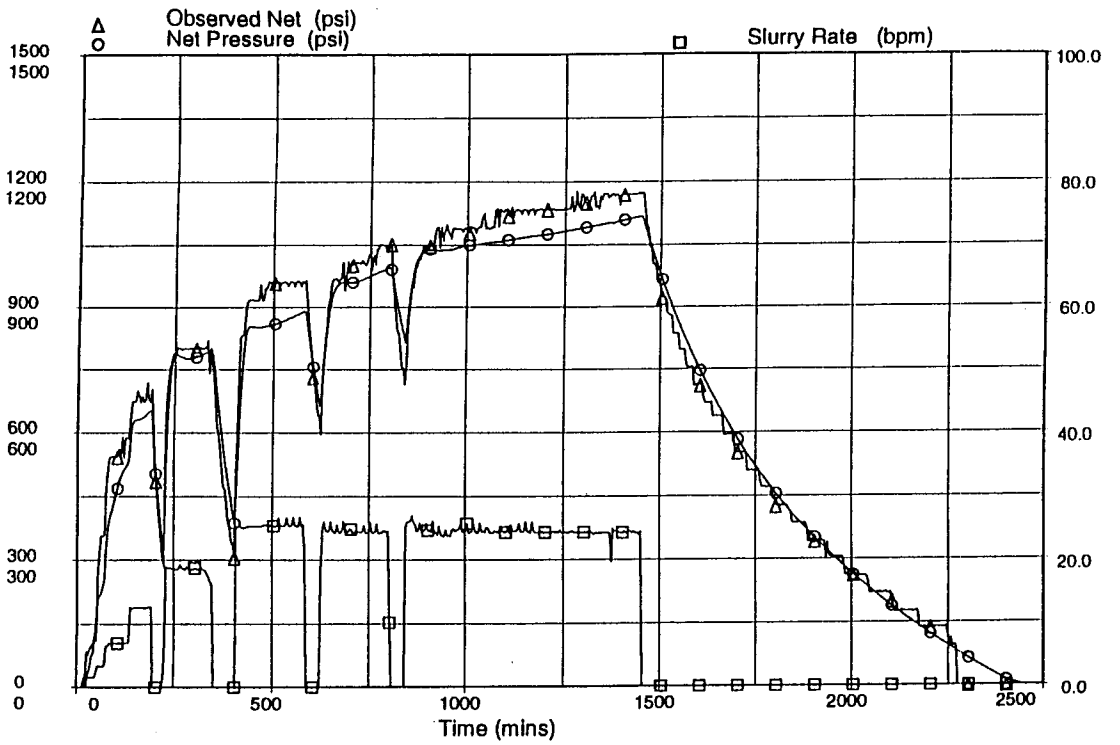


**Figure 5: Net Pressure Match for TG-2 Massive Fracture Treatment**

This net pressure match concluded that a fracture radius of 94 meters (310 ft) and a maximum total hydraulic fracture width of 58 mm (2.28 inches) was achieved. In addition, the net pressure matching also concluded that multiple (19 'equivalent') hydraulic fractures were created during the stimulation. As in the previous example, since no barriers to height growth were known to exist, the modeled fracture propagated radially from the wellbore.

While the massive frac of the TG-2 well failed to achieve the initial goal of establishing communication with the prolific Matsukawa reservoir, the series of tests performed did provide tremendous insight into the process of fracturing hydrothermal reservoirs and the range of achievable results. It was also the first time a real-time hydraulic fracture modeling technology had ever been employed in a geothermal reservoir.

## CONCLUSIONS

(1) Effective hydraulic fracture stimulation is essential to the technology of producing power from Hot Dry Rock reservoirs.

(2) Hydraulic fracture stimulation can also be applied to hydrothermal reservoirs to increase production (and improve the economics) by enhancing the communication with the reservoir's natural fracture system.

(3) Careful analysis of observed data from hydraulic fracturing treatments has revealed the inadequacy of conventional fracture modeling approaches in predicting created hydraulic fracture dimensions and geometry.

(4) Expanded (from conventional) physical modeling capabilities are required for realistic hydraulic fracturing modeling, particularly in geothermal reservoirs.

(5) Real-time analysis provides critical information on-site and *in time* to make necessary design changes during fracturing operations.

## ACKNOWLEDGMENTS

The authors express their appreciation to the New Energy and Industrial Technology Development Organization (NEDO) for giving us permission to present the results obtained in the "Development of Geothermal Hot Water Power Generation Plant" in MITI's the Sunshine Project, Japan. Much of the work discussed in this paper was performed using the FRACPRO simulator, developed by RES, Cambridge,

Massachusetts. We would also like to thank GRI for their continued support of research in the area of hydraulic fracturing. Finally, we express our gratitude to C.C. Fraley for assisting in the final draft of this manuscript.

## REFERENCES

1. Cleary, M.P., (1988), "Engineering of Hydraulic Fractures - State of the Art and Technology of the Future", Journal of Petroleum Technology, January 1988, pp. 13-21.

2. Katagiri K, Ott W.K., Nutlley B.G., (1980), "Hydraulic Fracturing Aids Geothermal Field Development", World Oil, December 1980, pp. 75-88.

3. Nakatsuka K, Takahashi H, Takanohashi M (1982), "Hydraulic Fracturing Experiment at Nigorikawa and Fracture Mechanics Evaluation", Proceedings of the First Japan-United States Joint Seminar on Hydraulic Fracturing and Geothermal Energy, Tokyo, Japan, November 1982.

4. Camborne School of Mines (1988), "Camborne Geothermal Energy Project Viscous Stimulation of Hot Dry Rock Reservoir", Department of Energy, Contractor Report, 1988.

5. Brown, D.W., (1992) "Update on the Long-Term Flow Testing Program", Geothermal Resources Council BULLETIN, volume 21, No. 5, May 1992, pp. 157-161.

6. Abe H, Hayashi K, (1992) "Fundamentals of Design Concept and Design Methodology for Artificial Geothermal Reservoir Systems", Geothermal Resources Council BULLETIN, volume 21, No. 5, May 1992, pp. 149-155.

7. Matsunaga I, Yamaguchi T, (1992), "A Three-Month Circulation Test at the Hot Dry Test Site in Hijiori, Japan", Geothermal Resources Council BULLETIN, volume 21, No. 5, May 1992, pp. 162-166.

8. Perkins T.K., Kern L.R., (1961), "Widths of Hydraulic Fractures", Journal Petroleum Technology, September 1961, pp. 937-949.

9. Geertsma J, de Klerk F., (1969), "A Rapid Method of Predicting Width and Extent of Hydraulically Induced Fractures", Journal of Petroleum Technology, December 1969, pp. 1571-1581.

10. Cleary M.P., Wright C.A., Wright T.B., (1991), "Experimental and Modeling Evidence for Major Changes in Hydraulic Fracturing Design and Field Procedures", Society of Petroleum Engineers Gas Technology Symposium, Houston, Texas", January 1991, pp. 131-146.

11. Johnson E, Cleary M.P., (1991) "Implications of recent Laboratory Experimental Results for Hydraulic Fractures", Society of Petroleum Engineers Rocky Mountain Regional Meeting and Low Permeability Reservoirs Symposium, Denver, Colorado", April 1991, pp. 413-428.

12. Wooten C.T., (1989) "Fracture Control is Enhanced by Real-Time Monitoring", The American Oil & Gas Reporter, August 1989, pp. 17-22.

13. Martinez A.D., Wright C.A., Wright T.B., (1993), "Field Application of Real-Time Hydraulic Fracturing Analysis", Society of Petroleum Engineers Rocky Mountain Regional Meeting and Low Permeability Reservoir Symposium, Denver, Colorado", April 1993, pp. 693-703.

14. Crockett A.R., Okusu N.M., Cleary M.P., (1986), "A Complete Integrated Model for Design and Real-Time Analysis of Hydraulic Fracturing Operations, Oakland, California", April 1986, pp. 221-233.

15. Geothermal Energy Department New Energy and Industrial Technology Development Organization (1987, "Fiscal Year 1987 Summary of Hot Dry Rock Geothermal Power Project in Japan", 1987. [ *Also referencing FY Reports from 1988, 1989, 1990 and 1991.*]

16. Hyodo M, Inoue K, Takasugi S, (1993), "Hydraulic Fracturing Test and Pressure Behavior Analysis at the HDR-1 Well", Hot Dry Rock Geothermal Energy Forum 1993, November 1993, section C-6.

17. Shinohara N, Takasugi S, (1993), "Fracture Design and the Result of Mini Hydraulic Fracturing, Employed for the TIGER Project", SEG Japan, June 1993.

18. Hyodo M., Shinohara N, Takasugi S, (1993), "Hydraulic Fracturing Test and Pressure Behavior Analysis at the TG-2 Well", SEG Japan, June 1993.

19. Ujo S, Shinohara N, Takasugi S, (1993), "Evaluation of Productivity Improvement by Hydraulic Fracturing Using PTS Logging at the TG-2 Well", SEG Japan, June 1993.

20. Okabe T, Shinohara N, Takasugi S, (1993), "Measurement Results and Evaluation of BHTV Logging and FMI Logging at the TG-2 Well", SEG Japan, June 1993.

21. Kawakami N, Takasugi S, (1993), "SP Monitoring During the Hydraulic Fracturing Using the TG-2 Well", SEG Japan, June 1993.

22. Tateno M, Wei Q, Hanano M, (1993), "Evaluation of Fracture Extension Created by Hydraulic Fracturing using AE measurement, employed for TIGER Project", SEG Japan, June 1993.

PROCEEDINGS, Nineteenth Workshop on Geothermal Reservoir Engineering
Stanford University, Stanford, California, January 18-20, 1994
SGP-TR-147

# Vapor Pressure Lowering in Brines and Implications for Formation of a High Temperature Reservoir

G. Michael Shook

Idaho National Engineering Laboratory
PO Box 1625 Idaho Falls, ID 83404-2107

## Introduction

That a "high temperature reservoir" (HTR) underlies a "typical" vapor-dominated reservoir under certain circumstances is well known (Drenick, 1986; Pruess et al., 1987; Walters et al., 1988). However, formation and behavior of such a feature is poorly understood. Recent theories regarding the behavior of the HTR fall into one of two broad categories: transient and steady state. In the transient models (e.g., Drenick, 1986; Walters et al., 1988; Truesdell, 1991), the HTR is a component of the typical vapor-dominated reservoir for a relatively short period of time.. These models generally assume either a recent boiling of a liquid system (a fossil liquid system; Drenick, 1986; Walters et al., 1988), or downward extension of the "typical" reservoir into hot dry rock (Truesdell, 1991). Steady state models (Shook, 1993a; Lai et al., 1994) consider the HTR as a steady component of the geothermal reservoir. As in the case of the transient theories, several different explanations are given for the formation of the HTR. For example, Shook (1993a) used vapor pressure lowering in a fractured domain to develop an HTR, whereas Lai et al. (1994) used non-uniform heating in a porous media in forming the HTR.

While any of these theories may indeed explain the formation of the HTR, perhaps the most significant implication of the differences is the variation in liquid saturation of the HTR. For example, the Lai et al. (1994) steady state model exists only at very low liquid saturations overall, and superheated conditions in the HTR. Shook (1993a), on the other hand, showed large liquid saturations in the HTR. Such differences in saturation have potentially large effects on hypothesized response to exploitation. It would seem, then, that additional physics and field observations must be incorporated in these models to better constrain the problem and converge upon the correct mechanism.

Recent studies may provide additional clues regarding development of the HTR at The Geysers. On the basis of fluid inclusion work, Moore (1992) suggests the presence of very saline brine (up to 40 wt % NaCl) in the HTR, with much lower salinities in the "typical" reservoir. Moore further suggests that low permeabilities within the HTR may be responsible for the salinity contrasts. However, at this time it is not known whether these fluid inclusion results apply to the current hydrothermal cycle of the reservoir.

Williams et al. (1993) presented heat flow studies of Northwest Geysers, and showed a thermal transient in the caprock in the northwest portion of the field that is not found to the southeast. On the basis of some one-dimensional heat conduction calculations, they conclude that this thermal transient may be caused by a temperature reduction of 40°C 5,000-10,000 years ago in the northwest portion of the field. A second possibility not considered by these authors is that a thermal perturbation occurred to the southeast, and that the thermal transient has already been attenuated nearer the source. From their figure 9, this would place the perturbation temporally about 20,000 years ago.

This paper summarizes some preliminary numerical simulations of the formation of a HTR. The numerical model TETRAD (Vinsome, 1991; Vinsome and Shook, 1993) was used in the study. A two-dimensional model was used, and a possible evolutionary scenario for The Geysers was simulated. Results of the study indicate that a HTR may form under a variety of conditions, and may either be two-phase or superheated. Using brine as the reservoir fluid tends to create a two-phase HTR, with a substantial concentration of salt in that zone. The HTR developed in this study appears to be transient in nature, but is cooling only very slowly.

## Reservoir Description

The reservoir model used in this study is a two-dimensional cross section of a fractured media. The Warren and Root (1963) model was used, with some matrix-matrix interactions allowed both vertically and horizontally. Dimensions of the domain are 400 m by 100 m areally, and 1200 m vertically. Fracture spacing was taken as 100 m.Petrophysical properties for the reservoir were taken from the literature, and are representative of Geysers rock. Fracture porosity and permeability were taken as 0.01 and $10^{-14}$ $m^2$ (10 md), respectively. Matrix properties used were $\varphi = 0.04$ and $k = 10^{-17}$ $m^2$ (10 μd). These properties were constant throughout the domain, except as noted below.

Relative permeability and capillary pressure curves are not available in the literature. The parametric curves used are given in Table 1. Endpoint relative permeabilities and curvatures for both permeability and capillary pressure differ from fracture to matrix, as summarized in the table. An arbitrarily large maximum capillary pressure of 40000 kPa (400 bars) at standard conditions was used for both

fractures and matrix. Capillary pressures are scaled as a function of temperature and as functions of permeability and porosity as described by Shook (1993b). Maximum capillary pressure at initial reservoir temperature is approximately 12,250 kPa (122.5 bar). Petrophysical properties are summarized in Table 1.

The modifications to the petrophysical properties noted above involve permeability and porosity at depth. Several authors have noted variations in permeability and porosity with depth (Gunderson, 1990; Williamson, 1989). Additional evidence presented by Sternfeld (1989) indicates a facies change at depth in the northwest portion of the field. To mimic this facies change, decreases in permeability and porosity in the rock matrix, and reduction of fracture porosity were made. This "facies change" is not uniform across the domain. Instead, it is relatively thick on one side, and pinches out toward the center of the domain. No attempt was made to invoke a gradual change in facies, but rather an abrupt in properties was made. In this portion of the domain, $k = 10^{-19}$ $m^2$ (0.1 μd) in the matrix, and $\varphi = 0.005$ for both fracture and rock matrix. The reservoir is depicted schematically in Figure 1.

**Model Description**

The model was initially assumed to be in hydrostatic equilibrium and at an initial temperature of 240°C. Pressure at the top of the reservoir was 3600 kPa, slightly above the saturation pressure of pure water. The reservoir fluid was a low-concentration brine, with a salt concentration of 3 wt %. Relative vapor pressure from osmotic effects for this salt concentration is approximately 0.95.

The model scenario follows that of Shook (1993a). A uniform heat flux of 0.5 $W/m^2$ was applied to the bottom of the reservoir, and the top of the reservoir was initially held at constant temperature and pressure. After 2000 years of equilibration, the system was perturbed by a sudden venting episode. The vent (simulated via a well) was open to the atmosphere for 60 years, and the vent rate constrained to less than 1.2 kg/s. After the vent episode, the reservoir was again allowed to equilibrate. The constant pressure/temperature boundary at the reservoir top was removed, and heat escapes the domain via conduction through the caprock.

Results from the base case simulation at t=20,000 years (18,000 yrs. after venting) are shown in Figures 2-4. The pressure profile shown in Figure 2 clearly shows vapor-dominant conditions throughout the domain. However, Figure 3 shows the presence of a high-temperature zone at depth opposite the vent. One significant feature of this simulated HTR is its non-uniform depth. The top of the HTR largely follows the "facies change" input, and therefore moves deeper toward the middle of the domain. As seen in Figure 4, the HTR is two-phase, with an average matrix liquid saturation of 0.4.

Although not shown on the figures, another interesting feature of the HTR is the chemical composition of the fluid. The initial salt content in this simulation was a uniform 3 wt. %. However, after the venting and subsequent re-equilibration, most of the salt remaining in the system is concentrated within the HTR. Simulated salt concentrations in the "typical" reservoir are less than 0.05 wt. %, whereas in the HTR concentrations vary from 20 to in excess of 40 wt %.

The time simulated was 50,000 years, or 48,000 years past the venting episode. Throughout the simulation, temperatures in the HTR changed, falling approximately 16°C in 45,000 years. Liquid saturations in the rock matrix increase modestly over the same time period. However, liquid saturations in the fractures in the HTR fluctuate over the entire simulation, with a period of several thousand years. Two distinct endpoints are observed: a "dry" cycle, where only a small mobile liquid phase is present, and a "wet" cycle, in which liquid saturations are about 30%. It is not clear at present if these fluctuations are a result of the boundary conditions or discretization scheme used, or if it is a valid cyclic response to the dynamic nature of the heat pipe.

In summary, the base case simulation displays several unique features typically associated with the HTR found at The Geysers. Its lack of uniform depth, in particular, indicates that a discontinuous facies change may be partially responsible for its development. Relatively large concentrations of salt provide the vapor-pressure lowering mechanism to allow liquid to exist in the HTR rock matrix. A cyclic pattern of liquid saturations in the fractures has been observed; however, it is not currently known whether this is a numerical artifact or a physical response of the system. Finally, changes is the thermodynamic properties of the HTR indicate that it is a transient feature, with temperature changes of about 0.33°C/1000 yrs.

**Sensitivity Studies**

A limited set of sensitivity studies have been conducted to determine HTR formation sensitivity to several of the input parameters. Mass fraction vented, salt content, and petrophysical properties of the HTR were varied in these simulations. In each of the following cases, a single change was made to the base case conditions.

When the vented fraction of mass in place was reduced to 35% (from about 50%), properties of the HTR changed accordingly. In this case, the HTR was liquid-dominated, with pressures and temperatures following a hydrostatic gradient and boiling with depth curve, and the top of the HTR is at a constant depth. This result appears similar to that of Lai et al. (1994) for low vapor saturations.

When salt is removed from the reservoir fluid, the character of the HTR is changed. The HTR forms with a non-uniform surface, as in the base case. In this case, however, the HTR is superheated. However, very little salt is required to develop a saturated HTR. For example, when the salt content was reduced to 1.6 wt. %, the HTR forms as observed in the base case, and again is saturated. Despite the reduced mass of salt initially present, concentrations in the HTR approach 30% by weight.

In both of these cases the HTR is much more transient in nature. For example, when no salt is present, the HTR disappears in about 30,000 years, and the entire model is a "typical" vapor-dominated reservoir, with very low liquid saturations..

A final case considered changes in both permeability and porosity in the fractured domain of the HTR. In this case, fracture permeability was reduced to $10^{-19}$ $m^2$ (0.1 μd), the same as in the matrix in the HTR. As in the base case, the HTR forms with a non-uniform surface, and similar temperature profiles are also observed. However, in this case, the pressure gradient is approximately 1 kPa/m, somewhat larger than has been reported in the literature. The liquid saturation in the HTR is larger in this case as well, with fracture liquid saturations approaching 60% and matrix liquid saturation in excess of 80%.

**Conclusions**

A numerical study that considers the formation and long-term behavior under pre-exploitation conditions has been conducted. Results from this study indicate the HTR may form under a variety of conditions, but salt in the reservoir fluid tends to cause the HTR to be two-phase. Including a "facies change" in the reservoir model can in certain cases lead to the development of an HTR with a variable surface depth. This lack of uniform depth and large salt concentrations, in particular, show an interesting agreement between numerical results and field observations.

Several points in this study still need to be resolved. First, the cyclic variations in liquid saturation in the HTR fractures must be better understood. Also, abrupt changes in reservoir properties were assumed for the HTR. Additional studies are planned to examine the effect of gradational changes on HTR formation. Finally, two-dimensional heat flow in the caprock will be considered in an effort to better constrain the possible timing and location of the simulated venting episode.

**Acknowledgments**

The author wishes to thank J.L. Renner and D.D. Faulder for a review of the manuscript, and Jackie Brower for help with manuscript layout. Funding for this work was provided by the U.S. DOE, Assistant Secretary for Energy Efficiency & Renewable Energy, Geothermal Division, under DOE Contract NO DE-AC07-76ID01570. Mention of specific products and/or manufacturers in this document implies neither endorsement of preference nor disapproval by the U.S. Government, any of its agencies, or of EG&G Idaho, Inc. of the use of a specific product for any purpose.

**References**

Drenick, Andy, "Pressure-Temperature-Spinner Survey in a Well at The Geysers," *Proceedings*, 11th Workshop on Geothermal Reservoir Engineering, Stanford University, Stanford, CA., January 21-23, 1986 pp 197-206.

Gunderson, R.P., "Reservoir Matrix Porosity at The Geysers from Core Measurements," *Transactions*, Geothermal Resources Council, Vol. 14(2), August, 1990 pp 1661-1665.

Lai, C.H., G.S. Bodvarsson, and A.H. Truesdell, "Modeling Studies of Heat Transfer and Phase Distribution in Two-Phase Geothermal Reservoirs," Geothermics, in press, 1994.

Moore, J.N., "Thermal and Chemical Evolution of The Geysers Geothermal System, California," *Proceedings*, 17th Workshop on Geothermal Reservoir Engineering, Stanford University, Stanford, CA., January 29-31, 1992 pp 121-126.

Pruess, K., R. Celati, C. Calore, and G. Cappetti, "On Fluid and Heat Transfer in Deep Zones of Vapor-Dominated Geothermal Reservoirs," *Proceedings*, 12th Workshop on Geothermal Reservoir Engineering, Stanford University, Stanford, CA., January 20-22, 1987, pp 89-96.

Shook, G.M., "Numerical Investigations into the Formation of a 'High Temperature Reservoir'," *Proceedings*, 18th Workshop on Geothermal Reservoir Engineering, Stanford University, Stanford, CA., January 26-28, 1993(a), in press.

Shook, G.M., "Generalization of Vapor Pressure Lowering Effects in an Existing Geothermal Simulator," EG&G Report # EP-10781, June 1993(b) 16 pp.

Sternfeld, J.N., "Lithologic Influences on Fracture Permeability and the Distribution of Steam in the Northwest Geysers Steam Field, Sonoma County, California," *Transactions*, Geothermal Resources Council, Vol. 13, October, 1989, pp 473-479.

Truesdell, Alfred H., "The Origin of High-Temperature Zones in Vapor-Dominated Geothermal Systems," *Proceedings*, 16th Workshop on Geothermal Reservoir Engineering, Stanford University, Stanford, CA., January 23-25, 1991 pp 15-20.

Walters, M.A., J.N. Sternfeld, J.R. Haizlip, A.F. Drenick, and Jim Combs, "A Vapor-Dominated Reservoir Exceeding 600° F at The Geysers Sonoma County, California," *Proceedings*, 13th Workshop on Geothermal Reservoir Engineering, Stanford University, Stanford, CA., January 19-23, 1988 pp 73-81.Warren, J.E., and P.J. Root, "The Behavior of Naturally Fractured Reservoirs", *Society of Petroleum Engin. J.*, Sept. 1963, pp 245-255.

Vinsome, P.K.W., "TETRAD User's Manual," Dyad Engineering, Calgary, Alberta, 1991.

Vinsome, P.K.W. and G.M. Shook, "Multipurpose Simulation," *J. Petroleum Science and Engineering*, **9** (1), March, 1993, pp. 29-38.

Williams, C.F., S.P. Galanis Jr., T.H. Moses Jr., and F.V. Grubb, "Heat-Flow Studies in the Northwest Geysers Geothermal Field, California," *Transactions*, Geothermal Resources Council, Vol. 17, October, 1993.

Williamson, K.H., "Reservoir Simulation of The Geysers Geothermal Field," *Proceedings*, 15th Workshop on Geothermal Reservoir Engineering, Stanford University, Stanford, CA., January 23-25, 1990.

**Table 1: Petrophysical Properties and Initial Conditions**

| **Petrophysical Properties** | Matrix | Fractures |
|---|---|---|
| Porosity | 0.04 | 0.01 |
| Permeability (md) | 0.01 | 10. |
| Relative Permeabilities | | |
| $k_{rl} = k^o_{rl}\,(S)^{e_l}$ | $k^o_{rl} = k^o_{rv} = 1$ | $k^o_{rl} = k^o_{rv} = 1$ |
| $k_{rv} = k^o_{rv}\,(1 - S)^{e_v}$ | $e_l = 4.;\ e_v = 2.5$ | $e_l = 2.;\ e_v = 1.5$ |
| $S = \frac{S_l - S_{lr}}{1 - S_{lr} - S_{vr}}$ | $S_{lr} = 0.4;\ S_{vr} = 0.05$ | $S_{lr} = 0.05;\ S_{vr} = 0$ |

Rock Heat Capacity = 1. kJ/kg
Rock Density = 2650 kg/m$^3$
Rock Thermal Conductivity = 2.1 W/m°C
Matrix Block Size = 100. m
Heat Flux = 0.5 W/m$^2$

**Initial Conditions**
Pressure = Hydrostatic Gradient, $P_{avg}$ = 7960 kPa
Temperature = 240° C
Salt Concentration = 3. wt. %

**Grid Data**
Nx = 4 Ny = 1 Nz = 24
Dx = 100 m Dy = 100 m Dz = 50 m

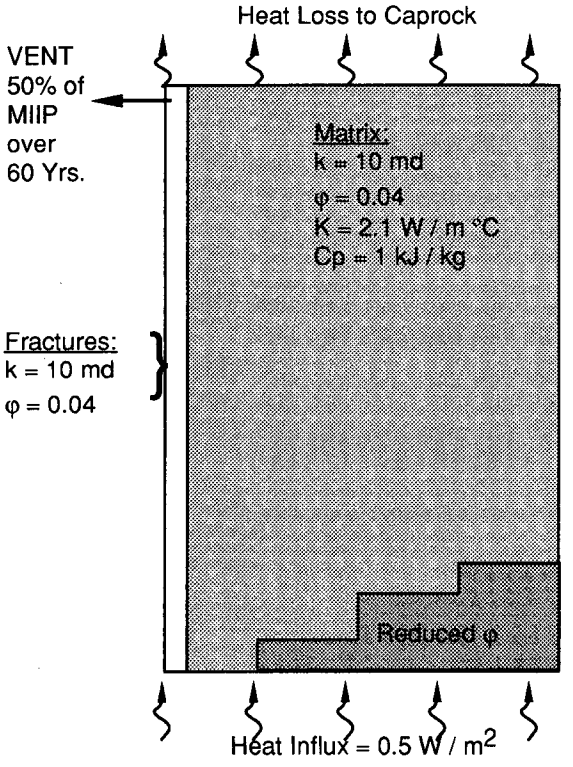


**Figure 1. A schematic of the reservoir model.**

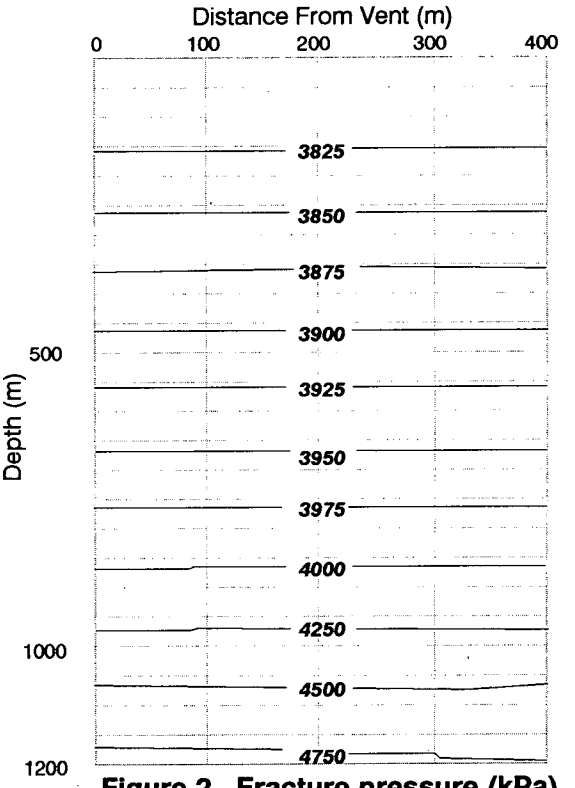


**Figure 2. Fracture pressure (kPa) profile at t=20,000 years**

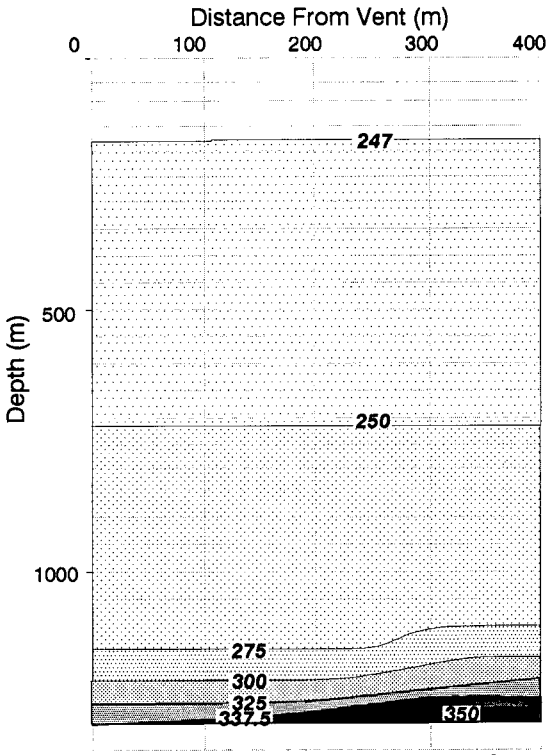


**Figure 3. Fracture temperature ( °C) profile at t=20,000 years**

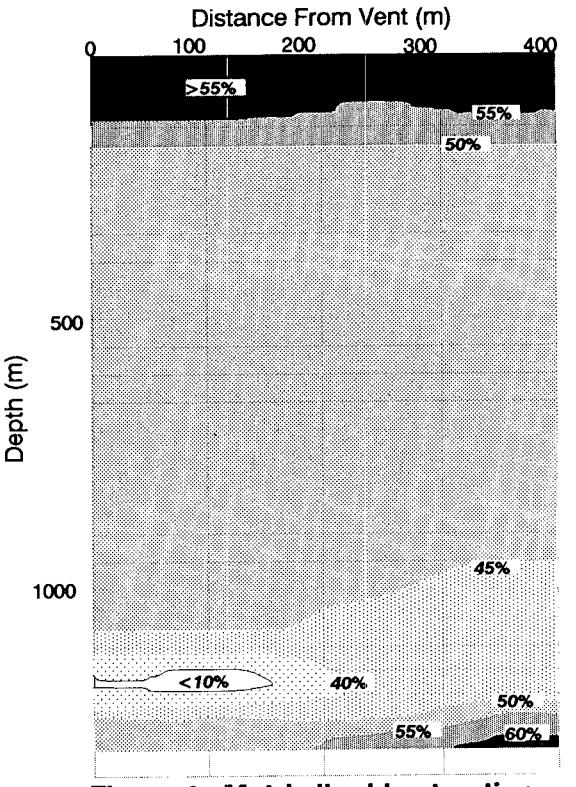


**Figure 4. Matrix liquid saturation profile at t=20,000 years**

PROCEEDINGS, Nineteenth Workshop on Geothermal Reservoir Engineering
Stanford University, Stanford, California, January 18-20, 1994
SGP-TR-147

# THE EFFECTS OF $CO_2$ ON STEAM ADSORPTION

**Steve Palar and Roland N. Horne**

Stanford University
Stanford, CA 94305

## ABSTRACT

Water adsorption in geothermal reservoir materials was investigated by transient flow technique using steam and $CO_2$ gas. Theoretical and experimental results indicate that water adsorption exists in vapor-dominated type of reservoir, but experiments in the past have been limited to pure gases.

The common presence of $CO_2$, a non-condensible gas, in a geothermal reservoir necessitated a study of the effect of partial $CO_2$ concentration on adsorption. Experimental laboratory work using a crushed Geysers rock sample at low pressure was carried out. Transient pressure exerted by steam pressure inside the sample was measured against time during a desorption process. It was found that the partial presence of $CO_2$ did not significantly affect the adsorption of water.

## INTRODUCTION

It is believed that vapor-dominated geothermal reservoirs (e.g. The Geysers) have liquid water in their pore space. The existence of the liquid water has been detected by using the following approaches :
- gravity & seismic method (Denlinger, 1979)
- material balance method (Ramey, 1990)

More steam production has been observed from The Geysers than be accounted for by means of superheated vapor thermodynamics. Due to the density difference between water and steam, large quantities of steam can be stored in a form of adsorption. The theory of adsorption provides a good explanation for the existence of the liquid water in this type of reservoir.

The presence of non-condensible gases is common in geothermal fields. The mole percentage of the non-condensible gases varies among reservoirs. It was reported that up to 80 % concentration of these gases was measured in Italy's Bagnore geothermal field. Total non-condensible gas in the Geysers varies from 4,000 to 80,000 ppm by weight (Haizlip and Truesdell, 1992).

$CO_2$ is by far the most common non-condensible gas found in a geothermal field. In The Geysers, Truesdell et al. (1992) reported that the measured concentration of this gas in ppm by weight ranged as follows :

| | |
|---|---|
| Northwest Geysers | 7,450 - 55,500 |
| Central & Southwest G. | 2,080 - 11,500 |
| Southeast Geysers | 94.70 - 734 |

In comparison, the geothermal fluids from New Zealand's Broadland field had 10 % of $CO_2$.

## ADSORPTION OF WATER

The term adsorption used here refers to surface adsorption. There are two types of surface adsorption, physical and chemical. The main differences are that physical surface adsorption, also called physisorption, occurs at low temperature and has a lower heat of adsorption.

The presence of liquid water in a porous dry steam reservoir can be caused by capillarity and/or adsorption depending on the pore size. In his study on adsorption in porous media, Hsieh (1980) discounted the effect of capillarity, but not adsorption in micropores, which are pores with radii less than 20 Å.

Surface adsorption plays a major role in the retention of liquid water in micropores at pressures below the saturation pressure. Since the density of hot liquid is approximately ten times greater than that of steam vapor, up to ten times the mass of the steam can be stored as adsorbed water at elevated temperatures.

The adsorbed liquid water in a porous media creates a pressure lowering of the saturated vapor pressure at a particular temperature. This explains the presence of the two-phase water and steam, under conditions that would normally be superheated.

This adsorbed liquid water has different properties than non-adsorbed water. Economides, et. al. (1982) wrote that properties, such as density, compressibility and viscosity might be different for the two waters. Moreover, the molecules of adsorbed water are very compact.

Using kinetic theory, Langmuir (1916) investigated surface adsorption. His modified isotherm equation is :

$$X = \frac{\frac{P}{P_{sat}}}{A + B\frac{P}{P_{sat}}}$$

where :
X denotes the weight ratio of the adsorbate (steam) to the adsorbent (rock).
P / $P_{sat}$ represents the ratio of pressure to the saturation pressure of steam at a particular temperature. Terms A and B are constants and both determine the shape of the isotherm.

The limiting condition of this equation is that only one adsorption layer forms at each adsorption site. Intuitively this might not be true, however it has been found (Nghiem and Ramey, 1991) that this equation successfully matches the experimental data.

# EFFECTS OF $CO_2$ ON ADSORPTION

$CO_2$ is characterized by its high saturation pressure. The presence of $CO_2$ in the binary mixture of $CO_2$ and water will elevate the saturation vapor pressure (dew point) of pure water at a temperature. The single saturation pressure line of pure water is replaced by bubble point and dew point curves for the mixture.

The amount of elevated pressure above the normal saturation vapor pressure for the pure water can be calculated if the composition of $CO_2$ and the temperature are known. The equilibrium constant K, which is the ratio of vapor phase to liquid phase, for the $CO_2$ and $H_2O$ can be calculated accordingly (Sutton, 1976).

Solubility of $CO_2$ in the adsorbed water and non-adsorbed water is not the same (Economides, et al. 1982). The equilibrium constant K, for the adsorbed water is much larger than the non-adsorbed water. As a result, the solubility of $CO_2$ in the adsorbed water is much less. Economides et al. calculated the solubility of $CO_2$ in the non-adsorbed water and found that the mole fraction of $CO_2$ would range from 0.0005 to 0.001 in a typical geothermal reservoir. Thus the presence of $CO_2$, if any, is mainly in the pore space away from the adsorbed water.

# EXPERIMENTAL WORK

## Apparatus and Procedure

The equipment for this transient pressure experiment is on loan to Stanford Geothermal Program from USGS. The schematic diagram of the equipment is shown in Figure 5. It basically consists of 3 main systems :

- The Air Bath System
- The Vacuum System
- The Data Recording System

Pneumatic valves inside the enclosed air bath are controlled from the outside of the air bath. Also located outside the air bath are a vacuum pump and a data logger.

A sample was prepared beforehand by crushing and sieving it to a predetermined mesh size. The uniform and homogeneous sample was then placed in a 2-ft sample holder, located inside the air bath. Entrapped air inside the sample was subsequently evacuated by means of a vacuum pump for at least 24 hours.

The air-free sample then was ready to receive steam. The steam was generated inside the air bath. After an equilibrium was reached, the transient pressure experiment could be performed.

Two pressure transducers are located on ends of the sample holder. The experiment started when the bottom end of the sample holder was exposed to atmospheric pressure. The pressure change on top of the sample was recorded by the top transducer, connected to the data recording system. This transient pressure change over time is depicted in Figures 2 and 4.

The temperature in this experiment was maintained at about $125^0$ C ($257^0$ F), which corresponds to a saturation steam pressure of 33.7 psia (steam table). This was the initial pressure of the steam inside the sample prior to the run.

The sample used was from Calpine Corporation's South Geysers well MLM-3, cored from a measured depth of 1325 m (1320 m TVD). The composition of this sample is mainly $SiO_2$ (67 %) and $Al_2O_3$ (12 %) by means of x-ray fluorescent test.

Two samples with mesh sizes of 20-45 and 45-150, and with measured permeability of 37.5 darcy and 0.207 darcy respectively, were subsequently used. The finer sample was extensively used due to its longer desorption time.

## Experimental Result

The experiment is actually a desorption process, so the isotherms inferred are for desorption rather than adsorption.

Herkelrath, et al. (1983), experimenting with the transient flow of steam in porous media, observed a delay in the steam pressure breakthrough. The delay was attributed to adsorption. Their work ushered in a series of adsorption investigations by Luetkehans (1988), Harr (1991) and Qi (1993).

In order to compare the effects of sample size, the steam-only runs from the two different sample sizes are shown in Figure 1. Starting from the same initial pressure, the coarser-size sample did breakthrough earlier than the finer-size sample.

Interestingly both slopes of the semi-log graph are approximately 1 bar/cycle. The starting times for the decrease in pressure are 0.45 and 75 seconds respectively for the coarser and finer samples. It took 10 times longer than those times to reach its corresponding atmospheric pressure (Fig. 1).

Using a computer program developed by Qi (1993), it is possible to infer the shape and the parameters of the adsorption isotherm from the transient pressure data. The program utilized the 1-D finite-difference simulator developed by Nghiem and Ramey (1991) and modelled the isotherm profile based on the Langmuir equation. The inferred isotherms from the two experiments using the 20-45 Mesh size sample is shown in Figure 3. The isotherm of the 45-150 Mesh size sample is yet to be measured, pending the calculation of its porosity.

The shapes of the isotherms from the two experiments are both concave upward, however the values of the isotherm parameters A and B are very different. This is not surprising since the pressure versus time curves of the two runs are not identical, but show a time shift. This time shift might be caused, among other things, by a discrepancy in the quantity of steam inside the sample prior to the desorption run.

Observations of the 100-% $CO_2$ runs for both samples show that when the initial $CO_2$ pressures are below the saturation steam pressure for that temperature, the shape of the corresponding curves do not display a steep decline and the pressure transmission is not delayed. Adsorption does not occur with $CO_2$. The steep pressure drop is only characterized by runs starting from the saturation steam pressure at that temperature.

Furthermore, it is observed that the transient pressure curves of steam-only and of mixture of steam and $CO_2$ do not show a noticeable difference. The partial presence of $CO_2$, up to a 36 % concentration, apparently did not affect the steam's pressure curve. This indicates that steam adsorption is unaffected by the presence of up to 36 % $CO_2$. Higher $CO_2$ concentration has not been tried yet.

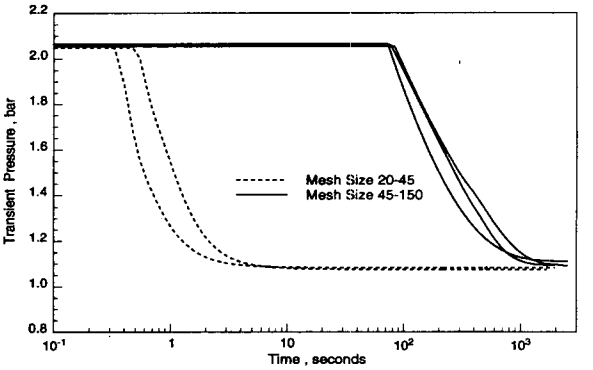


Figure 1: **Comparison of Mesh Size**

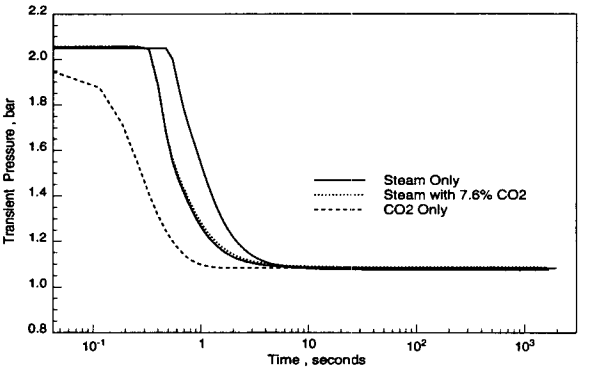


Figure 2: **Experiment with 20 - 45 Mesh Size**

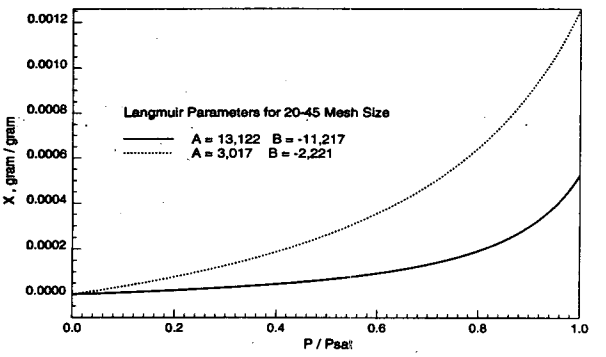


Figure 3: **Inferred Langmuir Isotherm**

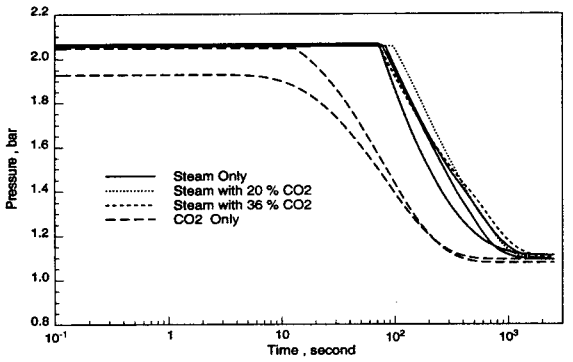


Figure 4: **Experiment with 45 - 120 Mesh Size**

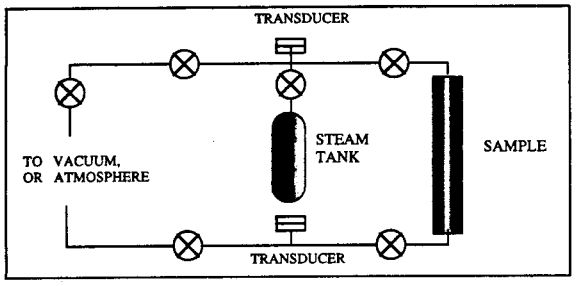


Figure 5: **Schematic Diagram of Apparatus**

# CONCLUSION

Based on this laboratory work, it is apparent that the partial presence of $CO_2$ does not affect the adsorption of steam in the samples used.

This work by no means conclusively answers all the questions related to the effect of $CO_2$ on adsorption, however it presents a preliminary understanding of the effects.

# ACKNOWLEDGMENTS

We thank the U.S. Department of Energy, Geothermal Division, for the support of this work, under Contract No. DE FG07 90 1D12934.

We also thank USGS, Calpine Corporation and UURI (University of Utah Research Institute) for making this work possible.

# REFERENCES

1. Denlinger, R.P.: "Geophysical Constraints on The Geysers Geothermal Field, Northern California", Ph.D. Thesis, Stanford University, (1979).

2. Ramey, H.J., Jr.: "Adsorption in Vapor-Dominated Systems", Proc. Eighth Geothermal Program Review, San Francisco, 63-67, (1990).

3. Haizlip, J.R., and Truesdell, A.H.: "Noncondensible Gas and Chloride Are Correlated in Steam at The Geysers", Monograph on The Geysers Geothermal Field, Geothermal Resources Council's Special Report No. 17, 139-143 (1992).

4. Truesdell, A.H., Box, W.T., Jr., Haizlip, J.R., and D'Amore, F.: "A Geochemichal Overview of The Geysers Geothermal Reservoir", Monograph on The Geysers Geothermal Field, Geothermal Resources Council's Special Report No. 17, 121-132 (1992).

5. Hsieh, C.H.: "Vapor Pressure Lowering in Porous Media ", Ph.D. Thesis, Stanford University, (1980).

6. Economides, M., Ostermann, R., and Miller, F.G.: " Implications of Adsorption and Formation Fluid Composition on Geothermal Reservoir Evaluation", Proc. International Conference on Geothermal Energy, Florence, Italy, Vol. 1, 149-162 (1982).

7. Nghiem, C.P. and Ramey, H.J., Jr.: "One-Dimensional Steam Flow in Porous Media", *Stanford Geothermal Program Report*, No. SGP-TR-132, (1991).

8. Langmuir, I.: "The Constitution and Fundamental Properties of Solids and Liquids, Part I. Solids", *J. Amer. Chem. Soc.*, Vol. 38, 2221-2295, (1916).

9. Sutton, F.M.: "Pressure-Temperature Curves for a Two-Phase Mixture of Carbon Dioxide and Water", *New Zealand J. of Sc.*, Vol. 19, 297-301, (1976).

10. Herkelrath, W.N., Moench, A.F., and O'Neal II, C.F.: " Laboratory Investigation of Steam Flow in a Porous Medium", *Water Resources Research*, Vol. 19, No. 4, 931-937 (1983).

11. Luetkehans, J.: "A Laboratory Investigation of Steam Adsorption in Geothermal Reservoir Rocks", Master's Thesis, Stanford University, March, (1988).

12. Harr, M.S.: "Laboratory Measurement of Sorption in Porous Media", Master's Thesis, Stanford University, August, (1991).

13. Qi, M.: "Estimation of Adsorption Parameters from Experimental Data", Master's Thesis, Stanford University, May, (1993).

PROCEEDINGS, Nineteenth Workshop on Geothermal Reservoir Engineering
Stanford University, Stanford, California, January 18-20, 1994
SGP-TR-147

# MEASUREMENT OF SURFACE AREA AND WATER ADSORPTION CAPACITY OF THE GEYSERS ROCKS

Shubo Shang, Roland N. Horne and Henry J. Ramey Jr.

Petroleum Engineering Department
Stanford University, CA 94305--2220

## ABSTRACT

The measurement of the quantity of adsorbed water on geothermal reservoir rocks allows a more realistic estimation of reserves for vapor-dominated geothermal reservoirs. This study measured adsorption/desorption isotherms of water vapor on rock samples from Calpine Co.'s well MLM-3, both core fragments and well cuttings from Coldwater Creek steamfield and a number of well cuttings from well Prati State 12, Northwest Geysers steam field. Surface areas of these rock samples were measured using nitrogen adsorption at 77K. The results of these measurements suggest that surface area is a crucial factor in determining the amount of water adsorption. Analysis of the water adsorption data indicates that adsorption is the dominant phenomena in the matrix of the reservoir rock at relative pressures below 0.8. Depending on the structure of the rock, capillary condensation contributes considerably to the total water retention at relative pressure between 0.8 and 1.0. However, there is no clear distinction between adsorption and capillary condensation and it is difficult in the experiments to determine when complete saturation occurs.

A significant result of these experiments was the demonstration that well cuttings show adsorption characteristics very much like those obtained from core fragments. This should allow further adsorption measurements to be made more extensively and at lower cost.

## INTRODUCTION

Adsorption of water onto vapor-dominated geothermal reservoir rocks, and the adsorbed water as a possible storage mechanism for these reservoirs have been a topic of much discussion for the last few years (Ramey, 1990). However, water adsorption data on reservoir rocks, particularly at high temperature, are still scarce. Furthermore, there has been no systematic study to evaluate the possible variation of the adsorbed quantity with rocks from different parts of a reservoir. Available experimental data in our laboratory show that the amount of water adsorbed varies depending on the types of rock studied (Shang et al., 1993, 1994). This indicates that the adsorbed quantity on rocks from different depths of a well may change since the structure as well as the lithology of the rock vary with location. Such information is important in terms of both understanding the reservoir production behavior and aiding the design of reinjection processes.

This paper presents results of our continuing effort on water adsorption research. Included in the paper are water adsorption isotherm measurements on rock samples from Calpine Corporation well MLM-3, South Geysers field, both core fragments and well cuttings from Coldwater Creek steamfield and a number of well cuttings from well Prati State 12, Northwest Geysers field. Surface areas of these samples were also measured.

## MULTILAYER ADSORPTION ISOTHERMS

The general characteristics of physical adsorption and the commonly used adsorption isotherms were reviewed previously (Shang, et al., 1994). The following is a brief summary of the Brunauer, Emmett and Teller (BET) isotherm, and the Frankel-Halsey-Hill (FHH) isotherm. These two isotherm equations are used to analyze the measured adsorption data in this study.

### BET Isotherm

The BET isotherm was developed to account for multilayer adsorption (Brunauer, et al., 1938), and it has the following form,

$$\frac{q}{q_m} = \frac{b\left(p/p^o\right)}{\left(1-p/p^o\right)\left(1-p/p^o+b\,p/p^o\right)} \qquad (1)$$

where $q$ is the amount adsorbed, $q_m$ is the amount adsorbed at monolayer coverage, $p$ is pressure, $p^o$ represents the saturation vapor pressure of the adsorbate at the relevant temperature, and $b$ is a constant. This isotherm has been widely used to determine the surface area of an adsorbent from experimental data in the relative pressure range of $0.05<p/p^o<0.3$. However, the best fitting BET equation normally predicts too little adsorption at low pressures and too much adsorption at high pressures (Adamson, 1990). The BET isotherm was only used to extract surface area from nitrogen adsorption data.

### FHH isotherm

The FHH (Halsey, 1952) equation was developed based on an assumed variation of adsorption potential with distance from the surface, and generally fits multilayer

adsorption data over a wide relative pressure range (Adamson, 1990). The isotherm equation is written as follows,

$$\left(\frac{q}{q_m}\right)^n = \frac{A}{\ln\left(p^o/p\right)} \quad \text{with} \quad A = \frac{\varepsilon_o}{x_m^n RT} \tag{2}$$

where $x_m$ is the film thickness at the monolayer point, $A$ and $n$ are empirical parameters, and $\varepsilon_o$ is the potential of the solid surface for adsorption. The above equation can be further simplified into a two parameters correlation for the purpose of fitting adsorption isotherm as follows,

$$q^n = \frac{B}{\ln\left(p^o/p\right)} \tag{3}$$

where $B$ is a lumped parameter containing information about the capacity of the surface for adsorption. The FHH isotherm is attractive for its simple mathematical form, and was used to fit water adsorption isotherms in this study.

**Adsorption and Saturation**

In dealing with reservoir engineering problems, saturation is a parameter of great concern. The amount of water adsorbed at any given temperature and pressure can be converted to saturation according to the following equation,

$$S_w = \frac{1-\phi}{\phi}\frac{\rho_r}{\rho_w} q \tag{4}$$

where $\phi$ is the porosity of the rock, $\rho_r$ and $\rho_w$ are the densities of the rock and the adsorbed water, respectively.

## APPARATUS

The apparatus used for water adsorption test is an automated sorptometer from Porous Material Inc. (PMI). It is a BET type sorptometer, and the measurement is based on changes in gas pressure before and after exposing to the sample. A detailed description of the PMI sorptometer has been given previously (Harr, 1991, Shang et al., 1993).

The surface area of the rock samples were measured using nitrogen adsorption at 77K. In principle, the PMI sorptometer should serve the purpose of surface area measurement as well. However, the design of the sorptometer has a limited capacity for sample size and the liquid nitrogen level cannot be maintained accurately during the test. This is crucial since the reservoir rocks we deal with have low surface area. The measurements were carried out using a surface area analyzer, Gemini 2370 on loan from Micromeritics. The Gemini 2370 uses a flow-gas technique in which nitrogen flows into both the sample and the balance tubes at the same time. The only difference between the two tubes is the presence of the sample in one of them. The delivery rate of nitrogen into the sample tube is controlled by the rate at which the sample can adsorb nitrogen onto the surface. The rate of flow into the balance tube is controlled to give the same pressure. The quantity adsorbed at a given pressure is measured by pressure difference in the two vessels connected to the two tubes. The BET equation was then used to fit the adsorption data to give surface area.

## RESULTS AND DISCUSSION

**Tests on MLM-3 Rock**

Figure 1 shows an example of the adsorption/desorption isotherms on Calpine Co's well MLM-3 rock obtained at 120°C. For engineering convenience, the amount of water adsorbed was converted into saturations using Eqn. 4. A rock density of 2.7 g/cm$^3$ and bulk water density of 0.943 g/cm$^3$ was used. The major uncertainty is porosity which is difficult to measure for low porosity rocks. A porosity of 2% was used in the calculation. Significant hysteresis exists and persists to very low pressure. The possible causes for the observed hysteresis are structural

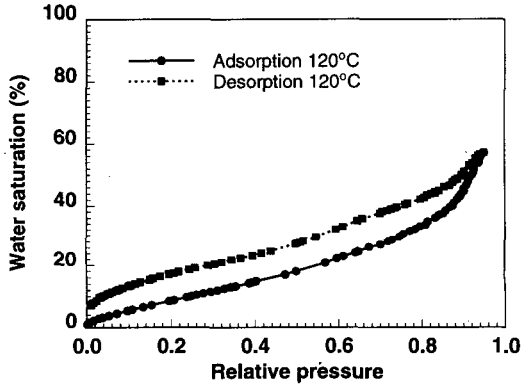


Figure 1 Isotherms for sample MLM-3

heterogeneity of the rock, capillary condensation and chemical interaction of water molecules with rock surface as explained previously (Shang et al., 1994).

The simplified FHH equation, Eqn. (4), was used to fit the adsorption isotherm shown above. Figure 2 shows the measured and fitted isotherms for Calpine Co's well MLM-3 rock. With fitted parameter values of 0.76 for B and 1.4 for n, the FHH equation fits the adsorption isotherm reasonably well.

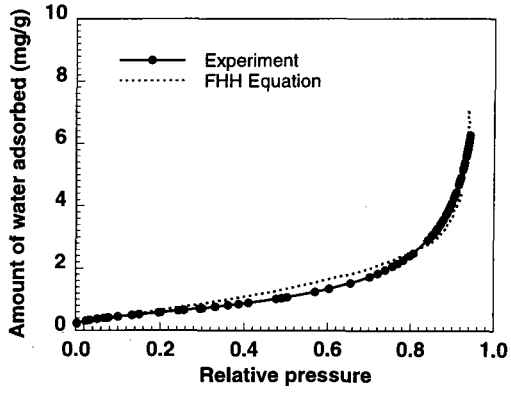


Figure 2 Comparison of measured and fitted isotherm on MLM-3 sample

The effect of temperature on water adsorption has been shown to be sample dependent (Hsieh & Ramey, 1983, Herkelrath et al., 1983). Water adsorption tests were carried out on well MLM-3 rock at temperatures from 90 to 130°C and Figure 3 shows the results of these tests. At low relative pressure, changes in the amount of water adsorbed with temperature is small. As relative pressure increases, the effect of temperature on water adsorption becomes more appreciable. Chemical interaction of water molecules with rock surface and its subsequent enhancement on water retention is one of the possible reasons for the observed temperature effect. The effect of temperature on water retention requires further study.

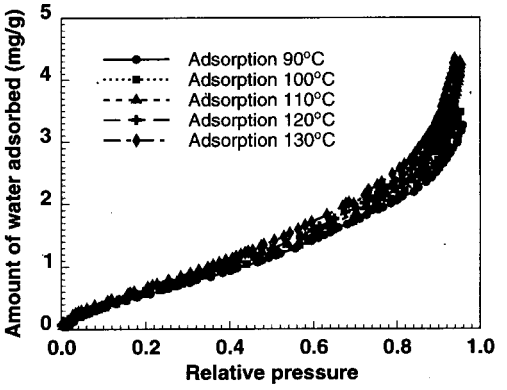


Figure 3 Adsorption isotherms on MLM-3 sample at different temperatures

## Comparison on Core and Well Cuttings

Reservoir rock samples in the form of core or core fragments are not readily available in specified locations. However, well cuttings are. In order to decide whether water adsorption on well cuttings represents that on the core, tests were performed on both core fragments and well cuttings of the same well location from the Coldwater Creek steamfield. Initial tests showed substantially more adsorption on the well cuttings than that on the core fragments. It was found that the presence of some foreign material (tentatively identified as clays from the drilling process) was the source of contribution to the higher adsorption on the well cuttings. Due to its distinguishing color, these foreign particles were easily removed. Figure 4 shows a comparison of the two adsorption isotherms obtained at 120°C. Considering experimental error, the agreement between the two data sets is acceptable. Thus, we concluded that it will be acceptable to use well cuttings from different parts of the Geysers for systematic water adsorption tests.

## Measurement of Surface Area

It has been shown that the amount of adsorption depends on the type of geologic media and that the surface area of the media is a crucial factor in determining the quantity adsorbed (Shang et al., 1994). It is, therefore, important to

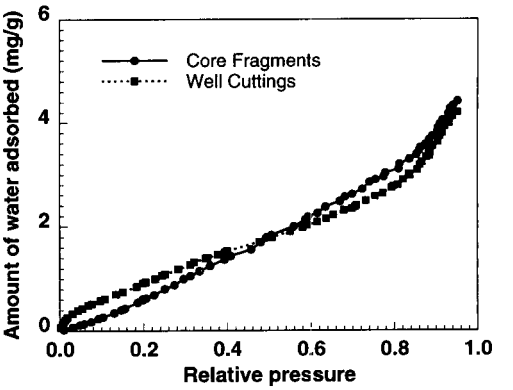


Figure 4 Comparison if adsorption isotherms on core and well cuttings

measure the surface area of the rock samples used for water adsorption tests. Such measurements were carried out using the Gemini 2370 surface area analyzer described previously. The results for 10 well cuttings samples from well Prati State 12, Northwest Geysers, and other samples discussed earlier are summarized in Table 1. Examination of Table 1 shows that for a depth span of 4600 feet, the measured surface area varies from 0.7 to 3.2 $m^2/g$ and the variation appears to be random. This clearly reveals the heterogeneous nature of reservoir rocks.

## Adsorption Capacity and Surface Area

Figure 5 shows a comparison of water adsorption isotherms obtained on seven Prati State 12 well cuttings at 120°C. The depth and the measured surface area of these samples are shown in Table 1. For all the samples studied, adsorption dominates the process of water retention for relative pressures up to about 0.8. As pressure is further increased, capillary condensation becomes more important. At a given pressure, the amount of water adsorbed varied considerably among the seven samples. The variation appears to be random with respect to depth. However, it does depend on the surface area of the samples. Knowing the surface area of the samples, we can express the amount adsorbed as weight per unit surface. Figure 6 shows the comparison of the isotherms on the basis of unit surface. If physical adsorption is the only process occurring, the isotherms should fall onto the same curve. This is not the case, however, particularly at high relative pressures when capillary condensation contributes substantially to the total water retention. This supports our previous conclusion that the surface area of a rock sample is a primary factor in determining its water adsorption capacity and capillary condensation is a dominant process in water retention at high relative pressures.

## CONCLUSIONS

Water adsorption/desorption hysteresis exists on the rock samples investigated. While rock heterogeneity and

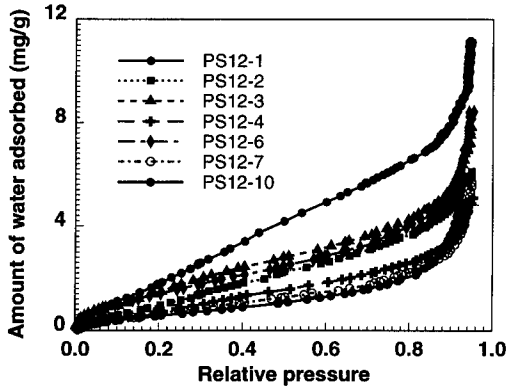


Figure 5 Comparison of adsorption isotherms on PS12 well cuttings

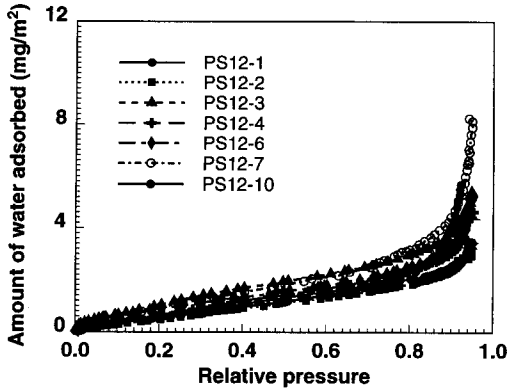


Figure 6 Comparison of adsorption isotherms based on surface area

**Table 1 Summary of the measured surface area**

| Sample ID | Measured Depth (feet) | Surface Area ($m^2/g$) |
|---|---|---|
| PS12-1 | 4800-4900 | 3.2 |
| PS12-2 | 5300-5400 | 2.0 |
| PS12-3 | 5800-5900 | 1.4 |
| PS12-4 | 6300-6400 | 1.1 |
| PS12-5 | 6800-6900 | 1.3 |
| PS12-6 | 7300-7400 | 1.6 |
| PS12-7 | 7800-7900 | 0.7 |
| PS12-8 | 8300-8400 | 1.0 |
| PS12-9 | 8800-8900 | 1.1 |
| PS12-10 | 9300-9400 | 0.9 |
| Cold Water Creek Core | 6260 | 1.4 |
| Cold Water Creek Cuttings | 6260 | 1.7 |
| Calpine Co.'s Well MLM-3 | 4330 | 1.1 |

capillary condensation are the commonly recognized source of hysteresis, chemical interaction also contributes to the hysteresis particularly at low pressures. The amount of water adsorption at a given relative pressure increases with increasing temperature.

Well cuttings can be used as substitutes for core samples for water adsorption studies. The amount of water adsorption depends on the type of geologic media and surface area is a crucial factor in determining the quantity adsorbed. Adsorption isotherms on different samples compare well for relative pressures below 0.8 when the comparison is based on unit surface area. The deviation at high relative pressures is due to the presence of capillary condensation. It is, thus, logical to suggest that surface area and porosity comprise the essential parameters in determining the capacity of a reservoir rock for water retention.

## ACKNOWLEDGMENTS

The authors acknowledge the financial support from US Department of Energy, Geothermal Division, Contract Number DE-FG07-90ID12934. We thank Mr. Paul Pettit for help with the equipment.

## REFERENCES

Adamson, A.W., Physical Chemistry of Surfaces, Wiley, 1990.

Halsey, G.D., Jr., "On Multilayer Adsorption", J. Am. Chem. Soc., **74**, 1082 (1952).

Herkelrath, W.N., Moench, A.F. and O'Neal II, C.F., "Laboratory Investigation of Steam Flow in a Porous Medium", Water Resources Research, **19(4)**, 931--937 (1983).

Hsieh, Chih-Hang, "Vapor Pressure Lowering in Porous Media", PhD Thesis, Stanford University, 1980.

Hsieh, Chih-Hang and Ramey, H.J., Jr., "Vapor-Pressure Lowering in Geothermal Systems", SPEJ, 23(1), 157--167 (1983).

Harr, M.S., "Laboratory Measurement of Sorption in Porous Media", MS Report, Stanford University, 1991.

Ramey, H.J., Jr., "Adsorption in Vapor-Dominated Systems", Geothermal Program Review VIII, April 18-20, 1990, San Francisco, CA.

Shang, S.B., Horne, R.N. and Ramey, H.J., Jr. "Experimental Study of Water Adsorption on Geysers Reservoir Rocks", 18th Annual Worshop Geothermal Reservoir Engineering, January 1993.

Shang, S.B., Horne, R.N. and Ramey, H.J., Jr., "Study of Water Adsorption on Geothermal Reservoir Rocks", submitted to Geothermics, 1994

PROCEEDINGS, Nineteenth Workshop on Geothermal Reservoir Engineering
Stanford University, Stanford, California, January 18-20, 1994
SGP-TR-147

# THE EFFECTS OF ADSORPTION ON INJECTION INTO GEOTHERMAL RESERVOIRS

John W. Hornbrook and Roland N. Horne

Stanford University

## ABSTRACT

The effects of an adsorbing phase on the injection of liquid and eventual production of vapor from a low-porosity, vapor dominated geothermal reservoir was studied. The magnitude of delay caused by adsorption, diffusion partitioning, preferential partitioning, and permeability variation were compared. Results were then compared to measured tracer production data at the Geysers to determine the most likely delay mechanism for injected tracer at the Geysers.

A one-dimensional numerical model describing vapor flow in a porous medium in the presence of a sorbing phase was used to investigate the delay of injected tracer caused solely by the sorbing phase. An analytical model was used to describe delay effects due to diffusion partitioning of tracer from the vapor phase into the liquid phase. Properties of steam and tracer used in Geysers tracer studies were compared to determine the effects of preferential partitioning. Finally, a streamline model of a tracer study was used to determine the magnitude of permeability delays possible using permeability values measured at the Geysers.

It was concluded that adsorption alone has very little effect on the delay of injected tracer indicating that little recharge of the adsorbed mass occurs for a typical injection program at the Geysers. Diffusion partitioning was shown to have a larger effect on tracer delay than adsorption while preferential partition was shown to have no effect. Permeability variation was shown to have the largest effect on tracer delay. Tracer delay was shown to be approximated closely by known permeability variations even when adsorption and diffusion effects are ignored.

## INTRODUCTION

Adsorbed liquid has long been known to significantly contribute to the mass stored in geothermal reservoirs. Measurements of adsorption isotherms in a range of porous solids and with a variety of fluids (Hsieh and Ramey, 1981) showed that adsorption can be significant in many geothermal and natural gas reservoirs. Application of measured adsorption data to volumetric analysis of the Geysers led to the conclusion that most of the initial mass in the reservoir was probably stored as an adsorbed liquid (Economides and Miller, 1985). Recent measurements of adsorption in Geysers core material indicate that at high pressures, the low porosity portions of the Geysers reservoir may be almost completely saturated by an adsorbed phase (Shang, et. al., 1993). These same measurements have also provided increasingly accurate descriptions of adsorption isotherms in the Geysers allowing increasingly accurate estimates of the effects of an adsorbed phase on reservoir performance for a wide range of pressures.

Due to pressure decline in the Geysers, injection programs have been undertaken in a number of areas in the reservoir. The purpose of these injection programs is to increase reservoir pressure, replace produced liquid mass, and ultimately increase production rate and the productive life of the reservoir. In order to assess the effectiveness of injection programs it is necessary to closely monitor the propagation of injected liquid in the reservoir. Monitoring of injected fluid may be accomplished either by monitoring production and pressure response in the reservoir or by introducing tracer along with the injected liquid and studying the production of the tracer. Production of the tracer provides information on the propagation of injected liquid in the reservoir.

In the Geysers, several tracer tests have been carried out and tracer production has been used to infer characteristics of the fluid propagation through the reservoir. In general, production of tracer at the Geysers has been characterized by long production times indicating some delay mechanism which significantly spreads the tracer concentration in the reservoir. It is the purpose of this paper to investigate the possible tracer delay mechanisms at the Geysers and to determine the size of delay of each. Specifically, the effects of adsorption on tracer delay are investigated to determine the influence of adsorption on injection programs at the Geysers.

## INJECTION AT THE GEYSERS

Injection of cooling tower condensate began at the Geysers in 1969 with an injection to production ratio of 5 %. At initiation of the injection program, all injectate was cooling tower condensate. In 1980, fresh water injection, extracted from Big Sulfur Creek, was initiated into the Units 1-6 area. A second fresh water facility began providing water for injection in 1983. Fresh water injection hit a peak of 7 % of production in 1983 while total injection has stayed fairly constant at 20 - 25 % since the early 70's.

In general, two strategies have been used at the Geysers -- deep injection and shallow injection. In deep injection, outlying wells with deep steam entries are used as injectors in order to minimize downward channeling of liquid water to nearby wells. Effects of deep injection are often difficult to quantify and while short term benefits have been observed, it has been assumed that most of the benefits are long term (UNOCAL, 1992). The shallow injection strategy uses injection wells with steam entries higher than surrounding wells and relies on the vaporization of injected water as it channels toward surrounding production wells. Since breakthrough of shallow injectate is usually fairly rapid, benefits of shallow injection are generally short term. A number of injection programs have been undertaken at the Geysers. Some successful programs are outlined below.

Unit 14 injection, begun in 1983, and Unit 17 injection, begun in 1988 were both deep injection projects. The programs met with limited success, but both projects had some short term benefits.

Units 9-10 injection, initiated in 1992, was a shallow injection project, UNOCAL's first, and was expected to provide short-term benefits. Increased production was almost immediate, but problems with watering out of producers limited the program's success.

In September 20, 1989, the LPA injection program was initiated with injection into C-11 (Enedy, et. al., 1992). The LPA injection program was very successful and resulted in both recharge of liquid mass and increases in production. It demonstrated that injection can be used as a means to increase production from the Geysers reservoir and increase the efficiency of heat extraction from the reservoir.

Planning of future successful injection programs must rely on an understanding of the mechanisms which affect the flow of injected fluids. In this paper, the mechanisms which can delay the production of injected tracer are studied. By understanding the magnitude of tracer delay caused by several reservoir mechanisms, conclusions can be drawn about which characteristics of the reservoir must be studied to increase the efficiency of injection programs.

## TRACER DELAY MECHANISMS

Mechanisms which may delay the propagation of tracer initially in the vapor phase are adsorption, diffusion partitioning, preferential partitioning, and permeability and flow length variations within the reservoir. Adsorption delays injected tracer when reservoir pressure is increased by injection and some of the injected mass is adsorbed and becomes immobile. Since tracer which resides in the vapor phase is also immobilized by adsorption, the rate of propagation of the tracer can be reduced. Another way in which the adsorption process reduces the propagation of tracer is by decreasing the rate of pressure decline in the reservoir. Since pressure drawdown is reduced by desorption of adsorbed liquid, pressure gradients in the reservoir are decreased and the flow velocity of vapor is also decreased.

Diffusion partitioning refers to the diffusion of tracer from the flowing vapor phase into the immobile adsorbed phase due to a concentration gradient. Diffusion partitioning occurs even in the absence of net mass transfer between the vapor and adsorbed phases. If diffusion is large with respect to convection of the vapor phase, concentration equilibrium between the two phases may be assumed instantaneous and the delay in tracer propagation due to diffusion can be calculated.

Due to the heterogeneous nature of Geysers reservoir material, permeability variations and differences in the flow path lengths between an injector and producer can also cause delays in the propagation of injected tracer. Estimates of flow path lengths for a given well pair and use of measured permeabilities in the Geysers can be used to calculate the probable spread in the production concentration of tracer due to these effects.

## NUMERICAL MODEL

A numerical model was constructed to study the effects of adsorption on the propagation of injected tracer. A one-dimensional, linear flow model with constant cross section and rock properties was used to model adsorption effects. An implicit pressure, explicit saturation and temperature solution scheme was used. It was assumed that the adsorbed phase is immobile and that the only flowing phase is vapor. The numerical model was validated against known analytical solutions describing the flow of constant compressibility liquids and against analytical solutions for the flow of highly compressible liquids in the presence of a sorbing phase (Hornbrook, 1994). The numerical model was shown to match all analytical solutions exactly. Adsorbed phase properties were assumed to be identical to saturated liquid water which has been shown to be valid for the Geysers geothermal reservoir (Hornbrook, 1994).

## EFFECTS OF ADSORPTION ON TRACER PROPAGATION

The purpose of this section is to delineate the effects of adsorption on tracer propagation in a porous media. In order to isolate the effects of adsorption, the effects of diffusion, preferential partitioning, and permeability variations were ignored.

Since the tracer considered in this report is tritiated water which behaves very much like water, the propagation of tracer was modeled as the propagation of a water component:

$$(1)\quad y_i^{n+1}T_{i+1/2}\left(p_{i+1}-p_i\right)^{n+1}-y_{i-1}^{n+1}T_{i-1/2}\left(p_i-p_{i-1}\right)^{n+1}-\frac{\Delta x}{\Delta t}\left[\left(y_{vi}\phi_i\rho_{vi}S_{vi}\right)^{n+1}-\left(y_{vi}\phi_i\rho_{vi}S_{vi}\right)^{n}\right]-\frac{\Delta x}{\Delta t}\left[\left(y_{ai}\phi_i\rho_{ai}S_{ai}\right)^{n+1}-\left(y_{ai}\phi_i\rho_{ai}S_{ai}\right)^{n}\right]+y_{inj}Q_{inj}-y_{prod}Q_{prod}=0$$

where, the subscripts *a* and *v* refer to the adsorbed and vapor phases, respectively, the subscripts *i* refer to block numbering, and the superscripts refer to time steps in the numerical computation.

Adsorbed phase saturation is related to an adsorption isotherm by:

$$(2)\quad S_a = \frac{1-\phi}{\phi}\frac{\rho_r}{\rho_a}X(p/p_s)$$

where, X denotes the mass adsorbed per mass of rock at a given relative pressure ($p/p_S$).

In Eqn. 1, the pressures, saturations, and fluid properties determined at the end of each time step in the computation of mass transport of vapor are used to compute the mass fraction of injected mass in the vapor phase, $y_V$, in each block. In order to calculate the mass fraction in the vapor phase explicitly, a relation between the mass fraction in the adsorbed phase and in the vapor phase is needed. Since the goal in this section is to isolate adsorption effects, it was assumed that the mass fraction of injected tracer in the adsorbed phase is a weighted average of the fraction adsorbed at the old time step and the change in adsorbed mass over the time step:

$$(3)\quad y_a^{n+1} = \frac{y_v^{n+1}\Delta_t S_a + y_a^n S_a^n}{S_a^{n+1}}$$

By making the assumption that concentrations are a function of the adsorptive process and are not affected by diffusion, the effects of adsorption are isolated.

By varying initial and boundary conditions in numerical simulation of tracer flow, the range of adsorption effects on tracer propagation may be determined.

In the numerical simulations described below, the following form of the langmuir equation was used to describe adsorption isotherms:

$$(4)\quad X\left(\frac{p}{p_s}\right) = d\left[\frac{c(p/p_s)}{1+(c-1)(p/p_s)}\right]$$

where, c is the shape factor which determines the rate at which sorption occurs, and d is the magnitude factor which determines the maximum amount adsorbed at a relative pressure of 1.0.

Figure 1 shows a range of isotherms with d=1 and with c varying over the entire range of shapes considered in this research.

Figure 2 shows tracer profiles in a 4 m long simulated core for injection when steady state conditions have been reached in the core. Injection and production rates in the core were held constant for these experiments and steady-state conditions were allowed to develop. When steady state conditions had developed, the injection block pressure was approximately 7 MPa while the production block pressure was about 0.5 MPa. Clearly, when steady-state is reached, the presence of an adsorbed phase increases the propagation rate of tracer. This is due to the fact that the amount adsorbed at a given point in the reservoir is constant and, therefore, the area open for flow is reduced. This causes an increase in the tracer flow rate which is initially in the vapor phase.

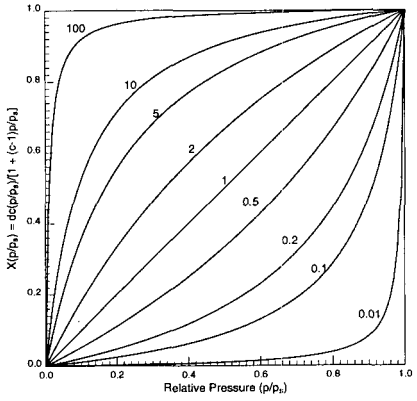


Fig. 1: Langmuir isotherms

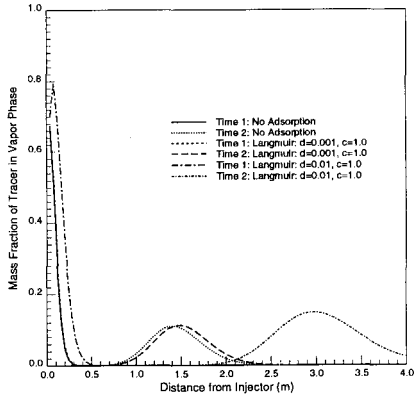


Fig. 2: Steady state flow

Figure 3 shows the tracer propagation in a core for conditions similar to those described above except that steady state conditions were not allowed to develop. In this case, the tracer begins moving faster due to a reduced flow area but eventually decreases in velocity due to adsorption of the vapor in which the tracer resides. The concentration of tracer when adsorption is occurring is also reduced due to loss of mass of the tracer to the adsorbed phase. Results shown in Figure 3 represent extreme conditions for the isotherm selected because the range between injection and production pressures is still large. Despite such large pressure differences, the tracer delay is shown to be only about 30%.

Figure 4 shows the rate of production of tracer injected into a 4 m long core. In this simulation, conditions approximating those at the Geysers were chosen to determine the likely effects of adsorption on tracer delay at the Geysers. Core temperature was set at a constant 300 C and injection was initiated at a relative pressure of 0.5. While the temperature is higher than that at the Geysers, the relative pressure is analogous. Tracer production is shown for injection with no adsorption, and for injection with adsorption for two controlling langmuir isotherms. In both cases, the magnitude factor is 0.01 which corresponds to an initial adsorbed phase saturation of 75%. This is an

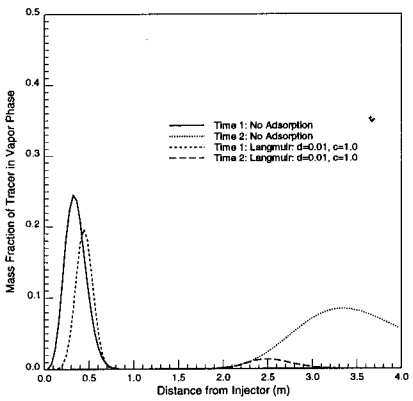


Fig. 3: Transient flow

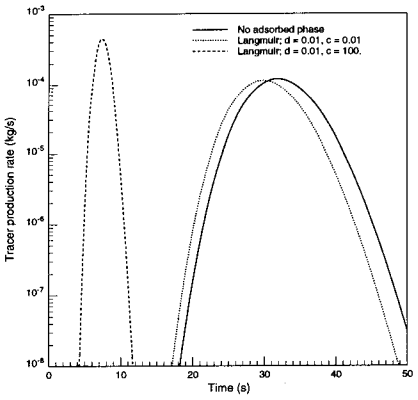


Fig. 4: Approximate Geysers tracer response

extreme case but is used to highlight adsorption effects. The shape factors used are 0.01 which is a concave up isotherm similar in shape to isotherms measured at the Geysers and 100 which represents a concave down isotherm for which desorption only occurs at low pressures.

It is shown in Figure 4 that the presence of an adsorbed phase increases the propagation of injected tracer. The reason for this increase in propagation is that the isotherms are nearly flat for relative pressure corresponding to initial injection into the core. Therefore, very little adsorption occurs to reduce the concentration of tracer in the vapor phase and very little pressure support is received by the production well to reduce the flow rate of vapor.

Based on these numerical experiments and others (Hornbrook, 1994), it was concluded that adsorption plays a very minor role in the transport of injected tracer in geothermal reservoirs. In the Geysers reservoir, tracer transport is probably increased slightly by the presence of an adsorbed phase.

## EFFECTS OF DIFFUSION PARTITIONING ON TRACER PROPAGATION

Diffusion of tritiated water into the immobile adsorbed water phase was considered as a possible mechanism for delay of injected tracer. In order to understand the likelihood of diffusion partitioning, the relative sizes of the convective and diffusive fluxes must be computed and compared. The porosity in the Geysers and in other geothermal reservoirs is often very complicated (Fig. 5) with flow taking place mainly in the fractures and adsorbed phase storage occurring in the interparticle porosity (Gunderson, 1993). By comparing the convective flux computed using measured Geysers permeability and an estimated diffusive flux of tracer, it is possible to determine the range of permeabilities for which instantaneous diffusive equilibrium is likely.

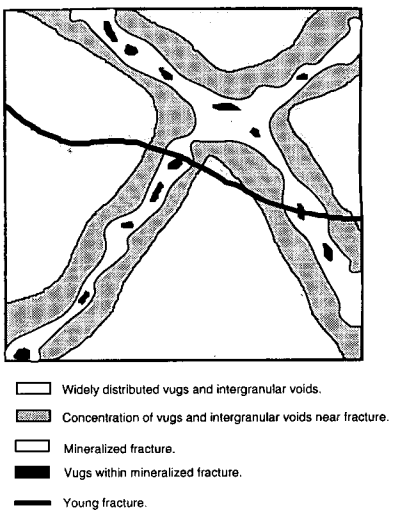


Fig. 5: Pore structure at Geysers (after Gunderson)

The diffusive flux of tracer is described by Fick's Law:

$$(5)\quad v_{diff} = -D_{mol}\frac{\partial C}{\partial x}$$

where, $D_{mol}$ represents the molecular diffusivity into a bulk phase. The diffusivity of tritium has been reported as $2.3 \times 10^{-5}$ $cm^2/s$ (Leap, 1992). In porous material, however, the diffusivity of a substance is decreased due to the tortuosity of porous matrix (Aris, 1975).

$$(6)\quad D_{pore} = D_{bulk}\left[\frac{\phi}{a^2}\right]$$

where, a is the actual pore length per distance in the direction of diffusion. Assuming that the interparticle porosity is about 1% (Gunderson, 1993) and that the measure or tortuosity, a, is 2, the maximum

diffusivity of tritiated water out of the vapor phase and into the adsorbed liquid phase was estimated to be $5.8 \times 10^{-10}$ m/s. Assuming Darcy's law is a valid model for convective flux, the range of flow rates likely in the Geysers was found to be $2.9 \times 10^{-5}$ to $2.9 \times 10^{-9}$ m/s, Thus, except in the extremely low permeability regions of the reservoir, convective flux is significantly greater than the diffusive flux. Since is was demonstrated that, for at least some regions of the Geysers reservoir, diffusive partitioning is important, computations of delay caused solely by diffusion were made. An analytical solution for convection and diffusion of a tracer in the presence of an immobile phase has been constructed (Antunez, 1984). In the derivation, instantaneous concentration equilibrium between the phases was assumed. The expression for concentration as a function of location and time for constant injection of tracer into a porous media initially free of tracer is:

$$(7) \quad \frac{C(x,t)}{C_0} =$$

$$\frac{1}{2}\exp\left[\frac{xu_v}{K}\right]\operatorname{erfc}\left[\frac{x\sqrt{\frac{S_v\rho_v + S_a\rho_a}{KS_v\rho_v}}}{2\sqrt{t}} - \frac{\frac{u_v}{K}\sqrt{t}}{2\sqrt{\frac{S_v\rho_v + S_a\rho_a}{KS_v\rho_v}}}\right]$$

$$+ \frac{1}{2}\exp\left[\frac{xu_v}{K}\right]\operatorname{erfc}\left[\frac{x\sqrt{\frac{S_v\rho_v + S_a\rho_a}{KS_v\rho_v}}}{2\sqrt{t}} + \frac{\frac{u_v}{K}\sqrt{t}}{2\sqrt{\frac{S_v\rho_v + S_a\rho_a}{KS_v\rho_v}}}\right]$$

In order to isolate the effects of diffusive partitioning, steady state flow conditions were assumed. When steady state flow conditions prevail, pressure at a given point in the reservoir is constant and, therefore, adsorption does not occur as vapor flows. This allows the study of diffusion into the immobile adsorbed liquid phase. In Eqn. 3, the vapor velocity, $u_V$ is given by:

$$(8) \quad u_v = \frac{q_{sc}}{\phi S_v}$$

From Geysers data, the velocity of vapor was computed as about $8 \times 10^{-6}$ m/s in the very low permeability regions of the reservoir where diffusion effects are large. From adsorption isotherm measurements (Shang, et. al, 1993) the saturation of adsorbed liquid was found to be about 3%. Saturated vapor and liquid properties were used in computations. The effects of diffusion partitioning on tracer propagation are shown in Figure 6. Tracer profiles with no adsorbed phase present and with an adsorbed phase saturation approximating conditions at the Geysers are shown. The effective velocity of injected tracer is shown to be reduced by about a factor of two due to diffusion into the adsorbed phase.

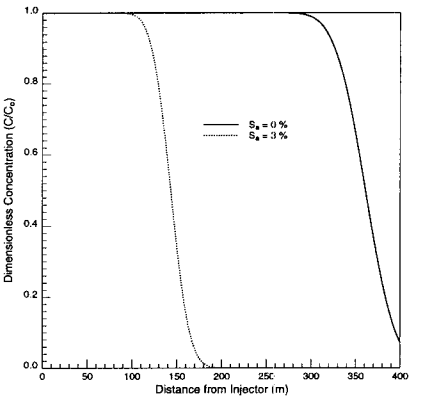


Fig. 6: Diffusion tracer delay

## EFFECTS OF RESERVOIR HETEROGENEITY ON TRACER PROPAGATION

In order to investigate the effects of reservoir heterogeneity on the propagation of injected tracer, a model of the reservoir must be constructed which captures the flow characteristics of the reservoir. In this research, a stream tube model was constructed because it allows application of the linear flow model to complicated flow patterns. The DX-8 tracer injection test was modeled by assuming steady state flow between the injector and surrounding producers. Excess production was made up by introduction of surrounding imaginary injection wells. The reservoir was assumed to be homogeneous. Based on reported flow rates, and including the producers accounting for about 90% of recovered tracer, streamlines were generated for the DX-8 tracer study. Figure 7 shows developed streamlines for all wells included in the study.

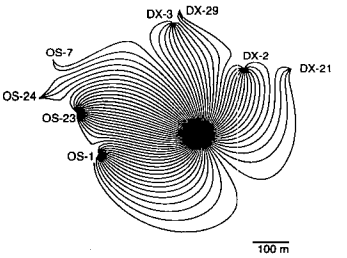


Fig. 7: Total DX-8 Streamlines

A single well pair was chosen to perform experiments on reservoir heterogeneity. The DX-8/OS-23 well pair was chosen because OS-23 accounted for approximately 34% of all produced tritium. The streamlines for the DX-8/OS-23 well pair are shown in Figure 8, and the tracer concentration in the produced vapor is shown in Figure 9. Concentration data are calculated from reported tritium production rate data (UNOCAL, 1991).

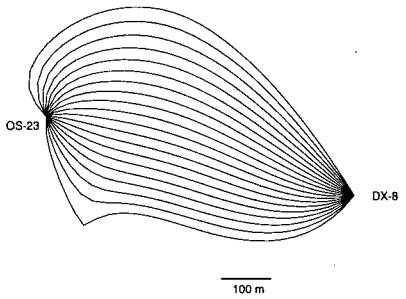


Fig. 8: OS-23/DX-8 Streamlines

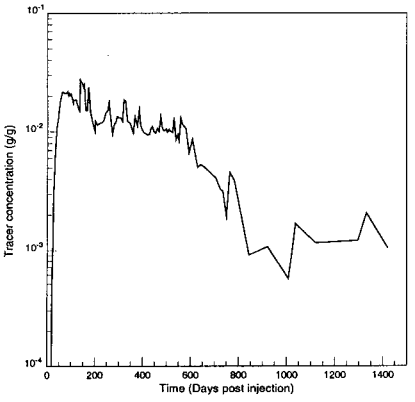


Fig. 9: Measured tracer concentration

Using the length of each stream tube shown in Figure 8 and the average cross-sectional area of each tube, a linear model of each tube was constructed. The permeability was varied in these stream tubes based on reported Geysers permeability. Slug injection of tracer was simulated and tracer concentration in the production block was monitored for each linear stream tube. By normalizing the initial breakthrough concentration of tracer to the measured value, and computing production tracer concentrations for all stream tubes, the effects of permeability and well separation on tracer propagation can be studied. Figure 10 shows a comparison of measured and computed concentrations. Production block concentrations for two of the stream tubes are shown to illustrate the range in tracer response possible for known Geysers permeabilities and well separations. The figure shows that even without adsorption or diffusion partitioning effects, the permeability and geometric variations present in the Geysers are sufficient to cause measured production delays in injected tracer.

Therefore, in designing injection programs, the communication between injection and production wells is the most important constraint with both diffusive partitioning and adsorption effects insignificant in comparison.

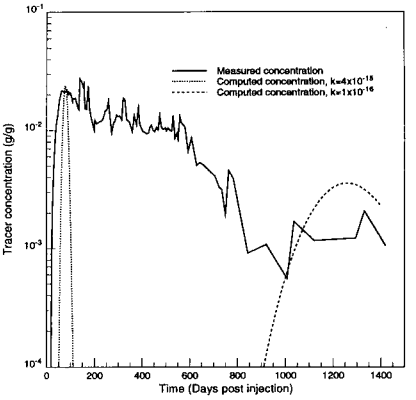


Fig. 10: Computed tracer concentration

## CONCLUSIONS

Based on the results described above, the following conclusions about the effects of adsorption and other delay mechanisms on the propagation of injected tracer are:

1. The effects of adsorption on tracer propagation are small for adsorption saturations likely in geothermal reservoirs. For conditions likely at the Geysers, the presence of an adsorbed mass probably slightly increases the rate of propagation of injected tracer.

2. The effects of diffusive partitioning of tracer are large than those due to adsorption alone. In the Geysers, instantaneous concentration equilibrium does not occur in high permeability portions of the reservoir, but in low permeability regions diffusive partitioning may reduce tracer flux by as much as 50%.

3. Preferential partitioning due to differences in the boiling characteristics of the tracer and the carrying liquid does not occur to any measurable degree in the Geysers. The saturation curve for tritium is nearly identical to that of water.

4. Permeability and geometric variations, without any adsorbing or diffusive partitioning effects, is sufficient to explain tracer production characteristics at the Geysers. Thus, by far the largest factors in the design of injection programs are the reservoir permeability in the region of the injector and the separation between injector and producer pairs.

## NOMENCLATURE

Variables

| | | |
|---|---|---|
| C | Mass Concentration | Dimensionless |
| D | Diffusivity | $m^2/s$ |
| k | Permeability | $m^2$ |
| p | Pressure | Pa |
| Q | Mass flow rate | kg/s |
| q | Volumetric flux | $m^3/s$ |

| | | |
|---|---|---|
| S | Saturation | Dimensionless |
| T | Transmissibility | kg/(m$^2$ Pa s) |
| t | Time | s |
| u | Velocity | m/s |
| X | Adsorbed amount | g-ads./g-rock |
| x | Distance | m |
| y | Mass fraction | Dimensionless |
| $\mu$ | Viscosity | Pa s |
| $\phi$ | Porosity | Dimensionless |
| $\rho$ | Density | kg/m$^3$ |

Subscripts and Superscripts

| | |
|---|---|
| a | Adsorbed phase. |
| bulk | Bulk phase. |
| diff | Diffusive quantity. * |
| i | Counter for a block in numerical model. |
| mol | Molar quantity. |
| n | Time step counter in numerical model. |
| pore | Residing in a pore. |
| r | Rock. |
| s | Saturation conditions. |
| t | Denotes time operator. |
| v | Vapor phase. |
| 0 | Initial condition. |

## ACKNOWLEDGMENTS

The authors thank the Department of Energy, Geothermal Division, who provided funding for this research under contract number DEFG0790ID12934.

## REFERENCES

Antunez, E. U.: *Semi-Analytic Approach to Analyze Single Well Tracer Test*, Ph.D. dissertation, Stanford University, 1984.

Aris, R.: *Mathematical Theory of Diffusion and Reaction in Permeable Catalysis*, Clarendon Press, Oxford, 1975.

Economides, M.J. and Miller, F. G.: "The Effects of Adsorption Phenomena in the Evaluation of Vapor Dominated Geothermal Reservoirs," *Geothermics* (1985) 14, No. 1, pp. 3-27.

Enedy, S. Enedy, K., and Maney, J.: "Reservoir Response to Injection in the Southeast Geysers," *Monograph on the Geysers Geothermal Field*, C. Stone (ed.), Geothermal Resources Council (1993), Special Report No. 17, pp. 211-220.

Gunderson, R. P.: "Porosity of Reservoir Graywacke at the Geysers," *Monograph on the Geysers Geothermal Field*, C. Stone (ed.), Geothermal Resources Council (1993), Special Report No. 17, pp. 89-93.

Hornbrook, J. W.: "The Effects of Adsorption on Injection Into and Production From Vapor-Dominated Geothermal Reservoirs," Stanford University Thesis, 1994.

Hsieh, C. H. and Ramey, H. J. Jr.: "Vapor-Pressure Lowering in Geothermal Systems," SPE 9926 presented at the 1981 SPE Annual Technical Conference and Exhibition, Bakersfield, Nov., 15.

Shang, S., Horne, R. N., and Ramey, H. J. Jr.: "Experimental Study of Water Vapor Adsorption on Geothermal Reservoir Rocks," Stanford Geothermal Program Technical Report, Dec., 1993.

UNOCAL, "DX-8 Tritium Study", DOE Report, 1991.

UNOCAL, "UNOCAL Position Report on Injection", Draft Report, 1992.

PROCEEDINGS, Nineteenth Workshop on Geothermal Reservoir Engineering
Stanford University, Stanford, California, January 18-20, 1994
SGP-TR-147

# DOUBLE-DIFFUSIVE CONVECTION IN LIQUID-DOMINATED GEOTHERMAL SYSTEMS WITH HIGH-SALINITY BRINES

Curtis M. Oldenburg, Karsten Pruess, and Marcelo Lippmann

Earth Sciences Division
Lawrence Berkeley Laboratory
Berkeley, CA 94720

## ABSTRACT

Variations in temperature and salinity in hypersaline liquid-dominated geothermal systems like the Salton Sea Geothermal System (SSGS) tend to be correlated such that liquid density is relatively constant in the system. The tendency toward small density variations may be due to connectivity with a surrounding regional aquifer at multiple depths in the stratigraphic column. We present numerical simulation results for natural convection in geothermal systems like the SSGS in hydraulic connection with a constant-density aquifer. Natural convection where there are two sources of buoyancy such as heat and salt, with different diffusivities, is called double-diffusive convection. Simulations of double-diffusive convection are carried out using our general-purpose reservoir simulator TOUGH2 with a newly developed two-dimensional heat and brine transport module (T2DM) that includes Fickian solute dispersion. The model includes an accurate formulation for liquid density as a function of temperature and salinity. Our simulation results show many features that are consistent with observations of the SSGS, making conceptual models that involve hydraulic connectivity with a surrounding aquifer appear plausible. The generality of our model makes the results broadly applicable to systems similar to the SSGS.

## I. INTRODUCTION

Although temperature and salinity variations are large in liquid-dominated geothermal systems such as the Salton Sea Geothermal System (SSGS) in southern California, they tend to be correlated such that liquid density differences are small. Liquid density data from wells across the SSGS field show that overall differences average about 10%, with density larger at greater depths in the system. Meanwhile temperature data show a conductive cap underlain by a convective hydrothermal system. These data define a fundamental paradox of the SSGS: liquid density changes are small with density stably stratified, yet temperature profiles imply that convective heat transfer occurs.

It must be kept in mind that large-scale stable density profiles do not preclude local free convection as local gravitational instabilities can arise due to the different diffusivities of the buoyancy-producing components, such as heat and salt. Free convection caused by two sources of buoyancy with different diffusivities is called double-diffusive convection. The potential significance of double-diffusive convection and associated layered convection for conceptual models of the SSGS was pointed out by Fournier (1990). Recent numerical simulation results (Rosenberg, 1991) of porous media convection show that layered double-diffusive convection is a transient phenomenon.

Constraints on conceptual models of the SSGS are provided by the wealth of observations and data collected through the years. A comprehensive early discussion of the thermodynamics of the field was published by Helgeson (1968). Recent reviews of the state of knowledge of the SSGS have been presented by Younker et al. (1982), Newmark et al. (1986) and Fournier (1990). The essential observations which any conceptual model must account for are: (1) temperature and salinity variations should be correlated such that the variation of liquid density with depth is small; (2) vertical temperature gradients should be larger near the surface and smaller in deeper parts of the system; (3) brine concentrations should increase sharply at depth as hypersaline brine is encountered; and (4) the temperature of the hypersaline brine should be above 260 °C.

In this paper, we present results of simulations of a convective scenario in which a temperature- and salinity-stratified system is heated from below while in hydraulic connection with an adjacent constant-density aquifer. The plausiblity of the scenario for the SSGS will be evaluated with respect to the constraining observations presented above. The idealized system modeled is sufficiently general that the results can be broadly applied to other geothermal systems similar to the SSGS.

## II. DENSITY FORMULATION

Following the work of Reeves et al. (1986) and Herbert et al. (1988), we adopt a mixing model in which the aqueous phase consists of two components, a concentrated brine with mass fraction $Xb$, and pure water with mass fraction $X_W = 1 - Xb$. The brine component is taken as aqueous NaCl solution. Assuming the volumes of pure water and brine are additive, we obtain for the mixture density ($\rho$) the equation

$$\frac{1}{\rho} = \frac{V_m}{M_m} = \frac{1 - Xb}{\rho_w} + \frac{Xb}{\rho_b} \qquad (1)$$

where the density of each component is given by $\rho_W = M_W/V_W$ and $\rho_b = M_b/V_b$ . The density of pure water at elevated temperatures is calculated from equations given in the steam tables of the International Formulation Committee (1967), while the temperature dependence of brine density is calculated using a coefficient of thermal expansivity:

$$\alpha_b = -\frac{1}{\rho_b}\left(\frac{\partial \rho_b}{\partial T}\right) \qquad (2).$$

Tabulated densities in Pitzer et al. (1984) show that the coefficient of thermal expansivity for pure water is more than two times larger than the coefficient of thermal expansivity for a concentrated brine solution. For pure brine, we define the coefficient of thermal expansivity ($\alpha_b$) by specifying two reference brine temperatures and densities ($\rho_{0b}$ and $T_{0b}$, $\rho_{2b}$ and $T_{2b}$) obtained from the tables of Pitzer et al. (1984). The coefficient of thermal expansivity for the brine is applied through the exponential relation

$$\rho_b = \rho_{0b}\, exp(-\alpha_b\,(T-T_{0b})) \qquad (3).$$

Subsequent to the calculation of the thermal effects on density for each component, the mixing relation (Eq. 1) is applied to obtain the density of the mixture. The calculated densities agree to within 3% with data tabulated in Pitzer et al. (1984) across the applicable range of temperatures and salinities. The method has been coded as an extension to EOS7, a TOUGH2 thermophysical properties module for water, brine and air (Pruess, 1991b).

Plotted in Fig. 1 are results of the above model for the density of brine as a function of temperature and brine mass fraction ($Xb$) where $Xb$ = 1.0 corresponds to a 24.98 wt. % NaCl solution. Pressure is set at $10^5$ Pa (1 bar) above the saturation pressure (Psat). Superimposed on the density isopleths are temperature and salinity (TDS) of 45 fluid samples of low TDS brines, hypersaline brines, and mixed brines from the SSGS (Williams, 1988; Williams and McKibben, 1989). In superimposing these data, we implicitly assume the predominant solid is NaCl and that TDS = 24.98 wt. % corresponds to $Xb$ = 1.0. (Note that the mixed brines do not represent reservoir conditions but are mixtures of low-TDS and hypersaline brines).

The data in Fig. 1 show that while temperature and salinity are correlated, the reservoir fluid is not at uniform density. Higher densities occur at hotter (deeper) levels making the reservoir density-stratified. Furthermore, the densities are generally in the range 850–950 kg m$^{-3}$ rather than the oft-quoted 1000 kg m$^{-3}$. We note here also that viscosity varies by a factor of two between pure water and pure brine but such changes have been neglected in the present study.

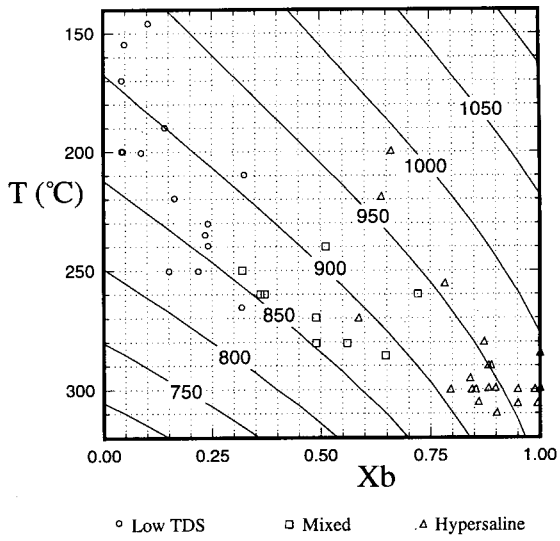


Figure 1. Density (kg m$^{-3}$) of NaCl brines as a function of temperature and brine mass fraction. Superimposed are fluid temperature and TDS data for the SSGS from Williams (1988) and Williams and McKibben (1989). The mixed fluids are thought to be mixtures of hypersaline and low-TDS fluids and do not represent true reservoir conditions.

## III. TRANSPORT MODEL

The general conservation equations solved by the integral finite difference method (IFDM) in TOUGH2 (Pruess, 1987, 1991a) consist of balances of mass accumulation and flux and source terms over all grid blocks into which the flow domain has been partitioned. The flux term has contributions from Darcy flow, molecular diffusion, and hydrodynamic dispersion and can be written

$$\mathbf{F}^{(\kappa)} = X^{(\kappa)}\,\mathbf{F} - \rho\,\overline{\mathbf{D}}^{(\kappa)}\nabla X^{(\kappa)} \qquad (4)$$

for single-phase conditions where $\kappa$ = 1,2 denotes the fluid components ($\kappa$ = 1: water, 2: brine). The advective flux is given by Darcy's Law:

$$\mathbf{F} = \rho\ \mathbf{u} = -\frac{k}{\mu}\rho\left(\nabla P - \rho\ \mathbf{g}\right) \qquad (5).$$

The second term on the right-hand side of Eq. 4 is the dispersion term. We have implemented a standard model for dispersion which accounts for both molecular diffusion and hydrodynamic dispersion (deMarsily, 1986). In the dispersion model, $\overline{\mathbf{D}}$ in Eq. 4 is the dispersion tensor, a second order, symmetric tensor with one principal direction in the average (Darcy) flow direction, and the other normal to it. Dispersion is written in terms of dispersion coefficients in the longitudinal ($D_L$) and

transverse ($D_T$) directions relative to the flow direction where

$$D_L^\kappa = \phi \cdot \tau \cdot d^\kappa + \alpha_L u \qquad (6)$$

$$D_T^\kappa = \phi \cdot \tau \cdot d^\kappa + \alpha_T u \qquad (7).$$

Here $\phi$ is porosity, $\tau$ tortuosity of the medium, $d$ molecular diffusivity, $\alpha_L$ longitudinal dispersivity, $\alpha_T$ transversal dispersivity, and $u$ magnitude of the Darcy velocity. Thus, the dispersion tensor of Eq. 4 can be written as

$$\overline{\mathbf{D}}^\kappa = D_T^\kappa \bar{\mathbf{I}} + \frac{(D_L^\kappa - D_T^\kappa)}{u^2} \mathbf{u}\,\mathbf{u} \qquad (8)$$

Substituting Eq. 8 into Eq. 4 gives the corresponding mass flux of component $\kappa$ due to molecular diffusion and hydrodynamic dispersion:

$$\mathbf{F}_d^{(\kappa)} = -\rho D_T^\kappa \nabla X^{(\kappa)} - \rho \frac{(D_L^\kappa - D_T^\kappa)}{u^2} \mathbf{u} \left(\mathbf{u} \cdot \nabla X^{(\kappa)}\right) \qquad (9).$$

In the discretized equations solved in TOUGH2, the interface conductivity arising from the molecular diffusion terms in Eqs. 6–7 is derived from harmonic averages of the properties of the two connected grid blocks. Note from Eq. 9 that full Darcy velocity and mass fraction gradient vectors are required at each interface between grid blocks. In the usual IFDM, only the vector components normal to the interface are known directly. In order to calculate dispersive transport, the parallel components must be interpolated from neighboring direct values. The details of the interpolation and calculation of the dispersive flux, along with verification studies, are presented in Oldenburg and Pruess (1993).

The transient equations are solved with a fully implicit time-stepping scheme in TOUGH2. The simulator uses a fully coupled residual-based solution technique that is efficient for strongly coupled flow problems such as double-diffusive convection. Solution of the resulting system of linear equations was accomplished with a bi-conjugate gradient solver with incomplete LU decomposition as preconditioner (Greenbaum, 1986; Seager, 1992; Moridis, private communication, 1993).

## IV. CONNECTION TO ADJACENT AQUIFER

In this section, we present results of simulations of convection in an idealized system representing a liquid-saturated hypersaline geothermal system in hydraulic connection with a constant-density aquifer. The domain is shown in Fig. 2 along with boundary and initial conditions. The two-dimensional domain is 2500 m on a side, with 25 grid blocks in the $Y$-direction, and 27 grid blocks in the $Z$-direction. This highly idealized system is sufficiently general that the results will have broad applicability.

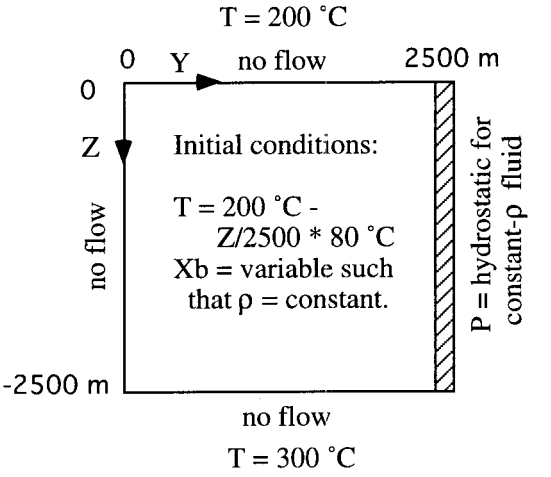


Figure 2. Boundary and initial conditions for the model. The right-hand side represents a constant-density aquifer with a linear temperature profile and corresponding brine mass fraction profile such that the density of the liquid is exactly 925 kg m$^{-3}$.

The boundary condition on the right-hand side was established as gravity equilibrium in a column of liquid linearly stratified in temperature from 200 °C at the top to 280 °C at the bottom. The mass fraction of brine is adjusted such that the density is constant with depth and equal to 925 kg m$^{-3}$. This constant-density column of liquid is assigned an effectively infinite volume making it inactive (its properties do not change with time). The column is directly connected to the hydrothermal system. The entire hydrothermal system is initially identical in $T$ and $Xb$ to the inactive column. At $t = 0$, the temperature at the bottom of the system is raised to $T$ = 300 °C. We initialized the lower left-hand corner of the system with slightly elevated temperatures to initiate clockwise convection. Brine does not enter or leave the system except through the right-hand side boundary.

Parameters were chosen to approximate average conditions at the SSGS (Table 1). The porosity of the medium was set to a uniform value of .20. The permeability was set to be anisotropic, with the vertical permeability 100 times smaller ($k_Z$ = 5 x 10$^{-15}$ m$^2$) than the horizontal permeability ($k_Y$ = 5 x 10$^{-13}$ m$^2$). This is believed to be a reasonable approximation for the sedimentary section at the SSGS. Numerical values for properties of the liquid and of the medium are given in Table 1.

Shown in Figs. 3–5 are computed temperature, brine mass fraction, and density fields at three different times. In Fig. 3a, we observe at early time ($t$ = 10,000 yrs.) that decreased density due to heating along the bottom drives a

convective plume. The upward flow is supplied with liquid from the lowest part of the right-hand side column. The liquid flowing horizontally along the bottom heats up and flows upward to a depth of 1500 m. The plume encounters cooler regions as it moves upward. Upward flow occurs only as long as the density of the plume is less than the ambient density of 925 kg $m^{-3}$. Thus the plume turns at about 1500 m and flows horizontally into the right-hand side column. Horizontal flow is favored by the anisotropic permeability field. The brine mass fraction field (Fig. 3b) shows the plume carrying concentrated brine upward in the thermal plume. The density field (Fig. 3c) shows that the largest densities are at the leading edge of the plume. This is due to the cooling of concentrated brine solutions at this edge. Only where the brine is hot will its density be low enough to drive a convective plume upward.

At $t$ = 20,000 yrs. (Fig. 4), the plume reaches a depth of 800 m before the fluid flows horizontally into the right-hand side column. By $t$ = 30,000 yrs (Fig. 5), the plume has reached the top of the domain. Temperature profiles at $Y$ = 200 m and $Y$ = 1250 m are plotted in Fig. 6. In the upper part of the domain, note the concave upward profile with depth early in time changing into a concave downward profile at later times.

Table 1. Properties of the liquid and porous medium.

| quantity | value | units |
|---|---|---|
| porosity ($\phi$) | .2 | – |
| heat capacity of rock ($C_P$) | 1000. | J $kg^{-1}$ $°C^{-1}$ |
| formation heat conductivity ($K$) | 1.8 | J $s^{-1}m^{-1}$ $°C^{-1}$ |
| molecular diffusivity ($d$) | $2 \times 10^{-8}$ | $m^2$ $s^{-1}$ |
| Y-direction permeability ($k_Y$) | $5 \times 10^{-13}$ | $m^2$ |
| Z-direction permeability ($k_Z$) | $5 \times 10^{-15}$ | $m^2$ |
| transverse dispersivity ($\alpha_T$) | 1. | m |
| longitudinal dispersivity ($\alpha_L$) | 10. | m |
| tortuosity ($\tau$) | 1. | – |
| density of rock ($\rho_R$) | 2650. | kg $m^{-3}$ |
| density of brine (at 200 °C) ($\rho_{0b}$) | 1066. | kg $m^{-3}$ |
| density of brine (at 300 °C) ($\rho_{2b}$) | 979.9 | kg $m^{-3}$ |

## V. DISCUSSION

Results from the simulations show some compelling resemblance to SSGS field data. We observe first that the correlation of $T$ and $Xb$ in the simulations leads to relatively small density variations just as observed in the field. The most concentrated brines correlate with the highest temperatures, typically above 250 °C. Second, we note the sharp temperature gradient near the top of the system (Fig. 6c) and the decreasing gradient within the plume. This type of temperature profile is similar to that observed in the SSGS. Temperature reversals (decreasing temperature with depth) are also observed in the SSGS (Newmark et al., 1986). Our results show reversals as the hot plume travels horizontally into the adjacent aquifer. Newmark et al. (1986) note that the curvature of the temperature profiles in the SSGS is concave downward in the center of the system and concave upward a distance away from it. These authors explain that this corresponds to colder groundwater entering the system or thermal waters leaving the system from the center. Clearly our simulation results involve flow leaving the system from the center in the upper parts of the system. It is interesting that the simulation results show the inflection in the temperature profiles evolves with time, with concave upward profiles early and concave downward profiles later on. If episodic heating due to magmatic intrusion occurs in the SSGS, the shape of such profiles may change with time.

Absent from our simulation results are hot, hypersaline brine pools thought to occur in the SSGS (Williams, 1988; Williams and McKibben, 1989). It is likely that the horizontal flow favored in the system could place cooler, fresher water from a surrounding aquifer on top of hot, hypersaline water in the center of the geothermal system. We assumed in our model a connected aquifer with variable temperature and salinity, but there is no reason to expect that the properties of the surrounding aquifer are the same all around the periphery of the field. In fact, regional groundwater flow through the SSGS might lead to varying properties in the adjacent aquifer. Perhaps where this aquifer is less saline, water could flow inward toward the center over denser hypersaline brines to produce the sharp brine interfaces thought to be present in the SSGS.

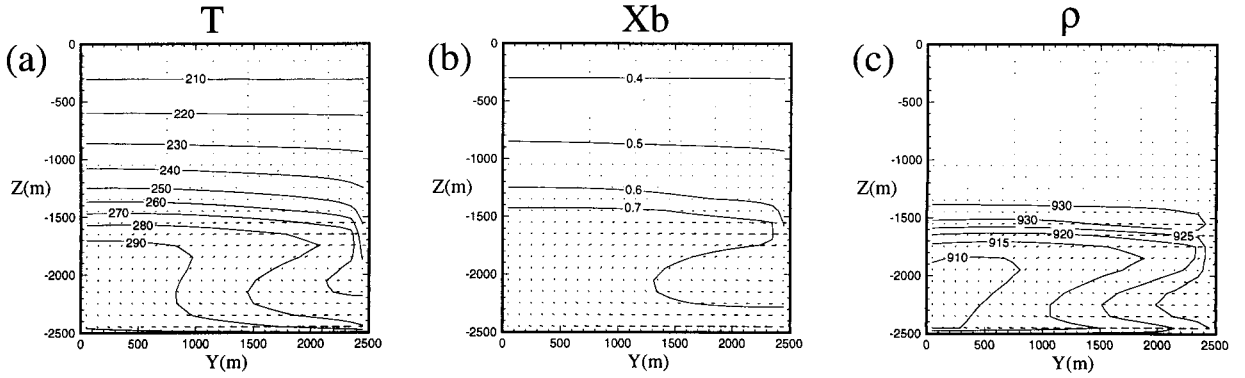


Figure 3. Computed results at $t$ = 10,000 yrs. (a) Temperature field (°C). (b) Brine mass fraction field. (c) Density field (kg $m^{-3}$). Results show the early plume and associated horizontal flow out from and into the constant-density right-hand side.

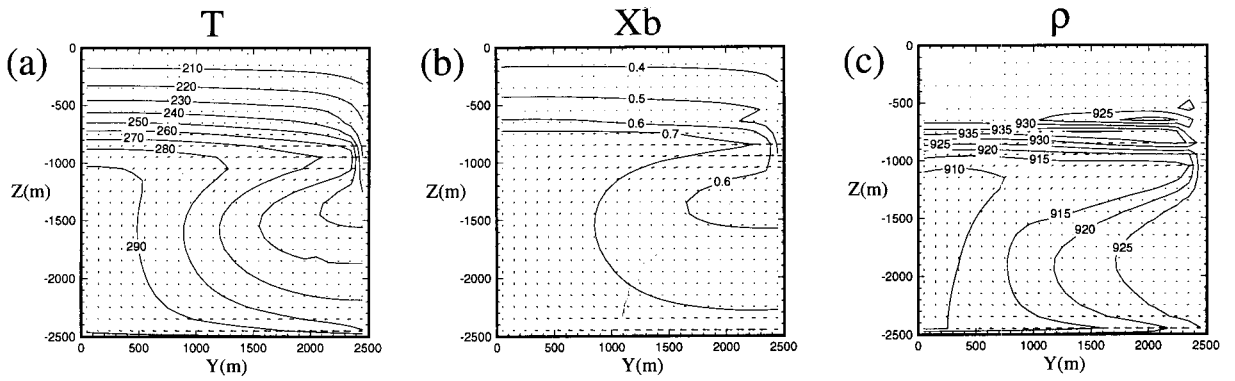


Figure 4. Computed results at $t$ = 20,000 yrs. (a) Temperature field (°C). (b) Brine mass fraction field. (c) Density field (kg $m^{-3}$).

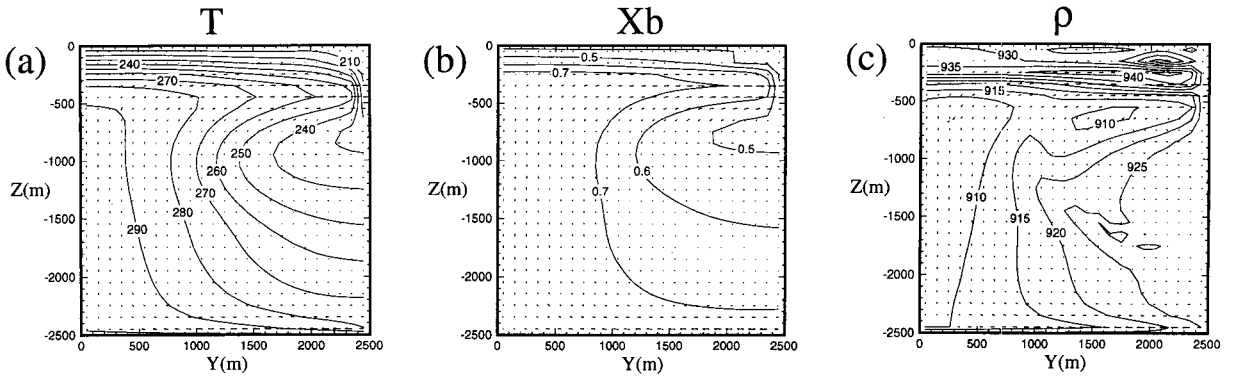


Figure 5. Computed results at $t$ = 30,000 yrs. (a) Temperature field (°C). (b) Brine mass fraction field. (c) Density field (kg $m^{-3}$).

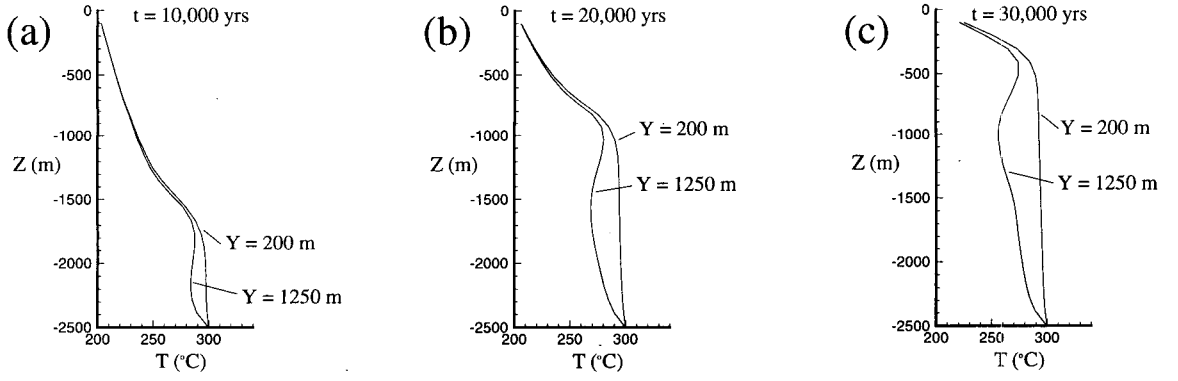


Figure 6. Computed temperature profiles at $Y$ = 200 m and $Y$ = 1250 m. (a) $t$ = 10,000 yrs. (b) $t$ = 20,000 yrs. (c) $t$ = 30,000 yrs. The temperature profile in the upper part of the system near the center of the field is concave upward early in time and concave downward later in the simulation.

## VI. CONCLUSIONS

Numerical simulation results of double-diffusive convection in a hypersaline liquid-dominated geothermal system that is in hydraulic connection with a constant-density aquifer show many of the characteristics observed in the SSGS. The consistency of results for a highly idealized model system with field data points to the potentially wider applicability of a conceptual model that includes strong connectivity to a surrounding aquifer. The particular features observed in the SSGS and reproduced by the model include (1) correlation of $T$ and $Xb$ such that liquid density variations are modest, (2) sharp temperature profile near the top and decreasing gradient with depth, and (3) temperature reversals caused by lateral flow of hot brine. The model does not produce hypersaline brine pools, but lateral flow could cause such pools depending on the conditions in the aquifer. The generality of the model makes our results broadly applicable to systems similar to the SSGS.


### Acknowledgment

This work was supported by the Assistant Secretary for Energy Efficiency and Renewable Energy, Geothermal Division, of the U.S. Department of Energy under Contract No. DE-AC03-76SF00098. The authors thank their colleague George Moridis for providing a package of preconditioned conjugate gradient solvers.


### Nomenclature

| | | |
|---|---|---|
| $d$ | molecular diffusivity | $m^2\ s^{-1}$ |
| $\underline{D}$ | dispersion coefficient | $m^2\ s^{-1}$ |
| $\mathbf{D}$ | dispersion tensor | $m^2\ s^{-1}$ |
| $\mathbf{g}$ | acceleration of gravity vector | $m\ s^{-2}$ |
| $\mathbf{F}$ | Darcy flux vector | $kg\ m^2\ s^{-1}$ |
| $\mathbf{I}$ | identity matrix | |
| $k$ | permeability | $m^2$ |
| $K$ | thermal conductivity | $J\ s^{-1}\ m^{-1}\ °C^{-1}$ |
| $M_b$ | mass of brine | kg |
| $\mathbf{n}$ | outward unit normal vector | |
| $P$ | total pressure | Pa |
| $t$ | time | years |
| u | magnitude of Darcy velocity vector | $m\ s^{-1}$ |
| $\mathbf{u}$ | Darcy velocity vector | $m\ s^{-1}$ |
| $V$ | volume | $m^3$ |
| $X$ | mass fraction | |
| Y | Y-coordinate | |
| Z | Z-coordinate (positive upward) | |

### Greek symbols

| | | |
|---|---|---|
| $\alpha$ | intrinsic dispersivity | m |
| $\alpha_b$ | thermal expansivity of brine | $°C^{-1}$ |
| $\mu$ | dynamic viscosity | $kg\ m^{-1}\ s^{-1}$ |
| $\phi$ | porosity | |
| $\rho$ | density | $kg\ m^{-3}$ |
| $\tau$ | tortuosity | |

### Subscripts and superscripts

| | |
|---|---|
| $b$ | brine |
| $L$ | longitudinal |
| $m$ | mixture |
| $0b$ | first reference value for brine |
| $2b$ | second reference value for brine |
| $T$ | transverse |
| $w$ | water |
| $\kappa$ | mass components |

## REFERENCES


deMarsily, G., *Quantitative Hydrogeology*, Academic Press, San Diego, CA, pp. 230-247, 1986.

Fournier, R.O., Double-diffusive convection in geothermal systems: The Salton Sea, California, geothermal system as a likely candidate, *Geothermics*, *19*(6), 481–496, 1990.

Greenbaum, A., Routines for solving large sparse linear systems, Lawrence Livermore Nat. Laboratory, Livermore Computing Center, *Tentacle* (January 1986), 15–21.

Helgeson, H.C., Geologic and thermodynamic characteristics of the Salton Sea geothermal system, *Am. J. Sci.*, *266*, 129–166, 1968.

Herbert, A.W., Jackson, C.P., and Lever, D.A., Coupled groundwater flow and solute transport with fluid density strongly dependent on concentration, *Water Res. Res.*, *24* (10), 1781-1795, 1988.

International Formulation Committee, A formulation of the thermodynamic properties of ordinary water substance, IFC Secretariat, Düsseldorf, Germany, 1967.

Newmark, R.L., P.W. Kasameyer, L.W. Younker, P.C. Lysne, Research drilling at the Salton Sea Geothermal Field, California: The shallow thermal gradient project, *Transactions of the American Geophysical Union EOS*, *67*(39), 698–707, 1986.

Oldenburg, C.M. and Pruess, K., A two-dimensional dispersion module for the TOUGH2 simulator, *Lawrence Berkeley Laboratory Report LBL- 32505*, 1993.

Pitzer, K.S., J.C. Peiper, and R.H. Busey, Thermodynamic properties of aqueous sodium chloride solutions, *J. Phys. and Chem. Ref. Data*, *13*(1), 1–102, 1984.

Pruess, K., TOUGH User's Guide, Nuclear Regulatory Commission, Report NUREG/CR-4645, June 1987 (also *Lawrence Berkeley Laboratory Report, LBL-20700*, June 1987).

Pruess, K., TOUGH2 - A General Purpose Numerical Simulator for Multiphase Fluid and Heat Flow, *Lawrence Berkeley Laboratory Report LBL-29400*, May 1991a.

Pruess, K., EOS7, An equation-of-state module for the TOUGH2 simulator for two-phase flow of saline water and air, *Lawrence Berkeley Laboratory Report LBL-31114*, August 1991b.

Reeves, M., Ward, D.S., Johns, N.D., and Cranwell, R.M., Theory and implementation of SWIFT II, the Sandia Waste-Isolation Flow and Transport Model for Fractured Media, *Report No. SAND83-1159*, Sandia National Laboratories, Albuquerque, N.M., 1986.

Rosenberg, N.D., Numerical studies of fluid flow and heat and solute transport in hydrothermal systems, Ph.D. dissertation, University of California, Santa Barbara, 138 p., 1991.

Seager, M.K., A SLAP for the Masses, Lawrence Livermore Nat. Laboratory Technical Report *UCRL-100267*, December 1988.

Williams, A.E., Delineation of a brine interface in the Salton Sea Geothermal System, California, *Geothermal Resources Council, Transactions*, *12*, 151–157, 1988.

Williams, A.E. and M.A. McKibben, A brine interface in the Salton Sea geothermal system, California: Fluid geochemical and isotopic characteristics, *Geochimica et Cosmochimica Acta*, *53*, 1905–1920, 1989.

Younker, L.W., P.W. Kasameyer, and J.D. Tewhey, Geological, geophysical, and thermal characteristics of the Salton Sea Geothermal Field, California, *J. Volcanol. Geotherm. Res.*, *12*, 221–258, 1982.

PROCEEDINGS, Nineteenth Workshop on Geothermal Reservoir Engineering
Stanford University, Stanford, California, January 18-20, 1994
SGP-TR-147

# Viscous Fingers in Superheated Geothermal Systems

**Shaun D. Fitzgerald[1], Andrew W. Woods[1] & Mike Shook[2]**

1 Institute of Theoretical Geophysics, Department of Earth Sciences, University of Cambridge, Downing Street, Cambridge, CB2 3EQ, England

2 Idaho National Engineering Laboratories, EG&G Idaho Inc.,

## Abstract

In this paper we investigate the physical controls upon the rate of vaporization of liquid as it is injected into a porous layer containing superheated vapour. We develop a simple model of the process and show that if liquid is injected at a relatively high rate, a small fraction of the liquid vaporizes and the porous layer becomes filled with hot liquid. In contrast, at low rates of injection a large fraction of the liquid may vaporize. We also describe a new and fundamental instability that can develop at a migrating liquid-vapour interface if the rate of injection is sufficiently small. This phenomenon is manifest in the form of liquid fingers growing from a liquid-vapour interface and is investigated through the use of analytical, experimental and numerical techniques.

## Introduction

Vapour-saturated geothermal reservoirs are recharged as liquid invades the pore spaces in the hot rock and vaporizes (Truesdell & White 1973). However, the rapid development of the vapour-dominated geothermal fields like The Geysers in California, and the significant fluid extraction in excess of the natural recharge has caused a depletion of the fluid levels within the reservoirs (Enedy 1989). The generating capacity of power plants installed within The Geysers region as of mid-1991 was approximately 2000 MW. As a result of the depletion of fluid reserves, the reservoir can only supply 1500 MW (Kerr 1991). This shortage of 500 MW has alarmed many commercial operators since this has affected the economics drastically. Depletion of fluid reserves has been observed in nearly all exploited geothermal reservoirs and this is to be expected locally around production wells. However, if exploitation of a reservoir is to be economical, the overall reservoir pressure needs maintaining to a certain degree. Hence, an exploitation scheme which addresses this problem is necessary for all reservoirs.

Active water injection schemes have been designed to regenerate the vapour and hence maintain the vapour pressure at The Geysers (Enedy et al. 1991). However, the optimal injection rate depends upon the particular situation. Understanding the underlying physical controls upon the rate of vaporization of liquid and the mass fraction of liquid which vaporizes helps to determine these conditions.

As a simple model we consider the injection of liquid into a porous layer as a mechanism to provide artificial recharge of fluid. Most of the energy within a geothermal reservoir is stored in the rock, and by increasing the rate of recharge into the reservoir, the rate at which hot fluids can be extracted from it can be maintained or increased (Schroeder et al. 1982; Pruess & Enedy 1993).

In this paper we describe results of our analysis of the physical controls upon the rate of vaporization of liquid as it is injected into a geothermal reservoir. The paper is divided into two parts. In the next section we analyse the vaporization of liquid at a planar liquid-vapour interface and describe how both the rate of vaporization and fraction of liquid which vaporizes change as the rate of injection is varied. In the subsequent section we investigate the stability of such planar vaporizing interfaces and show that for sufficiently slow rates of injection the interface actually becomes unstable. A series of analytical,

experimental, and numerical investigations identify that this instability is manifest in the form of fingers at the liquid-vapour interface.

**Vaporization of a planar interface**

As liquid migrates through hot porous rock and vaporizes, the rate of vaporization is governed by the amount of heat released by the rock and by the ability of the vapour to migrate ahead of the interface. In order to quantify the rate of vaporization and the mass fraction of liquid which can vaporize, equations for the conservation of mass and energy at the moving liquid-vapour interface are coupled with the Clausius-Clapeyron equation relating the interfacial pressure and temperature, and an equation describing the motion of the vapour ahead of the interface. Details of the physical processes and relevant equations are given by Woods & Fitzgerald (1993).

By solving the system of equations described above, we find that as the liquid flow rate increases, the interfacial pressure also increases (Figure 1). As a result, the interfacial temperature increases, reducing the heat released by the hot rock for vaporizing liquid. This in turn lowers the mass fraction of liquid which vaporizes (Figure 2); however, the total mass of vapour produced per unit time is greater owing to the greater flow rate (Figure 3).

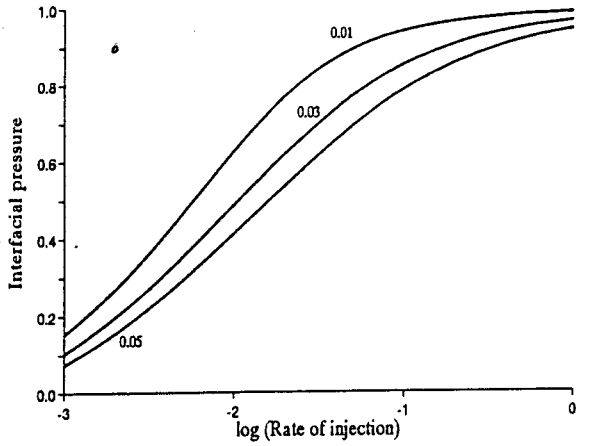


**Figure 1. Interfacial pressure as a function of rate of injection from a vertical well. Curves are given for various reservoir porosities.**

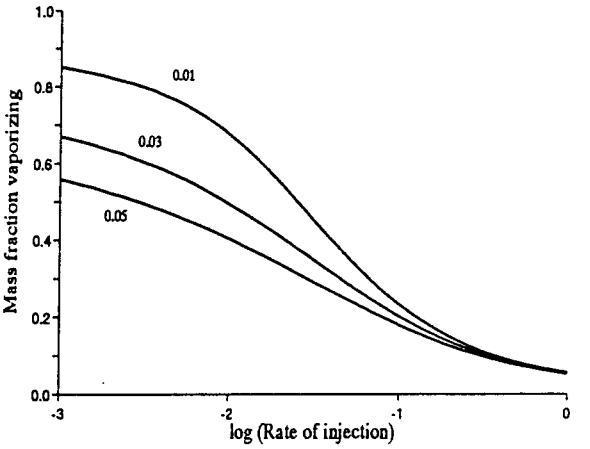


**Figure 2. Mass fraction vaporixing as a function of rate of injection from a vertical well. Curves are given for various reservoir porosities.**

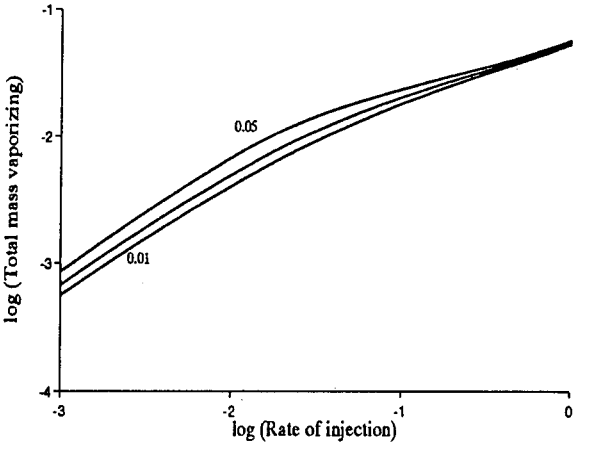


**Figure 3. Rate of production of vapor as a function of rate of injection from a vertical well. Curves are given for various reservoir porosities.**

These issues are discussed in greater detail by Woods & Fitzgerald (1993). They identify a fundamental paradox between the short term need for a high rate of vapour regeneration and the longer term objective of removing the thermal energy from the reservoir through extraction of vapour. In the next section we show that at low flow rates, for which the mass fraction of liquid which vaporizes is high, the situation is somewhat more complex. The assumption that the liquid vapour interface remains planar is not always satisfied. This affects

the above results concerning the fraction of the liquid which vaporizes, the rate of vaporization and the residual thermal energy stored in the reservoir.

**Interface Stability**

The results we described above hinge upon the assumption that the liquid vapour interface remains planar. However, this need not be the case if the pressure gradient in the vapour ahead of the interface exceeds that in the liquid just behind the interface. This effect is somewhat analogous to the Saffman-Taylor instability which develops in a porous layer when a more viscous fluid is displaced by a less viscous fluid (Saffman & Taylor 1958). The instability arises when a finger of the fluid behind the interface advances ahead of the interface. Because the pressure gradient in this finger is smaller than that of the surrounding fluid, the finger advances.

Appealing to the analogy with the Saffman-Taylor instability, we can derive a simple condition which identifies the flow rates for which the interface may be unstable. The pressure gradient in the liquid just behind the interface is given by Darcy's Law (Bear 1972)

$$\vec{\nabla} P_l = - \frac{\mu_l}{k} u_l \qquad (1)$$

where $u_l$ is the Darcy velocity of the liquid, k the permeability of the rock and $\mu_l$ the dynamic viscosity of the liquid. Similarly in the vapour, the pressure gradient is given by

$$\vec{\nabla} P_v = - \frac{\mu_v}{k} u_v \qquad (2)$$

We can relate these pressure gradients by noting that, if the mass fraction which vaporizes is F, then the mass flux of vapour $\rho_v u_v = F \rho_l u_l$ and so

$$\frac{\vec{\nabla} P_v}{\vec{\nabla} P_l} = F \frac{\mu_v \rho_l}{\rho_v \mu_l} = F \frac{\eta_v}{\eta_l} \qquad (3)$$

If this ratio is greater than unity an instability may develop. Typically, the ratio $\eta_v / \eta_l \approx 10$ for water and water vapour at pressures of 6 - 30 atmospheres and temperatures of 150 - 250°C. Therefore, if the typical mass fraction vaporizing, F, exceeds about 10 - 20% the liquid-vapour interface may be unstable.

A more detailed calculation (Fitzgerald & Woods, 1994) including the effects of thermal diffusion and the differential rate of vapour production between the crests and base of the fingers shows that very short and very long wavelength perturbations may be stabilized. Therefore, there is typically a band of wavelengths which are linearly unstable if F is sufficiently large (Figure 4).

From Figure 2, we see that the instability may arise for dimensionless injection rates Q<0.1 since at such low rates of injection the mass fraction vaporizing is sufficiently large. Once the fingering develops the surface area of the liquid-vapour interface increases, enabling more vapour to migrate ahead of the liquid. As a result, the mass of liquid which vaporizes can increase and the injection process becomes more effective.

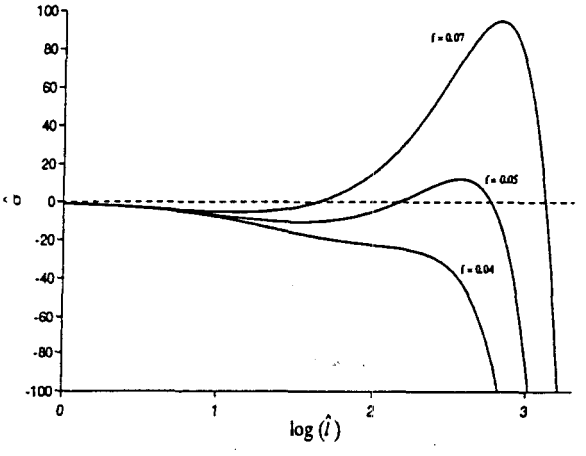


**Figure 4. Exponential growth rate of a finger as a function of wavenumber. Curves are given for three values of the mass fraction vaporizing. In these calculations the thermal diffusivity $k=3X10^{-6}$, $k/\alpha=5X10^{-4}$ and $v_l/v_v=0.042$.**

In order to demonstrate that the instability can indeed occur, we have conducted a series of experiments in which ether was injected into a cylindrically symmetric porous layer of hot sand bounded by two clear perspex plates (Fitzgerald & Woods 1994). As the ether spread radially from the source, a boiling front developed and ether vapour migrated ahead of the interface.

When the fraction vaporizing was sufficiently small, $F < (\eta_l / \eta_v)$, the advancing liquid-vapour front remained stable and circular. However, when a larger fraction of the ether vaporized, the liquid-vapour front developed fingers.

We plan to carry out a series of detailed numerical simulations of vaporizing liquid-vapour interfaces. Once we have reproduced the analytical stability criterion, we will then examine the nonlinear growth of the interfacial stability. This will enable us to determine the extent of the two-phase zone (the region in which liquid fingers are interspersed with vapour) and its impact upon the vaporization efficiency. We have conducted a series of preliminary calculations using the geothermal simulator TETRAD (Vinsome 1991).

Initial simulations of the case in which liquid is injected from a line source and in which the model domain is 2-dimensional indicate that for relatively high rates of injection the interface remains planar (Figure 5), while at lower flow rates the interface appears to become unstable.

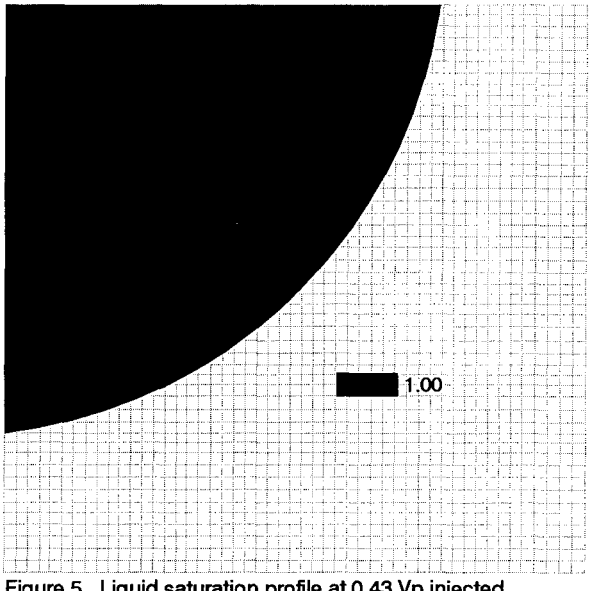


Figure 5. Liquid saturation profile at 0.43 Vp injected. Injection rate q=0.833 kg/s. Fraction vaporizing = 0.04. Five-point finite differencing.

However, these simulations have identified a number of difficulties inherent in the numerical simulation of a moving, vaporizing liquid-vapour interface and must, therefore, be regarded with caution.

The numerical predictions are highly sensitive to the finite difference scheme employed, the orientation and refinement of the grid and the boundary conditions. For example, simulations of the unstable case using 5-point and 9-point finite differencing schemes (Figures 6 and 7 respectively) lead to very different predictions of the evolution of the model interface. It is of paramount importance to resolve these dramatic discrepancies in the numerical simulations before we may build upon our analytical results and investigate the nonlinear growth of the interface numerically.

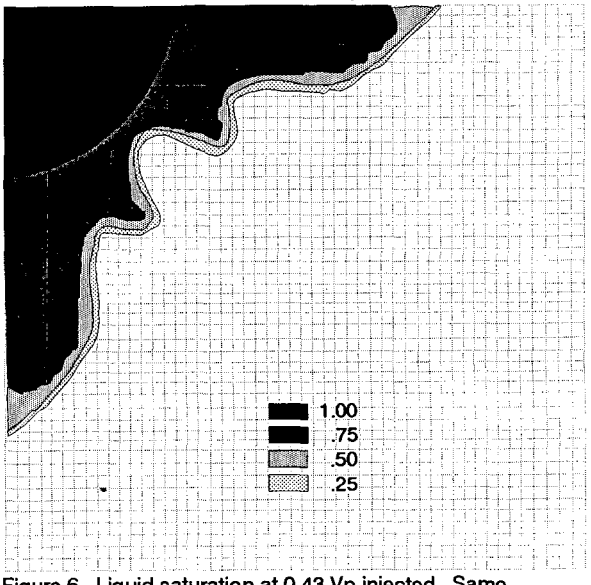


Figure 6. Liquid saturation at 0.43 Vp injected. Same conditions as in Figure 5, but q=0.0167 kg/s. Average fraction vaporizing = 0.58. 5-point finite differencing.

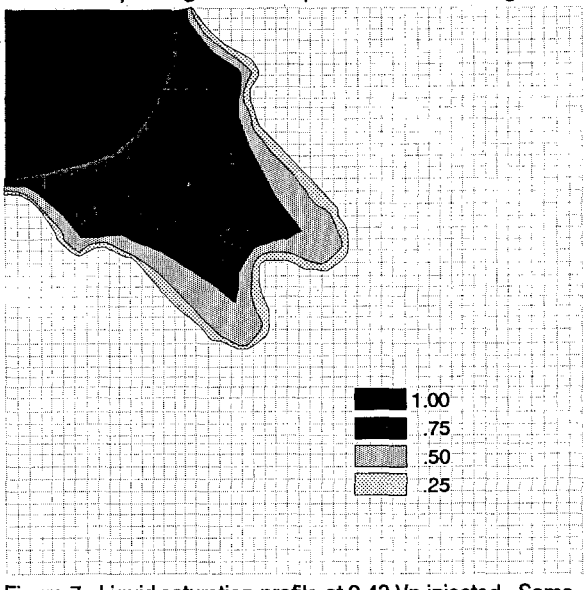


Figure 7. Liquid saturation profile at 0.43 Vp injected. Same conditions as in Figure 6, but 9-point finite differencing. Fraction vaporizing = 0.58.

## Conclusions

Vapour-saturated geothermal reservoirs may be recharged through the active injection and subsequent vaporization of liquid into the reservoir. As the rate of injection increases, the mass fraction of the liquid which vaporizes decreases although the overall rate of production of vapour increases. Furthermore, as the rate of injection increases, the temperature of the liquid-vapour interface increases. Therefore, owing to the thermal inertia of porous layers (Woods & Fitzgerald 1993) the liquid remaining in the reservoir is hotter, rendering the overall energy extraction through the vapour less efficient. We have described how, at low rates of injection, the liquid-vapour interface may become unstable and break up into fingers. This further increases the mass fraction of the liquid which can vaporize at low injection rates.

## Acknowledgments

SDF and AWW with to thank the Natural Environment Research Council for funding on this project. Funding for GMS was provided by the U.S. DOE, Assistant Secretary for Energy Efficiency & Renewable Energy, Geothermal Division, under DOE Contract NO DE-AC07-76ID01570. Thanks are due Jackie Brower, EG&G Idaho for manuscript preparation. Mention of specific products and/or manufacturers in this document implies neither endorsement of preference nor disapproval by the U.S. Government, any of its agencies, of EG&G Idaho, Inc. of the use of a specific product for any purpose.

## References

Bear, J. 1972 Dynamics of Fluids in Porous Media. Dover.

Bodvarsson, G. 1972, "Thermal problems in the siting of reinjection wells," Geothermics. 1(2) pp. 63-66.

Enedy, K.L. 1989, "The role of decline curve analysis at the Geysers," Trans. Geoth. Res. Counc. 13, pp. 383-392.

Enedy, S., Enedy, K. & Maney, J. 1991, "Reservoir response to injection in the southeast Geysers," Proc Stanford Geoth. Workshop 16.

Fitzgerald, S.D. & Woods, A.W. 1994, "The instability of a vaporisation front in a hot porous rock," Nature (in press).

Kerr, R.A. 1991, "Geothermal tragedy of the commons," Science 253, pp. 134-135.

Pruess, K., Calore, C., Celati, R. & Wu, Y.S. 1987, "An analytical solution for heat transfer at a boiling front moving through a porous medium," Int. J. Heat Mass Transfer. 30(12), pp. 2595-2602.

Pruess, K. & Enedy, S. 1993, "Numerical modeling of injection experiments at the Geysers," Proc. Stanford Geoth. Workshop 18.

Saffman, P.G. & Taylor, G.I. 1958, "The penetration of a fluid into a porous medium or Hele-Shaw cell containing a more viscous liquid," Proc. R. Soc. A. 245, pp. 312-329.

Schroeder, R.C., O'Sullivan, M.J., Pruess, K., Celati, R. & Ruffilli, C. 1982, "Reinjection studies of vapour-dominated systems," Geothermics 11(2), 93-119.

Truesdell, A.H. & White, D.E. 1973, "Production of superheated steam from vapor-dominated geothermal reservoirs," Geothermics. 2(3-4), 154-175.

Vinsome, P.K.W. 1991 TETRAD Users Manual. Dyad Engineering, Calgary, Canada.

Woods, A.W. & Fitzgerald, S.D. 1993, "The vaporization of a liquid front moving through a hot porous rock," J. Fluid Mech. 251, pp. 563-579.

PROCEEDINGS, Nineteenth Workshop on Geothermal Reservoir Engineering
Stanford University, Stanford, California, January 18-20, 1994
SGP-TR-147

# THE SOLUBILITY OF ELEMENTAL MERCURY IN WATER BETWEEN 30 AND 210°C

E. K. Mroczek

Institute of Geological and Nuclear Sciences
Wairakei Research Centre, P.B 2000
Taupo, New Zealand

## ABSTRACT

The solubility of elemental mercury ($Hg^0$) at temperatures between 30 and 210°C was determined by direct sampling of mercury saturated water contained in a fixed volume stainless steel autoclave. The temperature dependence of the solubility was best represented by the equation

$$\log_{10} x_{Hg} = -11.879 + 0.01206T$$

where $x_{Hg}$ is the mole fraction of dissolved $Hg^0$ and T is the temperature in degrees Kelvin.

At temperatures less than 100°C the best literature values are in good agreement with these results. At higher temperatures it is difficult to compare our data with previous studies as they show widely divergent results.

Comparison of field results for volatile mercury steam/water partitioning showed that up to $10^2$ times more mercury was retained in solution than would have been indicated from the theoretical distribution coefficients calculated from the solubility data. A kinetic limitation to the mercury steam/water distribution in the Webre separator was the most likely explanation although the presence of other nonvolatile mercury species could not be discounted.

## INTRODUCTION

The ability to predict the transport and partitioning behaviour of elemental mercury ($Hg^0$) during exploitation of geothermal reservoirs and power production requires reliable data for the vapour/liquid distribution coefficients. The distribution coefficient is derived from Henry's law constant which can be calculated from the solubility of elemental mercury. This study was undertaken because the large differences in $Hg^0$ solubility values between the few published experimental studies at temperatures above 100°C made it difficult to interpret field data collected at the Ohaaki geothermal field (Timperley and Mroczek 1989).

The importance of elemental mercury is that it appears to be the dominant chemical form of mercury found in chemical surveys of wells at New Zealand geothermal fields. This is in agreement with previous studies (Robertson et al. 1978) which showed that most if not all the mercury present in geothermal effluent is $Hg^0$, even at high $H_2S$ gas levels. Chemical modelling (Varekamp and Buseck 1984) has also shown that mercury transport occurs largely as $Hg^0$ in dilute hydrothermal systems with moderate amounts of S (<0.01 mol/litre).

## PREVIOUS WORK

At temperatures less than 100°C there have been numerous experimental solubility studies using a variety of measurement techniques. These studies also show a wide variation in values. The reason for the disagreement is not clear but trace contamination by air oxygen or not enough time allowed to attain the equilibrium solubility are commonly suggested reasons. Clever et al. (1985) reviewed and evaluated all available data and presented smoothed solubility data and smoothed Henry's constant equations over the temperature interval 273.15-393.15 K. The only high temperature study included in their evaluation was that of Sorokin (1973). Sorokin measured the solubility of mercury in water at temperatures of 573, 673 and 773 K at total pressures between 507 and 1013 bar. Samples were extracted from a flexible reaction cell autoclave at constant pressure and temperature. Clever et al. (1985) combined the hypothetical Henry's constant at the higher temperatures extrapolated to 1 bar with the Henry's constants calculated from the lower temperature data (277-346 K) of Glew and Hames (1971) to obtain an equation for Henry's constant over the temperature interval 393-773 K. Varekamp and Buseck (1984) also used the thermodynamic parameters calculated from Glew and Hames's (1971) data as well as Sorokin's (1973) data to calculate the solubility of $Hg^0$ to 250°C. Recently Gushchina et al. (1989) determined the solubility of mercury using a spectrophotometric technique at temperatures of 150, 200 and 250°C as well as evaluating previous work. Their results as well as those of Sorokin (1973), Sorokin's more recent experimental results and calculations as reported by Gushchina et al., Varekamp and Buseck's (1984) extrapolations, the smoothed literature interpolations of Clever et al. (1985) as well as selected low temperature

**Table 1.** Smoothed Mole Fraction Solubility, $-\log_{10} x_{Hg}$.

| t(°C) = | 30 | 60 | 72 | 100 | 120 | 150 | 200 | 210 | 250 | 300 |
|---|---|---|---|---|---|---|---|---|---|---|
| References | | | | | | | | | | |
| This Study | 8.22 | 7.86 | 7.72 | 7.38 | 7.14 | 6.78 | 6.17 | 6.05 | | |
| Sorokin (1973)*§ | | | | 7.38 | | | 5.33 | | | 4.42 |
| Sorokin calculated§ | 8.26 | 7.88 | 7.71 | 7.29 | 6.97 | 6.51 | 5.76 | 5.62 | 5.07 | 4.45 |
| Gushchina et al. (1989) | | | | | | 5.45 | 4.83 | | 4.21 | |
| Reichardt and Bonhoeffer (1931)* | | | | | 7.02 | | | | | |
| Sanemasa (1975) | 8.14 | 7.48 | | | | | | | | |
| Glew and Hames (1971) | 8.23 | 7.91 | 7.76 | | | | | | | |
| Varekamp, Buseck (1984) | 8.23 | 7.91 | 7.77 | 7.38 | 7.12 | 6.67 | 5.97 | 5.95 | 5.39 | |
| Clever et al. (1985) | 8.23 | 7.85 | 7.70 | 7.36 | 7.13 | | | | | |

*Experimental Data
§As reported by Gushchina et al. (1989)

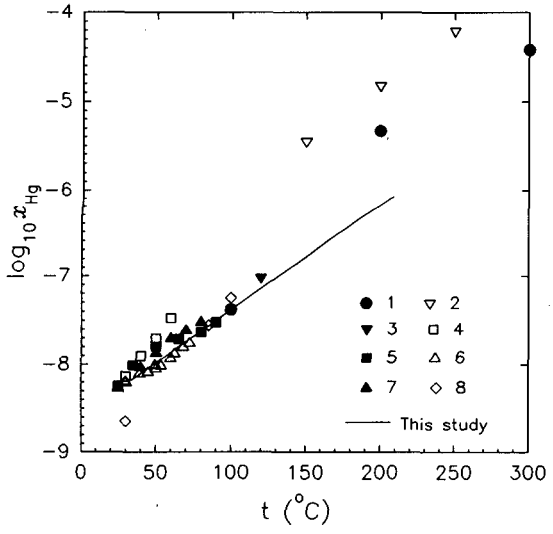


**Figure 1.** Comparison of experimental solubility values reported in the literature with the results from this study. 1 - Sorokin, 1973 (as reported by Gushchina et al, 1989), 2 - Gushchina et al., 1989; 3 - Reichardt and Bonhoeffer, 1931; 4 - Sanemasa, 1975; 5 - Choi and Tuck, 1962; 6 - Glew and Hames, 1971; 7 - Onat, 1974; 8 - Stock et al., 1934.

data are listed in Table 1. Figure 1 shows only the experimental data including more low temperature data below 100°C. As expected the Varekamp and Buseck's (1984) evaluations agree with Clever et al. (1985) due to the heavy weighting of the low temperature data of Glew and Hames (1971). At 150 and 200°C the solubility values of Gushchina et al. (1989) are significantly higher (1 log unit) than Sorokin's calculated values.

## EXPERIMENTAL

Distilled water was degassed and purged with nitrogen (99.99% minimum purity). Traces of oxygen in the gas were removed by passing the gas through a heated tube packed with copper turnings. A 100 $cm^3$ capacity 316 stainless steel autoclave containing about 0.1 to 0.5 g metallic mercury (BDH "Analar") was filled under nitrogen with 75 ml of water. In all runs, except #2, the water contained 0.001 mol $kg^{-1}$ hydrazine hydrate (BDH "Analar") to ensure no oxidation of mercury took place.

The autoclave was heated in a rocking furnace and the temperature was measured with a calibrated chromel-alumel thermocouple. The rocking was stopped 2 hours prior to sampling and the liquid was sampled through a short length of stainless steel capillary tubing using a low dead volume sampling valve directly into a weighed flask containing acidified 6% w/v potassium chromate solution. A pre-sample was first collected to clear the tubing of non-equilibrated fluid. Immediately after collection the sample was analysed for mercury using the flameless atomic absorption technique (Omang 1971).

At temperatures above 100°C equilibrium was only approached from below as the autoclave tended to leak with a reduction in temperature leading to higher but non-reproducible solubility values. In these experiments the liquid was equilibrated for between 4 and 31 days before sampling. The autoclave was thoroughly cleaned between runs including washing with hot nitric acid.

## RESULTS

The raw experimental mercury solubility results at temperatures between 30 and 210°C are presented in Table 2. The total pressure would have been slightly above saturated vapour pressure as the autoclave was not evacuated after filling under nitrogen. However the change in solubility due to such a small pressure increase is negligible. At 300°C the decrease in solubility is $3.4 \times 10^{-4}$ log units per bar (Sorokin, 1973). The standard deviation is a reflection of the uncertainties in the sampling and solubility method rather than the accuracy of the analytical technique (≈3%). The temperature

**Table 2.** Experimental Results, days = sampling time since commencement of run, n = No. of samples, t = temperature (°C), $x_{Hg}$ = mole fraction of mercury, SD = standard deviation, H = Henry's constant (bar), B = vapour/liquid distribution coefficient.

| Run | days | t | n | $x_{Hg}$x10$^9$ | SD | H | B |
|---|---|---|---|---|---|---|---|
| 1 | 14 | 58.5 | 6 | 20 | 3 | 1794 | 9603 |
| 1 | 20 | 78.8 | 3 | 22 | 1 | 5434 | 11931 |
| 2 | 5 | 89.6 | 3 | 44 | 5 | 5319 | 7609 |
| 3 | 5 | 131.5 | 2 | 104 | 4 | 17132 | 5882 |
| 4 | 4 | 90.5 | 3 | 39 | 2 | 5958 | 8235 |
| 4 | 7 | 91.3 | 3 | 36 | 3 | 6880 | 9223 |
| 4 | 11 | 91.3 | 3 | 32 | 1 | 7483 | 10030 |
| 5 | 9 | 60.3 | 3 | 18 | 1 | 2121 | 10439 |
| 5 | 11 | 60.3 | 3 | 12 | 1 | 3138 | 15441 |
| 5 | 14 | 60.3 | 2 | 17 | 1 | 2281 | 11227 |
| 6 | 4 | 39.8 | 3 | 10 | 1 | 1007 | 13756 |
| 6 | 7 | 39.3 | 3 | 10 | 1 | 933 | 13092 |
| 7 | 2 | 134.8 | 9 | 92 | 4 | 22382 | 6959 |
| 7 | 4 | 134.5 | 6 | 91 | 4 | 22401 | 7028 |
| 8 | 7 | 102.0 | 3 | 38 | 3 | 11726 | 10606 |
| 8 | 9 | 102.0 | 3 | 38 | 1 | 11011 | 9959 |
| 8 | 14 | 102.0 | 3 | 40 | 1 | 10731 | 9706 |
| 9 | 4 | 161.8 | 6 | 208 | 10 | 30164 | 4420 |
| 9 | 9 | 163.8 | 6 | 218 | 6 | 30357 | 4223 |
| 9 | 14 | 163.3 | 9 | 279 | 31 | 25501 | 3594 |
| 10 | 6 | 34.0 | 3 | 6.5 | 0.2 | 851 | 15959 |
| 10 | 8 | 34.0 | 2 | 6.40 | 0.02 | 835 | 15643 |
| 10 | 10 | 34.5 | 2 | 8 | 1 | 808 | 14743 |
| 11 | 6 | 185.5 | 6 | 515 | 41 | 29927 | 2435 |
| 11 | 8 | 185.0 | 6 | 469 | 4 | 29996 | 2470 |
| 12 | 6 | 104.2 | 3 | 49 | 4 | 10162 | 8499 |
| 12 | 8 | 107.5 | 3 | 55 | 6 | 11262 | 8398 |
| 13 | 6 | 54.0 | 3 | 12 | 1 | 1956 | 12972 |
| 13 | 9 | 57.5 | 2 | 15 | 1 | 2132 | 11962 |
| 14 | 28 | 207.8 | 3 | 1369 | 205 | 25357 | 1245 |
| 15 | 31 | 208.8 | 6 | 992 | 50 | 32350 | 1555 |

dependence of $\log_{10}x_{Hg}$, where $x_{Hg}$ is the dissolved mercury mole fraction, was linear within the experimental errors and the data is presented in Figure 2. The smoothed linear curve derived in this study is also shown in Figure 1 together with experimental results from previous work. The agreement at temperatures below 120°C is good but at 150 and 200 °C these results are over 1 log unit lower than those of Gushchina et al. (1989). The values are also lower than Sorokin's calculated results but the agreement is better, differing by about 0.4 log units at 150 and 200°C.

Henry's constant can be calculated from the solubility data assuming that $Hg^0$ is at equilibrium in the water and vapour phases, that the partial pressure of mercury ($P_{Hg}$) is such that the liquid mercury is in equilibrium with its aqueous solutions and assuming that the solubility of water in liquid mercury is negligible.

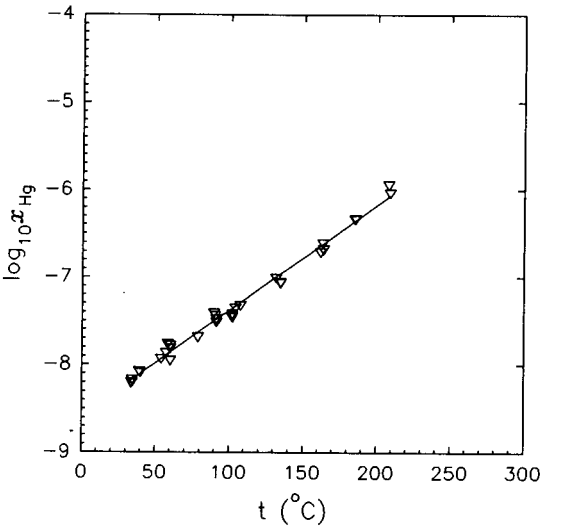


**Figure 2.** Temperature dependence of experimental and smoothed mole fraction solubilities.

Henry's constant (H) is calculated by

$$H = \frac{P^{o}_{Hg}}{x_{Hg_{(aq)}}} \qquad (1)$$

where $P^{o}_{Hg}$ is the vapour pressure of pure liquid mercury. From the ideal gas law the vapour/liquid distribution coefficient (B) can be calculated by

$$B = \frac{H\,Z}{R\,T} \qquad (2)$$

where Z is the specific molar volume of steam, R is the gas constant and T is the temperature in degrees Kelvin.

These simple relationships are expected to hold in these experiments and under most geothermal conditions because of the very low solubilities, vapour concentrations and partial pressures.

Henry's constants and distribution coefficients were calculated for each experimentally determined $Hg^0$ solubility using liquid mercury vapour pressures from Douglas et al. (1951). A least squares fit of the data showed that the best equation describing the temperature dependence of the data to be of the form

$$\log_{10}H = a + bT + c\log_{10}T + \frac{d}{T} \qquad (3)$$

where T is the temperature in degrees Kelvin. The regression for the distribution coefficients included the

**Table 3.** Regression Coefficients for Fitting Experimental Data in Table 2.

| | *a* | *b* | *c* | *d* | $r^2$ |
|---|---|---|---|---|---|
| $\log_{10}x_{Hg}$ | -11.88 | 0.012056 | - | - | 0.990 |
| $\log_{10}H$ | -535.94 | -0.13814 | 215.438 | 13944.2 | 0.992 |
| $\log_{10}B$ | -402.57 | -0.10581 | 161.042 | 11877.4 | 0.995 |

**Table 4.** Smoothed Elemental mole fraction Solubilities - $x_{Hg}$, Henry's Constants - H (bar) and Vapour/Liquid Distribution Coefficients - B. $\sigma$ = Standard Error of Estimate.

| t | $-\log_{10}x_{Hg}$ | $\sigma$ | $\log_{10}H$ | $\sigma$ | $\log_{10}B$ | $\sigma$ |
|---|---|---|---|---|---|---|
| 30 | 8.22 | 0.02 | 2.83 | 0.03 | 4.18 | 0.03 |
| 50 | 7.98 | 0.02 | 3.20 | 0.02 | 4.11 | 0.01 |
| 75 | 7.68 | 0.01 | 3.62 | 0.02 | 4.04 | 0.01 |
| 100 | 7.38 | 0.01 | 3.97 | 0.01 | 3.96 | 0.01 |
| 125 | 7.08 | 0.01 | 4.24 | 0.02 | 3.85 | 0.01 |
| 150 | 6.78 | 0.02 | 4.41 | 0.02 | 3.70 | 0.01 |
| 175 | 6.48 | 0.02 | 4.49 | 0.02 | 3.50 | 0.02 |
| 200 | 6.17 | 0.03 | 4.47 | 0.03 | 3.25 | 0.02 |
| 210 | 6.05 | 0.03 | 4.44 | 0.04 | 3.14 | 0.02 |

theoretical data value of 1 at the critical point of water. The regression coefficients for Equation 3 are listed in Table 3 and the smoothed calculated data is presented in Table 4.

The experimental and smoothed Henry's constants and distribution coefficients are presented in Figures 3 and 4 as well as the literature evaluations of Clever at al. (1985) and the experimental results of Gushchina et al. (1989). The agreement with the values of Clever et al. at low temperatures is good with greater deviations at high temperatures. The differences between Henry's constants and distribution coefficients calculated from Gushchina's et al. (1989) data are substantial because their solubility values are so much higher than found in this study.

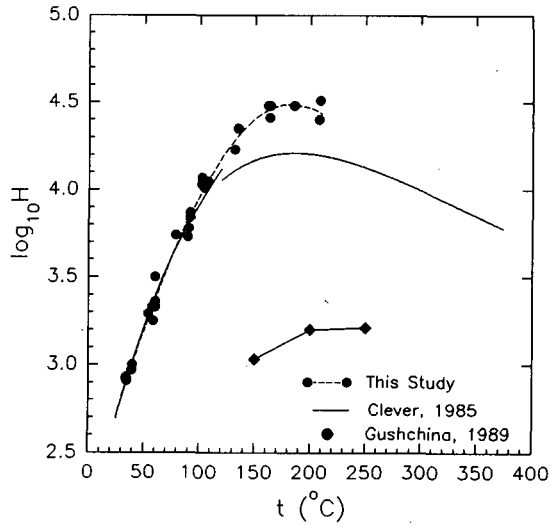


**Figure 3.** Temperature dependence of Henry's constant, H (bar) for dissolved elemental mercury.

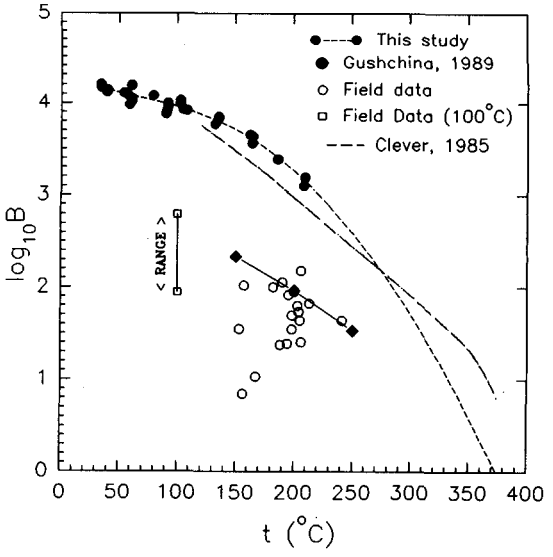


**Figure 4.** Experimental and field data for the temperature dependence of the distribution coefficient (B) of elemental mercury between aqueous vapour and liquid phases.

## DISCUSSION

### Experimental Solubility Values

Elemental mercury solubility values at temperatures above 100°C derived in this study are lower and the distribution coefficients higher than had been determined in previous experimental work. The attainment of equilibrium is critical for reliable solubility measurements. Glew and Hames (1971) showed that equilibrium at temperatures between 4 and 72°C was reached in less than 1 day under continuously stirred conditions while in the experiments of Gushchina et al. (1989) equilibrium at 150 and 250°C was attained in 8 and 2 hours respectively. Since the high temperature data of Gushchina et al (1989) and the mean literature value at 25°C was linear (log solubility vs. 1/T) they assumed their values were correct and suggested that equilibrium was not attained in all the other studies. This explanation seems unlikely given the equilibration times used in this study were between 2 and 31 days.

In this study hydrazine was used to ensure the mercury was not oxidized. Glew and Hames (1971) found that solubility was not affected by reducing agent (sodium

sulphite, hydrazine hydrate or sodium borohydride) concentrations between 0.001 and 0.02 mol $kg^{-1}$. At the higher temperatures association or complexing that might have occurred between the zerovalent elemental mercury and hydrazine or its decomposition products is likely to be negligible (Cobble, 1987) and obviously did not result in elevated total mercury solubilities. Sorokin (1973) took precautions to exclude oxygen and relied on the autoclave titanium to maintain reducing conditions relative to mercury and observed no oxidized mercury products. In the spectrophotometric method used by Gushchina et al. (1989) oxidized mercury would not have contributed to the $Hg^0$ absorption spectrum. However in their technique dissolved $HgCl_2$ was heated to 150°C and above to provide a known dissolved $Hg^0$ concentration. Oxidation may have affected the calibration which would have resulted in apparently higher $Hg^0$ solubility values. If this were the case they should not have obtained a consistent set of calibration data. According to the results of this study the lowest $HgCl_2$ concentration used would have resulted in oversaturation with respect to $Hg^0$ at 200 and 150°C. Gushchina et al. did not discuss the possibility of mercury oxidation by air affecting their results.

Comparison of Calculated Distribution Coefficients With Field Data

The major purpose of the study was to derive reliable mercury vapour/liquid distribution coefficients which can be used to calculate the steam and water mercury concentrations during boiling of geothermal fluid. The experimental data was compared with field data collected prior to the commissioning of the Ohaaki geothermal power plant (Timperley and Mroczek, 1989). In their study a portable Webre cyclone separator was used to collect steam and water samples of two phase fluid from a number of wells on the west bank of the Ohaaki geothermal field. An atmospheric (weirbox) water sample was collected at the same time as the samples at higher pressure. They found wide variations in mercury concentration between the wells, ranging from 16 to 181 ppb in the steam, 0.24 to 2.3 in high pressure separated water and 0.033 to 0.33 ppb in the weirbox water samples. High concentration in the Webre separated water samples were not correlated with high steam mercury concentrations, e.g. two samples separated at low pressure had 16 ppb steam concentrations and water concentrations of 2.3 and 1.5 ppb respectively. The results were not considered completely reliable. Possible reasons for the unreliability included imperfect separation in the Webre separator, slow kinetics for steam/water distribution in relation to fluid flow, the presence of non volatile mercury-sulphur species or oxidation of mercury during separation and sampling. However the data did not allow them to distinguish between these four effects. The mercury vapour/liquid distribution coefficients of these samples are plotted in Figure 4. The coefficients at atmospheric pressure were derived from the total discharge concentrations, which were calculated from mercury concentrations in steam and water from the Webre separated samples, and weirbox water mercury concentrations. The data shows wide scatter and the coefficients are significantly lower than the coefficients found in this study. The data is closest to the coefficients calculated from the solubility data of Gushchina et al. (1989) but in view of the previous discussion the agreement is considered to be fortuitous rather than an indication of the reliability of their results. If the experimentally derived ratios are to be of any use it is necessary to assess which of the reasons suggested by Timperley and Mroczek (1989) can best account for the discrepancy between the field and experimentally derived ratios.

Excluding two values which had significantly lower distribution coefficients the rest of the 21 Webre separated water samples were on average 48 times more concentrated than would have been expected from the experimentally derived coefficients. Imperfect steam/water separation in the Webre is an unlikely reason as the samples would have needed to be diluted by steam (carrying mercury with it) by an average of 2%. This level of dilution would require steam to water volume ratios of about 7 at 150 °C and 2 at 200°C. Separations better than 0.1% are possible with a mini Webre separator operated in the appropriate manner (Ellis and Mahon, 1977).

The presence of mercury species other than $Hg^0$ or oxidation of $Hg^0$ during sampling could also explain the lower distribution coefficients. Comparison of total steam mercury concentrations with on-line measurements using a mercury Zeeman spectrophotometer strongly supported the assumption that the steam phase species was elemental (Christenson and Persson, 1992). The on-line measurements taken over 1 hour varied between 21 to 23 ($\pm 1$) ppb compared to 22 ppb for a total mercury steam sample collected during this period.

The Webre separated water phase total mercury concentrations were always higher than corresponding weirbox samples. This suggested that the elevated Webre separated water mercury concentrations were not due to insoluble mercury sulphide as then the concentration would have been expected to increase on further flashing to atmospheric pressure. It is possible that aqueous mercury-sulphur species which are stable at the higher pressure but destabilize on flashing to atmospheric pressure could account for the nonvolatile fraction. It is not intended to present the results of chemical modelling here, but one preliminary calculation using the program SOLVEQ (Spycher and Reed, 1989) on an atmospheric BR9 water sample (typically pH 7.9 at 100°C, Hg(total) 0.033 ppb, $H_2S$(total) 2 ppm, ionic strength = 0.05) showed the water to be undersaturated (log Q/K = -3.3) with respect to cinnabar and except for $Hg^0$ all other mercury species were insignificant. For

this fluid at 100°C the equilibrium concentration of elemental mercury should have been less than 0.005 ppb.

Even if the formation of insoluble mercury sulphide was thermodynamically favoured the kinetics of the process are likely to be much slower than the time taken for separation and sample collection. In the Ohaaki power station only about 2 to 11% of the total incoming elemental mercury appears to be oxidized in the direct contact condenser and direct contact cooling tower (aerated condensate to steam ratio about 30:1). The amount of oxidized mercury is not constant and appears to be directly dependant on the colloidal sulphur burden in the circulating fluid (Timperley and Mroczek, 1989). The power station results suggest that the amount of mercury oxidation by sulphide may be much smaller than predicted thermodynamically because of slow kinetics compared to the rate of fluid flow through the system. In the field sampling situation the samples are collected quickly, directly into preservative and unlike the power station circuit water there is no sulphur due to the reducing conditions.

The reason for discrepancies between the experimentally derived distribution coefficients and the field work cannot be answered without further work but at this time the most favoured explanation is that there is a kinetic limitation on the mercury steam/water distribution.

## CONCLUSIONS

1. The temperature dependence of the solubility of elemental mercury in water is linear within experimental errors between 30 and 210°C.

2. The values above 150°C are lower than found in previous studies but equilibration times were long and a reducing agent was used to limit oxidation of mercury.

3. The derived steam/water distribution coefficients did not compare well with concentration ratios calculated from Webre steam and water separated samples collected at Ohaaki Geothermal field. The exact cause for this discrepancy has not been determined although a kinetic limitation on the steam/water distribution during separation appears to be the most likely answer.

## ACKNOWLEDGMENT

Acknowledgment to Electricity Corporation of New Zealand for permission to use mercury analyses of the Ohaaki production wells.

## REFERENCES

Choi S.S. and Tuck D.G. A Neutron-activation Study of the Solubility of Mercury in Water. J. Chem. Soc. #797, 4080, 1962.

Christenson B.W. and Persson W. Wairakei Research Centre Unpublished Results, 1992.

Clever H.L., Johnson S.A. and Derrick M.E. The Solubility of Mercury and Some Sparingly Soluble Mercury Salts in Water and Aqueous Electrolyte Solutions. J. Phys. Chem. Ref. Data, 14, 631, 1985.

Cobble J.W. A Theory on Mercury in Geothermal Fluid. EPRI Report #AP-5111, 1987.

Douglas T.B., Ball A.F. and Ginnings. Heat Capacity of Liquid Mercury Between 0° and 440°C; Calculation of Certain Thermodynamic Properties of the Saturated Liquid and Vapour. J. Res. Natl. Bur. Stand. 46, 334, 1951.

Ellis A.J. and Mahon W.A.J. Chemistry and Geothermal Systems. Academic Press, 1977.

Glew D.N. and Hames D.A. Aqueous Nonelectrolyte Solutions. Part X. Mercury Solubility in Water. Can. J. Chem. 49, 3114, 1971.

Gushchina L.V., Belevantsev V.L. and Obolenskiy A.A. Spectrophotometric Determination of the Solubility of $Hg_l$ in Water. Geokhimiya, No. 2, 274, 1989. [Geochem. Int. 26, 97, 1989]

Omang S.H. Determination of Mercury in Natural Waters and Effluents by Flameless Atomic Absorption Spectrophotometry. Anal. Chem. Acta 53, 415, 1971.

Onat E. Solubility Studies Of Metallic Mercury in Pure Water at Various Temperatures. J. Inorg. Nucl. Chem. 36, 2029, 1974.

Reichardt H. and Bonhoeffer K.F. The Absorption Spectrum of Dissolved Mercury. Z. Phys. 67, 780, 1931.

Robertson D.E., Fruchter J.S., Ludwick J.D., Wilkerson C.L., Crecelius E.A. and Evans J.C. Chemical Characterization of Gases and Volatile Heavy Metals in Geothermal Effluents, GRC Transactions, 2, 579 (1979).

Sanemasa I. The Solubility of Elemental Mercury Vapour in Water. Bull. Chem. Soc. Jpn. 48, 1795, 1975.

Sorokin V.I. Solubility of Mercury in Water at Temperatures from 300 to 500°C and Pressures from 500 to 1000 atm. Doklady Akademii Nauk SSSR, 213, 852, 1973. [Dokl. Chem. 213, 905, 1973]

Spycher N.F. and Reed M.H. SOLVEQ: A Computer Program for Computing Aqueous-Mineral-Gas Equilibria. 1989.

Stock A., Cucuel F., Gerstner F., Kohle H. and Lux H., Z. Anorg. Allg. Chem. 217, 214, 1934.

Timperley M.H. and Mroczek E.K. Mercury in Bore Fluids at Ohaaki, Wairakei Research Centre Memo to Electricity Corporation of New Zealand, 1989.

Varekamp J.C. and Buseck P.R. The Speciation of Mercury in Hydrothermal Systems, with Applications to Ore Deposition. Geochim. et Cosmochim. Acta, 48, 177, 1984.

PROCEEDINGS, Nineteenth Workshop on Geothermal Reservoir Engineering
Stanford University, Stanford, California, January 18-20, 1994
SGP-TR-147

# CHARACTERIZATION OF ROCK FOR CONSTRAINING RESERVOIR SCALE TOMOGRAPHY AT THE GEYSERS GEOTHERMAL FIELD

G. N. Boitnott
New England Research, Inc.

B. P. Bonner
Lawrence Livermore National Laboratory

## ABSTRACT

A suite of laboratory measurements are being conducted on Geysers graywacke recovered from a drilled depth of 2599 meters in NEGU-17. The tests are being conducted to characterize the effect of pressure and fluid saturation on the seismic properties of the graywacke matrix. The measurements indicate that the graywacke is an unusual rock in many respects. Both compressional and shear velocities exhibit relatively little change with pressure. Water saturation causes a slight increase in the compressional velocity, quantitatively consistent with predictions from the Biot-Gassmann equations. Shear velocity decreases with water saturation by an amount greater than that predicted by the Biot-Gassmann equations. This decrease is attributed to chemo-mechanical weakening caused by the presence of water. Measurements of $Q_s$ from torsion experiments on room dry samples at seismic frequencies indicate unusually high $Q_s$ (≈500). Water saturation decreases the shear modulus by 12 percent, again indicative of chemo-mechanical weakening. $Q_s$ is lower for the water saturated condition, but still relatively high for rock at low stress. Results of ultrasonic pulse propagation experiments on partially saturated samples are typical of low porosity rocks, being characterized by a monotonic decrease in compressional and shear velocity with decrease in saturation. An increase in shear velocity and low frequency shear modulus after vacuum drying indicates the presence of chemo-mechanical weakening resulting from the presence of small amounts of water.

## I. INTRODUCTION

Field seismic imaging experiments at the Geysers have indicated velocity, $V_p/V_s$, and attenuation anomalies associated with the dry stream reservoir [*O'Connell and Johnson*, 1991; *Zucca et al.*, 1994]. They observe an increase in compressional velocity and decrease in $Q_p$ with depth below the dry steam reservoir and suggest that they reflect changes in the degree of fluid saturation associated with the water/steam transition. However, this interpretation of the field seismic results has been hampered by a lack of knowledge of the physical properties of the reservoir rocks. Of particular interest is whether the observed variations of the field scale velocity and attenuation can be explained by the intrinsic properties of the matrix and its sensitivity to the degree of fluid saturation.

There are four phenomena typically assumed to be important in controlling the effect of saturation on velocities of rock. These can be summarized briefly as follows:

- **Local-Flow:** unrelaxed fluid in thin pore spaces and/or at grain contacts produces a frequency dependence on the measured velocity (see for discussion *Mavko and Jizba* [1991]). The presence of local-flow causes a visco-elastic like rheology exhibiting both velocity dispersion and attenuation. This effect is strongest at low effective pressures due to the increased compliance of and grain contacts and pores. The frequency band over which local-flow causes dispersion is largely unknown, however it is typically thought to be in the kHz to MHz range for most rocks.
- **Frame Weakening:** The presence of aqueous solutions in the pore space interacts with the rock matrix and alters the mechanical properties of the bulk material. Chemo-mechanical weakening of quartz and other minerals by the presence of water is well known and thus velocities measured under water saturated conditions should be lower than predictions based on the velocities of dry samples.
- **"Biot" effects:** the bulk modulus of the pore fluid acts to stiffen the pores to the deformation of the compressional wave, thus increasing the compressional velocity (see for discussion *Biot*, [1956a,b]). There is no similar effect on the shear modulus.
- **Density effects:** the addition of the pore fluid increases the bulk density of the material, thus decreasing both the compressional and shear velocities for a given set of elastic moduli.

The "Biot" and density effects combined constitute the Biot-Gassmann equations (see *Murphy*, [1982], *Winkler*, [1985]), which are commonly used for predicting the effects of fluid saturation on velocities at seismic frequencies. The experiments presented here are designed to determine which effects are active under various conditions of pressure, saturation, and frequency.

## II. ULTRASONIC VELOCITIES

A variety of ultrasonic pulse propagation experiments have been conducted on three samples of core from reservoir graywacke in the northeast Geysers (NEGU-17: drilled depth 2599 *m*). One plug was cored parallel (denoted X) and the other two cored perpendicular (Y1 and Y2) to the axis of the borehole. Identical tests were performed on Berea sandstone and Westerly granite for comparison, since measurements on Westerly and Berea have been used to infer seismic properties of geothermal areas [*Ito et al.*, 1979; *DeVilbiss*, 1980].

Each sample was nominally 1 inch in diameter and 1 inch long. Porosity was measured on the intact plugs using an $He^2$ gas pycnometer after drying in a vacuum at 80 C. The results are summarized in Table 1, illustrating that the graywacke exhibits very little porosity. The variation between the three samples reflects the fact that samples Y1 and Y2 contain veins with associated vugs and pores, while sample X was free of visible veins (see *Gunderson,* [1990] for a discussion of the porosity distribution in similar rocks). Included in Table 1 is the weight gain per unit volume after saturation with distilled water. For the NEGU-17 samples, each sample appears to have adsorbed more water than would be expected based on the pycnometer results (consistently by an amount of 9 mg/cc). This may be indicative of water absorbing minerals, however the pycnometer results should be viewed as preliminary and must be reproduced to make sure that very tight porosity (requiring unusually long pressure equilibration times) was not missed in the pycnometer results reported here.

TABLE 1

| Rock Type | Sample | Porosity | Grain Density | Weight Gain |
|---|---|---|---|---|
| | | % | g/cc | g/cc |
| NEGU-17 | X | 0.11 | 2.666 | 0.010 |
| NEGU-17 | Y1 | 0.93 | 2.659 | 0.018 |
| NEGU-17 | Y2 | 0.90 | 2.668 | 0.018 |
| Westerly | wd1 | 1.0* | 2.680 | 0.010 |
| Berea | bd1 | 20.67 | 2.690 | 0.191 |
| Berea | bd2 | 20.24 | 2.686 | 0.202 |

* assumed based on published data.

Compressional and shear ultrasonic velocities were measured as a function of confining pressure from 2 to 90 MPa. The results are summarized in Figure 1. Along with the dry and saturated ultrasonic velocities, the predicted velocities based on Biot-Gassmann equations are given for reference. Note that NEGU-17 sample exhibits different behavior from both Berea and Westerly in a number of ways.

In Berea, all four mechanisms listed above are thought to contribute to differences in dry and saturated velocities. The Biot-Gassmann effect appears to explain roughly half of the difference between dry and saturated compressional velocities. The rest is typically attributed to local-flow, although we should not ignore the presence of frame weakening. For shear, the saturated velocities are lower than predicted by Biot-Gassmann, implying that the amount of frame weakening is greater than the stiffening due to local-flow for shear. In contrast, for Westerly granite, both the compressional and shear velocities are greater saturated than dry, reflecting the fact that local-flow effects are dominant for both compressional and shear velocities.

For the NEGU-17 samples, compressional velocities are only slightly higher saturated than dry, being quantitatively consistent with the Biot-Gassmann predictions. This is unusual for measurements at ultrasonic frequencies, implying that local-flow is not important for the NEGU-17 matrix. Shear velocities are lower than predicted by Biot-Gassmann, particularly at high stress, suggesting that frame weakening is important. However, the reduction in shear velocity with saturation was not found in sample Y1, which exhibited similar compressional effects but no measurable effect of saturation on the shear velocity (as predicted by Biot-Gassmann). Thus the weakening may be anisotropic or spatially heterogeneous at the centimeter to decimeter scale. More testing is required to have confidence in this interpretation.

## III. TORSION AT SEISMIC FREQUENCIES

A sample from the same specimen of NEGU-17 core was also tested in a torsion apparatus at seismic frequencies (see *Bonner and Wanamaker,,* [1991] and *Bonner et al.,* [1992] for a more complete discussion of the apparatus and technique). The apparatus is a driven mechanical oscillator composed of a segmented torsional spring (the segments include the sample and two aluminum torsion bars) and an electromagnetic rotor. The first torsion bar is fixed to the frame of the apparatus. The rotor, which is fixed to the second torsion rod attached to the other end of the sample, is torqued by six electromagnets symmetrically arranged about the rod. Strains are measured by pairs of eddy current proximity detectors mounted on the torsion bars which are connected to the ends of the sample via collets. The strain measurement at the fixed end (which includes only the elastic response of the torsion bar), is used as a measure of the torque, while the other sensor measures the strain of the sample. Both the shear modulus and shear attenuation are computed as a function of frequency and shear strain amplitude while the sample is subjected to a continuous sinusoidal oscillation. The tests reported here where conducted at frequencies ranging from 4 to 40 *Hz* with peak shear strains from 1 to $3 \cdot 10^{-6}$. No end load or confining pressure were applied to the sample during testing.

One thin rod, 0.89 *cm* in diameter and 5.08 *cm* in length was cored parallel to the core axis. The sample was saturated with distilled water and tested. The specimen was then vacuum dried at 35 degrees C for 24 hours and retested while in a dry argon atmosphere. The results, along with a comparison of shear moduli with those computed from ultrasonic velocities are shown in Figure 2.

Water saturation has a dramatic effect on both the shear modulus and the attenuation. Shear modulus decreases with saturation by about 12 percent. This reduction, which is a clear indication of frame weakening due to the presence of water, is consistent with but much larger than the weakening observed in the ultrasonic data (most likely due to the different pressure conditions of the two types of tests). In both the dry and saturated results, there is a slight increase in shear modulus with frequency, with the saturated sample exhibiting a greater sensitivity to frequency than in the dry case. The shear moduli are relatively high for rock, but less than those determined from the ultrasonic velocities. This could reflect the difference in load on the samples and/or that there is moderate dispersion between seismic and ultrasonic frequencies (particularly for the saturated case). Shear attenuation increases with saturation and exhibits a significant increase with frequency, consistent with velocity/modulus dispersion at higher frequencies (i.e. between seismic and ultrasonic). Again, the frequency effect is largest for the saturated case, possibly indicating that the frame weakening is influencing (activating) anelastic/inelastic mechanisms of deformation.

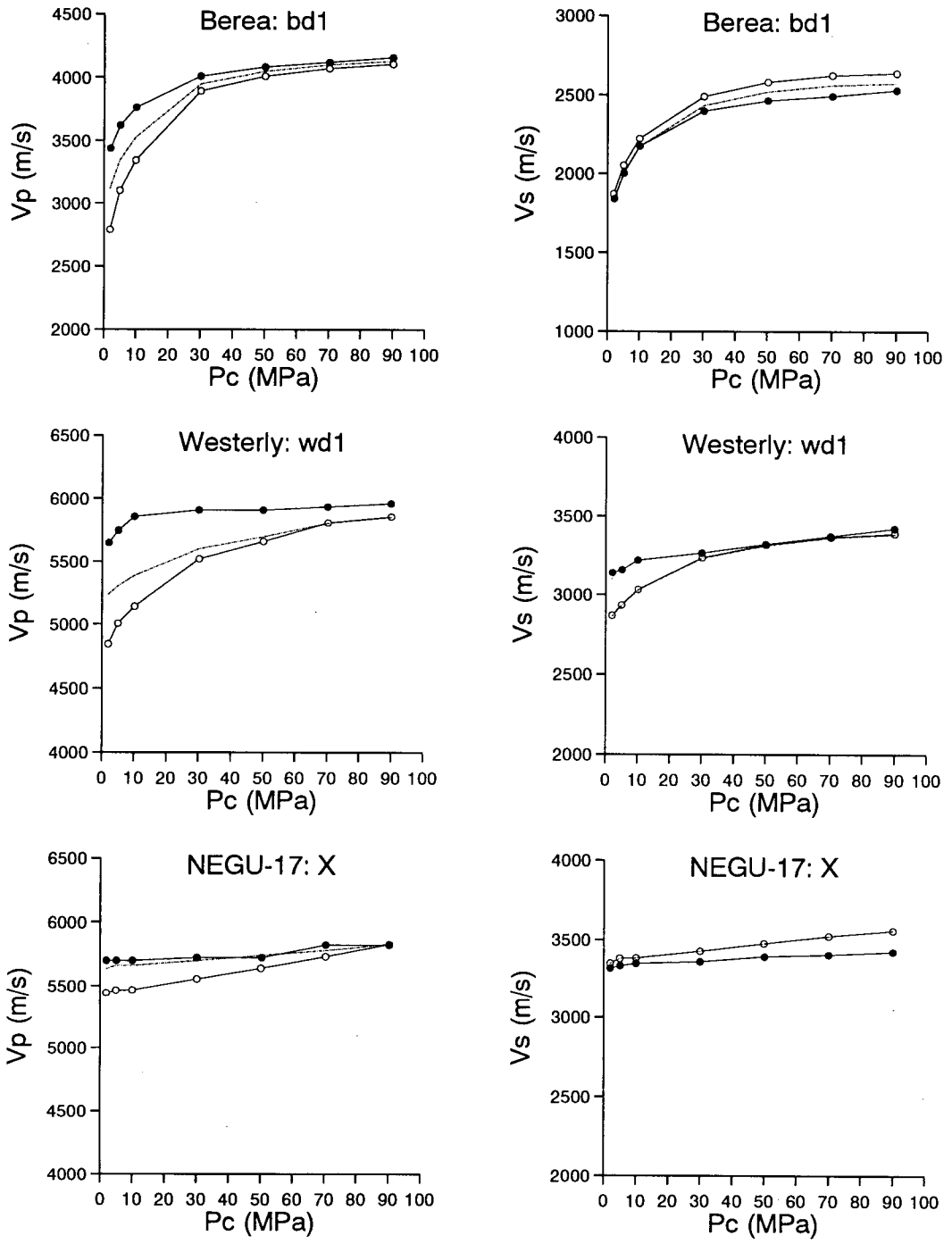


Figure 1: Ultrasonic velocities as a function of confining pressure for dry and saturated samples of Berea sandstone, Westerly granite, and NEGU-17 graywacke. Results on dry samples are shown with open circles and saturated with closed circles. The predicted saturated velocities using the dry velocities and the Biot-Gassmann equations are shown for reference (dot-dashed line).

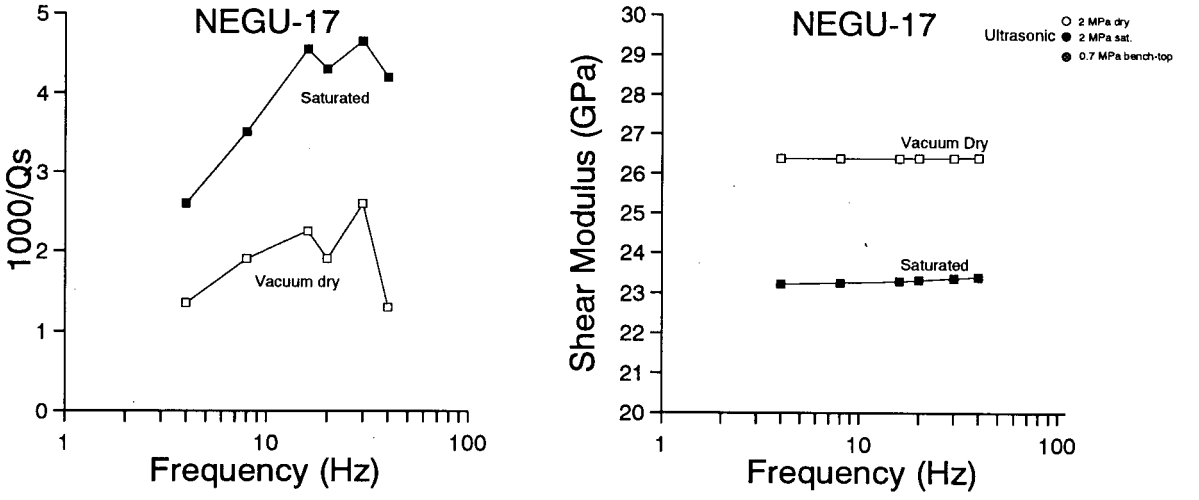


Figure 2: Shear attenuation and shear modulus as a function of frequency for NEGU-17 graywacke. The results for the dry case are shown with open boxes and the results for the saturated case are shown with closed boxes. Shear moduli computed from ultrasonic shear velocities are shown to the right (circles) for reference.

## IV. EFFECTS OF PARTIAL SATURATION

An important issue to be addressed is the effect of partial saturation on the acoustic velocities and attenuation. A number of studies have indicated that compressional wave attenuation and $V_p/V_s$ are quite sensitive to partial saturation. In addition, experiments on acoustic velocities through the steam-water transition ( *Ito et al.* [1979], *DeVilbiss-Munoz* [1980]) have illustrated a variety of phenomena which may be explainable (at least in part) by a simple partial saturation model. As a starting point, ultrasonic velocities have been measured as samples dried from fully saturated to room dry conditions. The results indicate a variety of responses, dependent on the dominant mechanisms of velocity dispersion for each rock type. Results of compressional and shear velocities as a function of time are shown in Figure 3.

For Berea, we see a complex response to drying which seems to reflect the separation of the various dispersion mechanisms from one another. The compressional velocity exhibits a sharp decrease with decreasing saturation from 100% to approximately 90%, reflecting the drainage of the larger pores and thus the loss of the Biot effect. The slight increase in compressional velocity for saturations from 90% to 10% reflects the decrease in bulk density due to the loss of pore fluid. Below 10% saturation, a relatively strong minimum in the compressional velocity is thought to reflect the loss of the local-flow stiffening (as the small compliant pores and grain contacts dry) followed by a recovery of the frame weakening effect during the final stages of drying. The shear velocity history is consistent with this interpretation, were we see a gradual increase in shear velocity from 100% to 10% (decrease in bulk density due to the loss of fluid). At about 10% saturation and below, a strong minimum in the shear velocity appears, reflecting the loss of the local-flow effect followed by recovery of the frame weakening. Note that in the shear response, the local-flow effect is of the same order as the frame weakening effect, consistent with our interpretation from the results in section II.

The response of the NEGU-17 graywacke and Westerly granite are quite different from that of Berea. In these samples, we see a monotonic decrease in both the compressional and shear velocities with drying. This may result from the fact that the drying of low porosity rocks is such that the water distribution is less uniform, not being able to selectively drain larger pores first. Thus the change in velocities are more gradual and monotonic with drying, reflecting loss of both local-flow and Biot effects.

For the case of the NEGU-17 graywacke (X), the degree of drying after 17 hours was only near 50%, and thus longer term tests are required to fully characterize the drying history. After the test, the sample was vacuum dried at 80 C and remeasured, the results being shown in Figure (3c). Here we see that further drying caused a decrease in compressional velocity and a slight increase in shear velocity, consistent with our observations of frame weakening for shear discussed in sections II and III.

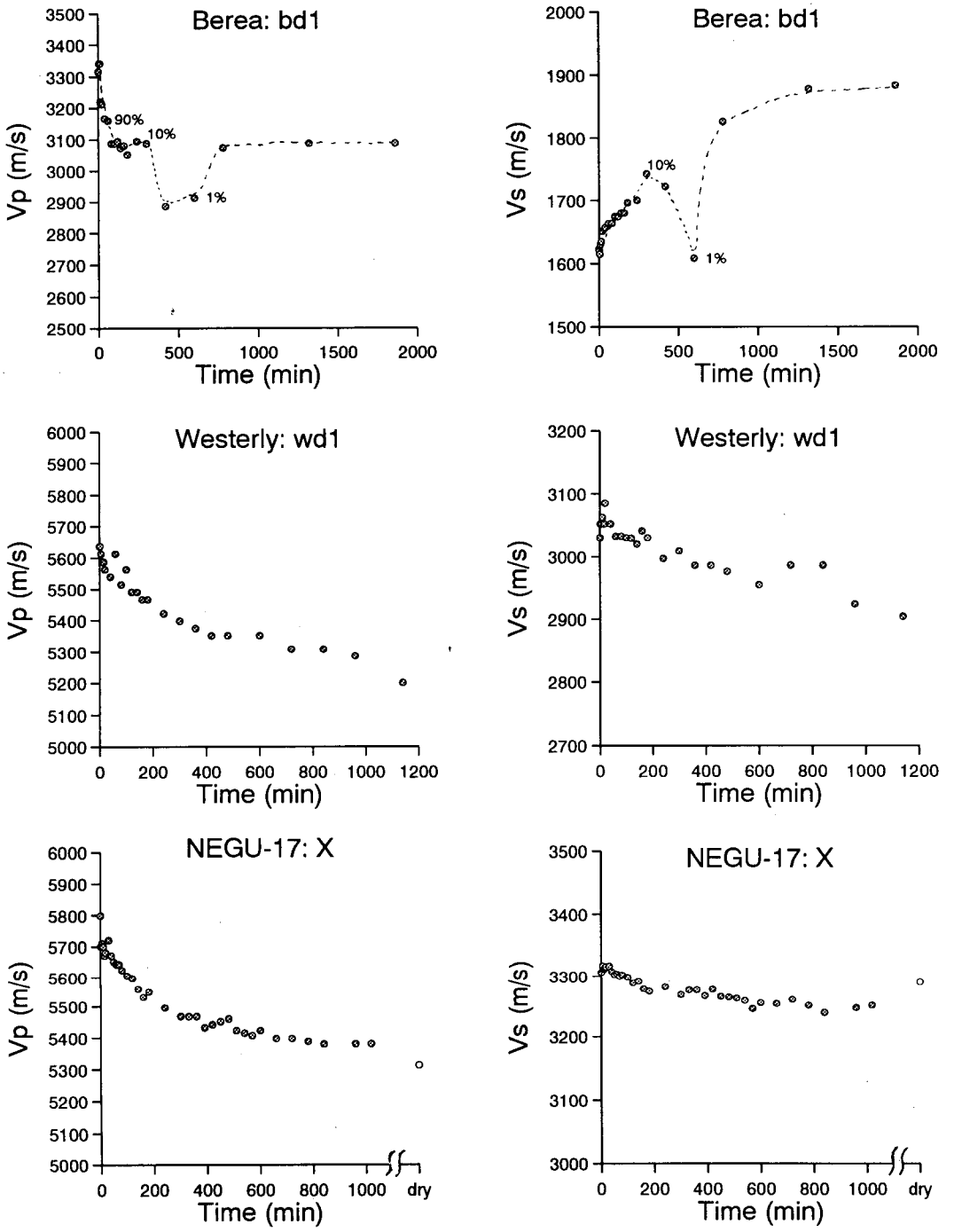


Figure 3: Compressional and shear ultrasonic velocities as a function of time during air-drying from a fully saturated state. The samples were subjected to a 0.7 MPa unconfined axial load during the tests. For the case of Berea sandstone, a complex relationship between velocity and saturation is observed (percentage saturation is shown at key points). In contrast, Westerly granite and NEGU-17 graywacke exhibit monotonic decreases in both compressional and shear velocities with decreasing saturation. For Westerly and NEGU-17, drying was not complete at the end of the test. For the NEGU-17 graywacke, velocities after vacuum drying are shown to the right of each plot.

## V. DISCUSSION AND CONCLUSIONS

Laboratory measurements on reservoir graywacke recovered from NEGU-17 indicate that the matrix is very tight, yielding high velocities and very low acoustic attenuation. The lack of a strong pressure effect on the velocities even at low confining stresses indicates that the porosity is confined to relatively stiff pores and/or mineralized grain contacts and micro-fractures (in contrast to other tight rocks such as Westerly granite where the presence of compliant micro-cracks are easily recognized in velocity vs. pressure data). Similarly, the effects of fluid saturation on ultrasonic velocities shows no evidence of a strong local-flow stiffening, again suggesting that the porosity is primarily in the form of stiff pores supported by welded grain contacts. Frame weakening due to the presence of water in the pore structure is a relatively large effect and is worthy of further investigation.

Based on the work of *Zucca et al.* [1994], compressional velocities in the reservoir range from 4400 to 5600 m/s. Their work suggests that the dry steam reservoir is correlated with low compressional velocities, exhibiting a velocity deficit on the order of 10 percent. Compressional wave attenuation appears low in these same regions, with $1/Q_p$ on the order of 0.008 as compared with higher values both above and below the dry steam reservoir (near 0.017). Comparing these observations with the laboratory data reported here, we see the following:

- Compressional velocities in the field are lower (on average) than the laboratory measured values, however the laboratory values are within the variation observed in the field. The laboratory measurements reported here, being made on intact matrix, should (and do) provide an estimate of the upper limit on field scale velocities at depth, and are quantitatively consistent with results of tomographic inversions [*O'Connell and Johnson*, 1991; *Zucca et al.*, 1994].
- Compressional velocities in the steam reservoir as low as 4400 m/s reported by *Zucca et al.,* [1994] are hard to explain based on the laboratory data, suggesting that the core studied here is not representative of the reservoir as a whole. This may be indicative of the presence of joints and fractures in the reservoir and their influence on the bulk (field scale) seismic properties. Alternatively, the effect of temperature and/or the presence of steam may be important and is currently under investigation. In particular, we expect that temperature should influence the frame weakening.
- The variation in $1/Q_p$ inferred from the field tomography (about a factor of 2) is consistent with what we find for the effects of saturation on $1/Q_s$. Quantitative comparison of field and laboratory measurements of $1/Q$ are made difficult by the fact that field measurements are values averaged over large volumes and based on relative measures of dispersion. In addition, estimating $1/Q_p$ from $1/Q_s$ is difficult for conditions of partial saturation without additional measurements.

## VI. ACKNOWLEDGMENTS

We would like to thank Jeff Hulen and Marshall Reed for selecting and obtaining the core for these measurements. This work has been funded by DOE contract DE-AC07-76IDO1570 to EG&G Idaho, Inc., subcontract C93-134002 to New England Research, Inc. Work at LLNL was funded by the DOE Office of Geothermal Energy.

## VII. REFERENCES

Biot, M. A., Theory of propagation of elastic waves in a fluid-saturated porous solid: I. Low-frequency range, *J. Acous. Soc. Amer.*, 28, 168-178, 1956.

Biot, M. A., Theory of propagation of elastic waves in a fluid-saturated porous solid: II. Higher frequency range, *J. Acous. Soc. Amer.*, 28, 179-191, 1956.

Bonner, B. P., and B. J. Wanamaker, Nonlinear attenuation effects outside the zone of macroscopic failure, *in* Explosion Source Phenomenology, Geophysical Monograph 65, AGU, 1991.

Bonner, B. P., D. R. Lesuer, C. K. Syn, and A. E. Brown, Damping measurements for ultra-high carbon steel/brass laminates, *in* Proceedings of the Damping of Multiphase Inorganic Materials Symposium, ASM International, Chicago, IL, 2-5 Nov., 1992.

DeVilbiss-Munoz, J. W., Wave dispersion and Absorption in partially saturated rocks, Ph. D. Thesis, Stanford U. 1980.

Gunderson, R. P., Reservoir matrix porosity at the Geysers from core measurements, *Geothermal Resources Council Transactions,* 14, 1661-1665, 1990.

Ito, H., J. DeVilbiss, and A. Nur, Compressional and shear waves in saturated rock during water-steam transition, *J. Geophys. Res.*, 84, 4731-4735, 1979.

Mavko, G. and D. Jizba, Estimating grain-scale fluid effects on velocity dispersion in rocks, *Geophysics*, 56, 1940-1949, 1991.

Murphy, W. F. III, Effects of microstructure and pore fluids on the acoustic properties of granular sedimentary materials, Ph. D. Thesis, Stanford U., 1982.

O'Connell, D. R. H., and L. R. Johnson, Progressive inversion for hypocenters and P wave and S wave velocity structure: Application to the Geysers, California, geothermal field, *J. Geophys. Res.*, 96, 6223-6236, 1991.

Winkler, K. W., Dispersion analysis of velocity and attenuation in Berea sandstone, *J. Geophys. Res.,* 90, 6793-6800, 1985.

Zucca, J. J., L. J. Hutchings, and P. W. Kasameyer, Seismic velocity and attenuation structure of the Geysers geothermal field, California, *Geothermics*, in press, 1994.

PROCEEDINGS, Nineteenth Workshop on Geothermal Reservoir Engineering
Stanford University, Stanford, California, January 18-20, 1994
SGP-TR-147

# Oxygen Isotope Geochemistry of The Geysers Reservoir Rocks, California

Richard P. Gunderson[1] and Joseph N. Moore[2]

1. Unocal Geothermal—Energy Resources Division, Santa Rosa, California 95406
2. University of Utah Research Institute, Salt Lake City, Utah 84108

## ABSTRACT

Whole-rock oxygen isotopic compositions of Late Mesozoic graywacke, the dominant host rock at The Geysers, record evidence of a large liquid-dominated hydrothermal system that extended beyond the limits of the present steam reservoir. The graywackes show vertical and lateral isotopic variations that resulted from gradients in temperature, permeability, and fluid composition during this early liquid-dominated system. All of these effects are interpreted to have resulted from the emplacement of the granitic "felsite" intrusion 1-2 million years ago. The $\delta^{18}O$ values of the graywacke are strongly zoned around a northwest-southeast trending low located near the center of and similar in shape to the present steam system.

Vertical isotopic gradients show a close relationship to the felsite intrusion. The $\delta^{18}O$ values of the graywacke decrease from approximately 15 per mil near the surface to 4-7 per mil 300 to 600 m above the intrusive contact. The $\delta^{18}O$ values then increase downward to 8-10 per mil at the felsite contact, thereafter remaining nearly constant within the intrusion itself. The large downward decrease in $\delta^{18}O$ values are interpreted to be controlled by variations in temperature during the intrusive event, ranging from 150°C near the surface to about 425°C near the intrusive contact. The upswing in $\delta^{18}O$ values near the intrusive contact appears to have been caused by lower rock permeability and/or heavier fluid isotopic composition there.

Lateral variations in the isotopic distributions suggests that the effects of temperature were further modified by variations in rock permeability and/or fluid-isotopic composition. Time-integrated water:rock ratios are thought to have been highest within the central isotopic low where the greatest isotopic depletions are observed. We suggest that this region of the field was an area of high permeability within the main upflow zone of the liquid-dominated hydrothermal system. The lowest water:rock ratios and permeabilities are found in the Northwest Geysers where the least depleted rocks occur.

## INTRODUCTION

Recent isotopic studies of steam from The Geysers geothermal field in northern California (Fig. 1) have documented large variations in both its $\delta D$ and $\delta^{18}O$ values (Gunderson, 1989; Truesdell et al., 1992). In the southern part of the field, $\delta D$ values of the steam range from -50 to -60 per mil and are similar to local meteoric waters, while in the northwest part of the field the $\delta D$ values of the steam are lighter (-40 to -50 per mil). The corresponding $\delta^{18}O$ values range from a low of -7 per mil in the south, again similar to meteoric waters, to as much as +3 per mil in the northwest.

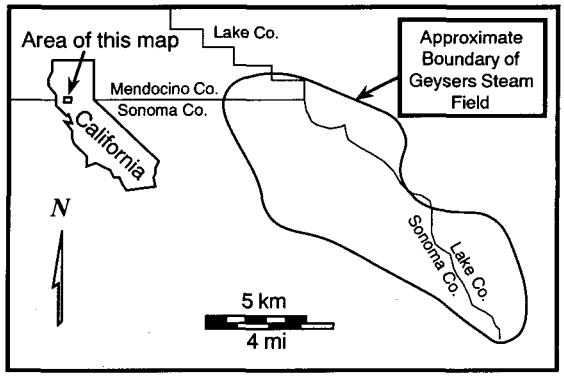


**Figure 1.** Location map of The Geysers.

Gunderson (1989) showed that there is a correlation between the oxygen isotopic compositions of the steam and the average isotopic composition of the reservoir rocks in the same wells. Based on this correlation, he suggested that the isotopic composition of the steam is partly controlled by equilibrium with the enclosing rocks. Because of the low porosities of the reservoir rocks (Gunderson, 1990), the isotopic composition of a relatively small amount of steam, which was initially held as liquid water in the pores and fractures, will be buffered by much larger volumes of rock.

Although the studies of Gunderson (1989) demonstrated the importance of the isotopic variations in the reservoir rocks, insufficient data were available at that time to characterize their extent and magnitude. In this paper, we expand significantly on earlier isotopic investigations of the rocks and vein minerals from The Geysers. These data are first used to document the isotopic structure of The Geysers on a field-wide basis. We then discuss possible factors that controlled the observed isotopic variations within the thermal system.

## ANALYTICAL TECHNIQUES

Whole-rock oxygen isotope analyses were performed on 551 samples of graywacke and 39 samples of felsite from 68 wells drilled throughout the field. With the exception of one well, where 30 m composite samples were analyzed, the analyses were performed on cuttings samples that were collected at intervals of 6 m. In addition to the whole rock analyses, $\delta^{18}O$ values were obtained on single crystals of vein quartz and calcite from 6 intervals in 4 wells in order to evaluate the isotopic composition of the fluids that precipitated these minerals. These samples had previously been used for fluid inclusion studies (Moore, 1992).

Prior to the whole-rock analyses, the cuttings were rinsed in cold water to remove any drilling mud and cleaned of drill steel with a hand magnet. The bulk rock samples were treated with acid to remove any carbonate and then reacted with bromine pentafluoride to extract oxygen from the silicate minerals (Clayton and Mayeda, 1963). The evolved $O_2$ was converted to $CO_2$ by combustion with graphite. The results are reported in parts per mil relative to SMOW. The NBS-28 quartz standard yielded an average $\delta^{18}O$ value of 9.5 per mil. Analytical precision based on multiple analyses of the standard was + 0.2 per mil. The samples were analyzed at Unocal's Science and Technology Center in Brea, California.

## GEOLOGIC RELATIONSHIPS

The Geysers steam field lies within the lithologically heterogeneous Franciscan Formation of Jurassic to Cretaceous age. This diverse unit is dominated by graywackes that are interlayered with argillite, chert, greenstone, and serpentinite (McLaughlin, 1981). The main steam reservoir is found dominantly within nonfoliated graywacke and an underlying granitic pluton that was emplaced more than 1.3 million years ago (Schriener and Suemnicht, 1981; Thompson, 1989; Dalrymple, 1992; Hulen and Nielson, 1993). This pluton, which is informally termed the felsite, is centrally located within the steam field and is generally considered to have provided the heat for a large liquid-dominated hydrothermal system that evolved into the present vapor-dominated regime (McLaughlin, 1981; Sternfeld, 1981; Thompson, 1989; Thompson and Gunderson, 1989; Moore, 1992). Highly foliated graywacke, and discontinuous lenses of mafic igneous rocks and chert occur primarily within the low permeability caprock of the system.

Alteration of the graywacke is related to two major events: early subduction-related regional metamorphism, and later contact metamorphism and associated hydrothermal alteration. During the Mesozoic, the Franciscan Formation underwent northeast-directed subduction that was accompanied by low-temperature, moderate- to high-pressure metamorphism (McLaughlin, 1981). The resulting metamorphic assemblages are found throughout the tectonic melanges and disrupted formations of the Geysers reservoir and caprock and are ubiquitously associated with quartz and calcite veining (Thompson, 1989).

More recent alteration of the Franciscan rocks at The Geysers is associated with the large liquid-dominated hydrothermal system that developed during the emplacement of the felsite. Alteration of the country rocks around the pluton included both recrystallization of the rock-forming minerals and deposition of a complex set of vein and selvage minerals. Recrystallization of the graywackes and argillites is most pronounced within distances of 300 to 600 m from the intrusion, where high temperatures caused the groundmass clays to recrystallize to phengite and biotite forming a biotite hornfels. At greater distances from the felsite, where temperatures were lower, the sheet silicates consist of equal amounts of illite and chlorite. At the shallowest depths, smectites and mixed-layer clays are present. Aside from these differences, the primary mineralogy of the altered graywackes is relatively uniform throughout The Geysers, consisting generally of about 45% quartz, 30% plagioclase feldspar, 20% sheet silicates, and 5% potassium feldspar.

During contact metamorphism and hydrothermal alteration of the Franciscan rocks, calcite in the early quartz-calcite veins was removed by dissolution and reacted to produce calc-silicate minerals (Gunderson, 1989; Hulen et al., 1991, 1992). Consequently, calcite is now generally restricted to the upper 300 m of the reservoir and the overlying caprock (Sternfeld and Elders, 1982; Thompson and Gunderson, 1989; Sternfeld, 1989; Gunderson, 1990; Hulen et al., 1991, 1992). With decreasing metamorphic grade and increasing distance from the intrusion, the following assemblages developed in the reopened Franciscan veins and in the newly formed fractures (Moore, 1992):

1. tourmaline + biotite + actinolite + clinopyroxene + epidote + quartz+ potassium feldspar (restricted to the biotite-hornfels zone);
2. actinolite + ferroaxinite + epidote + quartz + prehnite + potassium feldspar;
3. epidote + chlorite + quartz + potassium feldspar; and
4. quartz + potassium feldspar + calcite

Calcite and quartz related to The Geysers hydrothermal system can be distinguished from the older minerals by their morphologies and optical characteristics. In general, the Franciscan minerals are commonly anhedral in shape and clouded with numerous fluid inclusions, whereas quartz and calcite precipitated during the younger event contain only sparsely distributed fluid inclusions and often display well developed crystal forms.

## ISOTOPIC RESULTS

The $\delta^{18}O$ whole-rock values of the graywackes ranged from +2.3 to +15.6 per mil, while those of the felsite ranged from +4 to +10.5 per mil (Figure 2). The isotopic distributions are shown on plan maps and cross sections in Figures 3 and 4, respectively. The plan maps were constructed by averaging the isotopic values in each of the 610 m slices shown. In contrast, each of the

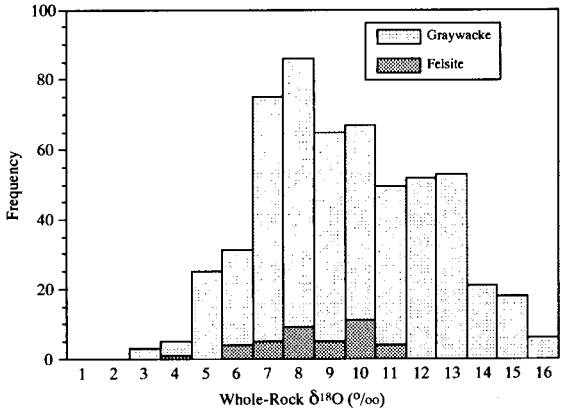


**Figure 2.** Range of isotopic compositions in per mil of graywacke and felsite samples.

| Well | Elevation | Wt % NaCl | O-18 (Qtz) | O-18 (Cc) | F.I. Temp | O-18 Calc | Comment |
|---|---|---|---|---|---|---|---|
| Thorne-6 | -469 | 0.0 | | 5.2 | 172 | -5.94 | 1 |
| Thorne-6 | -488 | 0.0 | 5.80 | | 253 | -2.95 | 2 |
| Thorne-6 | -516 | 0.2 | | 5.5 | 189 | -4.633 | 2 |
| CA 956-A4 | 376 | 0.1 | 5.20 | | 226 | -4.90 | 1 |
| DV-2 | -203 | 4.3 | 7.58 | | 282 | 0.05 | 3 |
| SB-26 | -175 | 0.6 | 6.06 | | 306 | -0.59 | 4 |
| PS-24 | -405 | 1.2 | 12.10 | | 223 | 1.84 | 2 |
| L'Esp-2 | -2462 | 15.7 | 10.13 | | 420 | 6.49 | 1 |

1-average of primary or pseudosecondary inclusions
2-average highest temperature secondary planes
3-average all inclusions probably pseudosecondary
4-data from Sternfeld (1981); average of all inclusions

**Table 1.** Oxygen isotopic compositions in per mil of quartz (Qtz) and calcite (Cc). Also shown are the average fluid inclusion homogenization temperatures (F.I. Temp) and range of salinities in weight percent NaCl equivalent (WT % NaCl). The sample elevations relative to mean sea level are given in meters (m). The calculated compositions in per mil of the waters in equilibrium with the minerals are denoted by O-18 calc.

individual data points was contoured in the cross sections. Thus, the cross sections display details that are not apparent in the plan maps.

Oxygen isotope analyses of the mineral separates are presented in Table 1. These samples yielded $\delta^{18}O$ values that ranged from +5.2 to +12.1 per mil for quartz and +5.2 to +5.5 per mil for calcite. The samples from Thorne 6 and CA 956A-4 are representative of the caprock in the southeastern part of the field while quartz from SB-26 and PS-24 are from the caprock in the central and northwestern parts of The Geysers respectively. Quartz from DV-2 is from a quartz-epidote vein deposited in tourmaline-bearing felsite within the steam reservoir. The isotope data from L'Esp 2 is from a quartz vein in graywacke that was metamorphosed to a biotite-rich hornfels. This sample is from the high-temperature reservoir.

## DISCUSSION

### Distribution of Oxygen Isotopes

Figures 3 and 4 show that $\delta^{18}O$ values of the Geysers graywackes are laterally and vertically zoned within the steam field. Samples from shallow depths display isotopic values typical of Franciscan rocks outside the geothermal field (Lambert and Epstein, 1992) while strongly depleted values are found above the top of the felsite intrusion near the center of the field. As discussed in greater detail below, the $\delta^{18}O$ values of the rocks show a clear spatial relationship to both the boundaries of the producing steam field and the felsite intrusion. Thus, the data provide independent evidence that intrusion of the felsite was responsible for the development of a large hydrothermal system that eventually diminished in size and evolved into the present steam reservoir.

The near-surface $\delta^{18}O$ values of Franciscan graywacke (above +610 m relative to mean sea level (msl)) obtained in this study range from +12 to +15.6 per mil and are similar to values obtained by Lambert and Epstein (1992) from shallow levels of The Geysers wells LF-19 and LF-15. In these wells, the graywackes yielded $\delta^{18}O$ values of +13 to +16 per mil and displayed no systematic variation within the depth range studied. Detrital quartz grains from the same depths yielded values ranging from +14.2 to +19.8 per mil. From these data, Lambert and Epstein (1992) concluded that the isotopic composition of the quartz was the result of regional metamorphism and that the shallow graywackes were essentially unaltered by recent hydrothermal activity. The lack of any significant variation in the near-surface oxygen isotope values obtained in our study further supports the conclusion that the isotopic composition of the graywacke was not differentially affected by hydrothermal alteration prior to emplacement of the felsite.

Below +610 m msl, the graywackes generally display depleted $\delta^{18}O$ values. With increasing depth, and toward the center of the field, the $\delta^{18}O$ values become progressively more depleted. Between +610 m and sea level, the lowest $\delta^{18}O$ values are found toward the southeastern end of the field above the shallowest part of the felsite intrusion (Fig. 5a). With increasing depth, this isotopic low is shifted northward, defining an elongate northwest-southeast area that is more centrally located within the steam field. Data below -1829 m msl reveal the presence of small, isolated isotopic lows.

In cross section, it is evident that the greatest isotopic depletions are found at distances of 300 to 600 m above the felsite (Fig. 4). These depletions occur within the biotite hornfels in both the normal and high-temperature reservoirs, and are characterized by $\delta^{18}O$ values that typically range from +4 to +7 per mil. As the felsite is approached, $\delta^{18}O$ values within the graywacke increase from these low values up to about +8 to +10 per mil at the intrusive contact. Within the intrusion itself, the whole-rock oxygen isotopic values generally remain fairly constant.

Figure 5a shows that the isotopic contours display a close relationship to the shape of the pluton, the steam reservoir, and major zones of surficial alteration. This coincidence suggests that these features are related to each other and that they were all influenced by the same structural controls. In contrast, there appears to be little relationship between the isotopic variations at

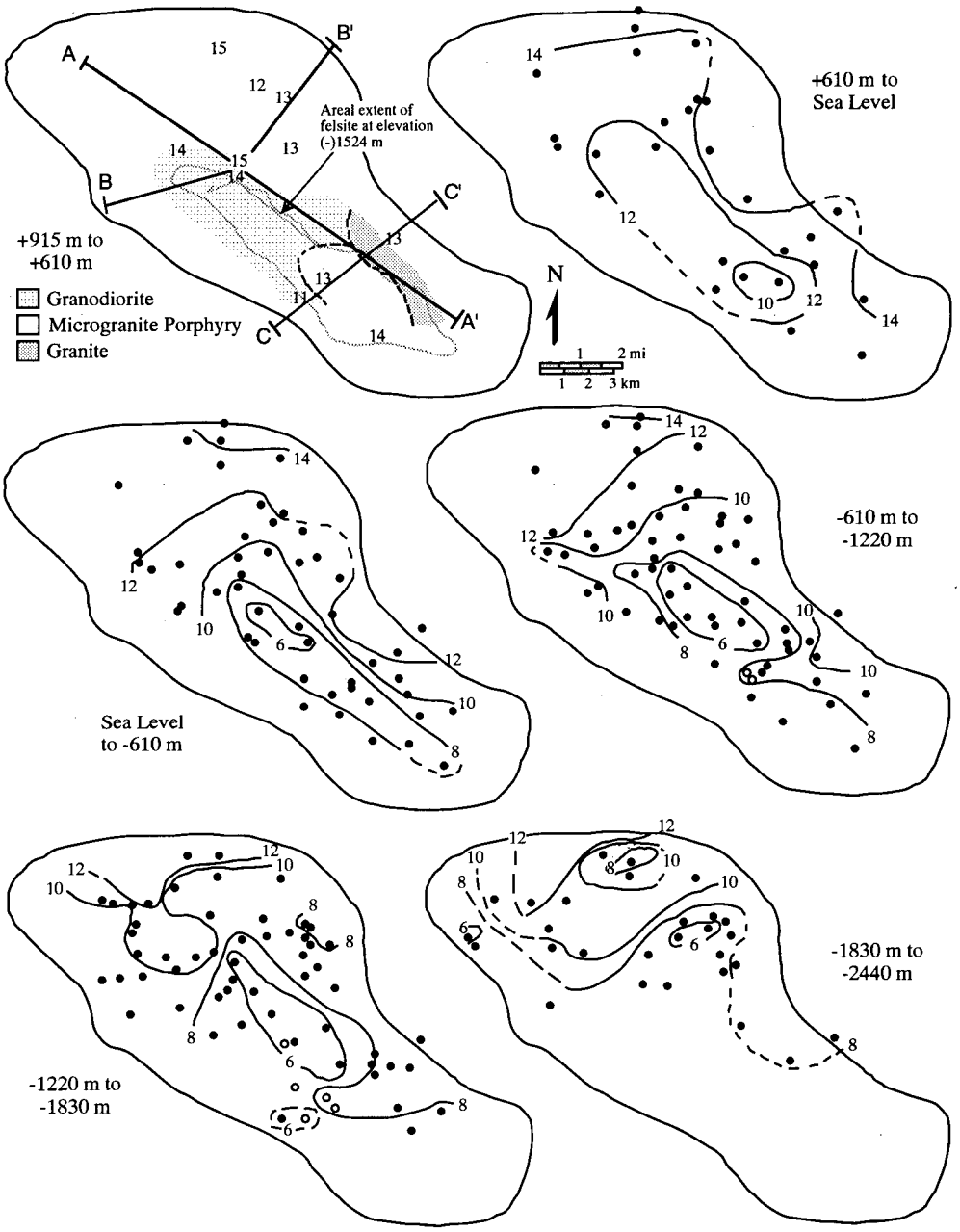


**Figure 3.** Distribution of the average $\delta^{18}O$ values in per mil of graywacke and felsite. The individual diagrams represent successive slices through The Geysers field. All elevations are shown relative to mean sea level. The solid dots represent samples of graywacke or mixtures of graywacke and felsite. Open circles denote felsite samples. The upper left hand diagram shows the distribution of the main granitic phases of the felsite (Hulen et al., 1993), the extent of the felsite at an elevation of –1524 m (Thompson, 1989), the locations of the cross sections given in Figure 4, and the average isotopic composition of graywackes between elevations of +915 and +610 m.

greater depth and regions of intense tourmaline mineralization in the felsite and hornfels (Fig. 5b). The lack of a clear isotopic signature in the overlying graywckes is surprising because the abundance of tourmaline implies that these were areas of locally high fluid flow that should have affected a large volume of the rock. This apparently was not the case. Instead, the isotopic data suggest that the fluids which deposited the tourmaline were unable to penetrate much above the top of the hornfels. This conclusion is further supported by fluid inclusion data which shows no evidence for the hypersaline fluids found in tourmaline-bearing veins at distances of more than 600 m from the intrusion (Moore, 1992). The upward mobility of these fluids could have been limited in part by ductile behavior of the hornfels, which is suggested both by the presence of highly con-

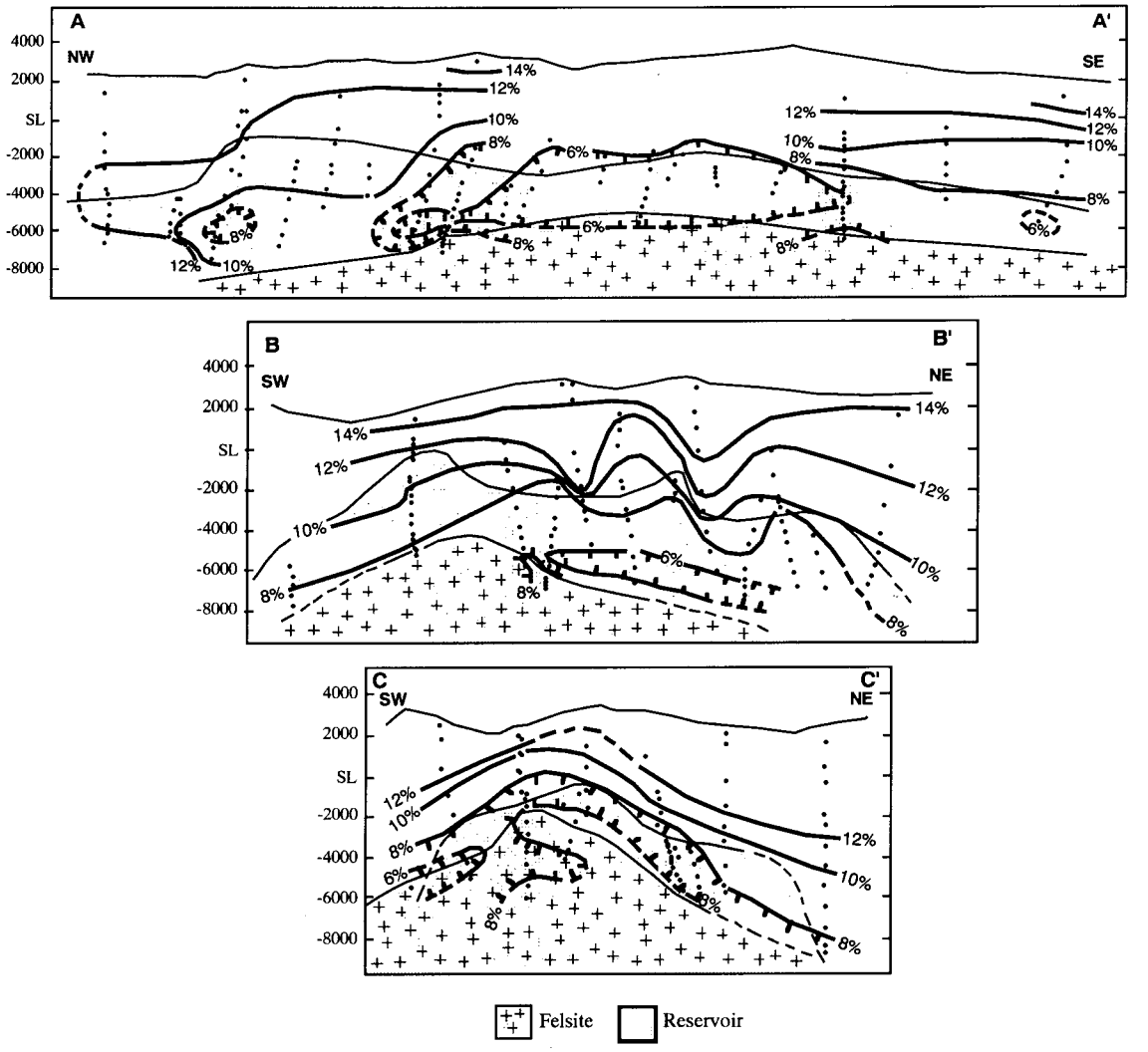


**Figure 4.** Cross sections through The Geysers field showing the distribution of $\delta^{18}O$ values in per mil with respect to the top of the steam reservoir and the felsite. All values were contoured in this figure. See Figure 3 for cross section locations.

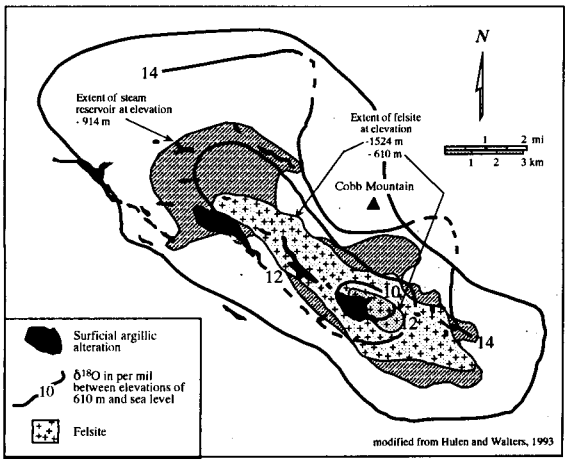


**Figure 5a.** Spatial relationships between the steam reservoir, felsite, surficial hydrothermal alteration, and the average $\delta^{18}O$ values in per mil of graywacke samples from +610 m msl to sea level. Modified from Hulen and Walters (1993)

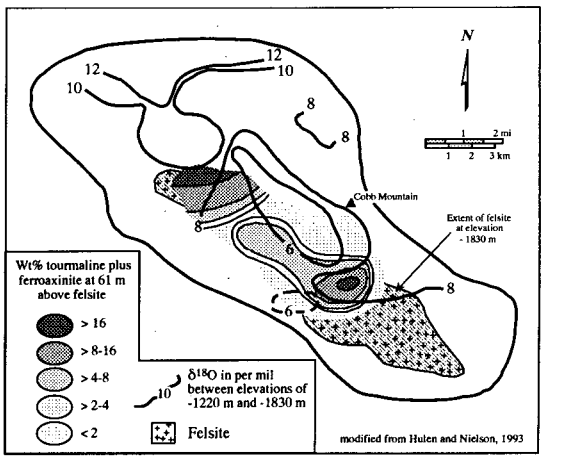


**Figure 5b.** Relationship between regions of strong tourmaline and ferroaxinite mineralization, the felsite, and the average $\delta^{18}O$ values in per mil of rocks from elevations between –1120 and –1830 m msl.

voluted Franciscan veins (Hulen, pers. comm., 1993) and by fluid inclusion data that imply high temperatures and lithostatic pressures (unpub. data).

At the depths shown in Figure 5b, the isotopically dominant feature, the central low, is developed within the graywacke in the contact metamorphic halo above the biotite-orthopyxone granite (refer to Fig. 3). This is the most extensive and apparently the oldest of the three major intrusive phases mapped by Hulen and Nielson (1993). The strong northwest elongation of the low parallels the major structural grain of the region, implying that this region was an area of preexisting and relatively intense fracturing that may have been enhanced by intrusion of the felsite.

**Origin of Isotopic Variations**

As noted above, the general pattern of oxygen isotopic depletions in the rocks strongly suggests a relationship to felsite emplacement. The specific vertical and lateral variations that make up this pattern are interpreted to have been caused by variations in the temperature, rock permeability, and composition of the fluids during the evolution of the hydrothermal system at The Geysers .

The most important isotopic feature shown in Figures 3 and 4 is the downward decrease in the $\delta^{18}O$ values from about +14 per mil near the surface to about +4 to +7 per mil within the hornfels at distances of 300 to 600 m above the intrusive contact. Extrapolation of fluid inclusion data suggest that the maximum temperatures ranged from about 425°C near top of the biotite hornfels to 150°C in the shallow cap rocks above the presently producing steam reservoir (Sternfeld, 1981; Moore, 1992). These temperatures, combined with the average mineral composition of the graywacke given above, yield water-rock fractionation factors of 2.4 and 12.7 per mil respectively. These values were calculated from the fractionation factors for water-quartz, -albite, -potassium feldspar, -muscovite, and -chlorite given by Matsuhisa et al. (1979), O'Neil and Taylor (1967), O'Neil and Taylor (1967), O'Neil and Taylor (1969), and Wenner and Taylor (1971) respectively. Thus, the inferred temperature gradient can itself account for a 10 per mil variation in the isotopic composition of the rocks, assuming that they equilibrated with waters of uniform isotopic compositions. This correspondence between the observed and calculated $\delta^{18}O$ values of the graywackes strongly suggests that temperature was the dominant process controlling the isotopic compositions of the rocks. These fractionation factors would require a water with a $\delta^{18}O$ of about +2 per mil.

Within the hornfels, the $\delta^{18}O$ values commonly increase by 1 to 3 per mil as the intrusion is approached. This opposite trend suggests that effects other than temperature influenced the oxygen isotope composition of the rocks in the immediate vicinity of the felsite. The most likely factors that could lead to this increase in $\delta^{18}O$ are a downward decrease in the water:rock ratios caused by decreasing permeabilities and equilibration of the rock with an isotopically heavier water. Both of these possibilities are reasonable, as measured matrix permeabilities of hornfels core samples are indeed considerably lower than the overlying graywackes, while isotopically heavy magmatic water could have readily been derived from the felsite. Evidence for the presence of such water is provided by the isotopic data and salinities of the inclusion fluids from the hornfels near the intrusive contact (see below), and by the presence of boron-rich waters.

The lateral isotopic gradients that result in the "bull's eye" pattern seen at intermediate depths in Figure 3 have two possible origins. The isotopically light "bull's eye" may have resulted from interaction with waters that were isotopically lighter than those found near the edges of the thermal system, or, more likely, from higher water:rock ratios in the center of the system. Higher water:rock ratios would imply that the isotopically lightest part of the system had the greatest permeabilities during the early development of the hydrothermal system at The Geysers. The present rates of steam production in the central part of The Geysers, however, are not anomalously high, suggesting that increased permeabilities are no longer present in this region.

Table 1 shows calculated $\delta^{18}O$ values of waters in equilibrium with vein calcite and quartz from Geysers cores and cuttings. These values, which ranged from -5.9 to +6.5 per mil, were calculated using the fractionation factors for quartz-water and calcite-water from Matsuhisa et al. (1979) and Freidman and O'Neil (1977) respectively, and pressure-corrected homogenization temperatures from the fluid inclusion data of Moore (1992) and Sternfeld (1981). Waters from the caprock in the southeastern part of the field (Thorne 6 and CA 958-3) display a relatively narrow range of $\delta^{18}O$ values between -5.9 and -3.0 per mil, while the fluid from the caprock in PS-24 and SB-26 (northern third of the Geysers), are substantially heavier (+1.8 and -0.6 per mil respectively). All of these samples are thought to belong to paragenetic sequence 4 (see above).

The low $\delta^{18}O$ values in the southeastern part of the field suggest that the fluids contained a large component of meteoric water. In contrast, the isotopically heavier waters from the northwestern third of the field are similar to the+2 per mil values determined for the early fluids from the rock-water fractionation factors (see discussion above). These heavier $\delta^{18}O$ values imply lower water:rock ratios, if it is assumed that the northwestern fluids were also meteoric in origin, or derivation from a different source. We favor the latter hypothesis. This conclusion is consistent with the relatively high fluid inclusion salinities of 1.2 equivalent weight percent NaCl determined for this sample from PS-24 and with the even higher salinities of up to 4 equivalent weight percent NaCl contained in fluid inclusions from other samples from the caprock in the Northwestern Geysers (Moore et al., 1989). These relatively high salinities suggest that the waters may be connate in origin or mixtures of magmatic and connate or meteoric water. The occurrence of these various water types in the region around The Geysers has recently been reviewed by Donnelly-Nolan et al. (1992).

In contrast to the shallower samples, the water responsible for deposition of the quartz veins in the biotite hornfels in L'Esp-2 had a $\delta^{18}O$ value of +6.5 per mil. This value lies within the region of primary magmatic waters (Sheppard et al., 1969). Such an origin is consistent with salinities of up to 31 weight percent NaCl in fluid inclusions from this sample and the occurrence of hypersaline inclusion fluids in other samples of the felsite and hornfels. Thus, the data demonstrate that the fluids responsible for the initial alteration of the hornfels were compositionally and isotopically different than the fluids that circulated through the upper portions of the hydrothermal system.

## CONCLUSIONS

The whole-rock $\delta^{18}O$ values of graywackes from The Geysers display systematic variations with respect to depth, location within the field, and grade of alteration. The dominant feature is an overall downward decrease in the $\delta^{18}O$ values of the graywackes as the underlying granitic intrusion is approached, with the lowest values in the center of the current steam system. The shallowest samples are characterized by $\delta^{18}O$ values of +12 to +15.6 per mil, which are typical of the weakly altered graywackes studied by Lambert and Epstein (1992), Sternfeld (1981), and Cole (1985). These high $\delta^{18}O$ values are found throughout the field at shallow depths, suggesting pre-intrusion isotopic homogeneity of the graywackes. Biotite hornfels, found at distances of up to 600 m from the intrusion, commonly displays the greatest isotopic depletions. This rock type occurs in both the normal and high-temperature reservoirs and is characterized, throughout most of the field, by $\delta^{18}O$ values that are as depleted as +4 to +7 per mil. Variations in temperatures determined from fluid inclusion and mineralogic data yield calculated rock-water fractionation factors that can account for $\delta^{18}O$ variations of 10 per mil. Thus, temperature variations provide an explanation for the overall vertical decrease in the $\delta^{18}O$ values of the rocks. As the intrusion is approached, the $\delta^{18}O$ values in the hornfels increase to a maximum of +8 to +10 per mil at the granitic contact. Corresponding values within the intrusive are similar and remain fairly constant with depth. We suggest that the effects of increasing temperature on the $\delta^{18}O$ values within the hornfels were offset by interaction with isotopically heavy waters of magmatic origin and possibly decreasing permeabilities.

Lateral variations in the pattern of isotopic values of the greywackes mimic the shape of the underlying felsite and display a strong zonation around a central low. The axis of this low, which is elongate in a northwest-southeast direction, is located in the center of the producing steam field slightly to east of the axis of the underlying granitic pluton and to the north of the shallowest portion of the intrusion. This low is interpreted as representing the central upwelling region of the early hydrothermal system that formed in response to the intrusion of the granite. The isotopic depletions in the graywackes imply that this region was characterized by the highest time-integrated water-rock ratios and permeabilities.

Rocks from the northwestern third of The Geysers field are consistently more enriched in oxygen-18 than the remainder of the system. As shown by Gunderson (1989), these gross lateral variations are also correlative with the isotopic composition of the early produced steam. These relationships suggest that lower water:rock ratios and hence lower permeabilities have characterized this part of the field throughout the evolution of The Geysers thermal system.

## ACKNOWLEDGEMENTS

We thank the management of Unocal for making the analyses and data reported here available for publication. Joe Beall kindly provided additional unpublished isotopic data. Mike Adams, Dave Cole, Pat Dobson, Brian Smith, and Mark Walters generously shared their ideas with us. The paper was reviewed by Mike Adams, Jeff Hulen, and Mark Walters whose suggestions are greatly appreciated. This work was supported in part by the U.S. Department of Energy, Contract No. DE-AC07-90ID12929. Such support does not constitute an endorsement by the U.S. Department of Energy of the views expressed in this publication.

## DISCLAIMER



## REFERENCES

Clayton, R. N., and Mayeda, T. K., 1963, The use of bromine pentafluoride in the extraction of oxygen from oxides and silicates for isotopic analysis: Geochim. Cosmochim. Acta v. 27, p. 43-52.

Cole, D., 1985, Oxygen, carbon, and sulfur isotope geochemistry of mineral phases from The Geysers (Aminoil Property): unpub. rept to Aminoil, U.S.A., 63 p.

Dalrymple, G. B., 1992, Preliminary report on 39 Ar/40Ar incremental heating experiments on feldspar samples from the felsite unit, Geysers geothermal field, California: U. S. Geol. Survey, Open-File Rept. 92-407, 15 p.

Donnelly-Nolan, J. M., Burns, M. G., Goff, F. E., Peters, E. K., and Thompson, J. M., 1993, The Geysers-Clear Lake area, California — Thermal waters, mineralization, volcanism, and geothermal potential: Econ. Geol., v. 88, p. 301-316.

Friedman, I., and O'Neil, J. R., 1977, Compilation of stable isotope fractionation factors of geochemical interest in M. Fleischer, ed., Data of Geochemistry: U. S. Geological Survey Prof. Paper 440-KK.

Gunderson, R. P., 1989, Distribution of oxygen isotopes and noncondensible gas in steam at The Geysers: Geothermal Resources Council Trans., v. 13, p. 439-445.

Gunderson, R. P., 1990, Porosity of reservoir graywacke at The Geysers: Geothermal Resources Council Trans., v. 14, p. 1661-1665.

Hulen J. B., and Nielson, D. L., 1993, Interim report on geology and hydrothermal alteration of The Geysers felsite: Geothermal Resources Council Trans., v. 17, p. 249-258.

Hulen J. B., and Walters, M. A., 1993, The Geysers felsite and associated geothermal systems, alteration, mineralization, and hydrocarbon occurrences in Fieldtrip Guidebook — The Geysers geothermal area and the McLaughlin gold deposit, California: Society of Econ. Geologists, in press.

Hulen, J. B., Nielson, D. L., and Martin, W., 1992, Early calcite dissolution as a major control on porosity development in The Geysers steam field, California— Additional evidence from Unocal well NEGU-17: Geothermal Resources Council Trans., v. 16, p. 167-174.

Hulen, J. B., Walters, M. A., and Nielson, D. L., 1991, Comparison of reservoir and caprock core from the Northwest Geysers steam field, California: Geothermal Resources Council Trans., v. 15, p. 11-18.

Lambert, S. J., and Epstein, S., 1992, Stable-isotope studies of rocks and secondary minerals in a vapor-dominated hydrothermal system at The Geysers, Sonoma County, California: Jour. Volcan. and Geothermal Res., v. 53, p. 199-226.

Matsuhisa, Y., Goldsmith, J. R., and Clayton, R. N., 1979, Oxygen isotope fractionation in the system quartz-albite-anorthite-water: Geochim. Cosmochim. Acta v. 43, p. 1131-1140

McLaughlin, R. J., 1981, Tectonic setting of pre-Tertiary rocks and its relation to geothermal resources in The Geysers-Clear Lake area in R. J. McLaughlin and J. M. Donnelly-Nolan, eds., Research in The Geysers-Clear Lake geothermal area, northern California: U. S. Geological Survey Prof. Paper 1141, p. 25-45.

Moore, J. N., 1992, Thermal and chemical evolution of The Geysers geothermal field, California: 17th Workshop on Geothermal Reservoir Engineering, Stanford Univ., p. 121-126.

Moore, J. N., Hulen, J. B., Lemieux, M. M., Sternfeld, J. N., and Walters, M. A., 1989, Petrographic and fluid inclusion evidence for past boiling brecciation, and associated hydrothermal alteration above the Northwest Geysers steam field, California: Geothermal Resources Council Trans., v. 13, p. 467-472.

O'Neil, J. R., and Taylor, H. P., 1967, The oxygen isotope and cation exchange chemistry of feldspars: Am. Mineral., v. 5, p. 1414-1437.

O'Neil, J. R., and Taylor, H. P., 1969, Oxygen isotope equilibrium between muscovite and water. Jour. Geophys. Res., v. 74, p. 6012-6022.

Schriener, A., Jr., and Suemnicht, G. A., 1981, Subsurface intrusive rocks at The Geysers geothermal area, California in M. L. Silberman, C. W. Field, and A. L. Berry, eds., Proceedings of the symposium on mineral deposits of the Pacific Northwest: U. S. Geological Survey Open File Rept. 81-355, p. 295-302.

Sheppard, S. M. F., Nielson, R. L., and Taylor, H. P., Jr., 1969, Oxygen and hydrogen isotope ratios of clay minerals from porphyry copper deposits: Econ. Geol., v. 64, p. 75777.

Sternfeld, J. N., 1981, The hydrothermal petrology and stable isotope geochemistry of two wells in The Geysers geothermal field, Sonoma County, California: M. S. Thesis, Univ. of California, Riverside, 202 p.

Sternfeld, J. N., 1989, Lithologic influences on fracture permeability and the distribution of steam in the Northwest Geysers steam field, Sonoma County, California: Geothermal Resources Council Trans., v. 13, p. 473-479.

Sternfeld, J. N., and Elders, W. A., 1982, Mineral zonation and stable isotope geochemistry of a production well in The Geysers geothermal field, California: Geothermal Resources Council Trans., v. 6, p. 51-54.

Thompson, R. C., 1989, Structural Stratigraphy and intrusive rocks at The Geysers geothermal field: Geothermal Resources Council Trans., v. 13, p. 481-486.

Thompson, R. C., and Gunderson, , R. P., 1989, The orientation of steam-bearing fractures at The Geysers geothermal field: Geothermal Resources Council Trans., v. 13, p. 481-485.

Truesdell A., Walters, M., Kennedy, M., and Lippmann, M., 1993, An integrated model for the origin of The Geysers geothermal field: Geothermal Resources Council Trans., v. 17, p. 273-280.

Wenner, D. B., and Taylor, H. P., 1971, Temperatures of serpentinization of ultramafic rocks based on $O^{18}/O^{16}$ fractionation between coexisting serpentine and magnetite: Contri. Mineral. and Petrol., v. 32, p. 165-185.

PROCEEDINGS, Nineteenth Workshop on Geothermal Reservoir Engineering
Stanford University, Stanford, California, January 18-20, 1994
SGP-TR-147

# LIQUID-VAPOR PARTITIONING OF NaCl(aq) FROM CONCENTRATED BRINES AT TEMPERATURES TO 350°C

J. M. Simonson, Donald A. Palmer, and R. W. Carter

Chemical and Analytical Sciences Division
Oak Ridge National Laboratory, Oak Ridge, TN 37831

## ABSTRACT

Compositions of coexisting liquid and vapor phases have been determined at temperatures from 250 to 350°C for brines containing NaCl and either HCl or NaOH by direct sampling of both phases from a static phase-equilibration apparatus. In these experiments, NaCl concentrations in the liquid phase ranged to 6.5 $mol \cdot kg^{-1}$, with corresponding vapor-phase NaCl concentrations varying strongly with temperature and brine composition. Acid or base was added to the brines to suppress unknown contributions of NaCl(aq) hydrolysis products to the observed volatilities. Thermodynamic partitioning constants for NaCl have been determined from the observed compositions of the coexisting phases combined with the known activity coefficients of NaCl(aq) in the liquid phase. An apparent dependence of the values of these partitioning constants on brine concentration is explained by considering the effect of decreasing pressure on the density of the vapor phase. Concentrations of HCl and NaCl in steam produced from various natural brines may be calculated as functions of temperature and brine composition based on these new results coupled with our previous determinations of the partitioning constants for HCl(aq). Application of these results to The Geysers will be discussed in terms of the composition of postulated brines which could be in equilibrium with observed steam compositions at various temperatures.

## INTRODUCTION

The production of acidic, chloride-containing steam from wells at The Geysers has resulted in corrosion of well casings and steam piping through attack by corrosive condensed fluids. In extreme cases corrosion has forced wells to be taken out of production. While the incidence of acid-chloride steam was originally considered a problem in the hotter producing regions of the northwest portion of The Geysers, recently the possible production of acid-chloride steam from the lower-temperature regions of the central portion of the field has received renewed attention. While the subject of acid-chloride steam chemistry has been modeled and discussed (TRUESDELL *et al.*, 1988; HIRTZ *et al.*, 1991), little new experimental information has been obtained on the partitioning of electrolytes between liquid and vapor phases over the temperature range commonly found in steam at The Geysers. The relative lack of reliable experimental values in this temperature range limits our ability to predict steam compositions over brines of varying pH and salinity. Conversely, given the observed composition and temperature of produced steam, the ability to predict a brine composition which would be in equilibrium with that steam phase is limited for many systems by a lack of data.

A number of aspects of the basic physical chemistry of geothermal systems are under investigation at ORNL, including solubility and speciation of aluminum in aqueous solutions, thermodynamics and phase relations in granitic melts, liquid-vapor distribution of stable isotopes in brines, and liquid-vapor distribution of HCl including the production of acid-chloride-containing steam. We have previously reported (SIMONSON and PALMER, 1993) measured values obtained in this program for the partitioning of HCl over HCl(aq) from 50 to 350°C. In a similar experimental study sponsored by the Electric Power Research Institute, we have measured liquid-vapor partitioning of $NH_4Cl$ over acidic and buffered aqueous solutions from 120 to 350°C (PALMER and SIMONSON, 1993) Ammonia and ammonium salts have been found in steam from The Geysers (HIRTZ *et al.*, 1991). Our recent experimental studies have addressed possible sources of acidity in steam from hydrolysis of alkaline-earth chlorides (Mg and Ca) at high temperatures through extensive series of measurements on brines containing NaCl. These latter experiments were performed both to determine quantitatively the effects of NaCl concentration on HCl partitioning, and to reinvestigate the partitioning of NaCl to steam from multicomponent brines. These new measurements of NaCl partitioning, coupled with experimental values for HCl partitioning from pure aqueous acid and from acidic NaCl brines, may be used to provide new estimates of steam composition above {NaCl + HCl}(aq) at temperatures ranging to the solvent critical temperature.

## EXPERIMENTAL

The apparatus and techniques used to equilibrate and analyze the samples taken in these equilibrium studies have

been described in detail previously. (SIMONSON and PALMER, 1993; PALMER and SIMONSON, 1993) The experimental method is based on the static equilibration of liquid and vapor phases at temperature in a chemically-inert, platinum-lined autoclave system (Figure 1).

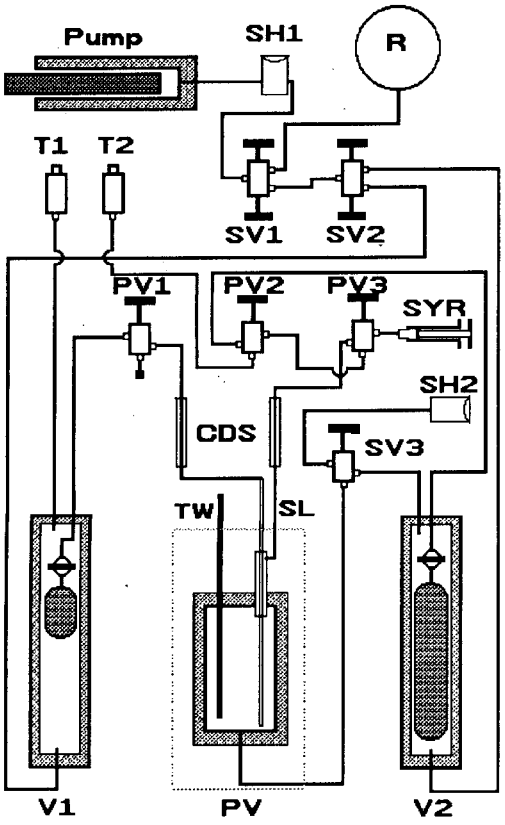


Figure 1. Static liquid-vapor equilibration apparatus and sampling equipment for partitioning measurements.

A stainless-steel pressure vessel PV of ca. 600 $cm^3$ internal volume, equipped with a platinum liner, is thermostated at the desired experimental temperature. The liquid phase is sampled into a syringe via platinum tubing and PEEK valve V3. Vapor-phase samples are drawn into a preweighed Teflon sample bag contained in the ambient-temperature pressure vessel V1 at a controlled rate (between 0.5 and 6 $cm^3\ h^{-1}$) by withdrawing water from the annular space of the pressure vessel using a positive-displacement pump. A second ambient-temperature pressure vessel V2 contains a large Teflon bag, connected to the platinum liner through capillary tubing and filled with the same solution as in the liner. The annular space of this pressure vessel contains distilled water, and is connected to the annular space surrounding the platinum liner; fluid transfer in this subsystem serves to equalize the pressure across the thin platinum liner.

Samples of the two phases were analyzed for chloride and sodium by ion chromatography, and for proton or hydroxide by acidimetric titration. The general procedure was to fill the liner approximately half-full with the desired solution and allow time for equilibration at the experimental temperature. Due to the preferential extraction of water from the system during vapor-phase sampling the liquid-phase molality increases over a series of samples for a particular loading of the system. Liquid-phase samples were taken both before and after obtaining a given vapor-phase sample, with the liquid-phase composition assumed to be the average of the two liquid samples. The overall increase in liquid-phase molality due to water extraction from a given set of samples was no more than a factor of two for any series of equilibrations. A tabular summary of the experimental conditions is given in Table 1.

Table 1. Summary of NaCl Partitioning Measurements.

| {NaCl + HCl}(aq) Runs | | |
|---|---|---|
| t(av)/°C | {m(Na)/m(H)}(aq) | I/(mol·kg$^{-1}$) |
| 297.5 | 5 - 14 | 0.1 - 0.3 |
| 322.6 | 7 - 25 | 0.1 - 0.3 |
| 347.5 | 15 - 59 | 0.2 - 0.5 |
| 297.5 | 90 - 170 | 1.6 - 2.5 |
| 322.5 | 100 - 230 | 1.4 - 1.9 |
| 346.8 | 200 - 620 | 2.0 - 3.6 |
| 247.2 | 140 - 470 | 3.3 - 6.3 |
| 249.4 | 42 | 0.9 |
| 298.6 | 32 - 70 | 0.6 - 0.9 |
| 244.3 | 150 - 290 | 3.0 - 4.1 |
| 294.9 | 140 - 520 | 2.1 - 3.6 |
| 318.1 | 300 - 800 | 3.2 - 4.5 |
| 345.4 | 50 - 340 | 1.1 - 3.0 |
| {NaCl + NaOH}(aq) Runs | | |
| t(av)/°C | {m(Cl)/m(OH)}(aq) | I/(mol·kg$^{-1}$) |
| 197.3 | 29 | 3.1- 4.6 |
| 248.4 | 30 | 2.5 - 3.1 |
| 297.5 | 30 | 2.8 - 3.7 |
| 321.5 | 30 | 2.8 - 4.4 |
| 343.9 | 30 | 2.7 - 4.8 |
| {NaCl + $MgCl_2$}(aq) Runs | | |
| t(av)/°C | {m(Na)/m(Mg)}(aq) | I/(mol·kg$^{-1}$) |
| 248.1 | 16 | 1.0 - 1.4 |
| 297.8 | 16 | 0.9 - 1.3 |
| 322.7 | 16 | 1.0 - 2.2 |
| 347.4 | 16 | 0.9 - 2.2 |

Measurements of NaCl volatilities were carried out over the mixed brines {NaCl + HCl}(aq), {NaCl + NaOH}(aq), and {NaCl + $MgCl_2$}(aq). The runs with excess acid or base were designed to eliminate the possibility of apparent transport of NaCl to the vapor phase as products of a

hydrolysis reaction of unknown extent; i.e., addition of either acid or base to a predominantly NaCl brine suppresses any appreciable hydrolysis of NaCl, with the vapor-phase molality of sodium ion indicating NaCl transport in the acidified experiments, and the chloride ion molality indicating NaCl partitioning in the basic runs. It should be noted from Table 1 that under the conditions of these measurements, HCl partitions preferentially to the vapor phase, resulting in 'stripping' of HCl from the liquid and a corresponding shift in the ratio m(Na)/m(H).

At high temperatures, {NaCl + $MgCl_2$} solutions are slightly acidic due to the hydrolysis of magnesium ion. While these measurements were performed primarily to determine the extent of hydrolysis of magnesium ion in NaCl(aq) at high temperatures, measurement of vapor-phase sodium ion molalities gave additional information on the partitioning of NaCl from acidic solutions.

## RESULTS AND DATA ANALYSIS

Following the procedure used in our analysis of liquid-vapor partitioning results for HCl and $NH_4Cl$ (SIMONSON and PALMER, 1993; PALMER and SIMONSON, 1993) it was assumed that NaCl was fully associated (unionized) in the vapor phase, and predominantly dissociated in the liquid. These assumptions lead to an expression for the equilibrium constant $K_D$ for the liquid-vapor phase distribution

$$K_D(NaCl) = \frac{m_v(NaCl)\gamma_v(NaCl)}{m_l(Na^+)m_l(Cl^-)\gamma_l(Na^+)\gamma_l(Cl^-)} \quad (1)$$

where $m_l$ and $\gamma_l$ are the molality and activity coefficient of a given species in the liquid phase; the corresponding quantities subscripted 'v' refer to the vapor phase. It should be noted that no speciation of solute is considered in the liquid phase, or equivalently, that the activity coefficients $\gamma_l$ in the liquid phase are stoichiometric values. On this basis it is not necessary to consider explicitly the formation of ion pairs in the liquid phase, provided that values of the stoichiometric activity coefficients are available. While this approach makes it unnecessary to assign speciation of electrolytes in the aqueous phase where such assignments are often poorly known or ambiguous, some additional uncertainty in the calculation of $K_D$ is introduced through neglect of speciation in common-ion systems where one component (e.g. HCl) may by strongly associated while the other (e.g. NaCl) is much less associated. This point will be discussed in further detail below.

The present experimental results give directly the compositions (molalities) of the coexisting liquid and vapor phases. In order to calculate $K_D$ using equation (1) it is necessary to calculate activity coefficients of NaCl(aq) in the aqueous medium of interest at the experimental temperature. Values of the stoichiometric mean-ionic activity coefficient $\gamma_\pm$(NaCl) approriate to pure NaCl(aq) media along the saturation vapor-pressure curve at temperatures to 350°C are available from the compilations of PITZER, PEIPER, and BUSEY (1984) and ARCHER(1992) at temperatures to 300 and 325°C, respectively, and are tabulated at 350°C by BUSEY, HOLMES and MESMER (1984). Noting that the former two compilations give values of $\gamma_\pm$ in good agreement with each other at temperatures to 300°C (the upper limit of applicability of the representation of PITZER *et al.*), we have adopted values for $\gamma_\pm$ from ARCHER for this work. At temperatures above 325°C, $\gamma_\pm$(NaCl) were interpolated from the 325°C values of ARCHER and the 350°C values reported by BUSEY *et al.*

Experimental studies leading to values of $\gamma_\pm$ for NaCl in mixed-electrolyte media at the temperatures of interest here are not available. To a reasonably good approximation the stoichiometric mean-ionic activity coefficient of NaCl(aq) in the mixture may be taken as $\gamma_\pm$ in pure NaCl(aq) media at the ionic strength of the mixture. This approximation has been used here for calculating $\gamma_\pm$(NaCl) in {NaCl + $MgCl_2$}(aq) mixtures, where reliable values of excess thermodynamic properties for $MgCl_2$(aq) solutions at high temperatures are not available. For the {NaCl + HCl}(aq) and {NaCl + NaOH}(aq) mixtures, excess thermodynamic properties for HCl(aq) are available to 375°C from SIMONSON *et al.* (1990). NaOH(aq) excess thermodynamic properties to 250°C are available from SIMONSON, MESMER, and ROGERS (1989); values at higher temperatures were calculated from extrapolated differences in NaOH(aq) and NaCl(aq) properties following the procedure adopted for $NH_4Cl$(aq) by PALMER and SIMONSON (1993). NaCl(aq) properties in the mixed-electrolyte media were then calculated from the approximate relation

$$\ln\gamma_\pm(NaCl) \approx \ln\gamma^*_\pm(NaCl) + y\Delta\phi^* \quad (2)$$

Quantities marked with an asterisk represent pure-electrolyte values at the ionic strength of the mixture, $\Delta\phi^* = \phi^*(NX) - \phi^*(NaCl)$ and $y = m(NX)/\{m(NX)+m(NaCl)\}$ where NX is HCl or NaOH. It is clear from Table 1 that m(NX) is never large relative to m(NaCl) in the present experiments, and that equation (2) should therefore provide a suitable approximate representation for the activity coefficient of NaCl(aq) in the mixed electrolyte.

The partitioning equilibrium constants $K_D$ calculated from the observed partitioning of NaCl between liquid and vapor phases for the various media considered here are shown graphically in Figures 2 and 3. The scatter in the experimental values, which may be as large as ±0.5 log units, particularly at lower temperatures, is indicative of the difficulty in determining quantitatively the very low

levels of NaCl in the vapor phase in the measurements at lower temperatures. As an example, at 250°C the liquid phase NaCl molality is more than six orders of magnitude greater than that of the vapor phase, leading to the possiblity of significant contamination of the vapor samples due to even a small amount of entrained liquid in the vapor phase. However, the consistency of the results as functions of sampling rate in the various media implies that contamination of the vapor samples with entrained liquid was not a significant problem in these experiments.

Within the precision of the experimental determinations, the approximations used to calculate activity coefficients in the liquid phase, and the assumption of unit activity coefficient for low levels of NaCl in the vapor phase, the

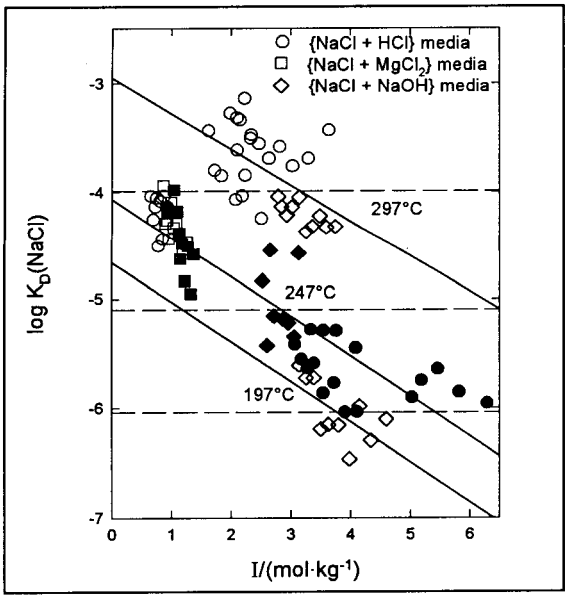


Figure 2. Liquid-vapor distribution constants for NaCl at low temperatures calculated from equation (1).

values of $K_D$ shown in Figures 2 and 3 should be independent of solution composition, as indicated by the horizontal dashed lines on these figures. However, linear regressions of the data (solid lines) show an apparent dependence of log $K_D$ on ionic strength which is larger than the experimental uncertainty. It is possible that the observed dependence is due to a failure of one or both of the assumptions concerning the value of the activity coefficients of NaCl in the liquid phase and the state of the solute in the vapor (associated NaCl with unit activity coefficient), or to systematic errors in the determination of equilibrium molalities of the two phases. However, $K_D$ decreases by approximately one order of magnitude on increasing ionic strength from infinite dilution to about 5 mol·kg$^{-1}$. If small amounts of the liquid phase were systematically entrained in the vapor-phase samples, it is expected that the calculated $K_D$ would increase with increasing liquid-phase molality. An error of 0.5 log units in calculating $\gamma_\pm$ is unlikely due to the precise information available for NaCl(aq) solutions and the relatively small effect of the other constituents of the mixed brines considered here. Significant dissociation of NaCl in the vapor phase, which could lead to an apparent decrease in $K_D$ with increasing ionic strength as calculated from equation (1) through overestimation of the molality of the associated molecule in steam at lower total vapor-phase molalities, seems unlikely due to the low density and dielectric constant of the vapor phase even at the highest temperatures considered here. Neglecting the presence of dissociated ions in the vapor phase is supported by calculations of the association constant of NaCl in steam as extrapolated from electrical conductance measurements at high temperatures (QUIST and MARSHALL, 1968). Finally, although little is known about the activity coefficient of the [assumed] associated NaCl in the vapor phase, it should be noted that the total vapor-phase NaCl molality near 347°C increases by only about a factor of five between the lowest (ca. 0.2) and highest (ca. 4.5) ionic strengths investigated in this work. Thus the activity coefficient of NaCl in the vapor phase would have to decrease quite strongly with increasing molality to give log $K_D$ values which are independent of ionic strength.

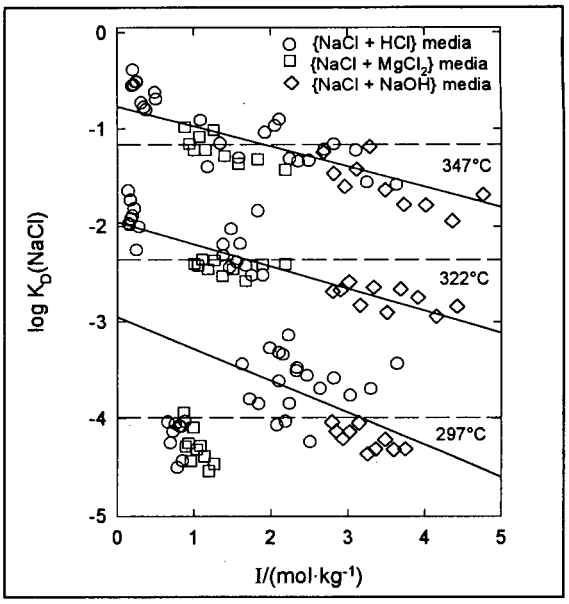


Figure 3. Liquid-vapor distribution constants for NaCl at high temperatures calculated from equation (1).

Equilibrium constants on a Gibbs free energy basis, such as those calculated for the partitioning of NaCl, are appropriate to conditions of constant temperature and pressure. As the ionic strength in these experiments increases the pressure decreases significantly, particularly at the higher temperatures. For example, at 347°C the observed experimental pressures decrease by more than 10% on increasing ionic strength from 0.2 to 4 mol·kg$^{-1}$. The effect of this pressure decrease on the liquid-phase

activity coefficient of NaCl is small, but may in principle lead to a significant change in $K_D$ depending on the magnitude of the volume change $\Delta V°$ for the reaction.

Recently PITZER and PABALAN (1986) have addressed the question of the thermodynamics of NaCl in steam, considering the formation of multiple hydrates of the neutral NaCl molecule in steam and including interparticle interactions based on statistical mechanical models of imperfect gases. Their working equation for the ratio of the total [volumetric] NaCl concentration in steam to the gas-phase NaCl concentration over pure NaCl(cr) was given in terms of a power series in the fugacity of water vapor, with coefficients given by the equilibrium constants for steam-phase hydrate formation. A somewhat similar but much less rigorous approach was adopted by STRYKOVICH *et al.* (1965) to describe both NaCl solubility in supercritical steam and liquid-vapor partitioning under subcritical conditions. These investigators used the density of water and steam as an independent variable in their representation of the data available to them, reflecting the assumed degree of hydration of NaCl.

The observed behavior of log $K_D$ values obtained in this study as illustrated in Figures 2 and 3 was represented with the fitting equation:

$$\log K_D = a + b/T + c \log \rho_l + d \log \rho_v \qquad (3)$$

where a = -33.31, b = 33829, c = 7.152, and d = 20.728; $\rho_l$ and $\rho_v$ are the densities of liquid water and steam respectively at the experimental conditions as calculated from the equation of state of HAAR, GALLAGHER, and KELL (1984).

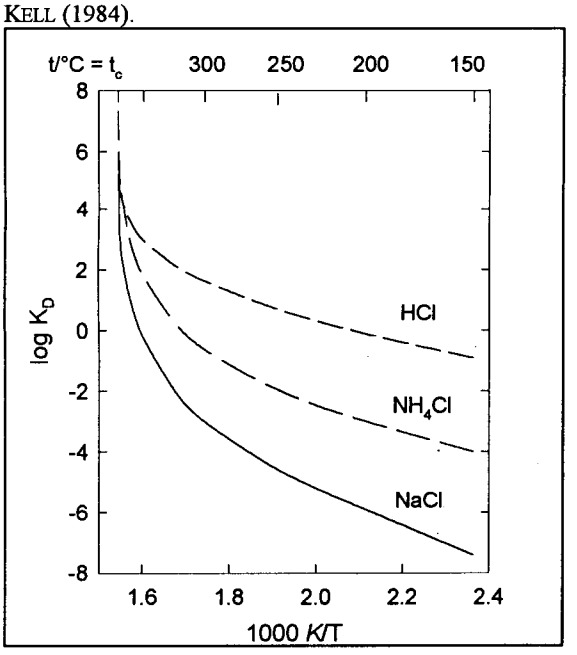


Figure 4. Comparison of liquid-vapor distribution constants of HCl, $NH_4Cl$, and NaCl at the saturation vapor pressure of pure water.

The parameters are based solely on a preliminary fit of the results of this study; the overall fit of the available subcritical partitioning data is expected to change somewhat as additional experimental results in the literature are incorporated fully into the data analysis. However, even with this provisional representation, it is possible to make comparisons of the results of this study with recent measurements on HCl and $NH_4Cl$ under similar conditions. Such a comparison is shown in Figure 4, where it is clear that HCl is significantly more volatile than $NH_4Cl$, which is in turn more volatile than NaCl at the same temperature.

Due to its fundamental importance the NaCl(aq) system is the most thoroughly investigated aqueous electrolyte at elevated temperatures and pressures. It is not possible here to review the extensive literature data on this system, nor to present detailed comparisons of the present measurements with previously available values. Of the previous studies of compositions of coexisting liquid and vapor phases in NaCl(aq), the work of Khaibullin and Borisov (1966) provides the most direct comparison with the present results. Among other studies the work of ÖLANDER and LIANDER (1950) and GOODSTINE (1974) include measurements at subcritical temperatures slightly above those considered here, and STEPHAN and KUSKE (1983) measured NaCl partitioning at constant pressures (120 and 160 bars) within the ranges of the present work. BISCHOFF, ROSENBAUER and PITZER (1986) reported steam compositions along the three-phase line near 300, 325, and 350°C, and have referenced the numerous other studies of NaCl(cr) solubility in steam. While detailed comparisons are still in progress, a comparison of the present results with those of KHAIBULLIN and BORISOV (1966) shows systematic differences at all temperatures. Above 300°C, $K_D$ calculated from the measurements reported here are higher by 1 log unit than those calculated from the results of KHAIBULLIN and BORISOV, with very similar trends as a function of liquid-phase ionic strength. This difference increases with decreasing temperature, with values calculated from equation (3) higher by nearly 2 log units at 200°C than those of KHAIBULLIN and BORISOV. Comparisons with the results of STEPHAN and KUSKE (1983) show somewhat smaller systematic deviations, with the present results again higher. These differences might indicate a systematic error in the present measurements due to the presence of small amounts of entrained liquid in the vapor-phase samples, or to some contamination of the vapor-phase samples with excess solute. The wide range of solution compositions and sampling rates used in this study was intended to minimize the possibility of unrecognized systematic errors, but this possibility cannot be completely discounted. Nevertheless, systematic sample contamination seems unlikely due to the observed agreement among the studies in the various media: ion-chromatographic analysis for sodium ion was used to determine the NaCl vapor-phase molality in the runs with excess HCl, whereas analysis for

chloride ion was the indicator used in the experiments with excess NaOH. Mass balance among all components of the vapor and liquid phases was observed in all experiments within the precision of the ion-chromatographic determinations. In their development of an equation of state for near-critical NaCl-$H_2O$, TANGER and PITZER (1989) noted that "the vapor compositions reported by KHAIBULLIN and BORISOV (1966) at or below 350°C are much too small to be consistent with the measurements of BISCHOFF *et al.* (1986)", which Tanger and Pitzer adopted along the three-phase curve. A full analysis of the available experimental results at temperatures below 350°C, which clearly is needed to address the discrepancies noted above, is currently in progress.

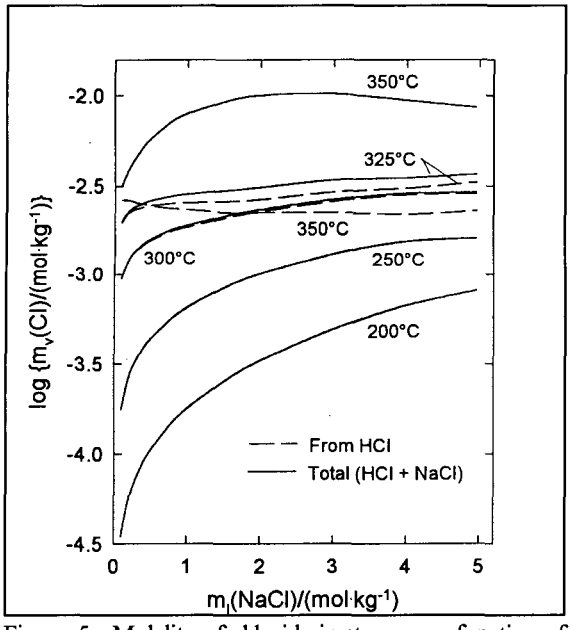


*Figure 5. Molality of chloride in steam as a function of temperature and NaCl(aq) molality for brines with pH = 3.*

The representation for the partitioning constant $K_D$ given in equation (3) may be combined with activity coefficients for NaCl(aq) to calculate the NaCl molality in steam in equilibrium with NaCl(aq) over wide ranges of temperature and liquid-phase molality. Partitioning constants and activity coefficients for other solutes may also be combined with the NaCl data to permit calculation of the steam composition over mixed electrolyte brines. As an example, the composition of steam in equilibrium with acidic NaCl(aq) solutions was calculated from the results of this study, combined with the equation for $K_D$ for HCl given by SIMONSON and PALMER (1993). Activity coefficients in the aqueous mixture were calculated from equation (2) using values for the pure-electrolyte activity and osmotic coefficients taken from BUSEY *et al.* (1984) for NaCl(aq), and from SIMONSON *et al.* (1990) for HCl(aq).

The calculated molalities of chloride in steam are shown in Figure 5. The total chloride molality in steam is indicated in this figure by the solid lines, while the contribution from HCl partitioning is indicated by the dashed curves. At a pH of 3 the contribution of NaCl partitioning to the total chloride molality in the steam is negligible at temperatures to 300°C, as indicated by the coincidence of the HCl-contribution and total-chloride curves at these temperatures. At higher temperatures the calculated vapor-phase chloride molality due to HCl partitioning decreases with increasing temperature even though the partitioning constant for HCl increases strongly (SIMONSON and PALMER, 1993). This behavior, which is due to the very low values of the activity coefficient for HCl in these media at high temperatures, has been verified experimentally (SIMONSON and PALMER, in preparation). At these higher temperatures the partitioning of NaCl contributes significantly to the total chloride molality in steam, increasing to near 0.01 $mol \cdot kg^{-1}$ over a wide range of liquid-phase ionic strength at 350°C. This high chloride molality in steam, corresponding to *ca.* 350 ppm, indicates the importance of NaCl partitioning to the total molality of chloride in steam at the highest temperatures encountered at The Geysers.

The presence of even low levels of solutes in the vapor phase may lead to the production of quite concentrated, and hence potentially corrosive, brines on condensation of a small percentage of the steam. This concentration process can also be accompanied by significant shifts in pH from that of the original brine. Calculation of the composition of condensates has been discussed in detail for geothermal brines by HIRTZ *et al.* (1991), and for the limiting case of infinitessimal condensate formation in all-volatile-treated steam generators by PALMER and SIMONSON (1993). These calculations are dependent on the process conditions of interest (steam formation and condensation temperatures; liquid-phase composition) and will not be discussed in detail here. However, it should be noted that equilibrium liquid and steam compositions may now be calculated for Na - H - $NH_4$ - Cl brines to 350°C based on experimental results from this laboratory, and that experiments currently in progress on sulfates, bisulfates and hydroxides should contribute significantly toward a description of liquid-vapor equilibria of "nonvolatile" components in a wide variety of mixed brines of importance in natural systems.

ACKNOWLEDGEMENTS

Research sponsored by the Geothermal Technology Division, Office of Conservation and Renewable Energy, U.S. Department of Energy, under Contract DE-AC05-84OR21400 with Martin Marietta Energy Systems, Inc.

REFERENCES


ARCHER D. G. (1992) Thermodynamic properties of the NaCl + $H_2O$ system II. Thermodynamic properties of NaCl(aq), NaCl·$2H_2O$(cr), and phase equilibria. *J. Phys. Chem. Ref. Data* **21**, 793-829.

BISCHOFF J. L., ROSENBAUER R. J. and PITZER K. S. (1986) The system NaCl-$H_2O$: Relations of vapor-liquid near the critical temperature of water and of vapor-liquid-halite from 300° to 500°C. *Geochim. Cosmochim. Acta* **50**, 1437-1444.

BUSEY R. H., HOLMES H. F. and MESMER R. E. (1984) The enthalpy of dilution of aqueous sodium chloride to 673 K using a new heat-flow and liquid-flow microcalorimeter. Excess thermodynamic properties and their pressure coefficients. *J. Chem. Thermodynamics* **16**, 343-372.

GOODSTINE S. L. (1974) Vaporous carryover of sodium salts in high-pressure steam. *Proc. Am. Power Conf.* **36**, 784-489.

HAAR L., GALLAGHER J. S. and KELL G. S. (1984) *NBS/NRC Steam Tables: Thermodynamic and Transport Properties and Computer Programs for Vapor and Liquid States of water in SI Units.* Hemisphere.

HIRTZ P., BUCK C. and KUNZMAN R. (1991) Current techniquies in acid-chloride control and monitoring at The Geysers. *Proc. Stanford Geo. Res. Eng. Workshop* **16**, 83-95.

KHAIBULLIN I. KH. and BORISOV N. M. (1966) Experimental investigation of the thermal properties of aqueous and vapor solutions of sodium and potassium chlorides at phase equilibrium. *High Temperature* **4**, 489-494.

ÖLANDER A. and LIANDER H. (1950) The phase diagram of sodium chloride and steam above the critical point. *Acta Chem. Scand.* **4**, 1437-1445.

PALMER D. A. and SIMONSON J. M. (1993) Volatility of ammonium chloride over aqueous solutions to high temperatures. *J. Chem. Eng. Data* **38**, 465-474.

PITZER K. S. and PABALAN R. T. (1986) Thermodynamics of NaCl in steam. *Geochim. Cosmochim. Acta* **50**, 1445-1454.

PITZER K. S., PEIPER J. C. and BUSEY R. H. (1984) Thermodynamic properties of aqueous sodium chloride solutions. *J. Phys. Chem. Ref. Data* 13, 1-102.

QUIST A. S. and MARSHALL W. L. (1968) Electrical conductances of aqueous sodium chloride solutions from 0 to 800°C and at pressures to 4000 bars. *J. Phys. Chem.* **72**, 684-703.

SIMONSON J. M., HOLMES H. F., BUSEY R. H., MESMER R. E., ARCHER D. G. and WOOD R. H. (1990) Modeling of the thermodynamics of electrolyte solutions to high temperatures including ion association. Application to hydrochloric acid. *J. Phys. Chem.* **94**, 7675-7681.

SIMONSON J. M., MESMER, R. E. and ROGERS, P. S. Z. (1989) The enthalpy of dilution and apparent molar heat capacity of NaOH(aq) to 523 K and 40 MPa. *J. Chem. Thermodynamics* **21**, 561-584.

SIMONSON J. M. and PALMER D. A. (1993) Liquid-vapor partitioning of HCl(aq) to 350°C. *Geochim. Cosmochim. Acta* **57**, 1-7.

STEPHAN K. and KUSKE E. (1983) Distribution of electrolytes over vapour and liquid phase in high pressure equilibria. *Chem. Eng. Fundamentals* **2**, 50-65.

STYRIKHOVICH M. A., MARTYNOVA O. I. and BELOVA Z. S. (1965) Some features of the carryover of sodium chloride from boiling water into steam. *Thermal Engineering* **12**, 115-118.

TANGER IV J. C. and PITZER K.S. (1989) Thermodynamics of NaCl - $H_2O$: A new equation of state for the near-critical region and comparisons with other equations for adjoining regions. *Geochim. Cosmochim. Acta* **50**, 973-987.

TRUESDELL A. H., HAIZLIP J. R., ARMANNSSON H. and D'AMORE F. (1988) Origin and transport of chloride in superheated geothermal steam. *Proceedings: Deposition of Solids in Geothermal Systems*, Reykjavik, Iceland, 16-19 August 1988, pp. 1-12.

PROCEEDINGS, Nineteenth Workshop on Geothermal Reservoir Engineering
Stanford University, Stanford, California, January 18-20, 1994
SGP-TR-147

# THEORETICAL STUDIES OF FLOWRATES FROM SLIMHOLES AND PRODUCTION-SIZE GEOTHERMAL WELLS

Teklu Hadgu, Robert W. Zimmerman and Gudmundur S. Bodvarsson

Earth Sciences Division
Lawrence Berkeley Laboratory
University of California
Berkeley, CA 94720

## ABSTRACT

The relationship between production rates of large diameter geothermal production wells, and slimholes, is studied. The analysis is based on wells completed in liquid-dominated geothermal fields, where flashing occurs either in the wellbore or at the surface. Effects of drawdown in the reservoir, and pressure drop in the wellbore, are included; heat losses from the wellbore to the formation are not presently included in our analysis. The study concentrates on the influence of well diameter on production rate. For situations where the pressure drop is dominated by the reservoir, it is found that the mass flowrate varies with diameter according to $W \sim D^{\alpha}$, where the exponent $\alpha$ is a function of reservoir outer radius, well diameter and skin factor. Similarly, when pressure drop in the wellbore is dominant, the scaling exponent was found to be a function of well diameter and pipe roughness factor. Although these scaling laws were derived for single-phase flow, numerical simulations showed them to be reasonably accurate even for cases where flashing occurs in the wellbore.

## INTRODUCTION

Drilling of slimholes instead of large diameter production-sized wells may be economically beneficial during the exploration phase of a geothermal prospect or during exploration of an undeveloped part of a producing reservoir. It has been reported that slimholes with diameters less than or equal to 4" could reduce the cost and time of drilling significantly (see for example, Entingh and Petty, 1992). Slimholes can also provide continuous cores which would help identify geological features more clearly. This report concentrates on the effect of wellbore diameter on production characteristics. Cost analysis, drilling practices and other relevant topics concerning slimholes are not discussed.

As fluid flows from the reservoir to the surface through the wellbore, pressure drawdown occurs both in the reservoir and in the wellbore. As pointed out by Pritchett (1993), it would be helpful to have a scaling law that allows the flowrate of a slimhole to be predicted from the flowrate of a normal-diameter hole under the same conditions. Following Pritchett, we will attempt to develop power-law scaling relationships to describe the effect of wellbore diameter on well output. We first carry out an analysis for single-phase flow, for which it is possible to derive some analytical expressions. We then discuss the case where flashing occurs at some point in the wellbore.

## PRESSURE DRAWDOWN IN THE RESERVOIR

Fluid flow from the reservoir into the wellbore has been studied by many investigators over the last half century or so, including processes such as the nature and direction of flow, transient or steady-state, single or two-phase, laminar or turbulent flow, and permeability reduction (well damage) or enhancement due to drilling and production/injection activities.

In these studies, reasonable simplifications have been suggested. For instance, the flow from the reservoir into the wellbore is sometimes assumed to be steady or quasi-steady, because flow equilibrates faster near the wellbore than in the reservoir as a whole (Pritchett and Garg, 1980). One could consider the direction of flow into the wellbore as spherical. However, with time it is assumed to approach horizontal radial flow. Other assumptions can also be made based on estimates of the amount and type of fluid, and the near-well reservoir behavior.

Consider the pressure drop that occurs in the reservoir as the fluid flows toward the wellbore. Imagine a bounded, circular reservoir, whose outer boundary $r = r_o$ is maintained at some pressure $p_o$ (see Fig. 1). If the wellbore has radius $r_w$, and the downhole wellbore pressure is maintained at $p_{wb}$, the steady-state flowrate under Darcy-flow conditions will be given by (Matthews and Russell, 1967, p. 21)

$$W = \frac{2\pi\rho kh}{\mu} \frac{(p_o - p_{wb})}{\ln(r_o/r_w) + s} \qquad (1)$$

where ρ is the fluid density, kh is the reservoir permeability-thickness product, μ is the fluid viscosity, and s is the well skin factor. This relation between pressure drop and flowrate will also hold during the transient process of production from a reservoir that is initially at uniform pressure, except at extremely small times that are of little practical relevance (see de Marsily, 1986, pp. 161-167). Hence, this relation is sufficiently general that it can be used as the basis of our scaling-law analysis. Equation (1) is often written in terms of the productivity index as

$$W = \frac{\rho PI}{\mu}\,(p_o - p_{wb}) \tag{2}$$

where PI is the productivity index, which can be expressed as

$$PI = \frac{2\pi kh}{\ln(r_o/r_w)+s} \tag{3}$$

If we compare two wells of different diameters that are producing under otherwise identical conditions, equations (1) and (3) predict that their flowrates will be in the ratio

$$\frac{W_1}{W_2} = \frac{PI_1}{PI_2} = \frac{\ln(2r_o/D_2)+s_2}{\ln(2r_o/D_1)+s_1} \tag{4}$$

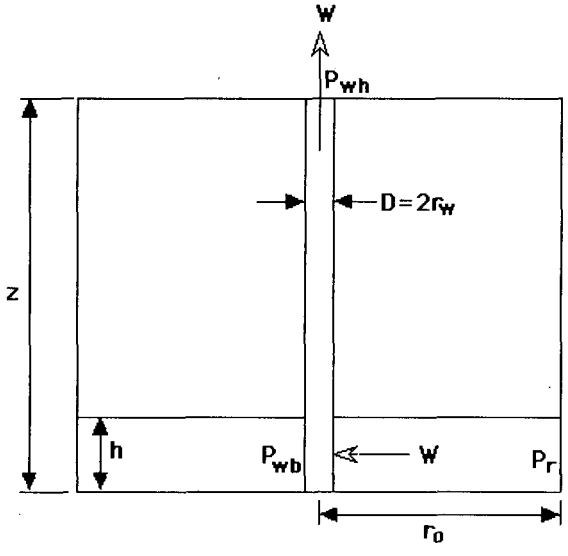


Fig. 1. Schematic diagram of the problem considered.

This ratio depends on the wellbore diameters, and also on the outer radius of the reservoir. In order to simplify the analysis that follows, we will assume that the skin factor does not depend on diameter, i.e., $s_1 = s_2$. However, if there was some knowledge of the variation of s with D, the method described below could be modified to account for this. For simplicity, and because power-law equations (representing different effects) can easily be combined, we will approximate equation (4) with a power-law. If $(PI_1/PI_2) = (D_1/D_2)^{\beta}$, then the exponent β would be given by

$$\beta = \frac{d\ln PI}{d\ln D} = \frac{D}{PI}\frac{dPI}{dD}. \tag{5}$$

In order to fit equation (4) to a power-law equation, we take its logarithmic derivative as in equation (5), and evaluate it at some reference diameter $D_2$. Specifically, we treat the parameters with subscript 1 as variables, and hold those with subscript 2 constant, and then set $D_1 = D_2$ when evaluating the derivative, to arrive at

$$\frac{D}{PI}\frac{dPI}{dD}\Big]_{D_1=D_2} = \beta = \left[\ln\left[\frac{2r_o}{D_2}\right] + s\right]^{-1} \tag{6}$$

Hence the ratios of the productivity indices and flowrates, between two otherwise identical boreholes, each having the same pressure drawdown in the reservoir, will be

$$\frac{W_1}{W_2} = \frac{PI_1}{PI_2} = \left[\frac{D_1}{D_2}\right]^{[\ln(2r_o/D_2)\,+\,s]^{-1}} \tag{7}$$

To estimate the ratio of mass flowrates, the outer radius $r_o$ and the skin factor s have to be determined. The skin factor may be obtained from well test analyses. For reservoir modeling exercises $r_o$ is the distance to the nodal point of the wellblock, the value of which depends on the type of computational grid selected. Hadgu et al. (1993) recently presented a method for determining the distance from the well to the nodal point of the wellblock. Similar studies have also been reported by Aziz and Settari (1979) and Pritchett and Garg (1980), among others.

If non-Darcy flow effects are important, equation (2) becomes inadequate; an analysis of this situation is given by Hadgu et al. (1993), Kjaran and Eliasson (1983), Hadgu (1989), Iglesias and Moya (1990) and Gunn and Freeston (1991), among others.

## PRESSURE DROP IN THE WELLBORE

The pressure drop in the wellbore is a sum of frictional, gravitational and accelerational components. For convenience, the following analysis ignores the accelerational pressure drop. For a comparison of output of large and small diameter wells, the parameters of interest will be friction factor λ, mass flowrate W, and the inside pipe diameter D.

First, consider the flow in the wellbore, temporarily ignoring the pressure drop in the reservoir itself. Under the assumption that the dynamic properties and pressure drop are the same for two wells with diameters $D_1$ and $D_2$, Pritchett (1993) proposed the following scaling law based on the ratios of the cross-sectional areas:

$$\frac{W_1}{W_2} = \frac{A_1}{A_2} = \left[\frac{D_1}{D_2}\right]^2 \quad (8)$$

A more accurate scaling equation in the form of a power-law can be formulated by considering the equations that govern wellbore flow, including the effect of frictional losses. The frictional and gravitational components of the pressure gradient can be expressed as

$$\frac{dp}{dz} = \left[\frac{dp}{dz}\right]_{fric} + \left[\frac{dp}{dz}\right]_{grav} = \frac{\lambda \rho v^2}{2D} + \rho g \quad (9)$$

where $\lambda$ is the Darcy friction factor and v is the mean fluid velocity, which is equal to $W/(\pi D^2/4)$. If we are comparing flows in two wellbores that occur under the same pressure drop, and assuming equivalent fluid properties, then equation (9) reduces to

$$\frac{\lambda v^2}{D} = \frac{2}{\rho}\left[\frac{dp}{dz} - \rho g\right] = \text{constant} = C \quad (10)$$

The friction factor depends on the Reynolds number, which is defined by

$$Re = \rho v D/\mu \quad (11)$$

as well as on the relative roughness of the wellbore casing, $\varepsilon/D$. One correlation that has been widely used to relate these parameters is the Colebrook equation (White, 1974, p. 498):

$$\frac{1}{\sqrt{\lambda}} = 1.74 - 4.605 \ln\left[\frac{2\varepsilon}{D} + \frac{18.7}{Re\sqrt{\lambda}}\right] \quad (12)$$

In order to find a relationship between flowrate and diameter, we first use equations (11) and (12) to eliminate explicit reference to Re and $\lambda$, to find

$$v = (CD)^{0.5}\left[1.74 - 4.605 \ln\left[\frac{2\varepsilon}{D} + \frac{18.7\mu}{\rho\sqrt{C}\, D^{1.5}}\right]\right]$$
$$\equiv (CD)^{0.5} f(D) \quad (13)$$

The first part of the right-hand side of the expression is already in the form of a power-law equation. The bracketed term f(D) is not of that form, but can be approximated by a power-law. If we assume

$$f(D) = \text{const.}\, D^{\alpha} \quad (14)$$

the parameter $\alpha$ would be given by

$$\alpha = \frac{d\ln f}{d\ln D} = \frac{D}{f}\frac{df}{dD} \quad (15)$$

We can calculate the derivative df/dD, and then evaluate expression (15) at some reference value $D = D_2$, to arrive at a value for the scaling exponent $\alpha$. Carrying out this differentiation, and then expressing the results in terms of Re and $\lambda$, we eventually find

$$\alpha = 4.605\sqrt{\lambda_2}\left[\left(\frac{2\varepsilon}{D_2} + \frac{18.7(1.5)}{Re_2\sqrt{\lambda_2}}\right) \Big/ \left(\frac{2\varepsilon}{D_2} + \frac{18.7}{Re_2\sqrt{\lambda_2}}\right)\right] \quad (16)$$

Equation (16) has a very weak dependence on Re, since the bracketed term varies only from 1, at high Reynolds numbers, to 1.5, at low Reynolds numbers. Hence, in order to arrive at a value of $\alpha$ that depends on as few parameters as possible, we now evaluate equation (16) in the limit of high Reynolds numbers. In this case, the bracketed term in equation (16) goes to 1.0, and for realistic values of $\varepsilon/D$, equation (12) can be approximated by

$$\sqrt{\lambda_2} = \left[-4.605 \ln(2\varepsilon/D_2)\right]^{-1} \quad (17)$$

Equation (16) then simplifies to

$$\alpha = -\left[\ln\left(\frac{2\varepsilon}{D_2}\right)\right]^{-1} \quad (18)$$

which depends only on the relative roughness of the casing. If we now combine equations (12, 13 and 14), we find

$$\frac{v_1}{v_2} = \left[\frac{D_1}{D_2}\right]^{0.5 - [\ln(2\varepsilon/D_2)]^{-1}} \quad (19)$$

Finally, we note that the flowrate is given by the product of the mean velocity and the cross-sectional area, so that

$$\frac{W_1}{W_2} = \frac{v_1 A_1}{v_2 A_2} = \frac{v_1}{v_2}\left[\frac{D_1}{D_2}\right]^{2.0} = \left[\frac{D_1}{D_2}\right]^{2.5 - [\ln(2\varepsilon/D2)]^{-1}} \quad (20)$$

If we assume typical values for the relative roughness in the range of $10^{-3}$ - $10^{-6}$, we find that the exponent in equation (20) depends weakly on roughness, and equals about $2.62 \pm 0.05$. For example, a relative roughness $\varepsilon/D_2 = 10^{-6}$ leads to an exponent of 2.58, whereas a value of $\varepsilon/D_2 = 10^{-3}$ gives an exponent of 2.66. This variation is probably less than the error introduced by fitting equation (13) with a power-law equation. Hence, taking into account the approximate nature of this analysis, one arrives at the following scaling law, which does not contain any reference to the roughness parameter:

$$\frac{W_1}{W_2} = \left[\frac{D_1}{D_2}\right]^{2.62} \quad (21)$$

The exponent 2.62 is close to the value of 2.56 that Pritchett (1993) found by fitting a power-law curve to numerically-computed values of W and D, assuming a wellhead pressure of 1 bar.

TOTAL PRESSURE DRAWDOWN

Assuming that the reservoir pressure ($p_r$) and the depth of the well (z) are known (Fig. 1), for a selected wellhead pressure ($p_{wh}$), the sum of pressure drops in the reservoir and in the wellbore, as fluid flows to the surface, can be written as

$$p_r - p_{wh} = \Delta p_{res} + \Delta p_{well} \qquad (22)$$

Using the deliverability equation (2), and assuming a linear drawdown relationship in the reservoir:

$$\Delta p_{res} = \frac{W\mu}{\rho PI} \qquad (23)$$

Pressure drop in the wellbore is subdivided into its components of friction, gravity and acceleration. For single-phase isothermal flow the acceleration term may be ignored. Thus,

$$\Delta p_{well} = \Delta p_{fric} + \Delta p_{grav} \qquad (24)$$

where $\Delta p_{fric}$ and $\Delta p_{grav}$ are the frictional and gravitational pressure drops in the wellbore, respectively. These components are further defined by:

$$\Delta p_{fric} = -\frac{\lambda \rho v^2}{2D} z \qquad (25)$$

$$\Delta p_{grav} = -\rho g z \qquad (26)$$

Equation (25) can be written in terms of mass flowrate instead of velocity, using the relationship

$$v = \frac{W}{\rho A} = \frac{4W}{\rho \pi D^2} \qquad (27)$$

Thus:

$$\Delta p_{fric} = -\frac{8z\lambda W^2}{\pi^2 \rho D^5} \qquad (28)$$

Substituting for the individual parameters, equation (22) can be written as:

$$p_r - p_{wh} = \frac{W\mu}{\rho PI} + \frac{8\lambda z W^2}{\pi^2 \rho D^5} + \rho g z \qquad (29)$$

Equation (29) indicates that the parameters which mainly affect pressure drop between the reservoir and the wellhead are discharge rate, productivity index, well depth and diameter, friction factor and fluid properties. If we assume isothermal flow both in the reservoir and in the wellbore, fluid properties will be approximately constant. For a comparison of output of large and small diameter casings, well depth can also be assumed to be constant. Thus, the parameters involved in the comparison of large and small diameter casings will be discharge rate, productivity index, friction factor and well diameter.

Equation (29) can now be rewritten in terms of W and D, with the help of equations for PI and $\lambda$. Note that $\lambda$ is in fact a function of W, as implicitly shown in equation (12), which implies that equation (29) is not simply a quadratic for W. However, we have found that for high Re, $\lambda$ can be approximated by equation (17), with little loss of accuracy. With this approximation, we can rearrange equation (29) as:

$$\frac{8\lambda z}{\pi^2 \rho D^5} W^2 + \frac{\mu}{\rho PI} W + (\rho g z - p_r + p_{wh}) = 0 \qquad (30)$$

with $\lambda$ given by equation (17). Equation (30) is a quadratic equation for W which is easily solved. The positive root in the solution for W must be taken, since W is by definition a positive quantity. The following is an example to study the relationship between mass flowrate and diameter for single-phase isothermal flow.

Example 1: A well completed in a liquid dominated geothermal reservoir, where the boundary conditions are chosen so that flashing occurs at the surface. If heat exchange with the rock formation is ignored, this is essentially a case of isothermal liquid flow. The reservoir and wellbore parameters are given in Table 1.

Table 1: Reservoir and Wellbore data for Examples 1 and 2.

| | Example 1 | Example 2 |
|---|---|---|
| reservoir pressure $p_r$ (bar) | 100 | 90 |
| reservoir temp. $T_r$ (°C) | 160 | 241 |
| wellhead pressure $p_{wh}$ (bar) | 7 | 7 |
| outer radius $r_o$ (m) | 88 | 88 |
| well depth z (m) | 1000 | 1000 |
| reference diameter $D_2$ (m) | 0.1 | 0.1 |
| pipe roughness $\varepsilon$ (m) | $4.5 \times 10^{-5}$ | $4.5 \times 10^{-5}$ |

Equation (30) was then used to solve for W in terms of D and kh. Fig. 2 shows the calculated values plotted as a ratio of mass flowrates vs. the ratio of diameters at different values of permeability-thickness product, using $D_2 = 0.1$ m as the reference diameter. The curve for kh = 100 D-m in Fig. 2, for example, contains straight line sections at low and high values of $D_1/D_2$. For small values of $D_1$, the pressure drop is dominated by the wellbore, and the curve follows equation (21). For larger values of $D_1$, there is less frictional pressure drop in the wellbore, and the pressure drop in the reservoir becomes relatively more important. In this region the curves approach asymptotes where slopes are given by equation (7). In the present example, s

= 0, $D_2$ = 0.1 m, and $r_o$ = 88 m, so that the exponent in the equation is 0.134.

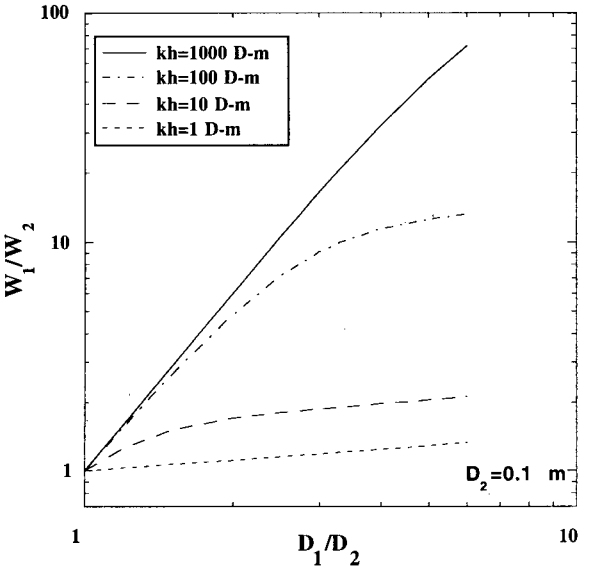


Fig. 2. Ratio of mass flowrate against diameter ratio, for different kh values, for single-phase isothermal flow (see Example 1).

TWO-PHASE FLOW IN THE WELLBORE

If the heat exchange between the wellbore and the surrounding rock formation is important, or two-phase flow exists in the reservoir or wellbore, changes in fluid properties become important. Thus, for non-isothermal single-phase or two-phase flow, fluid properties in the wellbore are not constant, and they have to be integrated over the length of the wellbore. In this case, equation (29) has to be written in the following form:

$$p_r - p_{wh} = \frac{W\mu_r}{\rho_r PI} + \frac{8W^2}{\pi^2 D^5}\int\frac{\lambda(\varepsilon/D,Re)}{\rho}d\zeta + g\int\rho\, d\zeta \qquad (31)$$

where $\rho_r$ and $\mu_r$ are the density and viscosity at reservoir conditions, $\zeta$ is a variable representing depth increment, and the integral is taken from $\zeta = 0$ to $\zeta = z$. Following is an example for two-phase flow.

Example 2: A well is open to a liquid-dominated geothermal reservoir, and flashing occurs in the wellbore. For this example heat exchange with the rock formation is ignored. The reservoir and wellbore parameters assumed are given in Table 1.

The wellbore simulator WFSA (Hadgu and Freeston, 1990) was used to solve for W in equation (31) in terms of D and kh. An iterative scheme was needed to equate the flow in the reservoir to that in the wellbore. Fig. 3 shows the calculated ratio of mass flowrates vs. the ratio of diameters at different values of kh. In this case the effect of fluid properties is evident, as fluid flashes at greater depths, longer columns of two-phase flow result. In Fig. 3, the plots for the higher kh values (i.e. 100, 10 and 1 D-m) show straight line portions for low $D_1/D_2$ values. This is similar to that of single phase flow where wellbore flow dominates.

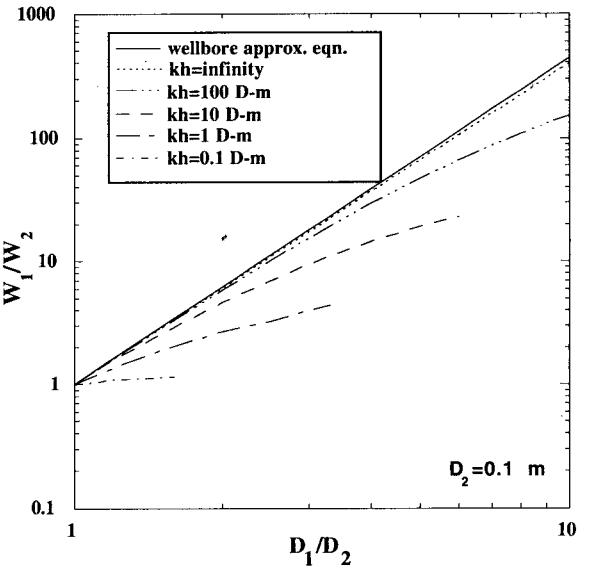


Fig. 3. Ratio of mass flowrate against diameter ratio for different kh values, with flashing occurring in the wellbore (see Example 2).

In this example the wellhead pressure is 7 bars, the undisturbed reservoir pressure is 90 bars, and the saturation pressure at the reservoir temperature of 241°C is 34 bars. Hence flashing will occur at some point between the reservoir far-field and the wellhead. As the wellbore diameter increases, the flow resistance in the wellbore decreases, and flashing occurs deeper. At some critical diameter D* flashing occurs at the bottom of the wellbore, when the bottomhole pressure equals the saturation pressure at the reservoir temperature. If the bottomhole pressure is reduced below the saturation temperature, flashing would occur in the reservoir. Our analysis does not include such cases since equation (31) assumes that fluid properties are constant in the reservoir. For flashing occurring both in the reservoir and in the wellbore a coupled numerical simulation of the flow processes in the reservoir and in the wellbore will be required. Hence our analysis, using equation (31), cannot be used to find the production curve when D is greater than D*.

Density changes also affect the pressure gradients, and the gravitational pressure gradient, which was constant in the single phase case, becomes important. At low flows and large wellbore diameters, the effect of frictional pressure gradient decreases, and the total pressure drop becomes dominated by gravity and reservoir drawdown.

The above analysis was made using the total pressure drawdown. The same parameters were also used to compare the pressure drop in the wellbore (i.e., no reservoir drawdown) with that of single-phase flow, by using equation (31) without the reservoir term. In order to evaluate the integral appearing in equation (31), we need to know how the density varies as a function of depth. To find the density profile, we use the wellbore simulator WFSA, which in effect performs the required integrations. The production rate, shown in Fig. 3 as the curve labeled k = infinity, is then compared with that produced by equation (20), which was developed for single-phase flow. The results are shown in Fig. 3, where it is seen that these two curves are quite close to each other, suggesting that equation (20) may also be used for some cases where flashing occurs in the wellbore.

For reservoir management purposes, it is useful to have plots of mass flowrate as a function of wellhead pressure, for given wellbore diameter values. Such production curves are shown in Fig. 4, for the case described in Example 2. In this case the wellhead pressure was not held constant. Equation (31) was used to compute values of W and $p_{wh}$ at constant diameter and kh. Fig. 4 shows the characteristic curves obtained for different diameters at a constant kh of 100 D-m. Note that the curves are identically shaped, but are displaced vertically on a semi-log plot; this can be explained as follows. For the parameters used in this example, kh is relatively high, and most of the flow resistance occurs in the wellbore. Hence, we see from equations (10) and (21) that

$$W(D) = f(p_{wh})\,(D/D_2)^{2.62} \qquad (32)$$

so that

$$\log(W(D)) = \log(f(p_{wh})) + 2.62\log(D/D_2)$$
$$= F(p_{wh}) + 2.62\log(D/D_2) \qquad (33)$$

Hence each curve should have the same shape, given by the function $F(p_{wh})$, but with a vertical offset equal to $2.62\log(D/D_2)$. As an example, consider the curve for D = 0.2 m, for which $D/D_2 = 0.2/0.1 = 2$. The calculated offset of $2.62\log(2) = 0.79$ is shown as a vertical line in Fig. 4, where it is seen to be very nearly equal to the actual vertical offset between the D = 0.2 m and D = 0.1 m curves. Note that the maximum discharge pressure is almost constant (about 22 bars in this example). This is consistent with the findings reported by Grant et al. (1982, pp. 138-139) and others, to the effect that the maximum discharge pressure depends only on the reservoir pressure and discharge enthalpy. Both of these parameters are constant in our analysis. For reservoirs with a lower permeability, the pressure drop in the reservoir becomes important, and a scaling law of the form given in equations (32) and (33) does not hold. For these cases, the production curves could be generated by solving equation (30) numerically for different values of $p_{wh}$.

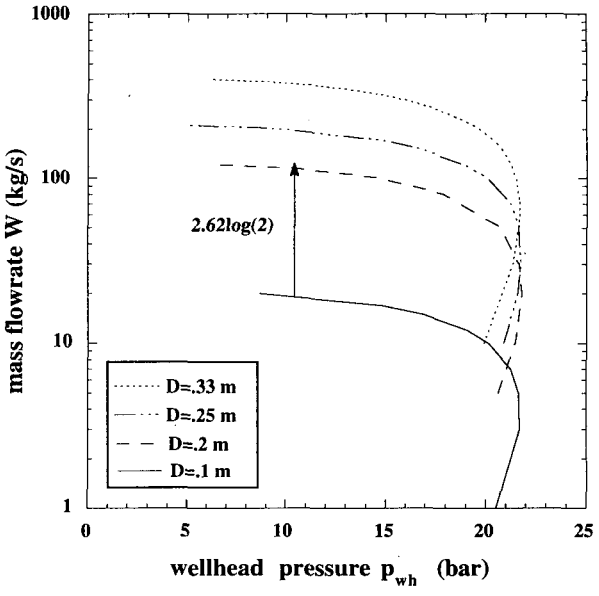


Fig. 4. Comparison of production of different diameter wells as a function of wellhead pressure. The curves are displaced vertically by an amount equal to $2.62\log(D/D_2)$.

## APPLICATION TO FIELD DATA

In this example we use field measurements to test the scaling law analyses. Production well PW3-3 and slimhole TH#1 are located in the Steamboat Hills geothermal field, Nevada, and are about 15 m apart. They have been drilled to similar total depths, and hence probably extend through similar geological structure. Data for both wells (from Goranson, 1993) are shown in Table 2.

Since both wells are located in a highly permeable reservoir, the production rates should be controlled by the wellbore. Thus, it seems appropriate to use the scaling law given by equation (20). To use the scaling law, the production data for both wells have to be similar, except for diameters and mass flowrates. However, in this case the wellhead pressures for the two wells are not equal. In order to apply the scaling laws to these data, we proceed as follows. Since static and flowing pressure and temperature profiles are available for TH#1, we first calculated the productivity index. Using equation (2) and the data in Table 2, the calculated value was $PI = 8.339 \times 10^{-11}$ m$^3$. Then using the calculated productivity index the, wellbore simulator WFSA (Hadgu and Freeston, 1990) was used to predict mass flowrate for well TH#1 at a wellhead pressure of 3.97 bars. Additional input data for wellbore simulation were obtained from Table 2, and a roughness value of $\varepsilon = 4.5 \times 10^{-5}$ m was selected. The computed values using the wellbore simulator were W = 2.07 kg/s and $p_{wb}$ = 22.78 bars. To predict the mass flowrate of the production well PW3-3, we used the scaling law given by equation (20):

$$W_1 = W_2 \left[ \frac{D_1}{D_2} \right]^{2.5 - [\ln(2\varepsilon/D2)]^{-1}} \quad (34)$$

For $\varepsilon = 4.5 \times 10^{-5}$ m, $D_1 = 0.318$ m, $D_2 = 0.076$ m and $W_2 = 2.07$ kg/s, equation (34) gives $W_1 = 91.6$ kg/s. The measured flowrate to well PW3-3 was about 84.2 kg/s, which is 8.8% less than the value predicted by the scaling law. Although this is not a direct verification of the utility of the scaling law, this agreement is encouraging, considering the assumptions made in the analysis, and the unavoidable inaccuracies in the measured data.

Table 2: Data on wells PW3-3 and TH#1, Steamboat Hills (from Goranson, 1993).

| | PW3-3 | TH#1 |
|---|---|---|
| total depth z(m) | 258.2 | 272.6 |
| casing diameter D(m) | 0.318 | 0.076 |
| openhole diameter D(m) | 0.311 | 0.070 |
| wellhead pressure $p_{wh}$ (bar abs.) | 3.97 | 3.07 |
| mass flowrate W (kg/s) | ~ 84.2 | 3.13 |
| static bottomhole pressure $p_r$ (bar abs.) | 22.83 | - |
| flowing bottomhole pressure $p_{wb}$ (bar abs.) | 22.76 | - |
| bottomhole temp. $T_{wb}$ (°C) | 166.1 | 162.8 |

## CONCLUSIONS

Analytical and numerical approaches to the characterization of output of different diameter geothermal wells have been presented. It is shown that flow processes in the reservoir and wellbore can be characterized by using scaling laws. The wellbore simulator WFSA (Hadgu and Freeston, 1990) was also used to provide numerical results to study flow processes when pressure drop in both the reservoir and wellbore are important. Future analysis should also include a study of the effect of wellbore heat losses to the formation. These studies need to be augmented with field data on slimholes and production size wells. Also, other topics concerning slimholes, such as well testing methodology, need to be studied to provide the basis for more effective use of slimholes.

## ACKNOWLEDGMENTS

This work was supported by the Assistant Secretary for Energy Efficiency and Renewable Energy, Geothermal Division, U.S. Department of Energy under Contract No. DE-AC03-76SF00098, and through a sub-contract with Sandia National Laboratories. The authors appreciate the careful technical review of this report by Marcelo Lippmann and Akhil Datta Gupta of LBL, and thank Judith Peterson of LBL for help in the preparation of the manuscript. They also thank Far West Capital, Inc., for allowing the use of their field data.

## REFERENCES

Aziz, K. and Settari, A. (1979), *Petroleum Reservoir Simulation*, Elsevier Applied Science Publishers, London.

de Marsily, G. (1986), *Quantitative Hydrogeology*, Academic Press, San Diego, Calif.

Entingh, D., and Petty, S. (1992), "Effects of Slim Holes on Hydrothermal Exploration Costs", *Geothermal Resourc. Counc. Trans., 16*, 73-81.

Grant, M.A., Donaldson, I., and Bixley, P. (1982), *Geothermal Reservoir Engineering*, Academic Press, New York.

Hadgu, T. (1989), "Vertical Two-Phase Flow Studies and Modelling of Flow in Geothermal Wells", *Ph. D. Thesis*, University of Auckland, New Zealand.

Hadgu, T. and Freeston, D.H. (1990), "A Multi-Purpose Wellbore Simulator", *Geothermal Resourc. Counc. Trans., 14*, 1279-1286.

Hadgu, T., Zimmerman, R.W., and Bodvarsson, G.S. (1993), "Coupling of a Reservoir Simulator and a Wellbore Simulator for Geothermal Applications", *Geothermal Resourc. Counc. Trans., 17*, 499-505.

Goranson, C. (1993), "Steamboat Hills Geothermal Field, Far West Capital, Inc., SB II and SB III Power Plants Lease Area Data Package", unpublished report, v. 1 to 3.

Gunn, C. and Freeston, D. H. (1991), "Applicability of Geothermal Inflow Performance and Quadratic Drawdown Relationships to Wellbore Output Curve Prediction", *Geothermal Resourc. Counc. Trans., 15*, 471-475.

Iglesias, E.R., and Moya, S.L. (1990), "Geothermal Inflow Performance Relationships", *Geothermal Resourc. Counc. Trans., 14*, 1201-1205.

Kjaran, S. P., and Eliasson, J. (1983), "Geothermal Reservoir Engineering Lecture Notes", *Report 1983-2*, U.N. Univ. Geothermal Training, Iceland.

Matthews, C.S., and Russell, D.G. (1967), *Pressure Buildup and Flow Tests in Wells*, Society of Petroleum Engineers, Richardson, Texas.

Pritchett, J. W., and Garg, S. K. (1980), "Determination of Effective Wellblock Radii for Numerical Reservoir Simulations", *Water Resourc. Res., 16(4)*, 665-674.

Pritchett, J.W. (1993), "Preliminary Study of Discharge Characteristics of Slim Holes Compared to Production Wells in Liquid-Dominated Geothermal Reservoirs", *Proc. 18th Workshop Geothermal Reservoir Engineering,* Stanford Univ., Stanford, Calif.

Pruess, K. (1987), "TOUGH User's Guide", *Report LBL-20700*, Lawrence Berkeley Laboratory, Berkeley, Calif.

White, F.M. (1974), *Viscous Fluid Flow*, McGraw-Hill, New York.

PROCEEDINGS, Nineteenth Workshop on Geothermal Reservoir Engineering
Stanford University, Stanford, California, January 18-20, 1994
SGP-TR-147

# Prospects for Universal Heat Mining: From a Jules Verne Vision to a 21st Century Reality

J.W. Tester, H.J. Herzog, Z. Chen, R.M. Potter, and M.G. Frank

MIT Energy Laboratory
Cambridge, MA 02139

## ABSTRACT

The extraction of heat or thermal energy from the Earth -- heat mining -- has the potential to play a major role as an energy supply technology for the 21st century. However, even if reservoir stimulation goals are achieved, the role of heat mining with today's energy prices and development costs is limited to only a small fraction of the earth's surface, specifically to geologically active regions where geothermal gradients are high. This paper examines the prospects for universal heat mining and the types of developments required to make it a reality.

A generalized multi-parameter economic model was developed for optimizing the design and performance of hot dry rock (HDR) geothermal systems by linking an SQP nonlinear programming algorithm with a generalized HDR economic model. HDR system design parameters selected for optimization include well depth (or initial rock temperature), geofluid flow rate, number of fractures and injection temperature. The sensitivities of the optimized design parameters, HDR system performance, and levelized electricity price to average geothermal gradient, fractured area/volume, maximum allowable geofluid temperature, reservoir flow impedance, well deviation, and fracture separation have been investigated.

Key technical and institutional obstacles to universal heat mining are discussed in a more general context. These include (1) developing methods for stimulating low permeability formations to provide sustained productivity with acceptable flow/pressure losses (2) dealing with barriers to change primary energy supply options when fossil energy resources are abundant and prices are low and (3) lowering the high drilling costs for developing the deep (>5 km) reservoirs required in low gradient areas. Advanced concepts in drilling technology that could lead to a linear as opposed to exponential relationship between cost and depth are discussed in light of their potential impact on heat mining.

## FUNDAMENTAL REQUIREMENTS AND TRADEOFFS

Hot Dry Rock (HDR) geothermal energy or, more generally, heat mining is envisioned by some as an environmentally sustainable primary energy supply that could replace our dependence on fossil and fissile fuels in the 21st century. In principle, thermal energy is extracted from the earth using extended oil and gas drilling and stimulation technology to create reservoirs that in many ways emulate natural hydrothermal systems. Thus HDR has all the advantages of natural geothermal energy, plus a few more. With HDR, water is recycled in a closed loop, and, with essentially no emissions, heat mining would not contribute to local or regional air or water pollution, global-scale problems of greenhouse gas build-up, or air or water quality-related health concerns (Tester *et al.*, 1989). Even with these positive attributes, HDR has been categorized as a very long-term alternative, one that has been portrayed like other renewables as a "Cinderella Option" (see Grubb, 1990).

Many potential private developers of HDR regard its current state of development too immature. In view of current energy markets and the perception that technology is inherently risky, private investment in heat mining has been very small. Although some concern about risk is certainly understandable, it seems disproportionate in that much of the required technology has either already been demonstrated for HDR specifically in government-supported R&D programs or represents an incremental extension of existing state-of-the-art techniques used for hydrocarbon or hydrothermal fluid extraction. Heat mining systems, like hydroelectric power plants, require a large, up-front capital investment that includes both the power conversion equipment and the "fuel" supply system. This built-in investment in the fuel supply system, of course, should partially reduce the risk for HDR over fossil-fired plants that face potentially unstable fuel prices.

National and international R&D programs have focused on demonstrating important heat mining requirements, such as the engineering of fractured systems in hot rock with low natural permeability (Batchelor, 1984a,b, 1987; Brown *et al.*, 1991; and Armstead and Tester, 1987). In the last 10 years, however, these programs have suffered from underfunding in the face of plentiful and cheap oil worldwide. With such subcritical support, technical milestones have not been fully realized and a few important development requirements still remain.

In the past 20 years, several economic forecasts and studies of HDR technology have been published. All of these inherently assume a set of reservoir performance levels and development costs for drilling, stimulation and power plant construction. Tester and Herzog (1990, 1991) reviewed and dissected seven HDR studies to establish base case conditions and parameter ranges for sensitivity studies, and to provide a revised level of economic predictions for heat mining. The studies reviewed were from Bechtel (1988); Cummings and Morris (1979); Murphy *et al.* (1982); Smolka and Kappelmeyer (1990); Shock (1986); Entingh (1987); and Hori *et al.* (1986). Later studies of HDR economics include those by RTZ consultants (1991) and Pierce and Livesay (1993). Although Milora and Tester (1976) and Armstead and Tester (1987) introduced more general economic modeling approaches for HDR systems to show the effect of resource grade, reservoir productivity and reservoir depth or temperature, these earlier studies did not tackle the non-linear, multi-parameter optimization problem of simultaneously selecting well depth, reservoir structure (eg. number and spacing of fractures), geofluid flow rate and redrilling management strategies to optimize performance at minimal cost. These design and operating choices are somewhat unique to heat mining systems. Figure 1 shows the tradeoffs between drilling/reservoir development and power plants costs that yield an optimal drilling depth (or initial rock temperature) for a specified HDR resource defined by its average geothermal gradient, ambient heat rejection conditions, and reservoir flow impedance. Effectively, one is trading off lower plant costs against higher individual well costs. Drilling deeper produces higher fluid production temperatures, which increases Second Law heat to work conversion efficiencies, thus reducing fluid requirements (lower kg/s per $kWh_e$ generated) and lowering corresponding power plant costs. While power plant costs in $/$kW_e$ tend to decrease monotonically with temperature, well drilling costs tend to increase exponentially with initial rock temperature (i.e. depth).

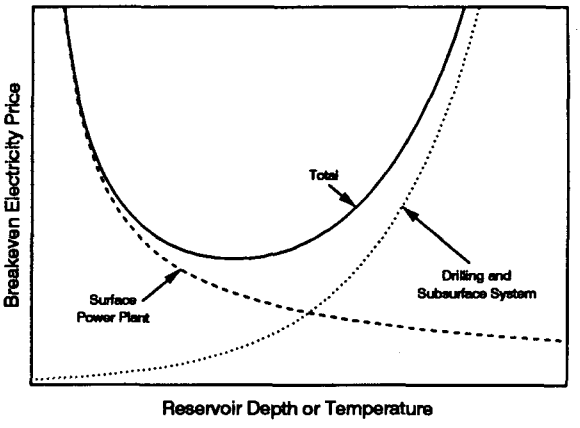


Fig. 1. Conceptual trade-offs in terms of breakeven electricity price (arbitrary scale) between power plant and drilling-related costs as a function of depth or initial reservoir temperature for a fixed geothermal temperature gradient.

In reservoirs with finite thermal lifetimes, temperature decline or drawdown will occur at different rates depending on the mass flow rate per unit of rock surface area or volume exposed to the circulating fluid. An optimal strategy to produce minimum costs requires a balanced state of utilization. The instantaneous power produced will scale as the product of the mass flow rate ($\dot{m}$) and the practical availability of the geofluid ($\eta_u \Delta B$) where $\eta_u$ is the utilization efficiency of the power cycle and $\Delta B$ is the thermodynamic availability (see Milora and Tester, 1976, and Tester, 1982, for details). Both $\eta_u$ and $\Delta B$ are strong functions of the geofluid temperature ($T$) such that the instantaneous power $P(t)$ per unit of effective reservoir size ($<A>$) is given by:

$$\frac{P(t)}{<A>} = \frac{\dot{m}(t)\,\eta_u(T)\,\Delta B(T)}{<A>} \qquad (1)$$

The magnitude of $P(t)/<A>$ is a measure of reservoir quality in terms of its productivity. Thermal drawdown rates scale directly with $\dot{m}(t)/<A>$, while electric power production potential varies with $\eta_u(T)\Delta B(T)$. As $\dot{m}(t)$ is increased for a fixed reservoir size ($<A>$), $T$ decreases faster and, since both $\eta_u(T)$ and $\Delta B(T)$ decrease rapidly as T declines, the overall productivity of the reservoir decreases and the resource is over-utilized as shown qualitatively in Figure 2. As $\dot{m}(t)$ is decreased below its optimal value, the temperature drawdown rate is reduced, but so is the productivity $P(t)/<A>$ in direct proportion to the decline in $\dot{m}$ (see Equation (1)). This condition corresponds to an under-utilization of the reservoir as shown in Figure 2.

## ECONOMIC ASSESSMENT MODEL DEVELOPMENT

A generalized multi-parameter economic model was developed for optimizing the design and performance of geothermal heat mining systems. This was accomplished by enhancing the MIT Energy Laboratory's existing HDR economic model (see Tester and Herzog, 1990, 1991). The major modifications included: reformulating our simple HDR reservoir representation by introducing a multiple parallel fracture conceptual reservoir with a well deviation parameter; adapting the model to an optimization environment and interfacing this revised HDR system model to a SQP (Successive Quadratic Programming) optimization package; and interfacing a levelized life-cycle cost (LLC) algorithm to the model and updating costs to 1991 dollars. As before, electricity production is calculated based on the geofluid (i.e. water) flow rate and the geofluid temperature using a utilization efficiency correlation. The electrical production is then corrected to account for the parasitic pumping requirement caused by system pressure drops minus the buoyancy-driven pressure gain. The model can calculate the electricity breakeven price through a fixed charge rate or LLC approach. The LLC code consistent with EPRI methodology developed by Los Alamos National Laboratory (Hardie, 1981) has been fully integrated into the revised HDR model. Results presented in this paper all use the LLC approach and are given in 1991 dollars. For simplicity, throughout the remainder of this paper we refer to this model as the HDR optimization model.

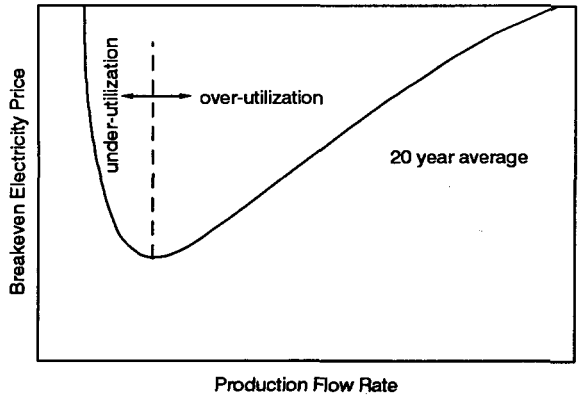


Fig. 2. Qualitative relationship for a specified heat mining resource (known gradient, reservoir area and impedance, depth, initial temperature, etc.) between breakeven electricity price and reservoir production flow rate, $\dot{m}$ (see Equation 1).

A proper understanding of the reservoir temperature drawdown rates is required to predict the geofluid temperature as a function of time. The HDR reservoir "conceptual model" incorporated into the HDR optimization model is a multiple parallel fracture system originally proposed by Gringarten, *et al.* (1975). A well deviation parameter is introduced to allow for rock formation temperature changes as a function of depth along the length of the wells. The reservoir model is labeled "conceptual" because there is insufficient evidence to prove that the parameters used to define the reservoir have exact physical meaning. Nonetheless, this conceptual model captures fundamental physical phenomena that influence the economics, such as finite thermal drawdown or decline in fluid production temperatures over the lifetime of the system. The envisaged HDR reservoir is composed of an injection and a production well which are drilled vertically to a certain depth and then deviate in parallel, linking a finite number of equispaced fractures of uniform thickness, separated by blocks of homogeneous impermeable rock. These fractures are all assumed perpendicular to the injection and production wells. Thus, the perceived reservoir looks like an inclined rectangular cubic rock mass connected to the surface by a well doublet. No heat flux is assumed across the reservoir boundary. Heat transfer in the rock mass is assumed normal to the fracture surfaces. Potential growth due to thermal stress induced effects is ignored. Water is injected at the surface, goes down the injection well, passes through the fractures with evenly distributed flow, up the production well and eventually to the power plant. Five parameters are used to define the geometry of the reservoir: well depth, well deviation, effective area of an individual fracture, number of fractures, and fracture separation. The model then predicts the well length, total effective area, average reservoir depth and average initial rock temperature. The drawdown behavior of the reservoir is predicted with a differential equation set that couples one-dimensional rock conduction to one-dimensional convection flow in planar fractures of uniform aperture.

The HDR optimization model is comprised of a non-linear equation system that can be solved explicitly. The manipulated variables are restricted by upper and lower bounds. Some of the model parameters are also subject to linear or non-linear inequalities. For example, the geofluid pressure at the bottom of the reservoir should be less than or equal to the fracturing critical pressure so as to minimize water loss. This mathematical structure requires a constrained, non-linear optimization algorithm that solves small-scale, highly non-linear problems effectively. The optimization objective is to minimize the levelized electricity price. Maximizing power generation, thermal output or geofluid availability can be specified as alternate objectives. In order to accelerate

convergence and prevent the optimization from falling into local minima, the control parameters are scaled to a magnitude of unity. Other details concerning the model and sensitivity analysis can be found in an MIT Energy Laboratory report (Herzog *et al.*, 1994).

In this study, the following parameters were designated as manipulated variables to be optimized:

- ***Drilling Depth.*** Given a geothermal gradient, optimal drilling depth is determined by balancing increased drilling costs (with depth) with the increased effectiveness in electric power production due to higher geofluid temperatures.

- ***Number of Fractures.*** With well separation and fracture spacing specified, the number of fractures is the parameter that determines the reservoir volume. Larger reservoir volumes result in lower temperature drawdown rates, but are penalized by higher capital costs and somewhat lower initial geofluid temperatures. For computational convenience, the number of fractures was treated as a continuous control parameter for optimization instead of a discrete variable, although only whole numbers make practical sense.

- ***Geofluid Flowrate.*** Larger geofluid flowrates increase the initial power generation while accelerating temperature drawdown.

Simulations were run on a range of average geothermal gradients varying from 20 to 100°C/km.

Other parameters defining the base case are given in Table 1. Economic and cost parameters were based on the commercial base case described in Tester and Herzog (1991), reflecting today's relatively higher drilling and completion costs. A three-dimensional plot of breakeven electricity price against geofluid flow rate and the number of fractures is presented in Figure 3 for the base case at a geothermal gradient of 50°C/km. Note the valley on the levelized electricity price surface from low geofluid flow rate and small number of fractures to high geofluid flow rate and large number of fractures. The valley is narrow at the low geofluid rate and small number of fracture end, and widens at the other end. From the figure it can be also seen that in a fairly large region the breakeven price surface is quite flat. The optimum occurs at a geofluid flow rate of 87.9 kg/s and 26.7 fractures with a breakeven electricity price of 9.2¢/kWh$_e$. The total temperature drawdown over the 20-year plant life is about 17.6%, i.e. $[T(t=0\,yr)-T(t=20\,yr)]/[T(t=0\,yr)-T_o]$ = 0.176, where $T(t)$ is the outlet fluid temperature at time $t$ and $T_o$ is the ambient heat rejection temperature.

**Table 1. Parameter Values for the Base Case**

| Parameter Description | Value |
|---|---|
| Maximum geofluid temperature | 330°C |
| Average surface temperature | 15°C |
| Ambient heat rejection temperature | 25°C |
| Temperature loss in production well | 15°C |
| Impedance per fracture | 2.57 GPa-s/m$^3$ |
| Water loss/total water injected | 5% |
| Rock density | 2700 kg/m$^3$ |
| Rock thermal conductivity | 3.0 W/m-K |
| Rock heat capacity | 1050 J/kg-K |
| Well deviation from vertical | 30° |
| Effective heat transfer area per fracture | 100,000 m$^2$ |
| Fracture separation distance (horizontal) | 60 m |
| Injection temperature | 55°C |
| Geofluid circulation pump efficiency | 80% |
| Plant life | 20 years |

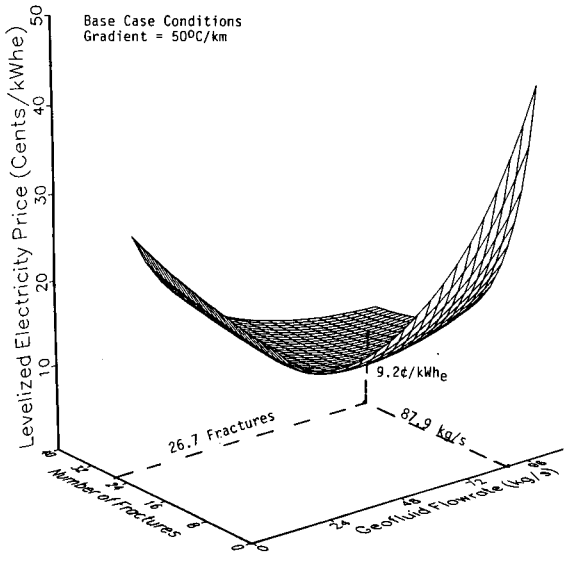


Fig. 3. HDR Optimization model results for the base case and a geothermal gradient of 50°/km. A plot of breakeven electricity prices are shown versus number of fractures and geofluid flow rate, with the optimal point indicated.

Figure 4 presents the percentage participation of each of the major key component costs in the breakeven electricity price calculation. As the geothermal gradient decreases, drilling and completion costs comprise a larger share of the overall costs. This variation highlights the importance of reducing drilling costs if HDR is to become an important energy supply technology in the low gradient areas that cover most of the world.

Figure 5 compares the HDR optimization model base case with the commercial base case from Tester and Herzog (1991). The levelized electricity prices predicted by the HDR optimization model are somewhat higher, partly because in this work redrilling/restimulation is not considered. While the breakeven electricity prices of the two models are comparable, the system designs are very different (see Table 2) due to the introduction of the Gringarten *et al.* (1975) reservoir conceptual model, which leads to a very conservative design.

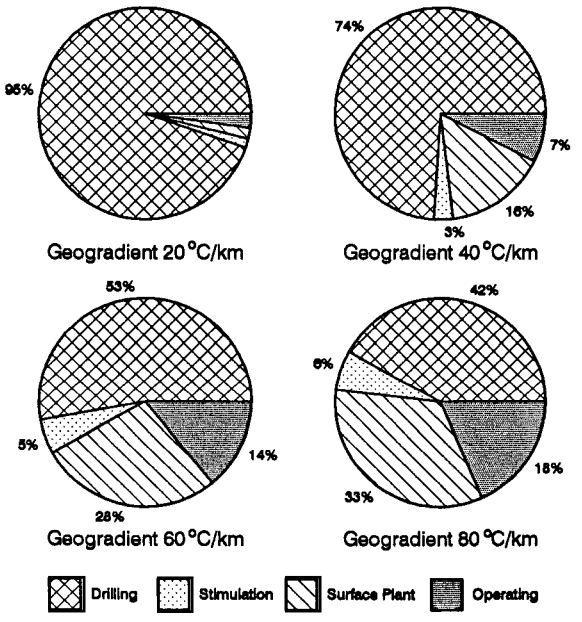


Fig. 4. Breakdown of component costs (drilling, stimulation, plant, and operating) for the HDR optimization model base case conditions at a range of geothermal gradients using today's technology and drilling costs.

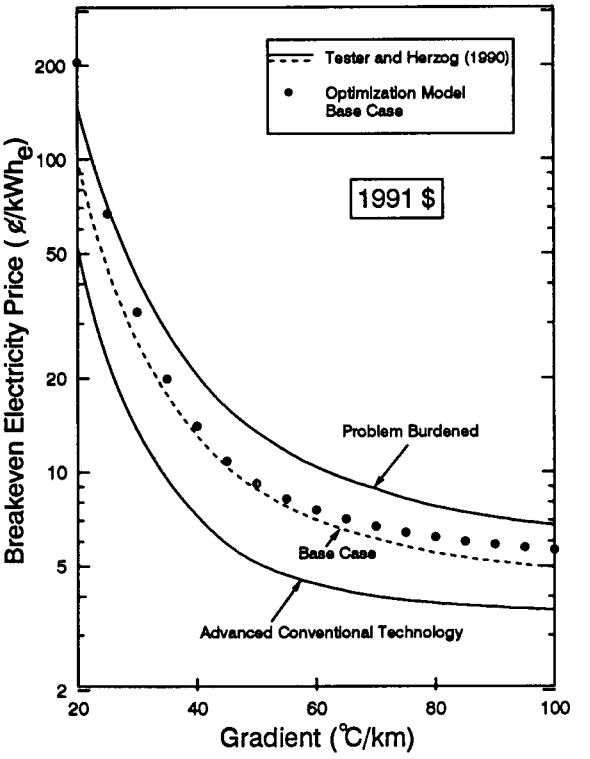


Fig. 5. Comparison of HDR optimization model base case results to those reported earlier in Tester and Herzog (1990, 1991).

Figure 6 shows the sensitivities of the three manipulated variables along with three calculated variables. At an average geothermal gradient below 40°C/km, well depth is determined by balancing drilling and completion costs with geofluid temperature. However, above 40°C/km, the drilling depth is always on the upper bound associated with maximum allowable geofluid temperature. In addition, for geothermal gradients above 40°C/km and a specified reservoir geometry, the higher the geothermal gradient is, the greater the temperature drop will be through the reservoir. That is why there is a clear trend to create smaller size reservoirs in higher geothermal gradient areas and larger size reservoirs in lower geothermal gradient areas. Because of this reservoir size differential, the optimal geofluid flow rate for a low geothermal gradient reservoir will be higher than that for a high geothermal gradient reservoir. Furthermore, the average electricity production for a single well pair over the plant life of 20 years decreases considerably with increasing geothermal gradient because of the smaller reservoir sizes and lower geofluid flows associated with the higher geothermal gradients.

**Table 2. System Design Comparison for a Single Well Pair**
**Old = Tester and Herzog (1991)**
**New = This Study**

| | 20°C/km | | 40°C/km | | 60°C/km | | 80°C/km | |
|---|---|---|---|---|---|---|---|---|
| | Old | New | Old | New | Old | New | Old | New |
| Breakeven Electricity Price (cents/kWh$_e$) | 85 | 205 | 11.9 | 14.0 | 6.6 | 7.6 | 5.3 | 6.2 |
| Well Depth (km) | 9.15 | 9.15 | 7.13 | 7.74 | 4.75 | 5.25 | 3.56 | 3.94 |
| Geofluid Flowrate (kg/s) | 75 | 46 | 75 | 92 | 75 | 81 | 75 | 66 |
| Effective Area (million m$^2$) | 1.2 | 2.04 | 1.7 | 2.93 | 1.6 | 2.48 | 1.6 | 1.94 |
| Net Power Output (MW$_e$) | 3.5 | 1.4 | 14.9 | 13.7 | 14.7 | 11.7 | 14.5 | 9.2 |

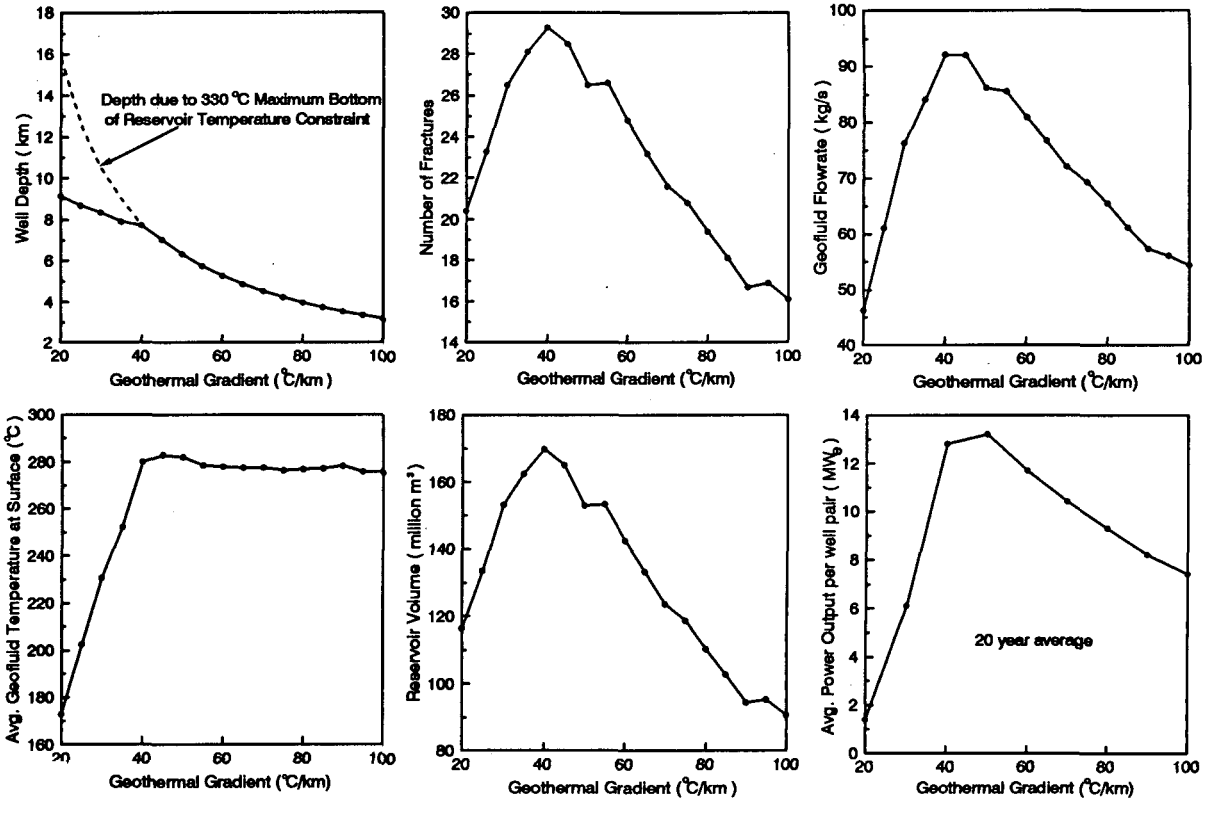


Fig. 6. Estimated values for key design parameters as a function of geothermal gradient for the HDR optimization model base case.

## TECHNICAL AND INSTITUTIONAL OBSTACLES TO UNIVERSAL HEAT MINING

The economic model simulation discussed in the previous section obviously contain a certain amount of speculation on our part. For example, to produce base case conditions we have made a number of assumptions regarding anticipated levels of reservoir productivity and performance that go beyond what has been achieved in field tests to date. In effect, we are dealing with the economic feasibility of heat mining somewhat retrospectively. In 1976, Milora and Tester assimilated data for commercial hydrothermal systems to establish a range of performance criteria as a goal for HDR. Later, Entingh (1987), various groups at Los Alamos (Cummings and Morris, 1979, and Murphy *et al.*, 1982) and in the UK (Batchelor, 1984 a,b, 1987), Armstead and Tester (1987), and Tester and Herzog (1990, 1991) refined these criteria somewhat. Frequently a rhetorical question was posed as to what resource and reservoir characteristics were needed to make HDR commercially competitive. For example, breakeven prices for HDR-generated electricity were estimated and compared to the competition from oil, gas, coal, or nuclear energy sources at current market prices. Basically, we have been able to show that our initial assumptions for base case conditions reported earlier (Tester and Herzog, 1990, 1991) were consistent with the more rigorous model developed in this study that treated the non-linear multi-parameter optimization problem. Moreover, this means that the original assumptions for reservoir productivity used earlier are still at a higher level than has been demonstrated in the field.

For mid- to high-grade resources (>40°C/km) at assumed reservoir productivities of 45 to 100 kg/s, 30 to 80 $MW_t$ per well pair and reservoir sizes large enough to ensure drawdown rates of 5% or less over 5 years of production, the HDR breakeven electricity price is 6-10¢/$kWh_e$. This assumes current drilling costs, power plant construction costs, and modest exploration and site development costs.

To achieve this base case level of reservoir production at Fenton Hill (a high-grade reservoir), a 5 to 10 fold reduction of flow impedance from current levels is needed with acceptable water losses. Clearly, more fundamental engineering experience is needed before HDR reservoirs can be constructed in an optimal fashion. There are no insurmountable technical barriers, but more knowledge of how to create large fracture systems in low permeability rocks is required before low impedance systems of sufficiently high productivity can be routinely engineered. The key implication here is that more time, effort, and funds should be invested in field demonstrations of heat mining. This approach will build the engineering knowledge base, technical know-how, and human resources required to develop heat mining commercially. One can think of the goal of demonstrating HDR reservoir productivity on a commercial scale as the first crucial step in the evolution of universal heat mining.

A successful demonstration would virtually guarantee commercial development of our mid- to high-grade HDR resource as an alternative to fossil or fissile-fired electricity generation. To achieve truly universal heat mining, the ubiquitously distributed low- grade (20-40°C/km) resource must become economically accessible. This will require more revolutionary developments. As seen in Figures 4 and 5, low gradient resources result in very high breakeven prices that are induced primarily by the high drilling cost component. At base case conditions for low-grade HDR, which includes reservoir productivities comparable to mid- and high-grade systems, electricity prices range from about 15 to 100¢/$kWh_e$ or a factor of 3 to 20 too high in today's marketplace. One can see from Figure 4, that as the gradient decreases from 80°C/km to 20°C/km the fraction of total costs due to drilling increases from 42% to 95%.

Even given the inherent speculative nature of these economic projections, it is still relatively safe to predict that heat mining will not become universal until a fundamental change in drilling and/or reservoir formation costs occurs to significantly lower costs. Although one could hypothesize that the discovery of new methods of creating HDR systems could result in enormous increases in productivity per well pair, it seems more probable based on the limitation of current heat mining concepts that a breakthrough in drilling technology is more likely to give the desired result. Such a breakthrough would involve a shift away from the exponential well cost versus depth functionality that has been observed historically for essentially all U.S. oil and gas drilling experience and, although offset to higher costs, for U.S. geothermal drilling experience as well. Figure 7 shows some of these data (see Herzog *et al.* (1994) and Tester and Herzog (1990, 1991) for the sources of data that are plotted). The base case/today's technology line represents average conditions for HDR-type well drilling using conventional rotary drilling technology. The problem-burdened and advanced conventional technology lines form the envelope of drilling costs

used in our sensitivity analysis that essentially captures the range of all HDR well cost data and predictions, again for rotary drilling technology. Joint Association Survey (JAS) (1978-1991) data are plotted for oil and gas wells average costs as well as for specific ultra deep wells. Note the scatter in the costs for ultra deep wells, caused primarily by variations in formation type and drilling programs.

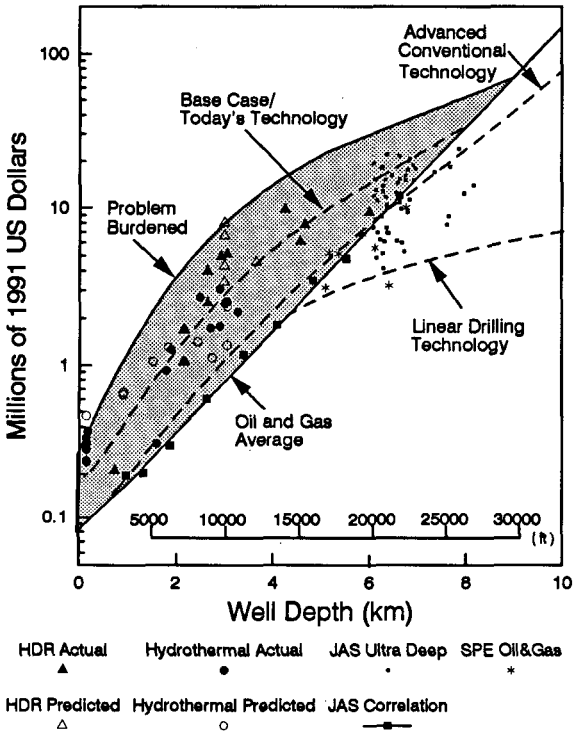


Fig. 7. Drilling costs for different technology levels used in the HDR model simulations. Also plotted are historical drilling costs for HDR, hydrothermal, oil and gas, and ultra-deep wells.

Figure 7 also shows a line for what we have called "linear drilling", where drilling costs for wells deeper than about 4 km no longer follow exponential JAS behavior -- rather costs become linear in depth at this point. We believe that such behavior is possible as a lower boundary on drilling costs when advanced technologies, such flame-jet thermal spallation or water-jet cavitation drilling methods, are employed in a fully integrated drilling system. However, for the moment it's not important what the specific enabling technology is -- only that it exists. Again we recognize we are speculating -- but let's see what happens to predicted heat mining development costs. Simulation results are shown in Figures 8 and 9 for the base case conditions cited in Table 1 but with linear rather than exponential drilling costs. In Figure 8, one notes the shift in the distribution of costs over what was found with conventional drilling technology shown in Figure 4. For example, for a 20°C/km resource only 51% rather than 95% of the total costs are due to drilling when a linear drilling model applies.

In Figure 9, the total US resource is divided into 5 classes or grades, each corresponding to an average gradient between 80 and 20°C/km. This amounts to a total supply of about 42,000 $GW_e$ from heat mining for a 20 year period. For reference the current US generating capacity is about 500 $GW_e$. The bar graph in Figure 9 compares the breakeven electricity price for each HDR grade using today's drilling costs to what would be possible with linear drilling technology. For the high grade classes (60-80°C/km) the effect of this advanced drilling technology, while significant, is not as striking as for the lower HDR grades (20-30°C/km) where such technology leads to the economic feasibility of heat mining in current energy markets.

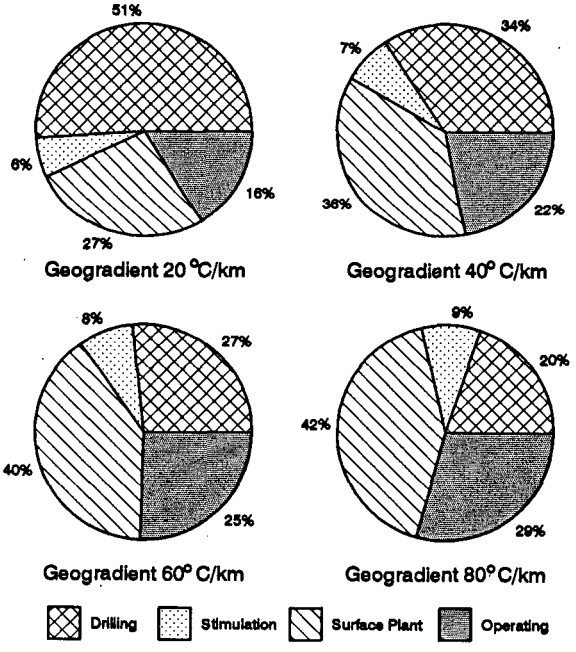


Fig. 8. Breakdown of component costs (drilling, stimulation, plant, and operating) for the HDR optimization model base case conditions at a range of geothermal gradients using linear drilling technology and costs.

## CONCLUSIONS AND RECOMMENDATIONS

A multi-parameter optimization model has been developed to specify reservoir design (well depth and spacing, effective fracture size and location) and operating conditions (flow rate, pressure drop) to minimize breakeven electricity prices. The effects of finite reservoir thermal drawdown, wellbore heat losses, and parasitic losses due to fluid recirculation have been included. Sensitivity of electricity price to

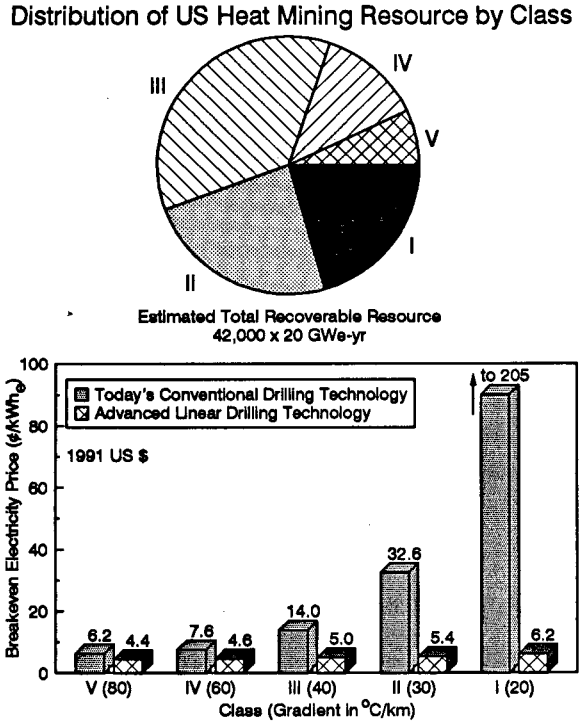


Fig. 9. Heat mining resource base for the U.S. Two sets of costs for producing electricity from this resource are shown -- one using today's conventional drilling technology and the other using advanced linear drilling technology.

resource grade, nominally expressed by the average geothermal gradient, and to important costs factors, such as individual well drilling costs as a function of depth, have been parametrically examined.

It is important to emphasize that the results reported in this paper are aimed at illustrating the sensitivity of electricity price to important reservoir and power plant design parameters and not to establish minimum costs for HDR-produced electricity. Base case conditions for the model simulations were selected somewhat conservatively based primarily on today's technology and costs for developing commercial hydrothermal geothermal resources. A key assumption throughout is that heat mining reservoir productivity levels (e.g. flow rate and impedance) can, in practice, match those found in existing hydrothermal systems. Field results to date from prototype HDR systems fall short of this goal. Based on current progress and potential, we strongly recommend continued field testing of heat mining concepts to achieve the reservoir productivity levels required for commercialization. For example, indications from recent testing of the high-grade Fenton Hill HDR system suggest that a sufficiently large reservoir system with acceptable water losses has been created -- it only lacks proper hydraulic connections to fully utilize its heat mining capacity (Duchane, *et al.*, 1991-1993).

For mid- to high-grade areas (>40°C/km), commercially competitive heat mining with risks and costs lower than estimated base case values will require somewhat higher levels of reservoir productivity and/or lower drilling costs. For universal heat mining that includes low-grade areas (20-40°C/km), a fundamental shift away from exponential drilling costs is needed. This will require revolutionary advances in drilling technology. Perhaps the proposed national program on advanced drilling and excavation could provide such technology (see Peterson, *et al.*, 1993).

## ACKNOWLEDGEMENT

The authors gratefully acknowledge the Geothermal Division of the U.S. Department of Energy for their partial support of this work. We received valuable suggestions and encouragement from J.E. Mock, A. Jelacic, J. Dunn, E. Drake, A. Diaz, W. Peters, P. Coleman, D. Duchane, P. Kruger, and B.A. Robinson.

## REFERENCES

Armstead, H.C.H. and J.W. Tester, *Heat Mining*, London: E.F. Spon (1987).

Batchelor, A.S., "Hot Dry Rock Geothermal Exploitation in the United Kingdom," *Modern Geology*, **9**, pp. 1-41 (1984a).

Batchelor, A.S., "Hot Dry Rock Reservoir Stimulation in the UK--An Extended Summary and An Overview of Hot Dry Rock Technology," presented at 4th Int. Conf. on Energy Options, The State of Alternatives in the World Energy Scene, London: IEE Papers (1984b).

Batchelor, A.S., "Development of Hot Dry Rock Systems in the UK," *IEE Proc. A*, **134**(5), pp. 371-380 (1987).

Bechtel National Inc. *Hot Dry Rock Venture Risks Investigation*, Final report for the U.S. Department of Energy under contract DE-AC03-86SF16385, San Francisco, CA (1988).

Brown, D.W., R.M. Potter, and C.W. Myers, "Hot Dry Rock Geothermal Energy - An Emerging Energy Resource with Large Worldwide Potential," in *Energy and the Environment in the 21st Century*, eds. J.W. Tester, D.O. Wood, and N.A. Ferrari, Cambridge, MA: MIT Press, pp.931-942 (1991).

Cummings, R.G. and G.E. Morris, *Economic Modeling of Electricity Production from Hot Dry Rock Geothermal Reservoirs: Methodology and Analysis*, Electric Power Research Institute report EPRI EA-630, Palo Alto, CA (1979).

Duchane, D.V., *et al.*, *Long-term Flow Test Operating Plan and Preliminary Results in the Phase II Hot Dry Rock Reservoir, Fenton Hill, NM*, Los Alamos National Laboratory memoranda and draft reports (1991-1993).

Entingh, D., *Historical and Future Cost of Electricity from Hydrothermal Binary and Hot Dry Rock Reservoirs, 1975-2000*, Meridian Corp. report 240-GG, Alexandria, VA (1987).

Gringarten, A.C., Witherspoon, P.A., and Ohnishi, Y., "Theory of Heat Extraction from Fractured Hot Dry Rock," *J. Geophysical Research*, **80**(8), p. 1120 (1975).

Grubb, M.J., "The Cinderella Options - A Study of Modernized Renewable Energy Technologies - Part 1- A Technical Assessment," *Energy Policy*, pp. 525-542 (July/August, 1990).

Hardie, R.W., *BICYCLE II: A Computer Code for Calculating Levelized Life-Cycle Costs*, Los Alamos National Laboratory report LA-8909 (1981).

Harrison, R. and P. Doherty, *Cost Modeling of Hot Dry Rock Systems, Volume 1: Main Report*, UK Department of Energy report ETSU G 138F-1 (1991).

Herzog, H., J. Tester, Z.Chen, and M. Frank, *A Generalized Multi-parameter Economic Model for Optimizing the Design and Performance of Hot Dry Rock (HDR) Geothermal Energy Systems*, Massachusetts Institute of Technology Energy Laboratory report forthcoming (1994).

Hori, Y. *et al.*, *On Economics of Hot Dry Rock Geothermal Power Station* and related documents, Corporate Foundation Central Research Institute for Electric Power, Hot Dry Rock Geothermal Power Station Cost Study Committee report 385001, Japan (1986).

*Joint Association Survey on Drilling Costs for Years 1978-1991*, American Petroleum Institute, Washington, D.C. (1978-1991).

Milora, S.L. and J.W. Tester, *Geothermal Energy as a Source of Electric Power*, Cambridge, MA: MIT Press (1976).

Murphy, H.D., R. Drake, J.W. Tester, and G.A. Zyvoloski, *Economics of a 75-MW$_e$ Hot Dry Rock Geothermal Power Station Based upon the Design of the Phase II Reservoir at Fenton Hill*, Los Alamos National Laboratory report LA-9241-MS (1982).

Peterson, C. *et al.*, "A Proposed National Program for Advanced Drilling and Excavation Technologies," Massachusetts Institute of Technology Energy Laboratory, Cambridge, MA (December, 1993).

Pierce, K.G. and B.J. Livesay, "Estimate of the Cost of Electricity Production from Hot Dry Rock," *Geothermal Resources Council Bulletin*, **22**(8), pp. 197-203 (1993).

RTZ Consultants Limited, *Conceptual Design Study for a Hot Dry Rock Geothermal System*, UK Department of Energy report ETSU G 153, (1991).

Shock, R.A.W., *An Economic Assessment of Hot Dry Rocks as an Energy Source for the U.K.*, UK Department of Energy report ETSU-R-34 (1986).

Smolka, K. and O. Kappelmeyer, "Economic Cost Evaluation of HDR Power Plants," in *Hot Dry Rock Geothermal Energy*, proceedings of the International Hot Dry Rock Geothermal Energy Conference, Camborne School of Mines, 27-30 June 1989, ed. R. Bario, London: Robertson Scientific Publications (1990).

Tester, J.W., "Energy Conversion and Economic Issues for Geothermal Energy," in *Handbook of Geothermal Energy*, ed. L.M. Edwards *et al.*, ch. 10. Houston, TX: Gulf Publishing (1982).

Tester, J.W., D.W. Brown, and R.M. Potter, *Hot Dry Rock Geothermal Energy -- A New Energy Agenda for the 21st Century*, Los Alamos National Laboratory report LA-11514-MS (1989).

Tester, J.W. and H.J. Herzog, *Economic Predictions for Heat Mining: A Review and Analysis of Hot Dry Rock (HDR) Geothermal Energy Technology*, Massachusetts Institute of Technology Energy Laboratory report MIT-EI-90-001 (1990).

Tester, J.W. and H.J. Herzog, "The Economics of Heat Mining: An Analysis of Design Options and Performance Requirements of Hot Dry Rock (HDR) Geothermal Power Systems," *Energy Systems and Policy*, **15**, pp. 33-63 (1991).

PROCEEDINGS, Nineteenth Workshop on Geothermal Reservoir Engineering
Stanford University, Stanford, California, January 18-20, 1994
SGP-TR-147

# MANAGING DECLINE : OPTIMISING GENERATION BY PREDICTION OF TWO-PHASE WELL PRODUCTIVITIES

*Allan W. Clotworthy*

Electricity Corporation of New Zealand, Geothermal Group
Private Bag 2001, Taupo, New Zealand

## ABSTRACT

Economic optimisation of the Ohaaki Geothermal Field dual-flash system indicated the requirement to program for sliding High Pressure turbine inlet pressures and the de-rating of individual wells to Intermediate Pressure. A wellbore simulator was used to generate output curves up to 5 years into the future to enable 'what-if' modelling for maximum electrical generation under different scenarios. The key to predicting future output curves as a function of wellhead pressure was predicting two-phase well productivities as a function of field pressure and enthalpy trends. Using a wellbore simulator to generate inflow pressure curves from output test data and matching measured downhole data showed that the Duns and Ros flow correlation produced a linear response with a consistent relationship to static pressures for most wells. This was used to generate predicted output characteristic curves up to 1998, enabling the modelling of varying turbine inlet pressures.

## INTRODUCTION

The rate of decline in steam produced from the Ohaaki geothermal steam field has been greater than was anticipated during the design of the power station. This has meant the need for management of the dual-flash system by reducing the inlet pressure to the High Pressure (HP) turbines in order to optimise electrical generation (Clotworthy and Brooks,1993). A gradual reduction in the inlet pressure of the HP turbines was recommended, to be combined with de-rating of individual wells from HP to Intermediate Pressure (IP) similar to the de-rating at Wairakei (Morris, 1983).

Prediction of future steam flows is the basis for scheduling de-rating of individual production wells. Normally a computer simulation would be used but this was not possible as we did not have a well-by-well model. The 3-D computer simulation run by the University of Auckland also was quite optimistic compared to extrapolations for individual wells. Decline curve projections have been conducted for dry steam fields such as The Geysers but have little theoretical basis for two-phase reservoirs. Nevertheless it has been found that projections of separated steam flows have been reliable over 2-3 years in predicting future HP steam flow trends. This is not viable for longer periods for a dual-flash system as changing enthalpies vary the HP/IP ratio. Varying the separation pressure also negates the use of the decline curve method. Because of the problems with detailed short-term 3-D model predictions and simple decline curve projections it was decided that individual well projections would be made using a wellbore simulator to produce characteristic curves at yearly intervals for 5 years into the future. These curves were used in a spreadsheet model to optimise the electrical generation as a function of turbine inlet pressures and allocation of wells as HP or IP producers.

## METHODOLOGY

The basis for the prediction method is estimating two-phase productivities of the wells into the future, so that the wellhead pressures can be calculated for varying mass flows. There do not appear to be any reliable measurements of two-phase productivities for geothermal wells (Gunn & Freeston, 1991) so it was decided to calculate the downhole feed pressures for each well from output tests using a wellbore simulator to see if an empirical relationship could be found relating mass flow to static feed pressure and enthalpy over time. Most of the wells showed a linear relationship between mass flow and feed pressure which was not strongly dependent on enthalpy. As this was rather surprising it was decided to test this in the field by direct measurement and determine which two-phase flow correlation to use for calculating wellbore pressure drops.

### *Experimental Tests*

The suggestion had been made that static pressures could be measured in wells with antiscalant injection tubing installed. I felt that this would be a good

opportunity to obtain productivity data during output tests. This was obtained by logging the mass flow and downhole and wellhead pressures simultaneously (Morris and Clotworthy, 1993).

Three wells have been tested to date. One well did not give useful data as the tubing was set below the major feed and the response of the secondary feed did not correlate with mass flow. The other two wells showed a linear relationship between mass flow and feed pressure, although one well showed unsteady behaviour.

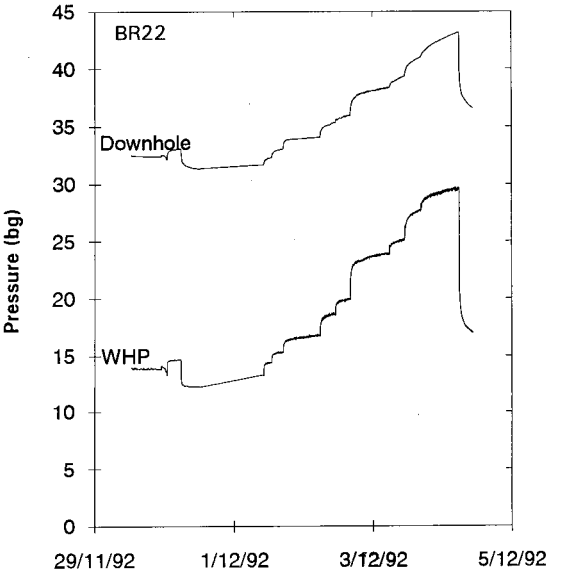


Figure 1a: Transient downhole and wellhead pressures during BR22 discharge test.

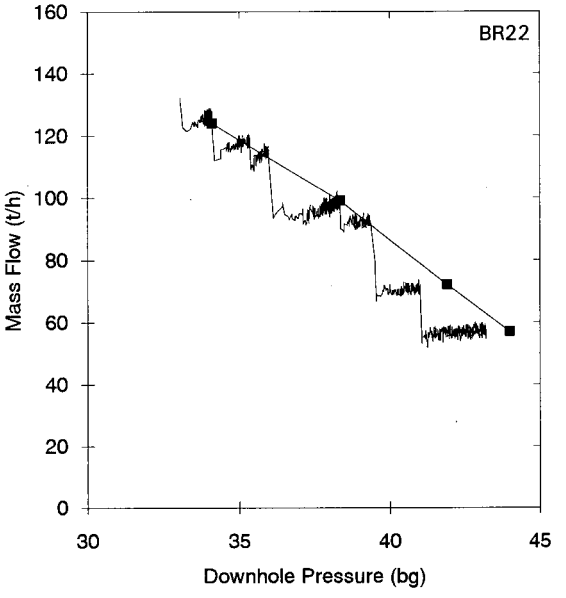


Figure 1b : Plot of downhole pressure at major feed versus mass flow for BR22. Last two pressures not stable and extrapolated to equal discharge volume.

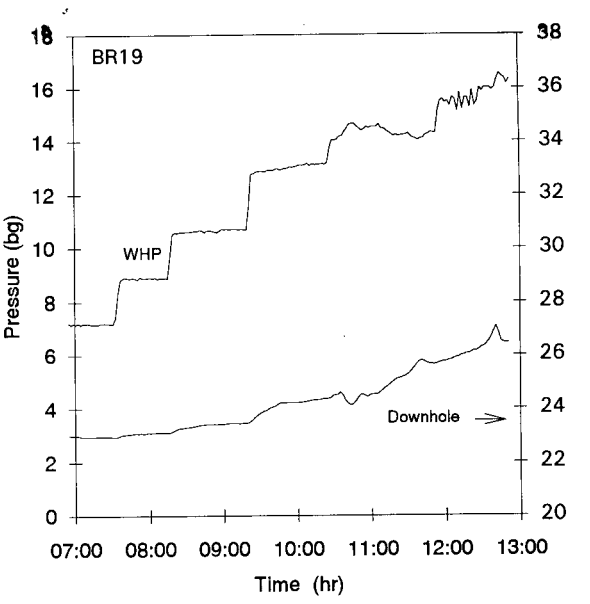


Figure 2a : Transient downhole and wellhead pressures during BR19 discharge test. Discharge unstable at last 2 flow rates.

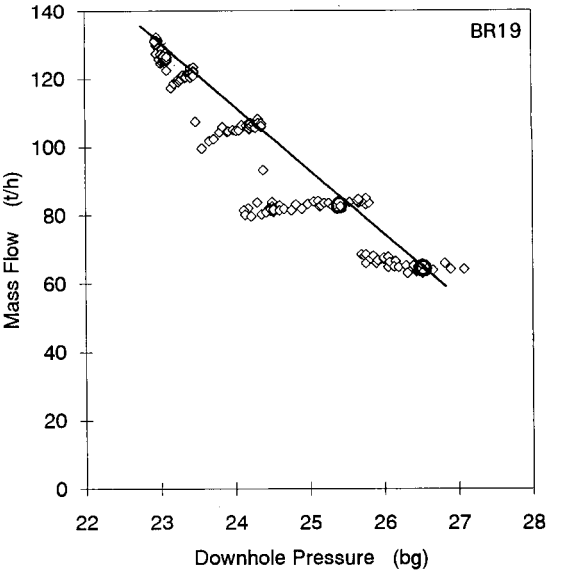


Figure 2b: Plot of downhole pressure at major feed versus mass flow for BR19. Estimates of stable pressures used for last 2 flow rates.

Using the *Wellsim* wellbore simulator (Gunn & Freeston, 1991a) to match the calculated versus actual wellhead pressures indicated that the Ros & Duns flow correlation was the most suitable for Ohaaki wells, in agreement with another recent comparison (Probst, Gunn & Anderson, 1992).

Matching of flowing survey data confirmed that the Duns and Ros correlation was the most suitable for Ohaaki.

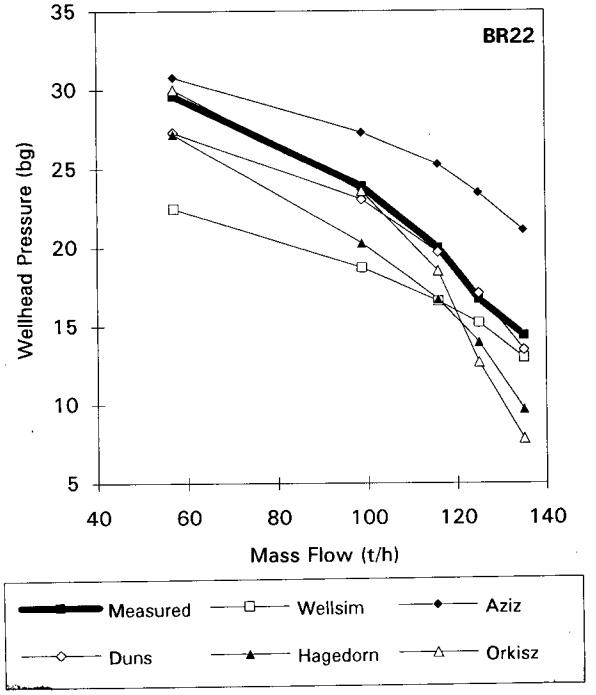


Figure 3 : Plots of wellhead pressures calculated using wellbore simulator and measured values for BR22.

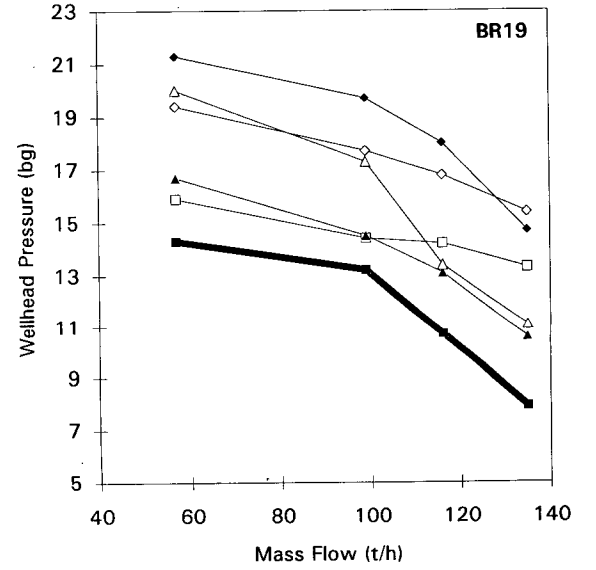


Figure 4 : Plots of wellhead pressures calculated using wellbore simulator and measured values. There was an apparent offset error in the downhole pressure at BR19.

*Calculation of productivities from output tests*

The Wellsim correlation was used in 1992 to calculate downhole pressures. The productivity curve generated was generally linear but did not correlate with the static

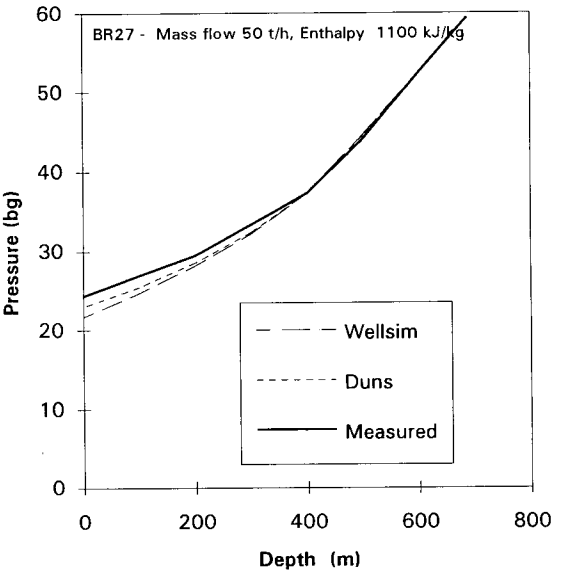


Figure 5 : Matching of flowing survey survey.

pressure so it was difficult to predict the trend for future years. In some cases the calculated flowing feed pressure was greater than the static pressure, especially for lower enthalpy wells.

In contrast the Duns correlation produced productivity curves which were also linear and extrapolated to the static pressure at zero flow. This meant that the complete curve could be generated from a single flowrate output test if the shut-in pressure was also known.

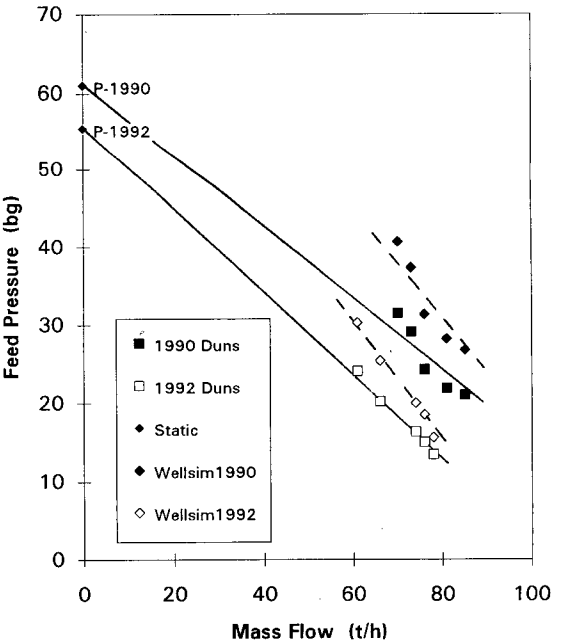


Figure 6 : Plot of feed pressure calculated from output test data for a typical well.

A number of wells deviated from this pattern. These deviations can be explained by multiple feeds or in some cases may be caused by calcite deposition in the formation adjacent to the wellbore. All the wells deviating had computed feed pressures which extrapolated to a pressure lower than the static pressure and were generally linear, except for wells with low enthalpies where the feed state changed from two-phase to liquid water at wellbore entry during the output test.

*Method of Prediction*

The future output characteristic curves were predicted for individual wells based on projections of the following parameters required by the wellbore simulator:

Flowing feed pressures were based on extrapolation of historic trends, taking into account predicted pressures from the 3-D computer model.

Future enthalpies were predicted using the history of the well together with chemical trends if available and the likely impact of groundwater inflows or injection returns. The enthalpies predicted by the 3-D model were not considered reliable enough to be used.

Gas concentrations in the total mass were predicted to decline slowly, based on historic trends and input from the chemists. The 3-D model gave poor historic matches to gas contents.

Using the above predicted parameters the wellbore simulator was run to calculate the wellhead pressures for an annual range of mass flows over the 5 year period.

*Limitations to the method*

As mentioned above a number of wells do not fit the pattern assumed, with linear productivity curves extrapolating to static pressure at zero flow. Of the 23 production wells at Ohaaki 12 give good fits to this pattern, 5 may fit but have poor data and 6 do not fit the pattern. There is added uncertainty for the latter group.

Interference between wells is ignored. There is only one proven case where wells have been shown to interact and generally the two-phase producers have substantial localised drawdown but do not appear to affect other producers. If adjacent producers do not change their relative flows then pressure declines are assumed continue to show a similar trend over the 5 year period.

Enthalpy variations with flow are ignored. This appears to give acceptable results because it is not the mass flow per se that is important but the separated steam flow. The mass flow usually makes a compensatory change when the enthalpy varies for two-phase producers so that the steam produced is the same.

The Duns & Ros flow correlation in *Wellsim* had problems with high mass flow, high enthalpy wells and the Wellsim flow correlation was used in one case.

## RESULTS

The 1991 extrapolation of separated steam flows had indicated a shortfall of steam in 1993 and this was verified.

In 1992 the method outlined above was used to estimate production until 1997. A shortfall of steam was predicted in mid-1993 and this was correct. The Wellsim flow correlation was used and did not produce productivity curves which could easily be correlated to reservoir pressure trends.

The latest revision uses the Duns & Ros flow correlation and appears to give more consistent trends. The 1993 prediction shows a substantially greater future decline than for 1992 but this is unlikely to be due to the method, but rather to the recent evidence of declining enthalpies in wells that were not affected in 1992.

A program of the work required to reconnect the wells to be de-rated and the revision of our contract with the transmission company to reflect the lower levels of guaranteed generation is under way.

The 3-D computer simulation had produced a much more optimistic prediction with full IP generation being maintained beyond 2000, compared to our prediction of a reduction in IP generation by 1997.

## SUMMARY

Direct measurement of productivities on two two-phase wells has shown that the Duns and Ros flow correlation for two-phase pressure drop is the most suitable method for Ohaaki wells.

Calculated two-phase productivities for Ohaaki wells, based on output test data and using a wellbore simulator to estimate flowing pressures at the feed zones, have been shown to be linear with mass flow and for the majority of wells extrapolate to the static pressure at zero flow. The wells which deviate from this pattern have low extrapolated pressures at zero flow and may be affected by a skin caused by calcite deposition.

The predictions generated can be used for planning of plant modifications to optimise output, make-up drilling

etc and to look in detail at interactions between the wells and surface plant in order to determine future bottlenecks.

There is a niche for the use of a wellbore simulator to produce predictions of future steam flows for a period of 1 - 5 years into the future for a two-phase geothermal steamfield, especially if the separation pressure is likely to vary. This method sits between simple decline curve extrapolation of separated steam flows and full computer simulation. It is more versatile than decline curve methods and enables optimisation of surface plant to be planned. It is much cheaper and faster than developing a fully detailed 3-D computer model and may be more reliable for individual well modelling. The computer model is required for longer-term predictions. An integrated reservoir simulator and wellbore simulator would be the best if it can be properly calibrated.

## ACKNOWLEDGMENTS

The author thanks the management of the Electricity Corporation of New Zealand Ltd for permission to publish this paper.

## REFERENCES

Clotworthy, A. W. and Brooks R. H. (1993), "Future Production Strategy - Ohaaki Geothermal Field", *Proc. of the 15th New Zealand Geothermal Workshop* pp 307-310.

Morris, C.J. and Clotworthy, A.W. (1993), "Electronic Logging of Output Tests", *Proc. 15th New Zealand Geothermal Workshop,* pp 327-330.

Morris, G. L. (1983), "The Conversion Of Wairakei From A Three Pressure To A Two Pressure Steam Supply System", *Proc. of the 5th New Zealand Geothermal Workshop*, pp 75-78.

Gunn, C and Freeston, D. (1991), "Applicability Of Geothermal Inflow Performance Performance And Quadratic Drawdown Relationships To Wellbore Output Curve Prediction", *Geothermal Resources Council TRANSACTIONS, Vol 15*, pp 471-475.

Gunn, C. and Freeston, D. (1991a), "An Integrated Steady-state Wellbore Simulation and Analysis Package", *Proc. 13th New Zealand Geothermal Workshop*, pp 161-166.

Probst, A., Gunn, C. and Anderson, G. (1992), "A Preliminary Comparison Of Pressure Drop Models Used In Simulating Geothermal Production Wells", *Proc. 14th New Zealand Geothermal Workshop*, pp 139-144.

Duns, H. and Ros, N. (1963). "Vertical Flow Of Gas and Liquid Mixtures In Wells", *Proc. 6th World Pet. Congress.*

PROCEEDINGS, Nineteenth Workshop on Geothermal Reservoir Engineering
Stanford University, Stanford, California, January 18-20, 1994
SGP-TR-147

# PARAMETRIC STUDY OF GRAVITY CHANGE ACCOMPANYING GEOTHERMAL RESERVOIR CHANGE CALCULATED BY NUMERICAL SIMULATION

Shinji Takasugi, Kazumi Osato, and Tatsuya Sato

Geothermal Energy Research and Development Co., Ltd., Tokyo 103, Japan

## ABSTRACT

We conducted feasibility studies of gravity monitoring based upon reservoir simulation.

At first, actual field data (although slightly modified) were used for constructing the conceptual model of a geothermal reservoir, particularly for shallow geothermal reservoir case study. Then the possibility of gravity monitoring was confirmed.

Secondly, in order to study the possibility of this for deep geothermal reservoir, we constructed simplified models for deep reservoir. Three models were prepared for our feasibility studies. These simulations showed us that we could also get fairly positive results, if we apply a very sensitive and stable gravity monitoring system.

As a next step, we will investigate gravity monitoring systems according to our feasibility studies.

## 1. INTRODUCTION

The Microgravity monitoring has been successfully applied in several geothermal areas such as Wairakei in New Zealand (Allis and Hunt, 1986), Takigami in Japan (Motoyama et al., 1992), and so on. If measurement is made inside and outside a field, the Microgravity changes might suggest zone where something must occur inside the field or its vicinity according to production and injection.

In this paper, we investigated the Microgravity changes relating to both deep reservoir which is deeper than approximate 3,000 meters, and shallow reservoir which is less than approximate 1,000 meters.

## 2. METHOD

### 2.1 Methodology

We prepared both shallow reservoir model and deep one, then we evaluated the gravity changes at surface and in borehole due to production and injection. Fig. 1 shows the procedure of calculation of gravity changes.

### 2.2 Reservoir Simulator and Way of Calculation of Gravity Changes

The TOUGH (Pruess, 1987) was used for our reservoir simulation and the Talwani method (Plouff, 1976) was applied for the calculation of gravity changes.

In our study, density changes were calculated at each block using changes of steam quality, vapor density, and liquid density at each block for reservoir simulation on TOUGH. Density changes are computed by the following equation.

$$\Delta\rho = \{ (sq_2 \times \rho s_2 + lq_2 \times \rho l_2) - (sq_1 \times \rho s_1 + lq_1 \times \rho l_1) \} \times \phi$$

$\Delta\rho$ :Density change  $sq$ :Steam quality
$lq$ :Lequid quality  $\rho s$ :Density of steam
$\rho l$ :Density of lequid  $\phi$ :Porosity
Subscript1:Natural state  Subscript2:After operation
$sq, lq, \rho s, \rho l$ are calcurated by TOUGH.

## 3. OUTLINE OF SIMULATIONS

### 3.1 Shallow Reservoir Model

(1) Natural state of shallow reservoir

Grid model for shallow reservoir is shown in Fig. 2. To construct this model actual field data such as borehole temperature and borehole pressure are referred to. Natural state simulations of 63 thousand years employ this conceptual model.

(2) Performance prediction simulation

Production corresponding to 10 MW is assumed for more than 20 years in the limited small area. Locations of production wells and injection ones at Layer-5 are presumed as shown in Fig. 3. Blocks for production and injection are located in Layer-3 and Layer-4, and all of separated water from steam shall be injected into the reservoir. Conditions of performance are as follows.

Production steam rate: 120 ton/hour (constant rate)
Separator pressure: 0.345 MPa
Enthalpy of injection water: 530 kJ/kg

(3) Gravity changes

Fig. 4 shows distribution of pressure, temperature, and steam quality of Layer-5 (depth of 100-300 meters) at the natural state and after 15 years of production and injection. Fig. 5 shows distribution of pressure changes, temperature ones, steam quality ones, and gravity ones of Layer-5 after 2.5 and 15 years of production. Changes of these parameters increase with change with time of 2.5 and 15 years of production.

Gravity increases at injection zone and decreases at production zone. These gravity changes correspond very well to the steam quality changes. At injection zone, steam quality decreases due to injection water, and distribution of gravity changes also agrees to high permeable zone as shown in Fig. 3.

3.2 Deep Reservoir Model

(1) Natural state of deep reservoir

Very simple model is introduced for this study, because we don't have enough data for deep reservoir yet.

Fig. 6 shows grid model for deep reservoir. In this model Layer-4 (depth of 1,500-2,000 meters) is impermeable and splits the shallow reservoir (Layer-5 and Layer-6) and the deep one (Layer-1, Layer-2, and Layer-3).

Average temperature of this model is 340°C after the natural state simulation of 63 thousand years.

(2) Performance prediction simulation

The following three deep reservoir types were examined.

Model A : No boundary between production zone and injection zone.
Model B (1): Boundary between production zone and injection zone.
Model B (2): Boundary, but different shape.

Fig. 7 shows distribution of permeability at Layer-1, Layer-2, and Layer-3 in deep reservoir model. This figure also shows locations of production wells and injection ones producing or injecting at Layer-2. All of separated water shall be injected into the reservoir as shallow model. Conditions of performance are as follows.

Production steam rate: 500 ton/hour
Separator pressure: 0.345 MPa
Enthalpy of injection water: 530 kJ/kg

(3) Gravity changes

Fig. 8 shows distribution of pressure changes, temperature ones, steam quality ones, and gravity ones at Layer-3 in deep reservoir model after 15 years of production.

Gravity changes are minus at production zone and its distribution is good coincident with the distribution of steam quality at Layer-3. Consequently we consider that the pressure of reservoir decreases dramatically due to expansion of two phase zone. Furthermore this distribution is also controlled by the boundary of reservoir at Layer-3. Refer to Fig. 7 about the distribution of permeability at Layer-3.

Temperature decreases at the area of injection zone due to injection water, and also at the area of production zone due to pressure draw down. Although density at injection zone ascends, it is difficult to see effect of these changes on gravity data.

## 4. CONCLUSION

We summarize the conclusion as follows.

a) The Microgravity changes depend upon expansion or reduction of two phase zone distribution by production and injection.

b) In our simulation, maximum changes are 50 micro gal at surface and more than this in borehole. Therefore, it is necessary to develop a very high accuracy Microgravity measurement system for successful monitoring.
c) In addition to high accuracy measurement, high density measurement is also essential to eliminate short period gravity changes in space because of shallow reservoir or ground water level.

## ACKNOWLEDGEMENTS

We would like to express our appreciation to the New Energy and Industrial Technology Development Organization (NEDO) for allowing us to use some of the results and data obtained in the project, "Development of drilling and production technology for deep-seated geothermal resources", which has been conducted since Fiscal Year 1992 in the Sunshine Project of MITI, Japan.

## REFERENCES

Allis, R.G. and Hunt, T.M. (1986), "Analysis of exploitation -Induced gravity changes at Wairakei geothermal field-," Geophysics, 51, 1647-1660.

Motoyama, T., Ehara, S., Mogi, T., and Akasaka, C. (1992), "Reservoir monitoring by observations of gravity changes -A case study of Takigami geothermal field-," Abstracts with Programs of 1992 Annual Meeting, Geothermal Research Society of Japan, A5.

Plouff, D. (1976), "Gravity and magnetic fields of polygonal prisms and application to magnetic terrain corrections," Geophysics, 41, 727-741.

Pruess, K. (1987), "TOUGH user's guide," LBL-20700.

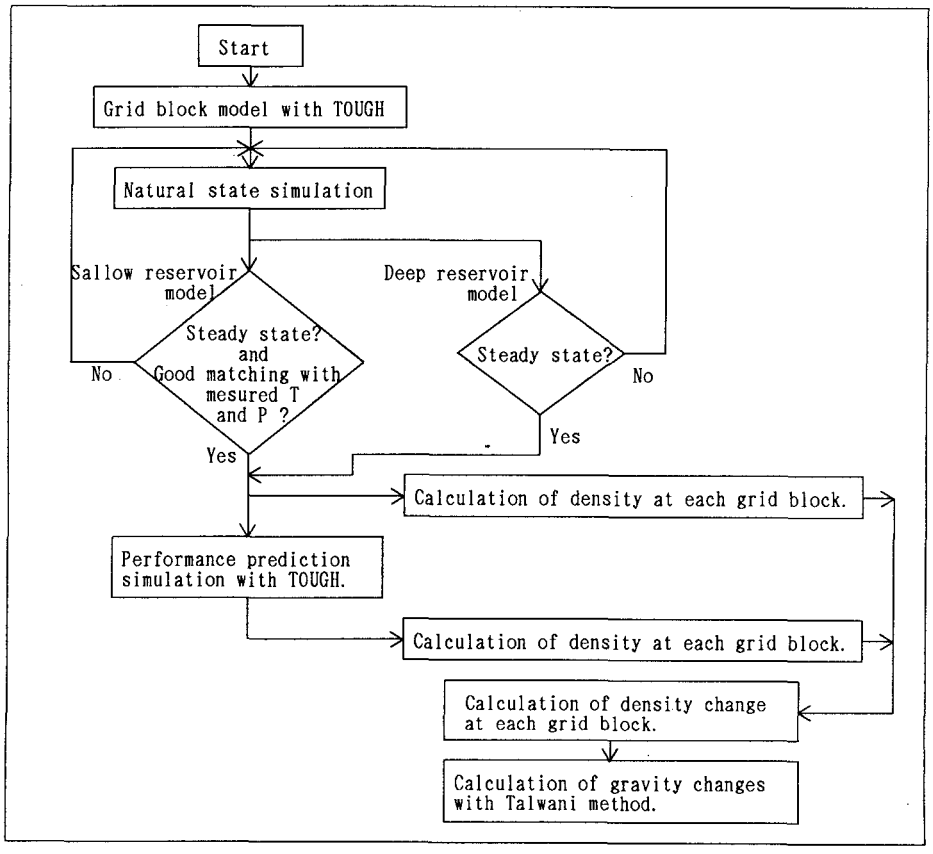


Fig. 1 Flow chart of calculation of gravity changes.

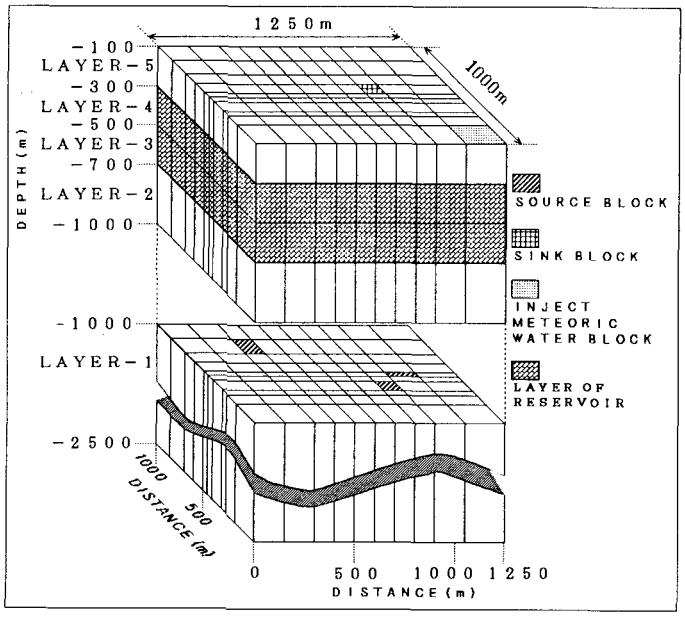


Fig. 2 Grid model for shallow reservoir.

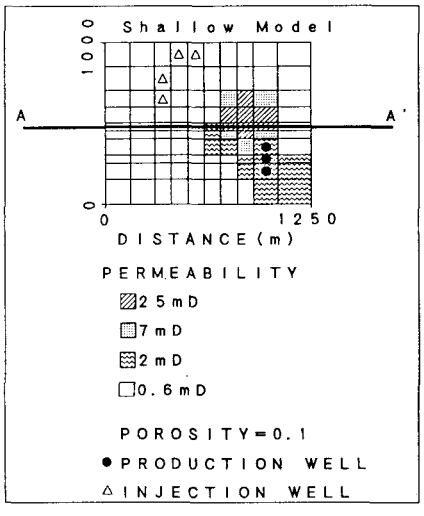


Fig. 3 Well location and distribution of permeability at Layer-5 in shallow reservoir model.

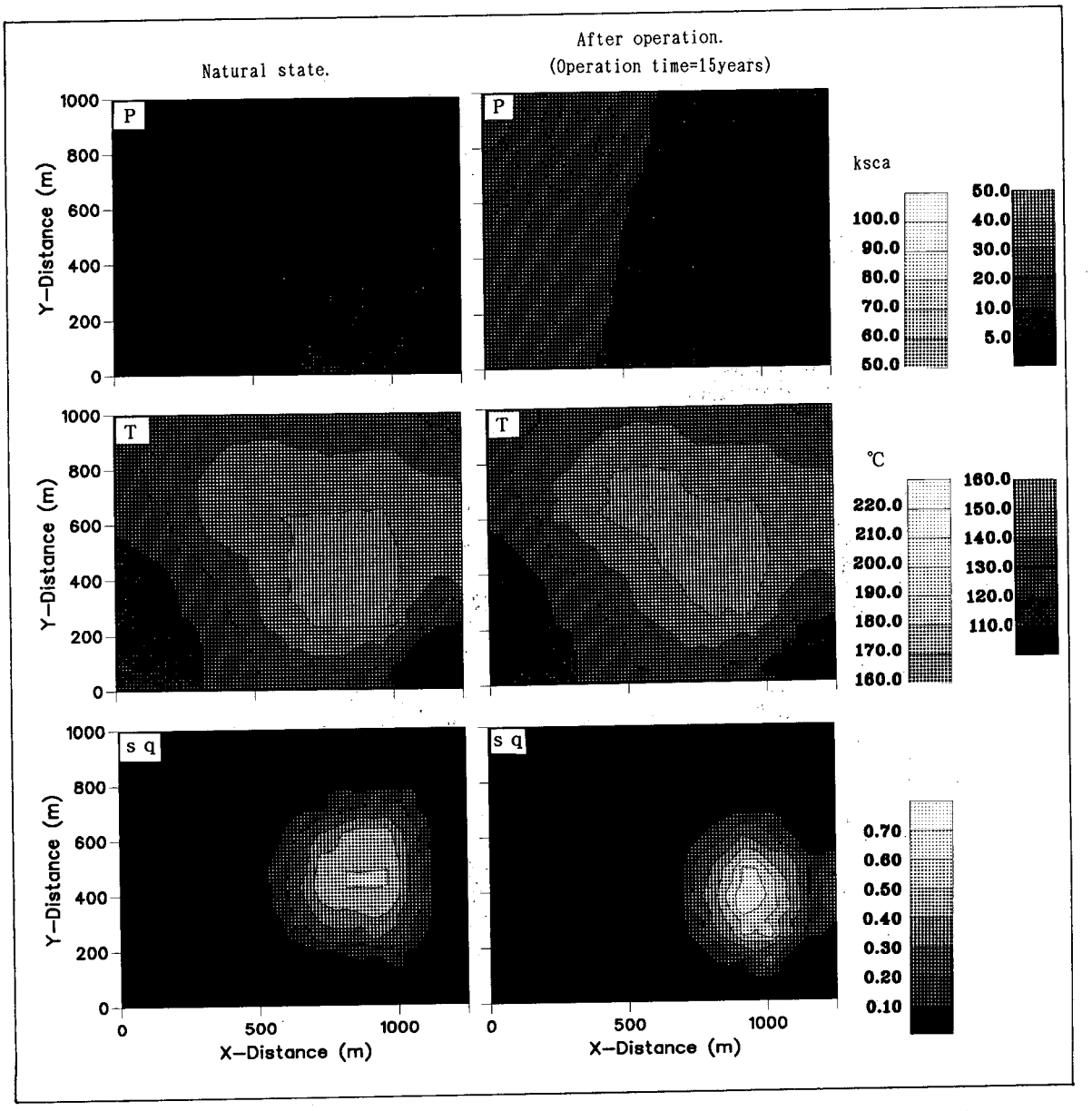


Fig. 4 Distribution of pressure (P), temperature (T), and steam quality (sq) at Layer-5 for shallow reservoir model. Figures of left side are the distribution of natural state and right side ones are the distribution after 15 years of production.

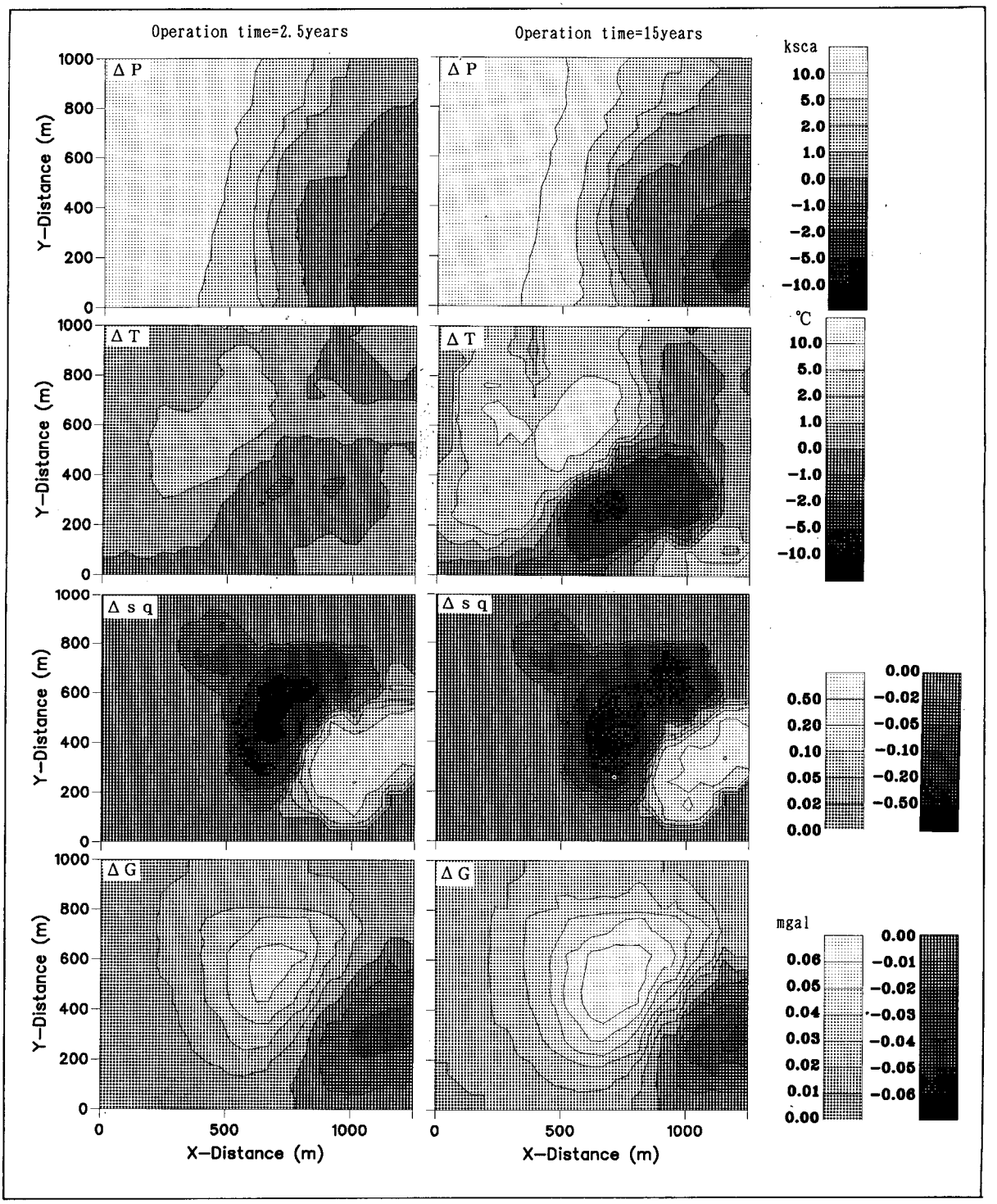


Fig. 5 Distribution of pressure changes (ΔP), temperature changes (ΔT), steam quality changes (Δsq), and gravity changes (ΔG) at Layer-5 for shallow reservoir model after 2.5 and 15 years of production.

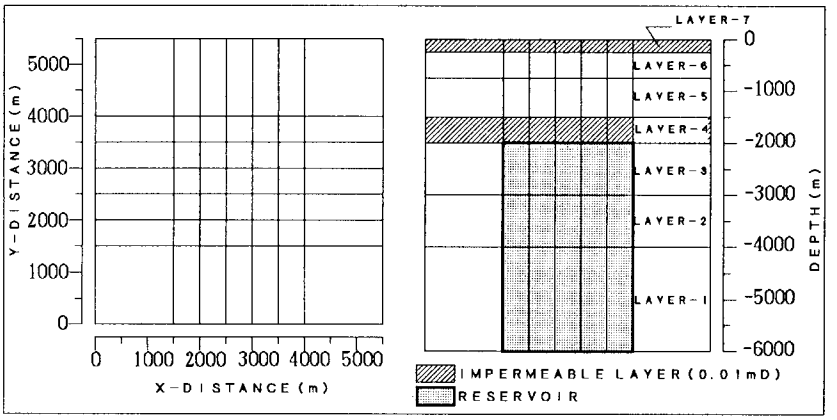


Fig. 6 Grid model for deep reservoir.

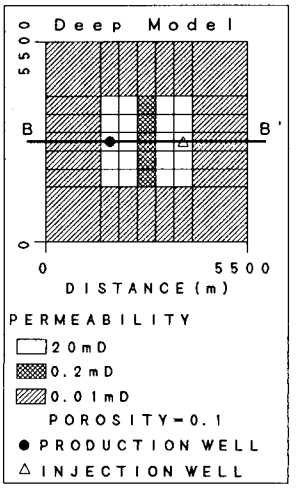


Fig. 7 Well location and distribution of permeability at Layer-1, Layer-2, and Layer-3 in deep reservoir model.

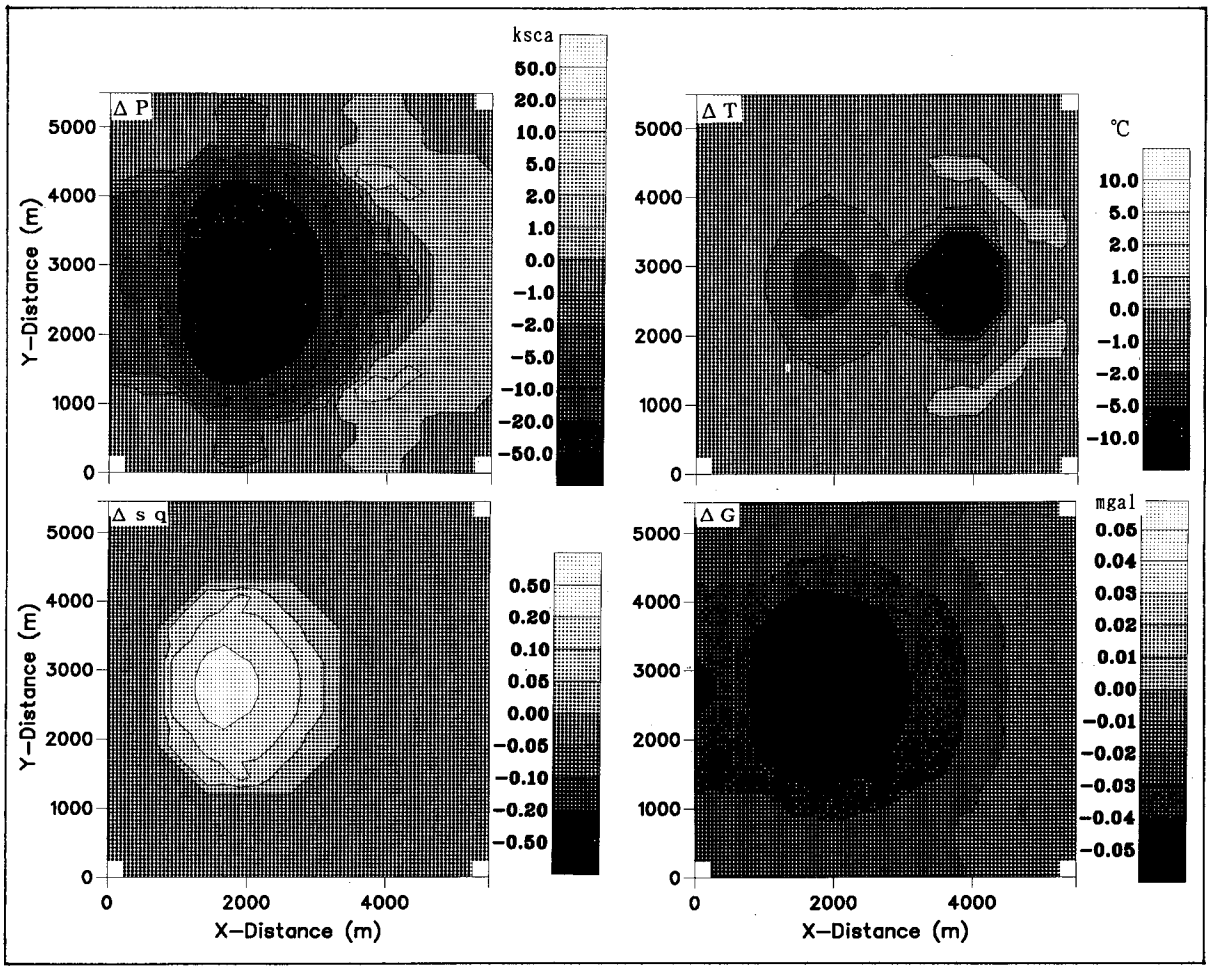


Fig. 8 Distribution of pressure changes (ΔP), temperature changes (ΔT), steam quality changes (Δsq), and gravity changes (ΔG) at Layer-3 for deep reservoir model after 15 years of production.

PROCEEDINGS, Nineteenth Workshop on Geothermal Reservoir Engineering
Stanford University, Stanford, California, January 18-20, 1994
SGP-TR-147

# SALT EFFECTS ON STABLE ISOTOPE PARTITIONING AND THEIR GEOCHEMICAL IMPLICATIONS FOR GEOTHERMAL BRINES

Juske HORITA, David R. COLE, and David J. WESOLOWSKI

Chemical and Analytical Sciences Division, Oak Ridge National Laboratory
P.O.Box 2008, MS 6110, Oak Ridge, TN 37831-6110

## ABSTRACT

The effects of dissolved salts (NaCl, KCl, $MgCl_2$, $CaCl_2$, $Na_2SO_4$, $MgSO_4$, and their mixtures) on oxygen and hydrogen isotope partitioning between brines and coexisting phases (vapor and calcite) were experimentally determined at 50-350°C and 300°C, respectively. In liquid-vapor equilibration experiments, for all of the salts studied, the hydrogen isotope fractionation factors between the salt solutions and vapor decreased appreciably (up to 20‰) compared to pure water-vapor. Except for KCl solutions at 50°C, the oxygen isotope fractionation factors between salt solutions and vapor were higher (up to 4‰) than, or very close to, that of pure water. The observed isotope salt effects are all linear with the molalities of the solutions. Mixed salt solutions mimicking natural geothermal brines exhibit salt effects additive of those of individual salts. The isotope exchange experiments of calcite-water at 300°C and 1 kbar yielded a fractionation factor of 5.9±0.3‰ for pure water and effects of NaCl consistent with those obtained from the liquid-vapor equilibration experiments.

The isotope salt effects observed in this study are too large to be ignored, and must be taken into account for isotopic studies of geothermal systems (i.e., estimation of isotope ratios and temperatures of deep-seated geothermal brines).

## INTRODUCTION

It has long been recognized that dissolved salts in water can change oxygen and hydrogen isotope partitioning between water and other phases (i.e., vapor, minerals) due to the hydration of ions upon the dissolution of salts in water. However, their effects have not been well determined at elevated temperatures (cf. Truesdell, 1974). We are currently conducting a series of hydrothermal experiments of the system brine-vapor or minerals to 350°C, in order to determine precisely the effects of dissolved salts abundant in brines on isotope partitioning at temperatures encountered in geothermal systems. The so-called "isotope salt effect" has important implications for the interpretation and modeling of isotopic data of brines and rocks obtained from geothermal fields. We will show how to use our new results of isotopic partitioning to help better evaluate energy resources of many geothermal fields.

## EXPERIMENTAL

We can determine the salt effect on oxygen and hydrogen isotope partitioning between liquid water and a coexisting phase A (vapor, minerals) from,

$$10^3\ln\Gamma = 10^3\ln\alpha_{\text{A-brine}} - 10^3\ln\alpha_{\text{A-pure water}} \quad (1)$$

where $\alpha$ is an equilibrium isotope fractionation factor between a phase A and liquid water. The isotope salt effect ($\Gamma$), which is caused by the dissolution of salts in water, can be more rigorously defined as follows,

$$\Gamma = \frac{a(HDO)/a(H_2O)}{X(HDO)/X(H_2O)} \text{ or } \frac{a(H_2{}^{18}O)/a(H_2{}^{16}O)}{X(H_2{}^{18}O)/X(H_2{}^{16}O)}$$

$$= \gamma(HDO)/\gamma(H_2O) \text{ or } \gamma(H_2{}^{18}O)/\gamma(H_2{}^{16}O), \quad (2)$$

where a, X, and $\gamma$ denote activity, mole fraction, and activity coefficient, respectively.

In order to examine the effects of dissolved salts on isotope partition, a series of vapor-liquid water equilibration experiments were carried out for NaCl solutions from 50 to 350°C, $CaCl_2$ solutions from 50 to 200°C, and for KCl, $MgCl_2$, $Na_2SO_4$, and $MgSO_4$ solutions from 50 to 100°C. Several mixed salt solutions mimicking natural geothermal brines (Salton Sea brine) were also studied at 50 to 100°C. In order to cover the wide range of temperature, three different liquid-vapor equilibration apparatus were employed, using both static and dynamic sampling techniques of water vapor. The overall errors in values of $10^3\ln\Gamma$ are ±0.1 to 0.15‰ ($1\sigma$) and ±1.0 to 1.5‰ ($1\sigma$) for oxygen and hydrogen isotopes, respectively.

The effect of dissolved NaCl on oxygen isotope

partitioning between calcite ($CaCO_3$) and water was also studied at 300°C and 1 kbar. Since complete isotope exchange of this reaction is not expected during the experiments, the partial isotope exchange method of Northrop and Clayton (1966) was used to calculate the equilibrium isotope fractionation factor. This technique gives errors of about ±0.2 to 0.3‰ (1$\sigma$).

## RESULTS AND DISCUSSION

### (1) Liquid-Vapor Equilibration Method

We first determined precisely liquid-vapor isotope fractionation factors of pure water from 25 to 350°C, because there are few precise data available in the literature above 100°C. All of our results and most of the literature data were then regressed to single equations valid from the freezing temperature (0°C) to the critical temperature of water (374.1°C),

$$10^3\ln\alpha_{l\text{-}v}(D)=1159(T^3/10^9)-1620(T^2/T^6)+794.8(T/10^3)-161.0+2.999(10^9/T^3) \quad (3)$$

within ±1.2‰ (1$\sigma$), and

$$10^3\ln\alpha_{l\text{-}v}(^{18}O)=-7.69+6.712(10^3/T)-1.666(10^6/T^2)+0.3504(10^9/T^3) \quad (4)$$

within ±0.11‰ (1$\sigma$) (Horita and Wesolowski, in review).

Liquid-vapor isotope fractionation factors of the single salt solutions (NaCl, KCl, $MgCl_2$, $CaCl_2$, $Na_2SO_4$, and $MgSO_4$) with different molalities were determined in order to calculate the isotope salt effects from the following equation,

$$10^3\ln\Gamma=10^3\ln\alpha_{l\text{-}v(\text{pure water})}-10^3\ln\alpha_{l\text{-}v(\text{brine})}. \quad (5)$$

Values of $10^3\ln\Gamma(D)$ for 0-6 molal NaCl solutions at 50 to 350°C, 0-5 molal $CaCl_2$ solutions at 50 to 200°C, and for 0-4 molal KCl, 0-5 molal $MgCl_2$, 0-2 molal $Na_2SO_4$, and 0-2 molal $MgSO_4$ solutions at 50 to 100°C were all positive and linear with their molalities within analytical errors. In other words, hydrogen isotope fractionation factors, $10^3\ln\alpha(D)$, between the salt solutions and vapor are always smaller (up to 20‰) than those of pure water. The magnitude of values of $10^3\ln\Gamma(D)$ is in the order $CaCl_2 \geq MgCl_2 > MgSO_4 > NaCl \approx KCl > Na_2SO_4$ at the same molalities at 50 to 100°C (see Fig. 1 for 100°C). Our results of NaCl solutions from 50 to 350°C together with those in the literature near and below room temperature show that values of $10^3\ln\Gamma(D)$ of NaCl solutions decrease from 2.6‰/molal at 10°C to 1.0‰/molal at 130°C, and are nearly constant from 130 to 300°C. Then, the values appear to increase to 2.0‰/molal at 350°C. The values of $10^3\ln\Gamma(D)$/molal for $CaCl_2$ solutions from 50 to 200°C, and of KCl, $MgCl_2$, $Na_2SO_4$, and $MgSO_4$ solutions from 50 to 100°C decrease slightly with increasing temperature.

Except for KCl solutions at 50°C, oxygen isotope salt effects, $10^3\ln\Gamma(^{18}O)$, in all of the salt solutions are negative or very close to zero; namely oxygen isotope fractionation factors, $10^3\ln\alpha(^{18}O)$, between the salt solutions and vapor are larger (up to 4‰) than, or very close to, that of pure water. Divalent cation salts ($Mg^{2+}$ and $Ca^{2+}$) exhibit oxygen isotope salt effects much larger than monovalent cation salts ($Na^+$ and $K^+$) (see Fig. 1 for 100°C). Values of $10^3\ln\Gamma(^{18}O)$ in $MgCl_2$ and $MgSO_4$ solutions are indistinguishable between 50 and 100°C, suggesting that cations determine oxygen isotope salt effects. Our results for the oxygen isotope salt effect of 0-6 molal NaCl solutions from 50 to 350°C show that NaCl has

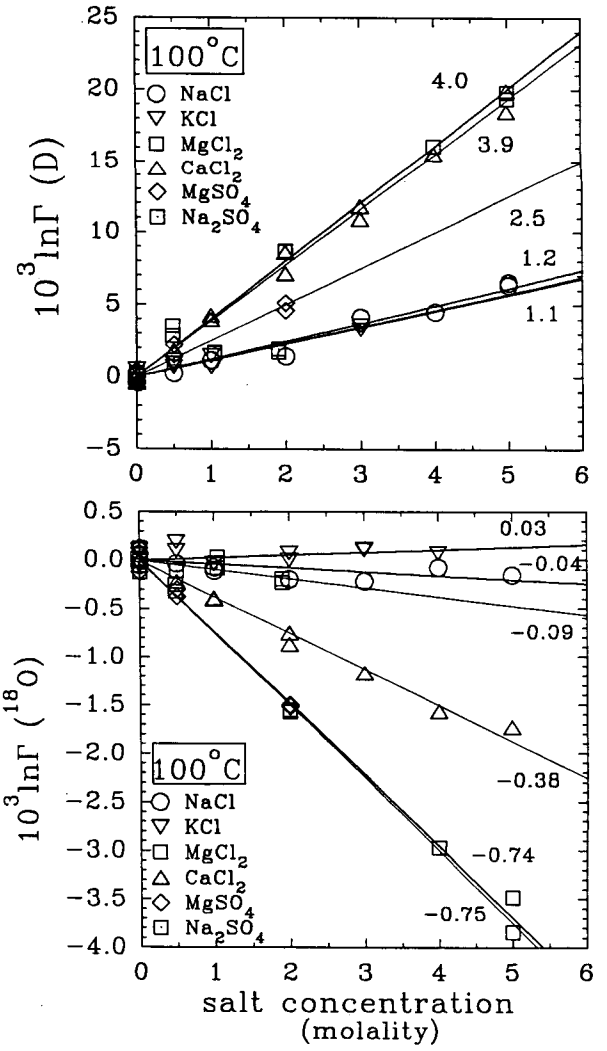


Fig. 1. Salt effect on liquid-vapor partitioning of oxygen and hydrogen isotopes at 100°C.

almost no effect on oxygen isotope partitioning to 200°C, but that values of $10^3\ln\Gamma(^{18}O)$ start to deviate to negative values at higher temperatures (Fig. 2). Our results for NaCl solutions clearly contradict those of Truesdell (1974) and Kazahaya (1986), who observed complex temperature and molality dependence (Fig. 2). Kazahaya (1986) employed a liquid-vapor equilibration method similar to ours, while Truesdell (1974) used a $CO_2$-brine equilibration method.

All of the results of the oxygen and hydrogen isotope salt effects in the single salt solutions determined between 50 to 100°C were satisfactorily regressed to an equation with a simple form,

$$10^3\ln\Gamma = m(a+b/T), \qquad (6)$$

where a (molality$^{-1}$) and b (K.molality$^{-1}$) are parameters, m molality of a salt solution, and T(K). The results of the fitting are shown in Table 1.

The oxygen and hydrogen isotope salt effects in mixed salt solutions of the system Na-K-Mg-Ca-Cl-$SO_4$, some of which mimic natural geothermal brines (Salton Sea), were measured using the liquid-vapor equilibration methods between 50 and 100°C. Then, we examined whether the measured isotope salt effects in the mixed salt solutions can be described as an additive property of the isotope salt effects of individual single salts contained in the mixed salt solutions; namely (Horita et al., 1993b)

$$10^3\ln\Gamma_{\text{mixed salt soln}} = \Sigma(10^3\ln\Gamma_{\text{single salt soln}}) = \Sigma\{m_i(a_i+b_i/T)\}, \qquad (7)$$

where i is the ith single salt in mixed salt solutions. Figs. 3a and 3b show that the measured oxygen and hydrogen isotope salt effects in the mixed salt solutions agree well with the calculated values using parameter values in Table 1 and Eqn (7) within analytical errors and uncertainty in the calculations. This is true even for the mixed salt solutions of chloride and sulfate anions with very high ionic strengths. Sofer and Gat (1972; 1975) and Horita and Gat (1989) also observed that this simple mixing rule applies to synthetic and natural chloride-mixed solutions at room temperature. Thus, Eqn (7) can be used to calculate oxygen and hydrogen isotope salt effects in complex natural brines, at least to 100°C.

(2) Calcite-Water Isotope Exchange Method

Hydrothermal experiments of partial isotope exchange were carried out on calcite-pure water at 300°C and 1 kbar for a duration of 126 days. A calculated equilibrium oxygen isotope fractionation factor, $10^3\ln\alpha_{\text{calcite-pure water}}$, was 5.9±0.3‰. From the experiments of calcite-1, 3, and 5 molal NaCl solutions, we obtained $10^3\ln\alpha_{\text{calcite-NaCl soln}}$ values of 5.6±0.2, 5.0±0.15, and 4.9±0.2 ‰ for 1, 3, and 5 molal NaCl solutions, respectively (Table 2). Oxygen isotope salt effects can be calculated from,

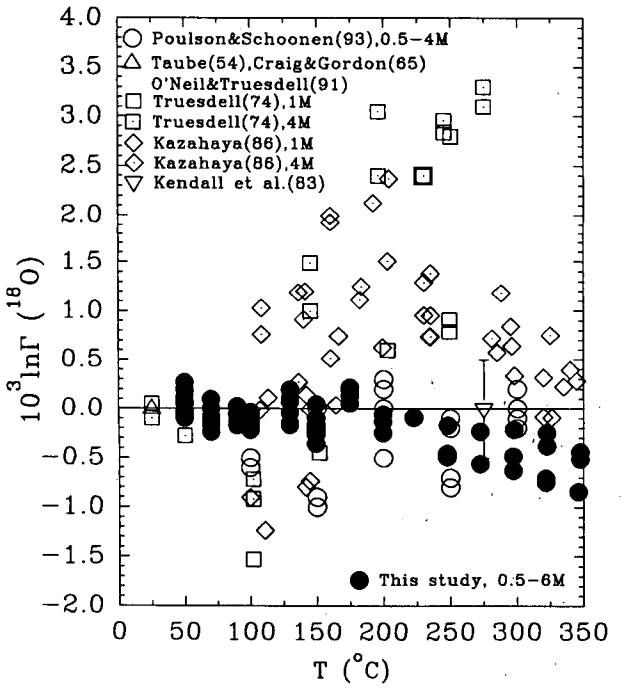


Fig. 2. Effect of NaCl on oxygen isotope partitioning.

Table 1. Results of least-squares fitting of the isotope salt effect in single salt solutions (Horita et al.1993a)

| salt | $10^3\ln\Gamma$ | parameter a | parameter b | T(°C) |
|---|---|---|---|---|
| NaCl | (D) | -2.89 | 1503.1 | 10-100 |
| | ($^{18}O$) | -0.015 | 0 | 25-100 |
| KCl | (D) | -5.10 | 2278.4 | 20-100 |
| | ($^{18}O$) | -0.612 | 230.83 | 25-100 |
| $MgCl_2$ | (D) | +4.14 | 0 | 50-100 |
| | ($^{18}O$) | +0.841 | -582.73 | 25-100 |
| $CaCl_2$ | (D) | -2.34 | 2318.2 | 50-100 |
| | ($^{18}O$) | -0.368 | 0 | 50-100 |
| $Na_2SO_4$ | (D) | +0.86 | 0 | 50-100 |
| | ($^{18}O$) | -0.143 | 0 | 50-100 |
| $MgSO_4$ | (D) | +8.45 | -2221.8 | 50-100 |
| | ($^{18}O$) | +0.414 | -432.33 | 0-100 |

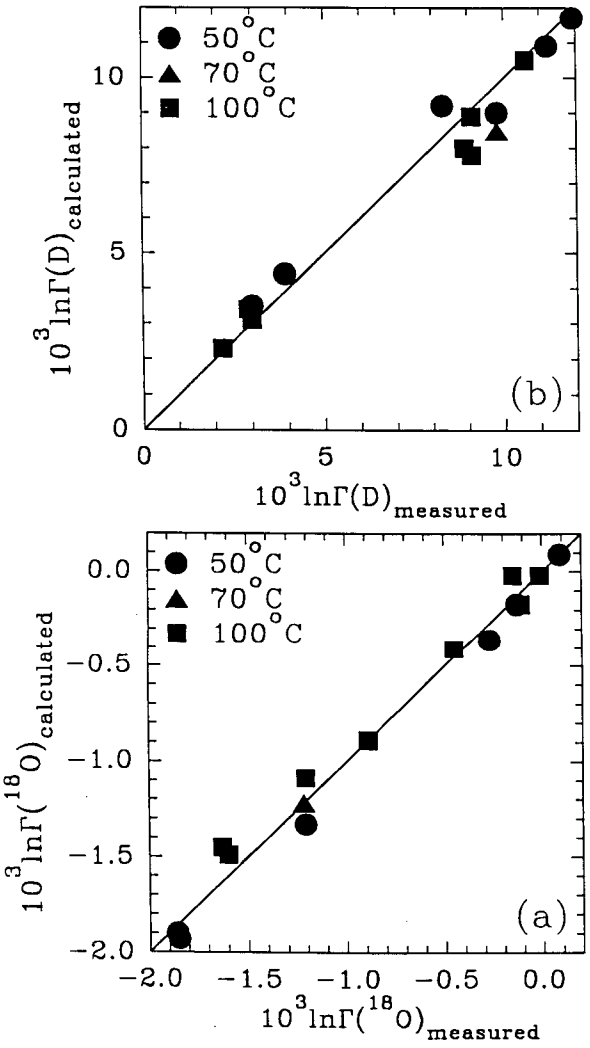


Fig. 3. Effects of mixed salt solutions on oxygen and hydrogen isotope partitioning at 50-100°C.

Table 2. Results of the isotope exchange experiments of calcite-water at 300°C and 1 kbar.

| NaCl | F(%) | $10^3\ln\alpha$ | $10^3\ln\Gamma(^{18}O)$ |
|---|---|---|---|
| pure water | 7.4 | 5.9±0.3 | |
| 1 molal | 19.0 | 5.6±0.2 | -0.3 |
| 3 molal | 22.7 | 5.0±0.15 | -0.9 |
| 5 molal | 25.0 | 4.9±0.2 | -1.0 |

F=fraction of isotope exchange

$$10^3\ln\Gamma(^{18}O)=10^3\ln\alpha_{calcite\text{-}NaCl\,soln}-10^3\ln\alpha_{calcite\text{-}pure\,water} \quad (8)$$

yielding $10^3\ln\Gamma(^{18}O)$ values of -0.3 to -1.0‰ (Table 2). The magnitude of these oxygen isotope salt effects obtained from the calcite-water experiments is consistent with those obtained from the liquid-vapor equilibration method at 300°C (-0.2 to -0.6‰ for 1 and 5 molal NaCl solutions) (Fig. 2).

A previous study on oxygen isotope fractionation in the system calcite-0.7 molal $NH_4Cl$ solution gave a $10^3\ln\alpha$ value of about 5.6‰ at 300°C (O'Neil et al., 1969, corrected in Friedman and O'Neil, 1977). Kendall et al. (1983) also carried out experiments for oxygen isotope fractionation factor of the system calcite-0.5 molal $NH_4Cl$±1 or 4 molal NaCl solution at 275°C. They found that the average oxygen isotope fractionation factors were 6.8±0.5‰ regardless of the presence of NaCl; the equation by O'Neil et al. (1969) yields 6.4‰ at 275°C. Thus, our results and those of O'Neil et al. (1969) and Kendall et al. (1983) are generally consistent with each other, although the effect of $NH_4Cl$ is not well determined.

## IMPLICATIONS FOR GEOTHERMAL STUDIES

In some geothermal fields, both steam and liquid water can be collected, and their oxygen and hydrogen isotopic compositions can be used as the water-steam isotope geothermometer, using Eqns (3) and (4). However, incomplete separation of steam and water, and partial condensation of steam after the phase separation often result in discordant, unreasonable temperatures for the phase separation. A third water-steam isotope geothermometer employs the slope in the $\delta D$-$\delta^{18}O$ diagram, given by the ratio of differences in oxygen and hydrogen isotopic compositions of water and steam samples,

$$\text{slope}=\Delta\delta D/\Delta\delta^{18}O=(\delta D_l-\delta D_v)/(\delta^{18}O_l-\delta^{18}O_v)$$
$$\simeq(1-\alpha_{l\text{-}v}(D)^{-1})/(1-\alpha_{l\text{-}v}(^{18}O)^{-1}) \quad (9)$$

Values of the slope were calculated from Eqns (3), (4), and (9) from 0 to 372°C, and shown in Fig. 4. The value of the slope decreases from about 8 near room temperature with increasing temperature, due to a rapid decrease in the value of the hydrogen isotope fractionation factor. The sign of the slope changes at about 229°C because of the cross-over of the hydrogen isotope fractionation factor. The effects of incomplete separation of water and steam, and partial condensation of steam on calculated temperatures of the phase separation using Eqn (9) are much smaller than those obtained from values of $\Delta\delta D$ and $\Delta\delta^{18}O$, alone. However, the water-steam isotope geothermometer using the value of $\Delta\delta D/\Delta\delta^{18}O$ should be limited to temperatures less than 250°C, due to large errors in the calculations above that temperature. Since dissolved salts in water

change both oxygen and hydrogen isotope fractionations factor between liquid water and steam, their effects must be taken into account for the evaluation of temperatures of the phase separation.

The importance of the isotope salt effect for evaluating reservoir temperatures of geothermal systems can be illustrated using a mineral-water isotope geothermometer. In active geothermal fields, isotopic compositions of brines and rocks obtained from bore holes have been used to estimate reservoir temperatures, assuming the attainment of isotope equilibrium. For example, samples of kaolinite and water obtained from a bore hole in a geothermal field give a measured $10^3\ln\alpha(D)_{kaol\text{-}water}$ value of -15‰. In order to calculate the underground reservoir temperature, the isotope salt effect of the water sample must be taken into account. The effects of 1 and 3 molal NaCl solutions and Salton Sea brine on the hydrogen isotope fractionation factor are shown in Fig. 5 as examples. The composition of Salton Sea brine is 3.14 molal $Na^+$, 0.882 molal $Ca^{2+}$, 0.588 molal $K^+$, and 5.76 molal $Cl^-$ (Williams and McKibben, 1989). The fractionation factor between kaolinite and pure water is taken from Liu and Epstein (1984). If the fractionation factor for pure water was inadvertently used for 1 and 3 molal NaCl solutions, and Salton Sea brine, the calculated isotope temperatures will be approximately 7, 24, and 59°C higher than the correct one, respectively.

Discrepancies reported in the literature between temperatures obtained from mineral-water isotope geothermometers and measured bore hole temperatures, homogenization temperatures of fluid inclusions, and other chemical geothermometers could be due to the disregard of possible isotope salt effect in waters in the calculations. The same principle should be applied to isotope geothermometers between brines and dissolved species (e.g., $SO_4^{2-}$), but isotope geothermometers using coexisting minerals or gaseous species (e.g., $CO_2$, $CH_4$) are independent of the isotope salt effect in brines.

Another important example is the estimation of isotopic compositions of fluids from which mineral assemblages were precipitated in geothermal fields. Isotopic data of minerals together with estimated temperatures of the precipitation of the minerals obtained from fluid inclusion microthermometry and/or other types of geothermometers can give the isotope ratios of the parental fluids, using mineral-water isotope fractionation factors. Alternatively, fluid inclusions in minerals can be extracted and their isotopic compositions can be determined, thus providing directly isotope ratios of the mineral-forming fluids. When fluids precipitating minerals in geothermal fields are brines, the isotope ratios of the fluids obtained by the above two approaches could be different due to the isotope salt effect in the brines (Truesdell, 1974).

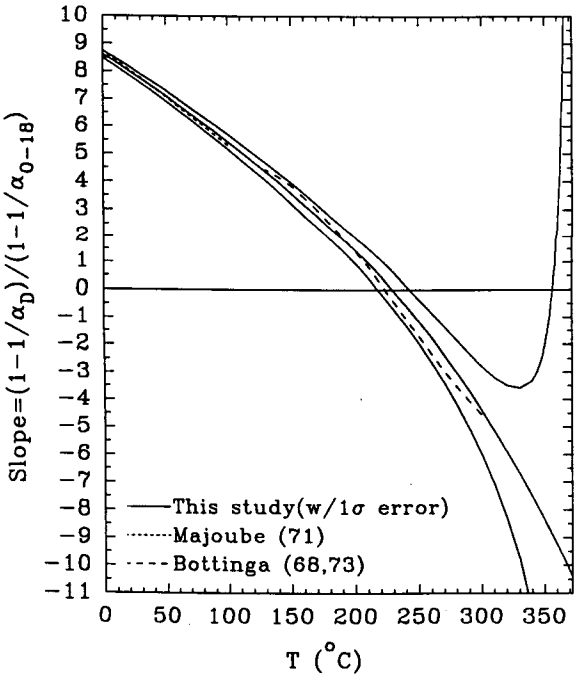


Fig. 4. Ratio of $\Delta\delta D/\Delta\delta^{18}O$ of water and steam samples as a function of temperature.

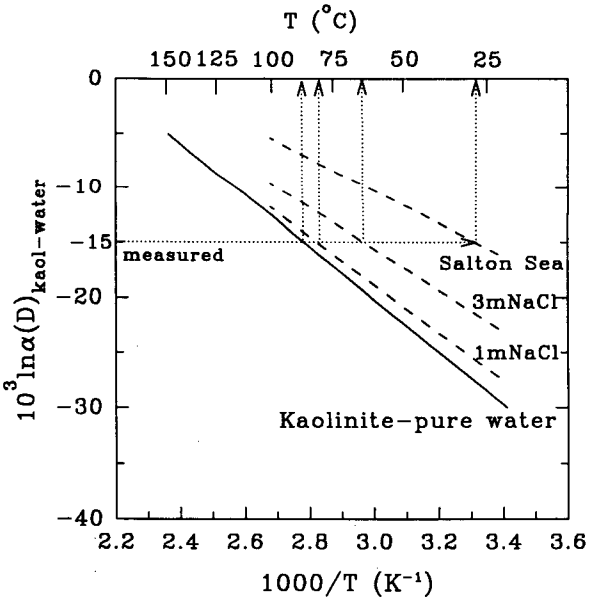


Fig. 5. Salt effect on kaolinite-water hydrogen isotope geothermometer.

## CONCLUSIONS

Our hydrothermal experimental studies demonstrate that salt effects on stable isotope partitioning between brines and other phases (vapor and minerals) indeed persist up to at least 350°C, but that the complex temperature and composition dependence reported in the literature is almost certainly an experimental artifact. Our new, precise results on isotope partitioning and salt effects permit a improved quantitative evaluation of the geochemical characteristics of geothermal systems.


## ACKNOWLEDGEMENT

This study was supported by the Geoscience Program of the Office of Basic Energy Sciences and the Geothermal Technology Program of the Office of Energy Efficiency and Renewable Energy, U. S. Department of Energy, under contract number DE-AC05-84OR21400 with Martin Marietta Energy Systems, Inc.


## REFERENCES


Bottinga, Y. (1968), "Isotopic fractionation in the system: calcite-graphite-carbon dioxide-methane-hydrogen-water," Ph.D. dissertation, U.C. San Diego.

Craig, H. and Gordon, L. I. (1965), "Deuterium and oxygen 18 variations in the ocean and the marine atmosphere," in *Stable Isotopes in Oceanographic Studies and Paleotemperatures* (ed. E. Tongiorgi), pp9-130.

Friedman, I. and O'Neil, J. R. (1977), "Compilation of stable isotope fractionation factors of geochemical interest," U. S. Geol. Surv. Prof. Paper 440-KK.

Horita, J. and Gat, J. R. (1989), "Deuterium in the Dead Sea: Remeasurement and implications for the isotope activity correction in brines," Geochim. Cosmochim. Acta, 53, 131-133.

Horita, J, Wesolowski, D. J., and Cole, D. R. (1993a), "The activity-composition relationship of oxygen and hydrogen isotopes in aqueous salt solutions: I. Vapor-liquid equilibration of single salt solutions from 50 to 100°C," Geochim. Cosmochim. Acta, 57, 2797-2817.

Horita, Cole, D. R., and J, Wesolowski, D. J. (1993b), "The activity-composition relationship of oxygen and hydrogen isotopes in aqueous salt solutions: II. Vapor-liquid equilibration of mixed salt solutions from 50 to 100°C and geochemical implications," Geochim. Cosmochim. Acta, 57, 4703-4711.

Kazahaya, K. (1986), "Chemical and isotopic studies on hydrothermal solutions," Ph.D. dissertation, Tokyo Institute Technology, 185p.

Kendall, C., Chou, I-M., and Coplen, T. B. (1983) "Salt effect on oxygen isotope equilibria," EOS, 334-335.

Liu, K. K. and Epstein, S. (1984), "The hydrogen isotope fractionation between kaolinite and water," Chem. Geol. (Isot. Geosci. Sec.) 2, 335-350.

Majoube, M. (1971), "Fractionnement en oxygène 18 et en deutérium entre l'eau et sa vapeur," J. Chim. Phys., 68, 1423-1436.

Northrop, D. A. and Clayton, R. N. (1966), "Oxygen isotope fractionations in systems containing dolomite," J. Geol., 74, 174-196.

O'Neil, J. R., Clayton, R. N., and Mayeda, T. K. (1969), "Oxygen isotope fractionation in divalent metal carbonates," J. Chem. Phys., 51, 5547-5558.

O'Neil, J. R. and Truesdell, A. H. (1991), "Oxygen isotope fractionation studies of solute-water interactions," In *Stable Isotope Geochemistry: A Tribute to Samuel Epstein* (ed. H. P. Taylor et al.), pp17-25, Geochem. Society.

Poulson, S. R. and Schoonen M. A. A. "An oxygen isotope study of NaCl-water interactions at 100-300°C," Isotope Geosci. (in press)

Sofer, Z. and Gat, J. R. (1972), "Activities and concentrations of oxygen-18 in concentrated aqueous salt solutions: Analytical and Geophysical implications," Earth Planet. Sci. Lett., 15, 232-238.

Sofer, Z. and Gat, J. R. (1975), "The isotopic composition of evaporating brines: Effects of the isotope activity ratio in saline solutions," Earth Planet. Sci. Lett., 26, 179-186.

Taube, H. (1954), "Use of oxygen isotope effects in the study of hydration of ions," J. Phys. Chem., 58, 523-528.

Truesdell, A. H. (1974), "Oxygen isotope activities and concentrations in aqueous salt solutions at elevated temperatures: Consequences for isotope geochemistry," Earth Planet. Sci. Lett., 23, 387-396.

Williams, A. E. and McKibben, M. A. (1989), "A brine interface in the Salton Sea Geothermal System, California: Fluid geochemical and isotopic characterization," Geochim. Cosmochim. Acta, 53, 1905-1920.

PROCEEDINGS, Nineteenth Workshop on Geothermal Reservoir Engineering
Stanford University, Stanford, California, January 18-20, 1994
SGP-TR-147

# Estimation of reservoir permeability using gravity change measurements

Trevor M. Hunt[a] and Warwick M. Kissling[b]

a *Institute of Geological and Nuclear Sciences, Wairakei Research Centre, Private Bag 2000, Taupo, New Zealand.*

b *Institute for Industrial Research and Development, P O Box 31 310, Lower Hutt, New Zealand.*

## ABSTRACT

Exploitation of a liquid-dominated geothermal system generally results in a transfer of mass that causes measurable changes in gravity. When the rate of mass transfer is controlled by the permeability of the reservoir rocks then analysis of measured gravity changes, using numerical reservoir simulation models, can yield values for reservoir properties. One such case is during the early stages of exploitation, during the formation and expansion of a 2-phase zone.

Calculations using MULKOM models show that for Wairakei field the gravity changes associated with permeabilities of 50 and 100 md would be clearly distinguishable (>50 microgal) in less than 2 years. A measured gravity change of -415 microgal between 1950 and 1961 suggests a permeability of 100 md for rocks in the upper part of the 2-phase zone. This value is consistent with those obtained from well tests.

## INTRODUCTION

The best documented behaviour of a liquid-dominated geothermal system during exploitation is probably that for Wairakei Geothermal Field where continuous production has taken place since 1958. In its natural (unexploited) state, Wairakei is believed to have contained a thin liquid-dominated 2-phase zone overlying a 1-phase deep liquid zone (Grant and Horne 1980; Donaldson et al 1983). The nomenclature used here is that used by Allis and Hunt (1986).

When exploitation began, production was mainly from the deep liquid zone beneath a small area (1 km$^2$) known as the Main Production Borefield (Fig. 1). Removal of fluid resulted in a pressure drop which caused boiling to occur in the upper part of the reservoir. The 2-phase zone expanded both laterally and vertically, and by the early 1970's was about 500 m thick. The 2-phase zone also divided into an upper zone ("steam zone" or "vapour-dominated zone") in which steam is the main pressure-controlling phase, and a lower zone ("liquid-dominated zone") in which liquid water is the continuous phase but boiling conditions exist and some steam is present (Allis and Hunt, 1986). The boundary between these zones is believed to be gradational, but there is little information available about the vertical distance over which the changes occur. The steam and liquid-dominated zones may not be homogeneous; liquid saturation in the steam zone may be smaller at the top of

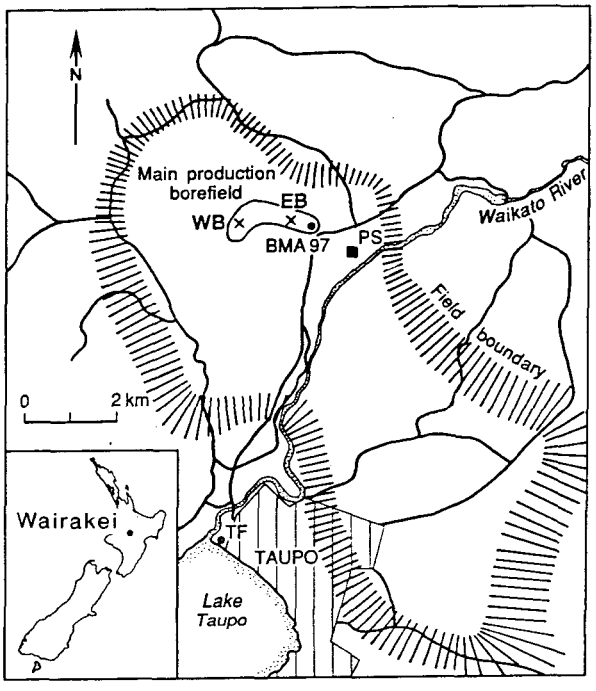


Fig. 1: Map of Wairakei Geothermal Field showing the location of the Main Production Borefield and its parts. EB = Eastern Borefield; WB = Western Borefield; TF = Taupo Fundamental benchmark; PS = geothermal power station.

the zone than at the bottom (Hunt, 1988). Pressures in the deep liquid zone fell by up to 2.5 MPa (25 bar), but have been relatively stable in most parts of the field since the early 1970's. However, gravity and pressure data suggest that in the Eastern Borefield (Fig. 1) the deep liquid level has risen by nearly 100 m since the early 1980's (Hunt, 1988).

Measured gravity changes have been used in New Zealand geothermal fields to: determine recharge over the whole field (Hunt, 1977); estimate changes in saturation in the steam zone in different parts of the field (Allis and Hunt, 1986); check the validity of numerical reservoir simulation models (Blakeley and O'Sullivan, 1985; Hunt et al, 1990a); and determine the path of reinjected fluid (Hunt et al, 1990b). In this paper we extend the application of gravity change measurements further by showing how, under certain circumstances, they can be used to determine the permeability (k) or permeability-thickness (kh) of the reservoir rocks. We use Wairakei field as an example because of its well-documented pressure and gravity data.

## PERMEABILITY MEASUREMENTS AT WAIRAKEI

The response of pressure in wells in the outer parts of the Wairakei field to changes in discharge from wells in the borefield is very rapid, and pressure changes over most of the field have been uniform, indicating very high values for horizontal permeability (Bolton, 1970).

Values of permeability (k) and permeability-thickness (kh) at Wairakei (Table 1) have previously been determined from (in approximate order of importance):

- Well tests such as interference and injection tests. Most published values are for the Eastern Borefield, and the results are poorly documented. Values range from 4-500 md for k, and from 10-170 d-m for kh.

- Reservoir simulation models which match response of the field to exploitation. Early models were 1-D matched only to pressure changes for a 5-10 year period; later models were 2½ or 3-D and matched pressure, temperature, recharge and enthalpy data over more than 20 years. Most later models were consistent with values of 25 - 50 md for horizontal permeability and 10 - 20 md for vertical permeability. Other modelling studies at Wairakei (Mercer et al, 1975; O'Sullivan et al, 1983) assumed values for permeability, and adjusted other parameters, (e.g. recharge coefficient and reservoir area).

- Laboratory measurements on core samples. All these measurements showed k« 1 md, however, they measure only pore permeability and do not take into account fracture permeability which is of much greater significance.

## GRAVITY CHANGES

The main causes of gravity changes resulting from mass changes in the reservoir according to Allis and Hunt (1986) are (in approximate order of importance):

- Liquid drawdown in the 2-phase zone.

- Saturation changes in the 2-phase zone (dry out due to steam loss, or cooling and condensation from invading groundwater).

- Changes in deep liquid density due to temperature changes.

The gravity effects of changes in deep liquid density due to pressure changes, pore compaction, and silica precipitation are generally negligible (Allis and Hunt, 1986).

The first two causes are associated with the transfer of large amounts of mass into or out of the 2-phase zone. In some cases (but not all) the rate of transfer of this mass is controlled, or at least significantly influenced, by the permeability of the rock in the 2-phase zone. The rate of mass transfer, together with fluid density and geometric factors, determine the rate of gravity change. Hence from the rate of gravity change, fluid density change, and the geometry of the 2-phase zone it is possible to calculate the permeability in the vicinity of the region of mass change.

## MODELLING

### *Conceptual Model*

The conceptual model for the development of the 2-phase zone as a result of production from the reservoir at Wairakei is of a boiling front expanding, both laterally and vertically (Fig. 2). Large density changes are associated with this development of the 2-phase zone and result mainly from the conversion of liquid water to steam. These density changes give rise to gravity changes.

### *Numerical Model*

To determine the permeability from gravity change data we set up a simple numerical reservoir simulation model for the initial exploitation of the Wairakei field and computed the theoretical gravity changes for different values of horizontal permeability.

The calculations were made using the simulator MULKOM (Pruess, 1983). To minimise computational time we chose for the model a homogeneous reservoir having radial geometry. The radius of the model was initially taken as 3 km, with element dimensions ranging from 100 m at the centre to 250 m near the boundary; each model element was 10 m thick and the total

TABLE 1: Summary of published values of permeability (k) and permeability-thickness (kh) of reservoir rocks at Wairakei Geothermal Field. v = vertical, h = horizontal, 1 md = $10^{-15}$ $m^2$.

| k (md) | kh (d-m) | Details | Reference |
|---|---|---|---|
| ***WELL TEST VALUES*** | | | |
| 100-500 | * | No details given | Elder 1966 |
| 4 h | * | Pressure response at WK223 to borefield production changes | McNabb et al 1975 |
| 4 h | * | Pressure transients at WK33 and WK36 | |
| * | 15-75 | Pressure build-up test on 4 dry steam wells | Grant 1978 |
| * | 14-33 | Steam fed wells WK4/2, 36, 42 (Eastern Borefield) | Grant 1980 |
| 50-500 | * | | Elder 1981 |
| * | 3 | Injection test on impermeable well WK301 | Allis et al 1985 |
| * | 10-100 | Interference tests during initial development | Electricorp 1990 |
| * | 100-150 | Measurements in monitor wells, Eastern Borefield, 1988-89 | |
| * | 100-170 | Injection test in Eastern Borefield | Hunt et al 1990b |
| ***VALUES DETERMINED FROM RESERVOIR SIMULATION MODELS*** | | | |
| 25 v | * | Simple 1-d model | Marshall 1966 |
| 11 | * | Simple 1-d steady state flow model | Donaldson 1968 |
| 12 v | * | From model for natural discharge | Grant 1970 |
| 4 | * | Calculated from temperature decrease due to production | McNabb et al 1975 |
| 7 h | * | From pressure drop in field | |
| 8 v | * | Calculated from natural output of whole field | |
| 25 | * | Gross permeability from single-phase model | Grant 1977 |
| 50 | * | Simple single-phase model of whole field | Robinson 1977 |
| 50 | * | Lumped parameter model with instantaneous drainage; pressure match | Sorey and Fradkin 1979 |
| 25 | * | Lumped parameter model with slow drainage; pressure match | |
| 40 | 18 | Unconfined aquifer model | Zais and Bodvarsson 1980 |
| 45 | * | Lumped parameter model with instantaneous drainage; pressure match | Fradkin et al 1981 |
| 27 | * | Lumped parameter model with slow drainage; pressure match | |
| 35 h | 30 -35 | Confined aquifer model, based on effects at Tauhara | Wooding 1981 |
| 20-300 h | * | Distributed parameter, 2D model; pressure, enthalpy, | Blakeley and O'Sullivan |
| 20 v | | recharge match | 1982 |
| 5 v | * | Calculated from natural output of field and pressure gradient | Donaldson et al 1983 |
| ***VALUES FROM LABORATORY MEASUREMENTS*** | | | |
| 1 | * | 30 specimens of various rock types, using water | Elder 1966 |
| 0.01-0.05 | * | Cores from WK37 (Eastern Borefield), pore pressure 100 bar, confining pressure 150-250 bar; using water | Pritchett et al 1978 |

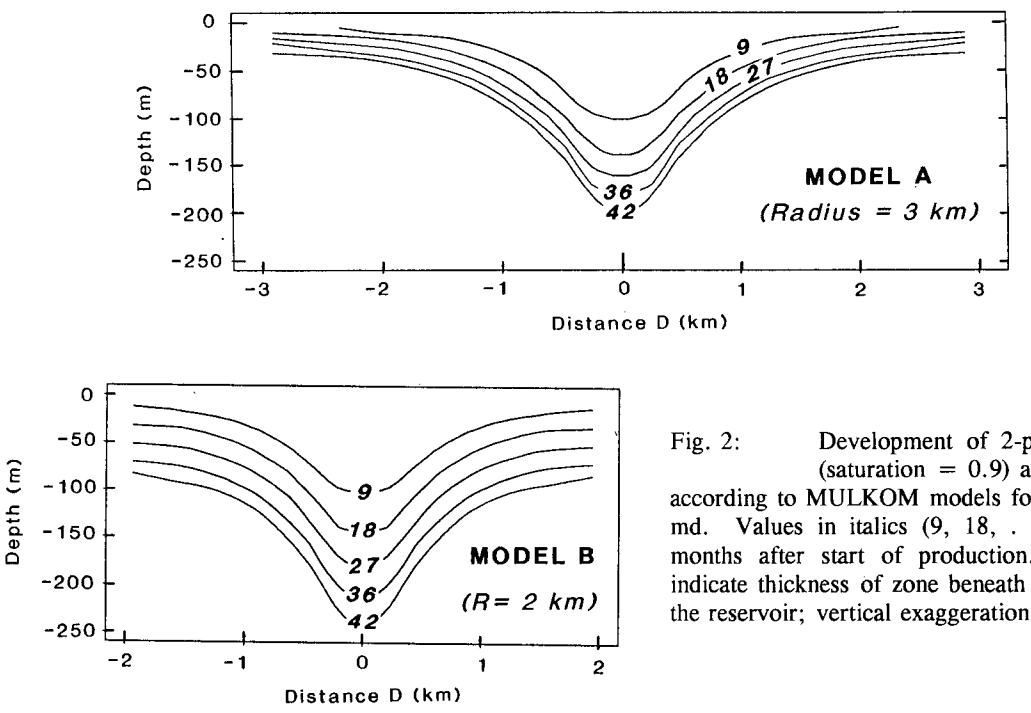


Fig. 2: Development of 2-phase zone (saturation = 0.9) at Wairakei according to MULKOM models for k = 100 md. Values in italics (9, 18, . .) indicate months after start of production. Depths indicate thickness of zone beneath the top of the reservoir; vertical exaggeration is 8x.

thickness was taken to be 500 m. The region of fluid withdrawal was taken to be 200 m thick, 900 m in diameter, located at the bottom centre of the model. The discharge rate was assumed to be 1200 kg/s; actually, mass output at Wairakei rose from about 460 kg/s in early 1958 to 1620 kg/s at the end of 1960 (Electricorp, 1990). The temperature of the liquid was taken (initially) to be 200°C, the (connected) porosity of the reservoir rocks to be 0.2, and pressures to be hydrostatic. Natural mass discharge from surface features was assumed to balance recharge: the natural discharge rate for the period 1958 - 1962 was about 400 kg/s and mass inflow into the 2-phase zone was 200 - 700 kg/s (Allis, 1981). Permeability was assumed to be isotropic. Saturation changes in the 2-phase zone were allowed to develop in the model with the residual liquid saturation set at 0.3 (Blakeley and O'Sullivan, 1985).

The output from MULKOM consists of values of pressure, temperature, and liquid saturation for each element in the model at specified times after production commences. From these values the density change ($\Delta\rho$) in each element for different periods of time was determined (Hunt et al, 1990a). The gravity effects ($\Delta g$) of the density changes in all the elements were then calculated by direct evaluation of the integral:

$$\Delta g(x_o,y_o,z_o) = \int_v G\Delta\rho(z - z_o)/R^3 dV$$

where $G$ is the Universal Gravitational constant (6.67 x $10^{-11}$ $Nm^2/kg^2$), and $R$ is the distance from the observation point $(x_o,y_o,z_o)$ to the volume element $dV$ at $(x,y,z)$.

Theoretical gravity changes with time, at the centre of the field, were calculated for reservoir permeabilities of 50, 100, and 200 md, for a period of 42 months from the start of production. The results (Fig. 3A) clearly show that gravity changes of greater than 100 microgal would be expected in the area above the production zone in 3-6 months from the start of production. More importantly, the size of the changes soon differs greatly for the assumed values of permeability. For example, after only 12 months the gravity change at the centre of the borefield is predicted to be nearly -330 microgal for a permeability of 50 md, and -180 microgal for a permeability of 200 md. After 36 months of production the difference in predicted gravity changes at the centre of the borefield, for permeabilities of 50 and 200 md, is about 300 microgal. The size of the theoretical changes, after a relatively short time, clearly exceed the errors in gravity change measurement and gravity changes that are likely to occur as a result of shallow groundwater level changes, topographic changes, or other influences (about 50 microgal). This shows that measurements of gravity change in the borefield area are a powerful tool for estimating reservoir permeability.

To check if the results were strongly model dependent we repeated the calculations for a model with radius 2

km (Model B, Fig.2), and at points 1 and 2 km from the centre (Fig. 3B, C). This data suggests that the gravity changes are most sensitive to differences in reservoir permeability at points close to the centre of the model, and here are not particularly dependent on the radius of the model. At distances of more than 1 km from the centre, however, discrimination is poor and the theoretical gravity values are influenced by the radius.

## RESULTS AT WAIRAKEI

Unfortunately, no precise gravity survey was made at Wairakei before production began; the first such survey was not made until August 1961, about 3.5 years after production had commenced. The only data available in the borefield area spanning the period of 2-phase zone development is a gravity change of -415 (±100) microgal between 1950 and 1961 at benchmark A97 (Hunt, 1977). This benchmark is located close to the centre of production in the early 1960s (Fig. 1). If it is assumed that there was no significant mass withdrawal before 1958, and the value of -415 microgal is plotted on Figure 3A, the point lies close to the theoretical gravity change curve for a permeability of 100 md. In view of the simplifications and assumptions made in setting up the model and the large error in the gravity change, this value for permeability must be considered only approximate. The value of 100 md is, however, consistent with values obtained by well tests and some previous simulation models and suggests that the method is viable. If gravity values at a few selected points in the borefield area had been measured immediately before production started and the measurements repeated at 6 to 12 month intervals for several years after production had begun, then a much better estimate of permeability could be made, especially if a more detailed model was used for the numerical simulation.


## ACKNOWLEDGEMENTS

This work was financed by the New Zealand Foundation for Science Research and Technology (Output Area 21 - Energy).


## REFERENCES


Allis, R.G.; Currie, S.A.; Leaver, J.D.; Sherburn, S. 1985: Results of injection testing at Wairakei Geothermal Field, New Zealand. 1985 International Symposium on Geothermal Energy: 289-294.

Allis, R.G. and Hunt, T.M., 1986: Analysis of exploitation induced gravity changes at Wairakei geothermal field. Geophysics, 51: 1647-1660.

Bolton, R.S. 1970: The behaviour of the Wairakei Geothermal Field during exploitation. Geothermics Special Issue, 2: 1426-1449.


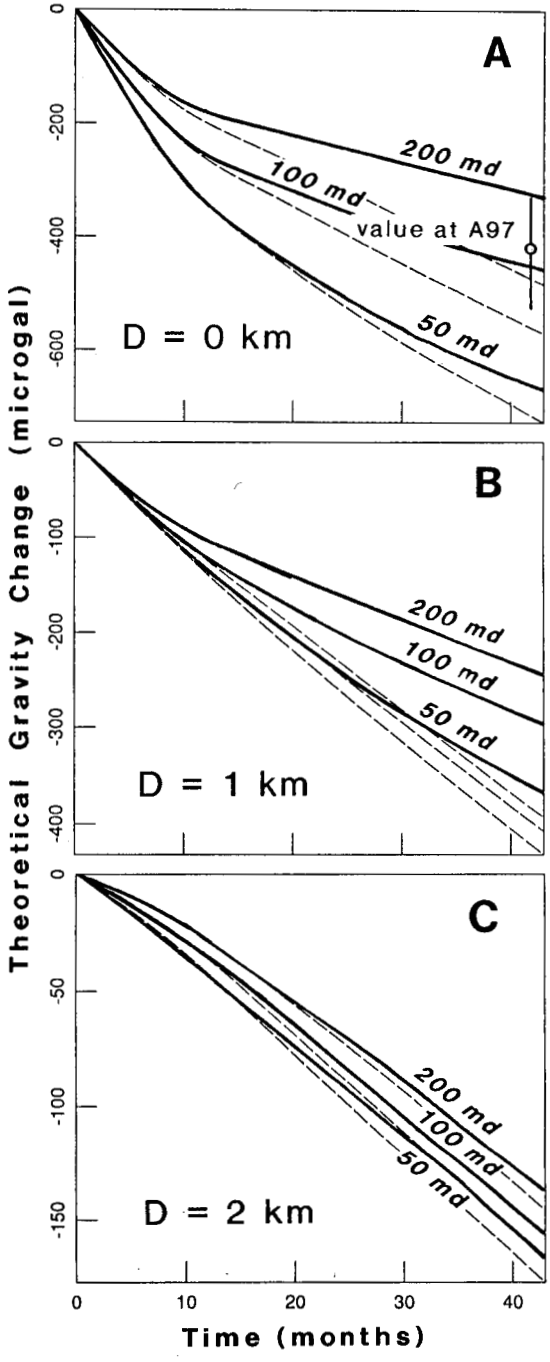


Fig. 3: Theoretical gravity changes for the 2-phase zone development at Wairakei for various values of permeability calculated using the MULKOM models (A, B). Solid lines indicate gravity changes calculated for Model A (R = 3 km); broken lines for Model B (R = 2 km). For clarity, only the lines for Model A are labelled with the values of permeability used. Note how quickly the difference between the lines exceed the significance level of the gravity measurements (approx. 50 microgal) for a point at the centre of the model.

Blakeley, M.R. and O'Sullivan, M.J. 1982: Modelling of production and recharge at Wairakei. Proceedings 4th NZ Geothermal Workshop: 23-31.

Blakeley, M.R. and O'Sullivan, M.J. 1985: Gravity changes predicted by numerical models of the Wairakei Geothermal Field. Proceedings 7th NZ Geothermal Workshop: 49-53.

Donaldson, I.G. 1968: The flow of steam water mixtures through permeable beds: a simple simulation of a natural undisturbed hydrothermal region. N.Z. J.Science, 11: 3-23.

Donaldson, I.G.; Grant, M.A.; Bixley, P.F. 1983: Nonstatic reservoirs: the natural state of the geothermal reservoir. Journal of Petroleum Technology, Jan 1983: 189-194.

Elder, J.W. 1966: Heat and mass transfer in the earth: hydrothermal systems. New Zealand DSIR Bulletin 169.

Elder, J. 1981: Geothermal Systems. Academic Press, London.

Electricorp 1990: Water right applications and impact assessment. Electricity Corporation of New Zealand.

Fradkin, L.J.; Sorey, M.L.; and McNabb, M.A. 1981: On identification and validation of some geothermal models. Water Resources Research, 17: 929-936.

Grant, M.A. 1977: Approximate calculations based on the simple one-phase model of a geothermal field. N.Z. J. Science, 20: 19-25.

Grant, M.A. 1978: Pressure changes in the two-phase zone at Wairakei. Geothermal Circular MAG 20. Unpublished internal report, Applied Mathematics Division, DSIR, Wellington.

Grant, M.A. 1980: Notes on Wairakei Wells 1-63. Geothermal Circular MAG 28. Unpublished internal report, Applied Mathematics Division, DSIR, Wellington.

Grant, M.A.; Donaldson, I.A.; and Bixley, P.F. 1982: Geothermal Reservoir Engineering. Academic Press, London.

Grant, M.A. and Horne, R.N. 1980: The initial state and response to exploitation of Wairakei Geothermal Field. Geothermal Resources Council Transactions, 4: 333-336.

Hunt, T.M. 1977: Recharge of water in Wairakei Geothermal Field determined from repeat gravity measurements. N.Z. Journal of Geology and Geophysics, 20: 303-317.

Hunt, T.M. 1988: Update on gravity changes in the main production borefield at Wairakei. Proceedings 10th N.Z. Geothermal Workshop: 129-132.

Hunt, T.M.; Allis, R.G.; Blakeley, M.R.; and O'Sullivan, M.J. 1990a: Testing reservoir simulation models for the Broadlands geothermal field using precision gravity data. Geothermal Resources Council Transactions, 14: 1287-1294.

Hunt, T.M.; Bixley, P.F.; Carey, B.S.; McCabe, W.M.; and Young, R.M. 1990b: Results of a 13-month reinjection test at Wairakei Geothermal Field, New Zealand. Geothermal Resources Council Transactions, 14: 1192-1200.

McNabb, A.; Grant, M.A.; and Robinson, J. 1975: Permeability estimates. Technical Report 34. Applied Mathematics Division, DSIR, Wellington, New Zealand.

Marshall, D.C. 1966: Preliminary theory of the Wairakei geothermal field. N.Z. J. Science, 9: 651-673.

Mercer, J.W.; Pinder, G.F.; and Donaldson, I.G. 1975: A Galerkin-Finite element analysis of the hydrothermal system at Wairakei, New Zealand. J. Geophysical Research, 80: 2608-2620.

O'Sullivan M.J.; Zyvoloski, G.A.; and Blakeley, M.R. 1983: Computer modelling of geothermal reservoirs. Report 318. Department of Theoretical and Applied Mechanics, Auckland University, New Zealand.

Pritchett, J.W., Rice, L.F. and Garg, S.K. 1978: Reservoir engineering data, Wairakei Geothermal Field, NZ. Systems, Science and Software, La Jolla, California (3 vols).

Pruess, K. 1983: Development of the general purpose simulator MULKOM. Report LBL-15500, Lawrence Berkeley Laboratory, University of California, Berkeley, United States of America.

Robinson, J.L. 1977: An estimate of the lifetime of the Wairakei geothermal field. N.Z. J. Science, 20: 27-29.

Sorey, M.L. and Fradkin, L.J. 1979: Validation and comparison of different models of the Wairakei geothermal reservoir. Proceedings 5th Workshop on Geothermal Reservoir Engineering, Stanford: 215-220.

Wooding, R.A. 1981: Aquifer models of pressure drawdown in the Wairakei-Tauhara geothermal region. Water Resources Research, 17: 83-92.

Zais, E.J. and Bodvarsson, L. 1980: Analysis of production decline in geothermal reservoirs. Report LBL - 11215. Lawrence Berkeley Laboratory, University of California, Berkeley, United States of America.

PROCEEDINGS, Nineteenth Workshop on Geothermal Reservoir Engineering
Stanford University, Stanford, California, January 18-20, 1994
SGP-TR-147

# NEW EVIDENCE FOR A MAGMATIC ORIGIN OF SOME GASES IN THE GEYSERS GEOTHERMAL RESERVOIR

A. H. Truesdell[1], B. M. Kennedy[2], M. A. Walters[3], and F. D'Amore[4]

[1]Consultant, Menlo Park, California
[2]Lawrence Berkeley Laboratory, Berkeley, California
[3]Russian River Energy Company, Santa Rosa, California
[4]International Institute for Geothermal Research, Pisa, Italy

## ABSTRACT

The Geysers vapor-dominated geothermal reservoir is known to have a wide range of gas concentrations in steam (<100 to >75,000 ppmw), but the variations in gas compositions and the origin of the gases have been little studied. Low gas concentrations and steam isotopes similar to meteoric waters are found in the SE Geysers, but steam high in gas and HCl from a high temperature reservoir (HTR) in the NW Geysers has been thought to be related to metamorphic or magmatic brine. New analyses of noble gas isotopes show that the highest gas steam from the HTR has high $^{3}He/^{4}He$ (8.3 Ra), and very low $^{36}Ar$ and radiogenic $^{40}Ar/^{4}He$, indicating a strong magmatic component and essentially no atmospheric or crustal noble gases. Other samples from the HTR show various amounts of atmospheric dilution of the magmatic gas and lower HCl and total gas contents. The occurrence of steam in the NW Geysers highly enriched in heavy isotopes of oxygen and hydrogen supports the indications of remnant magmatic fluid. The existence of this fluid strongly suggests that the HTR was formed by rapid heating and catastrophic boiling resulting from injection of magma.

## INTRODUCTION

Geothermal reservoir gases have been less studied than geothermal reservoir waters because there are fewer well-characterized "geothermometric" reactions among gas constituents. Recently there has been increased interest in gases because it has been discovered that isotopes of stable noble gases (He, Ne, Ar, Kr and Xe) provide long lasting tracers of the source of deep fluids originating in the mantle as well as shallower fluids of crustal and atmospheric origin (Lupton, 1983; Kennedy et al., 1985). In vapor-dominated systems such as The Geysers and Larderello, wells produce only steam without liquid so the isotopes of water and the chemical and isotopic composition of the accompanying gases provide the only geochemical indications of reservoir processes and fluid origins. At The Geysers water isotopes have been widely used to trace return of injected condensate and gas equilibrium calculations have been used to indicate reservoir temperatures and to provide indications of original liquid saturation.

The extraordinary high-temperature reservoir in the NW Geysers, containing steam with high $\delta^{18}O$, high gas and high HCl (Walters et al., 1988), has been considered to originate from rapid pressure decrease causing boil down of a hot water reservoir containing connate marine brines (Shook, this meeting) or to rapid temperature increase from injection of magma (Truesdell et al., 1993). The high gas and HCl in the high-temperature reservoir have made exploitation difficult and it is a matter of some importance to discover whether the HTR extends under the normal reservoir further south in The Geysers and will contribute steam high in HCl and gas to production as pressures are depleted.. For this reason a joint study has been undertaken by the Lawrence Berkeley Laboratory and the Geothermal Technology Organization. In this study noble gas isotopes and carbon isotopes in methane and carbon dioxide will be measured throughout The Geysers. The first results of noble gas isotope analyses of steam from the NW Geysers (Figure 1) are reported here and the implications of these results to the genetic model of The Geysers are discussed.

## NOBLE GAS ISOTOPES AS TRACERS IN GEOTHERMAL SYSTEMS

Noble gases are conservative tracers constraining the sources, evolution, and migration of fluids in the crustal regime. Terrestrial noble gases are of two genetic types: those indigenous to the Earth, inherited from meteoritic material through accretion, and those produced since Earth formation by natural processes such as radioactive decay or nuclear interactions. In simple Earth models, these two genetic types are contained in three sources. The first is the mantle which, because it is believed to be partially or non-degassed, is enriched in the indigenous or primordial noble gas component. The second is the crust which, due to outgassing during crust formation, tends to be enriched in radiogenic and nucleogenic components. The third is the atmosphere/hydrosphere produced through the natural degassing of the solid earth and therefore containing integrated mixture of the other two sources. Each of these sources is characterized by a distinct and different elemental and isotopic composition. For instance, volatiles from mantle magmas are enriched in $^{3}He$ with $^{3}He/^{4}He$ ratios attaining values as high as 9 Ra (Ra is the $^{3}He/^{4}He$ ratio in air, $1.4 \times 10^{-6}$) at mid-

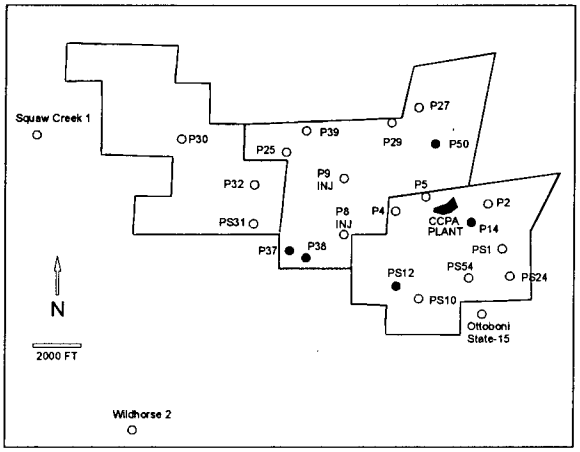


Figure 1. Locations of Coldwater Creek wells with noble gas compositions reported in Table 2 (filled circles).

ocean ridge (MOR) spreading centers, and 30 Ra associated with hotspot volcanism (e.g.- Hawaii, Yellowstone, Iceland), whereas volatiles derived from crustal sources far removed from any recent tectono-magmatic activity are enriched in radiogenic $^4$He with $^3$He/$^4$He ratios of 0.02 to 0.10 Ra. Origin of fluid contributions to a reservoir can, therefore, be readily identified through the occurrence of specific isotopic signatures.

Meteoric water is the primary source of atmospheric noble gases in crustal fluids, particularly in active geothermal systems. The solubility of noble gases in fresh water is known as a function of temperature up to and beyond the critical point and in brines at lower temperatures. Noble gas solubilities increase from He to Xe in a smooth, systematic fashion, facilitating multi-dimensional modeling of gas abundances. Henry's law (solubility) constants (partial pressure divided by the mole fraction in solution) are $>10^4$ bar. Their low solubility and conservative nature (low chemical reactivity) in geochemical systems make the noble gases especially adept detectors of processes such as phase separation and in favorable cases can be used to model the extent, path, and temperature of phase separation. Little is known of the inventory of atmospheric noble gases at The Geysers. It can be expected, however, that abundance variations can be used to model phase separation and fluid evolution and test fluid circulation models proposed on the basis of systematic variations of other geochemical and isotopic constituents. Furthermore assuming a uniform flux of magmatic $^3$He from the underlying volcanic system, fieldwide variations in ratios of $^3$He to atmospheric noble gases will provide a quantitative assessment of the influence of meteoric water.

In a preliminary survey of The Geysers geothermal field, Torgersen and Jenkins (1982) measured $^3$He/$^4$He ratios of ~6-9.6 Ra, indicative of direct magmatic input from volcanic sources (Table 1 and Figure 2). Furthermore, the highest $^3$He/$^4$He ratio (9.6 Ra) is on the high side of MOR values and implies an active magma beneath The Geysers. At the time of this survey the high-temperature reservoir had not yet been discovered, but one of their sampled wells (Ottoboni State 15) is in the NW Geysers.

## VARIATION OF NOBLE GAS ISOTOPES IN THE NW GEYSERS

Samples for noble gas studies, were collected from selected wells of the Coldwater Creek Steamfield (Figure 1) owned and operated by the Central California Power Agency No.1 (CCPA). Dry gases for noble gas analyses were collected in copper tubes sealed by cold welds. The gases were prepared and analyzed in the RARGA (Roving Automated Rare Gas Analysis) laboratory of LBL. The results are presented in Table 2. Because of the method of analysis the isotope ratios relative to a standard are more exactly known than the absolute abundances. For this reason the "F notation" is used in which ratios to $^{36}$Ar are normalized to air. In diagrams based on this notation, air plots at 1,1 and mixing between two components is linear. Table 2 also presents results in the delta notation as differences in parts per thousand from air. Finally the ratio, $^{40*}$Ar/$^4$He, in which $^{40*}$Ar is radiogenic $^{40}$Ar, is presented to show the degree of crustal influence.

Figure 3 shows the R/Ra values plotted against the ratio of $^{40*}$Ar/$^4$He. In this plot the linear relationship implies two component mixing. The end members are magmatic fluid (R/Ra $\geq$ 8.3 and $^{40*}$Ar/$^4$He $\leq$ 0.05, consistent with a mid ocean ridge mantle source) and a second fluid enriched in crustal gas (R/Ra $\leq$ 6.5 and $^{40*}$Ar/$^4$He > 0.25). The highest R/Ra value is for steam from well Prati 37. This steam also has the lowest value of $^{36}$Ar showing that there is almost no atmospheric influence. Note that steam samples from Prati 37 have had the highest total NC gas and highest HCl of the field (data from CCPA). On the basis of these analyses, the steam from this well has almost exclusively magmatic noble gases and possibly other magmatic gases as well, although these must have been modified by reaction with rock minerals. Nearby Prati 38 has lower R/Ra similar to other wells and much higher $^{40*}$Ar/$^4$He. This well has had maximum NCG about one fifth and HCl about one tenth of the maximum values for Prati 37, suggesting that the gradient of the magmatic gas was very sharp although the differences may recently have increased due to injectate return in Prati 38. All analyzed samples from wells to the west of Prati 37 are high in $^{36}$Ar (Figure 4), indicating a large atmospheric component.

## IMPLICATIONS FOR THE ORIGIN OF THE GEYSERS

The sharp boundary between strongly magmatic steam from Prati 37 and more ordinary steam to the west and

Table 1. Noble gas compositions of steam from The Geysers (Torgerson and Jenkins, 1982)

| Well | Type | $^3He/^4He$ E-6 cc/cc | He/Ne | R/Ra | R/Ra Ne corr. |
|---|---|---|---|---|---|
| McKinley-5 | g | 7.36 | 0.3 | 5.3 | |
| CA956-2 | g | 9.95 | >500 | 7.2 | 7.2 |
| | c | 9.50 | 2.3 | 6.9 | 7.7 |
| unknown | g | 13.11 | 28 | 9.5 | 9.6 |
| | c | 12.23 | 29 | 8.8 | 8.9 |
| Ottoboni State-15 | g | 11.16 | >500 | 8.1 | 8.1 |
| | c | 9.22 | 498 | 6.7 | 6.7 |
| DX state-30 | g | 9.48 | | 7.11 | |
| | c | 1.86 | >4 | 1.34 | 1.37 |
| Lakoma Fame-15 | g | 10.89 | 1.9 | 7.9 | 9.1 |
| | c | 11.88 | >500 | 8.6 | 8.6 |
| PDC-1 | g | 12.23 | >500 | 8.8 | 8.8 |
| | c | 12.40 | >500 | 9.0 | 9.0 |

Note: Sample type g, gas; c, condensate.

Table 2. Noble gas isotope compositions of steam from the NW Geysers (this study).

| Sample | [36Ar] E-7 cc/cc* | [4He] E-7 cc/cc* | F(4He) | +/- | F(22Ne) | +/- | F(84Kr) | +/- | F(132Xe) | +/- |
|---|---|---|---|---|---|---|---|---|---|---|
| P14 | 0.7710 | 65.800 | 511.02 | 4.81 | 0.6178 | 0.0060 | 1.7069 | 0.0127 | 2.954 | 0 145 |
| P37 | 0.3070 | 214.000 | 4168.07 | 107.61 | 0.8651 | 0.0411 | 1.5256 | 0.0874 | 2.895 | 0.638 |
| P38 | 1.6000 | 110.800 | 414.30 | 3.90 | 0.6066 | 0.0059 | 1.5880 | 0.0113 | 2.588 | 0 124 |
| P50 | 2.2650 | 57.960 | 153.24 | 1.44 | 0.4507 | 0.0036 | 1.6816 | 0.0115 | 2.630 | 0.129 |
| PS12 | 0.8063 | 71.700 | 532.70 | 5.02 | 0.6021 | 0.0068 | 1.6676 | 0.0137 | 2.874 | 0 138 |
| 10°C ASW | 13.3700# | 0.484# | 0 22 | | 0 2722 | | 1.9412 | | 3.677 | |
| 80°C ASW | 6.1600# | 0.532# | 0.52 | | 0.4962 | | 1 5227 | | 2.274 | |
| Air | 316.070+ | 52.784+ | 1.00 | | 1.000 | | 1.000 | | 1.000 | |

Notation: F(i) = [(i/36Ar)sample/(i/36Ar)air].
Notes: * ccSTP/ccNCgas, # ccSTP/ccWater, + ccSTP/cc

| Sample | R/Ra | +/- | Delta-20 | +/- | Delta-21 | +/- | Delta-38 | +/- | Delta-40 | +/- |
|---|---|---|---|---|---|---|---|---|---|---|
| P14 | 7.806 | 0.279 | 32.64 | 5.31 | 30.19 | 11.25 | -4.92 | 5.42 | 52.10 | 7.80 |
| P37 | 8.322 | 0.473 | 38.40 | 4.09 | 14.90 | 13.03 | -10.68 | 6.91 | 159.79 | 11.99 |
| P38 | 7.678 | 0.390 | 24.29 | 4.96 | 21.43 | 10.51 | -0.96 | 5.41 | 31.34 | 8.02 |
| P50 | 7.084 | 0.342 | 12.60 | 2.86 | 13.82 | 9.20 | -3.80 | 5.06 | 21.50 | 5.70 |
| PS12 | 7.165 | 0.379 | 18.00 | 3.77 | 30.13 | 11.48 | -4.61 | 5.11 | 52.52 | 7.49 |

Notation: Delta i = 1000[(i)sample/(i)air-1].

| Sample | 40*Ar/4He | +/- |
|---|---|---|
| P14 | 0.1804 | 0.0271 |
| P37 | 0.0678 | 0.0054 |
| P38 | 0.1338 | 0.0343 |
| P50 | 0.2483 | 0.0658 |
| PS12 | 0.1745 | 0.0249 |

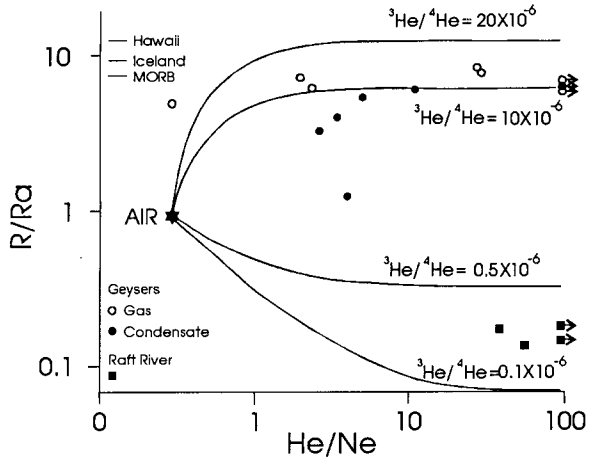


Figure 2. $^3He/^4He$ and Ne compositions of Geysers steam after Torgerson and Jenkins (1982). Their data for Raft River, a non-magmatic geothermal field are also shown.

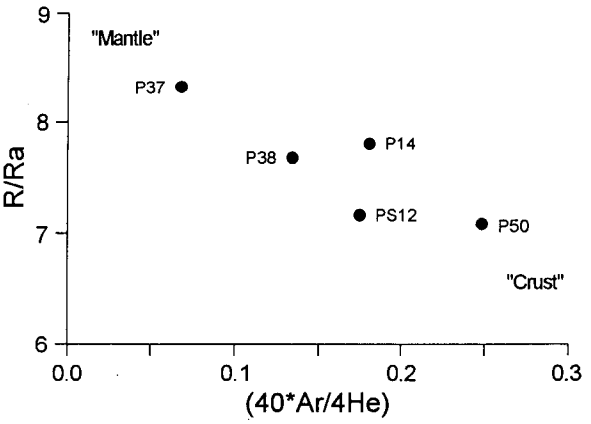


Figure 3. R/Ra plotted against 40*Ar/4He, an indicator of crustal influence

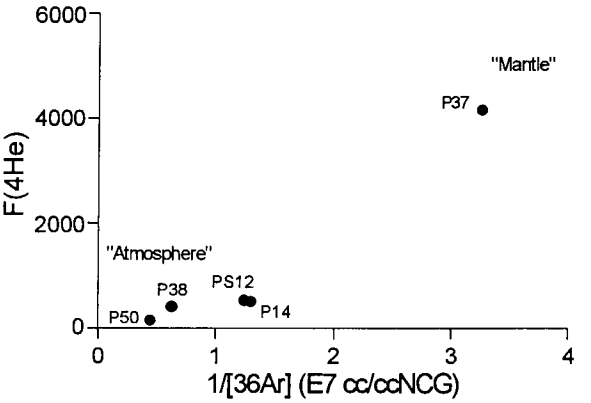


Figure 4. F(4He) plotted against 1/36Ar, an indicator of atmospheric influence.

northwest is a consequence of the lack of large scale convection in the high-temperature reservoir. This was pointed out by Truesdell et al. (1993) who hypothesized that there could be no saturated liquid layer at the bottom of the high temperature reservoir and that without such a layer, lateral steam flow within the reservoir could not occur.

In addition the existence of near-magmatic gas in the high-temperature reservoir argues against the formation of this reservoir by decompression of an earlier hot water reservoir. A hot water reservoir would most likely have been recharged by meteoric water bringing atmospheric gases into the reservoir and the strong boiling during decompression would have removed earlier formed magmatic gases. The formation of the high temperature reservoir by heating caused by massive emplacement of magma (as suggested by Truesdell, 1991) is in agreement with the persistence of magmatic gas. Heating and catastrophic boiling from this cause would have swept earlier atmospheric and crustal gases from the reservoir and replaced them with gases from the magma.

## ISOTOPES OF OXYGEN AND HYDROGEN ALSO INDICATE MAGMATIC INFLUENCE

Fieldwide compilations of oxygen-18 and deuterium at The Geysers show a remarkably wide range from near meteoric values in the SE Geysers to $\delta^{18}O > 3$ permil and $\delta D > -40$ permil in the NW Geysers (Haizlip, 1985; Truesdell et al., 1987; Gunderson, 1989). These isotopically heavy steam compositions have been suggested to result from the evaporation of connate seawater or of "metamorphic" water similar to that found in coast range mineral springs. D'Amore and Bolognesi (1994) recently reinterpreted the same data and suggested that the originating water may have been subducted seawater carried in the downgoing slab. In this interpretation they have extended the idea originally proposed by Giggenbach (1992) for geothermal waters associated with andesitic volcanism. There is in fact little expected isotopic difference between seawater that has been buried for long periods at normal earth temperatures (i.e. connate) or at elevated temperatures (metamorphic) and seawater that has moved with igneous rock from a subduction zone to a near-surface magma chamber and thence into a geothermal reservoir. This idea gains credibility from the noble gas compositions and is generally consistent with magmatic influence. Figure 5 shows the data approximately as presented by D'Amore and Bolognesi (1994).

## FUTURE DIRECTIONS

The analyses reported here cover a small part of The Geysers reservoir. We plan to enlarge our coverage as time and funds permit. We also plan to collect and analyze $\delta^{13}C$ in carbon dioxide and methane from much of the reservoir. The purpose of all of these analyses is to

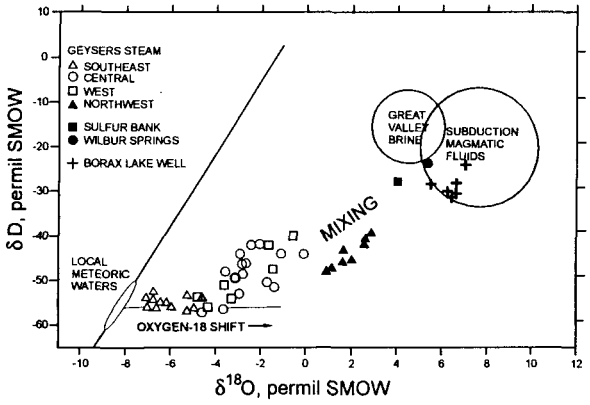


Figure 5. $\delta^{18}O$ and $\delta D$ compositions of initial Geysers steam and related waters. After Truesdell et al. (1987) and D'Amore and Bolognese (1994).

map in so far as possible the influence of the high-temperature reservoir. The carbon isotope geothermometer has been shown in field and experimental studies to be very slow to reequilibrate at temperatures below 300°C. Less certainly it appears to indicate the temperature of the formation of the gases. Preliminary studies by Shigeno et al. (1987) show variations of temperature within The Geysers with some samples showing the local reservoir temperature and others showing higher temperatures. Studies at Larderello have shown $CO_2$-$CH_4$ temperatures that are higher than those measured in wells but have similar variation (Panichi et al., 1977). Deep wells at Larderello have shown that the isotopic temperatures exist below the exploited reservoir.

## ACKNOWLEDGMENTS

We wish to thank John Stackleberg of CCPA for assistance in sample collection and Marcelo Lippmann of LBL for encouragement and helpful discussions. This work was supported by contracts from the Geothermal Technology Organization and The U.S. Department of Energy Geothermal Division and Office of .Basic Energy Sciences.

## REFERENCES

D'Amore, F. and Bolognesi, L., 1994, Isotopic evidence for a magmatic contribution to fluids of Larderello and The Geysers geothermal systems. Geothermics (in press).

Giggenbach, W.F., 1991, Isotope compositions of geothermal water and steam discharges: Ch. 9 in F. D'Amore ed., Application of Geochemistry in Geothermal Reservoir Dev., UNITAR/UNDP Rome, 253-273.

Gunderson, R.P., 1989, Distribution of oxygen isotopes and non-condensable gas in steam at The Geysers: GRC Trans. 13, 449-454.

Haizlip, J.R., 1985, Stable isotopic composition of steam from wells in the northwest Geysers, Sonoma County, California. GRC Trans. 9, 311-316.

Kennedy, B.M., Lynch, M.A., Reynolds, J.H. and Smith, S.P., 1985, Intensive sampling of noble gases in fluids at Yellowstone: I Early overview of the data; regional patterns. Geoch. et Cosmoch. Acta, 49, 1251-1261.

Lupton, J.E., 1983, Terrestrial inert gases: Isotope tracer studies and clues to primordial components in the mantle. Ann. Rev. Earth Sciences, 11, 371-414.

Panichi, C., Ferrara, G.C. and Gonfiantini, R., 1977, Isotope geothermometry in the Larderello geothermal field. Geothermics, 5, 81-88.

Shigeno, H., Stallard, M.L., Truesdell, A.H., and Haizlip, J.R., 1987, $^{13}C/^{12}C$ and D/H ratios of $CO_2$, $CH_4$ and $H_2$ in The Geysers geothermal reservoir. (abs.) EOS, 68, 439.

Torgersen, T., and W.J. Jenkins, 1982, Helium isotopes in geothermal systems: Iceland, The Geysers, Raft River and Steamboat Springs: Geoch. Cosmoch. Acta, 46, 739-748.

Truesdell, A.H., 1991, The origin of high-temperature zones in vapor-dominated geothermal systems: Proceedings, 16th Workshop on Geothermal Reservoir Eng., Stanford U., 15-20.

Truesdell, A.H., Walters, M.A., Kennedy, B.M. and Lippmann, M.J., 1993, An integrated model for the origin of The Geysers geothermal field. GRC Trans., 17, 273-280.

Truesdell, A.H., Haizlip, J.R., Box, W.T., and D'Amore, F., 1987, Fieldwide chemical and isotopic gradients in steam from The Geysers, Proc. 12th Workshop on Geothermal Reservoir Eng., Stanford U., 241-246.

Walters, M.A., Sternfeld, J.N., Haizlip, J.R., Drenick, A.F., and Combs, Jim, 1988, A vapor-dominated reservoir exceeding 600°F at The Geysers, Sonoma Co., California. Proc. 13th Workshop on Geothermal Reservoir. Eng., Stanford U., 73-81.

# NINETEENTH ANNUAL WORKSHOP ON GEOTHERMAL RESERVOIR ENGINEERING STANFORD UNIVERSITY

## *Participants List*


Jorge A. Acuna
Costarican Institute of Electricity
Geothermal Resources Department
OCE. P.O. Box 10032-1000
San Jose, Costa Rica
506-61-1959, FAX 506-61-1583

Willis J. Ambusso
Kenya Power Company, Limited
P.O. Box 785
Naivaska, Kenya
254-0311-20233/20234FAX

Emilio U. Antunez
L.B.L., Earth Sciences Division
1 Cyclotron Road, Bldg. 50E
Berkeley, CA 94720-0001
510-486-5866, FAX 510-486-4159

Fernando Ascencio-Cendejas
University of Mexico
Division de Estudios de Posgrado
Facultad de Ingenieria, UNAM
04510 Mexico, D.F. Mexico
525-622-3017/550-8712FAX 525-616-1073

Paul Atkinson
Unocal
3576 Unocal Place
Santa Rosa, CA 95403-1774
707-545-7600FAX 707-545-8746

Gudni Axelsson
Orkustofnun
Grensasvegur 9
108 Reykjavik, Iceland
354-1-69-6000, FAX 354-1-68-8896

Dan Ballantine
Pacific Gas & Electric
P.O. Box 456
Healdsburg, CA 95448
707-431-6070, FAX 707-431-6066

Ben Barker
UNOCAL Geothermal
3576 Unocal Place
Santa Rosa, CA 95403
707-545-7600, FAX 707-545-8746

Michael L. Barnes
UNOCAL Corp.
1201 W. Fifth St., Room 801
Los Angeles, CA 90017
213-977-6314, FAX 213-977-6333

Ruggero Bertani
ENEL-DPT/VDAG
Via Andrea Pisano, 120
56122
Pisa, Italy
50-53-5705, FAX 50-533290/50-535977

Bobbie Bishop-Gollan
Caithness
6111 Kelso Valley Road
Weldon, CA 93283
619-378-3972, FAX 619-378-2293

Grimur Björnsson
Orkustafnun
Grensasvegur 9
108 Reykjavik, Iceland
354-1-69-6000, FAX 354-1-68-8896

Kit Bloomfield
Pacific Gas & Electric
P.O. Box 456
Healdsburg, CA 95448
707-431-6070, FAX 707-431-6066

Timothy S. Boardman
California Dept. of Conservation
Div. of Oil, Gas, and Geothermal Resources
485 Broadway, Suite B
El Centro, CA 92243
619-353-9900, FAX 619-353-9594

Gudmundur (Bo) Bodvarsson
L.B.L., Earth Sciences Division
1 Cyclotron Road, Bldg. 50E
Berkeley, CA 94720-0001
510-486-4789, FAX 510-486-5686

Greg Boitnott
New England Research Inc.
76 Olcott Drive
White River Junction, VT 05001
802-296-2401, FAX 802-296-8333

Donald Brown
Los Alamos National Laboratory
P.O. Box 1663
Group EES-4, MS D443
Los Alamos, NM 87545
505-667-4318, FAX 505-667-8487

Raffaele Cataldi
ENEL - Italy
57, via Cesare Battisti
56125
Pisa, Italy
39-50-53-5454, FAX 39-50-53-5478

Paul E. Cavote
Northern California Power Agency
180 Cirby Way
Roseville, CA 95678
916-781-3636, FAX 916-783-7693

Wilson C. Clemente
Philippine Geothermal, Inc.
15th Floor, Metrobank Plaza
G.J. Puyat Avenue
Makati, Metro Manila, Philippines
632-817-8876

Allan W. Clotworthy
Electricity Corporation of NZ, Ltd.
Private Bag 2000
Taupo, New Zealand
064-07-3768216, FAX 064-07-374-8472

Jim Combs
Geo Hills Associates
27790 Edgerton Road
Los Altos Hills, CA 94022-3212
415-941-5480, FAX 415-941-5480

Jean Cook
Stanford Geothermal Program
Pet. Eng. Dept., Stanford University
Green Earth Sciences Bldg.
Stanford, CA 94305-2220
415/725-4744FAX 415/725-2099

John Copp
California Energy Company, Inc.
900 N. Heritage, Building D
Ridgecrest, CA 93555
619-499-2336, FAX 619-499-2308

John R. Counsil
Engineering Consultant
1148 Shadyoak Place
Santa Rosa, CA 95404
707-538-2288

Xianfa Deng
Stanford Geothermal Program
Pet. Eng. Dept., Stanford University
Green Earth Sciences Bldg.
Stanford, CA 94305-2220
415/725-4744FAX 415/725-2099

Allen Driscoll
Dames & Moore
221 Main Street, Suite 600
San Francisco, CA 94105
415-896-5858

David Duchane
Los Alamos National Laboratory
P.O. Box 1663, MS-D443
Los Alamos, NM 87545
505-667-9893, FAX 505-667-8487

Herman Dykstra
Consultant
838 Weaver Lane
Concord, CA 94518

Iraj Ershaghi
Univ. of Southern California
University Park
Los Angeles, CA 90089-1211
213-740-0323, FAX 213-740-0324

David Faulder
INEL
P.O. Box 1625
Idaho Falls, ID 83415-2107
208-526-0674, FAX 208-526-9822

Shaun D. Fitzgerald
University of Cambridge
Downing Street
Dept. of Earth Sciences
Cambridge CB4 1AE U.K.
44-223-33-3419, FAX 44-223-33-3450

Robert O. Fournier
U.S. Geological Survey
345 Middlefield Rd., MS-439
Menlo Park, CA 94025
415-329-5205, FAX 415-329-5203

Sabodh K. Garg
S-Cubed
P.O. Box 1620
La Jolla, CA 92038-1620
619-587-8438, FAX 619-755-0474

Colin Goranson
Consultant
1498 Aqua Vista Road
Richmond, CA 94805
510-234-0522, FAX 510-234-5881

Keshav Goyal
Calpine
1160 North Dutton, #200
Santa Rosa, CA 95401
707-527-6700, FAX 707-527-2422

Mohinder S. Gulati
UNOCAL Geothermal
P.O. Box 7600, Room 803
Los Angeles, CA 90051
213-977-7496, FAX 213-977-6333

Teklu Hadgu
L.B.L., Earth Sciences Division
1 Cyclotron Road, Bldg. 50E
Berkeley, CA 94720-0001
510-486-6474, FAX 510-486-4159

Jill Robinson Haizlip
Dames & Moore
221 Main Street, Suite 600
San Francisco, CA 94105
415-243-3733FAX 415-882-9261

Daniel Hayba
U.S. Geological Survey
National Center, MS-959
Reston, VA 22092
703-648-6180FAX 703-648-4727

Juske Horita
O.R.N.L., Chem. & Analytical Sciences Div.
P.O. Box 2008, MS-6110
Oak Ridge, TN 37831-6110
615-576-2750, FAX 615-574-4961

John Hornbrook
Stanford Geothermal Program
Pet. Eng. Dept., Stanford University
Green Earth Sciences Bldg.
Stanford, CA 94305-2220
415/725-4744FAX 415/725-2099

Roland Horne
Stanford Geothermal Program
Pet. Eng. Dept., Stanford University
Green Earth Sciences Bldg.
Stanford, CA 94305-2220
415/725-4744FAX 415/725-2099

Trevor M. Hunt
Inst. of Geol. & Nuclear Sciences
Wairakei Research Centre
Private Bag 2000
Taupo, New Zealand
64-7-374-8211, FAX 64-7-374-8199

Steve Ingebritsen
U.S. Geological Survey
345 Middlefield Road
Menlo Park, CA 94025
415-329-4422, FAX 415-329-4463

Steve Jones
Northern California Power Agency
P.O. Box 663
Middleton, CA 95461
707-987-3101, FAX 707-987-2088

Dennis Kaspereit
California Energy Company, Inc.
900 N. Heritage, Building D
Ridgecrest, CA 93555
619-499-2336, FAX 619-499-2308

M. Ali Khan
California Dept. of Conservation
Div. of Oil, Gas, and Geothermal Resources
50 D Street, Room 300
Santa Rosa, CA 95404
707-576-2385, FAX 707-576-2611

Warwick Kissling
Industrial Research, Ltd.
P.O. Box 31310
Lower Hutt, New Zealand
64-4-569-0000, FAX 64-4-569-0004

Ibrahim Kocabas
SDU, Isparta, Turkey
SDU, Jeoloji Muh. Bol.
Isparta, Turkey
90-246-237-0428x219FAX 90-246-237-0859

Paul Kruger
Stanford University
Civil Engineering Dept.
Stanford, CA 94305
415-725-2382, FAX 415-725-8662

Bert Landry
California State Lands Commission
200 Oceangate, 12th Floor
Long Beach, CA 90802
310-590-5201, FAX 310-590-5995

Marcelo J. Lippmann
L.B.L., Earth Sciences Division
1 Cyclotron Road, Bldg. 50E
Berkeley, CA 94720-0001
510-486-5035, FAX 510-486-5686

Jim Lovekin
California Energy Company, Inc.
900 N. Heritage, Building D
Ridgecrest, CA 93555
619-499-2322,FAX 619-499-2308

James V. McCarthy
California Board of Equalization
450 N. Street, MIC 64
Sacramento, CA 95814
916-445-4982, FAX 916-323-8765

H.K."Pete" McCluer
Consultant
P.O. Box 650
Mount Aukum, CA 95656
209-245-4171, FAX 209-245-4623

David Meade
U.S. Navy
Geothermal Program Office
China Lake, CA 93555
619-939-4057, FAX 619-939-2449

Anthony J. Menzies
GeothermEx
5221 Central Avenue, No. 201
Richmond, CA 94804
510-527-9876FAX 510-527-8164

John E. Mock
U.S. D.O.E., Geothermal Division
1000 Independence Avenue
Washington, DC 20585
202-586-5340, FAX 202-586-5124

Joseph N. Moore
UURI
391 Chipeta Way, Suite A
Salt Lake City, UT 84108
801-584-4428, FAX 801-584-4453

Paul B. Mount II
California State Lands Commission
200 Oceangate, 12th Floor
Long Beach, CA 90802
310-590-5201, FAX 310-590-5995

Eddie Mroczek
Inst. of Geol. & Nuclear Sciences
Wairakei Research Centre
Private Bag 2000
Taupo, New Zealand
64-7-374-8211, FAX 64-7-374-8199

Dennis L. Nielson
UURI
391-C Chipeta Way
Salt Lake City, UT 84108
801-584-4438, FAX 801-584-4453

Yuichi Niibori
Tohoku University
Dept. of Res. Engrg., Faculty of Engrg.
Aramaki, Aoba-ku
Sendai 980, Japan
81-22-222-1800, FAX 81-22-222-2114

Curtis Oldenburg
L.B.L., Earth Sciences Division
1 Cyclotron Road, Bldg. 50E
Berkeley, CA 94720-0001
510-486-7419, FAX 510-486-5686

Harry J. Olson
Univ. of Hawaii, Look Laboratory
811 Olomehani Street
Hawaii, HI 96813
808-522-5620, FAX 808-522-5618

Peter A. Omenda
Kenya Power Company, Limited
P.O. Box 785
Naivaska, Kenya
254-0311-20233/20234

Steve Palar
Stanford Geothermal Program
Pet. Eng. Dept., Stanford University
Green Earth Sciences Bldg.
Stanford, CA 94305-2220
415/725-4744FAX 415/725-2099

Susan Petty
Susan Petty Consulting
654 Glenmont Drive
Solano Beach, CA 92075
619-292-9055, FAX 619-292-9055

John W. Pritchett
S-Cubed
P.O. Box 1620
La Jolla, CA 92038-1620
619-587-8440, FAX 619-755-0474

Karsten Pruess
L.B.L., Earth Sciences Division
1 Cyclotron Road, Bldg. 50E
Berkeley, CA 94720-0001
510-486-6732, FAX 510-486-5686

Hector G. Puente
C.F.E. (Cerro Prieto)
P.O. Box 248
Calexico, CA 92231
65-53-6870, FAX 65-53-6269

Marshall Reed
U.S. D.O.E., Geoth. Div., CE-342
1000 Independence Ave., S.W.
Washington, DC 20585
202-586-8076, FAX 202-586-5124

Alex W. Reid, III
State Land Commission
200 Oceangate, 12th Floor
Long Beach, CA 90802
310-590-5201

Joel Renner
INEL
Box 1625
Idaho Falls, ID 83415-3830
208-526-9824, FAX 208-526-0969

Jose A. Rial
Univ. No. Carolina, Chapel Hill
Geology Dept., Mitchell Hall CB #3315
Chapel Hill, NC 27599
919-966-4553, FAX 919-966-4519

George F. Risk
Inst. of Geol. & Nuclear Sciences
P.O. Box 1320
Wellington , New Zealand
64-7-374-8211, FAX 64-7-374-8199

Jesus Rivera
University o9f Mexico
Div. Estudios Posgrado, Facultad de Ing.
Universidad Nacional Autonona de Mexico
04510 Mexico, D.F. Mexico
525-550-8702/622-3017FAX 525-616-1073

Peter Rose
UURI
391-C Chipeta Way, Suite A
Salt Lake City, UT 84108
801-584-4430, FAX 801-584-4453

Yukihiro Sakagawa
Japan Metals & Chemicals Co., Ltd.
72-2 Sasamori
Ukai, Takizawa-mura
Iwate 020-01, Japan
81-196-84-4114, FAX 81-196-84-6231

Fernando Samaniego
University of Mexico
Division de Estudios de Posgrado
Facultad de Ingenieria, UNAM
04510 Mexico, D.F., Mexico
525-622-3017/550-8712FAX 525-616-1073

Cengiz Satik
University of Southern California
Petroleum Engineering Dept.
Los Angeles, CA 90082-1211
213-740-0324, FAX 213-740-0323

R.C. Schroeder
Berkeley Group, Inc.
245 Gravatt Drive
Berkeley, CA 94705
510-849-1195, FAX 510-849-1196

Michael Shook
INEL
P.O. Box 1625, MS-2107
Idaho Falls, ID 83404
208-526-6945FAX 208-526-9822

John M. Simonson
Oak Ridge National Laboratory
P.O. Box 2008, Bldg. 45005, MS-610
Oak Ridge, TN 37831-6110

Cesar M. Sinson
Philippine Geothermal, Inc.
15th Floor, Metrobank Plaza Bldg.
Sen Gil Puyat Ave.
Makati, MM Philippines
632-817-8876

Mike Sorey
U.S. Geological Survey
345 Middlefield Rd., MS-439
Menlo Park, CA 94025
415-329-4420, FAX 415-329-4463

Paul Spielman
California Energy Company, Inc.
900 N. Heritage, Building D
Ridgecrest, CA 93555
619-499-2300, FAX 619-499-2308

Roman Sta. Maria
Philippine Geothermal, Inc.
15th Floor, Metrobank Plaza
Sen. G.J. Puyat Avenue
Makati, Metro Manila, Philippines
632-817-8876, FAX 632-817-8622

Mitchel Stark
UNOCAL
3576 Unocal Place
Santa Rosa, CA 95403
707-545-7600, FAX 707-544-6855

Kenso Takai
Geothermal Energy Res. & Dev. Co., Ltd.
Kyodo Bldgs., 11-7
Kabuto-cho, Nihonbashi, Chuo-ku
Tokyo 103, Japan
81-3-3666-5822, FAX 81-3-3666-5289

Shinji Takasugi
Geothermal Energy Res. & Dev. Co., Ltd.
Kyodo Bldgs., 11-7
Kabuto-cho, Nihonbashi, Chuo-ku
Tokyo 103, Japan
81-3-3666-5822, FAX 81-3-3666-5289

Jefferson W. Tester
M.I.T., Energy Laboratory
77 Massachusetts Avenue, E40-455
Cambridge, MA 02139
617-253-3401, FAX 617-253-8013

Shigeo Tezuka
Elec. Power Dev. Co., Ltd.
158-2, Miyanoharu
Oguni-cho, Aso-gun
Kumamoto, Japan
0967-46-2700, FAX 0967-46-4881

Richard P. Thomas
California Dept. of Conservation
Div. of Oil, Gas, and Geothermal Resources
801 K. Street, MS 20-21
Sacramento, CA 95814-3530
916-445-9686, FAX 916-323-0424

Alois A. Treybal
Montana Tech.
718 W. Galena St.
Butte, MT 59701
406-723-6883FAX

Alfred Truesdell
Entropy, Inc.
700 Hermosa Way
Menlo Park, CA 94025
415-372-6135, FAX 415-324-4009

Mark Walters
Russian River Energy Company
1573 Manzanita Avenue
Santa Rosa, CA 95404
707-538-2705

Kenneth H. Williamson
UNOCAL Geothermal
3576 Unocal Place
Santa Rosa, CA 95403
707-545-7600, FAX 707-545-8746

Phillip M. Wright
UURI
391 Chipeta Way, Suite C
Salt Lake City, UT 84108
801-584-4439, FAX 801-584-4453

Chris Wright
Pinnacle Technologies
600 Townsend Street, Suite 230W
San Francisco , CA 94103
415-861-1097, FAX 415-861-1448

# SUBJECT INDEX

# AUTHOR INDEX